Two-Photon Interactions in Proton-Proton Collisions with the ATLAS Experiment at the LHC

Mateusz Dyndal

UNIVERSITÉ PARIS-SUD

ÉCOLE DOCTORALE 517 :
PARTICULES, NOYAUX ET COSMOS

Laboratoire : CEA Saclay, DSM/Irfu/SPP

THÈSE DE DOCTORAT

PHYSIQUE

par

Mateusz DYNDAL

Two-Photon Interactions in Proton–Proton Collisions with the ATLAS Experiment at the LHC

Date de soutenance : 21/09/2015

Composition du jury

Directeur de thèse :	Laurent SCHOEFFEL	dr hab.
Co-directeur de thèse :	Mariusz PRZYBYCIEN	prof. dr hab.
Rapporteurs :	Nicole d'HOSE	dr hab.
	Antoni SZCZUREK	prof. dr hab.
Examinateurs :	Patrick PUZO	prof. dr hab.
	Piotr BOZEK	prof. dr hab.
Membres invités :	Wladyslaw DABROWSKI	prof. dr hab.
	Janusz CHWASTOWSKI	prof. dr hab.

Acknowledgements

I would like to express my deepest thanks to my supervisors for their guidance, attention and organizational support through all the years of my PhD studies, for the continuous help with scientific advice and useful suggestions and comments to this thesis.

Many thanks belong to my colleagues from the AFP group, especially Lada, Leszek, Libor, Tom and Michael for the fruitful collaboration in the simulation task and for introducing me to the technical parts of the project.

I am especially grateful to Emmanuel for his technical support and for showing me how professional the HEP analysis might look like.

I would also like to thank Alessandro, Jan, Andrew, Cristi, Massimo and Witold for their excellent support through the long and complex analysis approval process.

I am also very grateful to Oldrich, Tim and Oleg for their support and advices during the analysis setup procedure.

Contents

List of Figures

List of Tables

Abbreviations

ALFA	**A**bsolute **L**uminosity **F**or **A**TLAS
ALICE	**A** **L**arge **I**on **C**ollider **E**xperiment
AFP	**A**TLAS **F**orward **P**roton
AOD	**A**nalysis **O**bject **D**ata
ATLAS	**A** **T**oroidal **L**HC **A**pparatu**S**
BCM	**B**eam **C**ondition **M**onitor
BEH	**B**rout–**E**nglert–**H**iggs
BS	**B**eam **S**pot
CD	**C**entral **D**iffractive
CDF	**C**ollider **D**etector at **F**ermilab
CERN	**C**onseil **E**uropéen pour la **R**echerche **N**ucléaire
CFD	**C**onstant **F**raction **D**iscriminator
CL	**C**onfidence **L**evel
CMS	**C**ompact **M**uon **S**olenoid
CP	**C**harge-**P**arity
CSC	**C**athode **S**trip **C**hamber
CTP	**C**entral **T**rigger **P**rocessor
DAQ	**D**ata **A**c**Q**uisition
DD	**D**ouble-**D**iffractive
DIS	**D**eep **I**nelastic **S**cattering
DGLAP	**D**okshitzer–**G**ribov–**L**ipatov–**A**lterelli–**P**arisi
DPD	**D**erived **P**hysics **D**ata
DX	**D**ipole magnet number **X**
DY	**D**rell–**Y**an
ECal	**E**lectromagnetic **Cal**orimeter

EF	**E**vent **F**ilter
EM	**E**lectro**M**agnetic
EPA	**E**quivalent **P**hoton **A**pproximation
ESD	**E**vent **S**ummary **D**ata
EW	**E**lectro**W**eak
FCal	**F**orward **Cal**orimeter
FSR	**F**inal-**S**tate **R**adiation
GEANT	**GE**ometry **AN**d **T**racking
GSF	**G**aussian **S**um **F**ilter
GSW	**G**lashow–**S**alam–**W**einberg
HBP	**H**amburg **B**eam **P**ipe
HCal	**H**adronic **Cal**orimeter
HEC	**H**adronic **E**nd-**C**ap
HEP	**H**igh **E**nergy **P**hysics
HERA	**H**adron–**E**lectron **R**ing **A**ccelerator
HLT	**H**igh-**L**evel **T**rigger
HPTDC	**H**igh-**P**recision **T**ime-to-**D**igital **C**onverter
IBL	**I**nsertable **B**-**L**ayer
ID	**I**nner **D**etector
IP	**I**nteraction **P**oint
ISR	**I**ntersecting **S**torage **R**ing
L1	**L**evel **1**
L2	**L**evel **2**
LAr	**L**iquid **Ar**gon
LEIR	**L**ow **E**nergy **I**on **R**ing
LEP	**L**arge **E**lectron–**P**ositron collider
LHC	**L**arge **H**adron **C**ollider
LHCb	**LHC** – **B**eauty
LHCf	**LHC** – **F**orward
LO	**L**eading-**O**rder
LQbar	**L**-shape **Q**uartz **bar**
LS	**L**ong **S**hutdown
LUCID	**LU**minosity measurement using **C**herenkov **I**ntegrating **D**etector

MBTS	**M**inimum **B**ias **T**rigger **S**cintillators
MC	**M**onte **C**arlo
MCP-PMT	**M**icro**C**hannel-**P**late **P**hoto-**M**ultiplier
MD	ALFA **M**ain **D**etector
MDT	**M**uon **D**rift **T**ube
MIP	**M**inimum **I**onising **P**article
MoEDAL	**Mo**nopole and **E**xotics **D**etector **A**t the **L**HC
MS	**M**uon **S**pectrometer
ND	**N**on-**D**iffractive
NLO	**N**ext-to-**L**eading-**O**rder
OD	ALFA **O**verlap **D**etector
PDF	**P**arton **D**istribution **F**unction
PMT	**P**hoto-**M**ultiplier **T**ube
PS	**P**roton **S**ynchrotron
PSB	**P**roton **S**ynchrotron **B**ooster
Qbar	**Q**uartz **bar**
QCD	**Q**uantum **C**hromo**D**ynamics
QED	**Q**uantum **E**lectro**D**ynamics
QUARTIC	**QUAR**tz **TI**ming **C**herenkov
QX	**Q**uadrupole magnet number **X**
RDO	**R**aw **D**ata **O**utput
RHIC	**R**elativistic **H**eavy **I**on **C**ollider
RMS	**R**oot **M**ean **S**quare
ROI	**R**egion-**O**f-**I**nterest
RF	**R**adio-**F**requency
RP	**R**oman **P**ot
RPC	**R**esistive **P**late **C**hamber
SCT	**S**emi-**C**onductor **T**racker
SD	**S**ingle-**D**iffractive
SiD	AFP **Si**licon **D**etector
SM	**S**tandard **M**odel
SPS	**S**uper **P**roton **S**ynchrotron
T&P	**T**ag-and-**P**robe

TAN	**T**arget **A**bsorber **N**eutral
TAS	**T**arget **A**bsorber **S**econdaries
TCL	**T**arget **CoL**limator
TD	AFP **T**iming **D**etector
TDR	**T**echnical **D**esign **R**eport
TGC	**T**hin **G**ap **C**hamber
ToF	**T**ime-**o**f-**F**light
TOTEM	**TOT**al elastic and diffractive cross section measurement
TRT	**T**ransition **R**adiation **T**racker
UE	**U**nderlying **E**vent
vdM	**v**an **d**er **M**eer
WLS	**W**ave**L**ength **S**hifting
ZDC	**Z**ero **D**egree **C**alorimeter

Introduction

A considerable fraction of proton–proton collisions at high energies involve reactions mediated by photons. This fraction is dominated by elastic scattering, with a single photon exchange. Quasi-real photons can also be emitted by both protons, with a variety of final states produced. In these processes the proton–proton collision can be then considered as a photon–photon collision. At the Large Hadron Collider, these reactions can be studied with good experimental precision. This work presents my contribution to the development of the current understanding of two-photon processes at high energies. This dissertation is divided between the three main parts and each part is followed by a separate bibliography.

Part I contains a theoretical introduction in the field of two-photon physics. It begins with a presentation of the Standard Model and introduces necessary definitions. Next, a theoretical framework related to the different photon-interaction types in proton–proton collisions is explained. A proton absorptive correction formalism for exclusive photon–photon processes (developed by the author of this thesis) is also discussed. Finally, a comparison of different Monte Carlo generators for two-photon reactions in proton–proton collisions is presented.

Part II of the thesis briefly introduces the Large Hadron Collider, presenting the main points of its programme. A more detailed description of the ATLAS experiment is given, including sub-detectors, trigger and data processing. A large part is devoted to the ATLAS forward detectors, especially to the AFP project, which will extend the ATLAS forward physics programme by tagging scattered protons with non-zero energy losses. For the qualification work required in the ATLAS collaboration, the author significantly developed the ATLAS+AFP simulation software.

Part III describes in details a measurement of exclusive two-photon production of lepton pairs (electrons or muons) in proton–proton collisions at center-of-mass energy $\sqrt{s} = 7$ TeV with the ATLAS experiment at the Large Hadron Collider, performed completely by the author. Using 4.6 fb^{-1} of data, the fiducial cross sections for exclusive two-photon

production of lepton pairs have been measured and compared to the theory predictions corrected for proton absorptive effects.

The presented results are based on the work performed during the author's PhD studies. The majority of the results were presented during conferences and workshops and are published. This thesis is based on the following scientific work:

- ATLAS Collaboration (G. Aad et al.), *Measurement of exclusive* $\gamma\gamma \to \ell^+\ell^-$ *production in proton–proton collisions at* $\sqrt{s} = 7$ *TeV with the ATLAS detector*, Phys. Lett. **B749** (2015) 242–261.
- M. Dyndal and L. Schoeffel, *The role of finite-size effects on the spectrum of equivalent photons in proton–proton collisions at the LHC*, Phys. Lett. **B741** (2015) 66–70.
- ATLAS Collaboration (G. Aad et al.), *Technical Design Report for the ATLAS Forward Proton Detector*, CERN-LHCC-2015-009; ATLAS-TDR-024.
- M. Dyndal (on behalf of the ATLAS Collaboration), *Standard Model measurements with ATLAS*, The XXII International Workshop High Energy Physics and Quantum Field Theory, 24 Jun – 01 Jul 2015, Samara, Russia, ATL-PHYS-SLIDE-2015-353.
- M. Dyndal (on behalf of the ATLAS Collaboration), *The tracking system of the AFP detector*, 2$^{\text{nd}}$ Workshop on Detectors for Forward Physics at LHC, 28–30 May 2014, La Biodola, Isola d'Elba, Italy, ATL-FWD-SLIDE-2014-231.

Part I

Theoretical motivation

Chapter 1

The Standard Model

The Standard Model (SM) of particle physics is the best and most sensible theory which summarizes our understanding of the basic components of matter and their interactions in an unified scheme. The fundamental forces described by the theory are the electromagnetic force, the weak force and the strong force. While the first two forces are collectively described by the unified electroweak theory (a part of the SM), they appear to be two separate forces at low energy. The SM is a relativistic quantum field theory: it combines the fundamental principles of quantum mechanics with those of special relativity. At this moment, gravity is the only fundamental force not described by the SM; there is currently no fully consistent quantum theory of gravity.

1.1 Standard Model particles

1.1.1 Elementary particles

Ordinary matter is built up of atoms, with negatively charged electrons attracted to the positively charged nucleus. The electrons are bounded with the nucleus by the electromagnetic force. The nucleus consists of the nucleons: the positively charged protons and the electrically neutral neutrons. These consist of quarks bound together by the strong force: the proton consists of two up (u) quarks and one down (d) quark, while the neutron consists of two d quarks and one u quark. Therefore, an ordinary matter consists only of three elementary matter particles: the electron, the u quark and the d quark. Together with the electron neutrino, the electron and the u and d quarks make up the first generation of the SM matter particles.

These four particles constitute a so-called *first generation* matter particles. There are also heavier versions of these particles, with exactly the same properties as the first

	Leptons (ℓ)			Quarks		
	Particle	q_e	Mass [GeV]	Particle	q_e	Mass [GeV]
First	electron ($e^{\pm}$)	$\pm e$	0.0005	down ($d/\bar{d}$)	$\mp\frac{1}{3}e$	0.003
generation	neutrino ($\nu_e/\bar{\nu_e}$)	0	$< 10^{-9}$	up ($u/\bar{u}$)	$\pm\frac{2}{3}e$	0.005
Second	muon ($\mu^{\pm}$)	$\pm e$	0.106	strange ($s/\bar{s}$)	$\mp\frac{1}{3}e$	0.1
generation	neutrino ($\nu_\mu/\bar{\nu_\mu}$)	0	$< 10^{-9}$	charm ($c/\bar{c}$)	$\pm\frac{2}{3}e$	1.3
Third	tau ($\tau^{\pm}$)	$\pm e$	1.78	bottom ($b/\bar{b}$)	$\mp\frac{1}{3}e$	4.5
generation	neutrino ($\nu_\tau/\bar{\nu_\tau}$)	0	$< 10^{-9}$	top ($t/\bar{t}$)	$\pm\frac{2}{3}e$	173

TABLE 1.1: The main properties of the Standard Model matter particles.

generation particles, except for the mass, making up the second and third generations of matter particles. Each matter particle has its respective antiparticle, which has exactly the same mass, but opposite electric charge. All the elementary matter particles of the SM are spin-$\frac{1}{2}$ fermions, i.e. they obey to the Fermi–Dirac statistics. The fermionic elementary particle content of the SM is summarized in Table 1.1. The charged leptons are the electrons ($e^{\pm}$), muons ($\mu^{\pm}$), and tau leptons ($\tau^{\pm}$), all of which have electric charge $q_e = \pm e$. For each charged lepton generation, there is one electrically neutral lepton neutrino partner ($\nu_\ell/\bar{\nu_\ell}$). The quarks with electric charge $q_e = \pm\frac{2}{3}e$ are the up ($u/\bar{u}$), charm ($c/\bar{c}$), and top ($t/\bar{t}$) quarks, and those with electric charge $q_e = \mp\frac{1}{3}e$ are the down ($d/\bar{d}$), strange ($s/\bar{s}$), and bottom ($b/\bar{b}$) quarks.

In addition to the matter particles the SM introduces force particles, spin-1 gauge bosons, mediating the interactions between them. The electromagnetic (EM) force is mediated by the photon (γ), which is the quantum of EM radiation. The weak force is mediated by the $W^{\pm}$ and Z bosons, while the strong force is mediated by the gluons. While the photon and the gluons are massless, the $W^{\pm}$ and Z bosons are massive, with masses of 80.4 and 91.2 GeV, respectively [1]. The force carrier content of the SM is presented in Table 1.2. Finally, the only SM particle which is neither a matter particle nor a force particle, is the spin-0 Higgs boson (H). The existence of the Higgs boson explains why the $W^{\pm}$ and Z bosons, as well as the elementary fermions are massive (see Section 1.5 for details). Discovered in 2012 [2, 3], it was the last particle of the SM to be observed in experiment, with the mass measured to be 125.1 GeV [4].

1.1.2 Composite particles

All the leptons in SM can be observed in nature as free particles, as they do not experience the strong force. On the other hand, quarks are confined by the strong force, and they form bound states called mesons (consisting of quark–antiquark pair) and baryons (three-quark states). The mesons and baryons are collectively referred to as hadrons.

Force	Carrier	Relative strength	Range [m]
Strong	gluons	1	$\sim 10^{-15}$
Electromagnetic	photon (γ)	$\sim 10^{-2}$	∞
Weak	W^+, W^-, Z	$\sim 10^{-13}$	$\sim 10^{-18}$
Gravitational	?	$\sim 10^{-38}$	∞

TABLE 1.2: The main properties of the Standard Model force carriers.

As an example, the lightest electrically charged meson, π^+, consists of one up quark and one down antiquark. There are also other mesons with heavier quarks involved (charm, strange and bottom), in combination with lighter quarks as well as with each other. The J/ψ meson is an example of *charmonium*, with one charm quark and one charm antiquark.

Examples of baryons are the nucleons (protons and neutrons) and the Δ baryons. These look identical in composition to the nucleons. The difference lies in the way the spins of the quarks are aligned. In the $\Delta(1232)$ baryons, all three quark spins are aligned, while in protons and neutrons one of the three is always opposite the other two. The $\Delta(1232)$ baryons are unstable and quickly decay into a neutron or proton plus a pion of appropriate charge. A large number of baryons exist in the nature, with different relative numbers of c, s and b quarks involved.

The top quark, with a mass of 173 GeV[5], is the exception here. It is so heavy that it decays before it can form any bound state with the lighter quarks. The top quark decays almost entirely into W boson and b quark.

1.2 Quantum electrodynamics

1.2.1 The Dirac Lagrangian

The Lagrangian for a free, spin-$\frac{1}{2}$ particle describes a field of a single fermion $\psi(x^\mu)$ (so-called *spinor* field) with mass m. It follows the Dirac equation [6]:

$$\mathcal{L}_{\text{Dirac}} = \bar{\psi}(i\gamma^\mu\partial_\mu - m)\psi \iff (i\gamma^\mu\partial_\mu - m)\psi = 0 \ , \tag{1.1}$$

where $\bar{\psi}$ denotes Dirac adjoint: $\bar{\psi} = \psi^\dagger\gamma^0$. The γ^μ are the 4×4 Dirac matrices:

$$\gamma^0 = \beta; \quad \gamma^\mu = \beta\alpha_\mu \ , \tag{1.2}$$

given that the arbitrary matrices α_i and β satisfy the relations:

$$\beta^2 = \mathbb{1}; \quad \alpha_i^2 = \mathbb{1}; \quad \alpha_i\beta + \beta\alpha_i = 0 \text{ (for all } i); \quad \alpha_i\alpha_j + \alpha_j\alpha_i = 0 \text{ (for all } i \neq j) \; . \tag{1.3}$$

These relations are fulfilled by a certain set of 4×4 matrices, which can be constructed e.g. from the Pauli matrices [6]. The matrix γ^0 is included to ensure proper behavior in Lorentz transformations.

By studying the symmetries of Dirac Lagrangian, one can find that it is invariant under global transformation of the field phase U_θ, i.e. under rotation of the field in a complex plane:

$$\begin{aligned} \psi(x^\mu) &\xrightarrow{U(1)} \psi'(x^\mu) = e^{i\theta}\psi(x^\mu) \\ \bar{\psi}(x^\mu) &\xrightarrow{U(1)} \bar{\psi}'(x^\mu) = e^{-i\theta}\bar{\psi}(x^\mu) \; , \end{aligned} \tag{1.4}$$

where θ is an arbitrary real constant (the same over all space-time). This transformation is referred to as $U(1)$. It is unitary ($U_\theta^\dagger U_\theta = 1$), Abelian ($U_{\theta_1}U_{\theta_2} = U_{\theta_2}U_{\theta_1}$) and by definition global (since θ is not a function of space-time coordinates x^μ).

1.2.2 QED interaction Lagrangian

The Dirac Lagrangian (1.1) describes a free spin-$\frac{1}{2}$ particle, such as a free electron. An electromagnetic field can be introduced in terms of the four-potential, $A^\mu = (\phi, \vec{A})$, with the usual relations between the electromagnetic potentials and the electric ($\vec{E}$) and magnetic ($\vec{B}$) fields:

$$\vec{E} = -\nabla\phi - \frac{\partial\vec{A}}{\partial t}; \quad \vec{B} = \nabla \times \vec{A} \; . \tag{1.5}$$

A non-relativistic particle of charge q_e and mass m moving in an electromagnetic field is described by the Hamiltonian:

$$H = \frac{1}{2m}\left(i\nabla + q_e\vec{A}\right)^2 + q_e\phi \; . \tag{1.6}$$

One can see that the electromagnetic interaction follows the free particle wave equation using the following substitutions:

$$i\nabla \;\rightarrow\; i\nabla + q_e\vec{A}; \quad i\frac{\partial}{\partial t} \;\rightarrow\; i\frac{\partial}{\partial t} - q_e\phi \; , \tag{1.7}$$

which can be written using four-vector notation as

$$\partial_\mu \;\rightarrow\; D_\mu \equiv \partial_\mu + iq_eA_\mu \; . \tag{1.8}$$

The newly introduced operator D_μ is referred to as *covariant derivative*, which is defined as a derivative that transforms in such a way that Dirac equation remains unchanged.

Similar substitution can be used to introduce electromagnetic interactions also in the relativistic case. The electromagnetic Lagrangian can be constructed by including the free particle term from the Dirac equation (1.1):

$$\begin{aligned} \mathcal{L}_{\text{QED}} &= \bar{\psi}(i\gamma^\mu \partial_\mu - m)\psi - q_e \bar{\psi}\gamma^\mu \psi A_\mu \\ &= \bar{\psi}(i\gamma^\mu D_\mu - m)\psi \\ &= \mathcal{L}_{\text{Dirac}} + \mathcal{L}_{\text{int}} \ . \end{aligned} \tag{1.9}$$

The interaction Lagrangian, $\mathcal{L}_{\text{int}} = -q_e \bar{\psi}\gamma^\mu \psi A_\mu$, describes the interaction between the charged particle and the electromagnetic field.

Finally, one can add in the Lagrangian a term describing the free electromagnetic field:

$$\begin{aligned} \mathcal{L}_{\text{QED}} &= \bar{\psi}(i\gamma^\mu \partial_\mu - m)\psi - \frac{1}{4} F_{\mu\nu} F^{\mu\nu} - q_e \bar{\psi}\gamma^\mu \psi A_\mu \\ &= \mathcal{L}_0 + \mathcal{L}_{\text{int}} \ , \end{aligned} \tag{1.10}$$

where

$$F_{\mu\nu} = \partial_\nu A_\mu - \partial_\mu A_\nu \tag{1.11}$$

is the electromagnetic field tensor.

The Lagrangian above describes a quantum field of electromagnetic interactions. This theoretical framework is called *quantum electrodynamics* (QED). Maxwell in his unification of electricity and magnetism predicted the existence of electromagnetic waves, which in QED act as a gauge boson mediator, identified with the photon. This symmetry is also connected with a conservation law, in this case it is the conservation of electric charge q_e.

The so-called *QED vertex*, shown in Figure 1.1 can be associated with a particular vertex factor in the formula (see Section 1.6), when the *Feynman diagram* approach [6] is used to calculate a probability for a given process to occur. In the QED, one can obtain the vertex factor from

$$i\mathcal{L}_{\text{int}} = -iq_e \bar{\psi}\gamma^\mu \psi A_\mu \tag{1.12}$$

as $-iq_e\gamma^\mu$. For the electron or muon, $q_e = \pm e$, so the vertex factor is $\mp ie\gamma^\mu$.

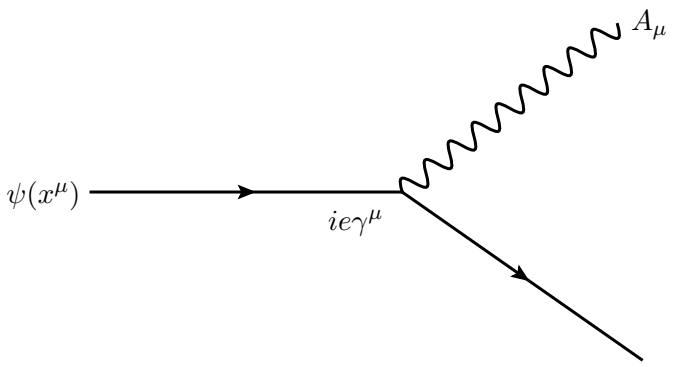

FIGURE 1.1: The basic vertex of QED in which a charged fermion couples to a photon. The vertex can be oriented such as to represent a fermion emitting a photon, an antifermion emitting a photon, a fermion–antifermion annihilating into a photon, a fermion or an antifermion absorbing a photon, or a photon splitting into a fermion–antifermion pair.

1.2.3 QED gauge symmetry

The free fermion Lagrangian from Section (1.2.1) is invariant under a global phase transformation. However, global phase transformations cannot affect any physical observable. Consequently, the phase of $\psi(x^\mu)$ is without any physical meaning. One can redefine the problem and require that the symmetry is a function of space-time, $\theta = \theta(x^\mu)$ (i.e. making it local), but the Dirac Lagrangian is no longer invariant under such transformation. This is only possible if one add to this Lagrangian a spin-1 gauge field A_μ, transforming like:

$$A_\mu(x^\mu) \to A'_\mu(x^\mu) = A_\mu(x^\mu) - \partial_\mu \alpha(x^\mu) \ . \tag{1.13}$$

Indeed, the QED Lagrangian remains unchanged under these transformations. Moreover, from the definition of the electromagnetic four-potential (1.5), it is clear that the transformation (1.13) leaves the electric and magnetic fields unchanged. The fermion field now undergoes the coupled transformation

$$\psi(x^\mu) \xrightarrow{U(1)^{\text{local}}_{em}} \psi'(x^\mu) = e^{i\theta(x^\mu)}\psi(x^\mu) = e^{ig\alpha(x^\mu)}\psi(x^\mu) \ , \tag{1.14}$$

where the constant g is a dimensionless measure of the strength of the interaction: formally referred to as the *coupling parameter*. In case of a quantum theory of electromagnetism, the coupling parameter can be identified with the electric charge $g \equiv q_e$, which is the quantity preserved by the invariance with respect to the local gauge transformation $U(1)^{\text{local}}_{em}$. One can also define the electromagnetic *coupling constant*:

$$\alpha_{em} = \frac{e^2}{4\pi} \ , \tag{1.15}$$

which determines the strength of the electromagnetic force on an electron/muon.

Finally, the QED gauge theory, as presented in (1.14), is the relativistic invariant way to describe the interactions mediated by massless spin-1 particles. Indeed, a massless spin-1 particle has only two physical polarizations. Then, the gauge invariance is a local symmetry that allows to remove the unphysical polarization of this spin-1 massless particle, while keeping Lorentz invariance explicit.

The QED created by Feynman [7, 8], Schwinger [9] and Tomonaga [10] was the first quantum field theory that provided a consistent relativistic quantum mechanical description of electromagnetism. The principle of gauge invariance has become a powerful tool to understand electromagnetism and very useful in describing the strong and weak interactions mechanism.

1.2.4 Running QED coupling

In quantum electrodynamics, an electron or muon is not treated as a single free particle. All particles with electric charge will emit a cloud of virtual photons around them. A virtual photon can afterwards annihilate into a pair of virtual charged particles, for example, e^+e^- pairs. A negatively charged muon, for instance, surrounded by a cloud of these e^+e^- pairs will repel the e^- particles and thus the e^+ particles will be preferentially closer to the muon. When probing such a structure from distance, the surrounding e^+ particles will *screen* the muon, what will affect the measured charge. A high-energy probe that manages to get closer to muon will see less effects from the virtual particles, so that the effective electric charge will increase.

A high-energy interactions can also explore so-called virtual-loop corrections to the photon propagator, as sketched in Figure 1.2. They can lead to the (unphysical) divergences when calculating physical processes in QED. To resolve the possible ultraviolet (i.e. high energy) divergences in QED, an arbitrary energy scale called the *renormalization scale* is introduced. For QED, the renormalization scale is defined as the minus of the four momentum squared, $Q^2 = -q^2$, where Q^2 is positive and represents the virtuality of the photon. The larger Q^2 (in GeV^2 unit), the more virtual is the photon. In particular, a real photon corresponds trivially to $Q^2 \simeq 0$.

The dependence of α_{em} on the renormalization scale Q^2 is known as *running* of the constant coupling. Following from an all-orders resummation of vacuum polarization diagrams, the evolution of QED coupling is conventionally parametrized by:

$$\alpha_{em} \to \alpha_{em}(Q^2) = \frac{\alpha_{em}(0)}{1 - \Delta\alpha_{em}(Q^2)} \ , \tag{1.16}$$

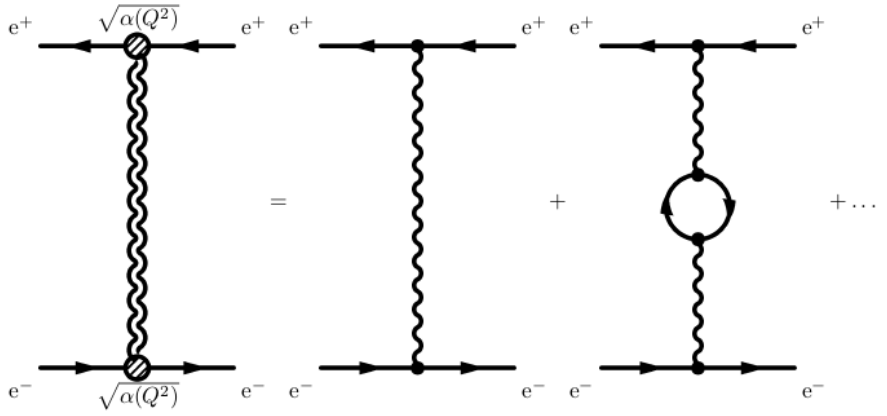

FIGURE 1.2: Feynman diagrams contributing to $e^+e^- \to e^+e^-$ scattering. The sum of all diagrams including zero, one, two or more virtual loop corrections is denoted by the diagram with the double-wavy photon propagator, with an electromagnetic coupling $\alpha(Q^2)$. Figure taken from [11].

where $\alpha_{em}(0) = 1/137.035999679(94)$ is the fine structure constant in the long-wavelength Thomson limit [12], and the term $\Delta\alpha_{em}(Q^2)$ controls the evolution. Figure 1.3 shows the evolution of the α_{em} with Q^2 determined from the $e^+e^- \to e^+e^-$ scattering measurements at large momentum transfers [11]. This provides an impressive evidence of the running of the electromagnetic coupling in the high-energy regime.

1.3 Quantum chromodynamics

In *quantum chromodynamics* (QCD), the theory describing the strong interaction, quarks appear in color triplets. Such a property was needed for explaining e.g. how quarks can coexist inside some hadrons without violating the Pauli exclusion principle [13]. The colour plays the role of the charge for every particle which interacts strongly. Each quark can exist in one of three colour states, e.g. red, green, blue, or 1, 2, 3. The antiquarks have anticolors, so the mesons can be colorless by consisting of e.g. a red and an "antired" quark. Therefore, only colourless objects (colour singlets, like mesons, or baryons containing red, blue and green quarks) can exist in nature as a free particles. This behavior is called *colour confinement*. Gluons, which represent the relevant spin-1 gauge field in QCD, carry both color and anticolor, e.g antired–blue or green–antiblue.

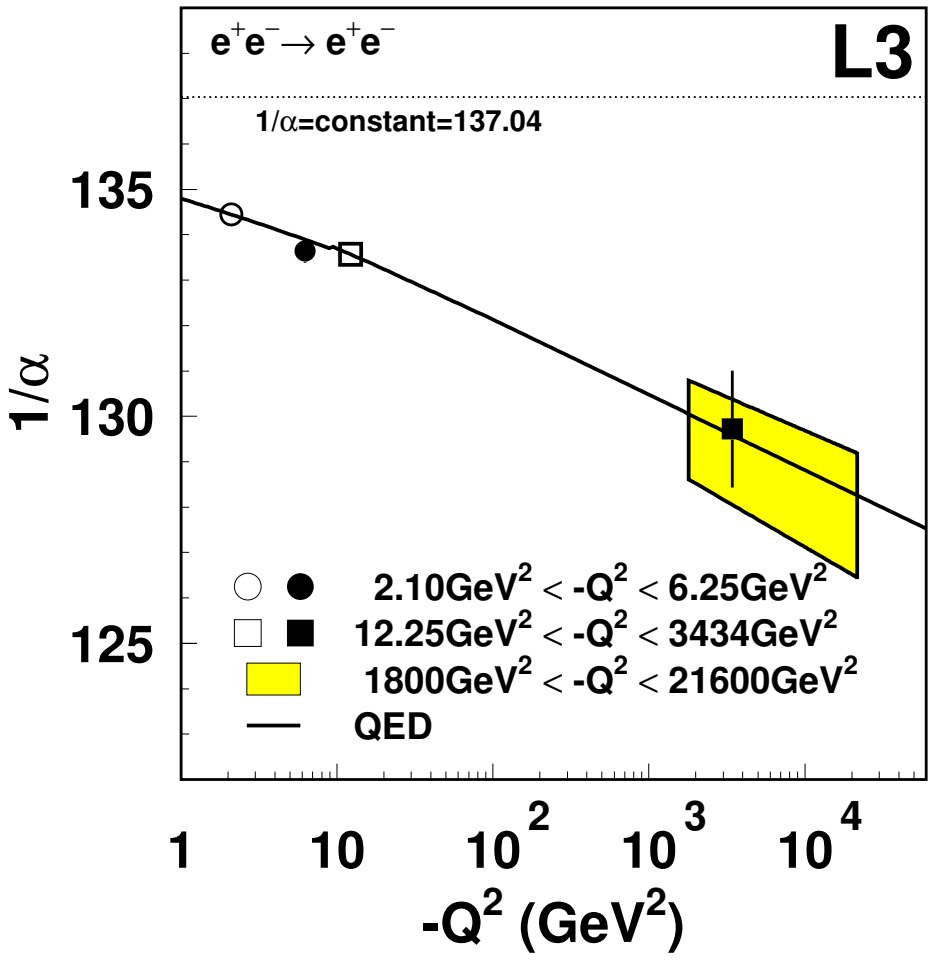

FIGURE 1.3: Evolution of the electromagnetic coupling with Q^2 determined from the measurements at large momentum transfers. The QED predictions are shown by the solid line. Figure taken from [11].

1.3.1 QCD gauge symmetry

The QCD Lagrangian representation allows to arbitrarily mix the quarks by acting on a three vector of quark wave functions:

$$\boldsymbol{\psi} = \begin{pmatrix} \psi_1 \\ \psi_2 \\ \psi_3 \end{pmatrix} , \tag{1.17}$$

where ψ_i is a regular Dirac spinor for a quark of color i. The Lagrangian for a specific-flavour free quark is:

$$\mathcal{L}_0 = \bar{\boldsymbol{\psi}}(i\gamma^\mu \partial_\mu - m)\boldsymbol{\psi} \ . \tag{1.18}$$

This Lagrangian is invariant under the non-Abelian $SU(3)_C$ transformations. Following the analogy to QED, the gauge invariant QCD Lagrangian for gluon field and a quark of the specific flavour is [14]:

$$\mathcal{L}_{\mathrm{QCD}} = \bar{\psi}(i\gamma^{\mu}\partial_{\mu} - m)\psi - \frac{1}{4}G^{k}_{\mu\nu}G^{\mu\nu}_{k} - \frac{g_s}{2}\bar{\psi}\gamma^{\mu}\lambda_k\psi G^{k}_{\mu} \ , \tag{1.19}$$

where the second term describes free gluon Lagrangian and the third term is responsible for quark–gluon interaction. The basic vertices describing QCD interactions are presented in Figure 1.4. In QCD the coupling parameter g_s acts on 8 vector fields[1] $G_{\mu} = \frac{1}{2}\lambda^i G^i_{\mu}$ represented by the λ^i $(i = 1, ..., 8)$ generators called *Gell-Mann matrices*. These gluon fields can be expressed in terms of field strength tensor [14]:

$$G^{i}_{\mu\nu} = \partial_{\mu}G^{i}_{\nu} - \partial_{\nu}G^{i}_{\mu} - g_s f_{ijk}G^{j}_{\mu}G^{k}_{\nu} \ , \tag{1.20}$$

where f_{ijk} are the $SU(3)$ structure constants that form a totally antisymmetric tensor.

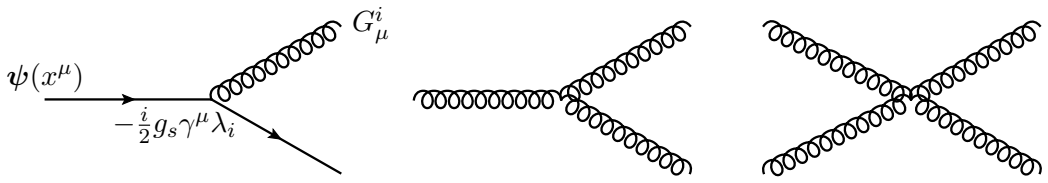

FIGURE 1.4: The basic vertices describing QCD interactions. The vertex factor for the quark-gluon coupling is $-\frac{i}{2}g_s\gamma^{\mu}\lambda_i$. The gluon self-coupling vertex factors are more complex and are not given explicitly.

1.3.2 Strong interaction coupling

In analogy to QED, the strong coupling constant α_s can be defined only with respect to the given energy scale squared, labelled as μ^2 below. This can be a hard scale (squared) involved in a reaction or the mass (squared) of a heavy particle. The dependence of a coupling constant on the energy-scale in QCD takes the form:

$$\alpha_s(\mu^2) \equiv \frac{g_s^2(\mu^2)}{4\pi} \approx \frac{1}{\beta_0 \ln\left(\frac{\mu^2}{\Lambda_{\mathrm{QCD}}}\right)} \ , \tag{1.21}$$

where Λ_{QCD} is the scale above which the effective QCD coupling becomes small and β_0 is the constant proposed and computed by Wilczek, Gross [15] and Politzer [16]. For values of μ^2 much larger than Λ_{QCD} the effective coupling is small and the perturbative QCD

[1] In QCD the presence of 8 gluon fields (gluons) is related with the $N^2 - 1 = 3^2 - 1 = 8$ generators of $SU(3)$ group

(pQCD) calculations provide a good description of the strong interaction physics. From the Equation (1.21) it is clear, that with increasing μ^2, the strong coupling becomes small for short distances. This means that quarks interact weaker at high energies, allowing perturbative calculations, and stronger at low energies, preventing the unbinding of baryons or mesons.

1.3.3 The parton model

In order to describe the internal structure of the proton, the *parton model* was proposed [17, 18]. In this model, the proton is assumed to be composed of a number of point-like constituents, termed as partons, defined in a reference frame where the proton has infinite momentum. Thus, the motion of any partons is slowed down by time dilation, and the proton charge distribution is Lorentz-contracted, such that incoming particles will be scattered instantaneously and incoherently. The most important ideas in the parton model are that partons are point-like and asymptotically free. The parton model was successfully applied to electron–proton (ep) *Deep Inelastic Scattering* (DIS) experiments: see some recent results in [19–22], where partons are matched to quarks and gluons inside the proton.

The DIS data allowed to extract the *Parton Density Functions* (PDFs) of a proton. They represent the probability densities to find a parton carrying longitudinal momentum fraction x of the proton at given energy scale (squared) Q^2. Here, Q^2 is the virtuality of the photon exchanged in the DIS ep collision. It can be noticed that the wavelength of the virtual photon is $\sim 1/Q$, which means that the photon probes smaller distances in the proton for larger Q^2 values. The distribution of partons for $Q^2 = 10$ GeV^2 as a function of the longitudinal momentum fraction x carried by the parton is shown in Figure 1.5. The valence quarks (xu_v and xd_v) dominate at values $x > 0.2$. Partons at small x ($x < 0.01$) values are mostly composed of gluons (xg) and sea-quarks (xS). At the LHC energies, the energy scales in various reactions are usually much larger than $Q^2 = 10$ GeV^2. The evolution of the PDFs to larger values of Q^2 is achieved through the *Dokshitzer–Gribov–Lipatov–Alterelli–Parisi* (DGLAP) [23–25] evolution equations. Then, PDFs and DGLAP equations are the fundamental components to describe the large number of physical processes at the LHC.

1.3.4 Diffraction

In hadron–hadron collisions majority of collision events are due to strong interaction exchanges. In general, there are different types of these processes:

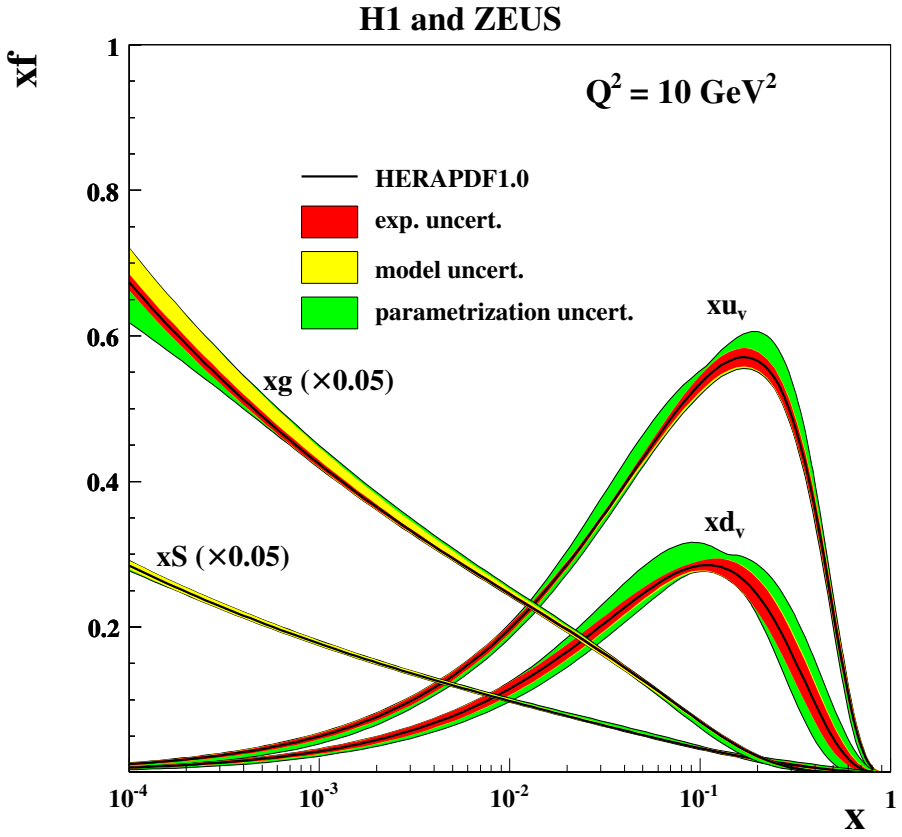

FIGURE 1.5: Distributions of partons in the proton as a function of longitudinal momentum fraction for $Q^2 = 10\ \mathrm{GeV}^2$ from a combined fit of H1 and ZEUS data. Figure taken from [19].

- inclusive (or non-diffractive) interaction,
- elastic scattering,
- single-diffractive (SD) interaction,
- double-diffractive (DD) interaction.

By its name, the last three interactions are of diffractive nature. They occur when no quantum numbers are exchanged between the scattered objects and, e.g. the net colour is equal to zero. A diffractive interaction can be described in QCD at the lowest order by the exchange of two gluons that together form a colour singlet [26]. However, this simple description cannot describe the observed data. This is why the concept of *Pomeron* has been introduced [27].

Elastic scattering is the simplest process to consider. Here the final-state hadrons are the same as in the initial state, with some four momentum transfer (squared), usually

labelled as t, in the reaction:

$$a + b \to a + b \ . \tag{1.22}$$

Depending on the value of t, scattering can occur in the Coulomb (photon exchange) or nuclear (Pomeron exchange) region. There is also a Coulomb–nuclear interference region allowed.

Single diffraction occurs as the following process:

$$a + b \to a + X \ , \tag{1.23}$$

where X represents any additional low-mass multi-particle state with the same quantum numbers as particle b. In single-diffractive processes, the particle a stays intact, whereas the other one dissociates into the state denoted by X. In analogy, the double diffraction is a process with:

$$a + b \to X + Y \ , \tag{1.24}$$

where X and Y are the low-mass multi-particle states of the same quantum numbers as particles a and b, respectively. In other words, there is no quantum number exchange between a and b.

The above definitions of hadronic diffractive reactions are mainly experimental. This is what is needed in the following. However, this is interesting to discuss briefly the origin of hadronic diffraction and thus why one expects important contributions of these reactions in hadron–hadron collisions at high energies. In fact, the phenomenon of diffraction is well known from classical wave theory and has its origin in the coherence of classical waves. In Quantum Mechanics (QM), high-energy elementary particles are described by QM waves. This brings to the direct counterpart of classical diffraction in the case of elastic scattering (and only in this case). Inelastic hadronic diffraction is more complex. In such processes, like in SD and DD, the internal structure of the interacting particle is probed. Then, one may consider a picture as follows: the incident hadron fluctuates into some basic states and then is scattered by the target hadron. Moreover, certain of these basic states will feel the strong interaction of the target (hadron) while other states will not. This is the large fluctuation in the absorption coefficients during the scattering process which is at the origin of the inelastic diffraction.

By contrast, non-diffractive processes involve the exchange of coloured objects, leading to the break-up of both interacting hadrons and particle production in the central and mid-rapidity regions. Schematic diagrams of non-diffractive, elastic, single and double-diffractive interactions are presented in Figure 1.6.

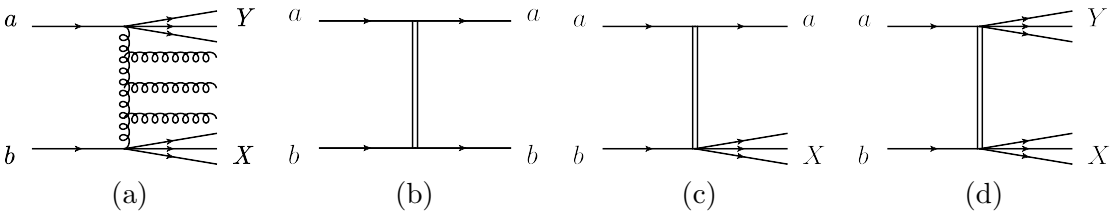

FIGURE 1.6: Schematic diagrams of different scattering processes in hadron–hadron collisions: (a) non-diffractive interaction, (b) elastic scattering, (c) single-diffractive process and (d) double-diffractive process. The vertical double line represents the Pomeron exchange.

1.4 The electroweak theory

The electromagnetic interaction occurs only between electrically charged particles. It is mediated by photons and has an infinite range. On the other hand, the weak interaction occurs between charged and uncharged leptons and quarks and has a very short range. While the electromagnetic and weak interactions are different, they have been combined into a single theoretical framework, known as the *Glashow–Salam–Weinberg* (GSW) model [28–30] with a $SU(2)_L \otimes U(1)_Y$ symmetry [14].

In the electroweak theory, all fermions are arranged by flavour, so that each of the three generations is represented as a pair of particles, so called *weak isospin doublets*. For leptons, each doublet consists of a charged lepton with a non-zero mass and a massless, neutral neutrino. One can define so-called *left-handed* (ψ_L) and *right-handed* (ψ_R) components of the fermion field ψ, using the chirality projection operators:

$$\begin{aligned} \psi_L &= L\psi; \quad L = \frac{1}{2}(1-\gamma_5) \\ \psi_R &= R\psi; \quad R = \frac{1}{2}(1+\gamma_5) \ , \end{aligned} \tag{1.25}$$

where

$$\gamma_5 = i\gamma^0\gamma^1\gamma^2\gamma^3\gamma^4 \ . \tag{1.26}$$

The weak interaction only takes into account left-handed fermions (and right-handed antifermions). To take this into account, the Lagrangian describing e.g. the free lepton (ℓ) and lepton neutrino (ν_ℓ) can be decomposed in the weak doublet scheme [14]:

$$\mathcal{L}_0 = \bar{\chi}_L i\gamma^\mu \partial_\mu \chi_L + \bar{\psi}^\ell_R i\gamma^\mu \partial_\mu \psi^\ell_R + \bar{\psi}^{\nu_\ell}_R i\gamma^\mu \partial_\mu \psi^{\nu_\ell}_R \ , \tag{1.27}$$

where the masses of the fermions are neglected and

$$\chi_L = \begin{pmatrix} \psi^{\nu_\ell}_L \\ \psi^\ell_L \end{pmatrix} \ . \tag{1.28}$$

The left-handed components of the fermion fields are now grouped in a weak isospin doublet ($I_3 = \pm\frac{1}{2}$ for $\psi_L^{\nu_\ell}$ or ψ_L^{ℓ}), while all the right-handed components form weak isospin singlets ($I_3 = 0$). One can also introduce so-called *weak hypercharge* Y to each field, such that the electric charge can be expressed with the Gell-Mann–Nishijima relation:

$$\frac{q}{e} = I_3 + \frac{Y}{2} \ . \tag{1.29}$$

To make the Lagrangian (1.27) invariant under $U(1)_Y^{\text{local}}$ transformations, one should introduce a new field B_μ, which couples to weak hypercharge with coupling strength denoted by g'. The $SU(2)_L^{\text{local}}$ symmetry gives rise to three fields W_μ^i ($i = 1,\ 2,\ 3$) which couple to weak isospin with coupling strength g.

The physical gauge bosons of electroweak interaction are the photon (γ), the $W^\pm$ and the Z, which do not correspond to the $SU(2)_L$ and $U(1)_Y$ representations given above. The W_μ^1 and W_μ^2 fields can be identified with the physical charged vector bosons by making the following transformations [14]:

$$\begin{aligned} W^+ \quad &: \quad W_\mu = \frac{1}{\sqrt{2}}\left(W_\mu^1 - iW_\mu^2\right) \\ W^- \quad &: \quad W_\mu^\dagger = \frac{1}{\sqrt{2}}\left(W_\mu^1 + iW_\mu^2\right) \ . \end{aligned} \tag{1.30}$$

When writing out the terms involving W_μ^3 and B_μ fields, one can define the physical photon A_μ and Z boson Z_μ [14]:

$$\begin{aligned} \gamma \quad &: \quad A_\mu = \cos\theta_{\text{W}} B_\mu + \sin\theta_{\text{W}} W_\mu^3 \\ Z \quad &: \quad Z_\mu = -\sin\theta_{\text{W}} B_\mu + \cos\theta_{\text{W}} W_\mu^3 \ , \end{aligned} \tag{1.31}$$

where θ_{W} is the weak mixing angle or Weinberg angle [31] that relates to the amount of mixing in the rotation of the fields. To preserve the A_μ couples to that electromagnetic current, one should have [14]:

$$g \sin\theta_{\text{W}} = g' \cos\theta_{\text{W}} = e \ . \tag{1.32}$$

This leads to the full electroweak Lagrangian, which takes the form (e.g. for charged lepton and its neutrino):

$$\begin{aligned}\mathcal{L}_{\mathrm{EW}} = \mathcal{L}_0 &- \frac{g}{\sqrt{2}}\left[\bar{\psi}_L^{\nu_\ell}\gamma^\mu\psi_L^\ell W_\mu + \bar{\psi}_L^\ell\gamma^\mu\psi_L^{\nu_\ell}W_\mu^\dagger\right] \\ &- \frac{g}{2\cos\theta_{\mathrm{W}}}\left[\bar{\chi}_L\gamma^\mu\tau_3\chi_L + 2\sin^2\theta_{\mathrm{W}}\bar{\psi}^\ell\gamma^\mu\psi^\ell\right]Z_\mu \\ &+ e\bar{\psi}_L^\ell\gamma^\mu\psi_L^\ell A_\mu \\ &- \frac{1}{4}B_{\mu\nu}B^{\mu\nu} - \frac{1}{4}W_{\mu\nu}^k B_k^{\mu\nu}\ ,\end{aligned} \tag{1.33}$$

where

$$\bar{\chi}_L\gamma^\mu\tau_3\chi_L = \bar{\psi}_L^{\nu_\ell}\gamma^\mu\psi_L^{\nu_\ell} - \bar{\psi}_L^\ell\gamma^\mu\psi_L^\ell\ , \tag{1.34}$$

and the last two terms in $\mathcal{L}_{\mathrm{ew}}$ are the kinetic terms of the gauge bosons, where the field strength tensors have the form:

$$\begin{aligned}B_{\mu\nu} &= \partial_\mu B_\nu - \partial_\nu B_\mu \\ W_{\mu\nu}^i &= \partial_\mu W_\nu^i - \partial_\nu W_\mu^i - g\epsilon_{ijk}W_\mu^j W_\nu^k\ .\end{aligned} \tag{1.35}$$

Here ϵ_{ijk} is the total antisymmetric tensor that builds the structure constant of the $SU(2)_L$. The neutral gauge bosons couple to left-handed as well as to right-handed particles, while the charged gauge bosons of the electroweak interaction only couple to left-handed particles.

Within the electroweak theory, the physical gauge bosons can be introduced. However, the masses of these gauge bosons would have to be zero, as possible mass terms in the electroweak Lagrangian,

$$m_W^2 W_\mu^\dagger W^\mu + \frac{1}{2}m_Z^2 Z_\mu Z^\mu\ , \tag{1.36}$$

would not be locally gauge invariant [14]. The fermion mass terms have to be also neglected, because they are not gauge invariant when taking into account the left-right chirality mixing. The way weak gauge boson and fermion masses are incorporated into the Standard Model is due to the spontaneous symmetry breaking, that is related to the *Brout–Englert–Higgs* (BEH) mechanism [32, 33].

1.5 The Brout–Englert–Higgs mechanism

To include the spontaneously broken symmetry into the electroweak theory, a scalar (Higgs) doublet Φ with hypercharge $Y = 1$ has to be introduced in the electroweak

Lagrangian through the terms [14]:

$$\begin{aligned}\mathcal{L}_{\text{Higgs}} &= (iD^{\mu}\Phi)^{\dagger}(iD_{\mu}\Phi) - V(\Phi) \\ &= (iD^{\mu}\Phi)^{\dagger}(iD_{\mu}\Phi) - \left[\mu^2\Phi^{\dagger}\Phi + \lambda\left(\Phi^{\dagger}\Phi\right)^2\right] \ . \end{aligned} \tag{1.37}$$

The potential $V(\Phi)$ is invariant under local gauge transformation. It has a degenerate ground state with $\mu^2 < 0$ and $\lambda > 0$:

$$\Phi^{\dagger}\Phi = -\frac{\mu^2\lambda}{2} \equiv \frac{v^2}{2} \ . \tag{1.38}$$

By choosing the ground state to be:

$$\Phi_0 = \frac{1}{\sqrt{2}}\begin{pmatrix}0\\ v\end{pmatrix} \ , \tag{1.39}$$

the $SU(2)_L \otimes U(1)_Y$ symmetry is broken towards $U(1)_{em}$ and photon obtains no mass.

Performing an expansion around the ground state value Φ_0, the Higgs doublet has the form:

$$\Phi = \frac{1}{\sqrt{2}}\begin{pmatrix}0\\ v + H(x^{\mu})\end{pmatrix} \ , \tag{1.40}$$

where $H(x^{\mu})$ is the Higgs field. The other three degrees of freedom are absorbed by the weak gauge bosons and represent the degree of freedom of mass of these bosons.

Using the form (1.40) of the Higgs doublet Φ, one can perform the covariant derivative for the kinetic terms of $\mathcal{L}_{\text{Higgs}}$ [14]:

$$D_{\mu}\Phi = -\left[\frac{ig}{2}\begin{pmatrix}W_{\mu}^3 & W_{\mu}^1 - iW_{\mu}^2\\ W_{\mu}^1 - iW_{\mu}^2 & -W_{\mu}^3\end{pmatrix} + \frac{ig'}{2}B_{\mu}\right]\frac{1}{\sqrt{2}}\begin{pmatrix}0\\ v+H\end{pmatrix} \ . \tag{1.41}$$

This particular choice of the ground state and the parametrization of the mixing of the gauge fields lead to the mass terms:

$$(iD^{\mu}\Phi)^{\dagger}(iD_{\mu}\Phi) = \frac{1}{2}(\partial_{\mu}H)(\partial^{\mu}H) + \frac{1}{4}(v+H)^2 g^2\left[W_{\mu}^{\dagger}W^{\mu} + \frac{1}{2\cos^2\theta_{\text{W}}}Z_{\mu}Z^{\mu}\right] \ . \tag{1.42}$$

The first term describes the Higgs boson. The remaining terms describe the interaction of the Higgs field with the electroweak bosons. The masses of the $W^{\pm}$ and Z bosons can be directly read off as

$$m_W = \frac{vg}{2} \ ; \quad m_Z = \frac{vg}{2\cos\theta_{\text{W}}} \ . \tag{1.43}$$

A coupling of the Higgs-doublet to the fermions is also needed to introduce gauge invariant fermion mass terms. This is described by the so-called *Yukawa couplings*. As an example, for the electrons, the mass term is:

$$\mathcal{L}_{\text{Yukawa}} = -G_e \left(\bar{\chi}_L \Phi \psi_R^e + \bar{\psi}_R^e \Phi^\dagger \chi_L \right) \ , \tag{1.44}$$

where $m_e = \frac{G_e v}{\sqrt{2}}$. One should indicate that this relation is not a prediction of the BEH theory, as G_e is a free parameter given by the experimentally measured electron mass. However, the interaction of the electron with the Higgs boson gives rise to the vertex factor: $-\frac{iG_e}{\sqrt{2}} = -\frac{im_e}{v}$. Therefore, the Higgs boson couples more strongly to heavier particles in the SM, which is also verified experimentally [34, 35].

The QCD and electroweak part of the Lagrangian combined with Higgs and Yukawa terms form the full Lagrangian of the Standard Model:

$$\mathcal{L}_{\text{SM}} = \mathcal{L}_{\text{QCD}} + \mathcal{L}_{\text{EW}} + \mathcal{L}_{\text{Higgs}} + \mathcal{L}_{\text{Yukawa}} \ . \tag{1.45}$$

1.6 From Lagrangian to event rate

Theories can meet with experiments by providing some verifiable predictions, usually in terms of a measurable quantities. So-called *Feynman rules* [6], obtained from the SM Lagrangian $\mathcal{L}_{\text{SM}}$ can be used to define a quantity expressing the likelihood of an interaction event between two particles, a *cross section*, σ:

$$\sigma = \frac{[\text{Transition rate}] \cdot [\text{Number of final states}]}{[\text{Initial particle flux}]} \ . \tag{1.46}$$

These rules describe the conversion of Feynman graphs into the matrix elements $\mathcal{M}$ of the corresponding processes. The matrix element is related with the differential cross section $\mathrm{d}\sigma$ using the relation:

$$\mathrm{d}\sigma \propto |\mathcal{M}|^2 \, \mathrm{d}\Phi \ , \tag{1.47}$$

where $\mathrm{d}\Phi$ denotes a differential volume of the phase-space.

The full matrix element is defined by the sum of all possible Feynman graphs with given initial and final states. For the full calculation also the processes of higher order in the perturbation series have to be taken into account. Since this is an infinite series with in general decreasing influence, calculations are initially performed at *leading-order* (LO). This means only processes with the minimal number of vertex factors are considered.

1.7 Experimental verification of the Standard Model

The Standard Model has been examined by many experimental tests. All the elementary particles and their properties predicted by the SM are experimentally confirmed with good precision. Over the past 20 years before the Large Hadron Collider (LHC) era, the SM has been strongly constrained by precision measurements of e.g. the properties of $W^{\pm}$ and Z bosons, and the top quark, all of which have been found to be in good agreement with theory [36].

At the LHC, apart of the discovery of the Higgs boson, many other measurements have been performed to test the compatibility with SM. These are summarized in Figure 1.7, where all the achieved measurements show no deviation from the theory predictions.

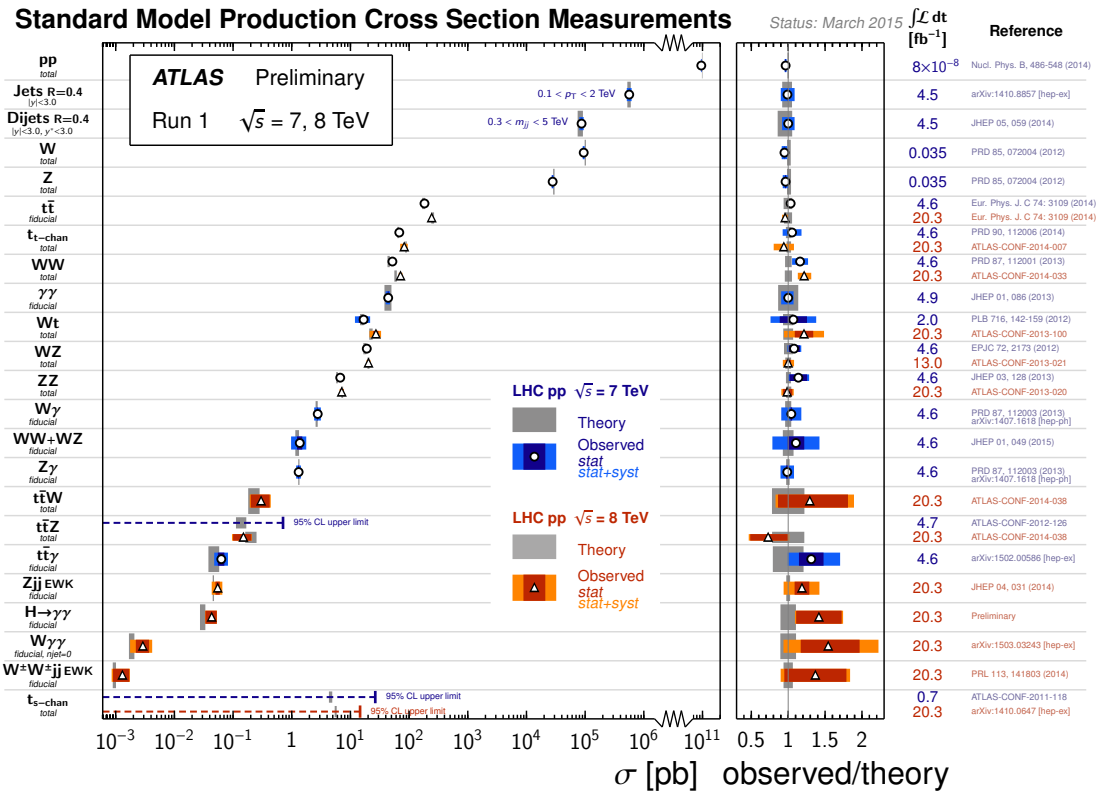

FIGURE 1.7: Detailed summary of several Standard Model measurements by the ATLAS experiment at the LHC, compared to the corresponding theoretical expectations. Figure taken from [37].

Chapter 2

Photon interactions at the LHC

This chapter is related to photon interaction properties at high energies. Firstly, the theoretical framework related to the different photon interaction types is explained in Sections 2.1–2.3. The experimental properties of photon-induced processes are explained in Section 2.4. Finally, the Monte Carlo (MC) event generators for photon-induced reactions are discussed in Section 2.5.

2.1 High-energy photon interactions

Photon interactions have been extensively studied at high-energy electron–proton (ep) collisions at *Hadron–Electron Ring Accelerator* (HERA) to test the hadronic structure of the proton [19], with the electron acting as a source of virtual photons. One can define k, k' and p as the four-momenta of the incident electron, scattered electron and incident proton (respectively). It can be noticed that the measurements presented in [19] come from e^-p or e^+p collisions. However, this does not make any difference for the discussion below. As already mentioned in Section 1.3.3, the photon emitted by the incident electron during the Deep Inelastic Scattering (DIS) reaction can be characterized by its virtuality $Q^2 = -q^2 = -(k - k')^2$, in terms of the four-momenta defined above. The invariant mass (squared) of the system produced in the reaction can be computed as $W^2 = (q + p)^2$. Then, for small virtualities Q^2 compared to W^2, the photon exchanged during the collision is *quasi-real*. This is schematically presented in Figure 2.1. When the initial proton stays intact after the interaction, the process is called *elastic*. The proton can be also excited (by the photon) to one of its resonant states, like $\Delta(1232)$ resonance. For larger photon virtualities and invariant masses W, a DIS process occurs. This reaction is sensitive to the momentum distributions of quarks in the proton.

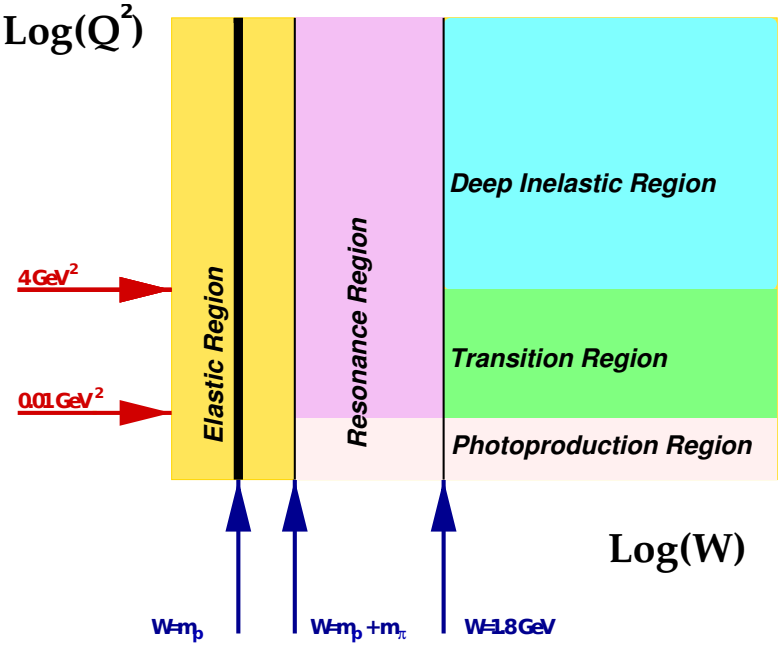

FIGURE 2.1: Different kinematic regions describing photon interaction with the proton. Figure taken from [38].

The photons can be radiated from both of the beam particles (electron and proton), and can produce a central state, like a pair of muons [39]. This state conserves the quantum numbers with respect to the net quantum numbers of initial two-photon system.

Similar phenomena have been observed in proton–antiproton ($p\bar{p}$) collisions at the Tevatron [40, 41] and in proton–proton (pp) collisions at the LHC [42–44]. Moreover, since the effective electromagnetic coupling increases with the charge of the colliding particle, nucleus–nucleus collisions are perfectly designed to induce the two-photon interaction. Indeed, the two-photon production of lepton pairs have been observed in Au-Au collisions at the *Relativistic Heavy Ion Collider* (RHIC) [45, 46] and in Pb-Pb collisions at the LHC [47].

Therefore, the LHC may be considered also as a photon collider, aiming to study a variety of photon-induced interactions.

2.1.1 Electron–muon elastic scattering

The electron–muon ($e\mu$) elastic scattering is the simplest example to study high-energy photon interactions. In the lowest order perturbation theory the reaction is described by the one-photon exchange diagram, presented in Figure 2.2. Using appropriate Feynman rules for QED, based on Equation 1.12, the matrix element for $e\mu$ scattering follows the

relation [48]:

$$\mathcal{M}_{e\mu\to e\mu} = \frac{1}{q^2}\left(e\bar{\psi}^e\gamma^\nu\psi^e\right)\left(e\bar{\psi}^\mu\gamma_\nu\psi^\mu\right) \ , \tag{2.1}$$

where q^μ is the electron four-momentum transfer and $q^2 = q_\mu q^\mu$ is the electron four-momentum transfer squared. It follows the approximation:

$$q^2 \simeq -4EE'\sin^2(\theta/2) < 0 \ . \tag{2.2}$$

Here E is the energy of the incident relativistic electron, E' is its final energy and θ is its scattering angle in the laboratory frame.

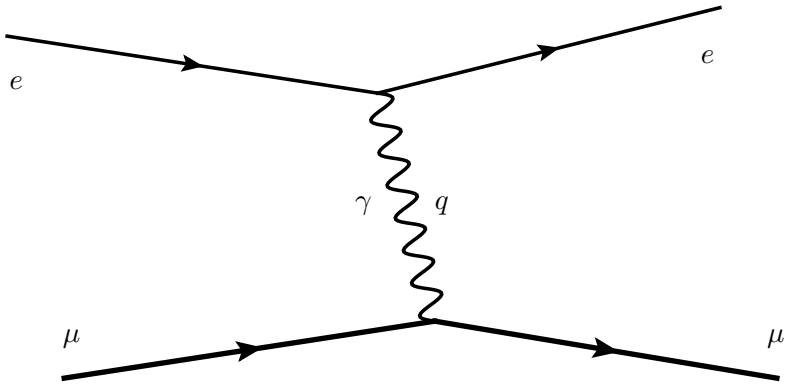

FIGURE 2.2: Leading-order, single-photon exchange diagram for electron–muon scattering.

Taking the modulus squared of the amplitude (2.1), multiplying by the appropriate phase-space and flux factors, one can find that the differential cross section for electron to be scattered in the solid angle $\mathrm{d}\Omega$ in the laboratory frame is [48]:

$$\frac{\mathrm{d}\sigma}{\mathrm{d}\Omega} = \frac{\alpha_{em}^2\cos^2(\theta/2)}{4E^2\sin^4(\theta/2)}\cdot\frac{E'}{E}\cdot\left[1-\frac{q^2}{2m_\mu^2}\tan^2(\theta/2)\right] \ , \tag{2.3}$$

where $\alpha_{em} = e^2/4\pi$ is the electromagnetic coupling constant and m_μ is the mass of the muon.

However, these simple results do not apply if the charge distribution of the target has some spatial extent (like in the proton).

2.1.2 Elastic ep scattering and proton form factors

In the lowest order perturbation theory of QED, the matrix element for the elastic ep scattering is very similar to $e\mu$ scattering. The only difference is that the relevant γp vertex factor is no longer point-like and should rather be given in the most general form possible for proton. In the case of elastic scattering from a fixed proton with a

charge distribution, $\rho_p(r)$, the scattering amplitude is modified by a form factor (in the non-relativistic limit):

$$F(q^2) = \int \mathrm{d}^3 r \; e^{-i\vec{q}\cdot\vec{r}} \rho_p(r) \; , \tag{2.4}$$

which corresponds to the Fourier transform of the charge distribution of the proton at rest.

In general, for the $ep \to ep$ reaction, the relation (2.1) can be extended to the form [48]:

$$\mathcal{M}_{ep\to ep} = \frac{1}{q^2} \left(e\bar{\psi}^e \gamma^\mu \psi^e\right) \left(e\bar{\psi}^p \Gamma_\mu \psi^p\right) \; . \tag{2.5}$$

In this relation, ψ^e and ψ^p are the electron and nucleon Dirac spinors respectively and

$$\Gamma_\mu = F_1(q^2)\gamma_\mu + \frac{\kappa_p}{2m_p} F_2(q^2) i\sigma_{\mu\nu} q^\nu + F_3(q^2) q_\mu \; , \tag{2.6}$$

where $\sigma_{\mu\nu} = \frac{i}{2}\left[\gamma_\mu, \; \gamma_\nu\right]$. The functions $F_i(q^2)$ are the electromagnetic *form factors* of the proton. $F_1(q^2)$ and $F_2(q^2)$ are the *Dirac* and *Pauli* form factors, respectively, while $F_3(q^2) \equiv 0$ in elastic ep scattering.[1] The mass of the proton is labelled as m_p and κ_p is the anomalous magnetic moment of the proton.

The form factors $F_1(q^2)$ and $F_2(q^2)$ are defined such that for $q^2 = 0$, which corresponds to the proton interacting with a static electromagnetic field, one has:

$$\begin{aligned} F_1(0) &= 1 \\ F_2(0) &= \kappa_p \; . \end{aligned} \tag{2.7}$$

Very often the linear combination of F_1 and F_2 is introduced, in terms of the *Sachs form factors* [49]:

$$\begin{aligned} G_E(q^2) &= F_1(q^2) - \frac{q^2}{4m_p^2} F_2(q^2) \\ G_M(q^2) &= F_1(q^2) + F_2(q^2) \; . \end{aligned} \tag{2.8}$$

From these considerations the differential cross section for elastic ep scattering can be calculated in terms of the form factors. The result is known as the *Rosenbluth formula* [48]:

$$\frac{\mathrm{d}\sigma}{\mathrm{d}\Omega} = \frac{\alpha_{em}^2 \cos^2(\theta/2)}{4E^2 \sin^4(\theta/2)} \cdot \frac{E'}{E} \cdot \left[F_1^2 + \frac{\kappa_p Q^2}{4m_p^2} F_2^2 + \frac{Q^2}{2m_p^2}(F_1 + \kappa_p F_2)^2 \tan^2(\theta/2)\right] \; , \tag{2.9}$$

[1] The F_3 type form factor appears when dealing with neutrino scattering

where θ is the scattering angle of the electron in the laboratory frame and E, E' is its initial and final energy, respectively. Also, since q^2 is negative in the scattering region, it is common practice to use $Q^2 = -q^2 > 0$. Experimentally F_1 and F_2 (or equivalently G_E and G_M) have been studied from $Q^2 \simeq 0$ to $Q^2 \simeq 10$ GeV^2 [50–57]. They are found to drop very rapidly as Q^2 increases, following the behavior:

$$G_E(Q^2) \approx \frac{G_M(Q^2)}{\kappa_p} \approx G_D(Q^2) \equiv \frac{1}{\left(1 + Q^2/Q_0^2\right)^2} \,, \tag{2.10}$$

the *dipole parametrization* with $Q_0^2 = 0.71$ GeV^2 parameter extracted from the measurements.

Form factors (or structure functions) exist as well for proton excitation processes, like $ep \to e\Delta(1232)$. However, all types of proton form factors are generally expected to decrease with four-momentum transfer, reflecting the spread in the charge and current distributions of the initial and final particles.

It is worth mentioning that in the general case, G_E and G_M, defined in Equations (2.7) and (2.10) cannot be expressed as the Fourier transforms of a charge density (in three dimensions of space). Indeed, it is known that the physical interpretation of the form factors is modified by some relativistic effects. This comes from the property that, in the relativistic quantum theory, an object of size R and mass m cannot be localized to a precision better than its Compton wavelength, $\sim 1/m$. Any attempt to do so with an external potential results in creation of particle–antiparticle pairs. Therefore, the static size of this system cannot be defined to a precision better than $\simeq 1/m$. Moreover, when the probing wavelength is comparable to $1/m$, the form factors are no longer determined by the internal structure alone. They contain, in addition, dynamical effects related with the Lorentz boost. The non-relativistic limit corresponds to $R \gg 1/m$.

However, it can be noticed that it is possible to recover the interpretation of the form factors as Fourier transforms of the charge distribution, with respect to the distance in the transverse plane, in the infinite momentum frame of the proton. The transverse plane is then a plane transverse to the direction of flight of the proton [58].

2.1.3 Two-photon fusion processes

Photon–photon ($\gamma\gamma$) interaction is the class of processes where photons are emitted from both colliding charged particles. The composed particle (like a proton) that emits a photon either survives and is scattered at small angle in case of elastic emission, or dissociates to some hadronic state in case of inelastic emission. This is shown in Figure 2.3. The colliding photons fuse to give a system of particles, X, which is centrally

produced. In the proton-dissociative case, either one or both colliding protons may be scattered inelastically. This is referred to as a *single* or *double proton-dissociative* interaction, respectively. If both colliding protons are scattered elastically, the reaction is called *exclusive*.

Assuming that the initial photon kinematics in the reaction is apriori known, the cross section for the sub-process $\gamma\gamma \to X$ can be calculated within the electroweak theory framework.

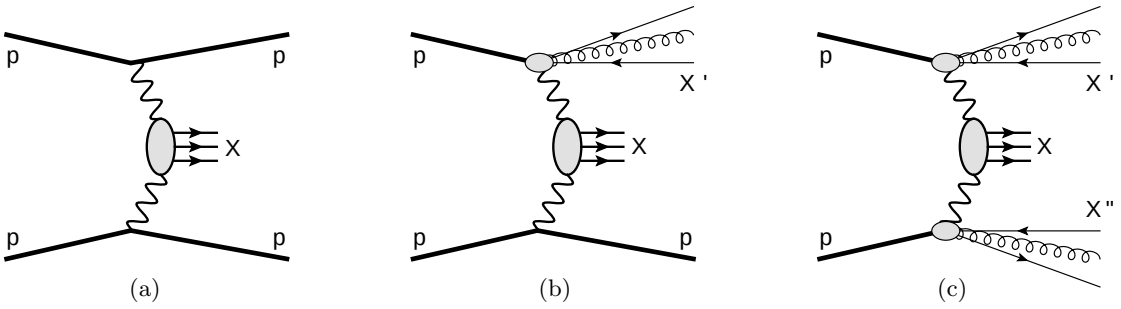

FIGURE 2.3: Schematic diagrams for (a) exclusive, (b) single proton-dissociative and (c) double proton-dissociative two-photon production of central state X in pp collisions.

Lepton pair production

The simplest process to consider in two-photon fusion reactions is the production of charged lepton pairs. For the electromagnetic production of a lepton pair using unpolarized photons, the sub-process cross section in the lowest order in α_{em} reads [59–61]:

$$\sigma_{\gamma\gamma\to\ell^+\ell^-} = \frac{4\pi\alpha_{em}^2}{W_{\gamma\gamma}^2}\left[\left(1+\frac{4m_\ell^2}{W_{\gamma\gamma}^2}-\frac{8m_\ell^4}{W_{\gamma\gamma}^4}\right)2\ln\left(\frac{W_{\gamma\gamma}}{2m_\ell}+\sqrt{\frac{W_{\gamma\gamma}^2}{4m_\ell^2}-1}\right)\right.$$
$$\left.-\left(1+\frac{4m_\ell^2}{W_{\gamma\gamma}^2}\right)\sqrt{1-\frac{4m_\ell^2}{W_{\gamma\gamma}^2}}\right]\Theta\left(W_{\gamma\gamma}^2-4m_\ell^2\right)\ , \qquad (2.11)$$

where m_ℓ is the mass of the lepton and $W_{\gamma\gamma}$ is the invariant mass of the photon–photon system. The Heaviside (step) function $\Theta\left(W_{\gamma\gamma}^2-4m_\ell^2\right)$, guarantees that the charged lepton pair can only be produced, if the center-of-mass energy of the two photons is larger or equal to twice the lepton mass. For quasi-real photons, the relation $W_{\gamma\gamma}^2 = 4\omega_1\omega_2$ holds, where ω_1, ω_2 are the energies of colliding photons. One can also introduce the Lorentz-invariant, two-photon center-of-mass rapidity $y_{\gamma\gamma} = \ln(\omega_1/\omega_2)$, which characterizes the scattering angle of the $\gamma\gamma$ system in high-energy limit (when $\omega_{1,2} \gg m_\ell$)

as[2]:

$$y_{\gamma\gamma} \simeq -\ln\left[\tan\left(\theta/2\right)\right] \ . \tag{2.12}$$

The formula (2.11) includes two leading-order diagrams shown in Figure 2.4, that had to be taken into account in the cross section calculation. Moreover, if the mass of the lepton is much larger than the invariant mass of the $\gamma\gamma$ system, and avoiding very forward and backward directions of lepton emissions[3], the formula (2.11) takes the simplified form [62]:

$$\sigma_{\gamma\gamma\to\ell^+\ell^-} \simeq \frac{4\pi\alpha_{em}^2}{W_{\gamma\gamma}^2}\left[\ln\left(\frac{1+\cos\theta_{\rm cut}}{1-\cos\theta_{\rm cut}}\right) - \cos\theta_{\rm cut}\right]\Theta\left(W_{\gamma\gamma}^2 - 4m_\ell^2\right) \ , \tag{2.13}$$

where the symmetric angular cut in the two-photon center-of-mass system

$$\theta_{\rm cut} < \theta < \pi - \theta_{\rm cut} \tag{2.14}$$

is imposed to avoid the limited detector acceptance in forward and backward regions. In the high-energy limit (with large $W_{\gamma\gamma}$ and fixed $\theta_{\rm cut}$) the cross section (2.13) drops like $1/W_{\gamma\gamma}^2$ for $\theta_{\rm cut} > 0$.

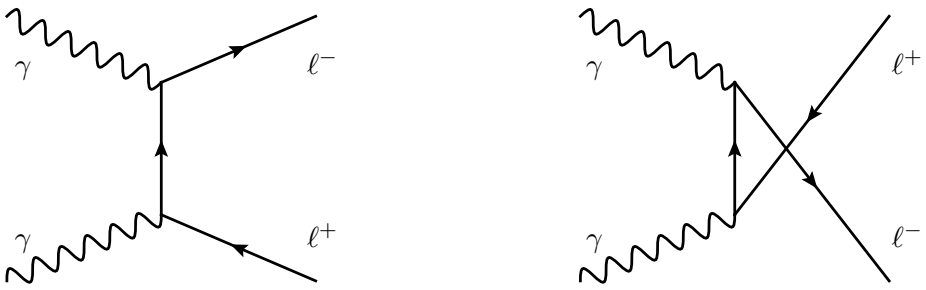

FIGURE 2.4: Leading-order diagrams for two-photon production of lepton pairs.

W boson pair production

Charged W bosons are also produced in pairs when created in two-photon fusion process. The elementary two-photon cross section for the photonic sub-process is given in lowest order (see Figure 2.5) by [61, 63]:

[2]See the Section 3.2.1 for more details

[3]In this case the leptons escape into the accelerator beam pipe and avoid detection

$$\sigma_{\gamma\gamma\to W^+W^-} = \frac{6\pi\alpha_{em}^2}{W_{\gamma\gamma}^2}\left[\sqrt{1-\frac{4m_W^2}{W_{\gamma\gamma}^2}}\left(1+\frac{4m_W^2}{W_{\gamma\gamma}^2}\right) - \frac{4m_W^2}{W_{\gamma\gamma}^2}\left(1-\frac{2m_W^2}{W_{\gamma\gamma}^2}\right)2\ln\left(\frac{W_{\gamma\gamma}}{2m_W}+\sqrt{\frac{W_{\gamma\gamma}^2}{4m_W^2}-1}\right) - \left(1+\frac{W_{\gamma\gamma}^4}{3m_W^4}\right)\frac{4m_W^2}{W_{\gamma\gamma}^2}\left(1+\frac{4m_W^2}{W_{\gamma\gamma}^2}\right)\right]\Theta\left(W_{\gamma\gamma}^2-4m_W^2\right) \ , \tag{2.15}$$

where m_W is the W boson mass and again, the step-function $\Theta\left(W_{\gamma\gamma}^2-4m_W^2\right)$ guarantees that the W boson pair can only be produced if the center-of-mass energy of the two photons is larger or equal to twice the boson mass. Similarly as for the charged lepton pairs, the cross section (2.15) can be expressed in terms of the fixed angular cut imposed in the two-photon center-of-mass frame [63]:

$$\sigma_{\gamma\gamma\to W^+W^-} = \frac{6\pi\alpha_{em}^2}{W_{\gamma\gamma}^2}\left[\beta\cos\theta_{\text{cut}} - \frac{4m_W^2}{W_{\gamma\gamma}^2}\left(1-\frac{2m_W^2}{W_{\gamma\gamma}^2}\right)\ln\left(\frac{1+\beta\cos\theta_{\text{cut}}}{1-\beta\cos\theta_{\text{cut}}}\right) + \left(\frac{1}{3}+\frac{m_W^4}{W_{\gamma\gamma}^4}\right)\frac{16\beta\cos\theta_{\text{cut}}}{1-\beta^2\cos^2\theta_{\text{cut}}}\right]\Theta\left(W_{\gamma\gamma}^2-4m_W^2\right) \ , \tag{2.16}$$

where $\beta = \sqrt{1-4m_W^2/W_{\gamma\gamma}^2}$ is the velocity of the W bosons in the $\gamma\gamma$ center-of-mass system. The cross section for $\gamma\gamma \to W^+W^-$ production approach constant at high-energies ($W_{\gamma\gamma}^2 \gg m_W^2$) and $\theta_{\text{cut}} = 0$:

$$\sigma_{\gamma\gamma\to W^+W^-} \xrightarrow{W_{\gamma\gamma}^2\to\infty} \frac{8\pi\alpha_{em}^2}{m_W^2} \ , \tag{2.17}$$

which makes the reaction dominant at high-energies, with respect to any other two-photon interaction process.

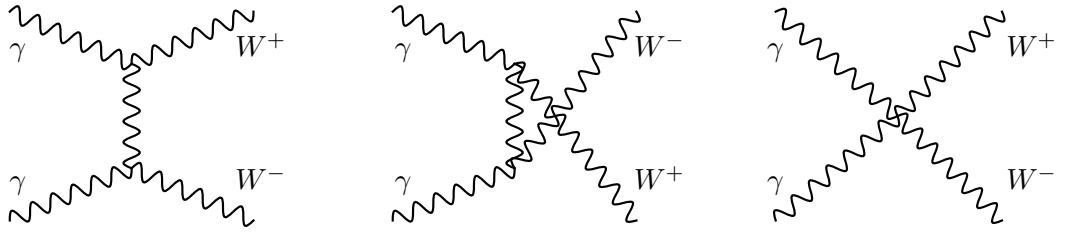

FIGURE 2.5: Leading-order diagrams for two-photon production of W boson pairs.

Higgs production

For the production of the Higgs boson one should notice that it can only be produced when the polarization vectors of the two photons are parallel to each other[4]. The two-photon production cross section of Higgs bosons is given by the following relation [61]:

$$\sigma_{\gamma\gamma\to H} = \frac{8\pi}{m_H}\Gamma_{H\to\gamma\gamma}\delta(W_{\gamma\gamma}^2 - m_H^2) \ , \tag{2.18}$$

where m_H is the mass of the Higgs boson, $\Gamma_{H\to\gamma\gamma}$ is its two-photon decay width and the $\delta(W_{\gamma\gamma}^2 - m_H^2)$ function ensures the energy conservation. The relevant leading-order diagrams that have to be taken into account in the $\gamma\gamma \to H$ cross section calculation are shown in Figure 2.6. The Higgs boson two-photon decay width, which enters into the elementary two-photon cross section is given by [61, 64]:

$$\Gamma_{H\to\gamma\gamma} = \frac{\alpha_{em}^2 g^2}{64\pi^3 m_W^2} m_H^3 |A_W + A_f|^2 \ , \tag{2.19}$$

where g is the weak coupling strength and the dimensionless quantities A_W, A_f reflects the contributions of W bosons, and fermions in the coupling between the Higgs boson and the two photons:

$$\begin{aligned} A_W &= \frac{1}{2} - \frac{m_W^2}{m_H^2} g\left(\frac{m_W^2}{m_H^2}\right) + \frac{3m_W^2}{m_H^2} + \frac{2m_W^2}{m_H^2}\left[2 - \frac{3m_W^2}{m_H^2}\right] g\left(\frac{m_W^2}{m_H^2}\right) \\ A_f &= -\sum_f \frac{q_f^2 m_f^2}{m_H^2}\left[2 - \left(\frac{4m_f^2}{m_H^2} - 1\right) g\left(\frac{m_f^2}{m_H^2}\right)\right] \ , \end{aligned} \tag{2.20}$$

where m_f denotes the mass of a fermion and q_f is its electric charge. The function $g(x)$ reads:

$$g(x) = \begin{cases} 2\arcsin^2\left(\frac{1}{2\sqrt{x}}\right) & x \geq \frac{1}{4} \\ \frac{\pi^2}{2} - 2\ln^2\left(\frac{1+\sqrt{1-4x}}{2\sqrt{x}}\right) + 2i\pi\ln\left(\frac{1+\sqrt{1-4x}}{2\sqrt{x}}\right) & x < \frac{1}{4} \end{cases} .$$

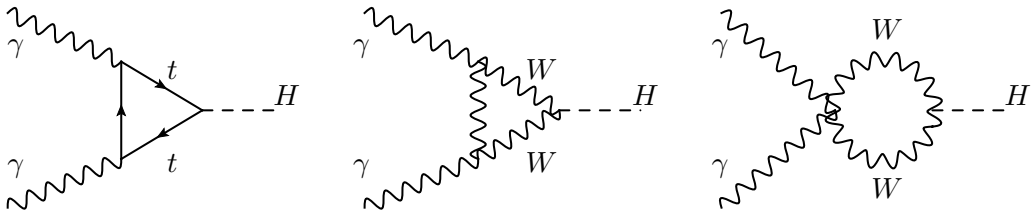

FIGURE 2.6: Leading-order diagrams for two-photon production of Higgs boson.

[4]Higgs boson is a scalar, spin-0 particle

2.2 The Equivalent Photon Approximation

Electrically charged particle moving at nearly the speed of light emits almost transverse electromagnetic (EM) fields[5]; the electric and magnetic fields have the same absolute value and are perpendicular to each other. As a consequence, an observer in the laboratory frame cannot distinguish between the EM field of a relativistic charged particle and the transverse component of the EM field associated with equivalent photons. This is an original idea of Fermi [65], which is schematically sketched in Figure 2.7. The idea was extended by Weizsacker [66] and Williams [67] who independently proposed the introduction of an equivalent (real) photon spectrum to compute the cross sections for the interaction of charged particles in their relativistic motion.

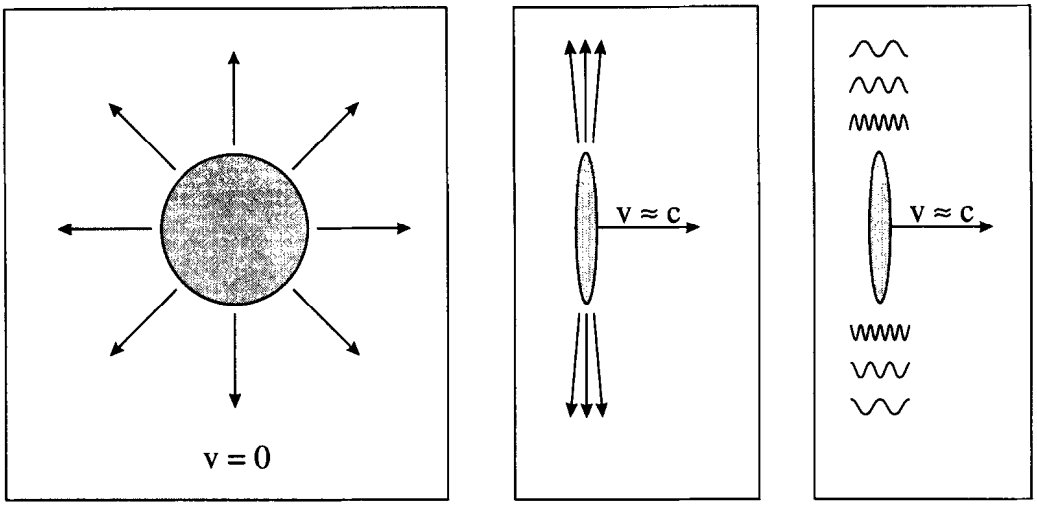

FIGURE 2.7: Sketch of the original Fermi's idea leading to the Equivalent Photon Approximation. As the velocity of the charge approaches the speed of light, its electromagnetic field becomes Lorentz-contracted and similar to a parallel-moving photon-cloud. Figure taken from [61].

The *Weiszacker–Williams flux* method was then extended to include the treatment of photon virtualities [59, 60]. The so-called *Equivalent Photon Approximation* (EPA) [61, 68, 69] is an approximative method to compute cross section of QED processes by considering them as interactions of fluxes of equivalent photons. The EPA can be successfully used to describe the majority of exclusive processes involving photon exchange, provided that the amplitude of a given process can be factorized into the photon exchange part and the process-dependent, photon interaction part:

$$\sigma^{\mathrm{EPA}}_{A_1A_2(\gamma\gamma)\to A_1A_2X} = \iint \mathrm{d}\omega_1 \; \mathrm{d}\omega_2 \; n_1(\omega_1) \; n_2(\omega_2) \; \sigma_{\gamma\gamma\to X}(W_{\gamma\gamma}) \; , \tag{2.21}$$

[5]This condition also includes the particles with non-zero magnetic moment, which can induce the EM fields

where the photons with energies ω_1 and ω_2, produced by the charged particles A_1 and A_2, can be described in terms of the equivalent photon spectrum, $n(\omega)$. In this approximation one should consider the photons as quasi-real and without polarization, which is valid only in the case of small-Q^2 photon exchange, where the condition $W^2_{\gamma\gamma} \gg Q^2$ should be always satisfied. Consequently, the EPA can only be applied when the cross section (2.21) is not sensitive to the virtuality of the photon, e.g. in the case of exclusive two-photon production.

2.2.1 Impact parameter dependent equivalent photon method

The photon flux $n(\omega)$ represents the electromagnetic radiation field which can be associated with the charged particle. This approximation is based on the property that the electromagnetic field of the relativistic charged particle is similar to the field of a light wave. Indeed, for a fast moving particle, its electromagnetic field is minimum in the direction of motion, with $|\vec{E}_{\parallel}| = q_e/z^2(1 - v^2/c^2)$, and maximum in the orthogonal (transverse) direction, with $|\vec{E}_{\perp}| = q_e/b^2/\sqrt{(1 - v^2/c^2)}$, where v is the constant speed of the particle, c the light velocity and z, b the distance to the charge q_e in the direction of motion and in the orthogonal direction, respectively. Then, it is obvious that when v is increasing close to c, $\vec{E}_{\parallel}$ is falling to zero while the field becomes mainly orthogonal ($\theta \simeq \pi/2$) with an angular spread in θ of order $\sqrt{(1 - v^2/c^2)}$.

The integrated equivalent photon distribution $n(\omega)$ indicates how many photons with energy ω are contained in the equivalent swarm of photons simulating the strong transverse electromagnetic fields of a charged particle moving with nearly the speed of light. However, one has no information on how many photons with a given frequency do occur at a certain transverse distance from the straight trajectory of the particle. Deriving the expression of the equivalent photon distribution of the fast moving proton without neglecting the transverse distance (or *impact parameter*) dependence means that one should determine this distribution as a function of the energy of the photon and the distance $|\vec{b}| \equiv b$ to the charged particle trajectory.

By definition, the photon distribution is given by the norm of the Poynting vector [61]:

$$n(\vec{b}, \omega) = \frac{1}{\pi\omega} \left| \vec{E}_{\perp}(\vec{b}, \omega) \right|^2 , \tag{2.22}$$

This expression describes the number of photons (per transverse area $\mathrm{d}^2\vec{b}$) of energy ω existing at a transverse distance b from the center of the charged particle. Obviously, this number does not depend on the orientation of $\vec{b}$ in the transverse plane, which implies $n(\vec{b}, \omega) = n(b, \omega)$.

In the first part of the derivation, one should assume that the projectile is point-like. This hypothesis will be relaxed in a second step. From the Coulomb's law for the EM field of a point charge, one can obtain immediately the transverse EM field of the fast moving point-like particle:

$$\vec{E}_\perp(b,t) = \frac{q_e}{\gamma^2}\frac{\vec{b}}{(t^2+\frac{b^2}{\gamma^2})^{3/2}} \ , \tag{2.23}$$

where t is time, q_e is the electric charge of the particle and γ its Lorentz contraction factor. One can take the Fourier transform of this expression, in order to obtain the field as a function of the variables $(\vec{b},\omega)$. It reads:

$$\vec{E}_\perp(b,\omega) = \frac{q_e}{\gamma^2}\int\frac{\mathrm{d}\omega}{2\pi}e^{i\omega t}\frac{\vec{b}}{(t^2+\frac{b^2}{\gamma^2})^{3/2}} \ . \tag{2.24}$$

Then, one can use a mathematical identity of Fourier integrals to rewrite Equation (2.24) in the form:

$$\vec{E}_\perp(b,\omega) = q_e\int\frac{\mathrm{d}^2\vec{q}_\perp}{(2\pi)^2}e^{-i\vec{b}\cdot\vec{q}_\perp}\frac{(-i\vec{q}_\perp)}{q_\perp^2+\frac{\omega^2}{\gamma^2}} \ , \tag{2.25}$$

where $\vec{q}_\perp$ is the transverse momentum of equivalent photons. From Equation (2.22), the relevant distribution of photons reads:

$$n(b,\omega) = \frac{q_e^2}{\pi\omega}\left|\int\frac{\mathrm{d}^2\vec{q}_\perp}{(2\pi)^2}e^{-i\vec{b}\cdot\vec{q}_\perp}\frac{(-i\vec{q}_\perp)}{q_\perp^2+\frac{\omega^2}{\gamma^2}}\right|^2 . \tag{2.26}$$

At this stage, the point-like hypothesis of the particle can be relaxed. Equation (2.26) becomes:

$$n(b,\omega) = \frac{q_e^2}{\pi\omega}\left|\int\frac{\mathrm{d}^2\vec{q}_\perp}{(2\pi)^2}e^{-i\vec{b}\cdot\vec{q}_\perp}\vec{q}_\perp\frac{F(q_\perp^2+\frac{\omega^2}{\gamma^2})}{q_\perp^2+\frac{\omega^2}{\gamma^2}}\right|^2 , \tag{2.27}$$

where $F(.)$ is the electromagnetic form factor of the source particle, that can be measured experimentally. Equation (2.27) can be simplified after writing $\mathrm{d}^2\vec{q}_\perp$ as $\mathrm{d}^2\vec{q}_\perp = q_\perp \mathrm{d}q_\perp \mathrm{d}\phi$. The integral over the azimuthal angle ϕ can be computed independently from the integral on the modulus $q_\perp$. For this, one needs to express $\vec{q}_\perp$ as $(q_\perp\cos\phi, q_\perp\sin\phi)$ and then, one can use the definition of the modified Bessel's function of first order $J_1(a) = \frac{1}{2\pi}\int_{-\pi}^{\pi}\mathrm{d}\phi\ e^{i\phi}e^{-ia\sin\phi}$. Altogether, the $n(b,\omega)$ reads [61]:

$$\begin{aligned} n(b,\omega) &= \frac{Z^2\alpha_{em}}{\pi^2\omega}\left|\int \mathrm{d}q_\perp q_\perp^2\frac{F(q_\perp^2+\frac{\omega^2}{\gamma^2})}{q_\perp^2+\frac{\omega^2}{\gamma^2}}J_1(bq_\perp)\right|^2 \\ &= \frac{Z^2\alpha_{em}}{\pi^2\omega}\left|\int \mathrm{d}q_\perp q_\perp^2\frac{F(Q^2)}{Q^2}J_1(bq_\perp)\right|^2 , \end{aligned} \tag{2.28}$$

where the Z is the electric charge of the colliding particle in the electron charge (e) units, and the virtuality of the photon is introduced:

$$Q^2 = -q^2 = q_\perp^2 + \frac{\omega^2}{\gamma^2} = q_\perp^2 + Q^2_{\text{min}}. \tag{2.29}$$

The minimum possible virtuality, Q^2_{min}, can be expressed as:

$$Q^2_{\text{min}} = \frac{m_p^2 x^2}{1-x}\ , \tag{2.30}$$

where m_p is the mass of the proton and x is the energy fraction of the proton carried by the photon, $x = 2\omega/\sqrt{s}$.

2.2.2 Equivalent photons of the proton

Using the form factor of the proton from Section 2.1.2, Equation (2.28) takes the form

$$n(b,\omega) = \frac{\alpha_{em}}{\pi^2\omega}\left|\int dq_\perp q_\perp^2 \frac{G_D(Q^2)}{Q^2}\left[(1-x)\frac{4m_p^2+Q^2\kappa_p^2}{4m_p^2+Q^2} + \frac{1}{2}x^2\frac{Q^2}{q_\perp^2}\kappa_p^2\right]^{\frac{1}{2}} J_1(bq_\perp)\right|^2, \tag{2.31}$$

where the dipole parametrization of the proton electromagnetic form factors are used and x is the energy fraction of the proton carried by the photon. It is worth to note that the electromagnetic coupling constant α_{em} is taken as $\alpha_{em}(Q^2 \simeq 0) = 1/137.035$ throughout the calculations, following the property that the photons entering the interaction are quasi-real.

The relation (2.31) for $n(b,\omega)$ corresponds to the equivalent photon distribution (for one proton) when the impact parameter dependence is taken into account. Equivalent photon distributions for 3.5 TeV proton are presented in Figure 2.8, as a function of the impact parameter for different photon energies. The overall shapes of these distributions can be easily understood. At very large b values, $n(b,\omega)$ behaves asymptotically as $\frac{1}{b}e^{-2\omega b/\gamma}$. At very small b values, the photon distributions are damped due to the effects of form factors and finite size of the proton. One can remark that Equation (2.21) can be re-derived from expression (2.31) after replacing $n(\omega_1)$ by the integral of $n(b_1,\omega_1)$ for all b_1, and similarly for the second photon variables independently.

Previous studies have been done using Equation (2.21) in order to compute cross sections at LHC energies for various exclusive two-photon processes in pp collisions, $pp(\gamma\gamma) \to ppX$, corresponding to different final states X [70, 71]. The EPA applied to pp collisions can be efficiently and conveniently used with Monte Carlo techniques. Some results obtained in this way are displayed in Figure 2.9 for different pp center-of-mass energies,

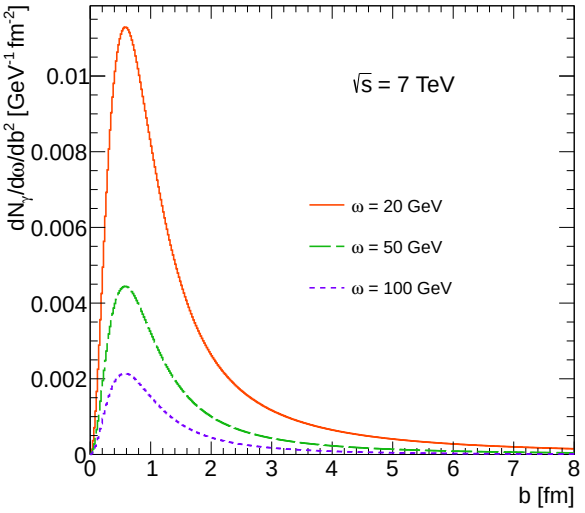

FIGURE 2.8: Equivalent photon distributions of the fast moving proton, with momentum of 3.5 TeV, for different energies of the photon, as function of the transverse distance b.

$\sqrt{s}$. The exclusive production of pairs of muons and pairs of W bosons have been generated using the HERWIG++ generator [72]. The exclusive production of the Higgs boson is computed according to *Higgs Effective Field Theory* (HEFT) [73–76]. Obviously, this reaction appears as a point in Figure 2.9, representing the total cross section, at the Higgs mass of 125 GeV. Finally, the exclusive production of pairs of photons (so-called *light-by-light scattering* [77]) has been generated using the FPMC generator [78] at large $W_{\gamma\gamma}$ where the $\gamma\gamma \to \gamma\gamma$ sub-process cross section is dominated by one-loop diagrams involving W bosons [79].

2.2.3 Proton finite-size effects

The full expression as given in Equation (2.31) is necessary when one wants to take into account effects that depend directly on the transverse space variables of the reaction. These effects occur e.g. when there are strong-interaction exchanges between the protons, in addition to the two-photon interaction. These extra contributions may alter the kinematic distributions of the final-state particles, and may also produce additional low-momentum hadrons. Therefore, when the finite sizes of colliding protons is considered, one should perform the replacement:

$$n(\omega_1)\ n(\omega_2) \to \iint \mathrm{d}^2\ \vec{b}_1 \mathrm{d}^2\vec{b}_2\ n(b_1,\omega_1)\ n(b_2,\omega_2)\ , \tag{2.32}$$

where the correlations between the transverse distances b_1 and b_2 prevent from performing the integrations independently. Indeed, there are important geometrical constraints to encode: the two photons need to interact at the same point outside the two protons,

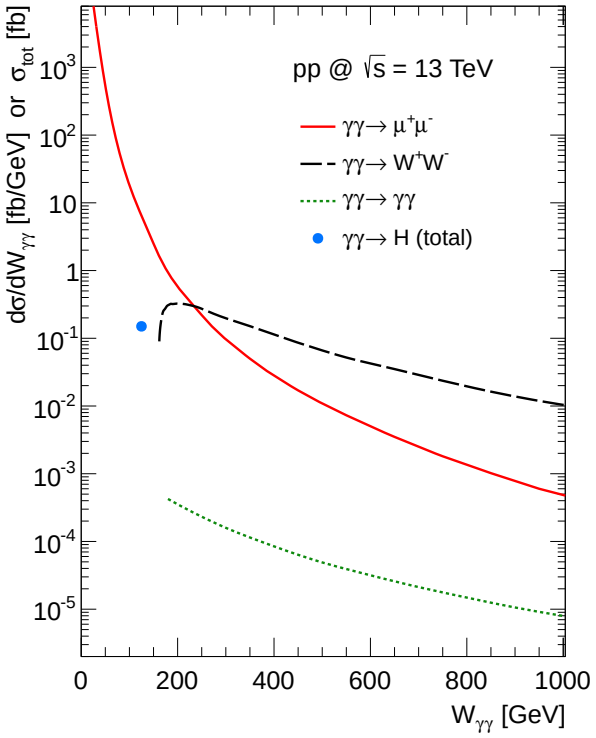

FIGURE 2.9: Differential cross sections for various processes $pp(\gamma\gamma) \to ppX$ at $\sqrt{s} = 13$ TeV generated using EPA formalism. For the exclusive Higgs production, the total cross section is shown. The exclusive production of pairs of photons has been generated at large $W_{\gamma\gamma}$ where the cross section is dominated by one-loop diagrams involving W bosons.

of radii r_p, while the proton halos do not overlap. This implies minimally that $b_1 > r_p$, $b_2 > r_p$ and $|\vec{b}_1 - \vec{b}_2| > 2r_p$ (see the Figure 2.10). The last condition clearly breaks the factorization in the variables b_1 and b_2 of the integral (2.32). In these conditions, the proton radius r_p is the radius determined in the transverse plane, that is taken to be 0.64 fm, as measured by the H1 collaboration [80]. It is worth to notice that it would be possible to keep the factorization by imposing stronger constraints, like $b_{1,2} > 2r_p$. However, this last condition prevents configurations where the two protons are very close and produce very energetic photon–photon collisions.

Equation (2.32) is a first step towards encoding proton finite size effects. They can be refined by including the so-called *pp non-inelastic interaction probability* [81], which depends explicitly on the transverse variables, $P_{\text{non-inel}}(|\vec{b}_1 - \vec{b}_2|)$. Then, Equation (2.32) takes the form:

$$n(\omega_1)\; n(\omega_2) \to \iint \mathrm{d}^2\vec{b}_1\; \mathrm{d}^2\vec{b}_2\; n(b_1,\omega_1)\; n(b_2,\omega_2)\; P_{\text{non-inel}}(|\vec{b}_1 - \vec{b}_2|)\;, \tag{2.33}$$

where the bounds of integrations are still $b_1 > r_p$, $b_2 > r_p$. The non-overlapping condition, $|\vec{b}_1 - \vec{b}_2| > 2r_p$, is not needed any longer. It follows as a consequence of the

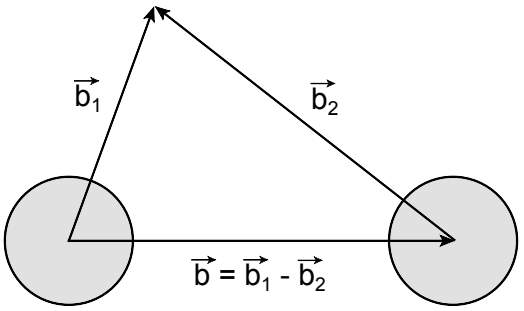

FIGURE 2.10: Schematic view of the two protons and the transverse distances $\vec{b}_1$ and $\vec{b}_2$. The difference $\vec{b} = \vec{b}_1 - \vec{b}_2$ is also pictured. It is clear from this view that the geometrical non-overlapping condition of the two protons corresponds to $|\vec{b}_1 - \vec{b}_2| > 2r_p$.

effect of the function $P_{\text{non-inel}}(|\vec{b}_1 - \vec{b}_2|)$. Indeed, this function represents the probability that there is no interaction (no overlap) between the two colliding protons in the impact parameter space. Following [81], one can make the natural assumption that a probabilistic approximation gives a reasonable estimate of the absorption effects. Then the pp non-inelastic interaction probability can be written as:

$$P_{\text{non-inel}}(b) = \left|1 - \exp\left[-b^2/(2B)\right]\right|^2 \ , \tag{2.34}$$

where the value of $B = 19.7$ GeV^{-2} is taken from a measurement at $\sqrt{s} = 7$ TeV by the ATLAS experiment [82]. At $\sqrt{s} = 13$ TeV, the extrapolated value $B = 21$ GeV^{-2} is used in the calculations. In Figure 2.11, the $P_{\text{non-inel}}(b)$ is compared with the step function $\Theta(b - 2r_p)$, which is the first approximation that can be performed to quantify a non-overlapping condition between both colliding protons. One should observe that both functions are roughly comparable. However, one can expect some deviations when performing more accurate computations of cross sections using $P_{\text{non-inel}}(b)$ in Equation (2.33), and then in Equation (2.21).

The first important issue is to quantify the size of the correction when one can take into account the finite size of colliding protons. Therefore, the survival factor can be defined as:

$$S^2_{\gamma\gamma} = \frac{\int_{b_1>r_p}\int_{b_2>r_p} \mathrm{d}^2\vec{b}_1\mathrm{d}^2\vec{b}_2 \ n(\vec{b}_1,\omega_1)n(\vec{b}_2,\omega_2) \ P_{\text{non-inel}}(|\vec{b}_1 - \vec{b}_2|)}{\int_{b_1>0}\int_{b_2>0} \mathrm{d}^2\vec{b}_1\mathrm{d}^2\vec{b}_2 \ n(\vec{b}_1,\omega_1)n(\vec{b}_2,\omega_2)} \ , \tag{2.35}$$

where the numerator contains the finite size effects encoded in the function $P_{\text{non-inel}}(b)$ and dedicated bounds of the integrations over $\vec{b}_1$ and $\vec{b}_2$, whereas the denominator represents the integral over all impact parameters with no constraint. Trivially, this factor will always be smaller than unity.

Then, the deviation with respect to unity will quantify the overestimation done when the finite size effects are neglected. This is first illustrated in Figure 2.12, where the two-dimensional dependence of $S^2_{\gamma\gamma}$ as a function of the energy fractions of the protons

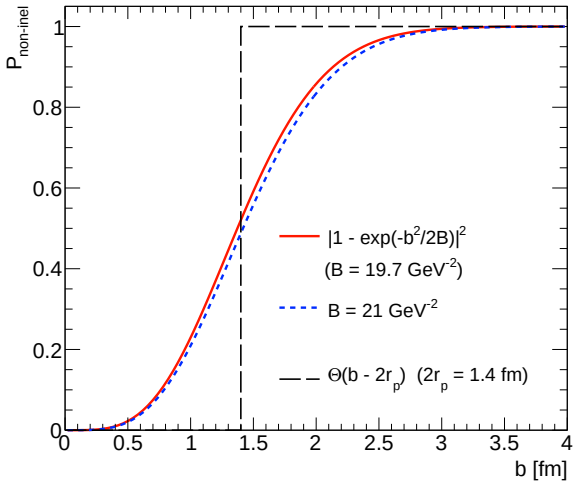

FIGURE 2.11: Function $P_{\text{non-inel}}(b) = |1 - \Gamma(b)|^2$ compared with the step function $\Theta(b - 2R)$. $P(b)$ representing the probability for no inelastic interaction in pp collision at impact parameter b.

carried by the interacting photons, x_1 and x_2, is presented. Then, the survival factor is displayed as a function of experimentally measurable variables in Figures 2.13 and 2.14. Figure 2.13 presents the behavior of the survival factor as a function of the center-of-mass energy of the photon–photon system ($W_{\gamma\gamma}$) at zero-rapidity. Different curves are displayed corresponding to the different center-of-mass energies, $\sqrt{s}$, for the pp collision. A common feature is observed. For all curves, the survival factor is decreasing as a function of $W_{\gamma\gamma}$, to reach values of ∼0.3 at $W_{\gamma\gamma} = 1$ TeV for $\sqrt{s} = 7$ TeV or 8 TeV and ∼0.4 at $W_{\gamma\gamma} = 1$ TeV for $\sqrt{s} = 13$ TeV. This is a large effect, due to the fact that for larger values of $W_{\gamma\gamma}$, smaller values of $b = |\vec{b}_1 - \vec{b}_2|$ are probed, and thus the integral at the numerator of the survival factor (2.35) becomes smaller. Indeed, when the photon–photon energy becomes larger and larger, this is understandable that the probability of no inelastic interaction becomes smaller and smaller. Figure 2.14 illustrates the behavior of the survival factor as a function of the rapidity of the photon–photon system, for different $W_{\gamma\gamma}$. Obviously, the same effect is observed, that when $W_{\gamma\gamma}$ increases the survival factor decreases. In addition, this figure shows the small dependence as a function of the rapidity $y_{\gamma\gamma}$. However, for possible measurements at the LHC, the rapidity domain covered is close to zero. Therefore, the dependence in $y_{\gamma\gamma}$ has a marginal effect.

Finally, one should notice that this formalism does not directly apply for the proton-dissociation processes, which are less well determined theoretically, and in particular require more significant corrections due to proton absorptive corrections.

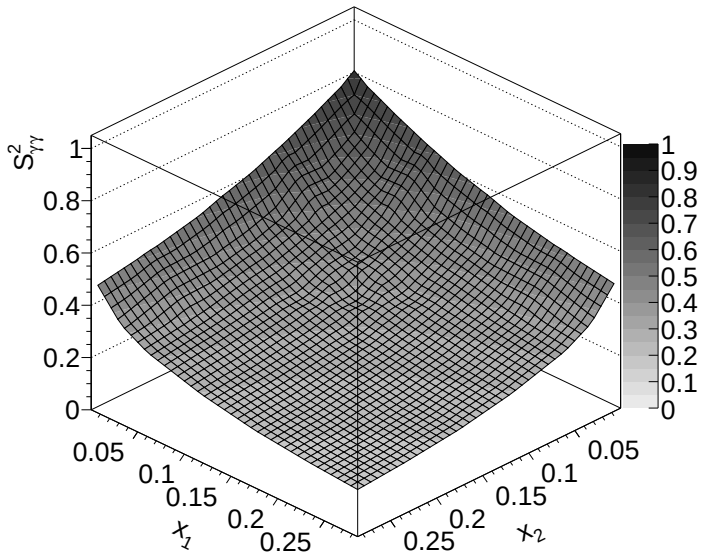

FIGURE 2.12: The survival factor as a function of the energy fractions of the protons carried by the interacting photons, x_1 and x_2.

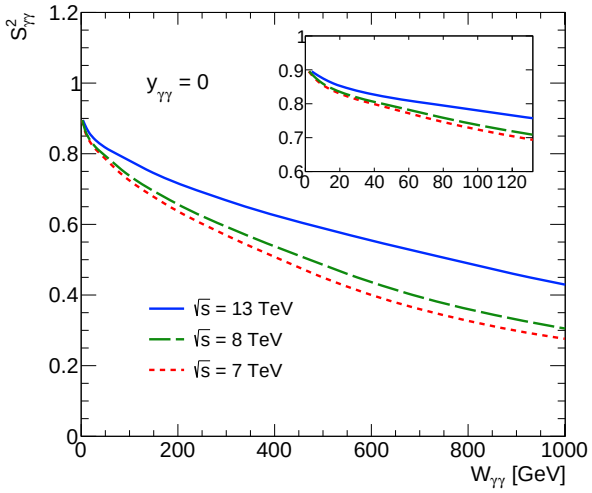

FIGURE 2.13: The survival factor at zero-rapidity as a function of the photon–photon center-of-mass energy.

2.3 Proton-dissociative reactions

For the inelastic case, in which the proton dissociates into a hadronic system N at low mass m_N, in general below 20 GeV, the proton form factors need to be replaced by the inelastic proton structure function, $F_2(z, Q^2)$, where z represents the longitudinal momentum fraction of the proton carried by the struck parton, see Section 1.3.3. At first approximation, the Q^2 dependence of F_2 can be neglected in the kinematic range

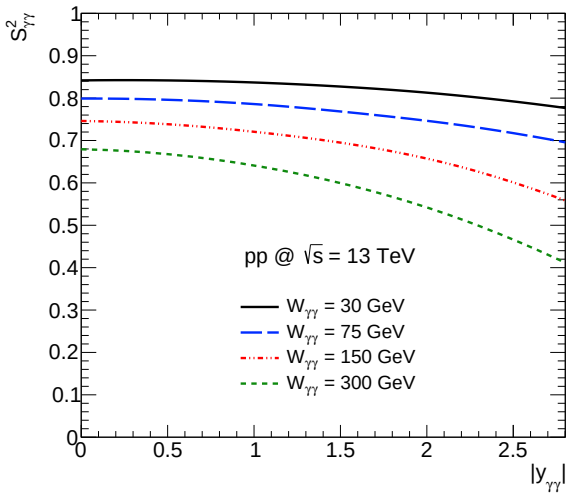

FIGURE 2.14: The survival factor for different photon–photon center-of-mass energies displayed as a function of the rapidity of the two-photon system.

of interest presented here. Then, the inelastic photon spectrum, n_i, reads [83]:

$$n_{\mathrm{i}}(x) = \frac{\alpha_{em}}{\pi x}\int_{z_{\min}}^{1}\frac{\mathrm{d}z}{z}F_2(z)\int_{Q^2_{\min}}^{\infty}\frac{\mathrm{d}Q^2}{z^2Q^2}\left(z(1-\frac{Q^2_{\min}}{Q^2})(1-x)+\frac{x^2}{2}\right), \tag{2.36}$$

where x is defined as in Section 2.2.2 as the energy fraction of the proton carried by the photon. In Equation (2.36), the bounds in Q^2 also depend on the z values, which means that the photon spectrum depends on the inelastic proton structure. Then, the simplest proton dissociation models rely on parametrizations of $F_2(z)$.

It can be noticed that the only difference between the elastic and the quasi-elastic processes is the treatment of the γp vertex. For proton excitation processes, where the low-multiplicity states are usually produced, the photon virtualities are usually below 5 GeV^2. For example, the Brasse parametrization [84], based on fits to the experimental data on the measurement of the total γp cross sections, is valid for photon virtualities $Q^2 < 5$ GeV^2 and masses of the dissociating system $m_N < 2$ GeV.

A more general expression can be written including also $O(\alpha_s)$ corrections, due to the quark–gluon interactions. Figure 2.15 shows four new diagrams which have to be considered at the $O(\alpha_{em})$ proton vertex. This includes initial and final-state gluon radiation as well as the photon–gluon production of quark and antiquark pair ($\gamma g \to q\bar{q}$).

Also from Equation (2.36), it is clear that the dissociative scenario is more complex to handle than the elastic one. In particular, the inelastic structure of the proton built up by quarks and gluons enters in the photon spectrum. It is possible to incorporate this effect by treating the photon from the proton as a parton - and construct the relevant "photon parton distribution", or *photon-PDFs*, $\gamma^p(x, Q^2)$ [85]. Since the emitted photon in such

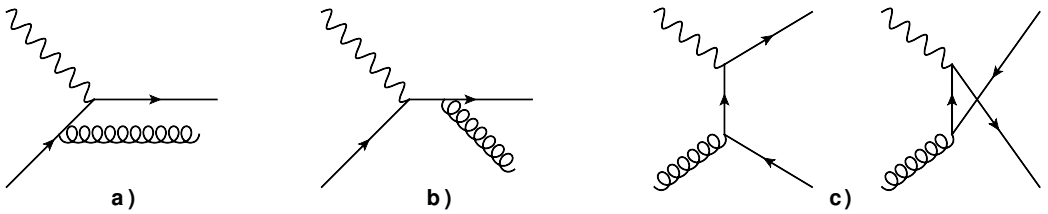

FIGURE 2.15: Higher-order diagrams for the $O(\alpha_s)$ corrections to the $\gamma q \to q$ process: (a) initial-state radiation, (b) final-state radiation, (c) quark pair production with interchange.

approach carries away some of the quark's momentum, the normal DGLAP evolution equations are slightly modified.

The only way to find out $\gamma^p(x, Q^2)$ is to perform a full global parton distribution function analysis with QED corrections included, and to compare with the results of a standard QCD-only analysis. The first qualitative estimates of the effect on the evolution of parton distribution functions was made in [86] for MRST2004QED PDFs, and later in [22] that defines the NNPDF2.3QED PDF set. The latter includes the fit also to the LHC data when constructing the photon-PDFs, starting from the initial scale of $\mu_0^2 = 2$ GeV^2. However, since the fits are performed to the inclusive pp and ep data, the final PDF set is affected by sizeable uncertainties, typically of order 50%.

2.4 Experimental considerations

The two-photon exchange reactions in a pp collider experiment can be characterized by striking experimental signatures. Indeed, for exclusive two-photon production of object X, large regions of the detector are free of any hadronic activity between the central state and the outgoing protons. Additionally, due to the very low photon virualities involved, the central state X has a very small transverse momentum, defined as $p_{T,X} = p_X \sin\theta$, where p_X is the total momentum of the object X.

For exclusive two-photon processes, each of the incoming proton survives, scattered at very small angle, and escapes undetected along the accelerator beamline. For a 7 TeV pp center-of-mass energy and two-photon invariant masses $W_{\gamma\gamma} > 10$ GeV, one can find that the average photon virtuality for the exclusive reactions is of the order of 0.01 GeV^2, which corresponds to proton scattering angles of the order of 20 µrad.[6] Far away from the experiment interaction point (IP), some dedicated devices may detect such protons and tag the photon-exchange reactions with the precise mass reconstruction of the centrally produced system. Studies on the installation of such forward proton-tagging stations at 204 m and 212 m of the IP within the ATLAS-AFP project are discussed in Chapter 6.

[6] This also validates the low photon virtuality approximation needed in the EPA approach

Unless both outgoing protons are detected, the semi-exclusive two-photon production, involving single or double proton dissociation, becomes an irreducible background to the fully exclusive reaction. However, due to the different photon virtualities, the proton-dissociative processes have significantly different kinematic distributions compared to the pure exclusive case, allowing an effective separation of the signal from this background. The experimental aspects related to the selection of exclusive events, based on the case of two-photon production of lepton pairs, are provided in Chapter 8.

The photon flux is proportional to the square of the colliding particle charge, so the photon fluxes can be enhanced by orders of magnitude when using nucleus–nucleus collisions for two-photon exclusive reactions. Considering Pb-Pb collisions at the LHC, this immediately leads to an enhancement factor of 10^7 in the total cross sections for two-photon exclusive processes in comparison to pp collisions. However, one should also consider the maximum available equivalent photon frequencies, which can be derived from the uncertainty principle [61]:

$$\Delta t \cdot \Delta E \simeq 1 \Longrightarrow \frac{R}{\gamma v} \cdot \omega \simeq 1 \overset{v \to c}{\Longrightarrow} \omega_{\text{max.}} \simeq \frac{\gamma}{R} \ , \tag{2.37}$$

where Δt is the collision time, γ is the Lorentz contraction factor, R denotes the nuclear radius and v the velocity of the nucleus. For the Pb-mode at LHC energies ($\gamma_{\text{nominal}} = 2750$) photons appear with energies only up to about 80 GeV contained in the electromagnetic fields of the nuclei.

2.5 Photon-induced MC generators for pp collisions

In order to test the reliability of MC generators in regard of two-photon processes in pp collisions, extended MC studies are performed with muon pair production in the final state as an illustration. Photon-induced processes in pp collisions are already implemented in various MC generators. For the simulation of exclusive processes, one can use:

- LPAIR [87, 88] - calculations include full leading-order QED process using specially developed algebraic form of the squared matrix element. The photon flux is implemented in the context of EPA. The VEGAS [89] algorithm is used for the cross section integration.
- HERWIG++ [72] - appropriate photon flux is implemented in the `BudnevPDF` function from `ThePEG` [90] software. Default functions are used for the final integration.

- FPMC [78] - this generator is based on the HERWIG [91]. Default HERWIG routines are used for the EPA photon flux and the final integration.

The proton-dissociative processes, both single- and double-dissociative are implemented in the LPAIR program. This generator uses the proton structure functions for each of the dissociative protons to calculate the final cross section. The Brasse [84] and Suri–Yennie [92] structure functions for proton dissociation are used. For photon virtualities $Q^2 < 5$ GeV^2 and masses of the dissociating system, $m_N < 2$ GeV, low-multiplicity states from the production and decays of Δ resonances are usually created. For higher Q^2 or m_N, the system decays to a variety of resonances, which produce a large number of forward particles. The LPAIR package is interfaced to JETSET [93], where the LUND [94] fragmentation model is implemented.

Apart from the structure functions approach in LPAIR, one can use exact photon-PDFs in the proton. This feasibility is already implemented in PYTHIA 8 [95]. After choosing the relevant PDFs, namely NNPDF2.3QED [96] or MRST2004QED[7] [86], PYTHIA 8 offers all machinery to simulate proton-dissociative processes. Depending on the multiplicity of the dissociating system, the default PYTHIA 8 string or mini-string fragmentation model is used for proton dissociation. All of these features should be valuable when exploring the new experimental regimes with two-photon processes at higher energy scales. Unfortunately, PYTHIA 8 provides only the double-dissociative process simulation.

2.5.1 Exclusive reactions

In order to test the compatibility of the different MC generators with respect to the exclusive dilepton processes, 100 000 events at $\sqrt{s} = 7$ TeV are generated for each generator. Furthermore, the kinematic cuts for leptons are imposed to account for the limited detector acceptance: only muons with $p_{\mathrm{T}}^{\mu} > 10$ GeV and $|\eta^{\mu}| < 2.5$ are considered. Moreover, additional requirement for dimuon invariant mass $m_{\mu^+\mu^-} > 20$ GeV is applied. Figure 2.16 shows dimuon invariant mass distribution comparison between the different MC generators. All three generators agree with each other within statistical uncertainties of the simulated event samples. The same agreement is observed in leading muon (i.e. the muon with higher transverse momentum) kinematic distributions (Figure 2.17). The total cross section comparison in the phase-space region considered is presented in Table 2.1.

[7] There are currently no other photon-PDFs available for this type of reactions

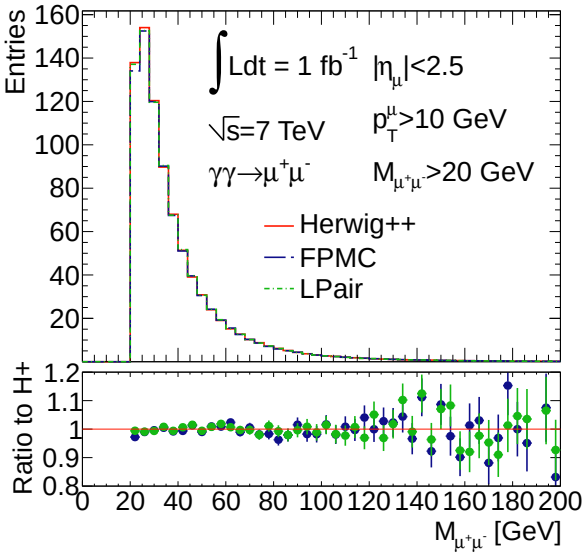

FIGURE 2.16: Dimuon invariant mass distribution comparison between HERWIG++ (red line), FPMC (blue) and LPAIR (green) event generators for exclusive $\gamma\gamma \to \mu^+\mu^-$ production in pp collisions. Distributions are normalized to 1 fb^{-1}. The ratios of FPMC (blue markers) and LPAIR (green) to HERWIG++ are also shown with statistical error bars.

Generator	HERWIG++	FPMC	LPAIR
Cross section	0.83 pb	0.84 pb	0.83 pb

TABLE 2.1: Total cross section comparison for exclusive $\gamma\gamma \to \mu^+\mu^-$ processes in pp collisions between various MC generators. For the muons, invariant mass cut, $m_{\mu^+\mu^-} > 20$ GeV, with $p_{\mathrm{T}}^{\mu} > 10$ GeV and $|\eta^{\mu}| < 2.5$ are used.

In order to verify the kinematic properties of the dimuon system, one can define the variable

$$\textit{dimuon acoplanarity} \equiv 1 - \left|\frac{\phi_{\mu^+} - \phi_{\mu^-}}{\pi}\right| = 1 - |\Delta\phi_{\mu^+\mu^-}|/\pi \ , \tag{2.38}$$

which represents the difference between azimuthal angles of the muons. This variable clearly shows when the muons are emitted back-to-back ($1 - |\Delta\phi_{\mu^+\mu^-}|/\pi = 0$) or are collinear ($1 - |\Delta\phi_{\mu^+\mu^-}|/\pi = 1$) in the transverse plane. Dimuon acoplanarity and transverse momentum difference ($\Delta p_{\mathrm{T}}^{\mu^+\mu^-} = |p_{\mathrm{T}}^{\mu^+} - p_{\mathrm{T}}^{\mu^-}|$) comparisons are presented in Figure 2.18. As expected, the dimuon acoplanarity distribution tends to zero - since the photons entering to the exclusive reaction are quasi-real. One can also observe the disagreement between FPMC and the other tested generators. This can be related with some problems with the EPA photon flux calculations in FPMC.

To cross-check the dimuon kinematic properties with respect to the longitudinal plane, it is preferable to use the scattering angle, θ, defined in two-photon rest frame. It is also equivalent to the angle between the lepton pair direction and the beam axis in the

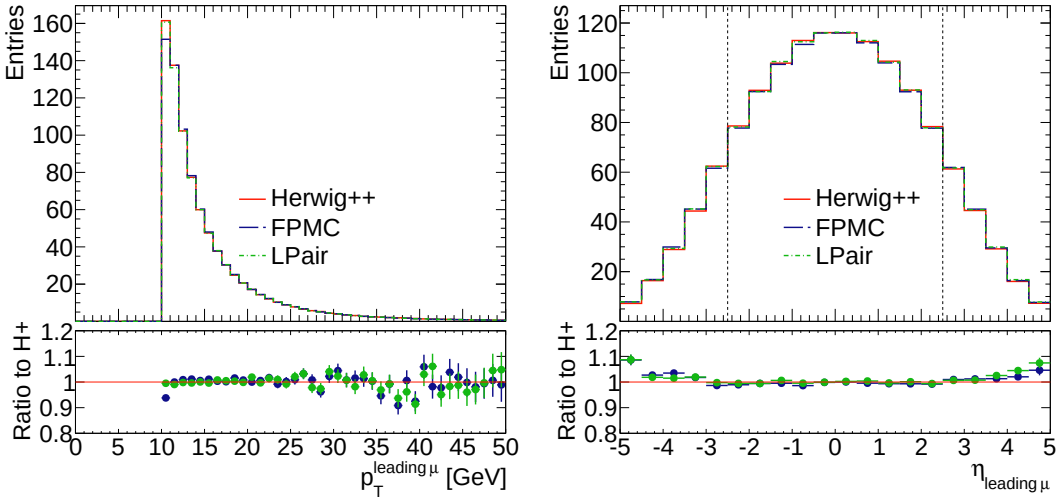

(a) (b)

FIGURE 2.17: (a) Leading muon transverse momentum and (b) pseudorapidity distributions for different MC generators for exclusive $\gamma\gamma \to \mu^+\mu^-$ production in pp collisions: HERWIG++, FPMC and LPAIR. Distributions are normalized to 1 fb^{-1}.

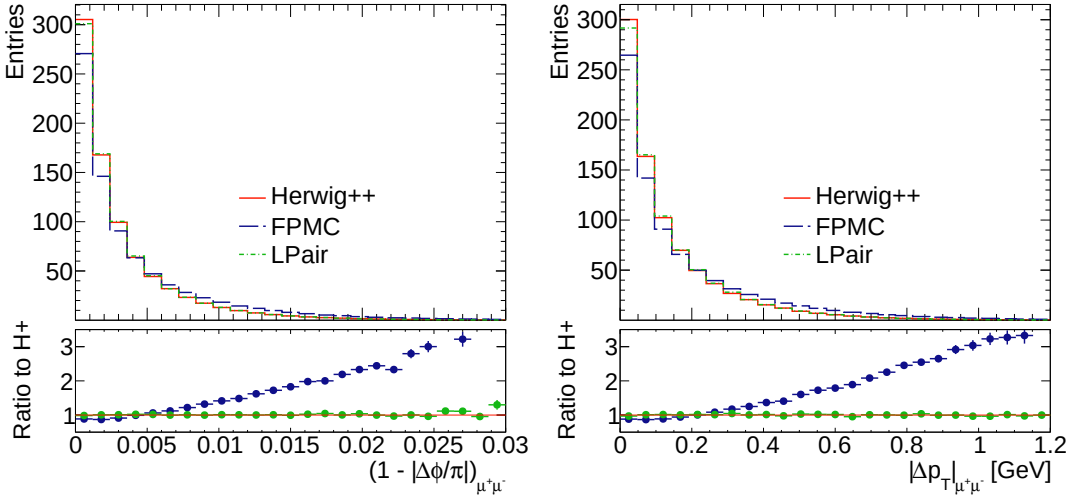

(a) (b)

FIGURE 2.18: (a) Dimuon acoplanarity and (b) muons transverse momentum difference distributions comparison between HERWIG++, FPMC and LPAIR generators for exclusive $\gamma\gamma \to \mu^+\mu^-$ production in pp collisions. Distributions are normalized to 1 fb^{-1}.

dilepton rest frame. One can use the relation:

$$\Delta\eta \equiv |\eta_{\mu^+} - \eta_{\mu^-}| = \ln\left(\frac{1 + |\cos\theta|}{1 - |\cos\theta|}\right) , \tag{2.39}$$

to easily calculate $|\cos\theta|$ function. Figure 2.19 shows the scattering angle distribution comparison for the three studied generators. A good agreement is observed. Since the elementary cross section for $\gamma\gamma \to \mu^+\mu^-$ sub-process reads as a function of $\cos\theta$:

$$\frac{\mathrm{d}\sigma}{\mathrm{d}\cos\theta} \propto \frac{1 + \cos^2\theta}{1 - \cos^2\theta} , \tag{2.40}$$

one could anticipate much narrowed behavior when $|\cos\theta| \to 1$. Since the pseudorapidity requirement is imposed on both muons, this results in the cross section suppression for $|\cos\theta| > 0.7$.

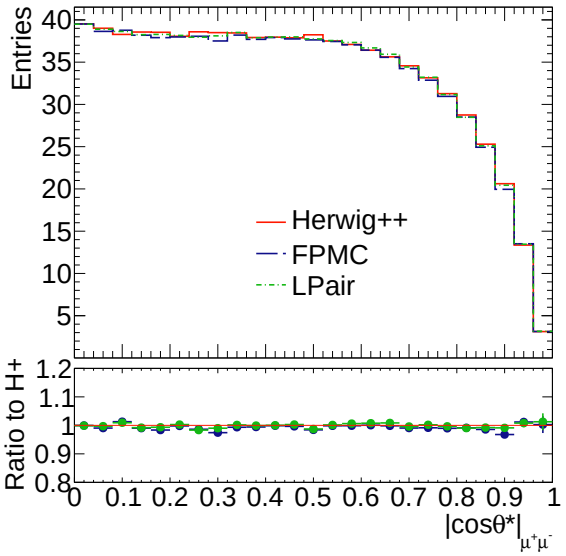

FIGURE 2.19: Comparison of scattering angle distribution between HERWIG++, FPMC and LPAIR event generators for exclusive $\gamma\gamma \to \mu^+\mu^-$ production in pp collisions. Distributions are normalized to 1 fb^{-1}.

2.5.2 Proton-dissociative reactions

Using the same kinematic lepton cuts, additional MC event samples are generated for single-dissociative (LPAIR) and double-dissociative (LPAIR, PYTHIA 8) processes. Figure 2.20 presents the pseudorapidity distribution of particles after the hadronization step[8] (excluding final-state muons from the hard $\gamma\gamma$ interaction). In case of the LPAIR generator, these particles are dominated by the resonances (proton beam remnants), which are emitted mostly in the region of large pseudorapidities. On the other

[8]See the Section 3.3.1 for more details about the hadronization process in MC generators

Generator	LPAIR	LPAIR	PYTHIA 8	PYTHIA 8
Process type	single-diss.	double-diss.	double-diss.	double-diss.
Photon-PDFs	-	-	NNPDF2.3QED	MRST2004QED
Cross section	0.87 pb	1.0 pb	3.7 pb	7.7 pb

TABLE 2.2: Total cross section comparison for proton-dissociative $\gamma\gamma \to \mu^+\mu^-$ processes in pp collisions between various MC generators and photon-PDFs. For muons, invariant mass cut, $m_{\mu^+\mu^-} > 20$ GeV, with $p_{\mathrm{T}}^{\mu} > 10$ GeV and $|\eta^{\mu}| < 2.5$ requirements are used.

hand, in PYTHIA 8 generator, photons are able to couple directly with quarks (see Section 2.3). Together with $O(\alpha_s)$ corrections, this results in emission of additional hadrons in the region of small rapidities. This leads also to the total cross section enhancement, as presented in Table 2.2.

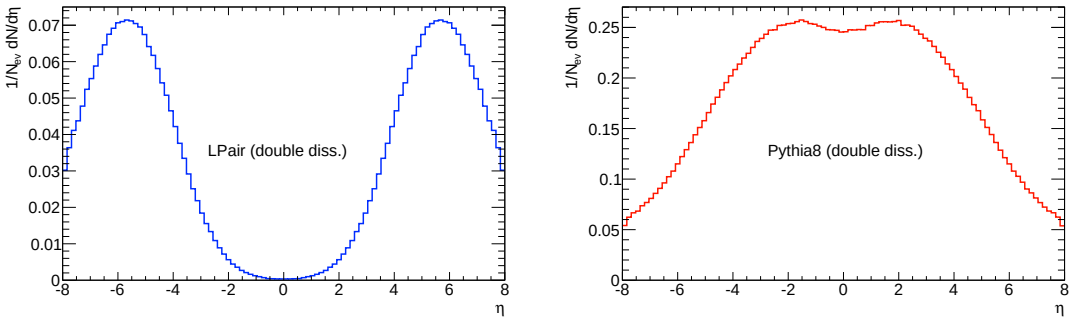

(a) (b)

FIGURE 2.20: Pseudorapidity distribution of particles produced after hadronization step for double-dissociative $\gamma\gamma \to \mu^+\mu^-$ processes in pp collisions for (a) LPAIR and (b) PYTHIA 8 (interfaced with MRST2004QED PDFs) generators.

In order to directly compare double-dissociative LPAIR with PYTHIA 8, one can impose additional pseudorapidity cut on the additional particles produced in an event ($|\eta^{\mathrm{particle}}| > 2.5$). This allows for approximate separation of the reactions with deep-inelastic photon-quark interactions. Figure 2.21 shows dimuon invariant mass distribution comparison for double-dissociative process modelling. Large incompatibility is observed between the LPAIR (PYTHIA 8 interfaced with MRST2004QED PDFs) and PYTHIA 8 interfaced with NNPDF2.3QED PDFs. This discrepancy is even more visible in the dimuon transverse momentum distribution presented in Figure 2.22. This fact can be used in discriminating different proton-dissociative models with respect to the experimental data.

One can also confront the ratio of proton-dissociative processes to the fully exclusive case. Assuming the imposition of $|\eta| > 2.5$ cut on the additional particles produced in an event (except muons produced via $\gamma\gamma$ interaction), all three components: exclusive,

single- and double-dissociative have the similar total cross sections: about 1 pb in the phase-space region considered.

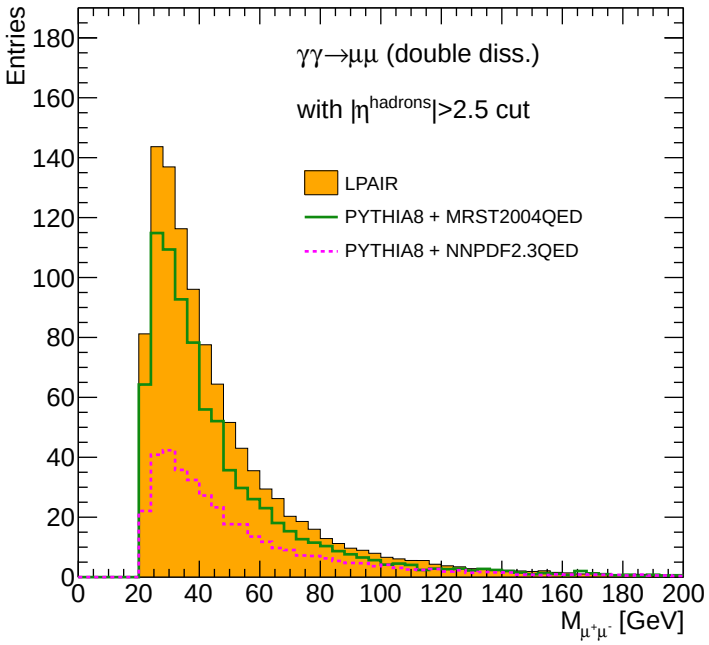

FIGURE 2.21: Dimuon invariant mass distribution comparison for various modelling of double-dissociative $\gamma\gamma$ reactions in pp collisions: events simulated with LPAIR (filled histogram), PYTHIA 8 interfaced with MRST2004QED (solid line) and PYTHIA 8 interfaced with NNPDF2.3QED (dashed line) are presented. Distributions are normalized to 1 fb^{-1}.

2.5.3 Comparison with Drell–Yan process

Photon-induced lepton production can become a non-negligible background to standard Drell–Yan (DY) processes [97], where the quark and antiquark pair annihilate to Z/γ^* boson. The latter decays to a pair of opposite charge, same flavour leptons. The DY process also dominates the inclusive spectrum of muon/electron pairs produced in pp collisions at the LHC. In order to simulate the contributions from DY processes, PYTHIA 8 with AU2 MSTW2008LO [98] set of tunable parameters is chosen with the same kinematic cuts for muons ($m_{\mu^+\mu^-} > 20$ GeV, $p_{\mathrm{T}}^{\mu} > 10$ GeV and $|\eta^{\mu}| < 2.5$). No other specific selection is used. Figure 2.23 presents dimuon invariant mass distribution comparison between the DY and various photon-induced reactions. The ratio of all photon-induced processes to DY can reach $\simeq$5% for the low dimuon invariant mass range. This comes mainly from the double-dissociative contribution (see the Table 2.2). The contribution from photon-induced processes could be even higher if one would include single-dissociative process simulation using PYTHIA 8 with photon-PDFs approach. Unfortunately, an exact implementation of such reactions is not yet available.

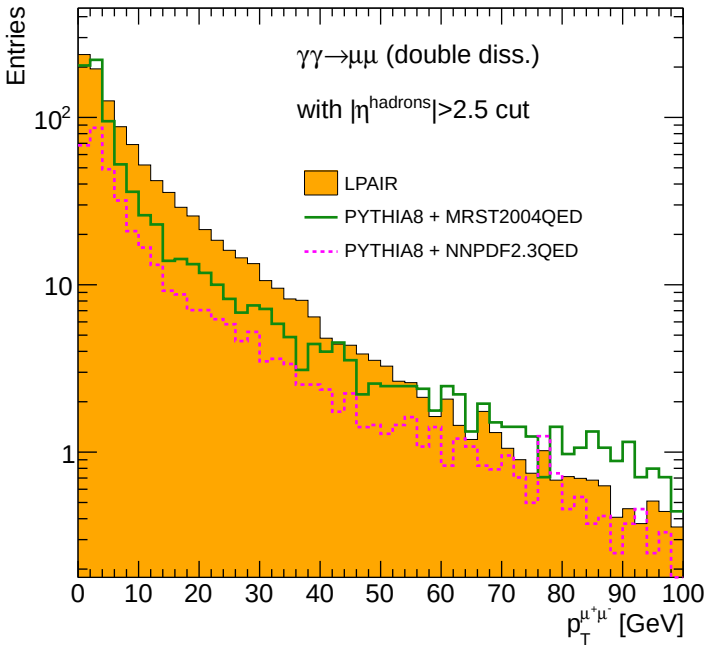

FIGURE 2.22: Dimuon transverse momentum distribution for various modelling of double-dissociative $\gamma\gamma \to \mu^+\mu^-$ reactions: events simulated with LPAIR (filled histogram), PYTHIA 8 interfaced with MRST2004QED (solid line) and PYTHIA 8 interfaced with NNPDF2.3QED (dashed line) are presented. Distributions are normalized to 1 fb^{-1}.

Dimuon acoplanarity and transverse momentum distributions are presented in Figure 2.24. The peaked shape of the exclusive distribution allows to distinguish this part both from the DY and proton-dissociative processes.

Finally, Figure 2.25 presents the scattering angle distribution. One could expect quite different shape in the DY processes associated with spin-1 particle exchange. Indeed the dependence in $\cos\theta$ of the leading-order cross section on $Z/\gamma^* \to \mu^+\mu^-$ process is:

$$\frac{\mathrm{d}\sigma}{\mathrm{d}\cos\theta} \propto 1 + \cos^2\theta \ , \tag{2.41}$$

which is, however, different from the expression (2.39). The differences occur mainly at high $|\cos\theta|$ values, which are suppressed by the dimuon kinematic cuts.

2.5.4 $\mathrm{e}^+\mathrm{e}^-$ and $\tau^+\tau^-$ channels

As it is known that the QED calculations of the sub-process $\gamma\gamma \to \ell^+\ell^-$ involve a dependence in the lepton mass (see Section 2.1.3), one can expect to observe some differences in the predictions with respect to the different lepton flavours involved. However, as shown in Table 2.3, predictions for exclusive $\gamma\gamma \to \ell^+\ell^-$ production cross sections for all three lepton flavours are almost the same. This comes from the fact that the dilepton

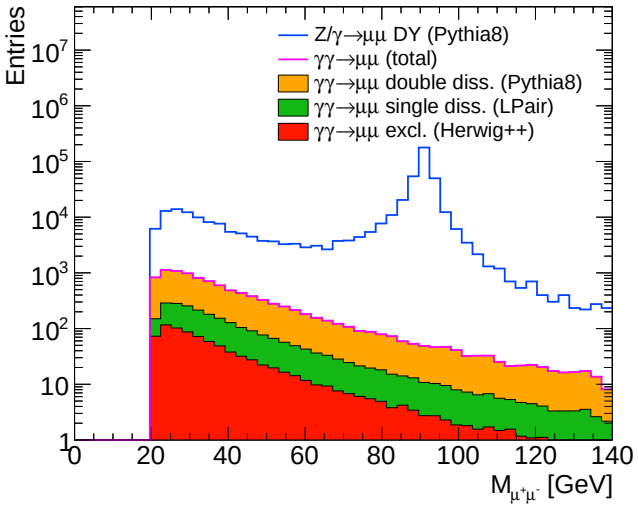

FIGURE 2.23: Dimuon invariant mass distribution comparison between the DY (blue line) and photon-induced processes (magenta line). Different contributions to $\gamma\gamma$ processes: exclusive (HERWIG++ in red), single-dissociative (LPAIR in green) and double-dissociative (PYTHIA 8 interfaced with MRST2004QED PDFs in yellow) are also shown. Distributions are normalized to 1 fb^{-1}.

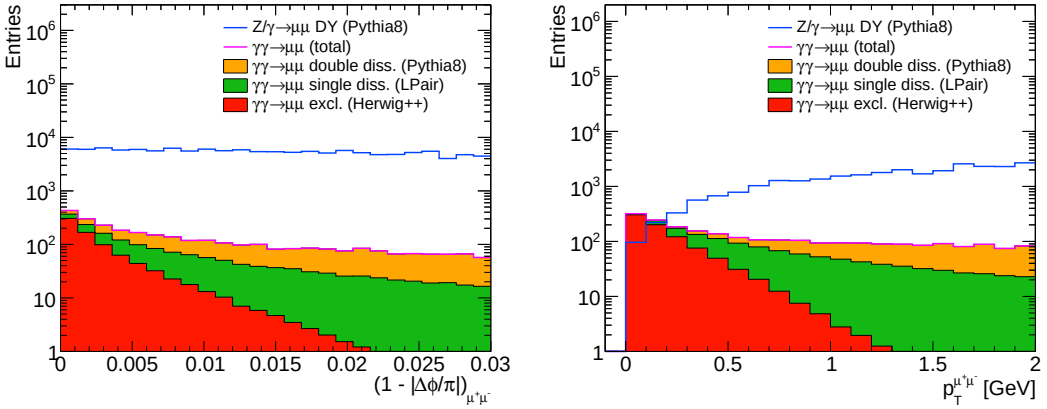

(a) (b)

FIGURE 2.24: Dimuon (a) acoplanarity and (b) transverse momentum distributions comparison between the DY and photon-induced processes. Distributions are normalized to 1 fb^{-1}.

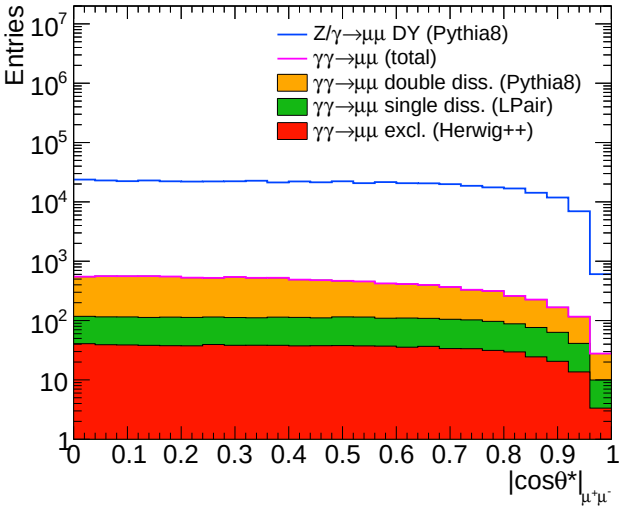

FIGURE 2.25: Scattering angle distribution comparison between the DY and photon-induced muon pair production. Distributions are normalized to 1 fb^{-1}.

Leptons	e^+e^-	$\mu^+\mu^-$	$\tau^+\tau^-$
Cross section	0.83 pb	0.83 pb	0.82 pb

TABLE 2.3: Total cross section comparison for exclusive $\gamma\gamma \to \ell^+\ell^-$ processes in pp collisions between different lepton flavours. Default HERWIG++ generator is used with $m_{\ell^+\ell^-} > 20$ GeV, $p_{\text{T}}^{\ell} > 10$ GeV and $|\eta^{\ell}| < 2.5$ cuts.

invariant mass considered is much above the tau lepton mass. Moreover, lepton pseudorapidity requirement ensures relatively large values of scattering angles, whereas the lepton mass dependence is expected only for very small scattering angles. A similar universality is observed in the dilepton invariant mass and leading lepton p_{T} distributions (Figure 2.26).

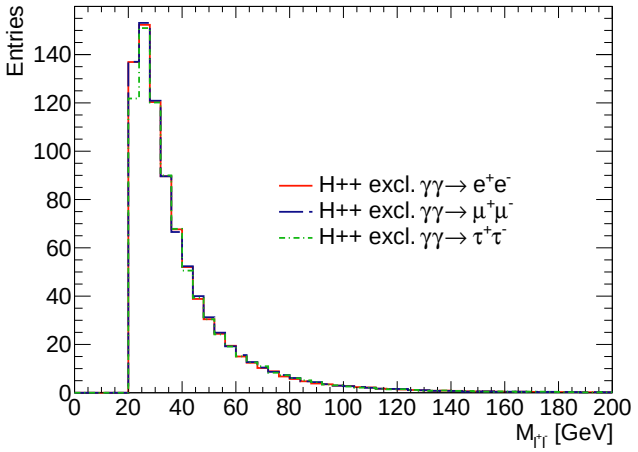

(a)

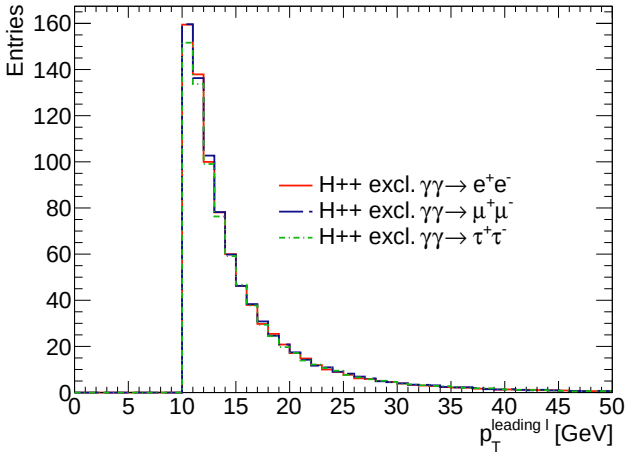

(b)

FIGURE 2.26: (a) Dilepton invariant mass and (b) leading lepton transverse momentum distributions comparison for exclusive $\gamma\gamma \to \ell^+\ell^-$ production between e^+e^-(red), $\mu^+\mu^-$(blue) and $\tau^+\tau^-$(green) channels. Default HERWIG++ generator is used with $m_{\mu^+\mu^-} > 20$ GeV, $p_T^\mu > 10$ GeV and $|\eta^\mu| < 2.5$ cuts. Distributions are normalized to 1 fb^{-1}.

Bibliography

[1] Particle Data Group Collaboration (K. A. Olive et al.), *Review of Particle Physics*, Chin. Phys. **C38** (2014) 090001.

[2] ATLAS Collaboration, *Observation of a new particle in the search for the Standard Model Higgs boson with the ATLAS detector at the LHC*, Phys. Lett. **B716** (2012) 1–29, arXiv:1207.7214 [hep-ex].

[3] CMS Collaboration, *Observation of a new boson at a mass of 125 GeV with the CMS experiment at the LHC*, Phys. Lett. **B716** (2012) 30–61, arXiv:1207.7235 [hep-ex].

[4] ATLAS and CMS Collaborations, *Combined Measurement of the Higgs Boson Mass in pp Collisions at $\sqrt{s} = 7$ and 8 TeV with the ATLAS and CMS Experiments*, Phys. Rev. Lett. **114** (2015) 191803, arXiv:1503.07589 [hep-ex].

[5] ATLAS, CDF, CMS and D0 Collaborations, *First combination of Tevatron and LHC measurements of the top-quark mass*, arXiv:1403.4427 [hep-ex].

[6] W. Cottingham and D. Greenwood, *An Introduction to the Standard Model of Particle Physics*. Cambridge University Press, 2007.

[7] R. Feynman, *Space - time approach to quantum electrodynamics*, Phys. Rev. **76** (1949) 769–789.

[8] R. Feynman, *Mathematical formulation of the quantum theory of electromagnetic interaction*, Phys. Rev. **80** (1950) 440–457.

[9] J. S. Schwinger, *On Quantum electrodynamics and the magnetic moment of the electron*, Phys. Rev. **73** (1948) 416–417.

[10] S. Tomonaga, *On a relativistically invariant formulation of the quantum theory of wave fields*, Prog. Theor. Phys. **1** (1946) 27–42.

[11] L3 Collaboration (P. Achard et al.), *Measurement of the running of the electromagnetic coupling at large momentum-transfer at LEP*, Phys. Lett. **B623** (2005) 26–36, arXiv:hep-ex/0507078 [hep-ex].

[12] P. J. Mohr, B. N. Taylor and D. B. Newell, *CODATA recommended values of the fundamental physical constants: 2006*, Rev. Mod. Phys. **80** (2008) 633–730, arXiv:0801.0028 [physics.atom-ph].

[13] F. Tkachov, *A Contribution to the history of quarks: Boris Struminsky's 1965 JINR publication*, arXiv:0904.0343 [physics.hist-ph].

[14] F. Mandl and G. Shaw, *Quantum field theory*. Wiley, 1993.

[15] D. J. Gross and F. Wilczek, *Ultraviolet Behavior of Nonabelian Gauge Theories*, Phys. Rev. Lett. **30** (1973) 1343–1346.

[16] H. D. Politzer, *Reliable Perturbative Results for Strong Interactions?*, Phys. Rev. Lett. **30** (1973) 1346–1349.

[17] R. P. Feynman, *Very high-energy collisions of hadrons*, Phys. Rev. Lett. **23** (1969) 1415–1417.

[18] J. Bjorken, *Asymptotic Sum Rules at Infinite Momentum*, Phys. Rev. **179** (1969) 1547–1553.

[19] H1 and ZEUS Collaborations (F. D. Aaron et al.), *Combined Measurement and QCD Analysis of the Inclusive e+- p Scattering Cross Sections at HERA*, JHEP **1001** (2010) 109, arXiv:0911.0884 [hep-ex].

[20] A. Martin et al., *Parton distributions for the LHC*, Eur. Phys. J. **C63** (2009) 189–285, arXiv:0901.0002 [hep-ph].

[21] H.-L. Lai et al., *New parton distributions for collider physics*, Phys. Rev. **D82** (2010) 074024, arXiv:1007.2241 [hep-ph].

[22] NNPDF Collaboration (R. D. Ball et al.), *Parton distributions for the LHC Run II*, JHEP **1504** (2015) 040, arXiv:1410.8849 [hep-ph].

[23] V. Gribov and L. Lipatov, *Deep inelastic e p scattering in perturbation theory*, Sov. J. Nucl. Phys. **15** (1972) 438–450.

[24] G. Altarelli and G. Parisi, *Asymptotic Freedom in Parton Language*, Nucl. Phys. **B126** (1977) 298.

[25] Y. L. Dokshitzer, *Calculation of the Structure Functions for Deep Inelastic Scattering and e+ e- Annihilation by Perturbation Theory in Quantum Chromodynamics.*, Sov. Phys. JETP **46** (1977) 641–653.

[26] E. Predazzi, *Diffraction: Past, present and future*, arXiv:hep-ph/9809454 [hep-ph].

[27] O. Nachtmann, *Pomeron physics and QCD*, arXiv:hep-ph/0312279 [hep-ph].

[28] S. Glashow, *Partial Symmetries of Weak Interactions*, Nucl. Phys. **22** (1961) 579–588.

[29] A. Salam and J. C. Ward, *Electromagnetic and weak interactions*, Phys. Lett. **13** (1964) 168–171.

[30] S. Weinberg, *A Model of Leptons*, Phys. Rev. Lett. **19** (1967) 1264–1266.

[31] J. Goldstone, A. Salam and S. Weinberg, *Broken Symmetries*, Phys.Rev. **127** (1962) 965–970.

[32] F. Englert and R. Brout, *Broken Symmetry and the Mass of Gauge Vector Mesons*, Phys. Rev. Lett. **13** (1964) 321–323.

[33] P. W. Higgs, *Broken symmetries, massless particles and gauge fields*, Phys. Lett. **12** (1964) 132–133.

[34] ATLAS Collaboration, *Measurements of Higgs boson production and couplings in the four-lepton channel in pp collisions at center-of-mass energies of 7 and 8 TeV with the ATLAS detector*, Phys. Rev. **D91** no. 1, (2015) 012006, arXiv:1408.5191 [hep-ex].

[35] CMS Collaboration, *Precise determination of the mass of the Higgs boson and tests of compatibility of its couplings with the standard model predictions using proton collisions at 7 and 8 TeV*, Eur. Phys. J. **C75** no. 5, (2015) 212, arXiv:1412.8662 [hep-ex].

[36] ALEPH and CDF and D0 and DELPHI and L3 and OPAL and SLD and LEP Electroweak Working Group and Tevatron Electroweak Working Group and SLD Electroweak and Heavy Flavour Groups Collaborations, *Precision Electroweak Measurements and Constraints on the Standard Model*, arXiv:1012.2367 [hep-ex].

[37] ATLAS Experiment Standard Model Results. twiki.cern.ch/twiki/bin/view/AtlasPublic/StandardModelPublicResults.

[38] M. Krasny, J. Chwastowski and K. Slowikowski, *Luminosity measurement method for LHC: The Theoretical precision and the experimental challenges*, Nucl. Instrum. Meth. **A584** (2008) 42–52, arXiv:hep-ex/0610052 [hep-ex].

[39] H1 Collaboration (A. Aktas et al.), *Muon pair production in ep collisions at HERA*, Phys. Lett. **B583** (2004) 28–40, arXiv:hep-ex/0311015 [hep-ex].

[40] CDF Collaboration (T. Aaltonen et al.), *Search for exclusive Z boson production and observation of high mass $p\bar{p} \to \gamma\gamma \to p + \ell\ell + \bar{p}$ events in $p\bar{p}$ collisions at $\sqrt{s}$ = 1.96 TeV*, Phys. Rev. Lett. **102** (2009) 222002, arXiv:0902.2816 [hep-ex].

[41] CDF Collaboration (T. Aaltonen et al.), *Observation of exclusive charmonium production and $\gamma + \gamma$ to $\mu^+\mu^-$ in $p\bar{p}$ collisions at $\sqrt{s} = 1.96$ TeV*, Phys. Rev. Lett. **102** (2009) 242001, arXiv:0902.1271 [hep-ex].

[42] CMS Collaboration, *Exclusive photon-photon production of muon pairs in proton-proton collisions at $\sqrt{s} = 7$ TeV*, JHEP **1201** (2012) 052, arXiv:1111.5536 [hep-ex].

[43] CMS Collaboration, *Search for exclusive or semi-exclusive photon pair production and observation of exclusive and semi-exclusive electron pair production in pp collisions at $\sqrt{s} = 7$ TeV*, JHEP **1211** (2012) 080, arXiv:1209.1666 [hep-ex].

[44] CMS Collaboration, *Study of exclusive two-photon production of W^+W^- in pp collisions at $\sqrt{s} = 7$ TeV and constraints on anomalous quartic gauge couplings*, JHEP **1307** (2013) 116, arXiv:1305.5596 [hep-ex].

[45] STAR Collaboration (J. Adams et al.), *Production of e^+e^- pairs accompanied by nuclear dissociation in ultra-peripheral heavy ion collision*, Phys. Rev. **C70** (2004) 031902, arXiv:nucl-ex/0404012 [nucl-ex].

[46] PHENIX Collaboration (S. Afanasiev et al.), *Photoproduction of J/psi and of high mass e+e- in ultra-peripheral Au+Au collisions at $\sqrt{s}$ = 200 GeV*, Phys. Lett. **B679** (2009) 321–329, arXiv:0903.2041 [nucl-ex].

[47] ALICE Collaboration (E. Abbas et al.), *Charmonium and e^+e^- pair photoproduction at mid-rapidity in ultra-peripheral Pb-Pb collisions at $\sqrt{s_{\rm NN}}$=2.76 TeV*, Eur. Phys. J. **C73** no. 11, (2013) 2617, arXiv:1305.1467 [nucl-ex].

[48] E. Leader and E. Predazzi, *An Introduction to Gauge Theories and Modern Particle Physics*. Cambridge University Press, 1996.

[49] F. J. Ernst, R. G. Sachs and K. C. Wali, *Electromagnetic Form Factors of the Nucleon*, Phys. Rev. **119** (1960) 1105–1114.

[50] R. Hofstadter, *Electron scattering and nuclear structure*, Rev. Mod. Phys. **28** (1956) 214–254.

[51] W. Albrecht et al., *Elastic electron - proton scattering at momentum transfers up to 245 F^{-2}*, Phys. Rev. Lett. **17** (1966) 1192.

[52] T. Janssens et al., *Proton form factors from elastic electron-proton scattering*, Phys. Rev. **142** (1966) 922–931.

[53] F. Borkowski et al., *Electromagnetic Form-Factors of the Proton at Low Four-Momentum Transfer*, Nucl. Phys. **B93** (1975) 461.

[54] G. Simon et al., *Absolute electron Proton Cross-Sections at Low Momentum Transfer Measured with a High Pressure Gas Target System*, Nucl. Phys. **A333** (1980) 381–391.

[55] R. Walker et al., *Measurements of the proton elastic form-factors for 1 GeV/c^2 < Q^2 < 3 GeV/c^2 at SLAC*, Phys. Rev. **D49** (1994) 5671–5689.

[56] E94110 Collaboration (M. E. Christy et al.), *Measurements of electron proton elastic cross-sections for 0.4 < Q^2 < 5.5 $(GeV/c)^2$*, Phys. Rev. **C70** (2004) 015206, arXiv:nucl-ex/0401030 [nucl-ex].

[57] I. Qattan et al., *Precision Rosenbluth measurement of the proton elastic form-factors*, Phys. Rev. Lett. **94** (2005) 142301, arXiv:nucl-ex/0410010 [nucl-ex].

[58] M. Burkardt, *Impact parameter dependent parton distributions and transverse single spin asymmetries*, Phys. Rev. **D66** (2002) 114005, arXiv:hep-ph/0209179 [hep-ph].

[59] M.-S. Chen et al., *Lepton pair production from two-photon processes*, Phys. Rev. **D7** (1973) 3485–3502.

[60] V. Budnev et al., *The process $pp \to ppe^+e^-$ and the possibility of its calculation by means of quantum electrodynamics only*, Nucl. Phys. **B63** (1973) 519–541.

[61] F. Krauss, M. Greiner and G. Soff, *Photon and gluon induced processes in relativistic heavy ion collisions*, Prog. Part. Nucl. Phys. **39** (1997) 503–564.

[62] A. Denner and S. Dittmaier, *Production of light fermion anti-fermion pairs in gamma gamma collisions*, Eur. Phys. J. **C9** (1999) 425–435, arXiv:hep-ph/9812411 [hep-ph].

[63] A. Denner, S. Dittmaier and R. Schuster, *Radiative corrections to $\gamma\gamma \to W^+W^-$ in the electroweak standard model*, Nucl. Phys. **B452** (1995) 80–108, arXiv:hep-ph/9503442 [hep-ph].

[64] R. Bates and J. N. Ng, *Nonstandard Higgs Scalar and Pseudoscalar Boson Production in ep and e^+e^- Colliders*, Phys. Rev. **D33** (1986) 657.

[65] E. Fermi, *On the theory of collisions between atoms and electrically charged particles*, Nuovo Cim. **2** (1925) 143–158, arXiv:hep-th/0205086 [hep-th].

[66] C. von Weizsacker, *Radiation emitted in collisions of very fast electrons*, Z. Phys. **88** (1934) 612–625.

[67] E. Williams, *Nature of the high-energy particles of penetrating radiation and status of ionization and radiation formulae*, Phys. Rev. **45** (1934) 729–730.

[68] V. Budnev et al., *The Two photon particle production mechanism. Physical problems. Applications. Equivalent photon approximation*, Phys. Rept. **15** (1975) 181–281.

[69] C. A. Bertulani and G. Baur, *Electromagnetic Processes in Relativistic Heavy Ion Collisions*, Phys.Rept. **163** (1988) 299.

[70] D. d'Enterria, M. Klasen and K. Piotrzkowski, *High-Energy Photon Collisions at the LHC*, Nucl. Phys. Proc. Suppl. **179B** (2008) 1.

[71] J. de Favereau de Jeneret et al., *High energy photon interactions at the LHC*, arXiv:0908.2020 [hep-ph].

[72] M. Bähr et al., *Herwig++ Physics and Manual*, Eur. Phys. J. **C58** (2008) 639–707, arXiv:0803.0883 [hep-ph].

[73] M. A. Shifman et al., *Low-Energy Theorems for Higgs Boson Couplings to Photons*, Sov. J. Nucl. Phys. **30** (1979) 711–716.

[74] B. A. Kniehl and M. Spira, *Low-energy theorems in Higgs physics*, Z. Phys. **C69** (1995) 77–88, arXiv:hep-ph/9505225 [hep-ph].

[75] S. Dawson and R. Kauffman, *QCD corrections to Higgs boson production: nonleading terms in the heavy quark limit*, Phys. Rev. **D49** (1994) 2298–2309, arXiv:hep-ph/9310281 [hep-ph].

[76] D. d'Enterria and J.-P. Lansberg, *Study of Higgs boson production and its b anti-b decay in gamma-gamma processes in proton-nucleus collisions at the LHC*, Phys. Rev. **D81** (2010) 014004, arXiv:0909.3047 [hep-ph].

[77] Z. Bern et al., *QCD and QED corrections to light by light scattering*, JHEP **0111** (2001) 031, arXiv:hep-ph/0109079 [hep-ph].

[78] M. Boonekamp et al., *FPMC: A Generator for forward physics*, arXiv:1102.2531 [hep-ph].

[79] S. Atag, S. Inan and I. Sahin, *Extra dimensions in $\gamma\gamma \to \gamma\gamma$ process at the CERN-LHC*, JHEP **1009** (2010) 042, arXiv:1005.4792 [hep-ph].

[80] H1 Collaboration (F. D. Aaron et al.), *Deeply Virtual Compton Scattering and its Beam Charge Asymmetry in $e^{\pm}p$ Collisions at HERA*, Phys. Lett. **B681** (2009) 391–399, arXiv:0907.5289 [hep-ex].

[81] L. Frankfurt et al., *Generalized parton distributions and rapidity gap survival in exclusive diffractive pp scattering*, Phys. Rev. **D75** (2007) 054009, arXiv:hep-ph/0608271 [hep-ph].

[82] ATLAS Collaboration, *Measurement of the total cross section from elastic scattering in pp collisions at $\sqrt{s} = 7$ TeV with the ATLAS detector*, Nucl. Phys. **B889** (2014) 486–548, arXiv:1408.5778 [hep-ex].

[83] C. Carimalo, P. Kessler and J. Parisi, *$\gamma\gamma$ Background of the Drell-Yan Process*, Phys. Rev. **D18** (1978) 2443.

[84] F. Brasse et al., *Parametrization of the q^2 dependence of $\gamma_V p$ total cross sections in the resonance region*, Nucl. Phys. **B110** (1976) 413.

[85] H. Spiesberger, *QED radiative corrections for parton distributions*, Phys. Rev. **D52** (1995) 4936–4940, arXiv:hep-ph/9412286 [hep-ph].

[86] A. Martin et al., *Parton distributions incorporating QED contributions*, Eur. Phys. J. **C39** (2005) 155–161, arXiv:hep-ph/0411040 [hep-ph].

[87] J. Vermaseren, *Two Photon Processes at Very High-Energies*, Nucl. Phys. **B229** (1983) 347.

[88] S. Baranov et al., *LPAIR: A generator for lepton pair production*, Proc. of Phys. at HERA (1991) 1478.

[89] G. P. Lepage, *A New Algorithm for Adaptive Multidimensional Integration*, J. Comput. Phys. **27** (1978) 192.

[90] L. Lonnblad, *THEPEG: Toolkit for High Energy Physics event generation*, DESY-PROC-2009-02 (2009) 733–736.

[91] G. Corcella et al., *HERWIG 6.5 release note*, arXiv:hep-ph/0210213 [hep-ph].

[92] A. Suri and D. R. Yennie, *The space-time phenomenology of photon absorption and inelastic electron scattering*, Annals Phys. **72** no. 1, (1972) 243 – 292.

[93] T. Sjöstrand, *High-energy physics event generation with PYTHIA 5.7 and JETSET 7.4*, Comput. Phys. Commun. **82** (1994) 74–90.

[94] B. Andersson et al., *Parton Fragmentation and String Dynamics*, Phys. Rept. **97** (1983) 31–145.

[95] T. Sjöstrand, S. Mrenna and P. Z. Skands, *A Brief Introduction to PYTHIA 8.1*, Comput. Phys. Commun. **178** (2008) 852–867, arXiv:0710.3820 [hep-ph].

[96] NNPDF Collaboration (R. D. Ball et al.), *Parton distributions with QED corrections*, Nucl. Phys. **B877** (2013) 290–320, arXiv:1308.0598 [hep-ph].

[97] S. Drell and T.-M. Yan, *Massive Lepton Pair Production in Hadron-Hadron Collisions at High-Energies*, Phys. Rev. Lett. **25** (1970) 316–320.

[98] ATLAS Collaboration, *Summary of ATLAS Pythia 8 tunes*, Tech. Rep. ATL-PHYS-PUB-2012-003, 2012.

Part II

The experimental tools

Chapter 3

The ATLAS experiment at the LHC

This chapter gives an overview of the ATLAS experiment at the LHC. It is used to perform the data analysis described in this thesis. Section 3.1 describes the main features of the Large Hadron Collider. Section 3.2 outlines the ATLAS detector and its components, together with trigger systems. Finally, the ATLAS simulation infrastructure is presented in Section 3.3.

3.1 The Large Hadron Collider

The *Large Hadron Collider* (LHC) [1] is currently the world's largest and most powerful particle accelerator. It is located at the *European Organization for Nuclear Research* (CERN) near Geneva in the Franco-Swiss border area.

It is a circular proton–proton (pp) collider placed 40–170 m underground[1], in the same tunnel of 27 km circumference originally built for its predecessor, the *Large Electron–Positron* collider (LEP) [2], operated from 1989 to 2000. The LHC is designed to provide pp collisions with up to $\sqrt{s} = 14$ TeV center-of-mass energy at an instantaneous luminosity of 10^{34} cm^{-2}s^{-1}. In addition to protons, the LHC can also collide lead–lead and asymmetric proton–lead beams.

[1] The LHC tunnel has an inclination of 1.4%, leading to a variation of its altitude of about ±60 m

3.1.1 CERN accelerator complex

The LHC is the last element of the accelerator complex chain at CERN, which is presented in Figure 3.1. Each of the other pre-accelerators injects the particle beam into the next accelerator in the chain, which brings the beam to an even higher energy. In this way, the particles are increasingly accelerated at each stage of the accelerator complex before they reach the main accelerator ring, the LHC.

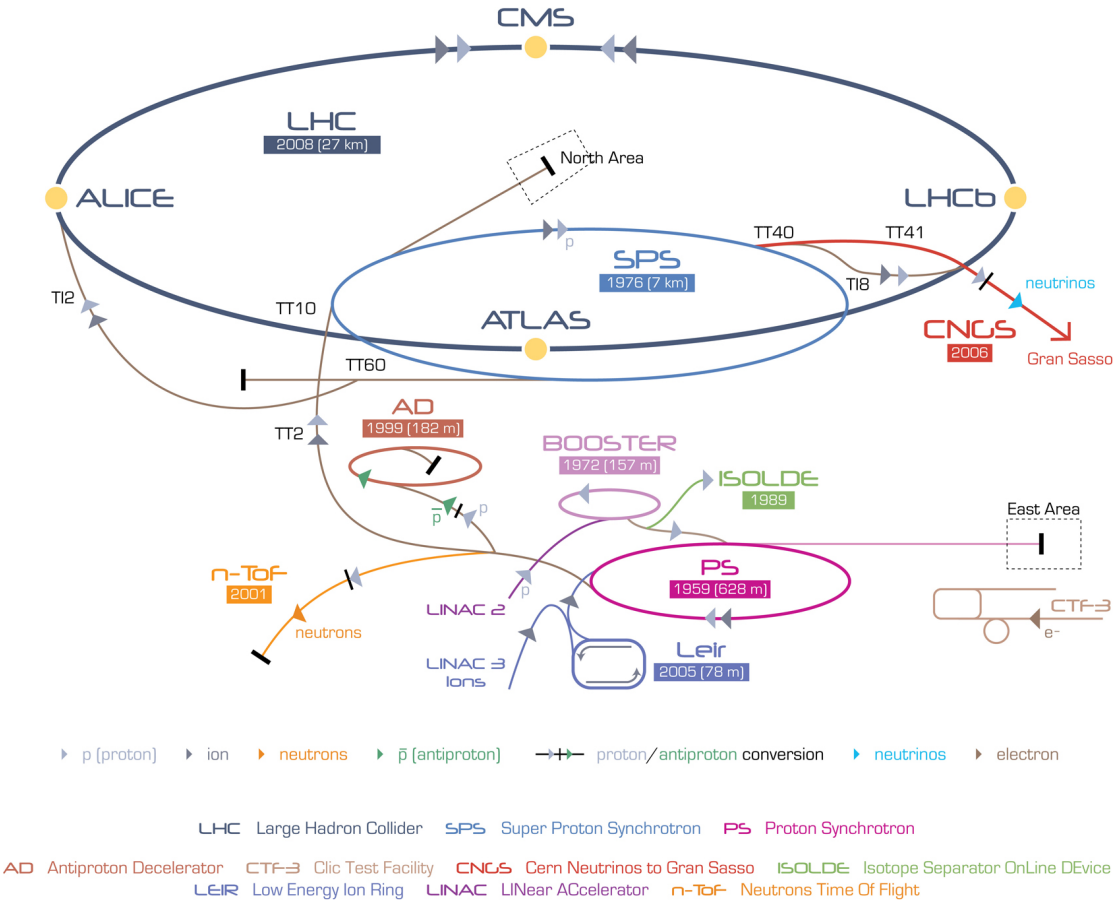

FIGURE 3.1: Schematic drawing of the CERN accelerator complex. Figure taken from [3].

Protons used in the LHC are obtained via the ionization process of hydrogen atoms using the *Duoplasmatron* source [4]. Protons are initially accelerated up to 50 MeV in the first accelerator of the complex, the linear accelerator *LINAC 2*. The protons are then injected into the *PS Booster* (PSB, 1.4 GeV) and then into the *Proton Synchrotron* (PS, 25 GeV). At this point, protons are injected to the *Super Proton Synchrotron* (SPS, 450 GeV). With this energy, protons are injected into two transfer lines of the LHC, resulting in two proton beams travelling in opposite directions inside the LHC beam pipes. The proton beams at the LHC travel in separate vacuum beam pipes and are maintained in a fixed orbit using 1232 superconducting dipole magnets that are cooled

to 1.9 K using liquid helium. The dipoles provide magnetic field strengths of up to 8.33 T. The beams are also focused using 392 main superconducting quadrupole magnets. Eight superconducting cavities operating at 400 MHz are generating the electric fields used for the particle acceleration. During the acceleration phase, each proton gain 485 keV energy per turn.

After accelerating up to the final energy, proton beams are brought to collision at four *interaction points* (IPs) along the LHC ring. Each of them is surrounded by an experiment: *ATLAS* [5] and *CMS* [6] are two general purpose detectors. They both cover almost the full solid angle and aim for high luminosities to discover rare processes. The *ALICE* [7] experiment is focused on the analysis of heavy ion collisions. The *LHCb* [8] experiment studies with great precision the decay of b-hadrons to investigate Charge-Parity (CP) symmetry violation. It is asymmetric and covers only a part of the phase space in pseudorapidity. Next to the four big experiments, several smaller ones are located close to the interaction points, such as *MoEDAL* [9] searching for magnetic monopoles, *LHCf* [10] that studies hadron interaction models used in cosmic ray analyses and *TOTEM* [11] for elastic and diffractive processes measurements.

3.1.2 LHC beam parameters

The instantaneous luminosity at the interaction points along the LHC can be determined by the beam parameters, using the formula:

$$\mathcal{L} = \frac{f_{\mathrm{r}} N_{\mathrm{b}} n_p^2 \gamma_{\mathrm{r}}}{4\epsilon_{\mathrm{n}} \beta^*} \cdot F(\theta_{\mathrm{c}}), \tag{3.1}$$

where f_{r} is the LHC revolution frequency, N_{b} is the number of bunches per beam, n_p is the number of protons per bunch, γ_{r} is the relativistic gamma factor and ϵ_{n} is the normalized transverse beam emittance (spread of the beam in position and momentum). β^* is called the *beta-function* at the collision point. It is a measure of how much the beam is squeezed towards the interaction point. $F(\theta_{\mathrm{c}})$ is the geometric luminosity reduction factor due to crossing angle of the beams, θ_{c}, at the interaction point.

The nominal revolution frequency of the LHC is 40.08 MHz. The LHC is also designed to circulate up to 2808 bunches per beam, each consisting of 1.15×10^{11} protons and separated by a time interval (*bunch spacing*) of 25 ns. In 2010, 2011 and 2012, during the first LHC run (Run-1) [12], bunch spacing of 50 ns was used for the largest part of pp data taking, reaching 1380 bunches circulating the LHC ring - which is the maximum number of bunches for such bunch spacing. During Run-1 protons are collided with 7 TeV center-of-mass energy during the year 2010–2011 and 8 TeV in 2012. During Run-2 (2015–2018), it is expected to reach the designed center-of-mass energy of $\sqrt{s} = 14$ TeV.

Parameter	2010	2011	2012	Nominal
$\sqrt{s}$ [TeV]	7	7	8	14
Maximum N_b	348	1380	1380	2808
n_p [$\times 10^{11}$]	1.2	1.5	1.6	1.15
ϵ_n [µm]	2.4–4	1.9–2.4	2.2–2.5	3.75
β^* [m]	3.5	1.5–1	0.6	0.55
θ_c [µrad]	200	240	290	285
Bunch spacing [ns]	150	75–50	50	25
Maximum $\mathcal{L}$ [$\times 10^{34}$ cm^{-2}s^{-1}]	0.02	0.4	0.76	1

TABLE 3.1: Summary of the most important LHC beam parameters during the 2010, 2011 and 2012 *pp* data taking campaigns. The nominal values of the design configuration are also shown.

The list of the most important LHC beam parameters is presented in Table 3.1. Since all parameter values gradually improved during the LHC Run-1, the actual values for 2010, 2011 and 2012 data taking periods are shown, together with the nominal configuration.

The number of collected events N_i that corresponds to a given reaction i depends on the corresponding cross section σ_i and the integrated luminosity $\int \mathcal{L}\, \mathrm{d}t$ accumulated by the experiment:

$$N_i = \sigma_i \int \mathcal{L}\, \mathrm{d}t\ . \tag{3.2}$$

In order to observe rare processes, LHC can collide protons at higher center-of-mass energies, compared to previous hadron–hadron accelerators. Moreover, high integrated luminosity can be delivered by the LHC machine.

The increasing instantaneous luminosity is followed by a larger number of *pp* collisions per single bunch crossing, μ. The mean number of interactions per bunch crossing, $\langle\mu\rangle$, can be calculated from the instantaneous luminosity (per bunch), $\mathcal{L}_{\mathrm{bunch}}$, as $\langle\mu\rangle = \mathcal{L}_{\mathrm{bunch}} \times \sigma_{\mathrm{inel}}/f_{\mathrm{r}}$, where σ_{inel} is the inelastic *pp* cross section. This effect is commonly known as *pile-up* and is an inevitable consequence at any high-luminosity collider experiment.

Since the interactions can be treated as independent of one another, the probability that n proton–proton interactions occur in a single bunch crossing, in a fixed beam setup, follows a Poisson distribution with a mean $\langle\mu\rangle$.

While the mean number of simultaneous interactions, $\langle\mu\rangle$, at the Tevatron never exceeded 6 [13], the LHC with its detectors are designed to cope even with $\langle\mu\rangle \simeq 40$ [14]. Maximum mean number of interactions per bunch crossing reached $\langle\mu\rangle = 4$ in 2010, $\langle\mu\rangle = 17$ in 2011 and $\langle\mu\rangle = 37$ in 2012 *pp* data taking campaigns. The peak instantaneous luminosity together with a maximum mean number of interactions per bunch

crossing, as delivered to the ATLAS experiment by the LHC, as a function of time over the LHC Run-1 *pp* data taking periods, is presented in Figure 3.2.

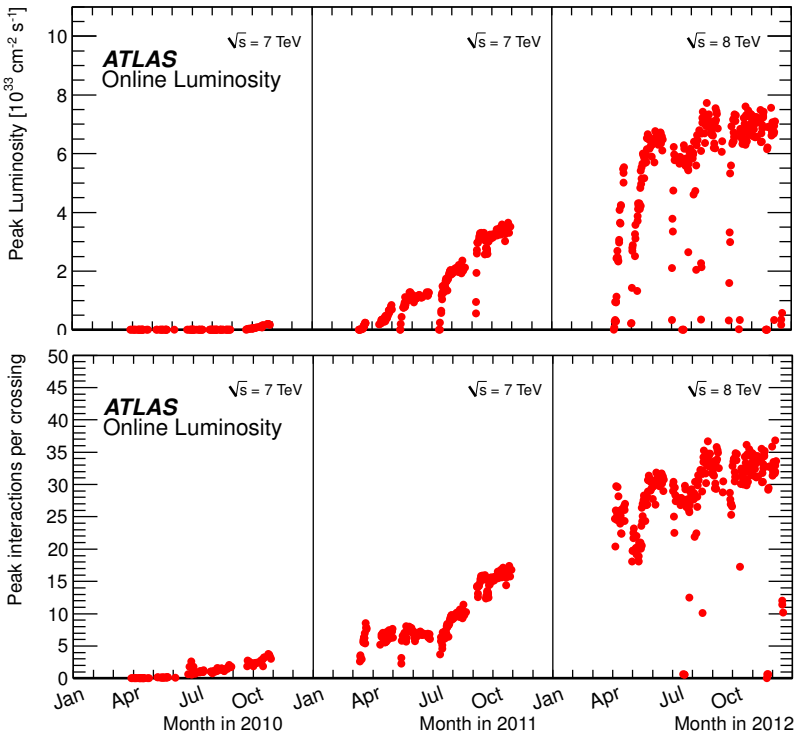

FIGURE 3.2: (a) Peak instantaneous luminosity and (b) maximum mean number of interactions per bunch crossing as delivered to the ATLAS experiment by the LHC during *pp* runs in 2010, 2011 and 2012. Figure taken from [15].

3.2 The ATLAS detector

A Toroidal LHC ApparatuS (ATLAS) [5] is by volume the largest detector installed on the LHC ring. The unprecedented high energy and luminosity of the LHC, implying higher particle multiplicities and radiation doses, have set new standards for the design of particle detectors. Requirements for the ATLAS detector have also been defined to cover a wide range of signatures from possible new physics phenomena which could appear at the TeV-energy scale, and to allow precise measurements of SM processes.

The anatomy of the ATLAS detector is sketched in Figure 3.3. It is forward-backward symmetric and covers almost the entire 4π solid angle. Each sub-system of the ATLAS detector is disposed around the interaction point forming a leek-like structure. In order to reconstruct charged particle momenta, large volumes of intense magnetic flux density are required to generate Lorentz forces sufficient to bend the trajectory of high-energy charged particles as they traverse the detector. The ATLAS system of magnets includes

a thin superconducting solenoid surrounding the tracking detectors, and three large superconducting toroids (one barrel and two end-caps) arranged around the calorimeters. The following sections describe the individual sub-detectors in more detail.

3.2.1 ATLAS coordinate system

ATLAS uses a right-handed, orthogonal coordinate system with its origin at the nominal interaction point in the center of the detector. The z-axis points along the anticlockwise beam direction, the x-axis points towards the center of the LHC ring, and the y-axis points upwards. In the transverse $(x-y)$ plane, cylindrical coordinates are used, with r denoting the radius and ϕ the azimuthal angle around the beampipe. The azimuthal angle can be written in terms of Euclidean coordinates as

$$\phi = \arctan\left(\frac{y}{x}\right) \ . \tag{3.3}$$

The polar angle θ is measured relative to the positive z-axis.

When describing the properties of a particle relative to the beam axis, it is convenient to construct a quantity with invariant properties under boosts along this axis. Such a quantity is the rapidity, defined as

$$y = \frac{1}{2}\ln\left(\frac{E+p_z}{E-p_z}\right) \ , \tag{3.4}$$

with E being the energy and p_z the longitudinal momentum of the particle (along the z-axis). For cases where the particle is massless or $E \gg m$, the rapidity can be approximated by the pseudorapidity, defined in terms of θ as

$$\eta = -\ln\left(\tan\frac{\theta}{2}\right) \ . \tag{3.5}$$

The pseudorapidity is very useful in the context of experimental particle physics, since the particle production is approximately constant as a function of η.

Therefore, the cylindrical coordinate system used is given by (ϕ, η, z). In this coordinate system, angular distances between two objects are given by $\Delta R = \sqrt{(\Delta\phi)^2 + (\Delta\eta)^2}$. The transverse momentum p_{T} and the transverse energy E_{T} are defined in the $x-y$ plane.

3.2.2 Inner Detector

The ATLAS *Inner Detector* (ID) [16] is designed to provide efficient pattern recognition and good momentum resolution for charged particles in the range $|\eta| < 2.5$ down to a

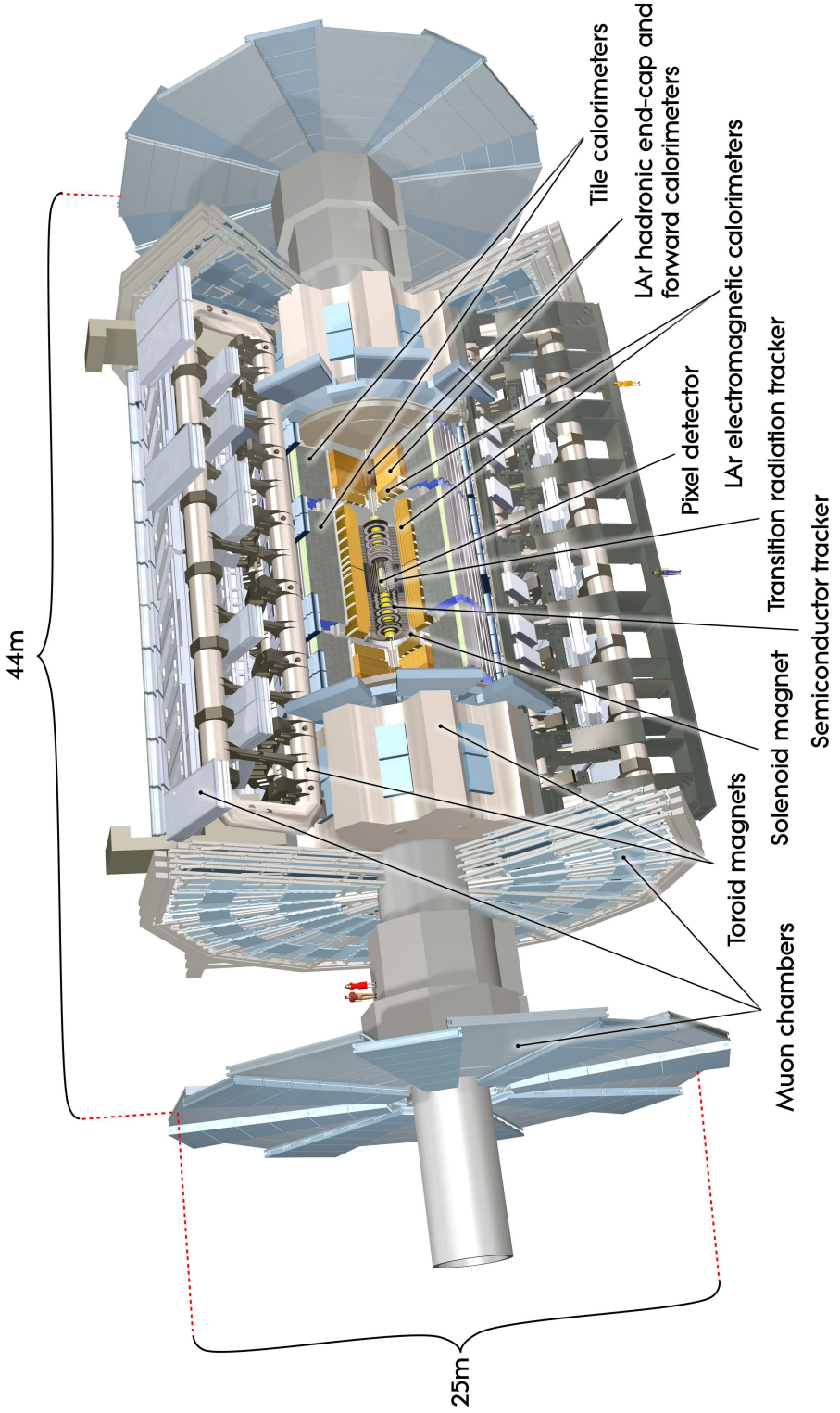

FIGURE 3.3: Schematic view of the ATLAS detector. The detector is approximately 25 high, 44 m long and weighs 7000 tonnes. Figure taken from [5].

p_{T} of 100 MeV. The ID is primarily used to reconstruct the positions of pp interaction vertices and to identify secondary decay vertices associated with relatively long lived states such as b-hadrons or τ leptons. The ID provides also additional electron identification capacity for $|\eta| < 2$ and 0.5 GeV $< p_{\mathrm{T}} <$ 150 GeV. The sub-detectors of the inner tracking detector in Figure 3.4, are the closest to the interaction point. The entire ID is enclosed in a solenoidal magnetic field of 2 T and its overall dimensions are 2.1 m in diameter and 6.2 m in length.

The Pixel Detector (Pixel) is the innermost tracking sub-detector [17] and therefore must be highly resistant to radiation damage. It consists of three concentric cylinders (barrel layers) and three disks in each end-cap, perpendicular to the beam axis. Every layer comprises of Pixel sensors: a 16.4×60.8 mm^2 wafers of silicon with 46 080 pixels, 50×400 µm^2 each. With over 80 million pixels, it has ≈90% of the total number of ATLAS readout channels. The Pixel operates at the initial bias voltage of 150 V, but it is expected to rise to up to 600 V to maintain a good charge collection efficiency.

As part of the planned detector upgrades during the long shutdown of the LHC that started in 2013 (LS1), a new layer closest to the beam pipe has been recently put in place, the so-called *insertable B-layer* (IBL) [18]. It is located between the existing pixel detector and a new smaller radius beam pipe at a radius of only 3.3 cm. Faster readout chips and two different silicon sensor technologies (thin planar and 3D sensors) were developed for IBL, in order to cope with high radiation and higher particle occupancies.

The Semi-Conductor Tracker (SCT) is located outside of the pixel detector and covers radial range between 30 and 51 cm. It is similar to the pixel detector but instead of the pixels, it consists of long silicon microstrips with a size of 120 mm by 80 µm, that are placed parallel to the beam line in the barrel and radially in the end-cap regions. Each SCT module consists of two arrays of strip sensors, off-set at a small stereo angle of 40 mrad to provide a z-position measurement in the barrel and r-position measurement in the end-cap. The silicon strip tracker is arranged in four concentric barrel cylinders and in six end-cap disks on both sides. The initial bias voltage of SCT strips is 150 V and is expected to rise to 350 V. The SCT, together with the Pixel, allows to reconstruct charged particle tracks with a momentum resolution of $\sigma_{p_{\mathrm{T}}}/p_{\mathrm{T}} = 0.05\% \cdot p_{\mathrm{T}}\ [\mathrm{GeV}] \oplus 1\%$.

The Transition Radiation Tracker (TRT) detector is installed after the SCT. It is comprised of 4 mm diameter and 1.44 (0.37) m long in the barrel (end-caps) straw tubes filled with a gaseous mixture of xenon (70%), carbon dioxide (27%) and oxygen (3%). The tubes form the cathodes of the system (operated at -1530 V) and each contains a grounded gold-plated tungsten anode. There are over 50 000 straw tubes in the barrel and 320 000 radial straws in the end-caps, with typically 30 TRT hits being registered on a well reconstructed track of a charged particle with $p_{\mathrm{T}} > 0.5$ GeV and $|\eta| < 2$. The

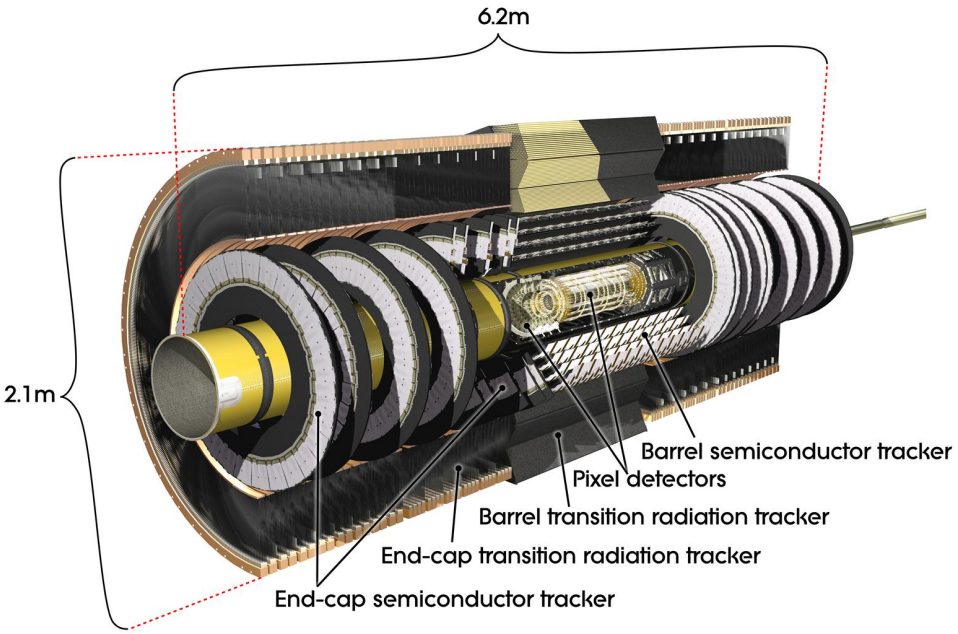

(a)

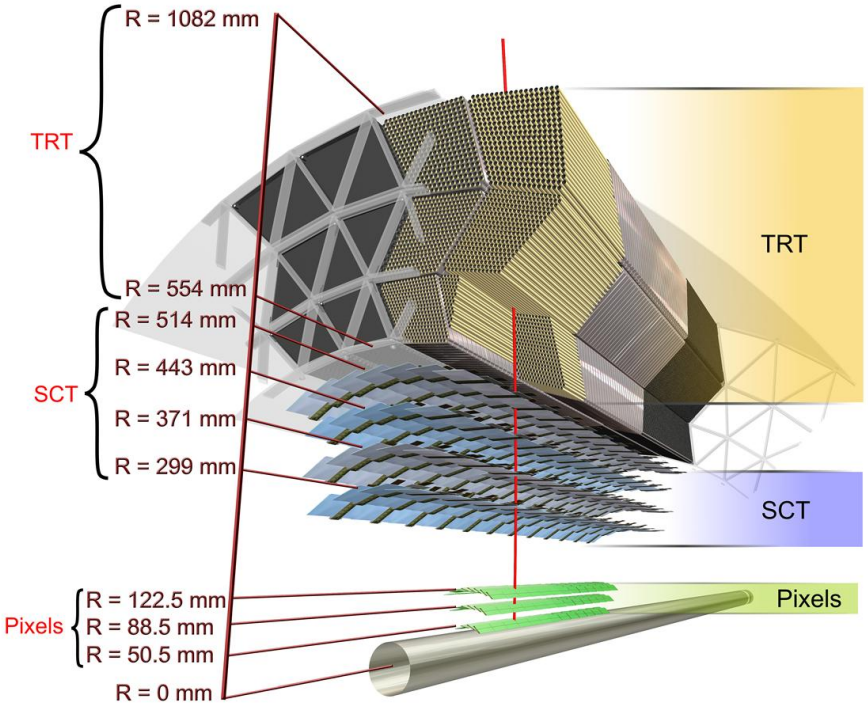

(b)

FIGURE 3.4: (a) Cut-away image of the ATLAS Inner Detector with sub-detectors labelled. (b) Scheme of the ATLAS Inner Detector barrel being crossed by a high-energy particle (red line). Figure taken from [5].

space between the layers of straw tubes are filled with radiators (polypropylene foils or fibres). A charged particle travelling through the radiator leads to a transition radiation which is emitted when passing through the material with different dielectric constants [19]. The intensity of the emitted transition radiation depends on the Lorentz γ factor of the particle passing through the TRT. For a given momentum, this allows separating heavy from light particles (for example electrons and pions).

3.2.3 Calorimeters

Calorimeters in HEP experiments are primarily used to absorb electrons, photons and hadrons created in the interaction, measuring their energy. The ATLAS calorimeter system consists of electromagnetic and hadronic calorimeters [5], as shown in Figure 3.5. All ATLAS calorimetric systems are of sampling type, where regions of an active sampling medium are alternated with a dense absorber material which induces particle showers.

The calorimeters cover the range $|\eta| < 4.9$ with the variable granularity. Over the same η region as the inner detector, the calorimeters are also finely segmented to perform precision measurements of electrons and photons. The rest of the calorimeter is of coarser granularity.

The Electromagnetic Calorimeter (ECal) is optimized to measure the energy of electrons and photons. Also, it provides electron and photon identification. It consists of two identical half-barrels, separated by a small gap (4 mm) at $z = 0$, covering the region $|\eta| < 1.475$, and two end-cap coaxial wheels covering a pseudorapidity range of $1.375 < |\eta| < 2.5$. Between the barrel and the end-cap regions, at $1.37 < |\eta| < 1.52$, so-called *crack* region exists in order to accommodate instrumentation and cooling infrastructure of the Inner Detector. This adds additional fraction of dead material in front of the EM calorimeter leading to significant particle energy loss. The ECal uses liquid argon (LAr) as active material and lead/stainless steel as passive material and has about 180 000 readout channels. Its granularity in terms of cell dimension, $\Delta\eta \times \Delta\phi$, varies as a function of η between 0.025×0.025 and 0.1×0.1. The thickness of the ECal has been also optimized as a function of η to improve the EM calorimeter performance in energy resolution, which is given by $\sigma_E/E = 10\%/\sqrt{E\ [\text{GeV}]} \oplus 0.7\%$.

The Hadronic Calorimeter (HCal) provides energy measurements of hadrons. The HCal uses two different construction techniques in the barrel and the end-cap parts. Steel is used as absorber and scintillating[2] tiles as active material for the barrel part.

[2] A scintillator is a material that exhibits the property of luminescence when excited by ionizing radiation

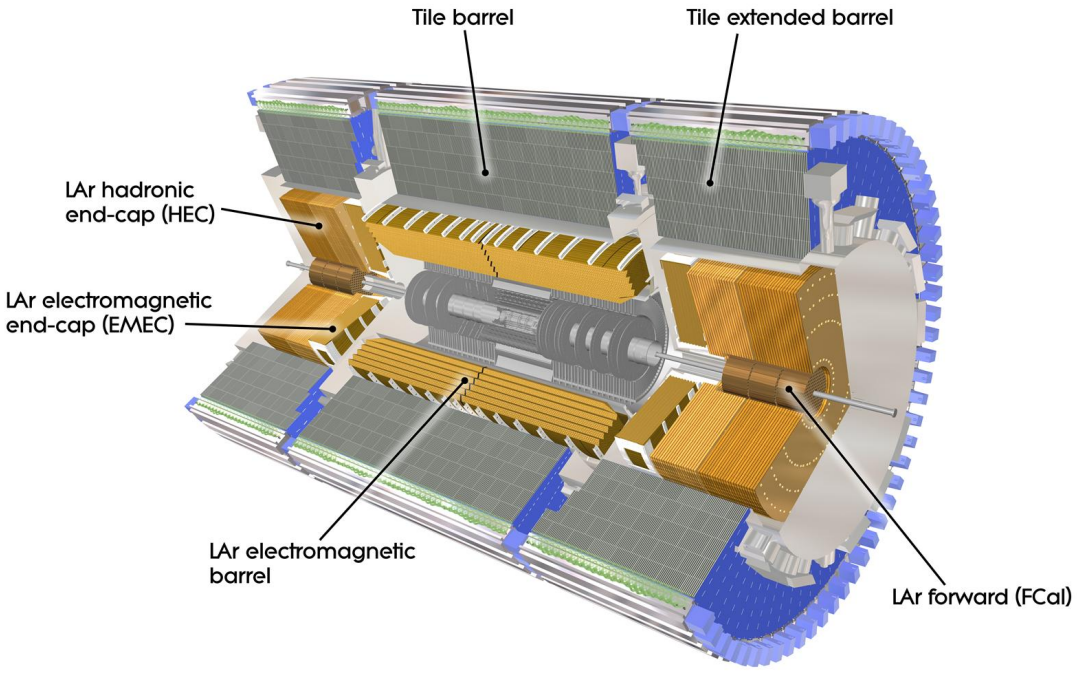

FIGURE 3.5: Schematic view of the ATLAS calorimeter system, showing the electromagnetic and hadronic calorimeters. Figure taken from [5].

It covers the region up to $|\eta| < 1.7$. In contrast, the *Hadronic End-Cap* (HEC) uses a LAr/copper combination and extends the HCal to $|\eta| < 3.2$. The granularity is chosen to be mostly $\Delta\eta \times \Delta\phi = 0.1 \times 0.1$. The hadronic calorimeter was designed to provide an energy resolution of $\sigma_E/E = 50\%/\sqrt{E\ [\text{GeV}]} \oplus 3\%$.

Forward Calorimeters (FCal) are the calorimeters placed in the forward region and due to the large radiation environment, they use LAr as an active material. As an absorber material, the first section of FCal uses copper and is optimized for EM showers. The remaining two sections use tungsten in order to cope with significant energy fluxes from forward hadrons. The FCal covers the range of $3.1 < |\eta| < 4.9$ and its energy resolution is given by $\sigma_E/E = 100\%/\sqrt{E\ [\text{GeV}]} \oplus 10\%$

3.2.4 Muon system

The *Muon Spectrometer* (MS) [20] is located outside the calorimeters, where it provides identification and reconstruction of muons. A toroidal magnetic field is causing curvature of the muon trajectory, which allows an additional muon momentum measurement. The information from the MS is then combined with the information provided by the ID to get a combined muon track. The MS is designed in such a way that it can measure

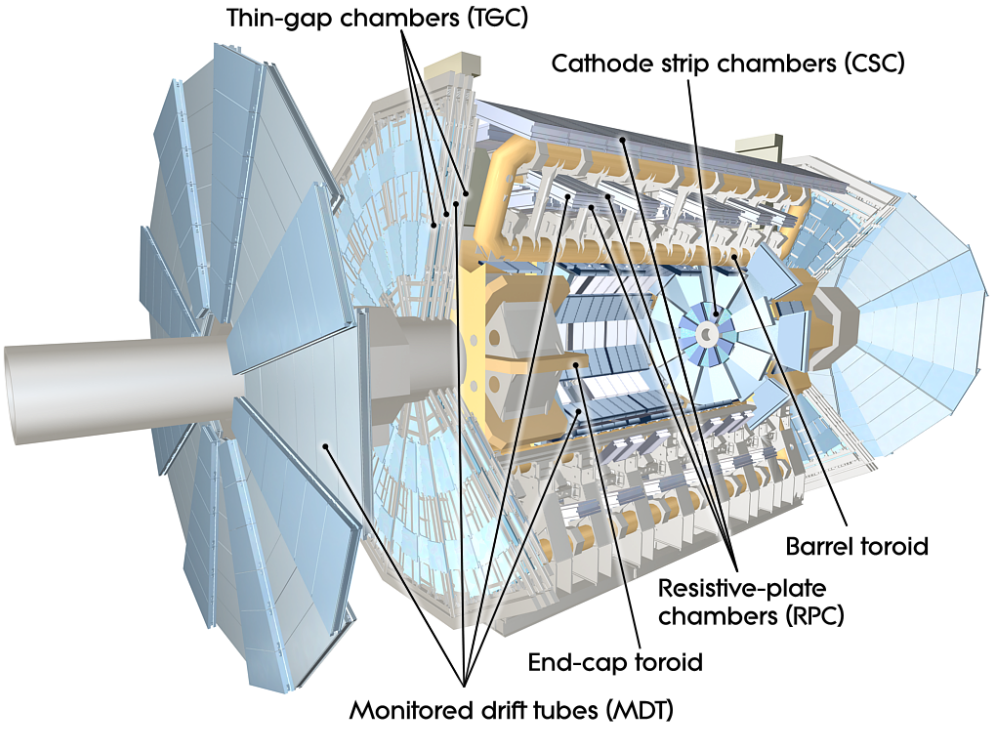

FIGURE 3.6: Schematic view of the ATLAS muon system. Figure taken from [5].

muon momenta from 3 GeV up to 3 TeV with good momentum resolution and charge identification.

The layout of the MS with its sub-detectors is shown in Figure 3.6. The MS is comprised of two main parts: a barrel region with the pseudorapidity coverage of $|\eta| < 1.0$ and the end-cap region covering $1.0 < |\eta| < 2.7$. A barrel toroid and two end-cap toroids produce a toroidal magnetic field of approximately 0.5 T and 1 T for the muon detectors in the central and end-cap regions, respectively.

Different experimental techniques are used in the MS. *Monitored drift tubes* (MDTs) are adopted for precision muon tracking in both the barrel and end-cap parts of the MS. The end-cap tracking is also supported by additional *Cathode strip chambers* (CSCs) with a high granularity in the pseudorapidity region of $2.0 < |\eta| < 2.7$ to cope with high particle fluxes. For muon triggering, *Resistive plate chambers* (RPCs) are used for the barrel and *Thin-gap chambers* (TGCs) for the end-cap part. The RPCs and TGCs provide also a secondary tracking information. The trigger muon systems have coverage up to $|\eta| < 2.4$. The whole MS provides about one million channels and a total resolution of $\sigma_{p_{\mathrm{T}}}/p_{\mathrm{T}} = 10\%$ for mouns with energy of 1 TeV.

3.2.5 ATLAS trigger system

Proton–proton collision rates at the LHC are heavily dominated by inelastic QCD processes with large cross section, in contrast to the interesting physics processes rates. Considering that one event has a size of about 1.5 MB, the collision rate provides too much data to store. Therefore, a fast and efficient selection procedure of physics events is designed to be able to keep approximately 1 GHz collision rate.[3]

The ATLAS trigger system [21] is divided into three levels: L1 [22], L2, and the *event filter* (EF). L2 and the EF are referred to collectively as the *High-Level trigger* (HLT) [23]. Each trigger level performs a stricter selection than the previous level. The hardware-based L1 trigger is able to make a decision using a limited amount of the detector information in less than 2.5 µs, reducing the rate from the initial 1 GHz to ≈75 kHz. In the next stages, the event rate is reduced to ≈3.5 kHz in L2, and to ≈200 Hz after the EF. Compared to the ATLAS design rates, the actual output rate during LHC Run-1 was 400 Hz on average, as the trigger system was able to handle a 5 orders of magnitude change of LHC instantaneous luminosity in 2010-2011, and its further increase of a factor 2 in 2012.

The L1 trigger electronics are located in the ATLAS cavern in order to reduce the latency in the trigger decision. Calorimeters and muon detectors (RPCs/TGCs) at reduced granularity are used to search for high momentum objects like electrons, photons, muons and jets. The results from the L1 triggers are processed by the *central trigger processor* (CTP), where information from different object types is combined. The CTP processes this information and forms on up to 256 distinct L1 triggers. The L1 trigger also defines *Regions-of-Interest* (ROIs) in each event: the (ϕ, η) coordinates of detector regions defined as interesting by the trigger selection procedure, where possible physics objects have been identified by L1. If an event is accepted, it is passed on to the second-level (L2) trigger.

The software-based L2 trigger uses the ROI information at full granularity and precision to reduce the amount of data to be transferred from the detector readout, needing on average approximately 40 ms to process an event. The final stage in the triggering is the EF, which is also software-based. The EF further reduces the event rate using offline analysis procedures, with the time budget of about 4 seconds/event, using additional information from the event that requires more advanced reconstruction algorithms. The HLT algorithms refine the trigger selection using not only the full information of the calorimeters and muon system data, but also information from the Inner Detector, enhancing the particle identification. For certain physics objects that ATLAS triggers on,

[3] Assuming pp bunch spacing of 25 ns and approximately 20 interactions per bunch crossing

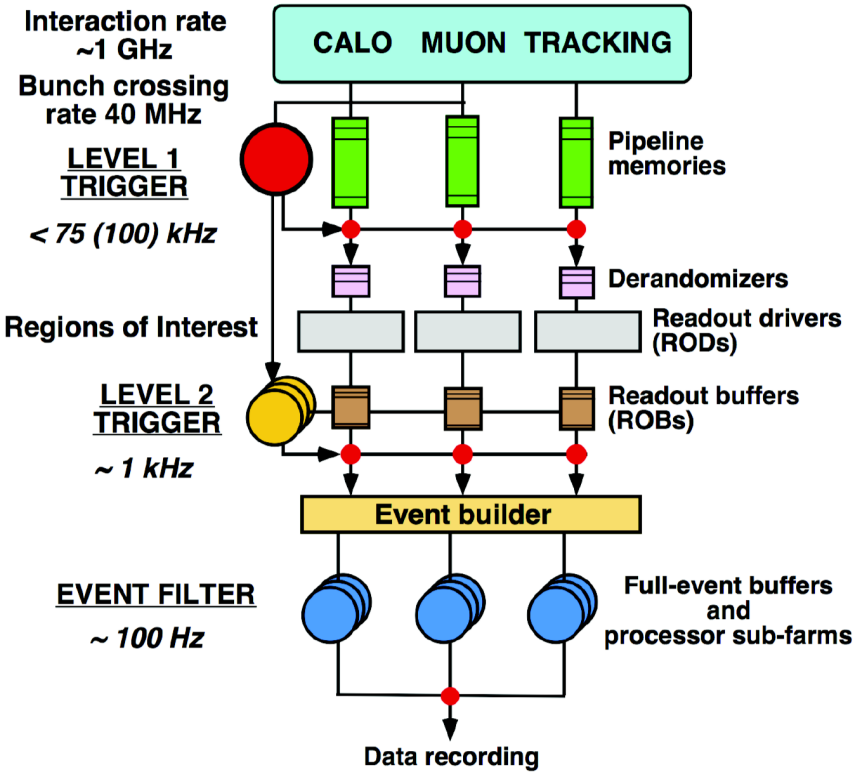

FIGURE 3.7: Schematic overview of the trigger and data acquisition systems in ATLAS. The specified rates should only be considered as orders of magnitudes. Figure taken from [24].

the production rate might be too high to record every single event passing the trigger. In such cases, *prescaled* triggers exist, which record only a certain fraction of the events that would normally pass the trigger, effectively reducing the recorded luminosity.

The ATLAS *data acquisition system* (DAQ) [23] receives and buffers the event data from each detector readout electronics (at the L1 trigger acceptance rate) over 1600 point-to-point readout links. It transmits the ROI data to the L2 trigger, and an event-building is performed for events passing the L2 selection criteria. These events are then received by the EF and, once accepted, moved to permanent event storage located at CERN.

Figure 3.7 summarizes the flow of data through the ATLAS trigger and data acquisition chain.

3.2.6 Data taking with ATLAS during LHC Run-1

As already mentioned in Section 3.1, the LHC Run-1 can be divided into three main data taking periods corresponding to the years 2010, 2011 and 2012. In 2010, the LHC delivered pp collisions at $\sqrt{s} = 7$ TeV corresponding to a total integrated luminosity of

48 pb^{-1}. The ATLAS experiment was able to record approximately 45 pb^{-1} out of the total integrated luminosity delivered by the LHC in 2010 [25]. In 2011, the collision energy remained the same but the total delivered luminosity increased to 5.46 fb^{-1}. The ATLAS detector recorded 5.08 fb^{-1}, which translates into a data taking efficiency of 93% [25]. In 2012, the *pp* collision energy was increased to $\sqrt{s} = 8$ TeV and a total integrated luminosity of 21.3 fb^{-1} was recorded by ATLAS out of the LHC delivered 22.8 fb^{-1}. Total integrated luminosity versus day delivered to and recorded by ATLAS during LHC Run-1 *pp* collisions is presented in Figure 3.8.

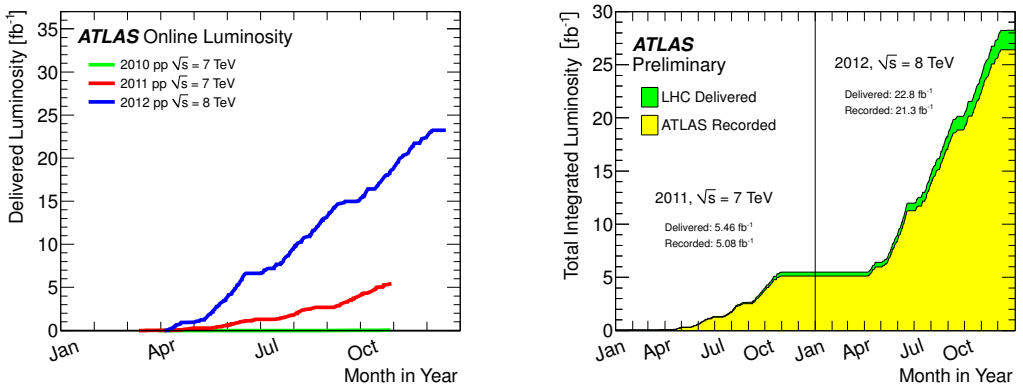

(a) (b)

FIGURE 3.8: (a) Total integrated luminosity versus day delivered to ATLAS during LHC Run-1 *pp* collisions. (b) Cumulative luminosity versus time delivered to and recorded by ATLAS in 2011 and 2012 *pp* collisions. Figures taken from [15].

ATLAS online data-taking can be divided into sub-periods. The time interval during which the luminosity is supposed to remain constant is called *Luminosity Block* (LB) and is approximately 2 minutes long. A *run* is a collection of luminosity blocks and its duration depends on the beam conditions. Status and functionality of all sub-detectors are known for each LB in every run. Thus, each physics analysis is required to use data only from "good" luminosity blocks in each run. For this purpose, a *Good Run List* (GRL) is prepared and used to determine the integrated luminosity for a given physics analysis.

During the LHC Run-1 operation, few *pp* runs were dedicated to special data taking when the relevant detectors, like TOTEM [11] and *ALFA* [26], were allowed to be inserted into the LHC beampipe. Such runs were characterized by a large value of the beta-function and therefore are called *high-*β^* runs.[4] It is worth to mention that the integrated luminosities collected during the dedicated runs are orders of magnitude smaller than the one gathered during nominal LHC Run-1 operation. This is related with large

[4] $\beta^* = 90$ m and 1000 m were used, to be compared with the nominal value of $\beta^* = 0.55$ m for high-luminosity *pp* runs

value of the beta-function (luminosity behaves like $1/\beta^*$) and lower number of colliding bunches and smaller number of protons per bunch during these runs.

3.3 ATLAS simulation infrastructure

In order to study the detector response for a wide range of physics processes and scenarios, a detailed detector simulation is mandatory. The simulated events are generated and reconstructed into a format, which is identical to that of the true detector. All of these components come together under the ATLAS simulation infrastructure [27]. The simulation program is integrated into the ATLAS software framework, ATHENA [28], and uses the GEANT4 simulation toolkit [29, 30].

3.3.1 Simulation chain

The simulation chain is generally divided into four steps, with a common data format required before the last stage of data processing. The steps that constitute the full procedure to produce simulated events are: *event generation*, *detector simulation*, *event digitization*, and *event reconstruction*. Figure 3.9 gives an overview of the standard simulation chain used in ATLAS.

The **event generation** step produces the events that result from the hard scattering process of the pp collisions. They are generated using a variety of Monte Carlo (MC) generator programs and can be saved in standard HepMC format [31]. These generator programs are usually configured so as to produce one physics process, where all the necessary model parameters are set. The generation of an high-energy pp collision event, where the QCD calculations are involved, can be factorized into different stages, as illustrated in Figure 3.10:

- *Hard scattering* process, where the partons (quarks/gluons, but also the photons) are created and undergo the reaction. The process is calculated based on matrix element computations, using fixed-order perturbation theory.
- *Parton showering* process, with multiple QCD bremsstrahlung in the initial (if the coloured partons are involved) and final state, evolving down to low momentum scales, until perturbation theory breaks down (called the *theory scale*).
- *Hadronization* process, which confines a system of QCD partons into colourless primary hadrons by utilizing phenomenological fragmentation models. The unstable primary hadrons decay into stable particles, which are expected to propagate through a part of the detector.

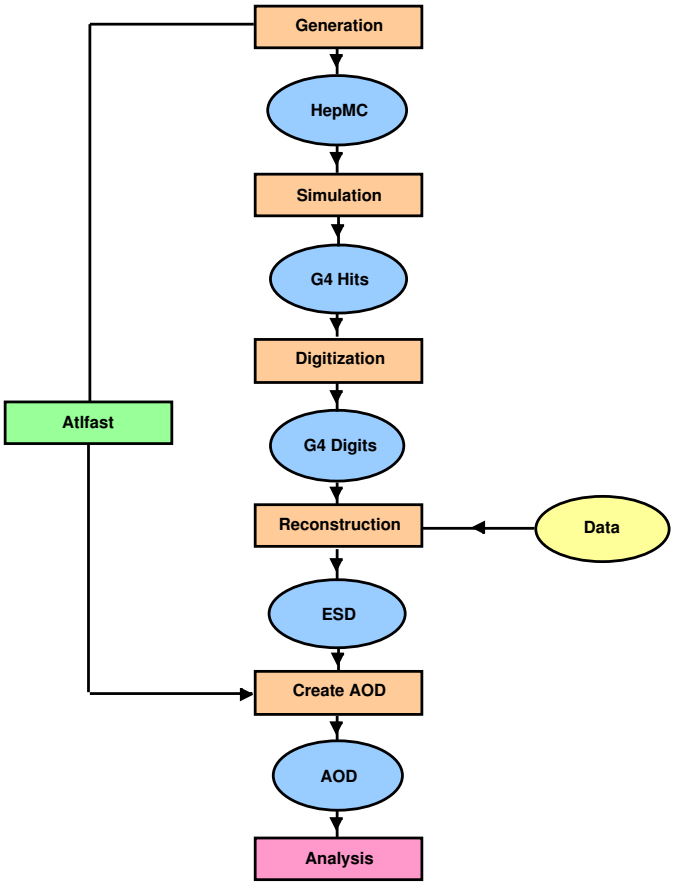

FIGURE 3.9: Overview of the standard simulation chain used in ATLAS. Elliptical-shaped boxes represent persistent data objects (or event collections), whereas rectangular boxes sets of algorithms applied.

- *Underlying event* (UE) process, where the secondary interactions between the proton remnants occur. It is based on parametrized phenomenological models, and typically produces additional soft hadrons throughout the event.

The distribution of partons within the incoming protons governs the probability of a particular interaction to take place. These distributions can be modelled by fitting parametrized functions, like the parton distribution functions (PDFs) or proton structure functions, to experimental data. These functions are then served as external inputs to the event generators. The details of the generated particles in the event, after all stages of event generation, are stored in what is called *MC truth* record.

The next step in the simulation chain is the simulation of the detector response to the particles created in the event generation. The **detector simulation** computes the paths of the particles while traversing the detector. Here, any kind of interaction with the detector material, or further possible decays of unstable particles are taken into account. In addition, the detector simulation computes the particle hits on sensitive

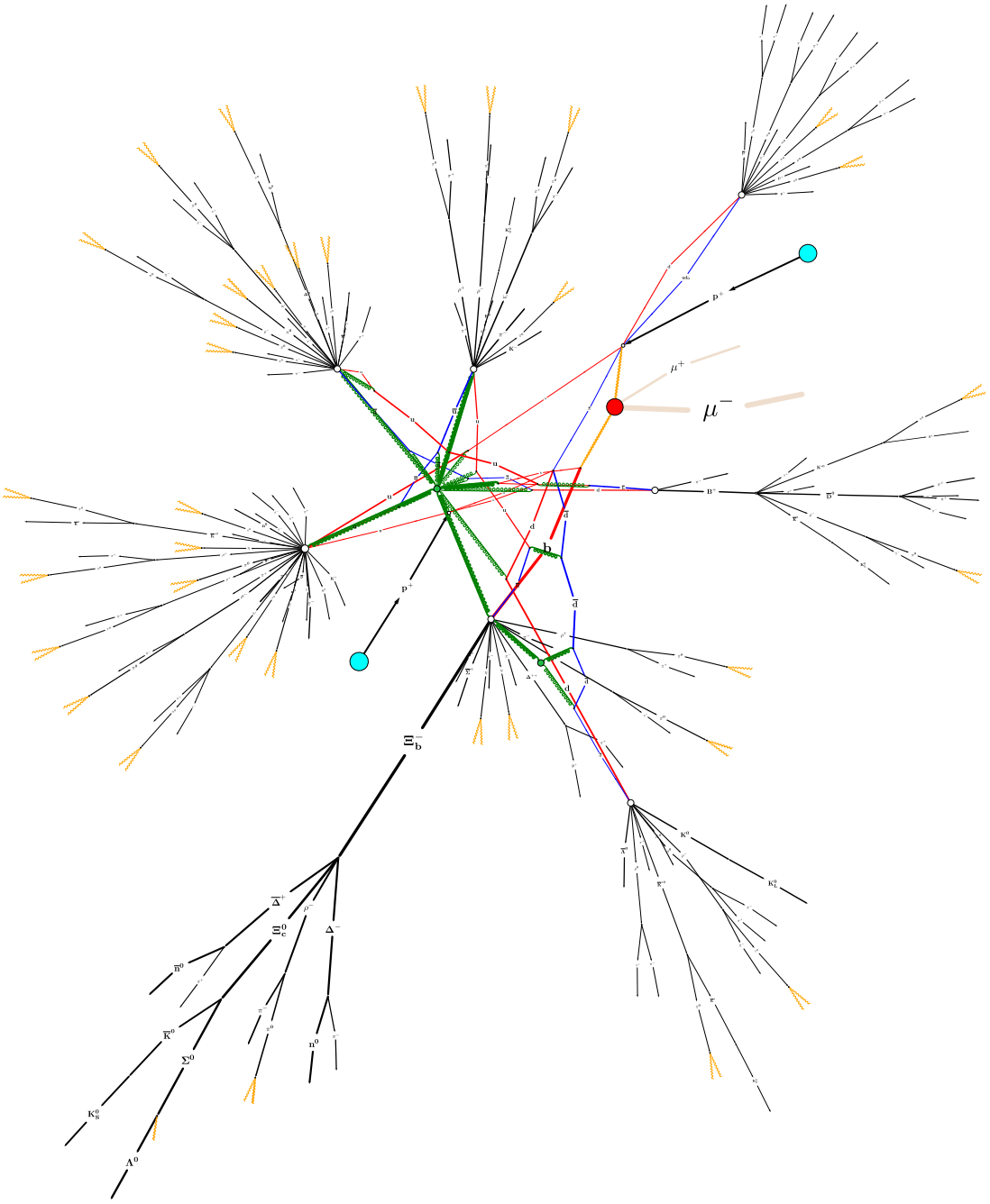

FIGURE 3.10: Illustration of a two-photon interaction (yellow waves) event in a proton-proton collision produced by an event generator. The hard scatter interaction (red blob) produces muon pair and is accompanied with additional QCD interactions (green springs) in the parton showering process, before the hadronization sets in (green blobs) and hadron decays (white blobs). The figure is prepared with MCViz [32].

detector elements. This information is stored in a dedicated output format, known as simulation *HITS*. The detector simulation usually ends when all particles are either stopped or left the detector volume.

After the detector simulation step, the simulation hits have to be translated into a data format which corresponds to a format retrieved from the detector during data-taking. For the simulation chain, this translation is carried out by the **digitization** [33]. The digitization takes as input the simulated hits and emulates the detector and electronics response, taking into account the intrinsic resolution of each detector. The digitization transforms the primary interaction of a particle with the sensitive detector material into the measurable quantities, such as the charge drifted to the readout modules. Besides creating realistic detector output signals, the digitization is responsible for introducing the simulated event pile-up. This is done by overlaying the detector simulations of different MC events and merging them into one common RDO (*Raw Data Object*) output for a single, pile-up enriched, event. At this step, the RDO file is produced, with the same data format used to record detector measurements after bytestream conversion.

Then, events obtained from the previous simulation step (or from detector measurements) needs to be interpreted in terms of finding particle properties. The **reconstruction** step is responsible for transforming the information held by the digits to a physics objects. This is done with various offline reconstruction algorithms that perform pattern recognition, track fitting and energy measurements. The output of reconstruction step is what is commonly used for physics analyses. Several formats exist, depending on the specific requirements. The *Event Summary Data* (ESD) keeps extended information for the physics objects at the detector level and can be used for validation purposes and performance studies. The *Analysis Object Data* (AOD) is derived from the ESD, with a significantly smaller size, and contains proper physics objects for physics analyses and further studies. The final format is the *Derived Physics Data* (DPD), which forms even smaller version of the AOD.

3.3.2 Detector simulation

The particles produced by the event generator in the first step of the simulation chain are propagated through a full model of the ATLAS detector based on the GEANT4 toolkit (*GEometry ANd Tracking*) [29, 30]. This allows to simulate the passage of particles through matter and their interactions with the detector material. The ATLAS detector geometry used in the simulations is built from databases containing the information describing the physical construction and conditions data. The model of the

ATLAS detector prepared for simulations (so-called ATLAS *GeoModel* [34]) is shown in Figure 3.11.

With GEANT4, it is possible to simulate interactions of particles with the matter over a wide range of particle energies. The toolkit is based on a number of physics models [35] describing many different kinds of particle - detector matter interactions. Physics models in GEANT4 are typically chosen as physics lists (e.g. the Quark-Gluon String Precompound model [36] and the Bertini Cascade model [37]). GEANT4 can also simulate the decays of unstable particles.

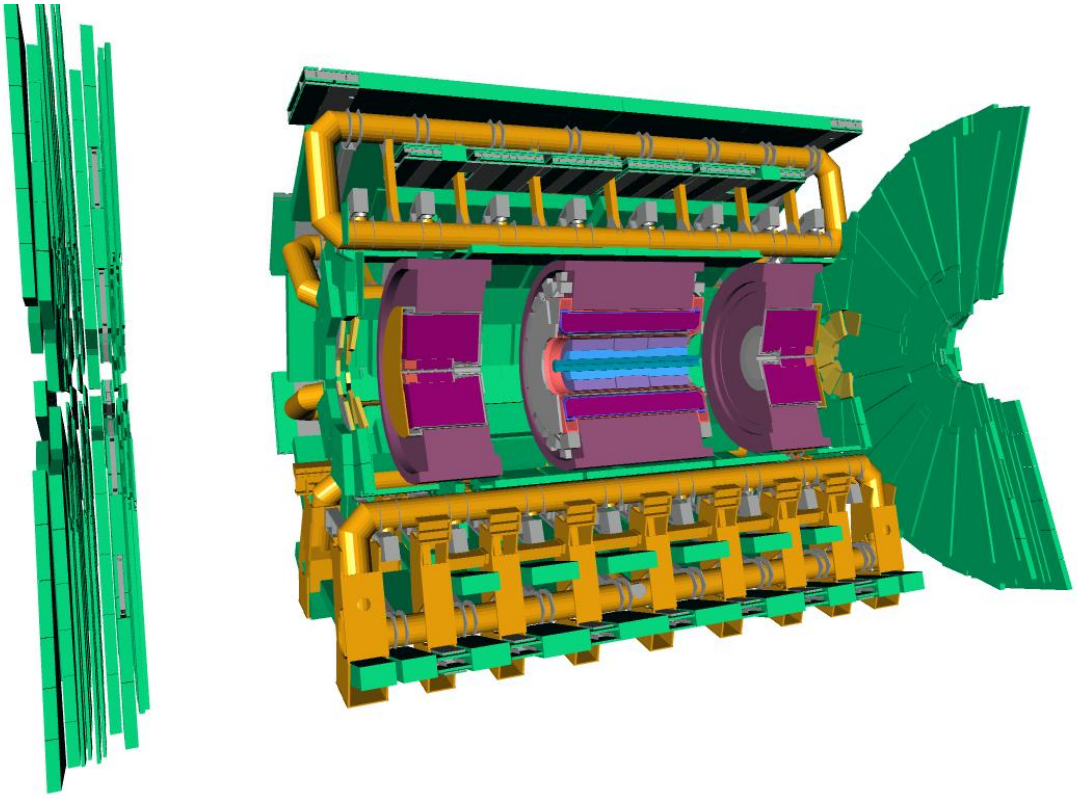

FIGURE 3.11: An example of the layout of the ATLAS detector used in the simulations. The calorimeter end-caps are shown in purple and the muon end-caps in green. The barrel toroid magnets are shown in yellow and the Inner Detector in blue. Figure taken from [27].

The GEANT4-based simulation step is the standard and most accurate detector simulation scheme applied in the ATLAS. However, this comes with an immense demand for computing resources. Almost 80% of the full simulation time with GEANT4 is spent for the progression of particle showers in calorimeters, mainly caused by particles such as electrons and photons, which produce large secondary particle cascades in the ECal. In order to reduce the burden on computing resources (and/or to increase the MC event statistics), the ATLFAST-II simulation [27] is used to reduce the simulation time by more than one order of magnitude. The ATLFAST-II parametrizes the longitudinal and

lateral energy profiles of electromagnetic and hadronic showers for the response of the calorimeters, when the full GEANT4 simulation is still used for the Inner Detector and Muon Spectrometer. The approach taken by ATLFAST-II is less accurate comparing to the full simulation, but the relevant parametrizations can be tuned to data.

3.3.3 ATHENA framework

ATHENA [28] is the ATLAS software framework based on the common Gaudi architecture [38], originally developed for LHCb. Major design principles of the ATHENA software are the clear separation of data and algorithms, and between transient (in-memory) and persistent (in-file) data. All levels of processing of ATLAS data, from high-level trigger to event simulation, reconstruction and analysis, take place within the ATHENA framework.

ATHENA releases are divided into several major projects [39], and all of the ATLAS simulation software (including event generation and digitization) resides in a single project. Each project consists of many different packages to allow flexible development of a wide range of shared components (or classes). The whole infrastructure uses object-oriented scripting to configure and load variety of algorithms and objects [28]. ATHENA highly relies on the external libraries, like CLHEP library [40], which include utility classes particularly designed for use in high energy physics software.

The major components of the ATHENA architecture are [28]:

- **Algorithms** provide the basic per-event processing capability of the framework. Each Algorithm performs a well-defined (and configurable) operation on some input data, in many cases producing some output data.
- **Tools**, in contrast to Algorithms, do not normally share a common interface so are more specialized in their manipulation, and they can be executed multiple times per event.
- **Services** are similar to the ATHENA Tools. Services usually provide more general tasks, designed to support the needs of the physicist (for example the message-reporting system, random-number generators, etc.).
- **Converters** are responsible for converting data from one representation to another. One example is the transformation of an object from its transient form to its persistent form.

- **Properties** can modify the operation of the components. Typically these are basic types (single numerical number), but can also be specified as having upper and lower bounds.

For storing data, ATLAS has adopted a scheme for separating transient from persistent objects [41]. This scheme can manage the data objects stored in transient form. It can also steer the transient/persistent conversion of data and can provide a dictionary allowing to identify and retrieve data objects in memory.

Chapter 4

Forward detectors in ATLAS

This chapter describes additional detectors covering the forward region of ATLAS. The existing devices will be characterized, together with future AFP detectors, proposed for measurements of diffractively scattered protons.

4.1 Existing forward detectors

The ATLAS experiment has several sub-detectors located in the acceptance region of large pseudorapidities (*ATLAS forward region*), i.e. in the direction of flight of the incident protons. These detectors, dedicated to different tasks, are listed below and described in details in the following sections. Three of these detector systems are placed in the very forward region: the *LUminosity measurement using Cherenkov Integrating Detector* (LUCID) [42] is a Cherenkov detector used for relative luminosity monitoring, the *Zero Degree Calorimeters* (ZDCs) [43] primary goal is to detect forward neutrons in heavy-ion collisions, and the *Absolute Luminosity For ATLAS* (ALFA) [26] measures elastically scattered protons down to very small scattering angles. Other sub-detectors located in the forward region of ATLAS are: the *Beam Conditions Monitor* (BCM) [44] designed for monitoring the beam background conditions within the Inner Detector (ID), and the *Minimum Bias Trigger Scintillators* (MBTS) [45], which are used primarily to trigger minimum-bias events (i.e. those with at least minimum proton–proton collision activity). All ATLAS forward detectors are symmetric with respect to the interaction point (IP) and have the same components on both sides.

The pseudorapidity coverage of ATLAS central and forward sub-detectors is shown in Figure 4.1.

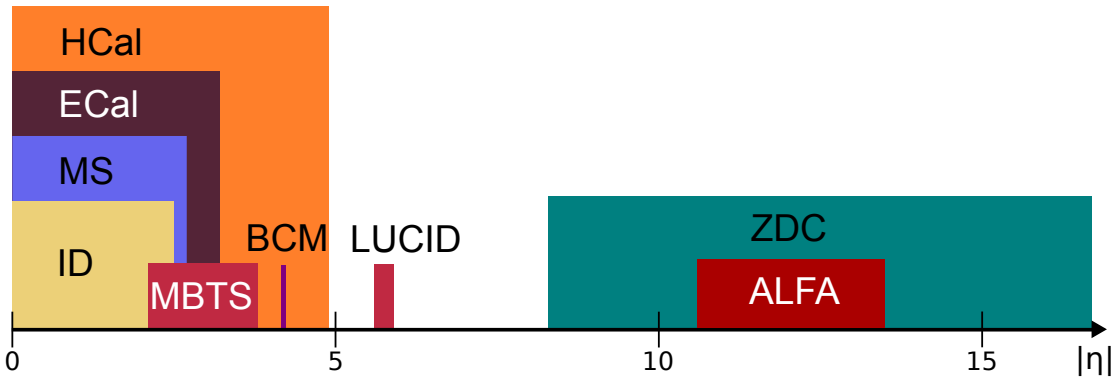

FIGURE 4.1: Pseudorapidity coverage of different ATLAS sub-detectors. The coverage of ZDC extends to $\eta = \pm\infty$.

4.1.1 ATLAS forward region

The ATLAS region of large pseudorapidities, where dedicated detectors are installed, consists mainly of LHC beampipe and magnetic elements.

The LHC collides two beams, which circulate in two horizontally displaced beam pipes. The beam pipes join into a common one about 140 m away from the interaction points. All insertion regions, where the main LHC experiments are located, have very similar designs. They consist of 13 main quadrupole magnets on both sides of the interaction point, out of which three on each side (so-called *triplets*) are situated in the common beamline and are used for final beam focusing. The triplet affects both beams, whereas the other quadrupoles will act on them independently.

The LHC region in vicinity of the ATLAS IP is shown in Figure 4.2. The final focusing triplet (Q1, Q2 and Q3) is positioned approximately 40 m from ATLAS IP. In addition, there are three more quadrupoles: Q4, Q5 and Q6, installed at the distances of 160 m, 190 m and 220 m, respectively. Between IP and 240 m two dipole magnets are installed: D1 at 70 m and D2 at 150 m away from the ATLAS IP. They are used for beam separation.

Besides forward detectors and magnets, there are few more LHC elements installed close to the ATLAS IP:

- *Target Absorber Secondaries* (TAS) - absorber for particles which could reach the quadrupole triplet. The first one is located in front of Q1, whereas the second one before the Q3 quadrupole magnet.
- *Target Absorber Neutral* (TAN) - absorber for neutral particles leaving the IP, located in front of the D1 dipole magnet on the side facing the ATLAS detector.

- *Target Collimators* (TCL4 and TCL5) - protect the superconducting magnets from quenching. TCL4 is installed before the D2 dipole and TCL5 before the Q5 quadrupole magnet.

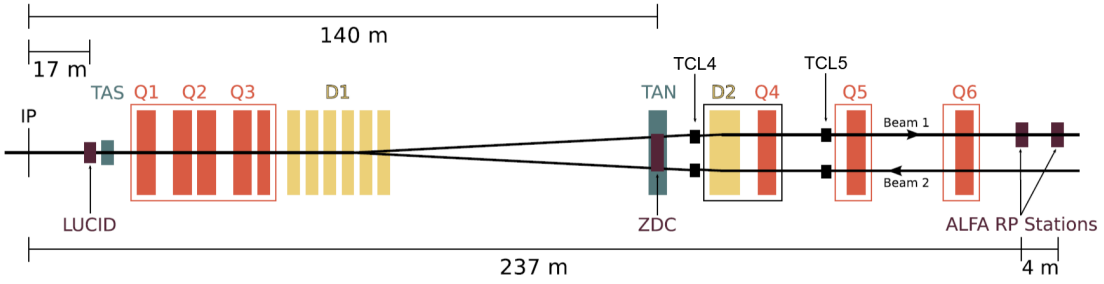

FIGURE 4.2: The LHC region in vicinity of the ATLAS IP: locations of forward detectors, dipole magnets (D), quadrupole magnets (Q), target collimators (TCL) and absorber systems (TAS, TAN) are shown. Figure taken from [46].

4.1.2 MBTS

The MBTS [45] detectors are located between the ECal end-cap cryostats and the Inner Detector. They are positioned at ±365 cm from the interaction point, perpendicular to the beam direction. Its specific geometry can be seen in Figure 4.3. The MBTS consist of 16 scintillator paddles per side (2 cm thick) organized into two disks. Each disk is divided into an inner and outer rings, which together cover the pseudorapidity region of $2.12 < |\eta| < 3.85$. The rings themselves are organized into eight independent sectors in ϕ. Light emitted by each scintillator segment is collected by *wavelength-shifting* (WLS) optical fibres and guided to *photo-multiplier tubes* (PMTs). Readout is done through fast electronics used in the ECal, which also communicate the MBTS response to the L1 trigger system.

The MBTS detectors are used during dedicated low instantaneous luminosity *pp* runs ($\mathcal{L} < 10^{32}$ cm^{-2}s^{-1}) [45] and during heavy-ion collisions [47] to provide a trigger on minimum collision activity from charged particles.

4.1.3 BCM

The BCM system [44] comprises one detector station on each side of the ATLAS detector at $\eta = \pm 4.2$. The stations are located about 1.84 m away from the interaction point and are made up of four modules (two vertical and two horizontal), positioned less than 6 cm from the beam. Each module includes two radiation-hard diamond sensors, read out by very fast and radiation-tolerant electronics.

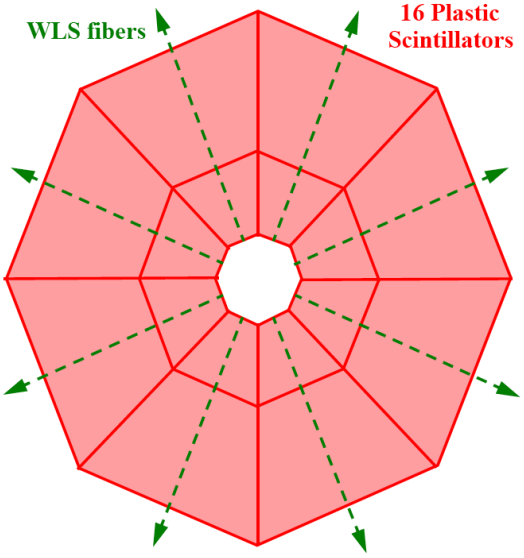

FIGURE 4.3: MBTS disk configuration. Figure taken from [45].

The BCM is designed to detect beam accidents that might damage the Inner Detector. Such accidents can arise, if several proton bunches hit the collimators in front of the detectors, producing enormous particle rates. In order to protect the ID, the BCM is included in the beam abort logic and can trigger a beam dump. The BCM detectors measure the difference in *time-of-flight* (ToF) between the two stations, distinguishing between background particles and particles from normal collisions at the IP. Therefore, another operational area of the BCM is bunch-by-bunch luminosity measurements.

4.1.4 LUCID

The LUCID [42] is a Cherenkov detector[1] and provides ATLAS with on-line monitoring of the instantaneous luminosity. Two detectors are located at a distance of $z = \pm 17$ m from the ATLAS IP on each side. They consist of 1.5 m long aluminium tubes of 15 mm diameter filled with C_4F_{10} gas, resulting in a Cherenkov threshold of 2.8 GeV for pions and 10 MeV for electrons. There are 20 tubes per side and they surround the beam pipe at a radius of 10 cm ($|\eta| \approx 5.8$). Cherenkov light is read out by a PMT at the end of each tube.

The benefit of a Cherenkov detector is that it is possible to determine the number of particles passing through a tube by measurement of the pulse height. The instantaneous luminosity can be measured from the rate of inelastic pp collisions as sampled by LUCID

[1] see the Section 5.3.1 for details about the Cherenkov radiation mechanism

in the forward region, under the principle that the number of detected particles is proportional to the number of inelastic interactions. LUCID provides also an independent trigger signal for use in the L1 trigger system.

4.1.5 ZDC

Two ZDCs [43] are installed at ATLAS, ±140 m from the interaction point, where the beam pipe splits from being a single tube through ATLAS to an individual tube for each beam. Each ZDC sits in slots inside the TAN and detects very forward ($8.3 < |\eta| < \infty$) neutral particles produced in the interaction. The ZDC is comprised of four modules, one electromagnetic and three hadronic (see Figure 4.4). The EM modules consist of tungsten plates as absorber, extended by steel plates, traversed by quartz rods forming an 8×12 matrix perpendicular to the beam axis. On the front of each module the rods are bent upwards and read out at the top by multi-anode PMTs. Therefore, the Cherenkov light induced by particle showers traversing the module provides both position and energy measurements. In order to get an improved measurement of the incident particle energy over that based on the position measuring rods, quartz strips are installed between the plates and read out from the top by PMTs. The hadronic modules are similar but in contrast to the EM modules the position-sensitive quartz rods are mapped in clusters of four into individual PMTs. Furthermore, only one out of three modules on each side is equipped with the position-sensitive rods.

The ZDC detectors occupies an important region of phase space for heavy-ion collisions, where it provides a measurement of the *centrality*[2] of each collision, which is strongly correlated to the number of very forward neutrons. The detector is also used as the primary trigger of low-centrality (so-called *ultra-peripheral*) events during heavy-ion runs. For *pp* collisions, the ZDC enhances the acceptance of ATLAS for minimum bias physics and also provides a minimum bias L1 trigger input.

4.1.6 ALFA

The ALFA experiment [26] aims to provide an independent measurement of the absolute luminosity and total *pp* cross section, in the Coulomb-nuclei interference region [48]. Since in this region, the four-momentum transfers between the interacting protons are small ($|t| \approx 0.001$ GeV^2), the protons are scattered at micro-radian angles. This requires, apart of the special *high-*β^* LHC optics, that the detectors have to be installed far away (typically hundreds of meters) from the interaction point and as close to the beam as possible.

[2]The elliptical cross-sectional overlap of the colliding nuclei

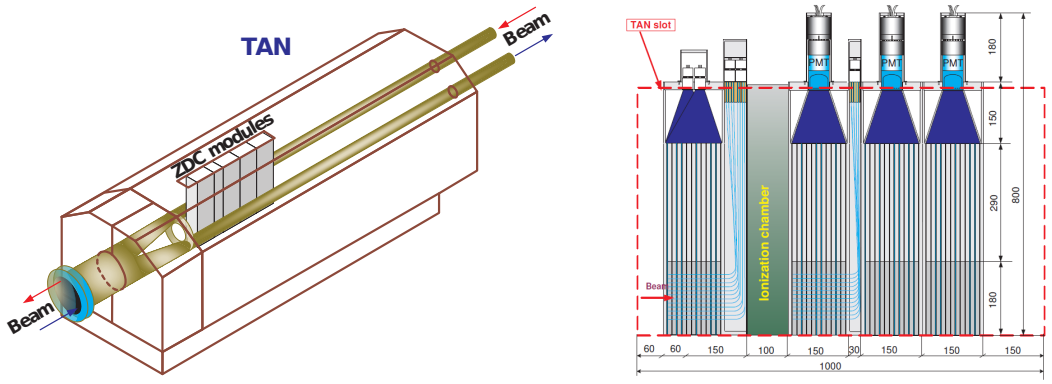

(a) (b)

FIGURE 4.4: (a) Transparent view of the TAN showing the beam pipe and location of ZDC modules. (b) ZDC modules as situated in TAN. Figure taken from [43].

The measurement of the absolute luminosity is based on the relation of the elastic scattering rate to the total interaction rate. This is called the *optical theorem* and states that the total cross section, σ_{tot}, is directly proportional to the imaginary part of the elastic-scattering amplitude at zero four-momentum transfer, $|t|$. To measure the total cross section, an independent measurement of the luminosity is required. This is needed to normalize the elastic cross section, σ_{el}. An extrapolation of the elastic cross section to $|t| \to 0$ gives the total cross section through the formula:

$$\sigma_{\text{tot}}^2 = \frac{16\pi}{1+\rho^2} \frac{\mathrm{d}\sigma_{\text{el}}}{\mathrm{d}|t|}\bigg|_{|t|\to 0} , \tag{4.1}$$

where ρ represents a small correction arising from the ratio of the real to imaginary part of the elastic-scattering amplitude and is taken from theory.

It is worth to notice that, apart from the elastic measurement, ALFA can also detect diffractivelly scattered protons.

Roman Pots

The ALFA detector system consists of eight tracking detectors housed in so-called *Roman Pots* (RP). The RP technique was used the first time at the ISR at CERN [49]. The RP beam interface has been also adopted by the TOTEM experiment [11] at the LHC. The Roman Pot concept is based upon a detector volume (the pot) that is separated from the vacuum of the accelerator by a thin window and connected with bellows which allow the insertion into the beampipe. The ALFA RP design [26] assumes that the detectors

could be moved as close as 1 mm to the beam in the vertical direction. A schematic view of the ALFA Roman Pot is shown in Figure 4.5.

The eight ALFA detectors are grouped into four stations, which are placed at $z = \pm 237.4$ m and $z = \pm 241.5$ m in the outgoing beams on both sides of the ATLAS IP. Each station consists of two RP (upper and lower) with tracking detectors approaching the beams in the vertical coordinate y.

Tracking detectors

The ALFA detectors are built using the scintillating fibre tracker technology. Since the ALFA detectors are planned to be used only during the special low instantaneous luminosity LHC runs, the applied technology is not radiation-hard. In the *Main Detector* (MD), traversing proton position is measured. In additional *Overlap Detectors* (OD), a measurement of the distance between upper and lower MDs is performed to align the detectors. Such a measurement is needed because the position of the movable RP with respect to the center of the beam is not fixed from one data-taking period to another. Both MD and OD are completed with trigger scintillator tiles providing a fast L1 trigger signal. These are used to select miscellaneous event topologies of e.g. elastically or diffractively scattered protons. Figure 4.6 shows the layout of the ALFA scintillating fibres and trigger counters in the single-station MD and ODs of the upper and lower detector, and their position with respect to the nominal beam trajectory.

The Main Detector consists of ten double-sided modules with 64 squared scintillating fibres in each. The fibres have a diameter of 500 µm, thus the effective area of the detector is approximately 32×32 mm^2. The fibres in each module are made of plastic and are glued on both sides of support plates made of titanium. The fibres are aluminized to reduce the light losses and optical cross-talk. At the front and back side of the plates the fibres are arranged at an angle of 45° to the vertical coordinate and are perpendicular to each other. The fibres are also arranged after each other in the direction of the beam, which results in a pattern of 10 alternating fibre layers which form "pixels". For a single plane the resulting pixels have a size of $d = 500$ µm, which corresponds to the base diameter of the fibres and gives an effective size of $d_{x,y} = 500/\sin(45°)$ µm $= 707$ µm in the $x - y$ plane.

The theoretical resolution for reconstructed proton position using single detector plane with pixels of size d_x in arbitrary x-direction can be calculated with the *Root Mean Square* (RMS) formula:

$$\sqrt{\int_{-d_x/2}^{d_x/2} \frac{x^2}{d} \mathrm{d}x} = \frac{d_x}{\sqrt{12}}. \tag{4.2}$$

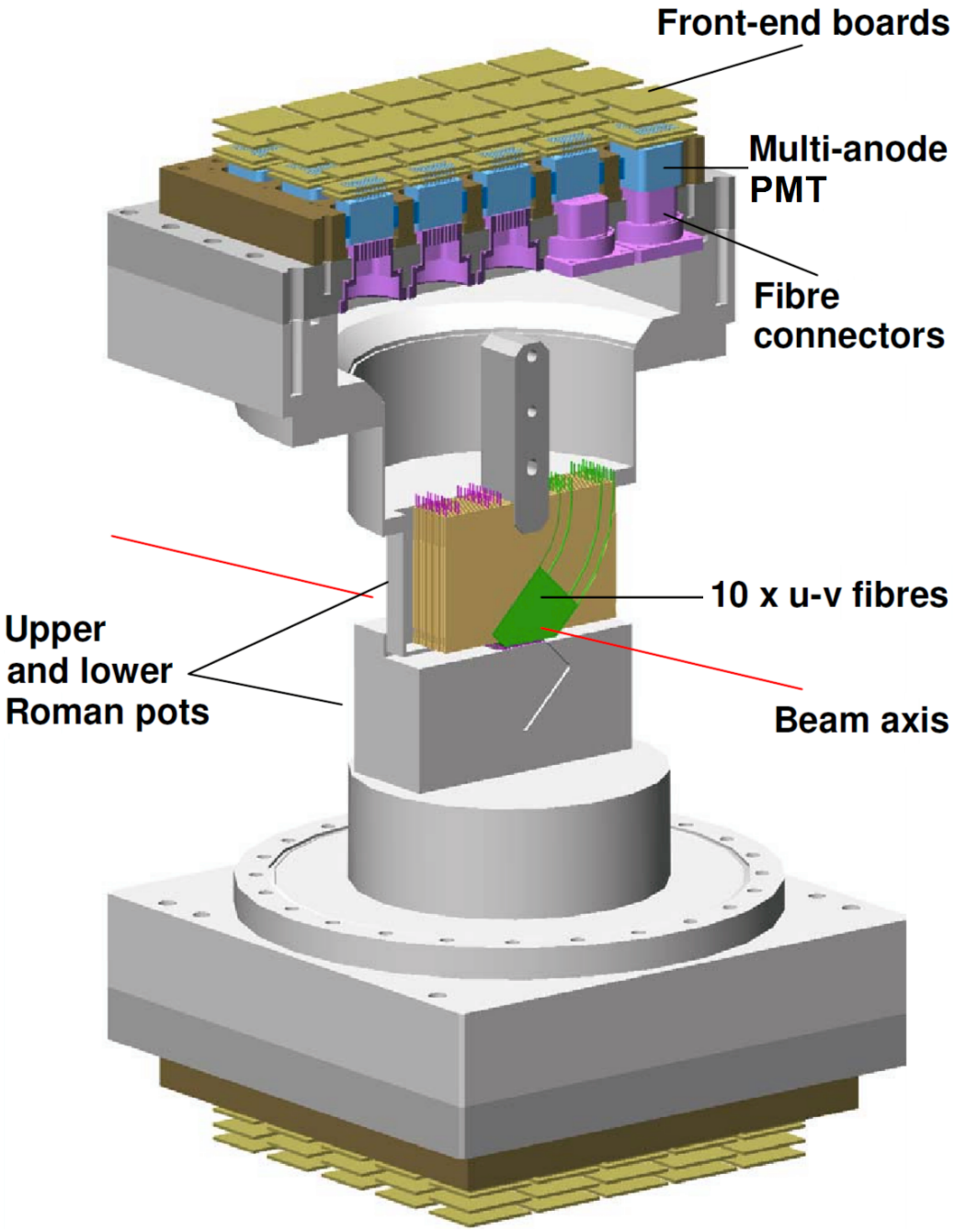

FIGURE 4.5: Schematic layout of the ALFA detector in the Roman Pot showing the scintillating fibres of tracker, the fibre connectors, the multi-anode PMTs and the front-end boards. Figure taken from [26].

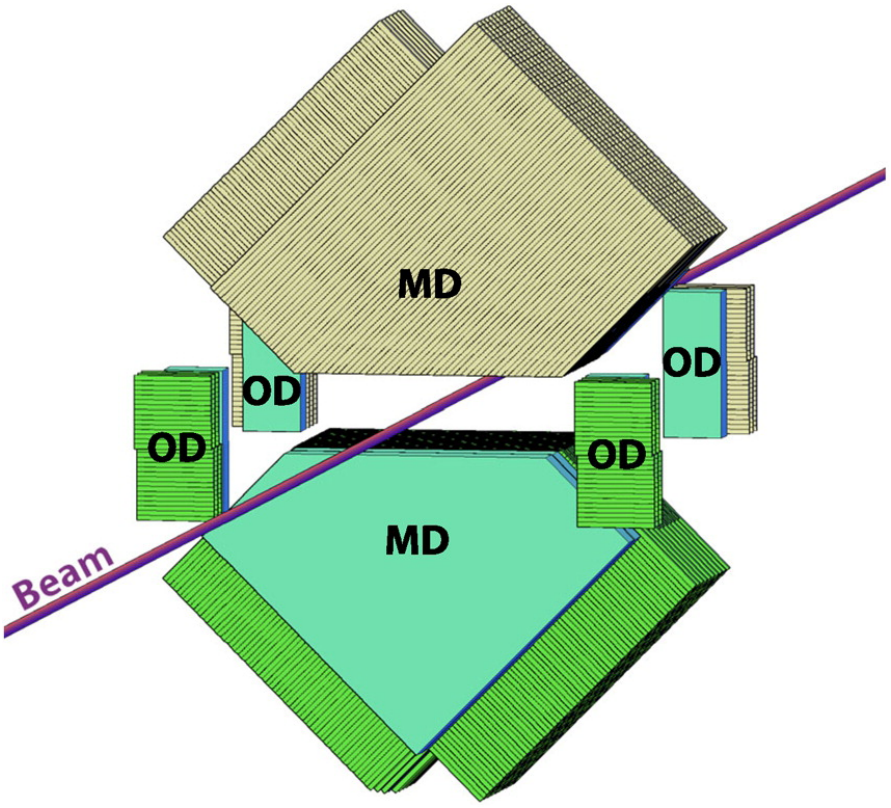

FIGURE 4.6: Layout of ALFA MD and OD with trigger counters with respect to the nominal beam position. Figure taken from [48].

This gives approximately 144 µm resolution for single ALFA fibre layer in both x and y directions. To further improve the resolution, fibre layers in the individual plates are *staggered* by multiples of 1/10 of the fibre size. The staggering procedure makes the effective ALFA pixel size ten times smaller, which results in theoretical resolution of 14.4 µm. In practice, the resolution is worsened by imperfect staggering, noise, cross-talks and fibre inefficiencies. The actual resolution of ALFA detectors was measured to be between 30 µm and 40 µm [50].

Geometrical acceptance

For all scattered proton measurements done using the ATLAS forward detectors, it is important to understand the connection between the proton four-momentum and its trajectory position in the detector. This dependence for various LHC optics is illustrated in Figure 4.7. This figure shows the positions of elastically and diffractively scattered protons with various transverse momenta in the ALFA detector plane at the nominal detector location. One can observe that the elastically scattered protons with very small transverse momentum do not reach the ALFA detector active area. Also, diffractively

scattered protons have negative value of x and positive values of y[3] and they mostly fly outside the ALFA detector acceptance for nominal $\beta^* = 0.55$ m (collision) optics. This means that for the collision optics ALFA covers only small kinematic phase space region of diffractive interactions. In the case of elastically scattered protons, more and more particles with small transverse momentum values reach the detector as β^* increase. Therefore, a dedicated *high-*β^* runs are crucial for ALFA elastic measurements.

4.2 The AFP project

The *ATLAS Forward Proton* (AFP) project [52] promises a significant extension of the physics reach of ATLAS by tagging and measuring the momentum and emission angle of diffractively scattered protons. This enables the observation and measurement of a range of processes where one or both protons remain intact and which otherwise would be difficult or impossible to study. Because diffractive processes generally have high cross sections, it is argued that significant diffractive physics results can be obtained with a few weeks of special runs in the LHC Run-2 period.

The installation of the AFP detectors is currently foreseen to occur in two phases: a first phase of a single-arm AFP ("0+2"), adequate for special low-luminosity running and the measurement of soft and hard single-diffractive (SD) physics. Installation may be attempted as early as during the scheduled 9-week long Winter 2015–2016 shutdown. Whether or not that will be possible, the second arm or the full system ("2+2") will be installed during the 19-week shutdown planned for Winter 2016–2017.

4.2.1 AFP physics program

The initial AFP physics program for LHC Run-2 is the study of diffractive processes in special low-luminosity runs.

Among all reactions that can be measured with AFP, the SD processes have the highest cross sections. This translates to relatively small amounts of integrated luminosity and run time ($\sim$1 pb^{-1}) required. On the other hand, these measurements must be done in an experimentally very clean environment, thus the optimal pile-up condition is $\langle\mu\rangle$ around 1. By studying single-diffractive jet production, one can probe the idea of Pomeron universality between ep and pp colliders, i.e. if the same object is mediating diffractive interactions at HERA and the LHC. Another interesting measurement is the measurement of diffractive gap survival probability factor. A detailed study into the

[3] Due to the non-zero beam crossing angle at the IP

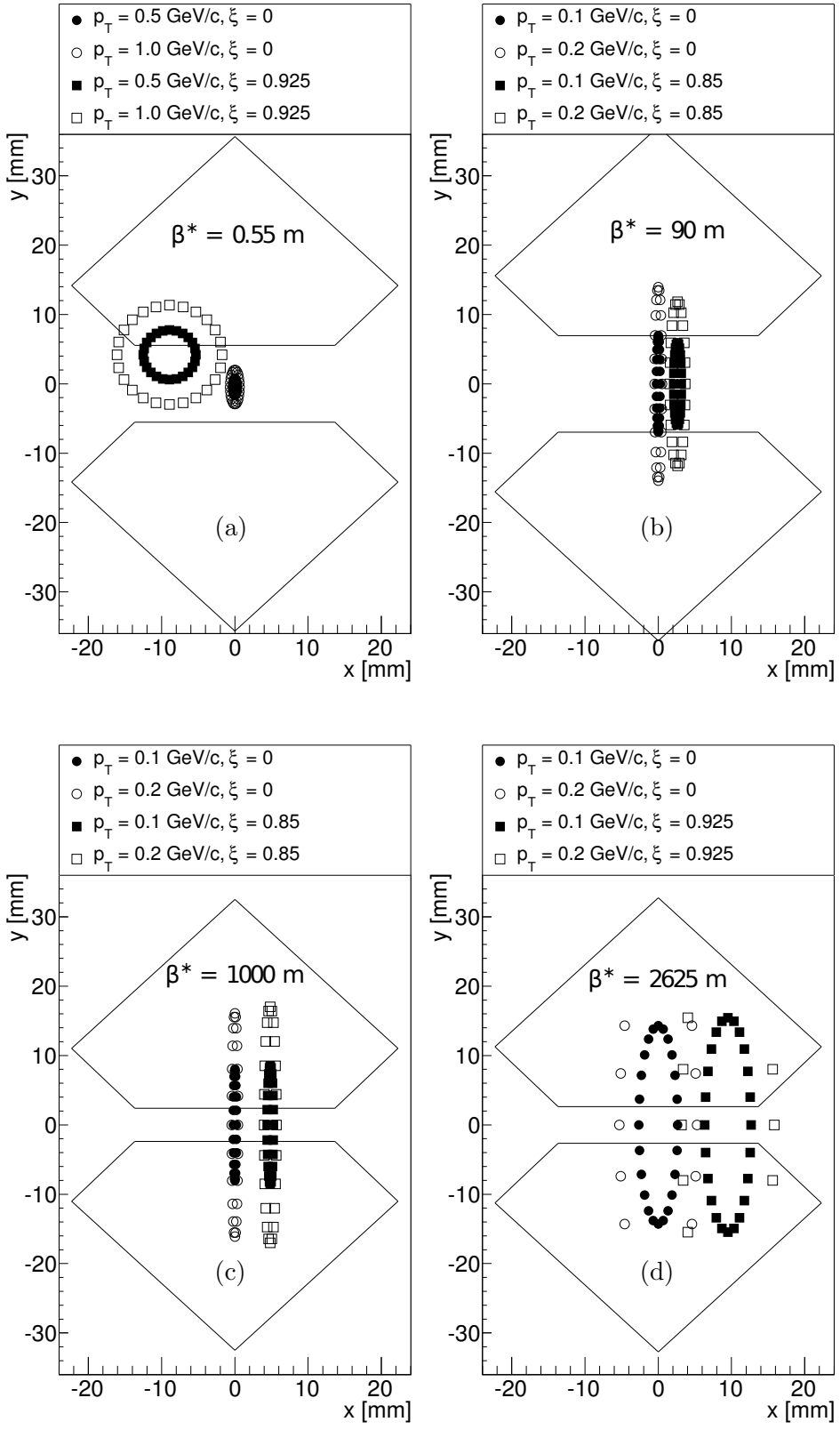

FIGURE 4.7: Proton positions with different relative energy loss (ξ_p) and transverse momentum (p_{T}^p) at the first ALFA station for the different LHC optics settings: (a) $\beta^* = 0.55$ m, (b) $\beta^* = 90$ m, (c) $\beta^* = 1000$ m and (d) $\beta^* = 2625$ m. The solid lines represent the ALFA detector active area. Figure taken from [51].

applicability of this factorization would be an interesting outcome of the AFP measurements. In particular, the presence of an additional contribution from other colourless exchanges can be studied. Good experimental precision will allow for comparison to theoretical predictions and differential measurements of the dependence of the survival factor on (for example) the mass of the central system. The other SD hard systems considered for AFP measurements in dedicated runs during LHC Run-2 are photons, photon+jet and electroweak bosons.

The AFP can be also very useful in measuring photon-induced reactions. In order to determine experimentally the nature of proton-dissociative processes, one can use single proton tagging to measure single-dissociative lepton pair production. With an integrated luminosity of the order of $\sim$10 pb^{-1}, this would give the access to e.g. the photon-PDFs in the proton: a quantities which are still poorly known at the LHC energies.

4.2.2 AFP detectors

The AFP detectors aim to measure protons that are emitted from a central interaction in the very forward directions. Protons suffering a moderate energy loss and emitted at µrad angles with respect to the beams will remain inside the beam pipe but separate from the beam axis because of the accumulated dispersion in the beam elements. At $\sim$200 m from the ATLAS interaction point (IP), they will be sufficiently separated from the nominal beam orbit so that they can be intercepted by detectors inserted into the beam pipe aperture. The deflection of the proton depends on the magnitude of the energy loss suffered, and also on the emission angle at the IP.

The locations available to AFP are at distances along the beam line of 204 m and 212 m from the ATLAS IP on both sides. They are shown in Figure 4.8 and lie between the Q5 and Q6 quadrupoles. The ALFA stations are located behind the Q6 quadrupole, at locations around 240 m. The chosen AFP locations are selected because they are available (i.e. empty of essential beam elements and instrumentation), and because they are located at positions of sufficient integral dispersion to make interception and measurement viable.

Beam interface

The search for a suitable detector-beam interface for AFP started within the framework of the FP420 collaboration [53]. The initial beam interface of choice was the *Hamburg Beam Pipe* (HBP), a movable section of beam pipe with a thin "floor" and entry/exit windows that would allow the detectors to approach the LHC beam as close as 3 mm.

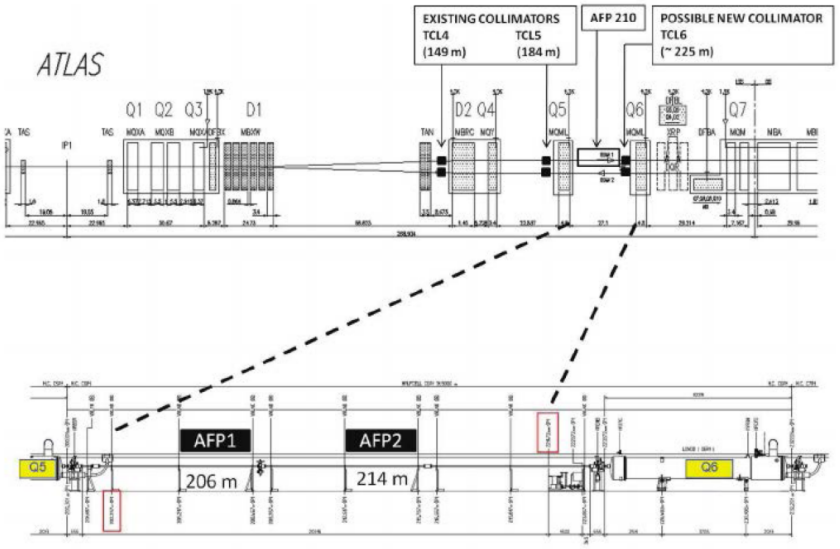

FIGURE 4.8: The locations of the AFP stations in the LHC lattice near the ATLAS interaction point. Only the positive-z arm of AFP is shown; the negative-z arm of AFP is nearly identical. The ALFA detector stations with vertical pots are located at about 240 m. Figure taken from [52].

The proposed HBP prototype is shown in Figure 4.9. This design was fully engineered and its radio-frequency (RF) impact on the LHC beam evaluated. With sloping entry and exit windows (similar to the sloping collimator jaws in use at the LHC), the HBP RF impact was shown to be equivalent to that of a Roman Pot. With the use of beryllium or aluminium windows, the interaction length of windows and floor was also shown to be acceptable. However, the HBP device has not been used previously at the LHC and is therefore considered more risky. Moreover, the cost of a single HBP station is estimated about three times that of a RP station. The RP beam interface has been already adopted by the ALFA [42] and TOTEM [11] collaborations and has shown to work reliably at the LHC. Hence, the AFP baseline beam interface chosen for the 210 m stations is the RP, with the parallel development of the HBP solution.

The AFP Roman Pot station contains the pot and the mechanics allowing it to enter the beam pipe aperture. The cylindrical pot orientation and its motion are horizontal, transverse to the beam direction. Since the present TOTEM horizontal station is perfectly suited for AFP, therefore it was decided to use TOTEM RP station design [11]. The design drawing of the AFP RP is shown in Figure 4.10. The most significant difference between AFP and TOTEM RP designs is that the AFP requires more flat area on the RP bottom. This is due to the generally larger size of detectors used. The material of the pot, as for many LHC beam elements, is a low-carbon, nitrogen-enhanced version of Type 316 molybdenum-bearing austenitic stainless steel.

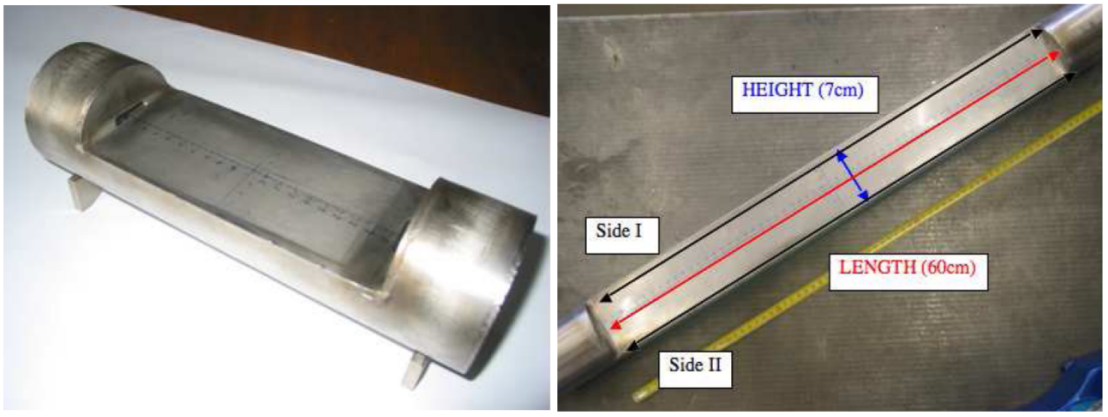

(a) (b)

FIGURE 4.9: Hamburg Beam Pipe prototypes: (a) view of a 200 mm long pocket and (b) 600 mm long pocket. Figure taken from [53].

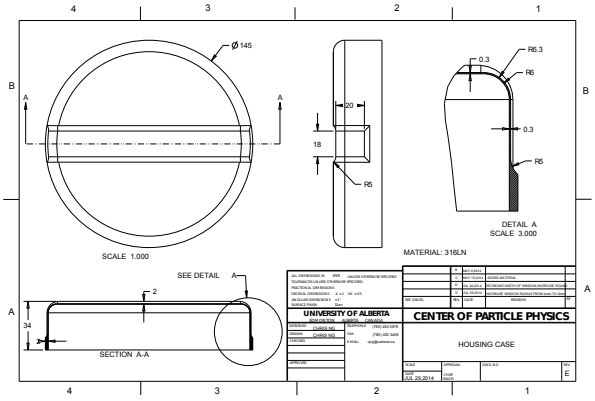

(a) (b)

FIGURE 4.10: The AFP Roman Pot design: (a) the drawing of the bottom "cup" of the Roman Pot and (b) the 3D visualization of the pot, including the cup, tubular section, and the vacuum flange. Figure taken from [52].

Tracking detectors

The AFP design foresees a high resolution pixelated silicon tracking system placed at 210 m from the ATLAS IP. Combined with the magnet systems of the LHC accelerator, the AFP *Silicon Detector* (SiD) system will provide the momentum measurement of the scattered protons. The full AFP SiD system will consist of four units (stations), each composed of many pixel sensor layers,[4] which will be placed in Roman Pots, two on each side of the ATLAS IP ("2+2"). However, for the first AFP phase ("0+2") the tracker will be reduced to two RPs at only one side of the ATLAS IP.

The needs for the AFP Silicon Detectors are as follows:

[4]The initial design assumed 6 layers/station, where 4 layers/station will be used with RP configuration

- To ensure good proton momentum resolution, the AFP SiD is required to provide a high spatial resolution of ∼10 µm (∼30 µm) per station in horizontal (vertical) direction.
- The AFP tracker must be able to approach the circulating beam closely, and therefore an "edgeless" device is required, i.e. the inactive region of the detector side facing the beam should have ∼200 µm.
- While in the measurement position only a few mm away from the beam, the AFP SiD units have to withstand a highly non-uniform irradiation profile with a high maximum fluence along the line of diffractively scattered protons.

Because of the above requirements, the AFP baseline tracking device is the 3D silicon pixel tracker, used for the ATLAS Inner Detector insertable B-layer (IBL) [18, 54]. The radiation environment for AFP is more benign than for the first layers of the ATLAS Inner Detector, but the irradiation varies strongly as function of the distance to the circulating beam. In addition, the choice of the 3D pixel sensor allows the use of the well-tested FE-I4b frontend chip [54] for readout. The chip operates with a 40 MHz externally supplied clock and provides readout for each pixel channel. Each channel contains an independent amplification stage, followed by a discriminator with adjustable threshold. The FE-I4b chip can also send a trigger signal, which is formed as the logical OR of all fired discriminators on the FE-I4b chip.

The AFP 3D pixel sensors for the first AFP phase were already fabricated [55] based on the p-type silicon wafers, with 230 µm thickness, and a very high resistivity (10 to 30 kW cm). The sensor design features an array of 336×80 pixels with a pixel size of 50×250 µm^2. This gives the AFP SiD sensor active area of 16.8 mm wide in horizontal (x) direction and 20 mm wide in y (vertical, the long direction of the pixels). Each pixel consists of 2 n^+-junction columns and 6 surrounding p^+-ohmic columns. In order to fulfill the AFP-specific needs, the 3D pixel sensors are slimmed at the vertical edge, leaving $100 - 200$ µm remaining extension from the sensor edge to the most external pixel columns. Figure 4.11 shows details of the 3D pixel sensor layout.

The construction of the AFP SiD should allow its easy and relatively fast installation or removal directly in the LHC tunnel, where the access time is usually very limited. In addition, the silicon sensors are rather fragile and they have to be protected against any mechanical stress. Therefore, the appropriate tracker holder has to be prepared. A preliminary design of the AFP SiD foresees a simple compact block of planes assembled together with a gap of about 10 mm between planes. Materials such as Si/Al alloy, aluminium nitride or a carbon fibre composite are considered as base materials for the manufacturing of the mechanical parts of the AFP SiD. These materials have a low

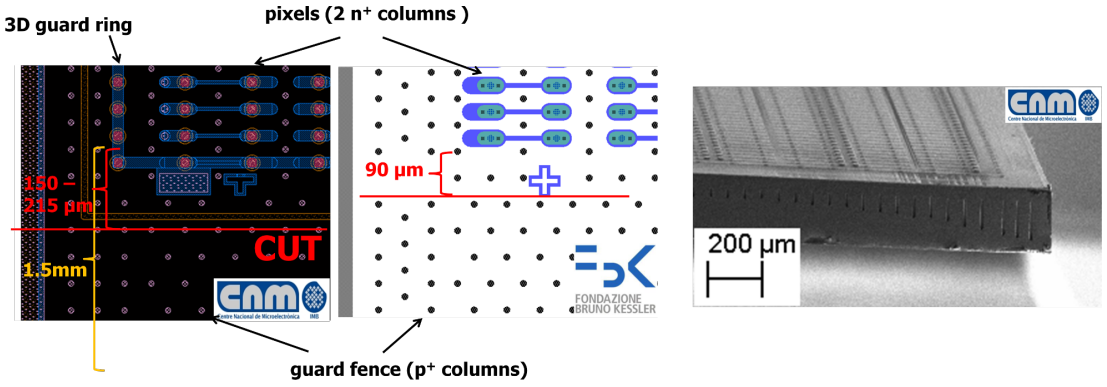

(a) (b)

FIGURE 4.11: (a) Sketch of a corner of a 3D pixel sensor and (b) a picture of a sensor after a diamond-saw cut. The cut lines for the AFP slim-edge prototypes are also indicated. Figure taken from [55].

thermal expansion coefficient which also provide high mechanical stiffness and overall stability of the tracker. The proposed AFP tracker assembly is shown in Figure 4.12. The plates are 1 mm thick, with a window underneath the silicon chip modules, and are covered with a thin layer of high thermal-conductivity foil, providing a heat exchange between the sensors and dedicated cooling system.

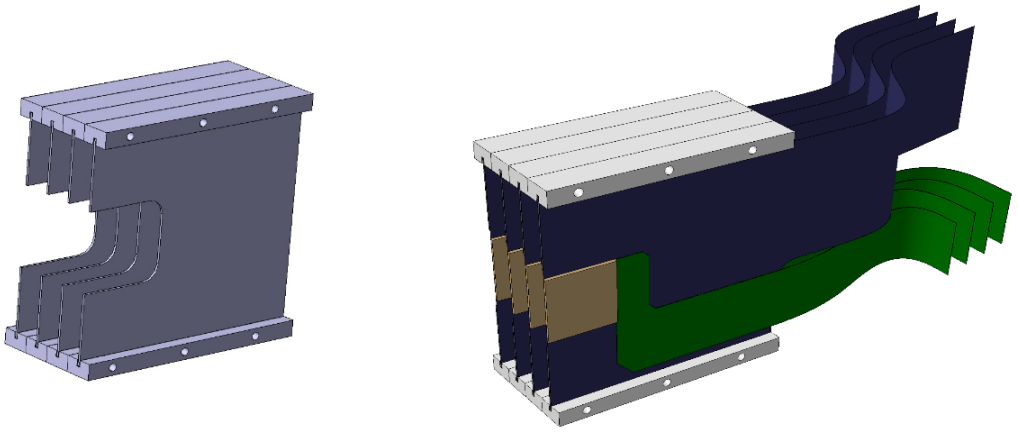

(a) (b)

FIGURE 4.12: The proposed AFP tracker assembly: (a) the bare tracker assembly of four planes and (b) the tracker assembled with sensors (gold), high thermal-conductivity foils (dark blue) and flex (green) interconnects. Figure taken from [52].

Timing detectors

When the average number of *pp* interactions per bunch crossing, $\langle\mu\rangle$, increases, forward proton *time-of-flight* (ToF) information becomes necessary to reject backgrounds. The level where timing becomes needed depends on the process under study, but in general,

the improved signal purity can be reached for any reaction with both intact protons tagged. The background mainly stems from protons (measured in the two AFP arms) that come from different single-diffractive interactions in the same bunch crossing.

Precision proton ToF measurements, t_{Right} and t_{Left} in the Right and Left AFP detector arms, permit the determination of the longitudinal origin (vertex) of the proton pair as

$$z_{\text{AFP}} = c \cdot \frac{t_{\text{Left}} - t_{\text{Right}}}{2} \ , \tag{4.3}$$

where c is the speed of light. The idea is that the matching of z_{AFP} with interaction vertices reconstructed by the ATLAS Inner Detector provides rejection of pile-up vertices if the time-of-flight resolution is sufficiently small.

At high LHC instantaneous luminosity, where the average number of interactions per bunch crossing can exceed 40 ($\langle\mu\rangle > 40$), the AFP *Timing Detector* (TD) system should have the following characteristics:

- 10 ps or better timing resolution, corresponding to ∼2.3 mm z_{AFP} position resolution
- geometrical acceptance that fully covers the 16.8×20 mm^2 active region of tracking detectors
- high efficiency to reconstruct the signal for diffractive protons (>90%)
- horizontal (x) segmentation in for multi-proton timing measurements
- L1 trigger capability
- radiation hard or tolerant for high integrated luminosity LHC runs

The original design of Timing Detectors for AFP relies on the measurement of Cherenkov light, emitted by the high-energy protons when passing through the dedicated radiator volume. Cherenkov light is prompt and therefore ideal for fast timing measurement, although the amount of light is small compared with scintillator. The design is based on *QUARtz TIming Cherenkov* (QUARTIC) detectors [56], proposed by FP420 [53] and further optimized by AFP for use with a Hamburg (movable) beam pipe.

Figure 4.13 shows the concept and layout of QUARTIC. The detector consists of straight synthetic quartz bars (Qbars) positioned at the Cherenkov angle with respect to the proton flight direction, and functioning both as a radiator producing Cherenkov light, and as a light-guide that funnels the light to the *microchannel-plate photo-multiplier* (MCP-PMT). MCP-PMT consists of a quartz faceplate and a photo-cathode followed

by two back-to-back chevroned microchannel plates read out by a single anode or multi-anode pads. They are compact (only few cm in depth) and provide a gain of about 10^6 for a typical operating voltage of 2 to 3 kV. The multi-bar configuration provides n independent measurements of the proton ToF, which can decrease the time resolution of a single TD (σ_t^{TD}), following the formula:

$$\sigma_t^{\mathrm{TD}} = \frac{\sigma_t^{\mathrm{bar}}}{\sqrt{n}} \ , \tag{4.4}$$

where n is the number of Qbars in beam direction (forming one row in horizontal direction) and σ_t^{bar} is time resolution of a single-bar detector. If several bars are to be read out by a single photo-detector, it is important that the light from each bar arrives at the MCP-PMT at approximately the same time, which occurs with the photo-detector face normal to the bars, as shown in Figure 4.13. Moreover, multiple-row configuration in horizontal direction gives the segmentation needed for multi-proton timing.

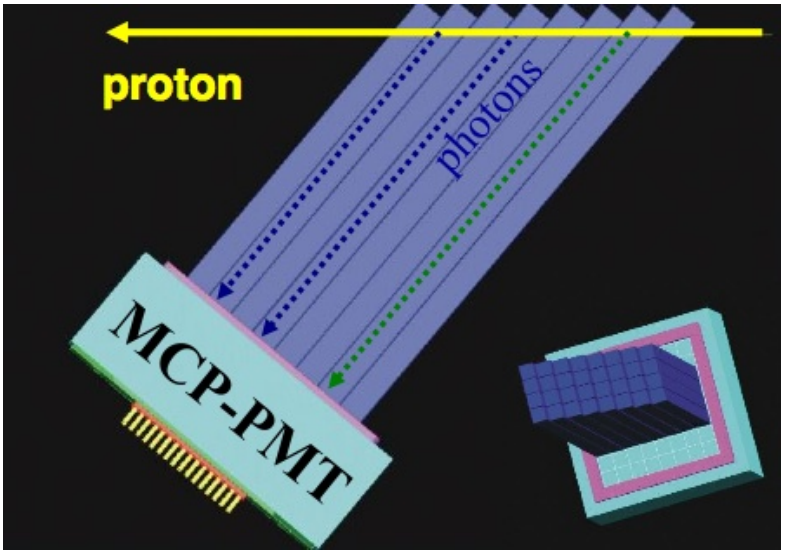

FIGURE 4.13: Conceptual drawings of a QUARTIC detector, showing the proton passing through eight bars of one row in horizontal (x) direction, providing eight measurements of the proton time. The 8×4 layout of QUARTIC bars is also shown. Figure taken from [53].

Initially proposed AFP Timing Detectors were a modified version of the original QUARTIC detectors, very similar in shape (straight bars) and concept. However, space constraints imposed by the cylindrical Roman Pot housing require that the light needs to be brought out perpendicular to the beam. Thus, the AFP TD quartz bars must be bent out of the z (beam) – y (vertical) plane into the x (horizontal) direction (parallel to the Pot axis). Therefore, they form a characteristic *L-shape quartz bar* (LQbar) pattern.

Figure 4.14 shows a drawing of the LQbar-based AFP TD concept, and a picture of the prototype implemented for the AFP beam tests. It contains 4×2 array of LQbars with

a 6 mm × 3 mm (first row), or 6 mm × 5 mm cross section (other rows). Cherenkov light travels up the bars and is converted to a signal by a specialized 4 × 4 pixel MCP-PMT. The MCP-PMT output signal is approximately Gaussian with a RMS of 300 ps. Photon statistics (the mean number of photo-electrons is about 10) affect the signal amplitude but keep the shape precisely. Then, the goal of the fast electronics is to further preserve the signal shape information and derive the best possible timing of the signal, independent of the signal amplitude. The approach chosen by the AFP is based on low-noise amplification followed by *constant fraction discrimination* (CFD) and *high-precision time-to-digital converter* (HPTDC) [57].

For the first AFP phase consisting in a single-arm two-station setup, the ToF system is of no great use except possibly for event triggering. However, installing a time-of-flight detector from the very beginning allows the characterization of the time profile of the protons from central interactions and from various background sources.

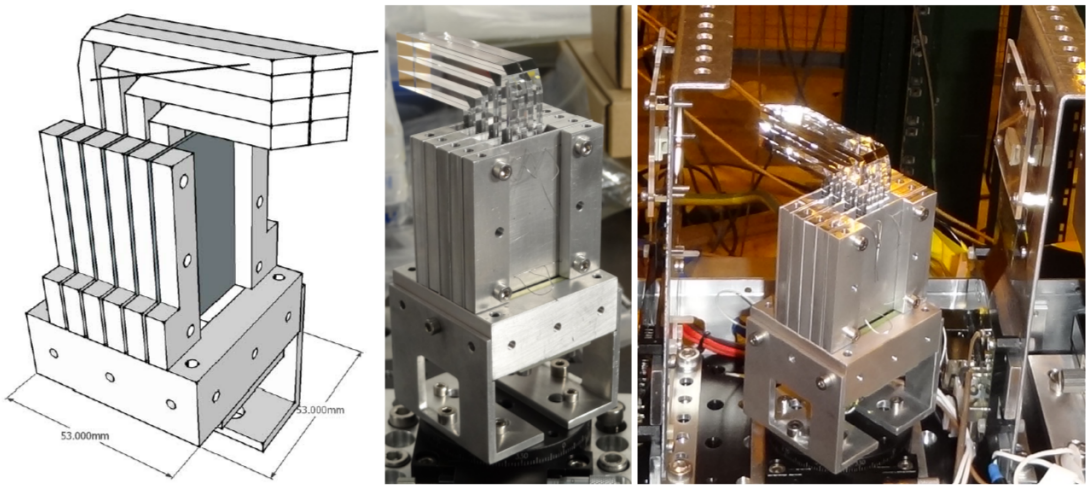

(a) (b)

FIGURE 4.14: (a) Drawing of a prototype of the LQbar-based AFP TD containing 4 rows of 2 bars. The straight line represents a diffractive proton trajectory. (b) The LQbar TD prototype installed in the beam test. Two 3D SiD planes are also visible. Figure taken from [52].

AFP detectors integration

The overall possible arrangement of individual AFP detectors is shown in Figure 4.15. The AFP beam interface at 204 m contains the first AFP Silicon Detector. The beam interface at 212 m contains a second, identical, AFP SiD followed by the AFP Timing Detector. Such configuration is mainly motivated by the relatively large nuclear

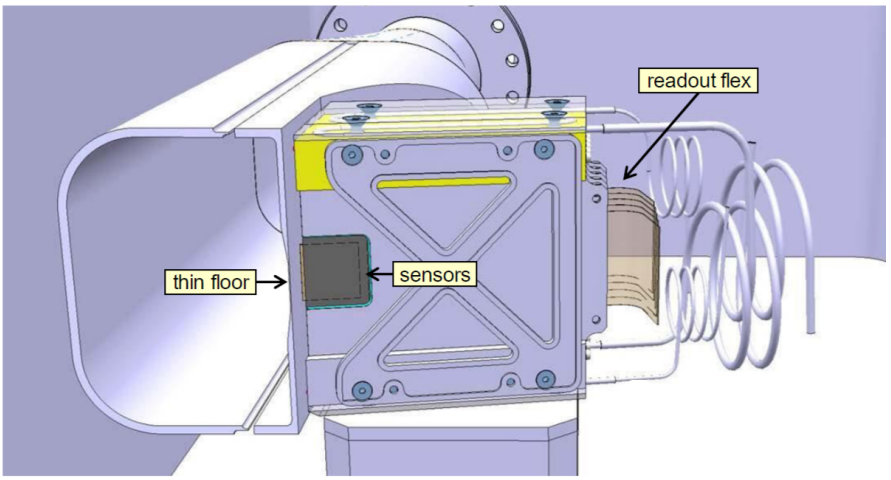

(a)

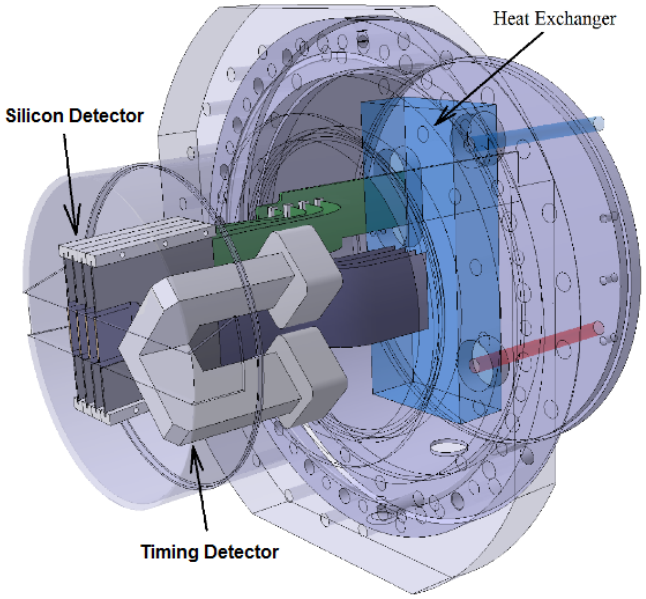

(b)

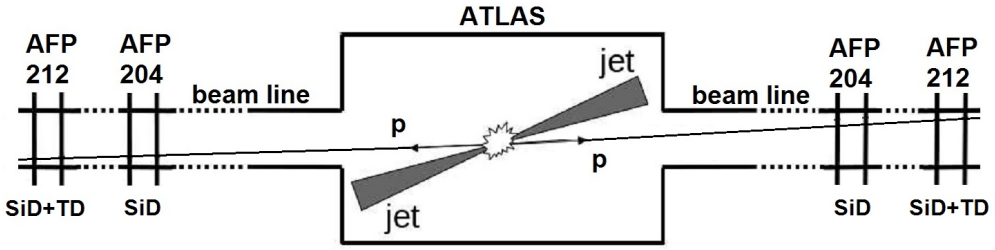

(c)

FIGURE 4.15: Sketch of the AFP detectors, at 204 m from the ATLAS IP inside an old-design HBP-based beam interface (a), and at 212 m with new-design RP-based stations (b). The sketch of the layout of the AFP stations at ±204 and ±212 m is also shown (c). The inner (±204 m) stations contain only SiD, where the outer (±212 m) both SiD and TD. Figure taken from [52].

interaction length[5] (3-6% per total thickness of 2-4 quartz radiators) of the TDs. Depending on the beam interface, Qbars (for HBP), or LQbars (for RP) are positioned at the Cherenkov angle of 48° with respect to the beam, and parallel to the floor (HBP), or bottom cup (RP). The SiDs are placed almost perpendicular to the beam (under a small tilt of 13° to minimize possible inefficiencies due to the columnar electrodes of the chosen 3D pixel technology).

[5]Nuclear interaction length is the mean distance travelled by a hadronic particle before undergoing an inelastic nuclear interaction

Chapter 5

Simulation of AFP detectors

This chapter describes in details the AFP detectors simulation. The simulation contains the implementation of ATLAS forward region, AFP detectors-beam interface, AFP Silicon and Timing Detectors. The author of this thesis significantly contributed to the development of models for simulated event digitization and reconstruction, both for AFP Silicon Detector (SiD) and Timing Detector (TD), together with so-called Fast Cherenkov model for optical photon transportation.

5.1 ATLAS forward region simulation

The AFP setup is designed to measure protons emitted at a very small scattering angles. Since the AFP sub-detectors (SiD and TD systems) have to be placed far away from the ATLAS interaction point, the protons are transported through several LHC magnets placed between the IP and AFP stations. The trajectory of the scattered protons deviates from the straight-line shape.

In order to simulate scattered proton positions and momenta at a given distance from the ATLAS IP, mapping tools are usually used [58, 59]. Such tools take as an input generator-level particles and calculate the required positions and momenta using matrices that describe magnetic elements (or fields) in the ATLAS forward region. There is also a possibility to make a full simulation of particle motion through the accelerator magnetic lattice, including all physical processes, using GEANT4 functionality [29].

The full GEANT4-based simulation of particle interactions in the ATLAS forward region is prepared within the ATHENA software framework [28]. There are several advantages of such approach. First, the full simulation allows the simultaneous treatment of multiple ATLAS forward detectors (i.e. in addition to AFP also ZDC and ALFA). Next,

secondary particles emerging in the forward region are also taken into account. For example, showers developing on the beam screen[1] elements of magnets can be studied. Additionally, it is possible to move and rotate magnets and vary their fields to study the effects of such modifications.

The model of the ATLAS forward region used in the simulation is shown in Figure 5.1. It is prepared using ATLAS GeoModel framework [34] and consists of the LHC beam pipe elements, starting at 19.06 m (the end of ATLAS cavern), and describing it till behind the ALFA detector, up to a distance of 269 m. All magnetic fields are included, based on the dedicated calculations prepared using FLUKA software [61]. Except for the beam pipe (including beam screens and adjustable collimators), there is presently no other material included in the simulation of the ATLAS forward region.

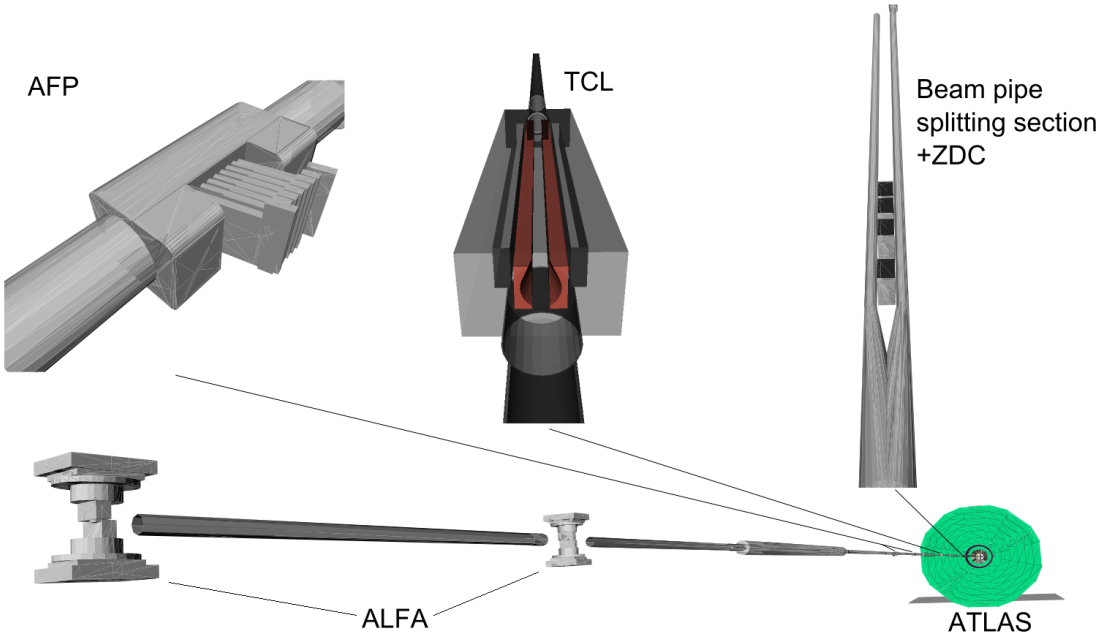

FIGURE 5.1: Simulation model of the ATLAS forward region containing different LHC beam pipe elements (including TCL and splitting section). The positions of ATLAS forward detectors are also shown. The figure is prepared using VP1 software [62].

5.2 AFP geometry

The geometry of AFP for GEANT4 simulation (AFP GeoModel) consists of models of detector-beam interface, silicon tracker and ToF spectrometer. All models are prepared within the ATLAS GeoModel framework [34] and are parametrized, such that their spatial dimensions can be easily adjusted, based on the final project requirements.

[1] Beam screen is a perforated co-axial liner, placed inside the beam pipe, that protects superconducting magnet against beam-induced heat and radiation. More details can be found in [60].

5.2.1 Beam interface

The AFP beam interface can be based either on Hamburg Beam Pipe solution, or Roman Pot configurations. In the simulation, models for both interfaces are implemented.

Based on the original model of the Hamburg Beam Pipe (HBP), the improved design of the HBP is considered, with tilted HBP entry/exit windows in order to minimize RF losses. The original HBP model is retained in the simulation and the tilted window is mimicked by the additional material - the HBP window thickness was changed to 300 µm / $\sin 11° \approx 1.57$ mm). The default thickness of the HBP floor layer in the simulation is chosen to be 300 µm. Figure 5.2 shows the visualization of the implemented HBP geometry. Two different versions of the AFP HBP are prepared. The *short HBP*, placed at ±204 m from the ATLAS IP, is designed to contain the inner AFP Silicon Detectors. The *long HBP* hold AFP SiD, together with the AFP Qbar-based TD, and is placed at ±212 m .

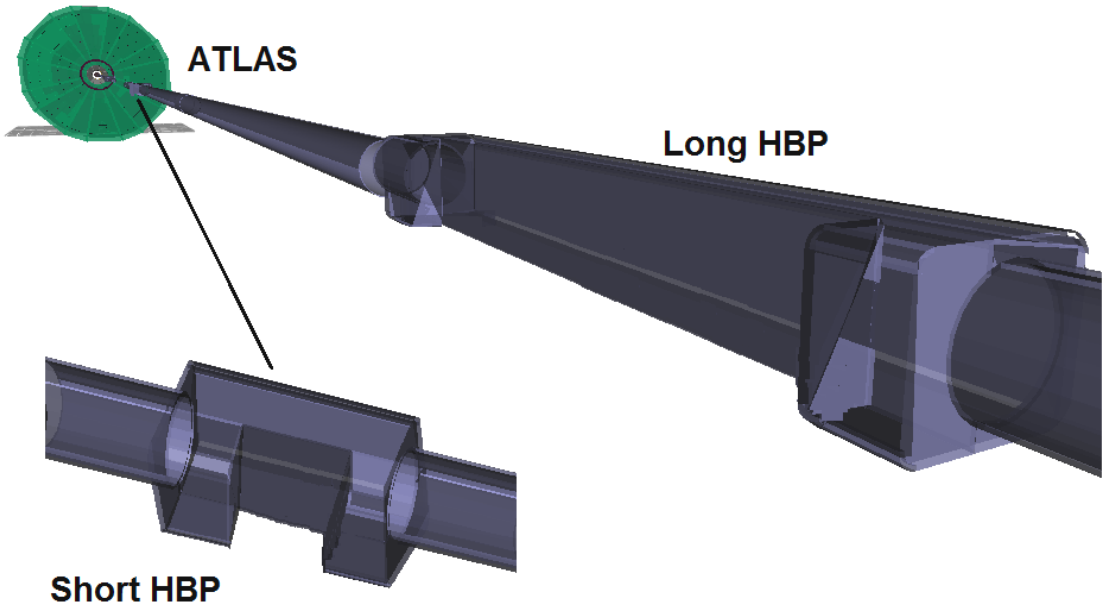

FIGURE 5.2: Simulation model of the short and long AFP Hamburg Beam Pipes. The length of the short and long pipes measured between the entrance and exit windows is 60 mm and 360 mm, respectively.

After studies of RF impedance and the cost considerations, the Roman Pot beam interface has been chosen as the AFP baseline. The model based on the AFP Roman Pot design is also incorporated in the simulation. It is shown in Figure 5.3. It consists of stainless steel cylinder of length of 119 mm and bottom cup with a 300 µm thick beryllium window. The default diameter of the pot is 140 mm.

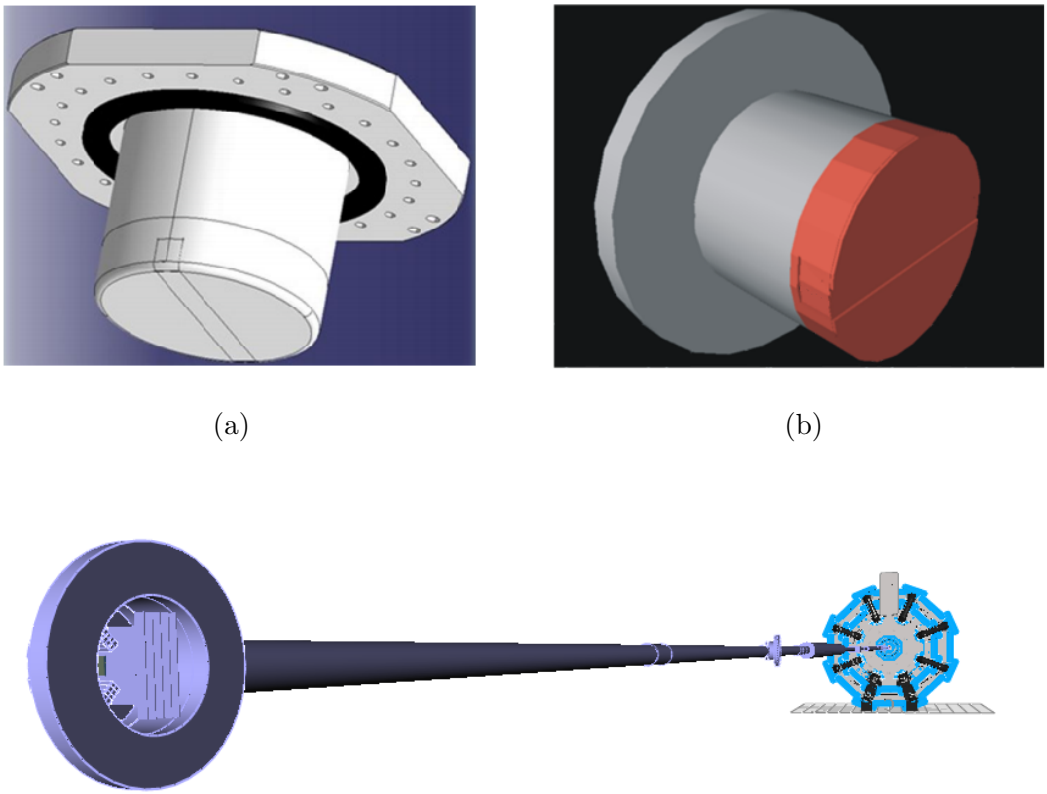

(a) (b)

(c)

FIGURE 5.3: Simulation model of the AFP Roman Pots. The technical drawing (a) is compared with the simulation implementation (b). The simulated alignment of the AFP Roman Pots with respect to the LHC beam pipe is also shown (c).

5.2.2 AFP Silicon Detectors

An initial simulated model of the AFP SiD has been prepared for usage with the Hamburg Beam Pipe interface. It includes 6 silicon sensor layers per HBP station. Each layer is mounted on a dedicated assembly with water sensor cooling implemented, as presented in Figure 5.4. The AFP SiD model was later changed to become close to the newly elaborated design, where the water cooling is no longer used. The final RP-based version of the detector will consist of 4 pixel sensor layers for each Roman Pot station.

Individual pixel sensor is simulated as a 250 µm thick silicon layer, with the area of 16.8×20 mm^2. The array of 336×80 pixels of size 50×250 µm is also considered. Based on the list of the energy deposits of the protons inside the silicon sensor (so-called GEANT4 hits [29]), the total deposited energy per pixel is calculated. For each hit, the following additional information is stored: the beginning and the end of the segment containing the hit and the physical properties of the particle, such as momentum and charge.

The AFP GeoModel tool allows parametrized staggering of silicon sensor planes in both horizontal and vertical directions, together with horizontal movement of AFP Silicon Detectors and their eventual vertical tuning. This should provide the required resolution and efficiency for the planned physics measurements and studies.

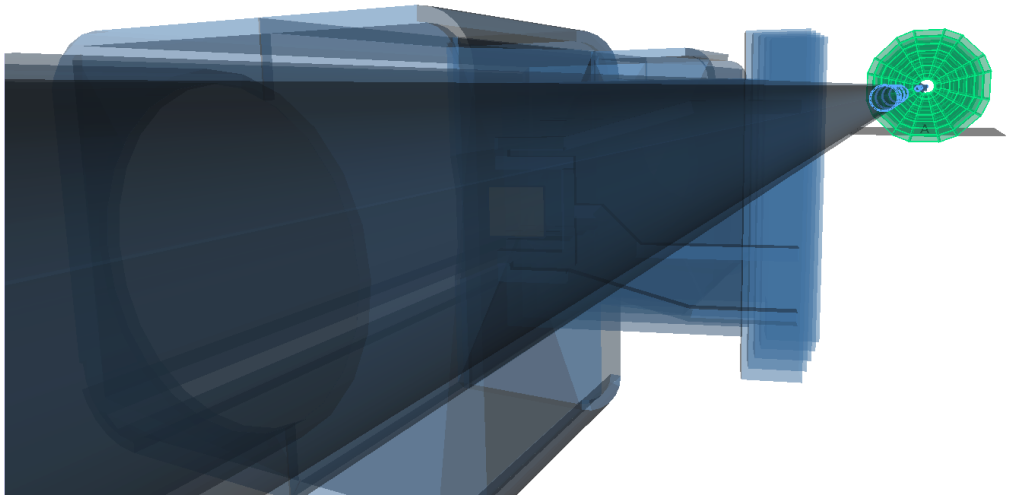

FIGURE 5.4: Simulation model of the AFP Silicon Detector for the HBP interface. Sensor planes with water cooling pipes are also visible.

5.2.3 AFP Timing Detectors

In the simulations the QUARTIC detectors [56] were initially implemented, in use with HBP-based configuration. The material properties of quartz radiators used in the simulations are summarized in Table 5.1. A full parametrization of the QUARTIC detectors allows various functions, e.g. to change number of simulated bars, their dimensions and relative spacing. An example of such configuration, designed for HBP interface is shown in Figure 5.5. A default HBP-based AFP simulation setup consists of two arrays of 8×4 Qbars per station, placed after each other in the beam direction. The rows of bars in the horizontal direction are separated by 4 mm and two detectors in a single HBP are placed with a relative 4 mm offset in the horizontal direction. The Qbar row segmentation is higher for bars placed closest to the beam axis and lower for more external bars. A cross section of the most internal bars in the row is 2 mm $\times$ 6 mm for detector placed closer to the ATLAS IP and 4 mm $\times$ 6 mm for detector placed further from the IP. For the external bars the cross section is 6 mm $\times$ 6 mm. This configuration provides a better geometrical acceptance of the AFP TD system, comparing to the original QUARTIC design, where the rows of bars are not separated.

Because of the adoption of the Roman Pot beam interface for AFP, a new LQBar timing radiator shape was devised. Each LQbar is geometrically divided into a radiator arm

Photon wavelength [nm]	Refractive index	Absorption length [cm]
200	1.541	83
250	1.510	95
300	1.488	104
350	1.475	111
400	1.470	120
450	1.465	122
500	1.462	125
550	1.460	128
600	1.458	130
650	1.456	130
700	1.455	130
750	1.450	130

TABLE 5.1: Relation between photon wavelength, refractive index and absorption length for synthetic quartz. Table taken from [56].

(vertical) traversed by the proton and a light-guide arm (horizontal) channelling the light to the photo-sensor. Therefore, several types of LQbar are implemented in GEANT4, depending on the material choice for radiator and light-guide separately [63]. This allows to compare benefits and drawbacks in consideration of light dispersion, losses and estimation of signal strength in LQbars. A possible alignment of the AFP Timing Detectors for the RP solution in the simulations is shown in Figure 5.6.

Both Qbar (in HBP) and LQbar (in RP) radiators are positioned at the Cherenkov angle of 48° with respect to the beam axis. Simulation of Cherenkov photons is performed when the simulated charged particle enters the quartz bar region. Generated Cherenkov photons are then propagated by total internal reflection, through the bars, to the MCP-PMT. The microchannel-plate is simulated as a thin (1 mm) layer of silicon, with the same cross section as a corresponding bar. Since the simulation of optical processes in GEANT4 is very time consuming, a Fast Cherenkov model has been implemented, which significantly speeds up the simulation step for AFP Timing Detectors. The formalism is implemented for the QUARTIC bar geometry, however, it can be extended for the LQbar detector geometry.

5.3 Fast Cherenkov algorithm

The simulation of Cherenkov light production is already taken into account in GEANT4. Since GEANT4 is treating each simulated particle individually, the simulation of such processes is very time consuming. Especially, if the information about every single optical photon needs to be stored, which is a crucial point in simulating the high precision

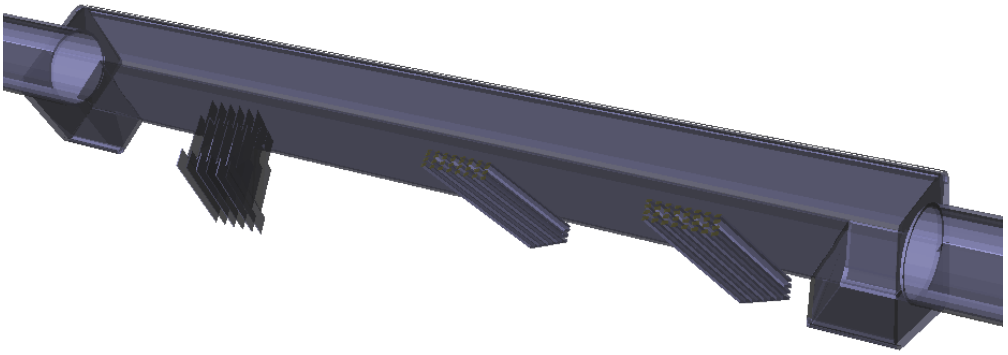

FIGURE 5.5: Simulation model of the AFP Timing Detectors for the HBP interface at ±212 m. Default setup consists of two detectors with a separated rows of bars, placed with a relative offset. AFP Silicon Detector planes are also shown.

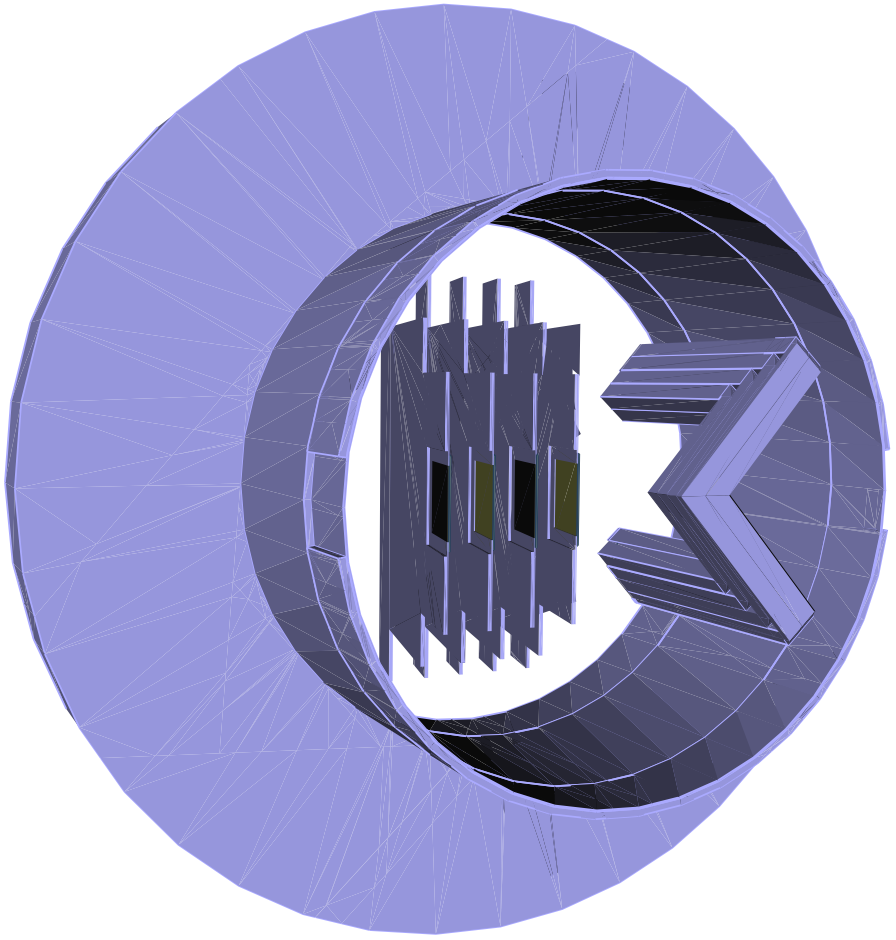

FIGURE 5.6: Simulation model of the AFP Silicon and Timing Detectors for the Roman Pot interface at ±212 m. Each Roman Pot at ±212 m includes AFP SiD consisting of 4 pixel sensor planes and the AFP TD formed with two arrays of 4×2 LQbars.

timing detectors [56]. An example of the simulated event with Cherenkov photons induced by a proton is shown in Figure 5.7. For 7 TeV proton crossing 6 mm thick quartz bar, on average 400 Cherenkov photons are generated. Each photon can undergo multiple reflections in the bar, before reaching MCP-PMT region, causing enormous CPU and memory consumption in the simulations.

To avoid poor simulation performance behavior, the Fast Cherenkov model is proposed. It is designed to handle the problem of efficient simulation in transportation of Cherenkov light through the straight radiator bars: from the generation to absorption point. Moreover, this formalism can be easily extended to the other radiator geometries.

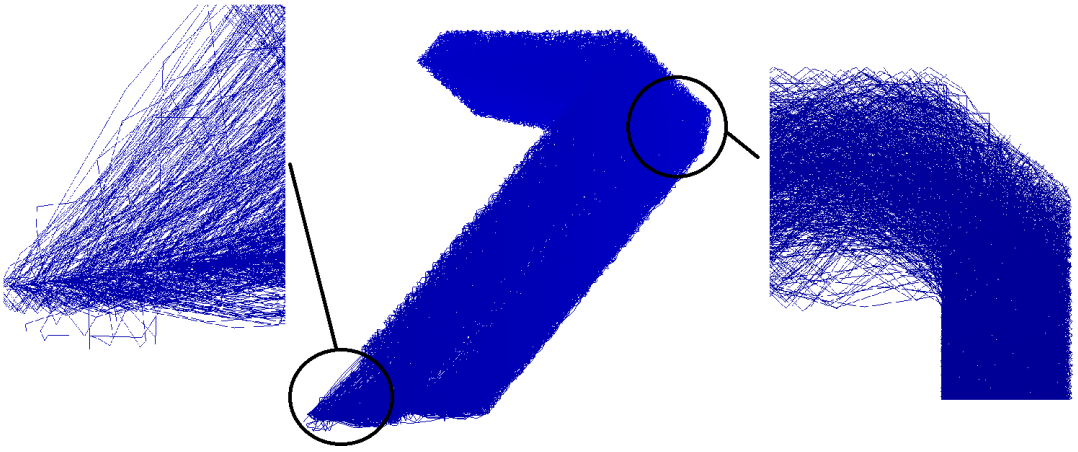

FIGURE 5.7: Simulated Cherenkov photons induced by 7 TeV proton when crossing two LQbars. For each bar, the number of generated photons is approximately 400.

5.3.1 Cherenkov photons

When a particle of charge q_e travels in a dispersive medium faster than the phase velocity of the light in that medium, it emits Cherenkov light. A particle travelling with a speed $\beta = v/c$ emits Cherenkov photons in a characteristic cone with the opening angle θ_{ch}, measured with respect to the particle momentum, and given by

$$\cos\theta_{\text{ch}} = \frac{1}{\beta \cdot n(\epsilon)} \ , \tag{5.1}$$

where $n(\epsilon)$ is the refractive index of the medium, which depends on the photon energy ϵ. Approximated relation for the number of generated Cherernkov photons in that medium (covering spatial dimension of x) is given by the relation [64]:

$$\mathrm{d}N = 370 \cdot q_e^2 \left[\frac{\text{photons}}{\text{eV} \cdot \text{cm}}\right] \left(1 - \frac{1}{\beta^2 \cdot n^2(\epsilon)}\right) \mathrm{d}\epsilon \mathrm{d}x \ . \tag{5.2}$$

GEANT4 provides a method of generating Cherenkov photons based on the above formulas [65]. In particular, the total number of photons produced is calculated according to the Poissonian distribution, with a parameter

$$\langle n \rangle = \frac{\mathrm{d}N}{\mathrm{d}x} \cdot \texttt{G4StepLength} \ , \tag{5.3}$$

where `G4StepLength` is a particle geometrical path length, simulated in GEANT4, where the interaction with matter (or transportation) occurs. The distribution of the photon energy (as well as the angle of emission) is sampled from the density function

$$g(\epsilon) = \left(1 - \frac{1}{\beta^2 \cdot n^2(\epsilon)}\right) = \sin^2 \theta_{\mathrm{ch}} \ . \tag{5.4}$$

5.3.2 General formalism

Fast Cherenkov model is based on effective photon length calculations. For QUARTIC bar geometry, photons are transported through the bar yielding multiple reflections, until they reach the photo-multiplier (MCP-PMT) region. A simple, two-dimensional example of such transportation is presented in Figure 5.8. Cherenkov photon is generated at the top of the bar of length L at a given angle α. Before it can reach the bottom part of the bar (MCP-PMT) it covers the effective path length

$$L_{\mathrm{eff}} = \frac{L}{\cos \alpha} \ . \tag{5.5}$$

This is a general formula on which the Fast Cherenkov model is based.

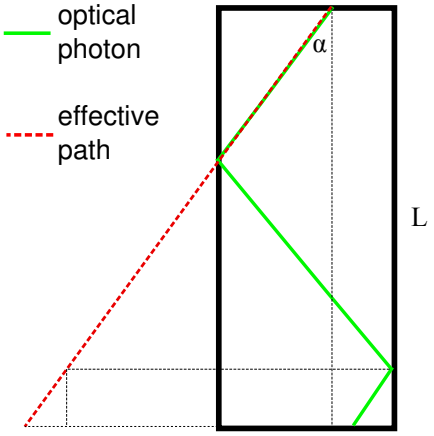

FIGURE 5.8: Example of a single photon transportation scheme for the QUARTIC bar of length L. Photon is generated at the angle α calculated with respect to L.

In the realistic three-dimensional scenario one has to introduce another angle δ to uniquely describe the initial direction of the photon. This is shown in Figure 5.9. The

bar is placed at the fixed angle with respect to the initial charged-particle momentum (shown as a red line). Interaction of the particle with the matter of the bar starts at P_{pre} and ends at P_{post} point. In P_{ch}, the generation of a single Cherenkov photon occurs (blue line), which travels through the bar with multiple reflections (denoted as #) until the absorption point (marked with $*$). In this case the Equation (5.5) takes the form

$$L_{\text{eff}} = \frac{y_0}{\cos\alpha \cdot \cos\delta} \,, \tag{5.6}$$

where y_0 denotes the distance from P_{ch} to the MCP-PMT, situated at the end of the bar. One should notice that L_{eff} does not depend on the initial proton x-position at a given set of angles.

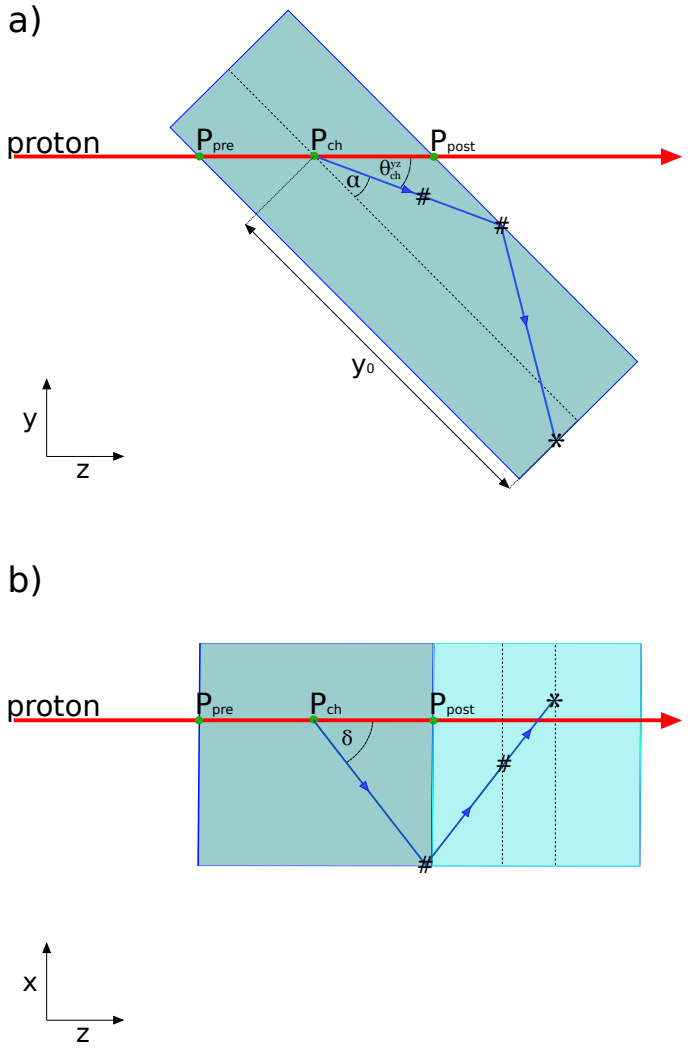

FIGURE 5.9: Schematic view of a single QUARTIC detector bar in (a) $y-z$ and (b) $x-z$ plane. Details are explained in the text.

5.3.3 Implementation in GEANT4

To implement the method in existing GEANT4 simulation code, it is preferred to perform calculations in the local coordinate system of hit bar. To do so, it is recommended to use appropriate GEANT4 class [66].

In order to generate the Cherenkov photons in the simulations, one can start with the randomization of the photon creation point, along the path of a charged particle. Knowing the initial and final particle positions inside the medium, the parametric equation of the line might be used:

```
G4double rand = G4UniformRand();
G4double PhotonX = PreProtonX + (PostProtonX-PreProtonX)*rand;
G4double PhotonY = PreProtonY + (PostProtonY-PreProtonY)*rand;
G4double PhotonZ = PreProtonZ + (PostProtonZ-PreProtonZ)*rand;
```

where `rand` is a random number generated in the $[0, 1]$ range, while `PreProton(X,Y,Z)` and `PostProton(X,Y,Z)` are the coordinates of initial and final GEANT4 step position.

The initial Cherenkov photon momentum can be calculated in two steps:

1. Generation of random position of the photon on the cone surface, defined by θ_{ch}, in the coordinate system with primary particle direction aligned with the z axis.
2. Rotation of the photon direction back to global reference system (using relevant GEANT4 method).

Having the initial photon generation point and its momentum, one can compute $\cos\alpha$ and $\cos\delta$ values. To do so, the scalar product can be used.

To account for the effect of absorption of photons inside the medium, the relevant probability needs to be determined:

$$p_{\mathrm{abs}} = 1 - \exp\left(-\mu_{\mathrm{abs}}(\epsilon) \cdot L_{\mathrm{eff}}\right) \ , \tag{5.7}$$

where $\mu_{\mathrm{abs}}(\epsilon)$ is the light attenuation coefficient of the radiator bar.

Since the transportation of the photons in QUARTIC bars is based on the total internal reflection, one can also specify the additional photon selection conditions. In the case of α and δ angles, defined in Equation (5.6), the conditions are

$$\begin{aligned} \sin\alpha\cos\delta &< \cos\theta_{\mathrm{c}} \\ \sin\delta &< \cos\theta_{\mathrm{c}} \ , \end{aligned} \tag{5.8}$$

where θ_c is a critical angle (angle of incidence above which the total internal reflectance occurs). If a given simulated photon does not satisfy these conditions, it will be refracted or absorbed, at the surface of the medium. In order to determine the total internal reflection conditions inside the radiator bar, one needs to find the dependencies between the projection and reflection angles. This is schematically shown in Figure 5.10. Keeping the same convention for angles α and δ, one can write the identities:

$$\begin{aligned} \cos\theta_{r1} &= \sin\alpha\cos\delta \\ \cos\theta_{r2} &= \sin\delta \ , \end{aligned} \tag{5.9}$$

where θ_{r1} and θ_{r2} are the reflection angles in a planes denoted as ① and ②, respectively.

To fulfill the total internal reflection conditions, the angles θ_{r1} and θ_{r2} must satisfy the conditions:

$$\begin{aligned} \theta_{r1} &< \theta_c \\ \theta_{r2} &< \theta_c \ , \end{aligned} \tag{5.10}$$

which can be expressed in terms of α and δ:

$$\begin{aligned} \sin\alpha\cos\delta &< \cos\theta_c \\ \sin\delta &< \cos\theta_c \ , \end{aligned} \tag{5.11}$$

where θ_c is a critical angle.

For precise photon timing simulations, one needs to specify the global time when photon is reaching the MCP-PMT region. An appropriate formula is given by

$$t = t_{pre} + \frac{z_0}{\beta \cdot c} + \frac{y_0}{v_g \cdot \cos\alpha \cdot \cos\delta} \ , \tag{5.12}$$

where:

- t_{pre} - global time of the incoming particle at P_{pre} point calculated with respect to the beginning of the simulated event,
- z_0 - distance between P_{pre} and P_{ch} points,
- v_g - group velocity of light in the medium.[2]

[2] $v_g = \dfrac{c}{n(\epsilon) + \epsilon \cdot dn/d\epsilon}$

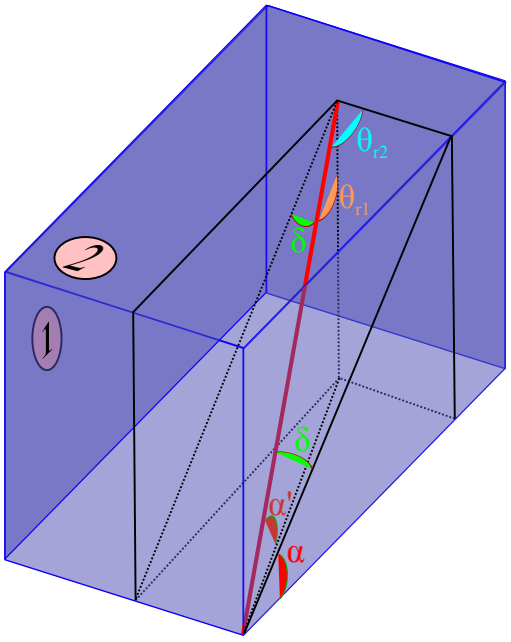

FIGURE 5.10: Cut projection of a single photon (red line) inside the Cherenkov detector bar. Details are explained in the text.

For a single incoming particle, the whole procedure has to be repeated n times, where n is an integer generated from Poisson distribution with parameter given by Equation (5.3). For secondary particles, the analogous process must be also reiterated.

5.3.4 QUARTIC bar simulation

As an example of method usability, simulation of single QUARTIC bar was performed. To reproduce the timing measurement of a single proton, complete GEANT4 simulation with default Cherenkov photons transportation was used as a default option. Then, the Fast Cherenkov model was implemented for the photons transportation. Figure 5.11 presents the simulated average photons time of arrival distribution (for MCP-PMT) in a single QUARTIC bar for 7 TeV protons and nuclear interactions turned on/off in GEANT4. One can observe a good agreement of Fast Cherenkov method with the full GEANT4 simulation on a picosecond scale: both in the distribution shape, as well as in the normalization (mean number of photons generated per bar). The consistency of the model is also observed in a simulated single event profile, which is presented in Figure 5.12.

Figure 5.13 shows comparison between the wavelength distributions of generated photons. As expected, Fast Cherenkov method fully reproduces the default GEANT4 Cherenkov photons energy spectra from the full simulation.

Comparing the CPU time-consumption of the method, it is over 100 times faster than the full simulation. This is a crucial aspect of usability of this model.

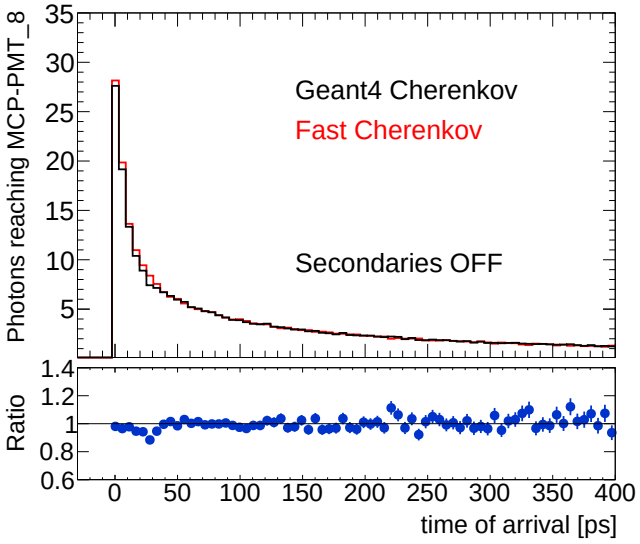

(a)

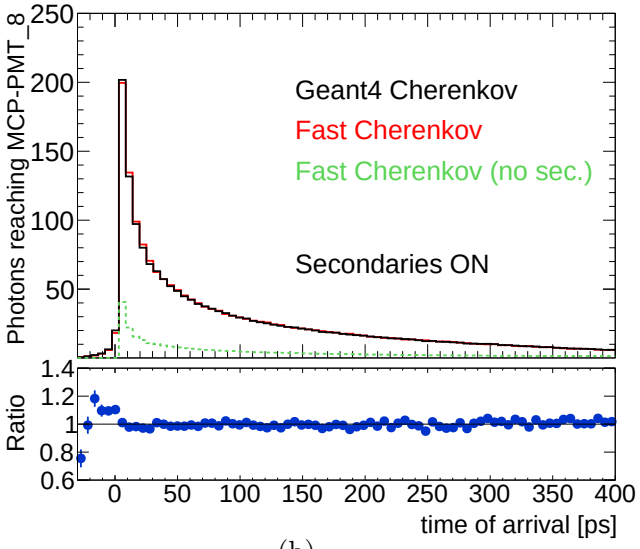

(b)

FIGURE 5.11: (a) Simulated Cherenkov photons time of arrival distribution in a single QUARTIC bar (last in a row of 8 bars) averaged over 1000 events with nuclear interactions turned off in GEANT4. Default GEANT4 simulation scheme is shown in black while the Fast Cherenkov model in red. (b) Same for the bar being last in a row and nuclear interactions switched on in GEANT4. For comparison, the Fast Cherenkov distribution from the configuration with nuclear interactions switched of is also shown (green dashed line).

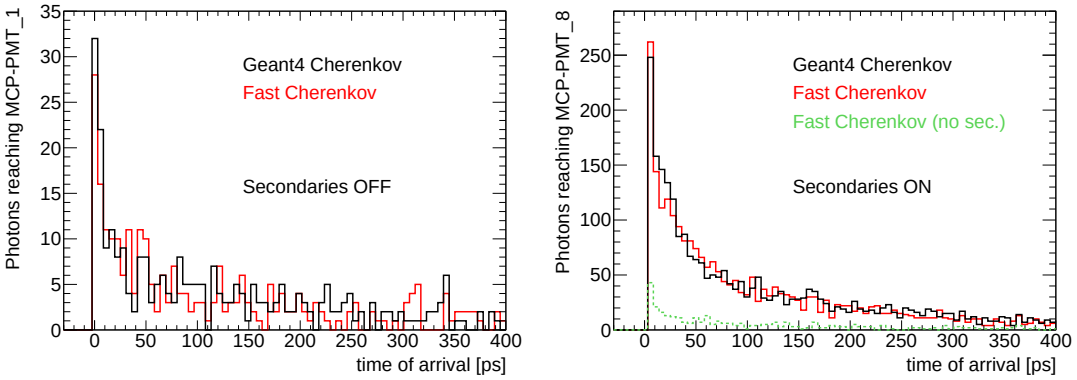

(a) (b)

FIGURE 5.12: (a) Simulated single-event Cherenkov photons time of arrival distribution in a single QUARTIC bar (first in a row of 8 bars) with nuclear interactions turned off in GEANT4. Default GEANT4 simulation scheme is shown in black while the Fast Cherenkov model in red. (b) Same for the bar being last in a row and nuclear interactions switched on in GEANT4.

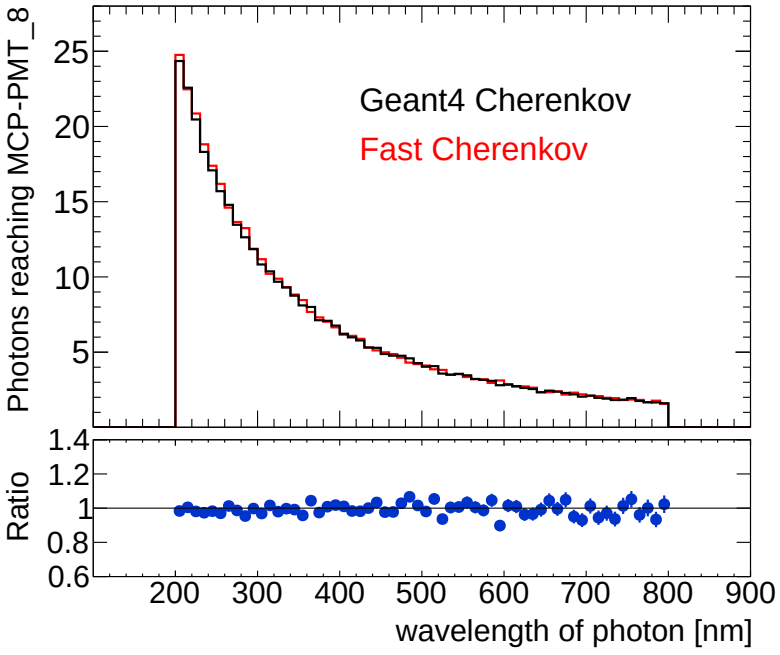

FIGURE 5.13: Wavelength distribution of the simulated Cherenkov photons reaching MCP-PMT in a single QUARTIC bar. Default GEANT4 simulation scheme is shown in black while the Fast Cherenkov model in red.

5.4 AFP data model

The AFP data model is implemented in the ATHENA framework and provides simulation hit collections and a corresponding digitization output, coming from both the AFP SiD and the AFP TD.

Hit collections store information about the hit position, time, deposited energy, and other parameters needed to resolve affected detector, such as the detector identification number or pixel position in the SiD plane. There is one hit/digitization/reconstruction collection per detector type.

The digitization collection for the AFP SiD stores the identification number of the station, the sensor planes and the hit pixels. The AFP TD collection contains station, detector and the bar identification numbers, together with the amplitude of the signal and the constant fraction discriminator time.

The reconstructed information from AFP SiD, stored in the corresponding collection, contains values of proton track positions, detector identification numbers, the number of hits and gaps used for track reconstruction, and the quality of the reconstructed track candidate. Similarly, the reconstructed ToF detector information consists of the detector and quartz bar row identification number, reconstructed time for a given row of radiator bars, the number of bars used in the proton ToF reconstruction, and possible pulse height saturation information of the bars.

The structure of the AFP D3PD format reflects the content of the abovementioned collections, which are stored in the corresponding data objects. This information is completed by the MC truth data object for simulated events, that cover the information about any generated forward particle kinematics.

5.5 AFP digitization

The AFP digitization algorithm is prepared within the general ATLAS scheme, which includes the possibility to add pile-up events. Prior to the digitization stage, GEANT4 hits from pile-up are overlaid to simulate the expected bunch spacing and number of bunch crossings.

5.5.1 Digitization in the AFP Silicon Detectors

For reasons of speed and flexibility, each AFP silicon sensor is treated as a single sensitive volume and there is no physical splitting into pixels at this step. The start and end

positions of each hit (in the global coordinate system of the ATLAS GeoModel) are transformed into local sensor coordinates. In the digitization step, the full track stub is split over corresponding pixels and for each pixel its coordinates (in pixel units: row and column numbers) and deposited energy are stored in the output data record. Since an electron-hole pair in silicon is produced for each 3.6 eV of deposited energy, the number of carrier pairs in each pixel is calculated in the AFP digitization algorithm. The pixel fires in case the number of pairs is higher than a pre-set threshold. At present, noise is not included in the AFP SiD digitization (and therefore no fake hits are generated). However, the expected noise is much lower than the threshold; a fact confirmed by all existing test beam measurements. Nevertheless, noise (e.g. due to different conditions in the LHC tunnel) could be added in future. For each pixel, its coordinates (in pixel units) and deposited energy are stored, together with the numbers that identify the station, detector (sensor plane) and, for future purposes, pixel discriminator time.

5.5.2 Digitization in the AFP Timing Detectors

For the AFP time-of-flight detectors, the number of Cherenkov photons and their arrival times is collected. The response of the photo-multiplier tube (MCP-PMT) to the Cherenkov photons is used to calculate the MCP-PMT output signal shape, and the signal is subsequently processed with a constant fraction discriminator function to obtain a digital representation of the pulse time (measured by HPTDC). A digital representation of the pulse amplitude is also recorded.

Each photon is allowed to convert to a photo-electron with a probability which is the product of two factors: a wavelength-independent geometrical collection efficiency (60%) and a wavelength-dependent quantum efficiency of the MCP-PMT photo-cathode ($<$ 25%). The conversion of a single photon to an electron is simulated by introducing an appropriate time-smearing (40 ps RMS)[3] and by adding a delay of 200 ps to the signal start time. In the next step, each electron is a source of a cascade of a Poisson-distributed number of electrons (a relatively small gain of 5×10^4 is assumed) which form a pulse with rise time of 400 ps and fall time of 400 ps. The pulse peak value is calculated as the highest number of electrons per 5 ps time bin observed in the pulse. The time recorded by HPTDC is calculated as the time when the pulse surpasses a constant fraction (50%) of its peak value as shown in Figure 5.14. All parameters in the digitization algorithm can be changed via dedicated ATHENA control file.

During the reconstruction step, all MCP-PMT sensors with the amplitude above the threshold that are placed in a single row of AFP quartz radiator bars are used to estimate

[3]The smearing by 40 ps covers the effect of the MCP-PMT transit time jitter only. Contributions from the pre-amplifier, CFD and HPTDC are not yet implemented.

the arrival time of a proton track candidate. In the simulation, the bars are considered as a fully independent sub-detectors, with no bar-to-bar cross-talks being implemented.

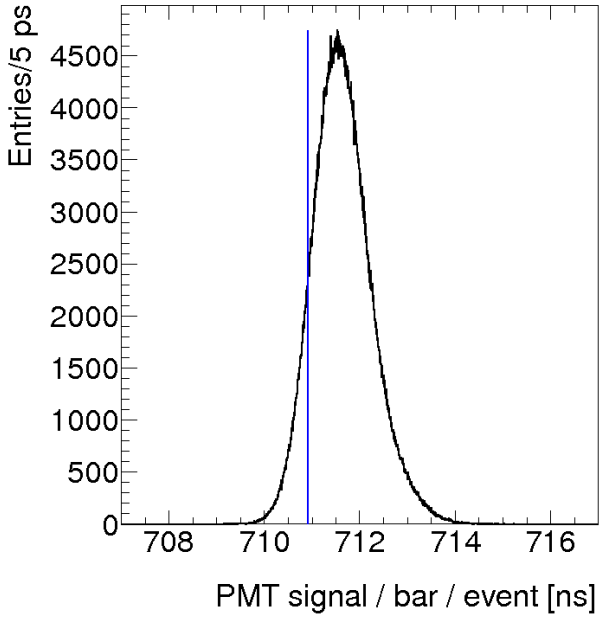

FIGURE 5.14: A typical simulated signal from a single AFP quartz bar in an event. The vertical line indicates the time (recorded by HPTDC) when the pulse passes a fixed fraction of its maximum amplitude. Figure taken from [52].

5.6 AFP reconstruction

5.6.1 Silicon tracker reconstruction

For proton track reconstruction from silicon tracker hits, the Kalman filter [67, 68] technique is employed. This approach minimizes the mean square estimation error, and is the optimal estimator of the state vector of a linear dynamical system. In case of the AFP SiD, a track pattern can be described by its 4-D state vector (straight-line motion), which can be parametrized as follows:

$$\mathbf{x} = (x,\ \mathrm{d}x/\mathrm{d}z;\ y,\ \mathrm{d}y/\mathrm{d}z)^T\ , \tag{5.13}$$

where x, y and z are the spatial coordinates in the ATLAS coordinate system, and z is the direction along the beam. In its linear form, the evolution of the state vector is described by the discrete system of linear equations:

$$\mathbf{x}(z_k) \equiv \mathbf{x}_k = \mathbf{F}_{k-1}\mathbf{x}_{k-1} + w_{k-1}\ , \tag{5.14}$$

where the matrix $\mathbf{F}_{k-1}$ relates the state at detector plane (step) $k-1$ to the state at step k. A random variable w describes the noise which can account, for example, for the effect of multiple scattering on the state vector. According to the AFP SiD track model, the matrix $\mathbf{F}_{k-1}$ has the form

$$\mathbf{F}_{k-1} = \begin{pmatrix} 1 & \Delta z_k & 0 & 0 \\ 0 & 1 & \Delta z_k & 0 \\ 0 & 0 & 1 & 0 \\ 0 & 0 & 0 & 1 \end{pmatrix} \tag{5.15}$$

and Δz_k denotes the distance between detector layers k and $k-1$.

An example from a single event with reconstructed charged-particle track trajectories in AFP SiD is presented in Figure 5.15. Typically, there are 20 or fewer hits per tracker in an event. Therefore, to save disk space and CPU consumption, the track reconstruction algorithm is invoked only if there are fewer than 1000 hit pixels in a given AFP station - otherwise this is considered the signature of a particle shower.

5.6.2 Time-of-flight detector reconstruction

In order to reconstruct a time from the AFP ToF detectors, only radiator bars with at least 10 effective photo-electrons are considered. The ToF track is formed from a single row of bars above threshold. The time associated with the ToF track is calculated as an average of times measured with unsaturated bars in the ToF track. Corrections for the different z-positions of the bars are applied (1 ps between adjacent bars).

Finally, a proton ToF correction for the y-position of the proton track is applied. This correction is considered only if the x-position of the reconstructed AFP SiD track matches the position of the reconstructed ToF track. The source of the correction is schematically shown in Figure 5.16. The size of this improvement is proportional to the proton y-position:

$$\frac{\mathrm{d}t}{\mathrm{d}y} = \frac{n}{c \sin\theta_{\mathrm{ch}}} - \frac{1}{c \tan\theta_{\mathrm{ch}}} \approx 3.7 \left[\frac{\mathrm{ps}}{\mathrm{mm}}\right] , \tag{5.16}$$

where n is the refractive index of quartz ($\approx$1.46), c is the speed of light and θ_{ch} is the Cherenkov angle ($\approx$48° for particles with $v \approx c$). The size of the correction is extracted from the simulation by performing a linear fit to the distribution of average proton ToF reconstructed by AFP TD as a function of proton y-position from AFP SiD. This is presented in Figure 5.17. The best-fit value is $\frac{\mathrm{d}t}{\mathrm{d}y} = 4.3 \pm 0.1$ ps/mm, which is consistent with the expected value of 3.7 ps/mm.

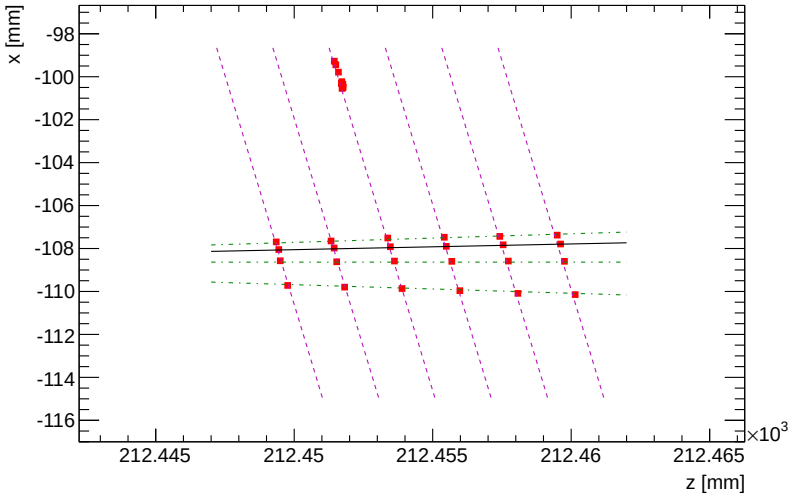

(a)

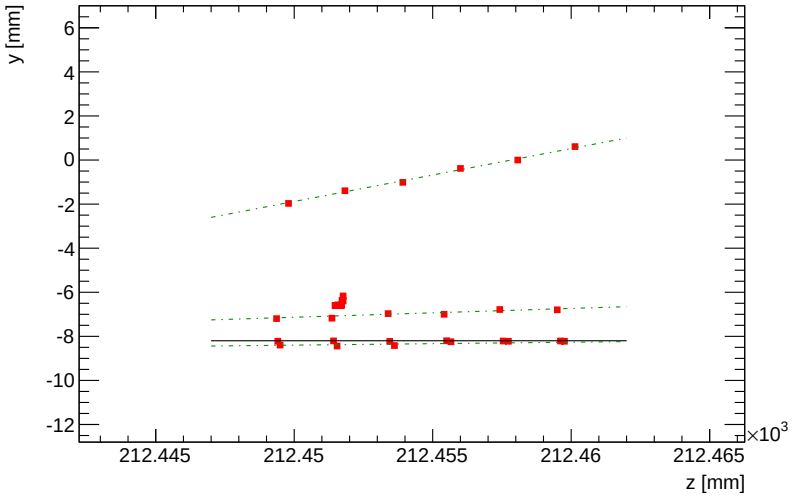

(b)

FIGURE 5.15: An example of reconstructed charged-particle trajectories in AFP SiD. The projections in (a) $x - z$ and (b) $y - z$ planes show the reconstructed proton trajectory (black solid lines) and additional tracks from showers (green dashed lines). Reconstructed tracks are formed using hit pixels (red markers) from the silicon planes (dashed magenta lines).

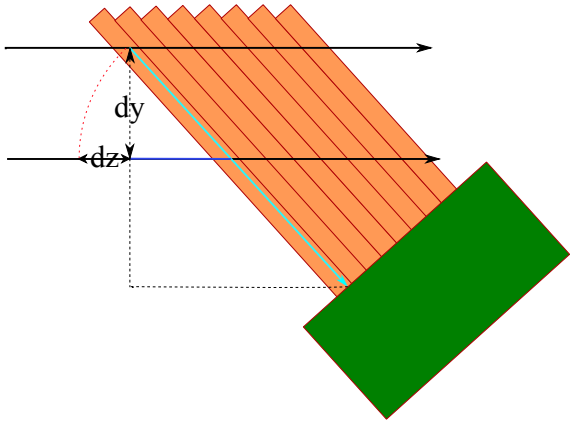

FIGURE 5.16: Schematic diagram of the source of the proton ToF correction needed to account for different proton y-positions. Two protons (black arrows) with the same ToF but different y-positions would have different values of ToF reconstructed by AFP TD bars (orange rectangles).

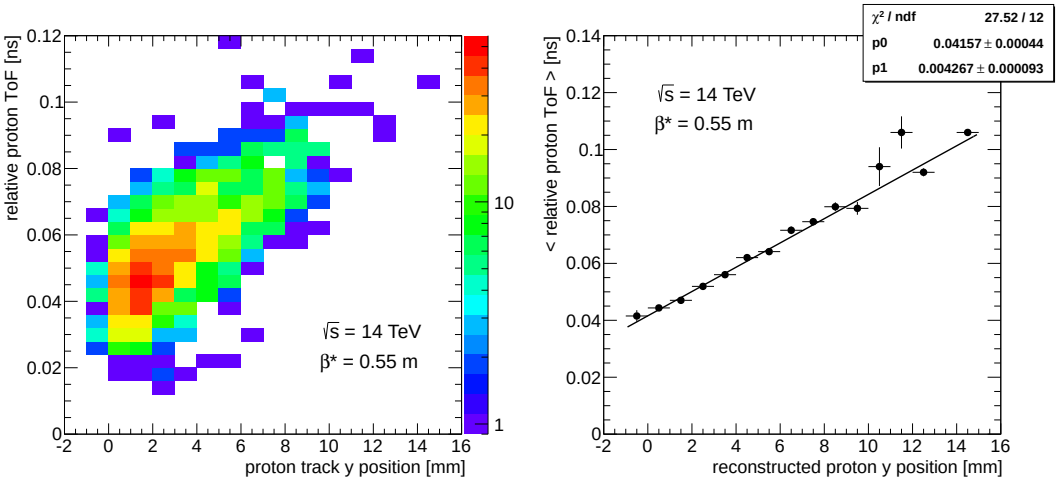

(a) (b)

FIGURE 5.17: (a) Correlation between the proton y-position reconstructed by AFP SiD and proton ToF from AFP TD. (b) Same but averaged over different ToF, with a linear fit performed to extract the relevant time correction.

5.7 Background simulations and expected AFP performance

AFP detectors aim to measure protons originating from primary interactions at the ATLAS IP. In that sense, real primary protons from soft or pile-up interactions form part of the genuine physics signal and are, for low-luminosity runs, an interesting component of the AFP physics program. For the high-luminosity program during the second AFP phase, which is not the main part of the first phase program, protons originating from pile-up interactions form a physics background that must be rejected by fast time-of-flight detectors and additional kinematic cuts.

The most important quality criteria for the AFP measurement are the proton reconstruction efficiency and signal-to-background rate. The proton efficiency is defined as the fraction of primary protons that would have reached the AFP geometrical acceptance but are lost or badly measured. Intimately connected to this is the rate of background particles seen in the AFP detectors. In the following sections sources of backgrounds, proton inefficiency, and ambiguities in the AFP measurements are discussed.

5.7.1 Backgrounds

While the signal in AFP detectors consists of primary protons, the AFP background consists of particles (protons or other particles like electrons, pions, muons) detected in the AFP, but that do not directly originate in the interaction point. This background has multiple origins and can be categorized as follows.

Beam-halo consists of protons in the 'tails' of the beam profile distribution. The amount of halo intercepted is strongly dependent on the distance of closest approach of the bottom part of the AFP beam interface to the circulating beam. Beam-halo can be reduced via dedicated LHC collimators, but is subsequently replenished by electromagnetic beam-lattice scattering, intra-beam scattering, and beam-beam elastic scattering in the interaction regions. The halo density and its profile is strongly affected by the tune of the LHC machine [69].

Beam-gas background: Beam protons may interact with the residual gas inside the beam pipe producing scattered protons, or showers of particles, that may impact the AFP detectors. Primary scattering products may also interact with LHC collimator jaws, beam screens, beam pipe walls, and other material upstream of AFP that can cause secondary shower products that enter the detectors. Beam-gas background is typically only a small component of the total background when only the beam pipe region between the IP and AFP is considered. However, when integrated over the LHC circumference, the total contribution to the lifetime reduction of the machine is significant, although

still sub-dominant [69]. Beam-halo and beam-gas interaction backgrounds are currently not implemented in the AFP simulation.

Secondary showers: High-energy primary particles produced in the IP in forward directions may cause interactions upstream of AFP, and the secondary particles (or secondaries) may reach the AFP detectors. Together with genuine (primary) protons from the IP, this is the dominant radiation source at the LHC and the elaborate LHC collimator hierarchy has been designed to deal with such radiation and protect the superconducting elements in the machine.

Back-scattering background: Already at $\langle\mu\rangle = 2$, the losses on Q6 magnet become unsustainable, especially with the AFP detectors inserted, such that a new collimator (TCL6) behind AFP is required for Q6 protection. In turn, TCL6 will cause some 'back-scattering' into the outer AFP stations. When AFP is operating, the possible upstream LHC collimator settings will have to be adapted not to obscure the AFP sensitive detector area.

Self-interaction background: Each AFP station is itself a target for particles inside the beam aperture and will cause interactions depending on the interaction length for traversing particles. Each inner station is also a potential source of showers that will be seen in the outer station.

5.7.2 Signal efficiency and proton survival

The signal for AFP is considered as a primary proton that is well measured in both AFP stations of a given arm. The proton inefficiency is defined as a fraction of these protons that would have reached the AFP geometric acceptance, but are lost or badly measured because of one of the two main effects.

Proton interactions in the AFP station: When the signal proton undergo an inelastic interaction in a station its tracker and/or ToF measurement may become unusable. This effect depends on the total interaction length of the detector station and detector material upstream (and nearby downstream) of the measurement itself. For this reason, the total nuclear collision probability will be kept well under 2% for the single-station AFP beam interface. The nuclear collision probability of the AFP SiD is estimated to be ≈0.7% for a 4-layer tracker, and about 9% (18%) for the rows of 4 (8) quartz radiator bars of the AFP TD.

Signal overlap and ambiguities: Signal overlap inefficiency occurs when another in-time particle, whether a genuine proton or a background, hits the same detector pixel as the signal and makes the proton signal unusable. Overlap particles are not considered a

serious issue in the tracker, because of its high degree of pixelation. In the ToF detector, the in-time particle or shower background has the possibility to 'flood' the fast time-of-flight detectors, which have limited spatial pixelation. Overlap particles hitting the same ToF quartz bars as the signal proton, may deform the timing signal and give rise to an unreliable ToF measurement. The magnitude of the overlap inefficiency is dependent on the LHC optics, luminosity, machine lattice, upstream material and beam conditions, and is therefore inherently difficult to be precisely calculated.

5.8 Simulated AFP performance

To demonstrate the expected AFP performance using full GEANT4 simulation, the configuration listed below is used. This configuration does not completely correspond to the latest detector design configuration but is sufficiently close for the simulation to remain valid.

- Two HBP-based AFP stations per ATLAS side (arm) placed at $z = \pm 204$ m (AFP 204) and $z = \pm 212$ m (AFP 212) from the IP. The thickness of the front window is set to 300 µm.
- Each station contains one SiD, the outer stations (at 212 m) contain a QUARTIC-based ToF detector in addition.
- Single SiD includes six silicon planes, separated by 10 mm (with a 13° tilt in the $x - z$ plane).
- Each Si layer has a sensor thickness of 250 µm and contains an array of 336×80 pixels of size 50×250 µm^2.
- Single ToF detector includes an array of 4×8 quartz bars (in $x - z$ plane), as described in Section 5.2.3.
- All AFP detectors are placed at $d = 1.8$ mm from the beam center (relatively to the edge of the active region of each detector).

In order to reconstruct the proton trajectory in AFP SiD, a number of quality cuts are introduced. A track is defined as a good one if the following criteria are fulfilled:

- Reconstruction quality: `trk_quality` > 6 (`trk_quality` $= N_{\text{hits}} + \frac{\chi^2_{\text{max}} - \chi^2_{\text{trk}}}{\chi^2_{\text{max}} + 1}$, where χ^2_{max} is taken to be 2.0 and χ^2_{trk} is the output from Kalman filtering). This cut prevents considering tracks with too small number of pixels, $N_{\text{hits}} < 6$, used for the reconstruction.

- Small slopes: $|\mathrm{trk}_{\mathrm{d}x/\mathrm{d}z}| < 0.003$ and $|\mathrm{trk}_{\mathrm{d}y/\mathrm{d}z}| < 0.003$. This cut selects for tracks which are almost parallel to the beam, as expected for primary protons and demonstrated in Figure 5.18.

- Small amount of tracks reconstructed in a given station: (a) $N_{\mathrm{trk}} = 1$ - default requirement, (b) $N_{\mathrm{trk}}^{\mathrm{inner}} \leq 2$ and $N_{\mathrm{trk}}^{\mathrm{outer}} \leq 5$ - robust set-up for high pile-up performance studies. This cut removes events with potential proton-nuclear interactions in the detector material. The reconstructed track multiplicity for different AFP stations is shown in Figure 5.19.

In addition to the requirements above, reconstructed tracks segments in the inner and outer station are required to be matched to each other, with a maximum distance: $|\mathrm{trk}_x^{\mathrm{inner}} - \mathrm{trk}_x^{\mathrm{inner}}| < 1.5$ mm and $|\mathrm{trk}_y^{\mathrm{outer}} - \mathrm{trk}_y^{\mathrm{outer}}| < 1.5$ mm. This is demonstrated in Figure 5.20.

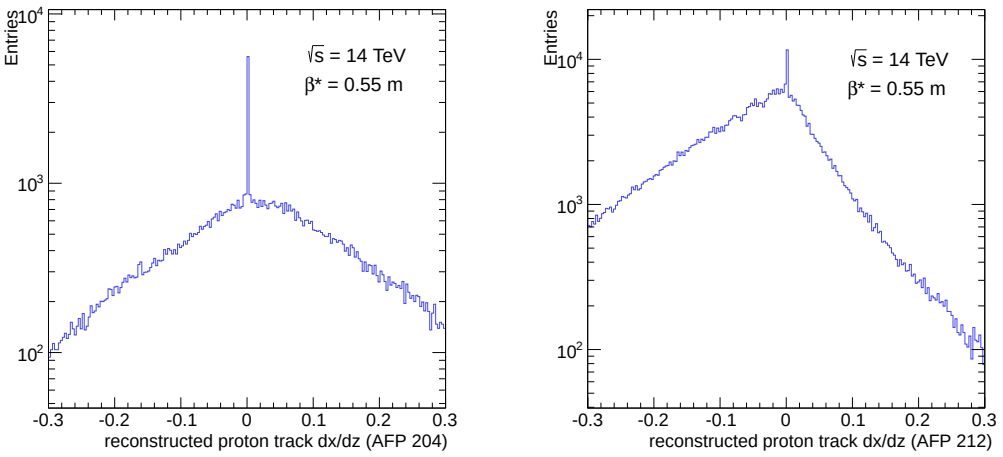

FIGURE 5.18: Reconstructed track slope ($\mathrm{d}x/\mathrm{d}z$) distribution for AFP SiD tracks satisfying reconstruction quality requirement for (a) inner and (b) outer AFP stations. Tracks originating from primary protons form sharp peaked structure around $\mathrm{d}x/\mathrm{d}z = 0$, where the showers form significantly wider structure.

For proton tracking-timing studies, a "good" event must also pass the following timing requirements:

- The number of collinear AFP TD radiator bars used for time reconstruction, $N_{\mathrm{TD}}^{\mathrm{rec}} = 8$, including a maximum number of saturated bars, $N_{\mathrm{TD}}^{\mathrm{sat}} \leq 4$.

- The extrapolated proton track trajectory must match a collinear set of bars (a "train") with reconstructed timing. If more than one track is pointing to the same train of bars, ToF reconstruction is not attempted. This occurs in about 5% of events for the two trains closest to the beam at high pile-up ($\langle\mu\rangle \sim 15$).

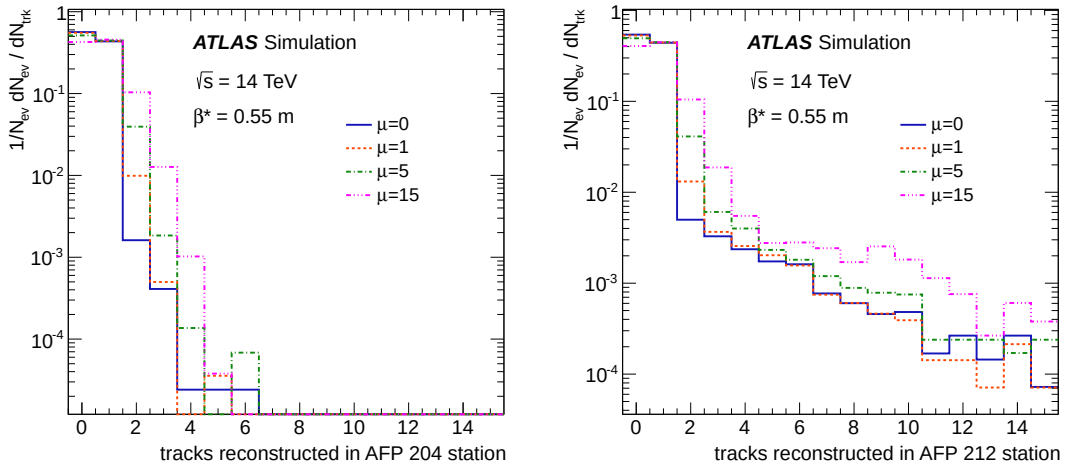

(a) (b)

FIGURE 5.19: Reconstructed track multiplicity in AFP SiD for (a) inner and (b) outer station before the track matching is included. Events are generated without any cut on the proton kinematics (i.e. $\xi_p < 1$). Approximately 50% of protons in the sample do not enter the AFP acceptance region ($0.015 < \xi_p < 0.15$) which results in no reconstructed track. Different pile-up scenarios are presented.

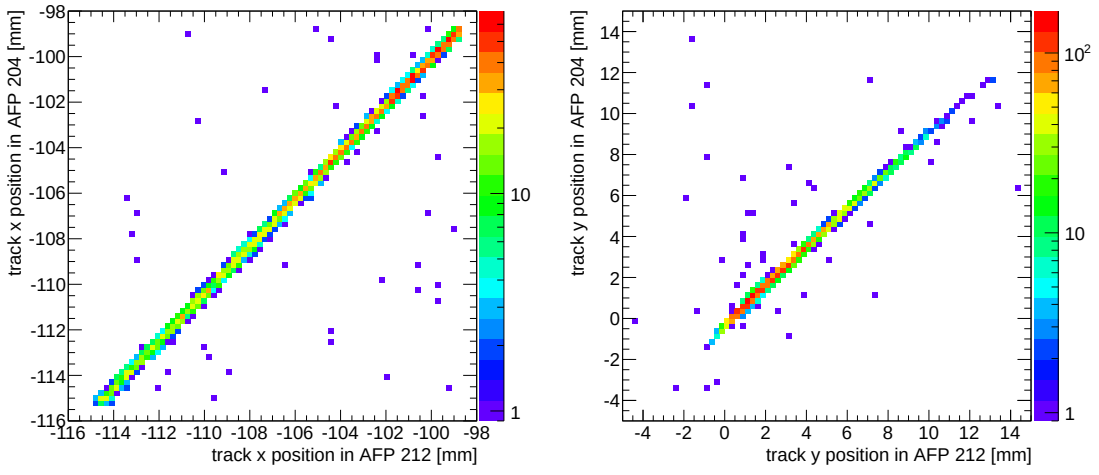

(a) (b)

FIGURE 5.20: Correlation between the (a) x and (b) y track positions reconstructed in inner and outer AFP station. Events passing the remaining selection criteria are shown.

5.8.1 Geometrical acceptance

The geometrical acceptance is defined as the ratio of the number of protons with a relative energy loss, ξ_p, transverse momentum, p_{T}^p and azimuthal angle ϕ_p that reach the forward detectors to the total number of scattered protons having the same ξ_p and p_{T}^p. The proton relative energy loss is defined with respect to the beam energy E_p as:

$$\xi_p = 1 - \frac{E'_p}{E_p} \,, \tag{5.17}$$

where E'_p is the energy of the scattered proton. Obviously, depending on ξ_p, p_{T}^p and ϕ_p, some scattered protons will not reach the forward detectors as they may be too close to the beam to be detected or hit an LHC element (collimator, beam pipe, magnet) upstream of the detector.

The geometrical acceptance for nominal LHC optics ($\beta^* = 0.55$ m) of the first AFP station (located at 204 m from the ATLAS IP) is shown in Figure 5.21a. For the collision optics the region of high acceptance (>80%) is limited by $p_{\mathrm{T}}^p < 3$ GeV and $0.02 < \xi_p < 0.12$. For comparison, the geometrical acceptance of ALFA detectors are shown in Figure 5.21b. This demonstrates the complementarity between the ALFA and AFP. As ALFA is designed to measure elastically scattered protons, its acceptance covers mainly the region around $\xi_p = 0$ in dedicated high-β^* runs. Unfortunately, this means that for the collision optics, ALFA covers only small kinematic phase-space region of $0.06 < \xi_p < 0.12$ and $p_{\mathrm{T}}^p < 0.3$ GeV. This gap could be filled by using the AFP detectors, which can measure protons up to much smaller ξ_p and larger p_{T}^p.

5.8.2 Detectors resolution

The difference between the true x position of the proton in the AFP station and a reconstructed track value is shown in Figure 5.22a. The obtained reconstruction resolution equals 14.8 µm (72 µm) in x (y). This is consistent with the values expected from the size of simulated pixels in a non-staggered set of tracking planes. In the final detector version the SiD planes will be staggered. Moreover, a better resolution per plane is expected for tracks reconstructed from the clusters, calculated using signal-charge interpolation [17]. Currently, a simple geometric mean is used to calculate the hit positions, if at least two adjacent pixels are hit in a single event. Staggering and charge-sharing interpolation techniques are expected to further improve the reconstruction resolution to 8 and 20 µm in x and y, respectively.

The reconstruction resolution of the ToF is evaluated using events satisfying selection criteria for both AFP arms (so-called double-tag events). The timing resolution is equal

to 15 ps with the current implementation of AFP TD. This value translates to 2.3 mm vertex z-position reconstruction resolution, as can be seen in Figure 5.22b.

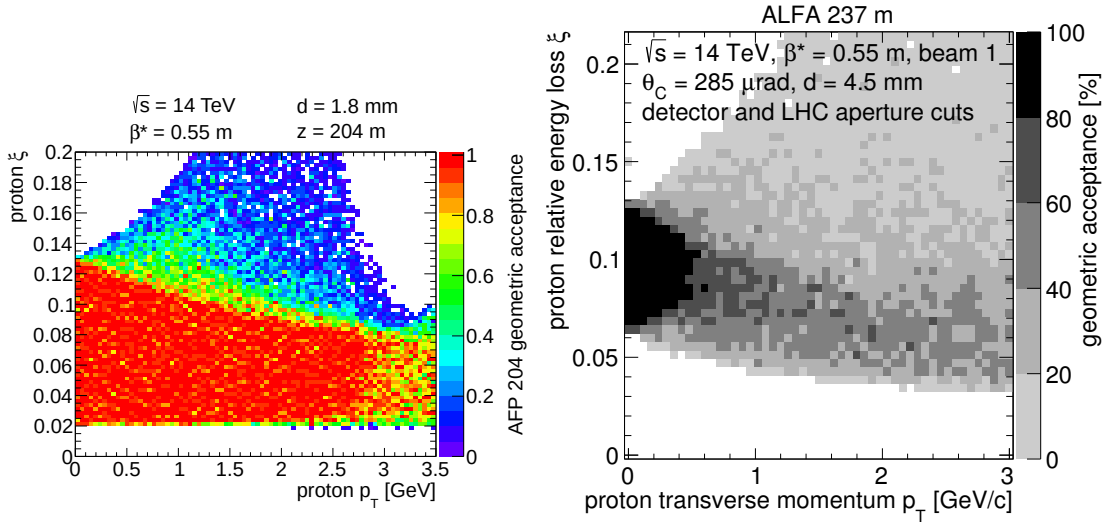

(a) (b)

FIGURE 5.21: Geometrical acceptance of the (a) AFP and (b) ALFA detectors as a function of the proton relative energy loss (ξ_p) and its transverse momentum (p_{T}^p) for nominal LHC optics settings. Figure (b) taken from [51].

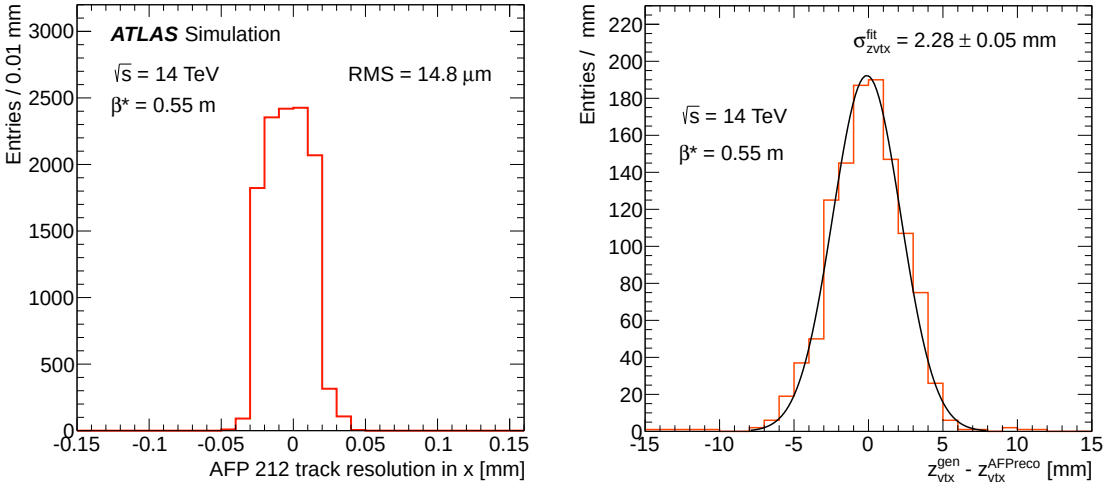

(a) (b)

FIGURE 5.22: (a) Reconstructed track x position resolution for the outer (AFP 212) SiD. (b) Reconstructed z-vertex position resolution using all ToF detectors and double-tag events.

5.8.3 Showers

As expected, not all forward protons can reach the AFP stations. If the energy lost by a proton is large enough ($\xi_p > 0.15$), it will hit the LHC aperture before the AFP

stations. In such case, a particle shower might be created, spoiling the measurement by populating the near or far AFP stations with a large number of tracks. A shower could also be produced inside the near station causing high multiplicity in the far station. This is shown in Figure 5.23a, where apart from protons, there are some tracks caused by showers. In order to clean the event from these, the selection criteria described above are applied. This removes almost all shower tracks in the sample as shown in Figure 5.23b.

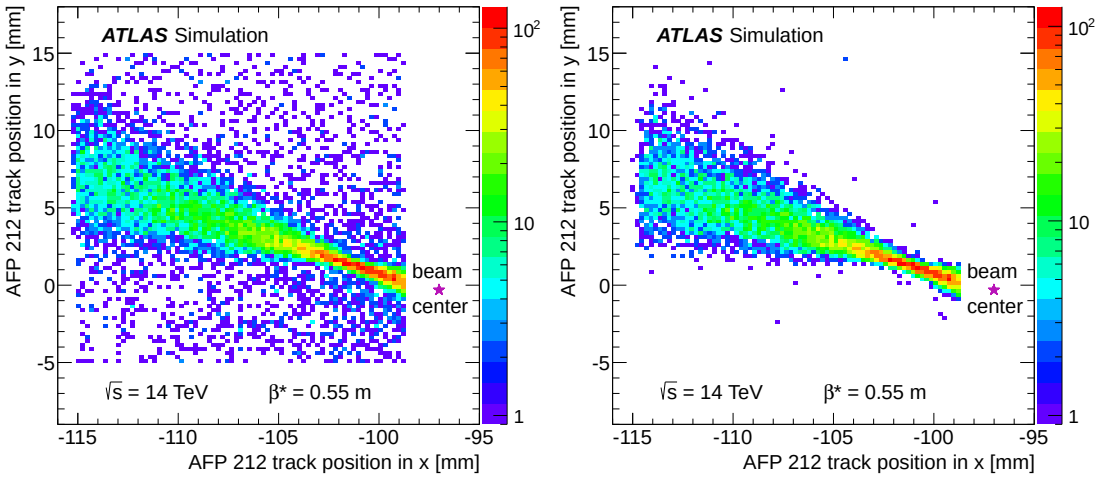

(a) (b)

FIGURE 5.23: $x - y$ track positions hitmap for the outer AFP SiD (a) before and (b) after track segment matching is required. Positions are calculated in the ATLAS Coordinate System (beam center is shifted). Tracks matched between inner and outer AFP stations are considered.

5.8.4 Proton reconstruction efficiency

To study the effect of pile-up interactions on the AFP proton reconstruction quality, simulated events with $\mu = 0$, 1, 5 and 15 are considered. A robust set of SiD+ToF cuts is chosen in order to account for the reconstruction of additional primary protons arriving from pile-up interactions. Figure 5.24 presents the track reconstruction efficiency for single-arm AFP SiD (in AFP 204 and 212 stations) as a function of proton relative energy loss. The tracking efficiency reaches 95% in $0.02 < \xi_p < 0.1$ for low pile-up contamination and 90% for $\mu = 15$.

The full proton reconstruction efficiency for single-arm detectors (including ToF information from the AFP TD) can be also considered. This is shown in Figure 5.25 for different pile-up scenarios. The average efficiency of the proton track plus time reconstruction is found to be ≈85% for $\mu = 0$, 1 and 76% for $\mu = 15$. These values demonstrate the excellent performance expected with the AFP detectors even in a high pile-up environment.

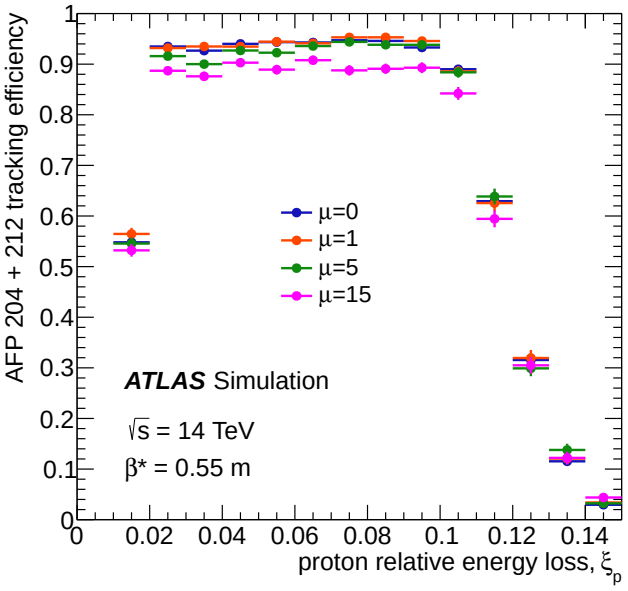

FIGURE 5.24: Proton track reconstruction efficiency for single-arm AFP SiD for different pile-up scenarios as a function of relative proton energy loss, ξ_p. Only tracks with segments matched between the inner (AFP 204) and outer (AFP 212) stations are included.

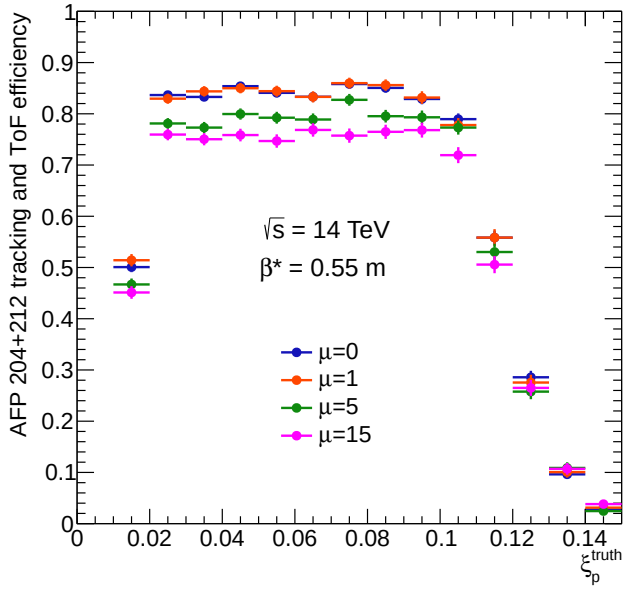

FIGURE 5.25: Proton track and ToF reconstruction efficiency for single-arm AFP SiD for different pile-up scenarios as a function of relative proton energy loss, ξ_p. Only tracks with segments matched between the inner (AFP 204) and outer (AFP 212) stations are included.

Bibliography

[1] L. Evans and P. Bryant, *LHC Machine*, JINST **3** (2008) S08001.

[2] R. Assmann, M. Lamont and S. Myers, *A brief history of the LEP collider*, Nucl. Phys. Proc. Suppl. **109B** (2002) 17–31.

[3] The CERN accelerator complex. `te-epc-lpc.web.cern.ch/te-epc-lpc/machines/pagesources/Cern-Accelerator-Complex.jpg`.

[4] A. A. Glazkov et al., *Duoplasmatron-type ion source with improved technical and operational performance for linear accelerator*, Proceedings of the 3. European particle accelerator conference **1** (1992) 993–995.

[5] ATLAS Collaboration, *The ATLAS Experiment at the CERN Large Hadron Collider*, JINST **3** (2008) S08003.

[6] CMS Collaboration, *The CMS experiment at the CERN LHC*, JINST **3** (2008) S08004.

[7] ALICE Collaboration (K. Aamodt et al.), *The ALICE experiment at the CERN LHC*, JINST **3** (2008) S08002.

[8] LHCb Collaboration (A. Alves et al.), *The LHCb Detector at the LHC*, JINST **3** (2008) S08005.

[9] J. L. Pinfold, *The MoEDAL Experiment at the LHC*, EPJ Web Conf. **71** (2014) 00111.

[10] LHCf Collaboration (0. Adriani et al.), *The LHCf detector at the CERN Large Hadron Collider*, JINST **3** (2008) S08006.

[11] TOTEM Collaboration (G. Anelli et al.), *The TOTEM experiment at the CERN Large Hadron Collider*, JINST **3** (2008) S08007.

[12] F. Bordry et al., *The First Long Shutdown (LS1) for the LHC*, MOZB202 (2013).

[13] CDF Collaboration (R. Blair et al.), *The CDF-II detector: Technical design report*, FERMILAB-DESIGN-1996-01, FERMILAB-PUB-96-390-E (1996).

[14] T. Varol, *Muon Performance in the Presence of High Pile-up in ATLAS*, arXiv:1212.0392 [hep-ex].

[15] ATLAS Experiment Luminosity Public Results. twiki.cern.ch/twiki/bin/view/AtlasPublic/LuminosityPublicResults.

[16] ATLAS Collaboration, *ATLAS pixel detector: Technical Design Report*, CERN-LHCC-98-013, ATLAS-TDR-11 (1998).

[17] ATLAS Collaboration, *ATLAS pixel detector electronics and sensors*, JINST **3** (2008) P07007.

[18] ATLAS Collaboration, *ATLAS Insertable B-Layer Technical Design Report*, CERN-LHCC-2010-013, ATLAS-TDR-19 (2010).

[19] B. Dolgoshein, *Transition radiation detectors*, Nucl. Instrum. Meth. **A326** (1993) 434–469.

[20] ATLAS Collaboration, *ATLAS muon spectrometer: Technical design report*, CERN-LHCC-97-22, ATLAS-TDR-10 (1997).

[21] ATLAS Collaboration, *Performance of the ATLAS Trigger System in 2010*, Eur. Phys. J. **C72** (2012) 1849, arXiv:1110.1530 [hep-ex].

[22] ATLAS Collaboration, *ATLAS first level trigger: Technical design report*, CERN-LHCC-98-14, ATLAS-TDR-12 (1998).

[23] ATLAS Collaboration, *ATLAS high-level trigger, data acquisition and controls: Technical design report*, CERN-LHCC-2003-022, ATLAS-TRD-016 (2003).

[24] ATLAS Collaboration, *ATLAS: Detector and physics performance technical design report. Volume 1*, CERN-LHCC-99-14, ATLAS-TDR-14 (1999).

[25] ATLAS Collaboration, *Improved luminosity determination in pp collisions at* $\sqrt{s} = 7$ *TeV using the ATLAS detector at the LHC*, Eur. Phys. J. **C73** (2013) 2518, arXiv:1302.4393 [hep-ex].

[26] ATLAS Collaboration, *ATLAS Forward Detectors for Measurement of Elastic Scattering and Luminosity*, Tech. Rep. CERN-LHCC-2008-004, ATLAS-TDR-18, 2008.

[27] ATLAS Collaboration, *The ATLAS Simulation Infrastructure*, Eur. Phys. J. **C70** (2010) 823–874, arXiv:1005.4568 [physics.ins-det].

[28] ATLAS Collaboration, *ATLAS computing: Technical design report*, CERN-LHCC-2005-022, ATLAS-TRD-017 (2005).

[29] GEANT4 Collaboration (S. Agostinelli et al.), *GEANT4: A Simulation toolkit*, Nucl. Instrum. Meth. **A506** (2003) 250–303.

[30] J. Allison et al., *Geant4 developments and applications*, IEEE Trans. Nucl. Sci. **53** (2006) 270.

[31] M. Dobbs and J. B. Hansen, *The HepMC C++ Monte Carlo event record for High Energy Physics*, Comput. Phys. Commun. **134** (2001) 41–46.

[32] Ebke, J. and Waller, P. and Brooks, T., *MCViz*, `mcviz.net`.

[33] J. Chapman et al., *The ATLAS detector digitization project for 2009 data taking*, J. Phys. Conf. Ser. **219** (2010) 032031.

[34] J. Boudreau and V. Tsulaia, *The GeoModel toolkit for detector description*, CERN-2005-002.353 (2005) 353–356.

[35] D. H. Wright et al., *Low and high energy modeling in GEANT4*, AIP Conf. Proc. **896** (2007) 11–20.

[36] G. Folger and J. Wellisch, *String parton models in GEANT4*, eConf **C0303241** (2003) MOMT007, `arXiv:nucl-th/0306007 [nucl-th]`.

[37] A. Heikkinen, N. Stepanov and J. P. Wellisch, *Bertini intranuclear cascade implementation in GEANT4*, eConf **C0303241** (2003) MOMT008, `arXiv:nucl-th/0306008 [nucl-th]`.

[38] G. Barrand et al., *GAUDI - The software architecture and framework for building LHCb data processing applications*, Comput. Phys. Commun. **140** no. 1-2, (2000) 92–95.

[39] E. Obreshkov et al., *Organization and management of ATLAS software releases*, Nucl. Instrum. Meth. **A584** (2008) 244–251.

[40] L. Lonnblad, *CLHEP: A project for designing a C++ class library for high-energy physics*, Comput. Phys. Commun. **84** (1994) 307–316.

[41] P. Calafiura et al., *The StoreGate: a Data Model for the Atlas Software Architecture*, `arXiv:cs/0306089`.

[42] P. Jenni and M. Nessi, *ATLAS Forward Detectors for Luminosity Measurement and Monitoring*, Tech. Rep. CERN-LHCC-2004-010, 2004.

[43] ATLAS Collaboration, *Zero degree calorimeters for ATLAS*, Tech. Rep. CERN-LHCC-2007-01, 2007.

[44] V. Cindro et al., *The ATLAS beam conditions monitor*, JINST **3** (2008) P02004.

[45] ATLAS Collaboration, *Performance of the Minimum Bias Trigger in p-p Collisions at* $\sqrt{s} = 7$ *TeV*, Tech. Rep. ATLAS-CONF-2010-068, 2010.

[46] K. Kreutzfeldt, M. Düren and H. Stenzel, *Measurement of elastic proton-proton scattering at* $\sqrt{s} = 7$ *TeV with the ALFA sub-detector of ATLAS at the LHC*. PhD thesis, Giessen U., 2014.

[47] ATLAS Collaboration, *Observation of a Centrality-Dependent Dijet Asymmetry in Lead-Lead Collisions at* $\sqrt{s_{NN}} = 2.77$ *TeV with the ATLAS Detector at the LHC*, Phys. Rev. Lett. **105** (2010) 252303, arXiv:1011.6182 [hep-ex].

[48] ATLAS Collaboration, *Measurement of the total cross section from elastic scattering in pp collisions at* $\sqrt{s} = 7$ *TeV with the ATLAS detector*, Nucl. Phys. **B889** (2014) 486–548, arXiv:1408.5778 [hep-ex].

[49] U. Amaldi et al., *The Energy dependence of the proton proton total cross-section for center-of-mass energies between 23 and 53 GeV*, Phys. Lett. **B44** (1973) 112–118.

[50] S. Ask et al., *Luminosity measurement at ATLAS - development, construction and test of scintillating fibre prototype detectors*, Nucl. Instrum. Meth. **A568** (2006) 588–600, physics/0605127.

[51] M. Trzebinski, J. Chwastowski and C. Royon, *Study of QCD and Diffraction with the ATLAS detector at the LHC*. PhD thesis, Cracow, INP and U. Paris-Sud 11, Dept. Phys., Orsay, 2013.

[52] ATLAS Collaboration, *Technical Design Report for the ATLAS Forward Proton Detector*,.

[53] FP420 Collaboration (M. G. Albrow et al.), *The FP420 Project: Higgs and New Physics with forward protons at the LHC*, JINST **4** (2009) T10001, arXiv:0806.0302 [hep-ex].

[54] C. Da Via et al., *3D silicon sensors: Design, large area production and quality assurance for the ATLAS IBL pixel detector upgrade*, Nucl. Instrum. Meth. **A694** (2012) 321–330.

[55] J. Lange et al., *3D silicon pixel detectors for the ATLAS Forward Physics experiment*, JINST **10** (2015) C03031, arXiv:1501.02076 [physics.ins-det].

[56] M. Albrow et al., *Quartz Cherenkov Counters for Fast Timing: QUARTIC*, JINST **7** (2012) P10027, arXiv:1207.7248.

[57] M. Mota and J. Christiansen, *A high-resolution time interpolator based on a delay locked loop and an RC delay line*, IEEE J. Solid-State Circ. **34** no. 10, (1999) 1360–1366.

[58] F. Schmidt, *MAD-X User's Guide*, mad.web.cern.ch/mad/.

[59] F. Schmidt, E. Forest and E. McIntosh, *Introduction to the polymorphic tracking code: Fibre bundles, polymorphic taylor types and exact tracking*, CERN-SL-2002-044-AP, KEK-REPORT-2002-3 (2002).

[60] P. Cruikshank et al., *Mechanical design aspects of the LHC beam screen*, Conf. Proc. **C970512** (1997) 3586.

[61] A. Ferrari et al., *FLUKA: A multi-particle transport code (Program version 2005)*, CERN-2005-010 (2005).

[62] T. H. Kittelmann et al., *The virtual point 1 event display for the ATLAS experiment*, J. Phys. Conf. Ser. **219** (2010) 032012.

[63] L. Nozka et al., *Design of Cherenkov bars for the optical part of the time-of-flight detector in Geant4*, Opt. Express **22** no. 23, (2014) 28984–28996.

[64] J. D. Jackson, *Classical electrodynamics; 3rd ed.* Wiley, New York, 1999.

[65] GEANT4, *Documentation: Cherenkov Effect*, http://geant4.web.cern.ch/geant4/G4UsersDocuments/UsersGuides/PhysicsReferenceManual/html/node37.html.

[66] GEANT4, *G4AffineTransform Class Reference*, www-zeuthen.desy.de/geant4/geant4.9.3.b01/classG4AffineTransform.html.

[67] R. E. Kalman, *A New Approach to Linear Filtering and Prediction Problems*, Trans. of the ASME–Journal of Basic Engineering **82D** (1960) 35–45.

[68] R. Fruhwirth, *Application of Kalman filtering to track and vertex fitting*, Nucl. Instrum. Meth. **A262** (1987) 444–450.

[69] R. Bruce et al., *Sources of machine-induced background in the ATLAS and CMS detectors at the CERN Large Hadron Collider*, Nucl. Instrum. Meth. **A729** (2013) 825–840.

Part III

The measurement

Chapter 6

Analysis objects

In this part of the thesis details of the data analysis and especially the measurement of exclusive two-photon production of lepton pairs (electrons or muons) in proton–proton collisions at $\sqrt{s} = 7$ TeV is discussed. The main physics objects used in this measurement are muons, electrons, tracks of charged particles and vertices. In the following sections, the identification and reconstruction of such objects will be explained.

6.1 Tracks and vertices

Tracks of charged particles play an important role in this analysis. They are used for vetoing the inclusive background, arising mainly from Drell–Yan-like events. Moreover, the reconstruction of vertices, i.e. the actual interaction points from which the primary interactions originate, is based on reconstructed trajectories of charged particles.

Track reconstruction algorithms are using the information from entire Inner Detector of the ATLAS experiment (Pixel, SCT, TRT). Tracks are identified based on so-called *inside-out* algorithm, which is implemented in a software called *NEW Tracking* (NEWT) [1]. Firstly, pattern recognition is performed, in order to identify information from a different hits (electronic signals registered by various Inner Detector modules). Here, a rough estimate of charged-particle trajectory is built. It is based on the creation of three-dimensional representation of the tracking detector measurements, which are then called `SpacePoint` objects, or *space-points*. While a single Pixel hit and the spatial coordinates of the pixel module surface form a space-point, the formation of a space-point from SCT information requires two hits in a single SCT module: one from the front and one from the back of the same module (as well as the spatial coordinates of the module itself). Combination of three of such space-points is then used to define a

`SpacePoint` seeded track (*seed*). For each seed, a transverse momentum is calculated and checked whether it is above the threshold. The track reconstruction algorithm used for the 2011 *pp* data reprocessing had a default threshold of $p_{\mathrm{T}} = 400$ MeV.

The final identification of a track candidate is performed using a combinatorial Kalman filter [2, 3]. The algorithm associates all compatible hits to the initial track seed, while iteratively updating the most probable trajectory of the charged particle. In this process, some ambiguities arise, leading to a very high number of track candidates. Many of these track candidates share hits, are incomplete or describe fake tracks, i.e. tracks where the majority of associated measurements do not originate from one single particle. Figure 6.1 shows an example how such ambiguities can arise. These ambiguities are resolved by assigning *track scores*, similar to likelihoods, based on refitting of each track candidate using a finer geometry. Only track candidates with the highest scores are accepted.

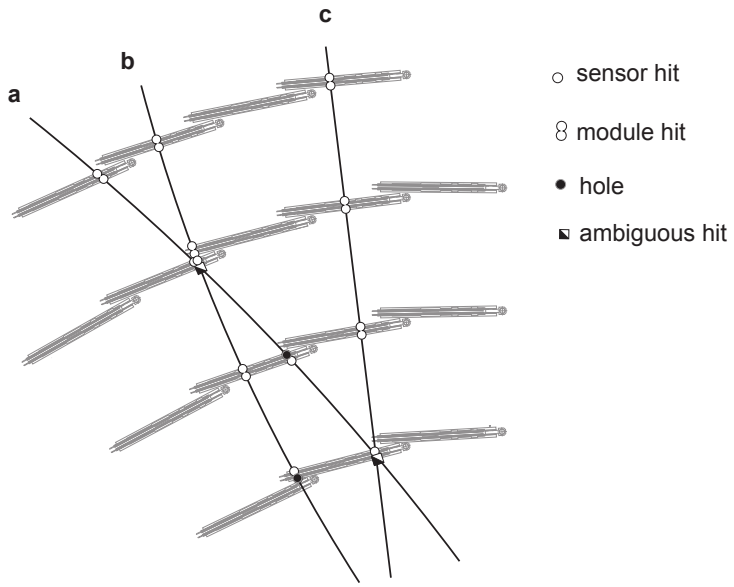

FIGURE 6.1: Simplified model of the ambiguity solving process, illustrated in the SCT. Tracks **a**, **b** and **c** have been found through the seeded track finding, but share several hits. Module hits (representing measurements on both sides of the SCT) result in a higher score than two single hits without associated backside module. If such a hit would be expected but is not found (hole) the track score receives a penalty. Figure taken from [1].

The next step is an extension of the accepted track candidates to the TRT detector. The components of a track candidate extracted from Pixel and SCT layers are not modified any more. Instead, fitting algorithms are used to find TRT hits compatible with the initial track candidate. Finally, a Kalman filter is used to determine whether the extended or the initial (silicon based) track candidate will be used as the final track. The obtained track parameters are used to define the charged-particle trajectory.

6.1.1 Track parameters

A track reconstructed in the Inner Detector can be approximated as a helix (according to charged-particle movement rules in a magnetic field) with its 5 parameters given with respect to some arbitrary reference point. In ATLAS, the reference point is usually the reconstructed vertex position, or the global origin of the coordinate system. Track parameters themselves are given in so-called *perigee* parametrization, which is one possible representation of a helix, where the perigee of a track is defined as a point of closest approach of the trajectory to the z-axis in a given reference frame.

The ATLAS perigee parameters, defined in [4] consist of:

- ϕ_0: azimuthal angle of the track direction at the perigee, i.e. the angle with respect to the x-axis in the $x-y$ (transverse) plane,
- θ: polar angle of the track direction, i.e. the angle with respect to the z-axis in the $r\phi - z$ plane,
- d_0: signed transverse impact parameter, closest distance to the z-axis in the transverse plane,
- z_0: longitudinal impact parameter, z-coordinate of the track at closest distance in the transverse plane,
- $\frac{q_e}{p}$: charge over momentum of the track.

This convention is schematically presented in Figure 6.2. Here also a sign of the impact parameter d_0 is defined: it is positive if the angle between the vector $\overrightarrow{OP}$ and direction of the track is $+\pi/2$, and negative if the angle is $-\pi/2$.

6.1.2 Vertices

Finding the common intersection points between sets of reconstructed tracks (vertices) allows to identify the pp interaction points, as well as the decay vertices of unstable particles produced in the collision. Identifying and reconstructing different vertices within one event relies on precise track reconstruction.

The reconstruction of vertices is performed using an iterative procedure based on all reconstructed tracks in a given event. The *adaptive vertex fitting* algorithm [5] which is based on a χ^2 minimization is used to determine the (primary) vertex position. The algorithm assigns tracks to vertices based on the distance (z-coordinate) of the track

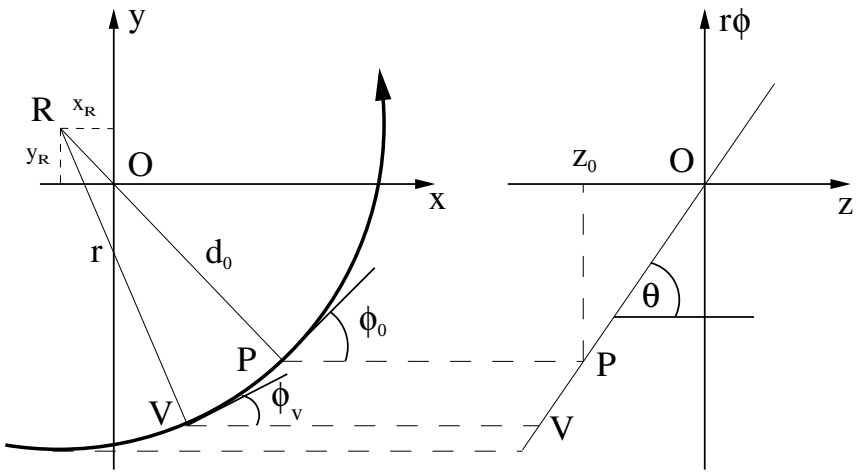

FIGURE 6.2: Definition of the ATLAS perigee parameters. The transverse and longitudinal impact parameters, d_0 and z_0 are determined using projections of the point of closest approach P of a track helix to the reference point O in the $x-y$ and $r\phi-z$ plane, respectively. The point R in the left hand plot represents the center of a track circle in the $x-y$ plane. For this track example, d_0 is positively signed.

and iteratively-updated vertex position. Tracks that are not assigned to any vertex are used as a seeds for other (secondary) vertices.

Most of the reconstructed tracks from a *pp* collision in ATLAS originate from the collision point, indicating the primary vertex of that collision. The *beam spot* (BS) defines in which region the *pp* collisions take place [6]. For 2011 data, it can be described by a three-dimensional Gaussian distribution with the standard deviation of $\simeq$56 mm in the beam direction and $\simeq$15 µm in both transverse directions. Beam spot position size (in z-coordinate) measured by ATLAS as function of time in 2011 *pp* runs is shown in Figure 6.3. Within this region, especially for high-luminosity runs of the LHC, more than one *pp* interaction per bunch crossing can take place.

6.1.3 Pile-up

Since the LHC physics programme is set out primarily to measure the electroweak symmetry breaking and to discover physics beyond the Standard Model, the processes of interest typically have very small cross sections, when compared to the total *pp* cross section. The design of the LHC is such that the luminosity is as large as technically possible, especially in terms of the properties of colliding beams (see Section 3.1.2). Thus, a high spatial density of protons within bunches brought to collision at the LHC and their frequency can give rise to the phenomenon of more than one simultaneous *pp* interaction being overlaid in a reconstructed event (pile-up).

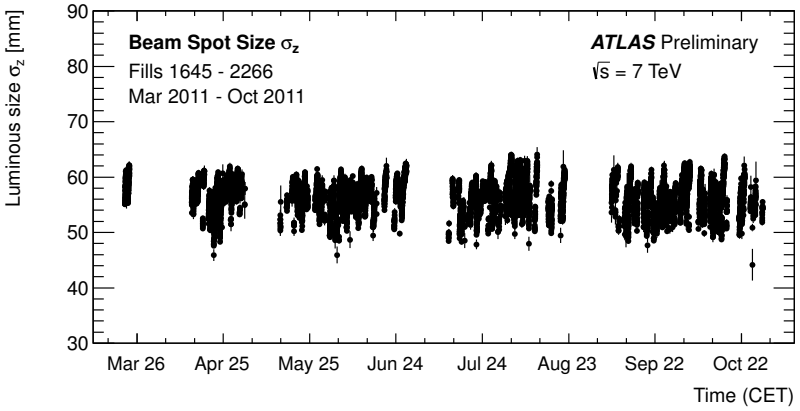

FIGURE 6.3: Beam spot size $\sigma_{z_{\mathrm{BS}}}$ in ATLAS over the course of pp running in 2011. The data points are the result of a maximum likelihood fit to the spatial distribution of primary vertices. Figure taken from [7].

Figure 6.4 shows a distribution of the mean number of interactions per bunch crossing, $\langle\mu\rangle$, for 2011 pp runs considered in the analysis. During that period, the averaged mean number of pp collisions per bunch crossing increased from 6 to 12 (with the averaged number of 9 for all 2011 pp runs).

The impact of these additional pp collisions, for any physics analysis, depend also on the total pp cross section, with its dominant inelastic component. A characteristic feature of those reactions is the production of charged hadrons - and therefore tracks in the reconstruction, that can overlay lepton tracks in the same vertex.

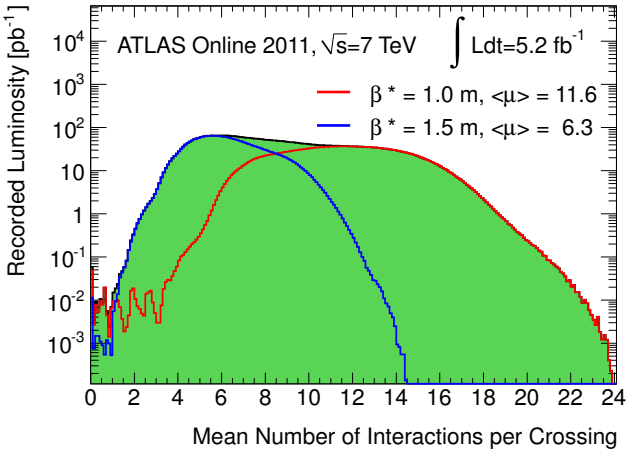

FIGURE 6.4: Luminosity-weighted distribution of the mean number of interactions per bunch crossing for 2011 pp runs. The plot is shown for data taken before and after the September Technical Stop where the collider beta function, β^*, was reduced from 1.5 m to 1.0 m. The integrated luminosity and the average $\langle\mu\rangle$ values are also given. Figure taken from [8].

6.1.4 Track and vertex selection

In this analysis charged-particle tracks are required to fulfill the following criteria:

- $p_{\mathrm{T}} > 400$ MeV - a default threshold of track reconstruction algorithm used for the 2011 *pp* data reprocessing.
- $|\eta| < 2.5$ to match geometrical acceptance of Inner Detector.
- A minimum of one Pixel hit and six SCT hits are required. A hit in the innermost Pixel layer (the *B-layer*) is required if the corresponding pixel module was active.
- The transverse and weighted-longitudinal impact parameters with respect to the vertex of association are required to be $|d_0| < 1.5$ mm and $|z_0 \sin(\theta)| < 1.5$ mm.
- A χ^2 probability of track fit, $p > 0.01$ is required for tracks with $p_{\mathrm{T}} > 10$ GeV, to remove mis-measured tracks (low momentum particles being reconstructed as having very high p_{T}) originating from the combination of a long non-Gaussian tail in the track momentum resolution with the steeply falling p_{T} spectrum.

The track selections are equivalent to the ones used in the underlying event in Z boson and jet events analyses [9, 10].

For MC truth selection of charged particles, for comparison to track observables, the following requirements are applied:

- $p_{\mathrm{T}} > 400$ MeV
- $|\eta| < 2.5$
- Non-zero electric charge
- Stable (`statuscode` $= 1$)
- $0 <$ `barcode` < 200000

The `statuscode` and `barcode` requirements account for selection of stable primary particles produced by the event generator (not secondary particles produced by GEANT4). A particle is being considered stable when its proper lifetime, $c\tau > 10$ mm.

Since this measurement is sensitive to the underlying event activity, tracks produced by the leptons originating from hard scattering process have to be removed from the collection of all charged-particle tracks in each event. Each selected track is probed

whether it falls into the cone, with respect to the reconstructed lepton direction, by calculating the ΔR distance between the lepton and track three-momentum vectors:

$$\Delta R = \sqrt{(\eta^{\ell} - \eta^{\mathrm{trk}})^2 + (\phi^{\ell} - \phi^{\mathrm{trk}})^2} \, . \tag{6.1}$$

The tracks from the reconstructed high-p_{T} leptons are excluded from the track collection by removing any tracks with $\Delta R < 0.01$ from the lepton. This results in removal of exactly two matched lepton tracks for 99.4% of events for $\mathrm{e}^{+}\mathrm{e}^{-}$ and $\mu^{+}\mu^{-}$ analysis channel and in both data and MC samples. If more than one track lies within the cone defined by ΔR requirement, track with highest $p_{\mathrm{T}}$is removed.

For vertices, a standard recommendation is to require each reconstructed vertex being consistent with the beam spot position (beam spot constraint is included in the data processing). For this analysis, each reconstructed vertex is required to have $N_{\mathrm{trk}} \geq 2$ tracks attached to it. Dilepton vertex is defined as the vertex with two matched lepton tracks.

6.2 Muons

Muon candidates are reconstructed in the ATLAS experiment from track segments in the various layers of the Muon Spectrometer (MS), matched with tracks found in the Inner Detector (ID). Depending on the criteria used for the muon identification, different types of reconstructed muons are available [11]:

- *Stand-alone* (SA): the muon trajectory is reconstructed only in the MS. SA muons allow to extend the acceptance range to $2.5 < |\eta| < 2.7$, which is not covered by the ID.
- *Combined* (CB): muon track reconstruction is performed independently in the ID and MS; the ID and MS tracks are later combined into one track. This type provides the highest muon purity, in terms of possible background rejection.
- *Segment-tagged* (ST): a track in the ID is classified as originating from muon if, once extrapolated to the MS, it is associated with at least one local track segment in the MDT or CSC muon chambers. This reconstruction technique is very useful in case of low p_{T} muons.
- *Calorimeter-tagged* (CaloTag): a track in the ID is classified as a muon, if it is associated to an energy deposit in the calorimeter compatible with a minimum ionising particle (MIP). This type has the lowest purity, but recovers acceptance regions with no MS coverage.

For the measurement presented in this thesis, CB muons are used.

There are several algorithms that implement the reconstruction strategies described above. Muons used in this analysis are reconstructed by so-called `STACO` algorithm, included in a dedicated algorithm chain [12]. The `STACO` algorithm is based on the statistical combination of independently measured tracks in the MS and ID which provides an improved momentum resolution and the possibility to reject muons from secondary interactions.

6.2.1 Inner Detector hits

Additionally, muon inner detector track must have a minimum number of hits in each silicon sub-detector:

- at least 1 pixel hit in the B-layer ($N_{\text{hits}}^{\text{BL}}$), unless the track passes from an uninstrumented or dead area of the B-layer,
- at least 1 hit in Pixel layers ($N_{\text{hits}}^{\text{Pix}}$) including the number of crossed dead pixel sensors ($N_{\text{dead}}^{\text{Pix}}$),
- at least 5 hits in the SCT ($N_{\text{hits}}^{\text{SCT}}$) including the number of crossed dead sensors ($N_{\text{dead}}^{\text{SCT}}$),
- less than 3 holes (no hit in a layer crossed by the track) in all silicon layers, Pixel ($N_{\text{holes}}^{\text{Pix}}$) and SCT ($N_{\text{holes}}^{\text{SCT}}$).

It is worth to mention that for all of those hit conditions, dead sensors count as observed hits, not as holes.

The muon reconstruction algorithm, when processing TRT information (pseudorapidity coverage $|\eta| < 2.0$) is unable to unambiguously assign a certain number of TRT hits to a muon track candidate. These hits are called *outliers* - in the sense they not necessarily contribute to the reconstruction of the muon track. For all muon candidates, the fraction of outliers is calculated as:

$$f_{\text{outliers}} = \frac{N_{\text{outliers}}^{\text{TRT}}}{N_{\text{hits}}^{\text{TRT}} + N_{\text{outliers}}^{\text{TRT}}} , \tag{6.2}$$

where $N_{\text{outliers}}^{\text{TRT}}$ denotes the number of outliers and $N_{\text{hits}}^{\text{TRT}}$ the number of TRT hits identified for the muon candidate. The requirements on TRT hits to be met by the muon candidate are based on its pseudorapidity. In the region of full TRT acceptance, $0.1 < |\eta^{\mu}| < 1.9$, it is required to have $N_{\text{hits}}^{\text{TRT}} + N_{\text{outliers}}^{\text{TRT}} > 5$ and $f_{\text{outliers}} < 0.9$.

Muon Selection
Object quality: Combined `STACO` muon
Kinematic acceptance: $p_{\mathrm{T}}^{\mu} > 10$ GeV
Geometrical acceptance: $\lvert\eta^{\mu}\rvert < 2.4$
ID hits requirements: $N_{\mathrm{hits}}^{\mathrm{BL}} > 0$ if expected $N_{\mathrm{hits}}^{\mathrm{Pix}} + N_{\mathrm{dead}}^{\mathrm{Pix}} \geq 1$ $N_{\mathrm{hits}}^{\mathrm{SCT}} + N_{\mathrm{dead}}^{\mathrm{SCT}} \geq 5$ $N_{\mathrm{holes}}^{\mathrm{Pix}} + N_{\mathrm{holes}}^{\mathrm{SCT}} < 3$ $N_{\mathrm{hits}}^{\mathrm{TRT}} + N_{\mathrm{outliers}}^{\mathrm{TRT}} > 5$ and $f_{\mathrm{outliers}} < 0.9$ for $0.1 < \lvert\eta^{\mu}\rvert < 1.9$
Impact parameter requirements: Longitudinal impact parameter: $\lvert z_0\rvert < 10$ mm Transverse impact parameter: $\frac{\lvert d_0\rvert}{\sigma_{d_0}} < 10$
Isolation requirement: $\sum_i p_{\mathrm{T}}^{i}/p_{\mathrm{T}}^{\mu} < 0.1$ in cone of $\Delta R < 0.2$

TABLE 6.1: Reconstructed muon definition used in the analysis.

6.2.2 Kinematic cuts

Selected muons are required to have transverse momentum, $p_{\mathrm{T}}^{\mu} > 10$ GeV and pseudo-rapidity, $|\eta^{\mu}| < 2.4$. In addition, kinematic cuts are applied to further reject muons coming from additional pile-up collisions and from multi-jet background. In particular, the ID track associated to the muon is required to originate from the primary reconstructed vertex. This requirement is implemented by requiring that each muon's flight path intersects the beam axis (z-axis) within 10 mm of the primary vertex and that the distance of closest approach to the dilepton vertex in the transverse plane $|d_0|$, divided by its resolution (σ_{d_0}), must be less than 10.

Finally, the ID track used in the CB muon must be isolated from other tracks to reject secondary muons from hadronic jets. The isolation requirement $\sum_i p_{\mathrm{T}}^{i}/p_{\mathrm{T}}^{\mu} < 0.1$ is calculated using all reconstructed tracks i in a cone of $\Delta R = \sqrt{(\eta^{\mu} - \eta^{i})^2 + (\phi^{\mu} - \phi^{i})^2} < 0.2$. Muons failing above isolation requirement are used to estimate multi-jet background, as described in Section 7.4.2.

A complete list of requirements, applied for each of the reconstructed muon is summarized in Table 6.1.

6.3 Electrons

The reconstruction of electrons in the central pseudorapidity region, $|\eta| < 2.47$, is based on electromagnetic calorimeter (ECal) *clusters* (energy deposits) which are associated to charged-particle tracks reconstructed in the ID. The electron reconstruction process consists of three steps [13, 14]:

- *Cluster reconstruction*: the basic building blocks for the reconstruction of electromagnetic clusters are longitudinal calorimeter towers of size 0.025×0.025 in $\eta - \phi$ plane, corresponding to the granularity of the middle layer of the electromagnetic calorimeter. A so-called *sliding-window* algorithm forms seed clusters of energy deposits in the ECal, with a minimum total transverse energy of 2.5 GeV within a window of size of 3×5 calorimeter towers.
- *Track association*: the electron track candidates are identified in the ID using the standard ATLAS track reconstruction algorithms. The tracks are extrapolated to the middle layer of the electromagnetic calorimeter and loosely matched to the seed clusters. This is done by requiring the angular distance between the extrapolated track and the electromagnetic cluster: $|\Delta\eta| < 0.05$ and $|\Delta\phi| < 0.1$ in the bending direction of the track (to account for bremsstrahlung losses), as well as $|\Delta\phi| < 0.05$ in the opposite direction. If more than one track is matched to a seed cluster, track with the smallest value of $\Delta R = \sqrt{(\eta^{\text{trk}} - \eta^{\text{cluster}})^2 + (\phi^{\text{trk}} - \phi^{\text{cluster}})^2}$ is preferred.
- *Electron candidate reconstruction*: the reconstructed electron energy is determined from the sum of the energy deposits in the cluster cells, corrected for the energy loss upstream of the calorimeter, a swell as lateral and longitudinal energy depositions in and beyond the electromagnetic calorimeter (lateral and longitudinal leakage). The electron direction, in terms of η and ϕ angles, is determined from the direction of the reconstructed ID track.

The behavior of high-energy electrons in the ID is dominated by radiative energy losses (bremsstrahlung) as they traverse detector material. This results in a significant inefficiencies, especially during the electron trajectory reconstruction. To improve the estimated electron track parameters, electron tracks are refitted using *Gaussian Sum Filter* (GSF) algorithm [15, 16]. The GSF algorithm is a non-linear generalization of the Kalman Filters, which allows to take into account the effect of bremsstrahlung in the electron trajectory reconstruction. This results in a much better azimuthal angle reconstruction resolution, compared to the default algorithm. This is shown in Figure 6.5.

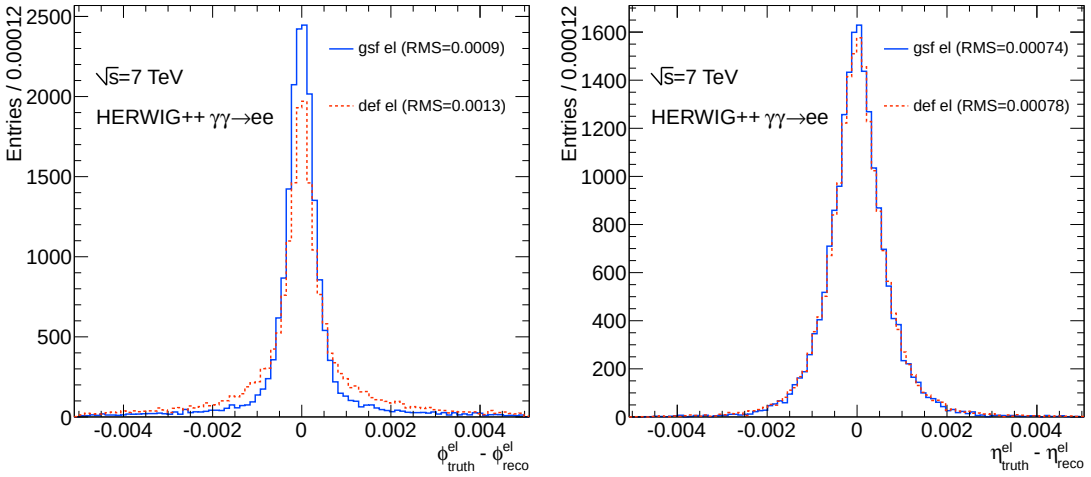

(a) (b)

FIGURE 6.5: Comparison of (a) azimuthal angle and (b) pseudorapidity reconstruction resolution for standard and GSF electron track reconstruction algorithms.

6.3.1 Loose and medium electrons

In the next step, identification criteria are applied to reconstructed electrons to increase the fraction of true signal electrons and reject background (fake) electrons from photon conversions and pion decays as well as hadronic jets. The electron identification sets base on the original classification into `loose`, `medium` and `tight` electrons in the order of decreasing efficiency and increasing purity [13, 14]. The tightened and more pile-up robust "`++`"-scheme defines `loose++`, `medium++`, and `tight++` selections and is used for the data taking periods in 2011.

The electron candidates selected in this analysis are required to fulfill a set of `medium++` cuts. For the estimation of QCD multi-jet background, a second set with less strict criteria (`loose++`) is used, see the Section 7.5.2.

`loose++` electrons

Electrons deposit most of their energy in the ECal, with some leakage into the adjacent hadronic calorimeter (HCal). For electrons reconstructed with $|\eta^{\text{cluster}}| < 0.8$ or $|\eta^{\text{cluster}}| > 1.37$, the hadronic leakage, R_{had1}, can be introduced. It is defined as the ratio of the transverse energy deposit in the first layer of the HCal and the EM cluster transverse energy. For $0.8 < |\eta^{\text{cluster}}| < 1.37$ the hadronic leakage, R_{had}, is calculated as the ratio of the total transverse energy deposit in the HCal and the EM cluster transverse energy. The cuts applied to these variables depend on the electron kinematics [14] and are designed to reject the potential selection of jets faking electrons.

The shape of the EM shower is then used to refine the electron selection. This shape can be characterized using the variable R_η. It is defined as a ratio of the energy in 3×7 cells over the energy in 7×7 cells, centered at the electron cluster position. The actual cut used also depends on the transverse energy and pseudorapidity of the electron [14]. Also the lateral shower width in the middle layer of the ECal, $w_{\eta 2}$, defined as the standard deviation of an energy-weighted distribution of the pseudorapidity of calorimeter cells, is used to check the quality of electrons:

$$w_{\eta 2} = \sqrt{\frac{\sum_i E_i \eta_i^2}{\sum_i E_i} - \left(\frac{\sum_i E_i \eta_i}{\sum_i E_i}\right)^2}, \tag{6.3}$$

where E_i is the energy and η_i is the pseudorapidity of cell i and the sum is calculated within a window of 3×5 cells. The cuts typically require $w_{\eta 2} < 0.02$ [14]. The width of the shower in the first (strip) layer of EM calorimeter:

$$w_{\mathrm{s,tot}} = \sqrt{\frac{\sum_i E_i (i - i_{\max})}{\sum_i E_i}}\ , \tag{6.4}$$

is also used to purify the electron selection. Here i runs over all calorimeter strips of energy E_i and $i_{\max}$ is the index of the highest-energy strip. Moreover, a requirement on the energy of the the largest and second largest energy depositions in the first layer of the ECal, $E_{\max 1}$ and $E_{\max 2}$, is used, requiring the:

$$E_{\mathrm{ratio}} = \frac{E_{\max 1} - E_{\max 2}}{E_{\max 1} - E_{\max 2}}\ , \tag{6.5}$$

to be close to unity.

A more robust (comparing to the initial selection) track-cluster match is required for electron passing the `loose++` criteria: $|\eta^e - \eta^{\mathrm{cluster}}| < 0.015$. The associated track is also required to have at least one Pixel hit and at least seven hits in all silicon layers.

`medium++` electrons

The `medium++` selection contains all the cuts made for `loose++` electrons, with more tight cut values for $R_{\mathrm{had1}}, R_{\mathrm{had}}, R_\eta, w_{\eta 2}, w_{\mathrm{s,tot}}$ and E_{ratio} [14].

The track-cluster match is also required to be tighter: $|\eta^e - \eta^{\mathrm{cluster}}| < 0.005$. In addition to the ID hit criteria in `loose++` selection, electron track is further required to have at least one B-layer hit for $|\eta^e| < 2.01$ (to reject electrons from photon conversions). The minimum number of Pixel hits is now required to be at least two for $|\eta^e| > 2.01$. To reject charged-hadron background, transition radiation in the TRT is required to be

identified with respect to the electron track. Finally, a cut on the transverse impact parameter of the electron track of $|d_0| < 5$ mm is imposed. This is done to suppress the background from electrons originating from heavy flavour quark decays, which tend to have larger values of $|d_0|$.

Object quality cuts

To avoid problems with the front-end boards of the liquid argon calorimeter (or other data quality issues), the electron candidates are required to pass the object quality cut: `el_OQ`&1446 == 0. The bitmask used, 1446, defines a bad electron and indicates that its cluster is affected by at least one of these three conditions: the presence of a dead frontend board in the first or second sampling layer, a dead region affecting the three samplings, or a masked cell in the core.

6.3.2 Kinematic cuts

As already mentioned, the energy of the electron candidate is taken from the calorimeter measurement, while the η^e and ϕ^e are taken from the tracker. Using the electron transverse energy defined in this way,

$$E_{\mathrm{T}}^e = E^{\mathrm{cluster}} / \cosh \eta^e, \tag{6.6}$$

electron candidates are required to have $E_{\mathrm{T}}^e > 12$ GeV. To select well measured electrons, i.e. to ensure the presence of ID tracking coverage and to avoid the transition region between the barrel and end-cap EM calorimeters (where the energy is not well measured), the electrons must be reconstructed using a cluster with $|\eta^{\mathrm{cluster}}| < 1.37$ or $1.52 < |\eta^{\mathrm{cluster}}| < 2.47$ in the absolute detector coordinate system. For compatibility with muons, additional requirement is imposed on the reconstructed electron pseudorapidity, $|\eta^e| < 2.4$.

All electron selection criteria are summarized in Table 6.2.

6.4 Trigger

As detailed in Section 3.2.5, the ATLAS trigger system consists of three stages: the hardware-based Level 1 (L1) trigger and the software-based Level 2 (L2) and Event Filter (EF) triggers.

Electron Selection
Object quality: `el_OQ`&1446 == 0
Identification criteria: `medium++`
Kinematic acceptance: $E_{\mathrm{T}}^{e} > 12$ GeV
Geometrical acceptance:
$\lvert\eta^{\mathrm{cluster}}\rvert < 2.47$, outside crack region $1.37 \leq \lvert\eta^{\mathrm{cluster}}\rvert \leq 1.52$
$\lvert\eta^{e}\rvert < 2.4$
ID hits requirements:
$N_{\mathrm{hits}}^{\mathrm{BL}} > 0$ if expected and for $\lvert\eta^{e}\rvert < 2.01$
$N_{\mathrm{hits}}^{\mathrm{Pix}} \geq 1$; $N_{\mathrm{hits}}^{\mathrm{Pix}} > 1$ for $\lvert\eta^{e}\rvert > 2.01$
$N_{\mathrm{hits}}^{\mathrm{Pix}} + N_{\mathrm{hits}}^{\mathrm{SCT}} \geq 7$
Impact parameter requirement:
Transverse impact parameter: $\lvert d_0\rvert < 5$ mm

TABLE 6.2: Reconstructed electron definition used in the analysis.

The L1 muon trigger utilises a measurement of particle trajectories made by two parts of the Muon Spectrometer (MS): the Resistive Plate Chambers (RPCs) in the barrel region and the Thin Gap Chambers (TGCs) in the end-cap region [17]. For events with electromagnetic clusters, the E_{T} is measured at L1 by trigger towers in a region of 0.1×0.1 in $\eta - \phi$ plane [17]. At L2 and EF steps, muons are reconstructed using Inner Detector (ID) and MS information [18]. Further requirements on the eT are also made at L2 and EF steps and additional quality criteria are imposed to the electron candidates [18].

Candidate events with dilepton final states are recorded with single- or dilepton (muon or electron) triggers. For single-muon trigger, different trigger sequences were used during the particular data-taking periods (labelled A–M for 2011 *pp* runs): `EF_mu18MG` or `EF_mu18MG_medium`, depending on the period, where the transverse momentum threshold of the muon was set to $p_{\mathrm{T}} = 18$ GeV. The term `MG` denotes an inside-out trigger, i.e. the trigger algorithm at the EF level that starts from the ID muon track and extrapolates it to the MS to produce a combined muon track. The dimuon trigger used in the analysis is `EF_2mu10_loose`. It requires two muons with minimum $p_{\mathrm{T}} = 10$ GeV, and is seeded at L1 by `2L1MU0` (indicated by the term `loose` in the chain name). The muon triggers used in the analysis are detailed in Table 6.4.

For single-electron trigger, there are `EF_e20_medium`, `EF_e22_medium` or `EF_e22vh_medium1` triggers used, where the `vh` denotes that additional corrections for hadronic leakage in

Single-muon trigger	Dimuon trigger	2011 period
`EF_mu18MG`	`EF_2mu10_loose`	B - K
`EF_mu18MG_medium`	`EF_2mu10_loose`	L - M

TABLE 6.3: Muon triggers used in the different 2011 data-taking periods in *pp* LHC runs.

Single-electron trigger	Dielectron trigger	2011 period
`EF_2e12_medium`	`EF_e20_medium`	B - J
`EF_2e12_medium`	`EF_e22_medium`	K
`EF_2e12_medium`	`EF_e22vh_medium1`	L - M

TABLE 6.4: Electron triggers used in the different 2011 data-taking periods in *pp* LHC runs.

HCal and dead material corrections were applied. Similarly, for the dielectron case, the `EF_2e12_medium` trigger is used. The electron triggers used in the analysis are summarized in Table 6.4.

The trigger efficiencies determined with the signal MC events after preselection, except the trigger requirement, are all close to (or above) 99% in both analysis channels [11, 14].

Chapter 7

Event reconstruction, preselection and background estimation

This chapter provides the informations about the reconstruction of general event properties as well as criteria requested to obtain basic data selection. In Section 7.1 the data event samples as well as the MC sets are introduced. Specific corrections applied to MC events in order to cover small differences from data are discussed throughout the Sections 7.3–7.5. In Sections 7.4 and 7.5, details concerning the background processes estimation are also provided. Finally, a common preselection criteria are applied to all data and MC events, before dividing further by specific exclusive event selection.

7.1 Data and Monte Carlo samples

7.1.1 Collision data

An analysis of collision data with a center-of-mass energy of $\sqrt{s} = 7$ TeV collected between February 28th and October 31st, 2011 is presented. A total integrated luminosity of 5.61 fb^{-1} was delivered by the LHC at a peak instantaneous luminosity of 3.65×10^{33} cm^{-2}s^{-1}, while an integrated luminosity of 5.25 fb^{-1} was recorded by the ATLAS experiment. The data collection was separated into periods, in which the trigger conditions remained stable, and the different 2011 data-taking periods are labelled A through M. Data-taking periods B–M are used in the analysis, as presented in Table 7.1.

A Good Run List (GRL) consists of a list of run numbers in which the LHC is circulating stable colliding beams and all critical ATLAS detector components are functioning properly. The data sample is selected using the official ATLAS GRL with configuration versions `DetStatus-v36-pro10`, `CoolRunQuery-00-04-08` and `WZjets_allchannels`.

Period	Run number range	Luminosity [pb^{-1}]
B – D	177986 – 180481	176.25
E – H	180614 – 184169	937.71
I	185353 – 186493	333.24
J	186516 – 186755	223.49
K	186873 – 187815	583.27
L – M	188902 – 191933	2401.77
2011	177986 – 191933	4591.01

TABLE 7.1: Run ranges and luminosities for each data-taking period in 2011 for *pp* LHC runs as collected by the ATLAS experiment.

The total integrated luminosity for the sample after GRL requirement is calculated to be $\int L\mathrm{d}t = 4.59$ fb^{-1} and the uncertainty associated with the luminosity measurement is 1.8% [19]. The calibration of the LHC luminosity was performed using dedicated beam-separation scans, also known as *van der Meer* (vdM) scans, where the absolute luminosity can be inferred from direct measurements of the beam parameter [20, 21].

7.1.2 Monte Carlo samples

Simulated event samples are generated in order to estimate the background and to correct the signal yields for detector effects. All Monte Carlo (MC) samples were provided by the official (MC11) campaigns of the ATLAS Production Group.

The signal event samples for exclusive $\gamma\gamma \to \ell^+\ell^-$ production are generated using HERWIG++ 2.5.1 [22] event generator, which implements the EPA formalism in *pp* collisions. The dominant background samples for photon-induced single proton-dissociative dilepton production are generated using LPAIR 4.0 [23, 24] with the Suri–Yennie [25] and Brasse [26] structure functions for proton dissociation. The LPAIR package is interfaced to JETSET 7.408 [27], where the LUND [28] fragmentation model is implemented. The HERWIG++ and LPAIR generators do not include any corrections to account for proton absorptive effects.

For the double-dissociative reactions, PYTHIA 8.175 [29] is used with the NNPDF2.3QED [30] photon-PDFs as a default option. Such modelling of this background contribution is chosen, since it provides the best description of the dilepton transverse momentum distribution observed in data, after event selection cuts are imposed (see Section 8.1.4). The absorptive effects in double-dissociative MC events are taken into account using the default multi-parton interactions model in PYTHIA 8 [31].

The POWHEG 1.0 [32–34] MC generator is used with the CT10 [35] PDFs to generate both the Drell–Yan (DY) $Z/\gamma^* \to \mathrm{e}^+\mathrm{e}^-$ and $Z/\gamma^* \to \mu^+\mu^-$ events. It is interfaced with

MCID	Process	Generator	Mass range [GeV]	Events	σ [pb]
185334	$\gamma\gamma \to e^+e^-$	HERWIG++	$20<m_{\ell^+\ell^-}<60$	500 000	25.322
185335	$\gamma\gamma \to e^+e^-$	HERWIG++	$60<m_{\ell^+\ell^-}<200$	200 000	1.275
185336	$\gamma\gamma \to e^+e^-$	HERWIG++	200<M	100 000	0.032
185337	$\gamma\gamma \to \mu^+\mu^-$	HERWIG++	$20<m_{\ell^+\ell^-}<60$	500 000	12.409
185338	$\gamma\gamma \to \mu^+\mu^-$	HERWIG++	$60<m_{\ell^+\ell^-}<200$	200 000	0.692
185339	$\gamma\gamma \to \mu^+\mu^-$	HERWIG++	$200<m_{\ell^+\ell^-}$	100 000	0.018

TABLE 7.2: Exclusive $\gamma\gamma \to \ell^+\ell^-$ signal production processes, cross sections σ and numbers of fully simulated MC events. The generators used to produce the MC events are also indicated with the appropriate identification numbers (MCID).

PYTHIA 6.425 [36] using the CTEQ6L1 [37] PDF set and the AUET2B [38] values of the tunable parameters to simulate the parton shower and the underlying event (UE). These samples are referred to as POWHEG+PYTHIA. The DY $Z/\gamma^* \to \tau^+\tau^-$ process is generated using PYTHIA 6.425 together with the MRST LO* [39] PDFs.

The production of top-quark pair ($t\bar{t}$) events is modelled using MC@NLO 3.42 [40, 41] and diboson (W^+W^-, $W^\pm Z$, ZZ) processes are simulated using HERWIG 6.520 [42]. The event generators used to model Z/γ^*, $t\bar{t}$ and diboson reactions are interfaced to PHOTOS 3.0 [43] to simulate QED final-state radiation (FSR) corrections.

For the DY background processes, i.e. $Z/\gamma^* \to \ell^+\ell^-$ ($\ell = e, \mu, \tau$), the samples are normalized to the perturbative QCD (pQCD) next-to-next-to-leading-order (NNLO) cross sections as provided by the FEWZ 3.1 [44, 45] program with MSTW2008 [46] PDFs. The theory uncertainties on those cross sections arise from the choice of PDFs (3%), from factorization and renormalization scale dependence, and the size of the correction from NLO and NNLO (4%). The $t\bar{t}$ cross section, is also scaled to pQCD NNLO accuracy, following calculations in [47–49]. The inclusive diboson samples are normalized to their respective NLO cross sections calculated with MCFM 5.8 [50] with MSTW2008 PDFs.

Details about the signal and all background MC samples used in the analysis are presented in Tables 7.2–7.5.

Finally, the passage of particles through the ATLAS detector is modelled using GEANT4, as described in Section 3.3.2. The simulated events are reconstructed and selected using the same software chain as for data.

MCID	Process	Generator	Mass range [GeV]	Events	σ [pb]
185343	$\gamma\gamma \to e^+e^-$	LPAIR	$20<m_{\ell^+\ell^-}<60$	500 000	5.146
185344	$\gamma\gamma \to e^+e^-$	LPAIR	$60<m_{\ell^+\ell^-}<200$	200 000	0.838
185345	$\gamma\gamma \to e^+e^-$	LPAIR	$200<m_{\ell^+\ell^-}$	100 000	0.035
185346	$\gamma\gamma \to \mu^+\mu^-$	LPAIR	$20<m_{\ell^+\ell^-}<60$	500 000	4.644
185347	$\gamma\gamma \to \mu^+\mu^-$	LPAIR	$60<m_{\ell^+\ell^-}<200$	200 000	0.777
185348	$\gamma\gamma \to \mu^+\mu^-$	LPAIR	200<M	100 000	0.033

TABLE 7.3: Single proton-dissociative $\gamma\gamma \to \ell^+\ell^-$ MC samples.

MCID	Process	Generator	Mass range [GeV]	Events	σ [pb]
185349	$\gamma\gamma \to e^+e^-$	LPAIR	$20<m_{\ell^+\ell^-}<60$	500 000	2.878
185350	$\gamma\gamma \to e^+e^-$	LPAIR	$60<m_{\ell^+\ell^-}<200$	200 000	0.569
185351	$\gamma\gamma \to e^+e^-$	LPAIR	$200<m_{\ell^+\ell^-}$	100 000	0.030
185352	$\gamma\gamma \to \mu^+\mu^-$	LPAIR	$20<m_{\ell^+\ell^-}<60$	500 000	2.905
185353	$\gamma\gamma \to \mu^+\mu^-$	LPAIR	$60<m_{\ell^+\ell^-}<200$	200 000	0.569
185354	$\gamma\gamma \to \mu^+\mu^-$	LPAIR	$200<m_{\ell^+\ell^-}$	100 000	0.030
129651	$\gamma\gamma \to e^+e^-$	PYTHIA 8	$20<m_{\ell^+\ell^-}<60$	500 000	24.54
129652	$\gamma\gamma \to e^+e^-$	PYTHIA 8	$60<m_{\ell^+\ell^-}<200$	500 000	2.412
129663	$\gamma\gamma \to e^+e^-$	PYTHIA 8	$200<m_{\ell^+\ell^-}<600$	200 000	0.1031
129661	$\gamma\gamma \to \mu^+\mu^-$	PYTHIA 8	$20<m_{\ell^+\ell^-}<60$	500 000	24.49
129662	$\gamma\gamma \to \mu^+\mu^-$	PYTHIA 8	$60<m_{\ell^+\ell^-}<200$	500 000	2.413
129663	$\gamma\gamma \to \mu^+\mu^-$	PYTHIA 8	$200<m_{\ell^+\ell^-}<600$	200 000	0.1033

TABLE 7.4: Double proton-dissociative $\gamma\gamma \to \ell^+\ell^-$ MC samples.

MCID	Process	Generator	Mass range [GeV]	Events	σ [pb]
108303	$Z/\gamma^* \to e^+e^-$	POWHEG+PYTHIA	$53.5<m_{\ell^+\ell^-}$	20 000 000	968
129806	$Z/\gamma^* \to e^+e^-$	POWHEG+PYTHIA	$38<m_{\ell^+\ell^-}<53.5$	3 000 000	84.0
185606	$Z/\gamma^* \to e^+e^-$	POWHEG+PYTHIA	$20<m_{\ell^+\ell^-}<38$	3 000 000	601
108304	$Z/\gamma^* \to \mu^+\mu^-$	POWHEG+PYTHIA	$53.5<m_{\ell^+\ell^-}$	20 000 000	968
129807	$Z/\gamma^* \to \mu^+\mu^-$	POWHEG+PYTHIA	$38<m_{\ell^+\ell^-}<53.5$	3 000 000	84.0
185607	$Z/\gamma^* \to \mu^+\mu^-$	POWHEG+PYTHIA	$20<m_{\ell^+\ell^-}<38$	3 000 000	601
106052	$Z/\gamma^* \to \tau^+\tau^-$	PYTHIA	$60<m_{\ell^+\ell^-}$	500000	835
105200	$t\bar{t}$	MC@NLO	-	15 000 000	177
105985	W^+W^-	HERWIG	-	2 500 000	389
105986	ZZ	HERWIG	-	250 000	4.69
105987	$W^\pm Z$	HERWIG	-	1 000 000	12.01

TABLE 7.5: Electroweak background MC samples.

7.2 Drell–Yan pair p_{T} reweighting

The description of the transverse momentum spectrum of the Z/γ^* boson by the POWHEG +PYTHIA generator shows a consistent deficit of events in the low-p_{T} range [51]. Therefore, for this analysis the $p_{\mathrm{T}}^{\ell^+\ell^-}$spectrum is reweighted to the pQCD NNLO RESBOS [52] prediction using CT10 PDFs, which models the data within 5% [51, 53, 54]. The differences between these MC generators are presented in Figure 7.1.

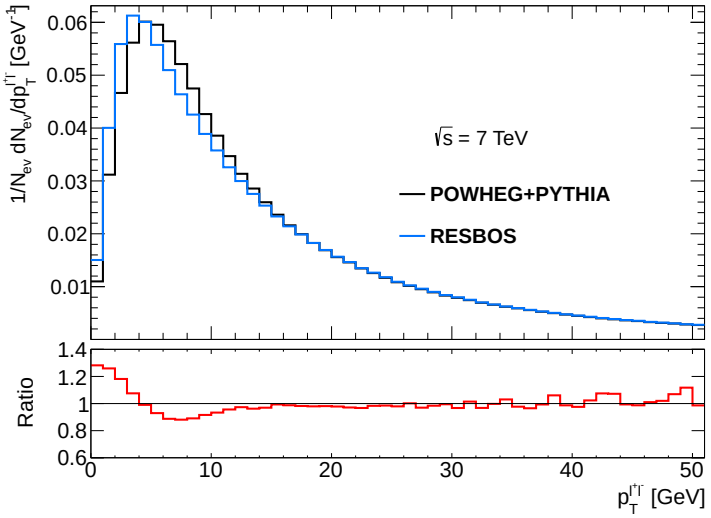

FIGURE 7.1: Truth transverse momentum of the dilepton system distribution for POWHEG+PYTHIA (black) and RESBOS (blue) MC generators. Events satisfying $m_{\ell^+\ell^-} > 20$ GeV, $p_{\mathrm{T}}^{\ell} > 10$ GeV and $|\eta^{\ell}| < 2.4$ requirements are shown.

7.3 Reconstructed vertices and pile-up correction

Multiple interactions per bunch crossing (pile-up) are accounted for by overlaying simulated minimum-bias events, generated with PYTHIA 6.425 using the AUET2B tune and CTEQ6L1 PDFs. The variations in pile-up conditions in 2011 are included in the simulation of MC events in order to match the different running conditions and the pile-up distribution observed in data.

Residual differences in the pile-up between data and MC simulation have been corrected by reweighting the Monte Carlo events to reproduce the average number of interactions per bunch crossing, $\langle\mu\rangle$, observed in data. This reweighting of the MC samples is performed using the official ATLAS tool from the ATHENA software framework. The distribution of the number of primary vertices and the $\langle\mu\rangle$ distribution in data and MC simulation after the pile-up reweighting are shown in Figure 7.2. It can be observed that the reweighted MC simulation accurately describes the distribution seen in the data.

Distribution of the z coordinate of the primary vertices has a quite large difference between data and MC simulations used in the analysis. The vertex z-coordinate position shape in MC events should be reweighted in order to match the distribution observed in data. The official ATHENA tool is used to perform this reweighting. The vertex z-coordinate position shape in MC simulation (dimuon vertices) before and after reweighting is shown in Figure 7.3 and compared to the shape observed in data.

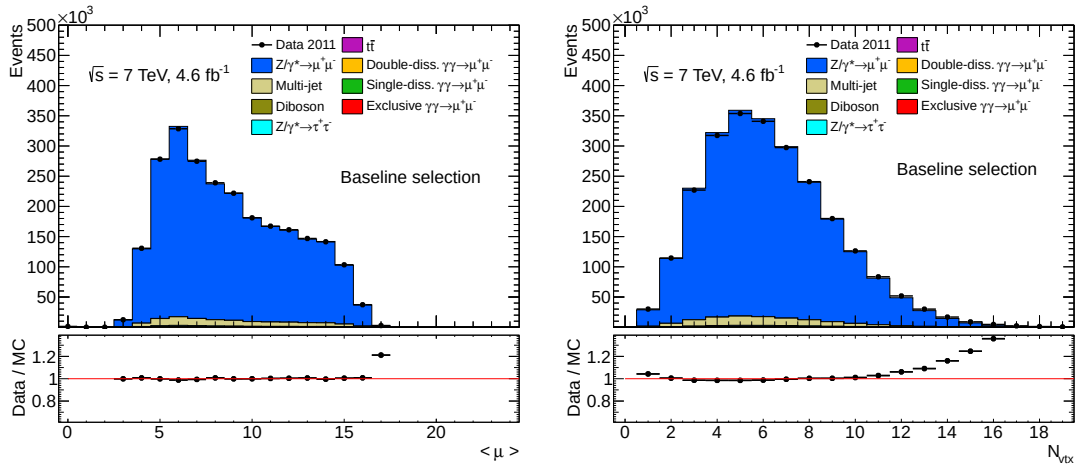

(a) (b)

FIGURE 7.2: Control distributions (a) of the average number of interactions per bunch-crossing $\langle\mu\rangle$ and (b) of the number of reconstructed primary vertices for $\mu^+\mu^-$ analysis channel after application of the pile-up reweighting. All MC expectations are scaled to the integrated luminosity of the data using the predicted cross sections.

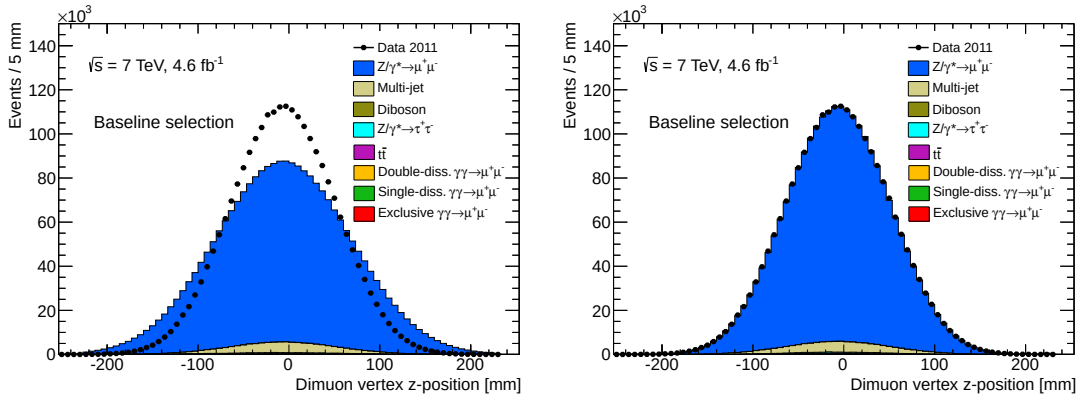

(a) (b)

FIGURE 7.3: Distributions of the z-position of the reconstructed dimuon vertex for $\mu^+\mu^-$ analysis channel. Data are compared to the MC simulation: (a) before and (b) after applying the vertex position reweighting procedure.

7.4 Event preselection in $\mu^+\mu^-$ channel

Dimuon events are preselected by requiring two oppositely charged same-flavour muons, as defined in Section 6.2. Only events that pass the muon trigger requirements from Section 6.4 are considered. Moreover, the dilepton invariant mass is required to be $m_{\mu^+\mu^-} > 20$ GeV.

7.4.1 Corrections to the Monte Carlo modelling

A list of corrections is applied to the MC simulation in order to improve its agreement with data. Official tools from the relevant ATHENA software packages are used.

Muon momentum scale and resolution. Before the reconstruction efficiency can be calculated, a correction must first be applied to the MC simulation to take into account the mis-modelling of the resolution response and momentum scale of the muon reconstruction. Previous ATLAS studies have been performed using so-called *tag-and-probe* (T&P) method with muons from Z boson decays in order to measure the difference in reconstructed muon momentum scale and momentum resolution between MC simulation and data [11]. Smearing factors, which can be applied to simulated muons, are provided by the software packages that employ the T&P procedure. Figure 7.4 shows the effect of the smearing on the p_{T} of the muons for the signal MC events. The error bars represent the RMS spread of the difference in p_{T}^{μ} before and after smearing correction is applied.

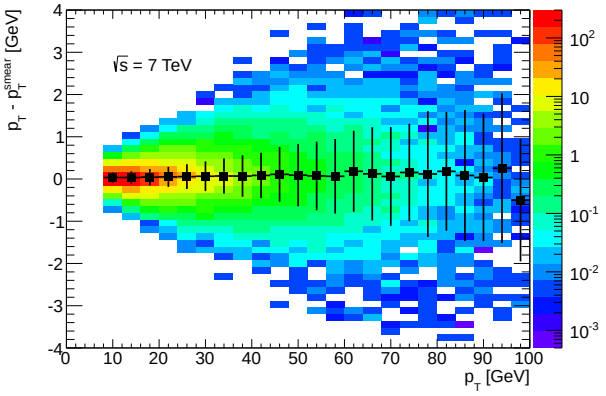

FIGURE 7.4: Size of the p_{T} smearing and momentum scale corrections for muons. The smearing and scale shifts are accounted for together. The error bars represent the RMS in each bin.

Muon reconstruction efficiency. The data-driven efficiency of the `STACO` muon reconstruction algorithm has been studied elsewhere in ATLAS using a T&P method with $Z/\gamma^* \rightarrow \mu^+\mu^-$ decays from data [11]. The results from this study are provided as another software tool within the ATHENA framework, which can be used to retrieve a scale factor to correct for the measured discrepancy between data and MC simulation. The tool provides a p_{T}-, η- and ϕ-dependent scale factor for each reconstructed muon (calculated after the p_{T} smearing has been applied). These factors are calculated for both muons in an event, and are multiplied together to give a single MC event weight associated with muon reconstruction correction. Figure 7.5 shows the muon reconstruction scale factor in bins of muon p_{T} and η, applied to the signal MC events.

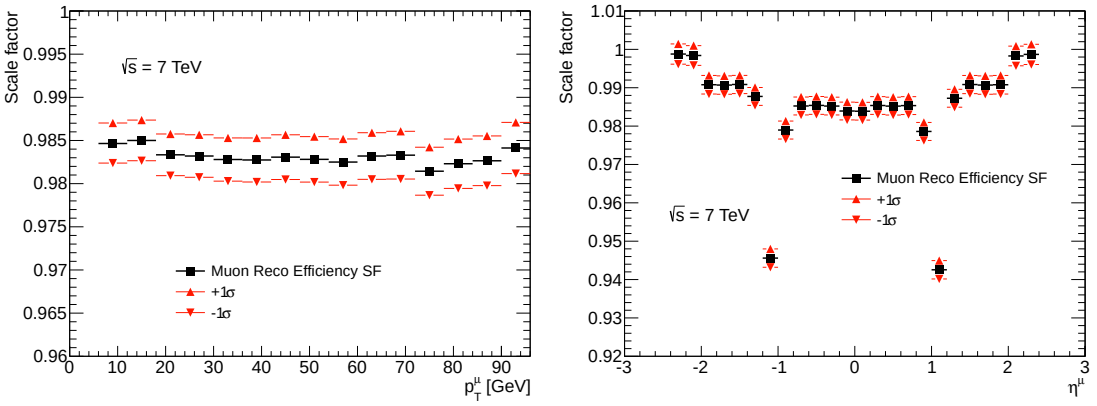

(a) (b)

FIGURE 7.5: Average muon reconstruction efficiency scale factor, in bins of (a) muon p_{T} and (b) muon η. The total uncertainties on the muon reconstruction efficiencies are also shown.

Muon trigger efficiency. Trigger scale factors correcting for the mis-modelling of triggers in the MC simulation are also applied using the official dedicated tool as detailed in [11, 55]. Moreover, the dimuon trigger efficiency scale factors for `EF_2mu10_loose` are obtained from the product of each single muon `EF_mu10_loose` efficiency scale factors. Figure 7.6 shows the `EF_mu10_loose` trigger corrections as a function of the p_{T} and η of the reconstructed muons. As an effect, these corrections decrease the MC predictions by about 0.5%.

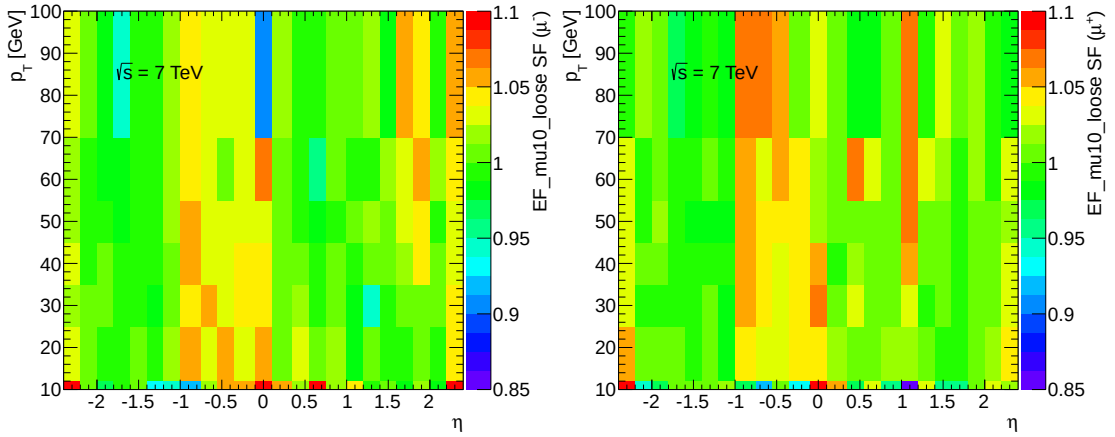

(a) (b)

FIGURE 7.6: Scale factors for `EF_mu10_loose` trigger efficiency as a function of muon η and p_{T} for (a) positively and (b) negatively charged muons.

7.4.2 Backgrounds

Backgrounds for the $\mu^+\mu^-$ channel can be divided in three categories: photon-induced, electroweak (EW) and QCD multi-jet backgrounds.

Photon-induced backgrounds. Single- and double-dissociative background reactions are estimated using MC simulations. Detailed MC generator studies for photon-induced processes are summarized in Section 2.5.

Electroweak backgrounds. EW backgrounds contain high transverse momenta muons from the weak boson decays. Significant contributions are $Z/\gamma^* \to \mu^+\mu^-$ and $Z/\gamma^* \to \tau^+\tau^-$ processes. In addition, the diboson (W^+W^-, $W^\pm Z$, ZZ) decays are considered, as well as $t\bar{t}$ pair production, where either one or both produced $W^\pm$ bosons decay into an muon. The contribution of these background processes to the final selection is estimated from the MC simulations.

QCD backgrounds. QCD background arises mostly from mis-identification of jets from $b\bar{b}$ and $c\bar{c}$ decaying to muon pairs. The predictions for these backgrounds suffer from dominated by large uncertainties and the available statistics is too low for the precision required in this analysis. Therefore, a data-driven technique has been adopted to estimate these processes, similarly as in [54, 56].

The QCD multi-jet sample has been selected requiring the same cuts as adopted for the signal selection but requiring same-charge muon pairs. This requirement strongly reduces the contamination of the sample from any EW process producing muon pair, and enhances QCD multi-jet contributions. Similar technique is used e.g. in the transverse momentum distribution of After all preselection requirements the QCD-enriched sample counts 150 000 same-sign muon pairs in the invariant mass range $m_{\mu^\pm\mu^\pm} > 20$ GeV. This is shown in Figure 7.7. The contamination of this sample has been investigated using signal and EW background MC events. It is estimated to be only ≈1% in the range $m_{\mu^\pm\mu^\pm} > 20$ GeV.

After selecting the QCD multi-jet sample from data, the expected fraction of QCD multi-jet events in the signal region is estimated using a template fit method. Maximum likelihood fit to the $m_{\mu^\pm\mu^\pm}$ distribution has been performed to extract the QCD multi-jet normalization factor. DY MC events have been used to prepare the dominant EW event template, adding to it the other EW processes, $\mathscr{P}(\mathrm{DY} + \mathrm{EW}_{\mathrm{other}})$. The same-sign dimuon sample has been used as a template for the QCD multi-jet background, $\mathscr{P}(\mathrm{QCD})$, that is assumed to follow the relation:

$$\mathscr{P}(\text{data}) \simeq p_0 \cdot \mathscr{P}(\text{DY} + \text{EW}_{\text{other}}) + p_1 \cdot \mathscr{P}(\text{QCD}) \ , \tag{7.1}$$

where $\mathscr{P}(\text{data})$ denotes the events observed in data. The p_i $(i = 0, 1)$ parameters of Equation 7.1 have been extracted from the fit, where p_0 is expected to be > 0.9 and p_1 is the QCD multi-jet normalization factor. The QCD multi-jet background fraction is found to be $\simeq$4% in the range $m_{\mu^\pm\mu^\pm} > 20$ GeV, comparing to all other expected contributions after the preselection step.

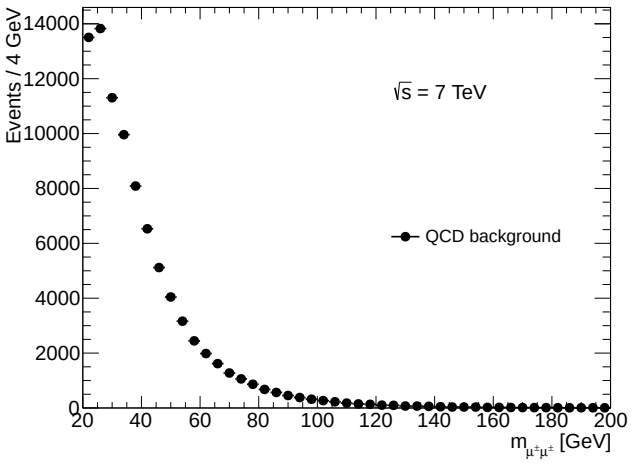

FIGURE 7.7: Invariant mass distribution of two same-sign muons for $20 < m_{\mu^\pm\mu^\pm} < 200$ GeV used to extract the QCD multi-jet background contribution.

7.4.3 Preselection results and control distributions

After applying all preselection requirements, the 2 422 745 dimuon candidate events are observed in data, for a total number of predicted events of 2 423 810. The total number of observed candidate events is therefore in excellent agreement with the sum of predictions for the different contributing processes. The individual contributions of different background processes are detailed in Table 7.6.

Kinematic distributions of observed preselected event candidates are compared to the prediction from the MC simulations in Figure 7.8. Figure 7.8a shows dimuon invariant mass, 7.8b transverse momentum of positively charged muon, 7.8c dimuon rapidity, 7.8d pseudorapidity of positively charged muon, 7.8e transverse momentum of the dimuon system, and 7.8f dimuon acoplanartity. The MC predictions for all distributions are found to be in good agreement with the data.

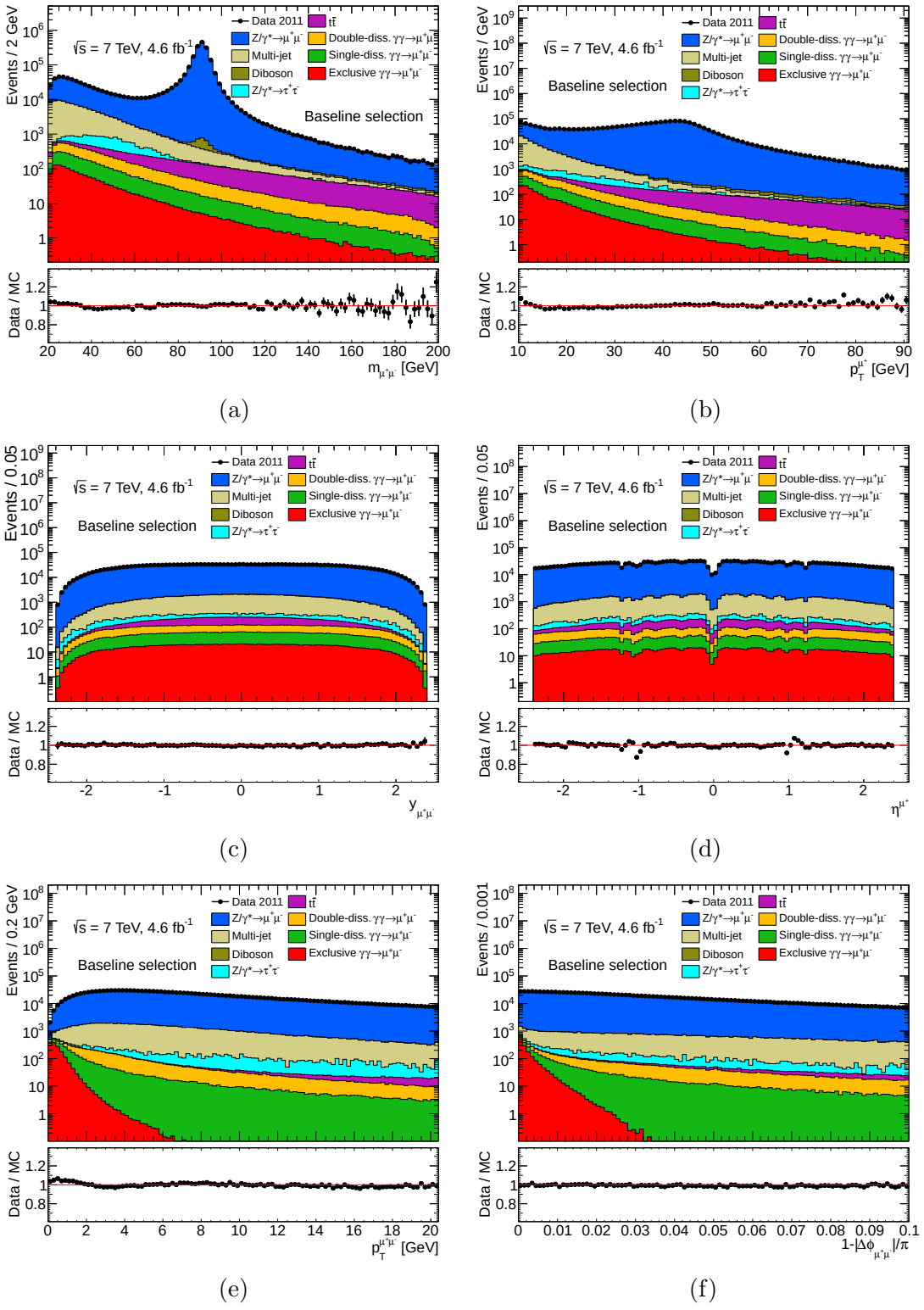

FIGURE 7.8: Control distributions of kinematic variables of the dimuons candidate after preselection citeria are applied. Data (black dots) are compared to the MC simulation (histograms). The error bars on the ratio take into account statistical uncertainties of the data and MC samples.

	Data	MC total	$Z/\gamma^* \to \mu^+\mu^-$	Multi-jet	$Z/\gamma^* \to \tau^+\tau^-$	$t\bar{t}$	Di-boson
Events	2 422 745	2 423 810	2 298 767	97 727	7606	6708	2870
	D-diss. $\gamma\gamma \to \mu^+\mu^-$		S-diss. $\gamma\gamma \to \mu^+\mu^-$		Exclusive $\gamma\gamma \to \mu^+\mu^-$		
Events	4394		3964		1774		

TABLE 7.6: Number of $\mu^+\mu^-$channel candidates after all preselection criteria in data, compared to the number of expected signal and background events. The multi-jet background is estimated using data-driven methods, whereas the other contributions are obtained from MC simulations.

7.5 Event preselection in e^+e^- channel

Dielectron events are preselected by requiring two oppositely charged same-flavour electrons, as defined in Section 6.3, with the dielectron invariant mass required to be $m_{e^+e^-} > 20$ GeV. Events passing the electron trigger requirements from Section 6.4 are considered.

7.5.1 Corrections to the Monte Carlo modelling

Various corrections are applied to correct for remaining mis-calibrations or mis-modelling of the electrons in MC simulations, as compared to data. Reweighting procedure applied to the MC events takes into account all corrections for electrons: including trigger efficiency correction, reconstruction and identification efficiency correction, energy scale and resolution corrections. Only official tools from the relevant ATHENA software packages are used.

Electron energy scale. The electromagnetic calorimeter energy scale is derived using full 2011 data set [57]. Corrections for the reconstructed electron energy scale are applied on an event by event basis and propagated trough the full analysis chain.

Electron energy resolution. Another correction that is applied on MC events is the reconstructed electron energy smearing [57]. The effect of electron energy resolution correction on the E_{T} of electrons in MC events is shown in Figure 7.9. The error bars show the RMS spread of the difference in E_{T} before and after scaling.

Electron trigger efficiency. The electron trigger efficiency in MC simulation does not match exactly the trigger efficiency observed in data. This difference can be corrected by applying relevant trigger efficiency scale factors on the MC events. The T&P method is also used to calculate the scale factors for the trigger requirements on the electrons [14]. The effect of this correction is shown in Figure 7.10, for the `EF_e12_medium`

and `EF_e12Tvh_medium` triggers, as a function of the E_{T} and η of the reconstructed electrons.

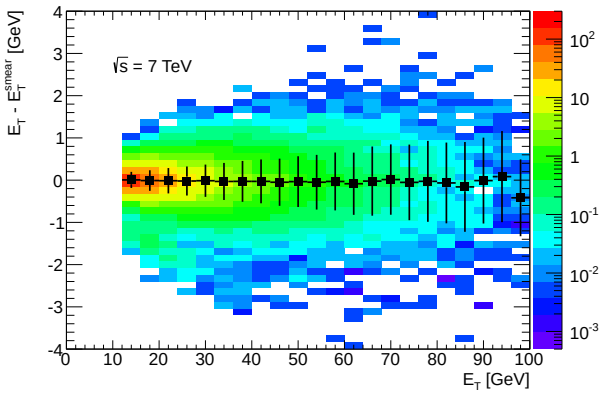

FIGURE 7.9: Size of the electron energy smearing in E_{T} for the exclusive signal MC events. The error bars represent the RMS in each bin.

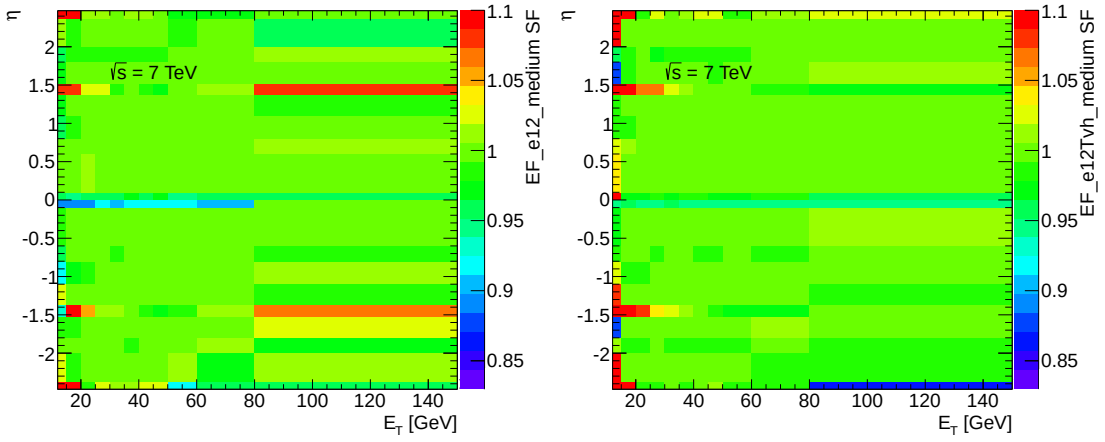

(a) (b)

FIGURE 7.10: Scale factors for (a) `EF_e12_medium` and (b) `EF_e12Tvh_medium` dielectron triggers efficiency as a function of E_{T} and η of electrons.

Electron reconstruction and identification efficiency. The electron efficiency was studied using the T&P method, as described in [14]. This correction needs to be applied on MC events in order to describe the electron efficiencies measured in data. The appropriate scaling factor distributions are shown in Figure 7.11.

7.5.2 Backgrounds

Backgrounds for the e^+e^- channel can be divided in three categories: photon-induced, EW and QCD multi-jet backgrounds.

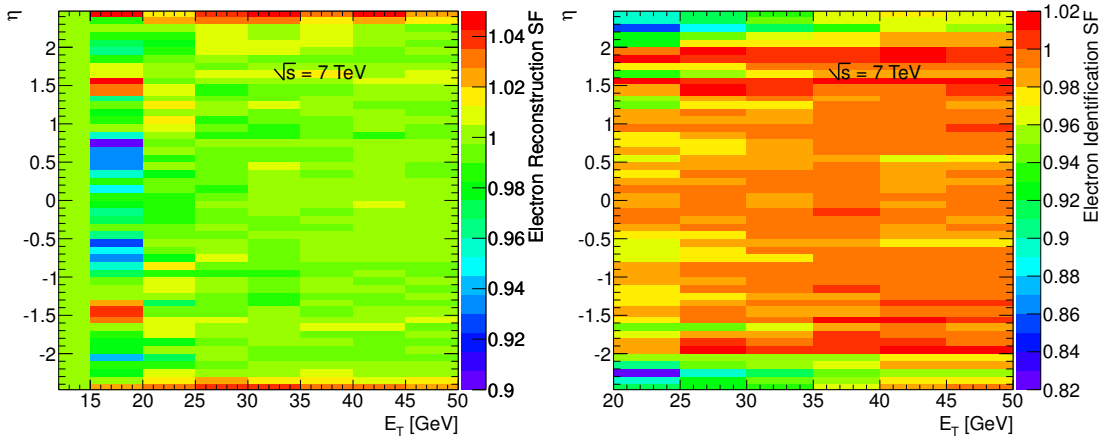

(a) (b)

FIGURE 7.11: Scale factors for (a) electron reconstruction and (b) identification efficiencies as a function of E_{T} and η of electrons.

Photon-induced backgrounds. Single and double dissociative background reactions are estimated using MC events. Detailed MC generator studies for photon-induced processes are summarized in Section 2.5.

Electroweak backgrounds. EW backgrounds contain real high transverse momenta electrons from the weak boson decays. Significant contributions are $Z/\gamma^* \to e^+e^-$ and $Z/\gamma^* \to \tau^+\tau^-$ processes. In addition the diboson decays (W^+W^-, $W^\pm Z$, ZZ) are considered, as well as $t\bar{t}$ pair production, where either one or both $W^\pm$ bosons decay into an electron. The contribution of these background processes to the final selection is estimated from the MC simulations.

QCD backgrounds. In order to calculate a contribution from QCD multi-jet events in the electron channel, a template fit method is used - similarly as for muons. The normalization factor is estimated using a maximum likelihood fit to the dielectron invariant mass distribution for events satisfying the preselection requirements.

In order to select QCD multi-jet template sample in the dielectron channel, the standard preselection is modified to enhance the QCD background. In this selection, the same trigger and electron kinematic requirements are used (except charge requirement), and events with two electrons failing `medium++` and passing `loose++` selection criteria are considered.

The dielectron invariant mass distribution for selected QCD multi-jet background events is shown in Figure 7.12. To check the possible contamination from signal events in the selected multi-jet sample, events with same-sign electron pairs are considered. No

difference in various dielectron kinematic distributions is observed, comparing to the QCD multi-jet sample extracted using the default selection requirements.

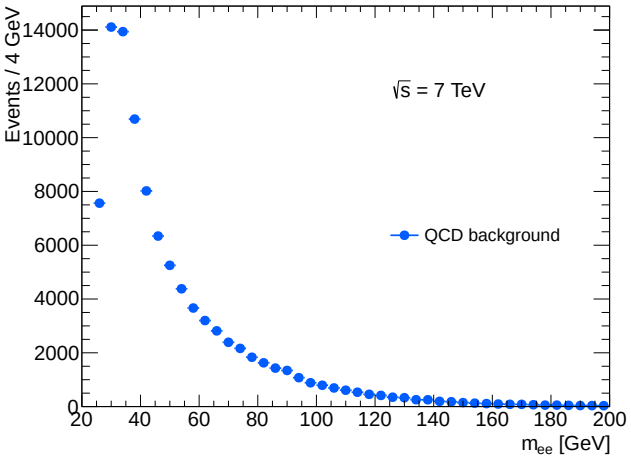

FIGURE 7.12: Invariant mass distribution of two electrons failing `medium++` selection criteria for $24 < m_{ee} < 200$ GeV used to extract the QCD multi-jet background contribution.

7.5.3 Preselection results and control distributions

After applying all preselection requirements, the 1 572 271 candidate events in the electron channel are observed in data, for a total number of predicted events of 1 559 431. The total number of observed candidates is in agreement with the sum of predictions for the different contributing processes. The individual contributions of different background processes are detailed in Table 7.7.

Typical kinematic distributions of observed preselected dielectron candidates are compared to the prediction from the MC simulations in Figure 7.13. Figure 7.13a shows dielectron invariant mass, 7.13b transverse energy of positively charged electron, 7.13c dielectron rapidity, 7.13d pseudorapidity of positively charged electron, 7.13e transverse momentum of the dielectron system, and 7.13f dielectron acoplanartity. The MC predictions for all distributions are found to be in agreement with the data.

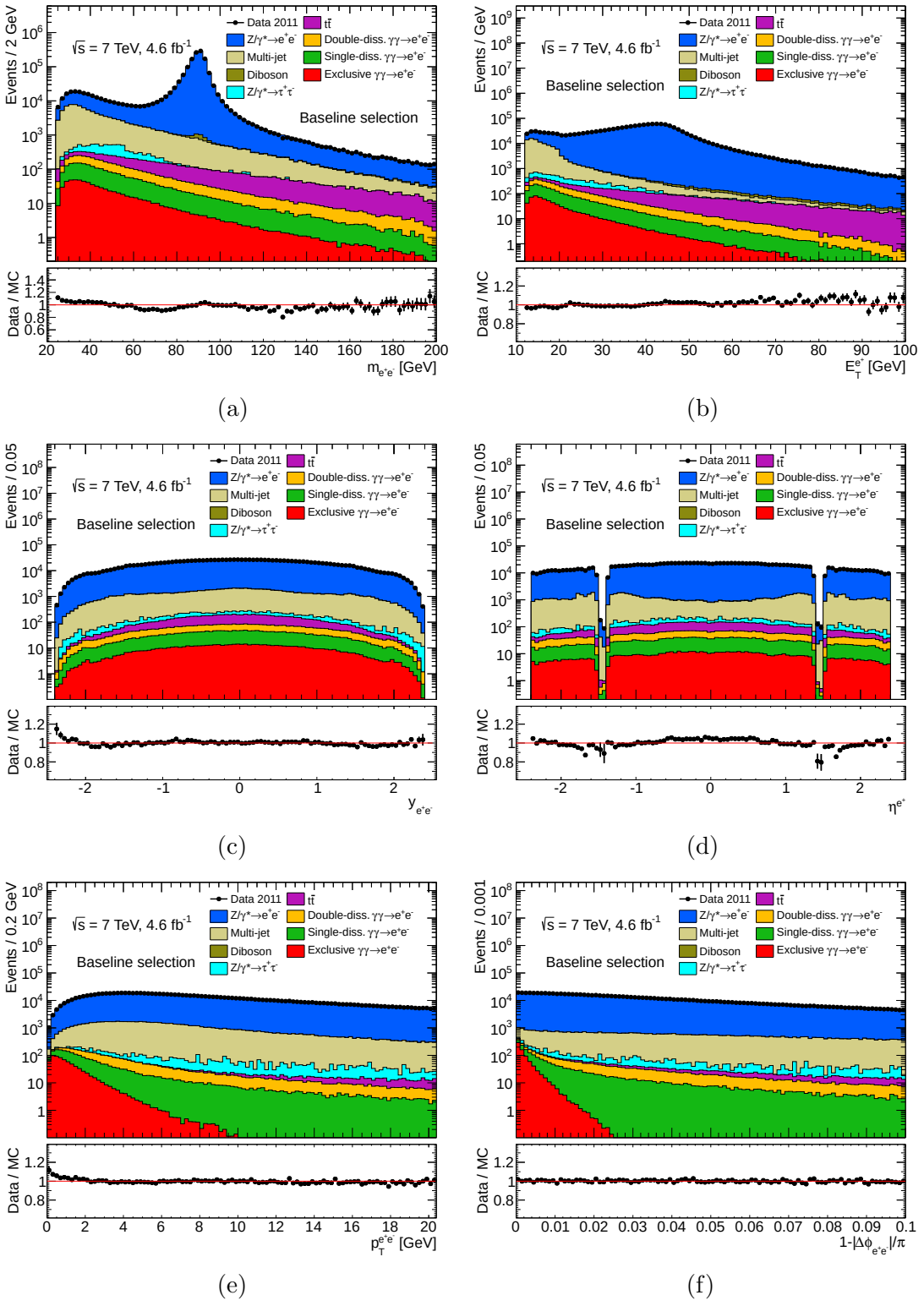

FIGURE 7.13: Control distributions of kinematic variables of the dielectron candidates after preselection citeria are applied. Data (black dots) are compared to the MC simulation (histograms). The error bars on the ratio take into account statistical uncertainties of the data and MC samples.

	Data	MC total	Z/γ^* $\to e^+e^-$	Multi-jet	Z/γ^* $\to \tau^+\tau^-$	$t\bar{t}$	Di-boson
Events	1 572 271	1 559 431	1 460 867	83 183	3758	4612	1945
	D-diss. $\gamma\gamma \to e^+e^-$		S-diss. $\gamma\gamma \to e^+e^-$		Exclusive $\gamma\gamma \to e^+e^-$		
Events	2072		2096		898		

TABLE 7.7: Number of e^+e^-channel candidates after all preselection criteria in data, compared to the number of expected signal and background events. The multi-jet background is estimated using data-driven methods, whereas the other contributions are obtained from MC simulations.

Chapter 8

Exclusive event selection and signal extraction

In this chapter, detailed cut-based event selection for $\gamma\gamma \to \mu^+\mu^-$ and $\gamma\gamma \to e^+e^-$ analysis channels is given. Section 8.1 discusses exclusive selection criteria used to obtain a high signal-purity event sample. Section 8.2 provides the detailed information about the method used to extract the exclusive signal fractions in the selected data sample.

8.1 Exclusivity selection

In order to select exclusive $\gamma\gamma \to \ell^+\ell^-$ candidates, a veto on additional track activity at and near the dilepton vertex is applied. It relies both on a charged-particle track multiplicity requirement at the primary vertex, and on the isolation of this vertex from nearby pile-up induced vertices and/or tracks.

Specifically, the exclusivity veto require that no additional charged-particle tracks (as defined in Section 6.1) be associated with the dilepton vertex, and that no additional tracks or vertices be found within longitudinal distance $\Delta z = \pm 3$ mm of the dilepton vertex.

These conditions are required to reject of Drell–Yan (DY) background, the impact of which is evaluated after correcting for data-simulation differences in the reconstructed charged-particle multiplicity distribution (Section 8.1.1). The optimization of the vertex isolation requirement is discussed in Section 8.1.2, and the overall efficiency of the exclusivity cuts is analysed in Section 8.1.3. The results of the selection, illustrated by control distributions, are presented in Section 8.1.4.

8.1.1 Corrections to track multiplicity in Z/γ^* MC

Figure 8.1 shows the distribution of the number of additional charged-particle tracks associated with the dilepton vertex for both analysis channels. The exclusive $\gamma\gamma \to \ell^+\ell^-$ MC events are peaked at low-multiplicity region ($N_{\text{trk}} \simeq 0$), with additional smearing caused by the pile-up-induced tracks. One can also find that all other charged-particle track multiplicity regions are dominated by the $Z/\gamma^* \to \ell^+\ell^-$ processes. Due to the mis-modelling of this distribution by the Z/γ^* MC events, the specific reweighting procedure is applied.

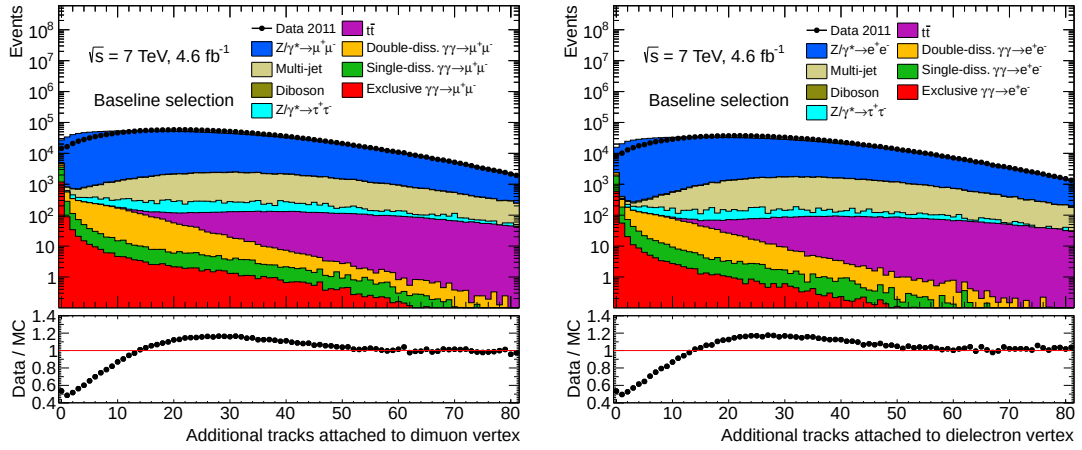

(a) (b)

FIGURE 8.1: Detector-level distribution of the number of charged-particle tracks for (a) $\mu^+\mu^-$and (b) e^+e^-analysis channels. Data (black dots) are compared to the MC simulations (histograms).

In order to find the relevant weight for Z/γ^* MC events, Z-peak region (70 GeV $< m_{\ell^+\ell^-} <$ 105 GeV) is used. This guarantees that the other sources of background are negligible comparing to the DY processes. Firstly, the reconstructed charged-particle multiplicity in data is unfolded to the particle-level. The correction procedure accounts for both on the effect of tracks originating from pile-up and ATLAS Inner Detector reconstruction inefficiency.

To correct the detector-level track multiplicity distribution for the presence of pile-up tracks, the same procedure is applied as in [10]. This procedure relies on the simple probabilistic approach for the pile-up track multiplicity description in the hard scattering vertex. One can express the probability to observe N tracks associated with this vertex as a sum of probability to have K reconstructed charged particles produced in the hard

process and $N - K$ pile-up tracks occasionally satisfying tracking selection cuts:

$$\mathscr{P}^{\text{reco}}(N) = \sum_{K=0}^{N} \mathscr{P}^{\text{PU}}(N-K)\mathscr{P}^{\text{hard}}(K) \ . \tag{8.1}$$

This problem can be inverted by constructing the relevant matrix:

$$\mathscr{P}^{\text{hard}}(N) = \sum_{K} U^{-1}_{NK}\mathscr{P}^{\text{reco}}(K) \ , \tag{8.2}$$

where $U_{NK} = \mathscr{P}^{\text{PU}}(N-K)$ for $N \geq K$ and 0 otherwise. The matrix U^{-1}_{NK} extracted from the Z/γ^* MC events is shown in Figure 8.2a.

The charged-particle multiplicity correction for track reconstruction inefficiency is taken care of in the Bayesian unfolding procedure, where the `RooUnfold` [58] package is used. Using the Z/γ^* MC events, the relevant response matrix is created. It is presented in Figure 8.2b. Then, the unfolding procedure with $k = 4$ number of iterations is applied for the multiplicity distribution already corrected for pile-up contamination. Charged-particle multiplicity distributions in Z-peak region before and after pile-up and track reconstruction inefficiency corrections are shown in Figure 8.3. The closure test performed on MC events shows a good agreement between the particle-level multiplicity distribution and the one obtained from simulated detector-level via pile-up removal and the correction for track reconstruction inefficiency.

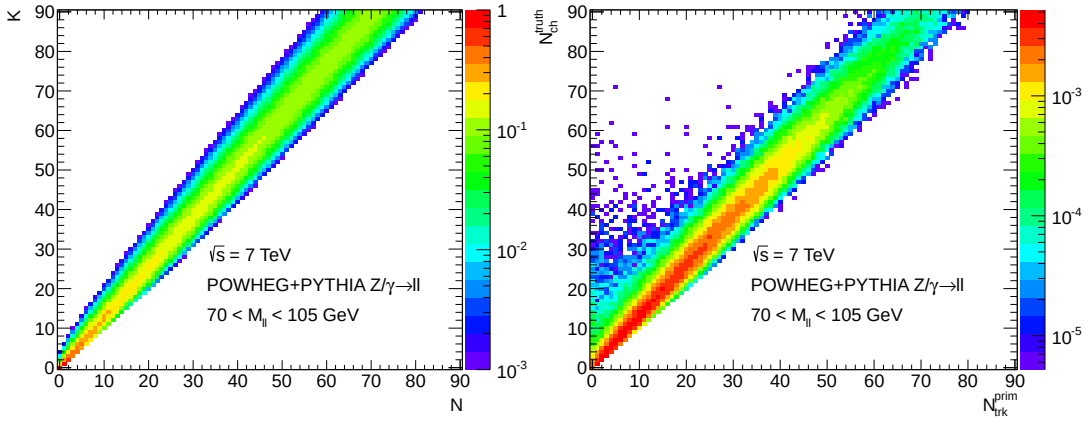

(a) (b)

FIGURE 8.2: (a) Matrix U^{-1}_{NK} constructed for pile-up unfolding procedure. (b) Response matrix for Bayesian unfolding for charged-particle track reconstruction inefficiency.

This procedure is repeated for data events in order to reweight the charged-particle multiplicity distribution in Z/γ^* MC events. A weight extracted from the corrected data distribution is shown in Figure 8.4. The reweighting procedure is validated on

both Z-peak region and invariant mass range with Z region removed. Detector-level distributions with corrected Z/γ^* MC events, including other background contributions are shown in Figure 8.5. Good agreement within $\pm 10\%$ is observed in the invariant mass range outside the Z-peak region. The small disagreement is caused by other background sources, especially QCD multi-jet events, with less precisely known underlying event topologies.

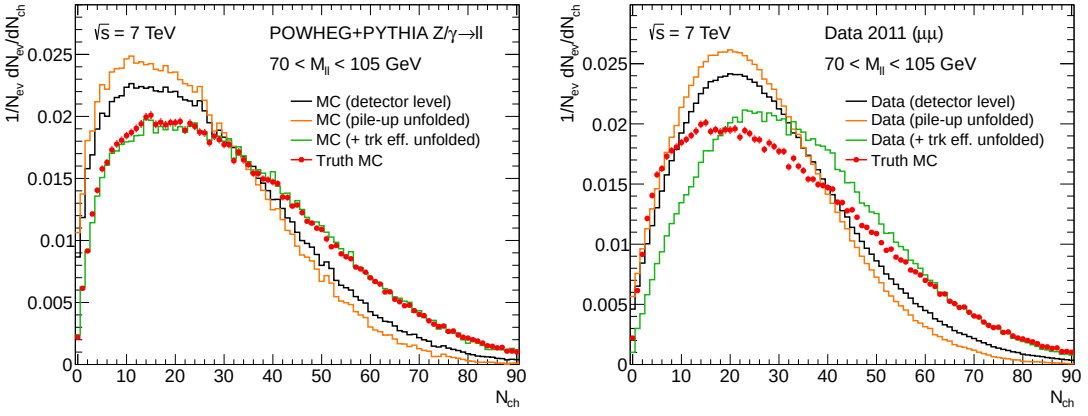

(a) (b)

FIGURE 8.3: (a) Z/γ^* MC distribution of the number of charged-particle tracks at the detector level, after pile-up removal and the track inefficiency correction to particle-level (solid lines), compared to the truth-level distribution (red markers). (b) Same but applied for data distribution (solid lines). For comparison, the truth-level distribution for Z/γ^* MC (red markers) is also shown - to be compared with the fully unfolded data (green line).

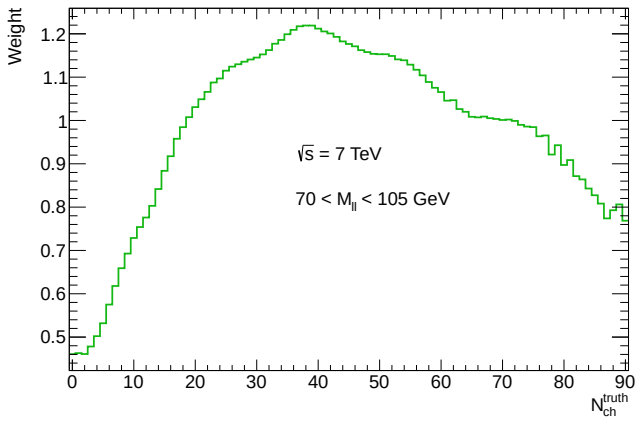

FIGURE 8.4: Weight applied for Z/γ^* MC events for charged-particle multiplicity correction. The weight is obtained by taking the ratio of unfolded data with truth-level distribution obtained from Z/γ^* MC events (See the Figure 8.3b)

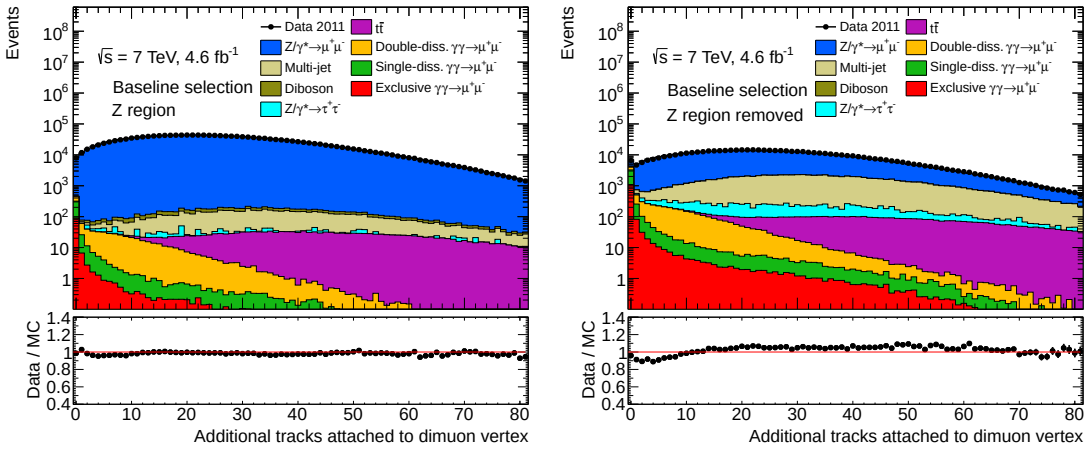

(a) (b)

FIGURE 8.5: Detector-level distributions of the number of charged-particle tracks after the charged-particle multiplicity reweighting procedure is applied to the DY MC events. (a) Z-peak region and (b) invariant mass range with Z region removed are shown. Data (black dots) are compared to the MC simulations (histograms).

8.1.2 Optimization of exclusivity veto region size

Standard tracking cuts defined in Section 6.1 ensure that there are no additional charged-particle tracks with a longitudinal distance $\Delta z \lesssim 1.5$ mm to the dilepton vertex. However, it is expected (for inclusive background events) that there might be some additional objects (tracks or vertices) at higher isolation distance values. Figure 8.6 shows the correlation between the dimuon vertex isolation distance and reconstructed charged-particle track multiplicity in the vertex with a closest distance to the dimuon vertex. Here the events with no additional tracks associated with the dimuon vertex are shown. In spite of the standard pile-up vertices pattern (isolation distance > 5 mm), a region with increased activity at low (< 5 mm) isolation distance values is present. This is due to the reconstruction of additional vertex built from the underlying event tracks in inclusive $Z/\gamma^* \to \ell^+\ell^-$ reactions.

This effect is fully reproduced by the MC simulation. Moreover, it is present only for the background-dominant inclusive DY events, where additional event activity in the dilepton vertex is expected. Dilepton vertex isolation distance distribution is shown in Figure 8.7. Indeed, the lower isolation distance region is dominated by the $Z/\gamma^* \to \ell^+\ell^-$ processes. In order to further remove this inclusive contribution, a cut on the vertex isolation distance is imposed. To maximize the sensitivity with respect to the exclusive $\gamma\gamma \to \ell^+\ell^-$ signal reactions, additional optimization studies are prepared. The idea relies on the maximization of signal significance in reference to the DY background

part. It is defined as:

$$significance = \frac{S}{\sqrt{S+B}} = \frac{N^{\text{excl.}}}{\sqrt{N^{\text{excl.}} + N^{\text{s-diss.}} + N^{\text{d-diss.}} + N^{\text{DY}}}} , \tag{8.3}$$

where $N^{\text{excl.}}$, N^{DY} denote the number of exclusive signal and Drell–Yan events, and $N^{\text{s-diss.}}$, $N^{\text{d-diss.}}$ number of single- and double-dissociative events accordingly.

Figure 8.8 presents the signal significance as a function of minimum dilepton vertex isolation distance requirement. Both $\mu^+\mu^-$ and e^+e^- distributions peak at $\Delta z \simeq 3$ mm and this value of cut is chosen for both analysis channels. One can also notice a lower averaged significance values for electrons. This is due to the lower statistics of data available in this channel. It is related with higher electron trigger thresholds in 2011 data in comparison with the muons.

The single- and double-dissociative $\gamma\gamma \to \ell^+\ell^-$ background contributions are irreducible using the vertex isolation distance cut. This is because the forward-particle states from proton dissociation are usually created in this reactions, which are produced outside the kinematic acceptance of the ATLAS Inner Detector. Therefore, the event topology for single- and double-dissociative backgrounds is very often similar to the exclusive signal process (no additional tracks attached to the dilepton vertex).

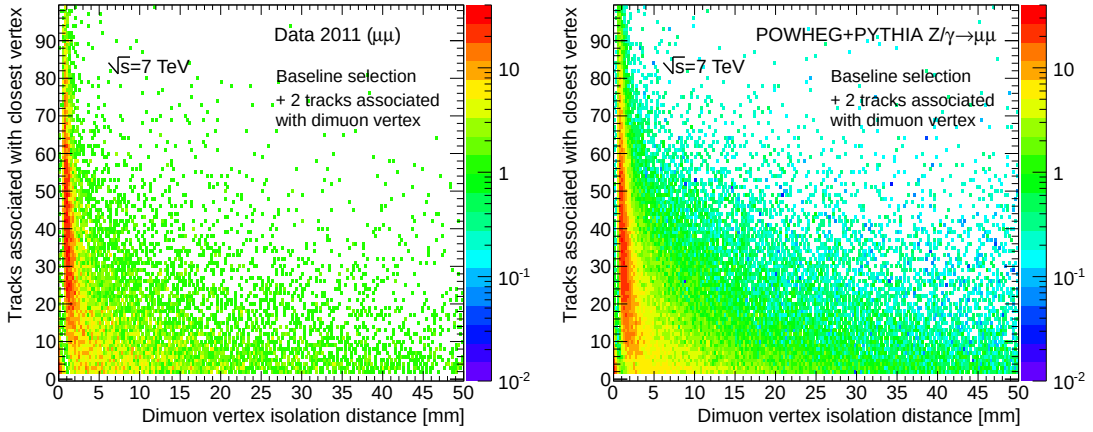

(a) (b)

FIGURE 8.6: Correlation between the isolation distance of the dimuon vertex and the number of charged-particle tracks associated with the secondary vertex that is closest to the dimuon vertex. (a) Data and (b) $Z/\gamma^* \to \mu^+\mu^-$ MC distributions are shown for events with no additional tracks attached to the dimuon vertex.

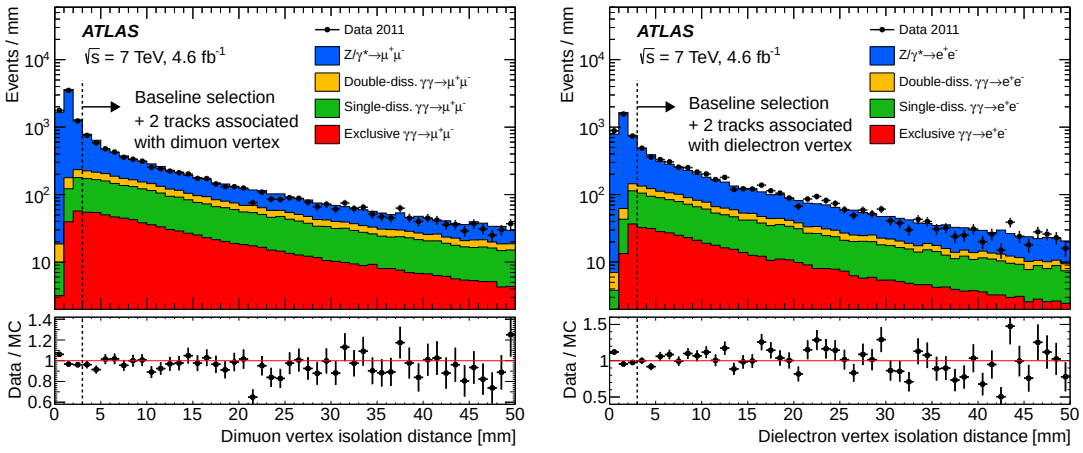

(a) (b)

FIGURE 8.7: Dilepton vertex isolation distance distribution for (a) muon and (b) electron channels for events with no additional tracks associated with the dilepton vertex.

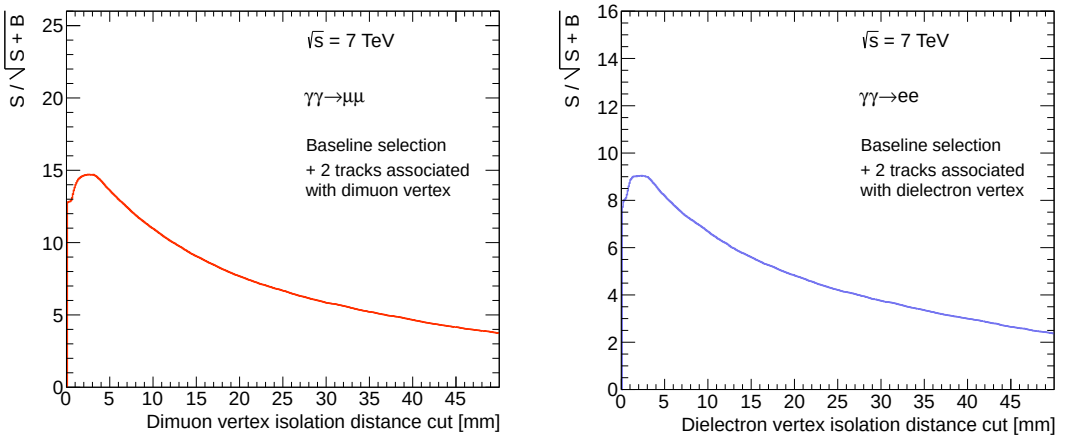

(a) (b)

FIGURE 8.8: Exclusive signal significance as a function of the dilepton vertex isolation distance cut for (a) $\mu^+\mu^-$and (b) e^+e^-analysis channels. Events with no additional tracks attached to the dilepton vertex and outside the Z region (i.e. 70 GeV $< m_{\ell^+\ell^-} <$ 105 GeV) are considered.

8.1.3 Exclusivity veto efficiency

Figure 8.9 shows the signal selection efficiency for the exclusivity veto defined in Section 8.1 (no additional tracks or vertices within $\Delta z = 3$ mm of the dilepton vertex), as a function of average number of interactions per bunch crossing. For both electrons and muons, the averaged efficiency is 74%, where it can reach 90% for $\langle\mu\rangle = 3$ and is above 60% for $\langle\mu\rangle = 16$, which is almost the highest value of number of interactions per bunch crossing in 2011 pp collisions.

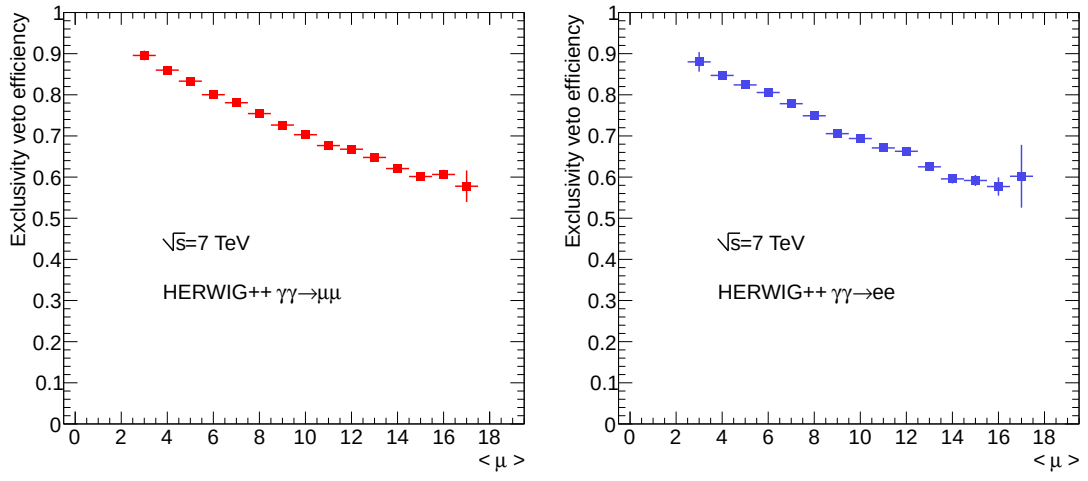

(a) (b)

FIGURE 8.9: Exclusivity veto efficiency for signal MC events as a function of average interactions per bunch crossing for (a) $\mu^+\mu^-$ and (b) e^+e^- analysis channels.

8.1.4 Exclusive selection results and control distributions

After exclusivity veto, 7940 events for $\mu^+\mu^-$ channel and 5410 events for e^+e^- channel are selected from data. Figures 8.10 and 8.11 present the control distributions for events after the veto in muon and electron channels, respectively. Good agreement between the data and MC simulation of various kinematic distributions is observed, both in the Z-peak region (70 GeV $< m_{\ell^+\ell^-} <$ 105 GeV) and outside of this region. Also, the Z region provides a cross-check of the residual inclusive DY contamination in the further event selection process. Some small disagreement observed in the electron channel can be covered by the systematic uncertainties. Here the uncertainties do not include NNPDF2.3QED PDFs uncertainty in double-dissociative part, simulated by PYTHIA 8. Moreover, the relevant structure functions uncertainty for single-dissociative reactions using LPAIR are not available, where they will further increase the total size of the systematic uncertainty related with the background modelling.

8.2 Exclusive cross section extraction

In order to suppress further the proton-dissociative and DY backgrounds, additional set of kinematic cuts should be imposed. At the same time, they enhance the relative contribution from exclusive (elastic) signal processes.

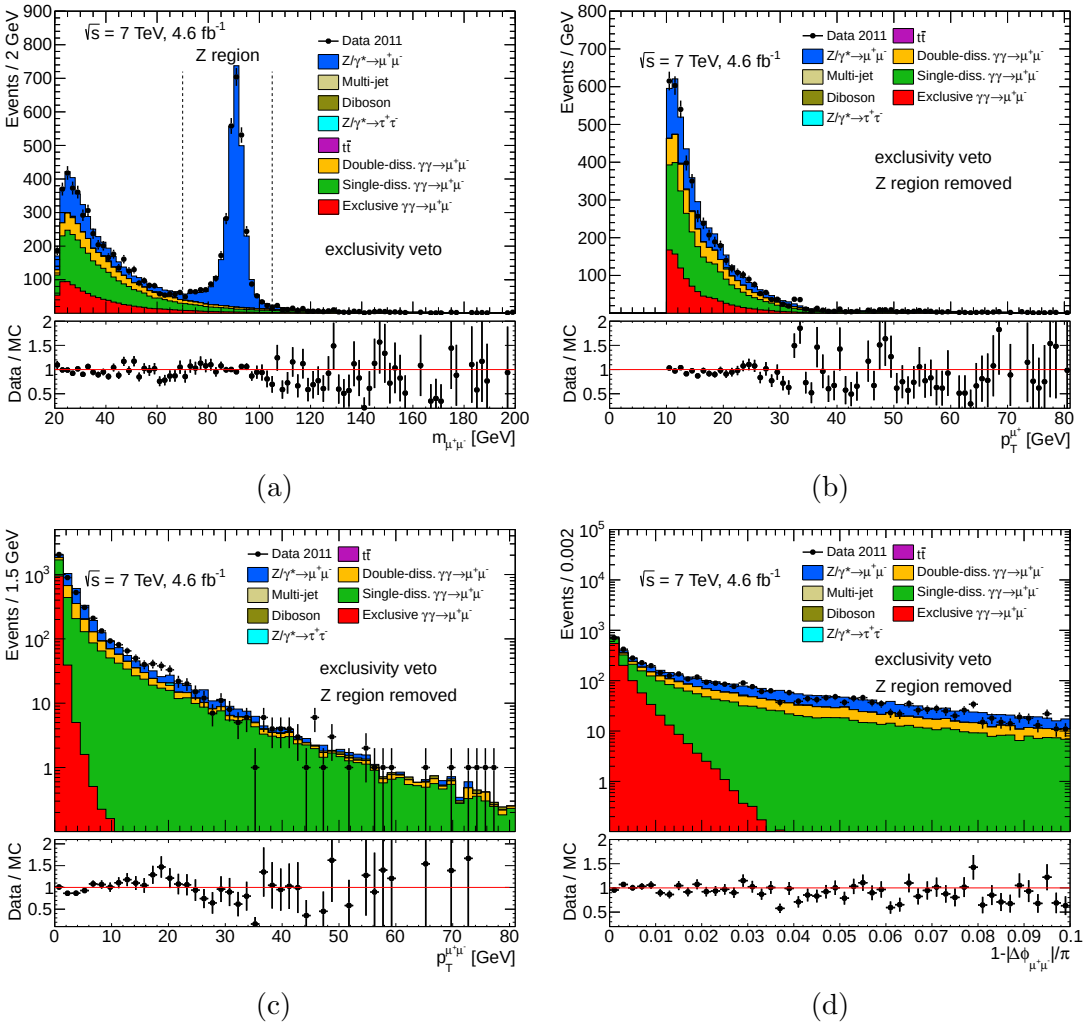

FIGURE 8.10: Control distributions for events passing the exclusivity veto in the muon channel. (a) Dilepton invariant mass, (b) transverse momentum of the positively charged muon, (c) dimuon transverse momentum and (d) dimuon acoplanarity distributions are presented. Exclusive and single-dissociative event yields are extracted in the region $p_{\mathrm{T}}^{\ell^+\ell^-} < 1.5$ GeV, as discussed in Section 8.2.2.

8.2.1 Elastic selection

Because of the very low photon virtualities in exclusive $\gamma\gamma \to \ell^+\ell^-$ reactions, the outgoing signal leptons are produced back-to-back in the transverse plane. Therefore, the selected lepton pairs are required to be balanced in their transverse momentum.

As a default option, requirement on the transverse momentum of the dilepton system is chosen. The value of $p_{\mathrm{T}}^{\ell^+\ell^-} < 1.5$ GeV is found to be sufficient to further reduce the background and almost not reduce the signal process. The distribution of invariant mass of the leptons after this requirement is shown in Figure 8.12. Clearly, the contribution from the $Z/\gamma^* \to \ell^+\ell^-$ and proton-dissociative processes is suppressed. However, the

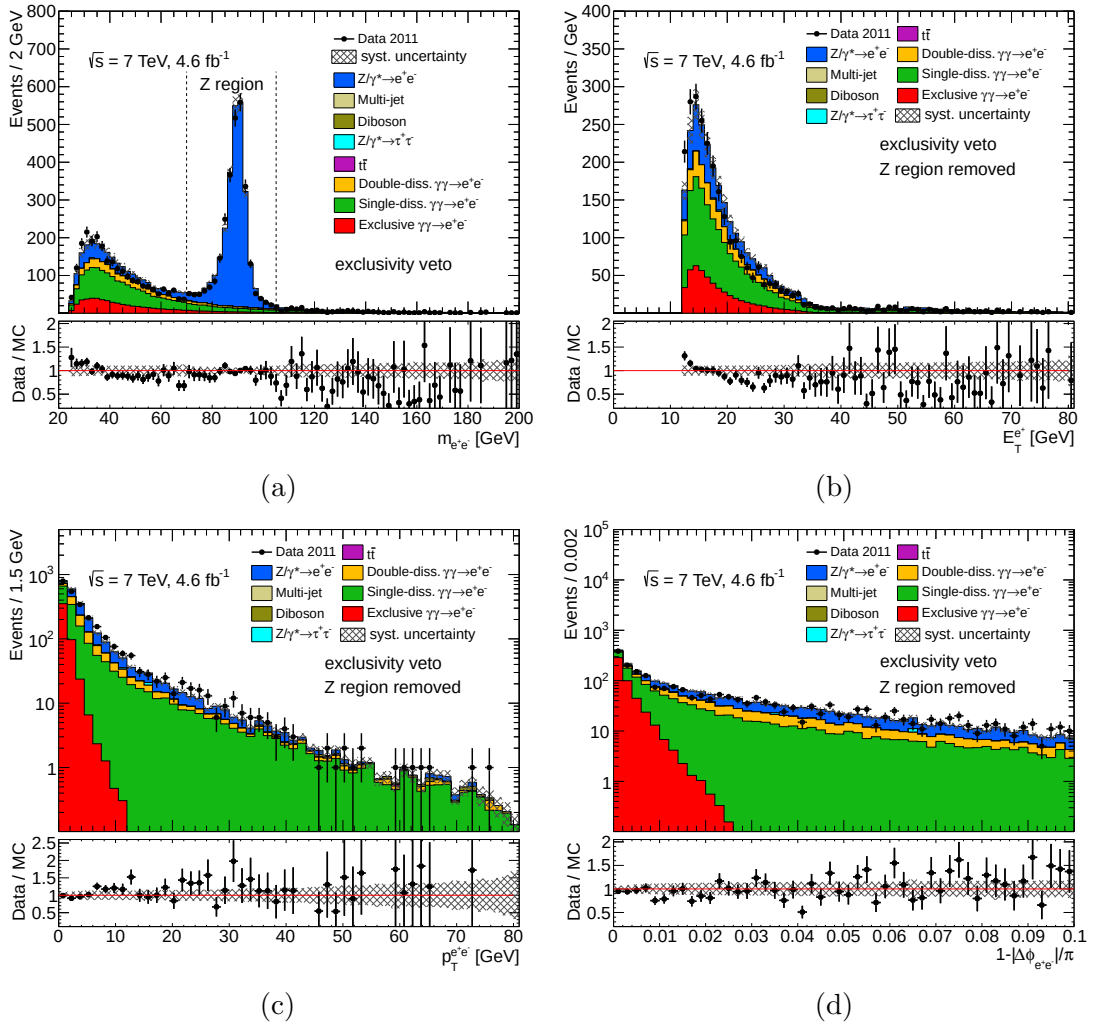

FIGURE 8.11: Control distributions for events passing the exclusivity veto in the electron channel. (a) Dielectron invariant mass, (b) transverse energy of the positively charged electron, (c) dielectron transverse momentum and (d) dielectron acoplanarity distributions are presented. Systematic uncertainties are shown as a shaded area. Exclusive and single-dissociative event yields are extracted in the region $p_{\mathrm{T}}^{\ell^+\ell^-} < 1.5$ GeV, as discussed in Section 8.2.2.

70 GeV $< m_{\ell^+\ell^-} <$ 105 GeV region is still dominated by the Z boson production. As a consequence, this region is excluded in the subsequent exclusive cross section extraction procedure.

Tables 8.1 and 8.2 present the effect of each step of the selection on the data and simulated signal and background samples for muon and electron channels, respectively.

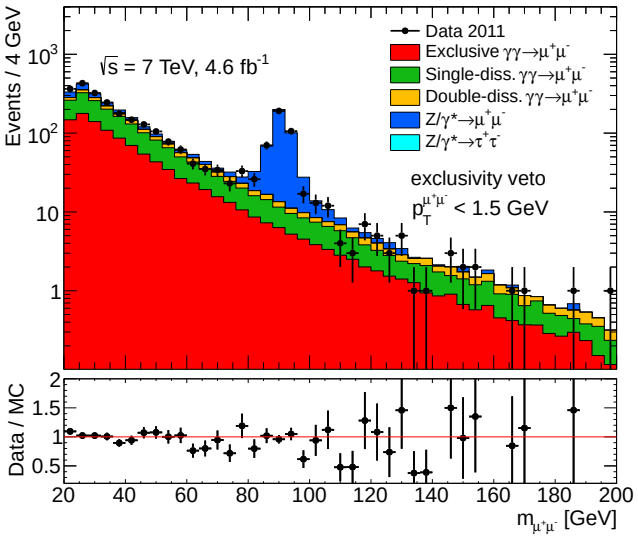

(a)

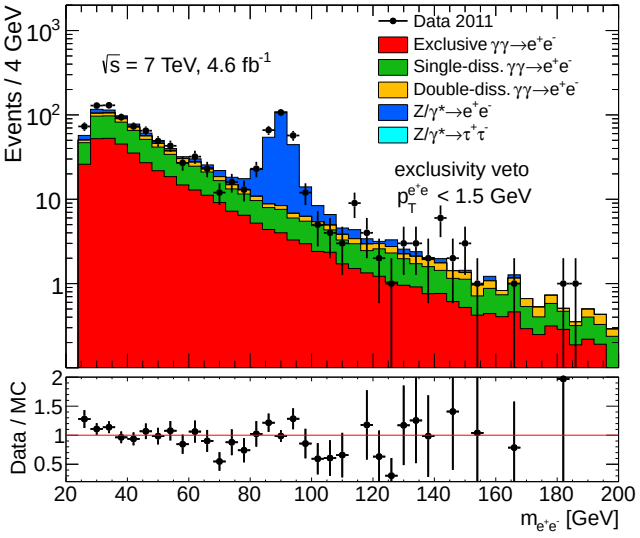

(b)

FIGURE 8.12: Distribution of the invariant mass of lepton pairs for events after exclusivity veto and elastic selection for (a) $\mu^+\mu^-$ and (b) e^+e^- analysis channels. Exclusive and single-dissociative event yields are extracted using fit procedure, as discussed in Section 8.2.2.

Selection	Data	Signal	S-diss.	D-diss.	$Z/\gamma^* \to \mu^+\mu^-$	$Z/\gamma^* \to \tau^+\tau^-$	Multi-jet	$t\bar{t}$	Diboson	MC Total
Initial preselection	2 422 745	1774	3964	4394	2 298 767	7606	97 727	6708	2870	2 423 810
3 mm exclusivity veto	7940	1313	2892	861	3960	8	1	0	6	9041
Z region removed	4729	1215	2618	757	1157	8	1	0	3	5759
$p_{\mathrm{T}}^{\mu^+\mu^-} < 1.5$ GeV	2124	1174	1085	160	211	3	0	0	0	2633
$1 - \left\lvert\Delta\phi_{\mu^+\mu^-}\right\rvert/\pi < 0.008$	1377	1064	499	59	73	3	0	0	0	1698

TABLE 8.1: Effect of sequential selection requirements on the number of events selected in data, compared to the number of expected signal and background events for muon channel. The multi-jet background is estimated using data-driven methods, whereas the other contributions are obtained from MC simulations. As an illustration, on the top of the elastic selection, the acoplanarity cut is used to further enrich the sample in elastic events.

Selection	Data	Signal	S-diss.	D-diss.	$Z/\gamma^* \to e^+e^-$	$Z/\gamma^* \to \tau^+\tau^-$	Multi-jet	$t\bar{t}$	Diboson	MC Total
Initial preselection	1 572 271	898	2096	2072	1 460 867	3758	83 183	4612	1945	1 559 431
3 mm exclusivity veto	5410	661	1480	475	3142	9	0	0	5	5772
Z region removed	2586	569	1276	379	601	8	0	0	3	2836
$p_{\mathrm{T}}^{\mathrm{e}^+\mathrm{e}^-} < 1.5$ GeV	869	438	414	75	103	2	0	0	0	1032
$1 - \lvert\Delta\phi_{\mathrm{e}^+\mathrm{e}^-}\rvert/\pi < 0.008$	596	414	221	30	36	2	0	0	0	703

TABLE 8.2: Effect of sequential selection requirements on the number of events selected in data, compared to the number of expected signal and background events for electron channel. The multi-jet background is estimated using data-driven methods, whereas the other contributions are obtained from MC simulations. As an illustration, on the top of the elastic selection, the acoplanarity cut is used to further enrich the sample in elastic events.

8.2.2 Maximum likelihood fit

After all selection criteria are applied, 2124 events remain for the muon channel, and 869 events are selected in the electron channel. From simulations, approximately half are expected to originate from exclusive production. The number of selected events in the data is below the expectation from the simulation, with an observed yield that is approximately 80% of the sum of simulated signal and background processes (see the Tables 8.1 and 8.2). This suppression is interpreted as due to proton absorptive effects, in which strong interactions between the protons can produce additional hadronic activity. These effects are not included in the MC generators used to model exclusive and single-dissociative processes, hence more MC events than expected pass the exclusivity veto and elastic selection requirements.

The exclusive $\gamma\gamma \to \ell^+\ell^-$ contribution is extracted from the data by performing a binned maximum-likelihood fit to the dilepton acoplanarity distribution for events passing the exclusivity veto and elastic selection. Templates obtained using MC events are used to model the exclusive signal, DY, single- and double-dissociative processes.

The fit includes two free parameters: the scale factors for exclusive ($f^{\text{excl.}}$) and single-dissociative ($f^{\text{s-diss.}}$) event yields. The double-dissociative and DY contributions are fixed in the fit procedure. Small contributions from other background processes ($Z/\gamma^* \to \tau^+\tau^-$, $\gamma\gamma \to \tau^+\tau^-$, $\gamma\gamma \to W^+W^-$) are neglected. The statistical asymmetric uncertainties for the yields are computed with `Minos` [59].

Muon channel. Figure 8.13 presents the best-fit to the data dimuon acoplanarity distribution. The individual signal and background yields from the fit are summarized in Table 8.3. The ratios of data to MC predictions (scale factors) for exclusive and single-dissociative contributions are also shown. This scale factor corresponds to the survival factor defined in Section 2.2.3 that quantifies the effect of proton absorptive suppression. Its deviation from unity can be interpreted as a direct consequence of the proton finite-size effects that impact photon–photon interactions in pp collisions. For the exclusive process, it is measured to be $f^{\text{excl.}}_{\gamma\gamma\to\mu^+\mu^-} = 0.791^{+0.041}_{-0.040}(\text{stat.})$, in good agreement with value of 0.801 calculated using phenomenological model described in Section 2.2.3. A comparable value, within the uncertainties, is obtained for the single-dissociative processes. Finally, a 68% and 95% confidence level (CL) contours in the ($f^{\text{excl.}} - f^{\text{s-diss.}}$) fit variable space are displayed in Figure 8.14.

Electron channel. The best-fit to the data dilepton acoplanarity distribution for electron channel is shown in Figure 8.15. Table 8.4 summarizes the individual signal

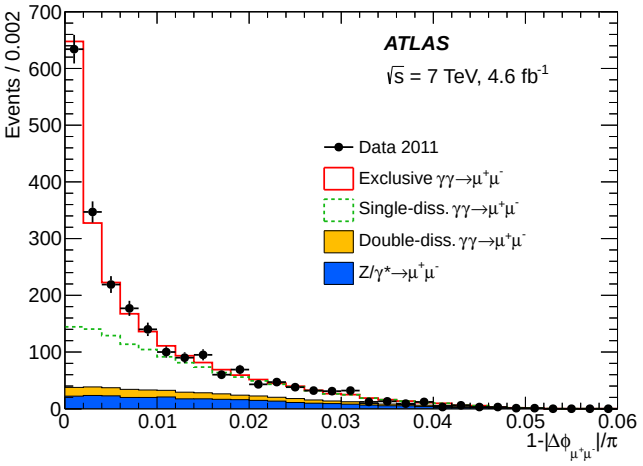

FIGURE 8.13: Dimuon acoplanarity distribution for the sample after full event selection. Data are shown as points with statistical error bars. The stacked histograms, in top-to-bottom order, represent the simulated exclusive signal, and the single-dissociative, double-dissociative and DY backgrounds. The exclusive and single-dissociative yields are determined from the fit described in the text.

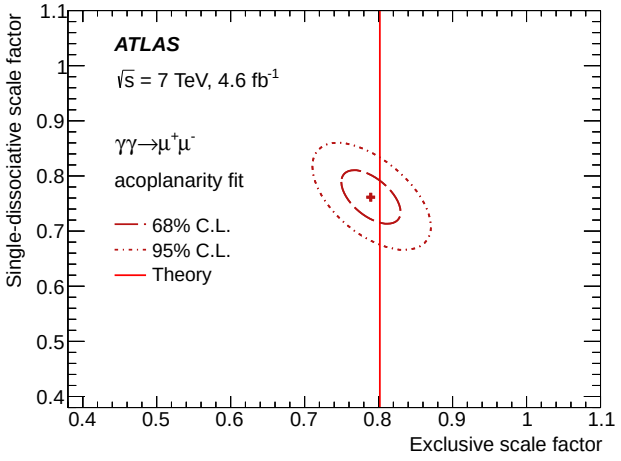

FIGURE 8.14: 68% and 95% confidence level (CL) contour plots for the signal vs. single-dissociative yield scale factors in the fitted parameter plane for the muon channel. The contours represent the statistical uncertainties on the measurement and the points indicate the best-fit values. Prediction for survival factor (proton absorptive correction) is also shown (red solid line).

$\text{Data/MC}_{\text{excl.}}$	$\text{Data/MC}_{\text{s-diss.}}$	$\text{Yield}_{\text{excl.}}$	$\text{Yield}_{\text{s-diss.}}$	$\text{Yield}_{\text{d-diss.}}$	Yield_{DY}
$0.791^{+0.041}_{-0.040}$	$0.762^{+0.049}_{-0.048}$	927 ± 47	826 ± 53	160	211

TABLE 8.3: Binned maximum-likelihood fit results for the muon channel.

$\text{Data/MC}_{\text{excl.}}$	$\text{Data/MC}_{\text{s-diss.}}$	$\text{Yield}_{\text{excl.}}$	$\text{Yield}_{\text{s-diss.}}$	$\text{Yield}_{\text{d-diss.}}$	Yield_{DY}
$0.863^{+0.070}_{-0.069}$	$0.759^{+0.080}_{-0.078}$	378 ± 31	314 ± 32	75	103

TABLE 8.4: Binned maximum-likelihood fit results for the electron channel.

and background yields from the fit, together with the scale factors to MC predictions for exclusive and single-dissociative contributions. Here again, the scaling factor for the exclusive signal yield, $f^{\text{excl.}}_{\gamma\gamma\to e^+e^-} = 0.863^{+0.070}_{-0.069}(\text{stat.})$, is found to be in a good agreement with the the predicted value of 0.798, using calculations from Section 2.2.3. Figure 8.16 presents 68% and 95% CL contours in the fit variable space for the electron channel.

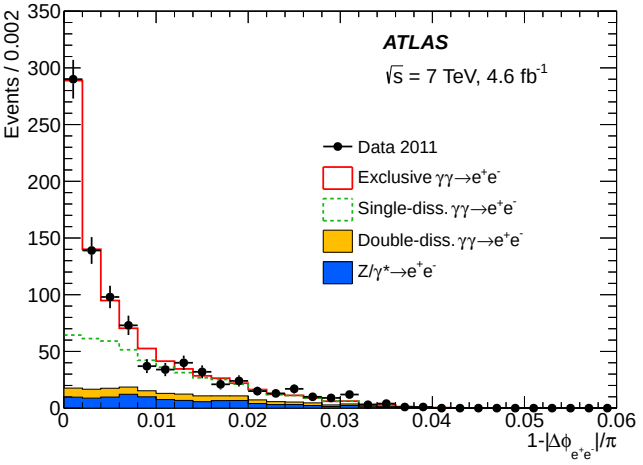

FIGURE 8.15: Dielectron acoplanarity distribution for the sample after full event selection. Data are shown as points with statistical error bars. The stacked histograms, in top-to-bottom order, represent the simulated exclusive signal, and the single-dissociative, double-dissociative and DY backgrounds. The exclusive and single-dissociative yields are determined from the fit described in the text.

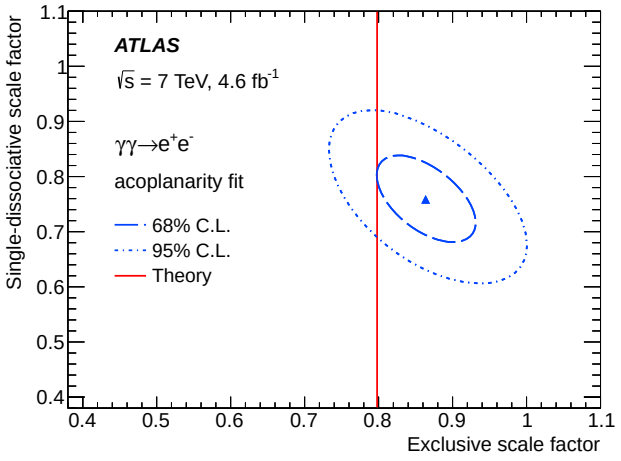

FIGURE 8.16: 68% and 95% CL contour plots for the signal vs. single-dissociative yield scale factors in the fitted parameter plane for the electron channel. The contours represent the statistical uncertainties on the measurement and the points indicate the best-fit values. Prediction for survival factor (proton absorptive correction) is also shown (red solid line).

Chapter 9

Systematic uncertainties and cross-checks

This chapter describes the procedure of estimating the statistical and systematic uncertainties associated with the analysis of exclusive $\gamma\gamma \to \ell^+\ell^-$ production. It is very important to estimate any possible systematic uncertainties which are those arising, for example, from the limited knowledge of the reconstructed physics objects, or the precision of the background processes control. The overall systematic uncertainty is obtained by adding in quadrature uncertainties from different sources.

9.1 Muon-related systematic uncertainties

The systematic uncertainties attributed to the muons originate from different sources: muon reconstruction efficiency, momentum scale and smearing, and muon trigger efficiency. The contributions are quantified by varying each systematic effect within its associated uncertainty and observing the fractional change in the number of events passing the signal extraction procedure.

Muon reconstruction efficiency. The uncertainty due to the muon reconstruction efficiency stems from the finite precision to which the MC scale factors for the muon reconstruction are determined [11]. The impact on the analysis is evaluated by varying scale factors within their uncertainties. The uncertainties are taken from the official ATHENA tool. A description of the calculation of this uncertainty can be found in [60]. The varied scale factors are applied to the analysis resulting in an altered signal yield.

Muon momentum scale and resolution. The determination of the p_{T} of the muon is affected by both the momentum scale and resolution uncertainties. In order to evaluate

Source	Value
Muon reconstruction efficiency	0.2%
Muon kinematics	0.5%
Muon trigger efficiency	0.6%

TABLE 9.1: Summary of the muon-related systematic uncertainties on the expected exclusive event yields.

the resolution uncertainty, the transverse momentum of the muon is varied through a dedicated tool, which is based on the measurements from [11].

Muon trigger efficiency. The systematic uncertainty on the efficiency of single- and dimuon triggers is calculated using the official tool, prepared based on the studies from [11, 55]. Variations of the trigger efficiency are applied on an event-by-event basis and propagated trough the full analysis chain up to the normalized cross section using exclusive $\gamma\gamma \to \mu^+\mu^-$ MC events.

Table 9.1 summarizes the muon-related systematic uncertainties. The overall contribution of these uncertainties on the exclusive cross section measurement is 0.8%.

9.2 Electron-related systematic uncertainties

The contribution of the systematic effects related with the electron reconstruction modelling is also determined. This contribution is evaluated by taking into account the uncertainties associated with the electron reconstruction and identification efficiency, energy scale and smearing, and electron trigger efficiency. The systematic uncertainties on the expected signal event yields are estimated as follows.

Electron reconstruction and identification efficiency. The differences observed in the reconstruction and identification efficiencies between the data and MC simulation are taken into account by weighting the simulation by the relevant scale factors [14]. The systematic uncertainty is then determined by varying the scale factors within their quoted uncertainties. The uncertainties on the scale factors are added in quadrature to obtain the combined electron reconstruction and identification uncertainty.

Electron energy scale and resolution. The uncertainty associated to the electron energy scale is obtained using the official tool that is based on [57]. A $\pm 1\sigma$ variations of the electron energy scale are applied on an event-by-event basis and propagated through the full analysis chain. The uncertainty associated to the description of the electron energy resolution by the MC simulation is calculated in a similar way.

Source	Value
Electron reconstruction and identification efficiency	1.9%
Electron scale	1.0%
Electron smearing	0.9%
Electron trigger efficiency	0.7%

TABLE 9.2: Summary of systematic uncertainties on the expected exclusive event yields related with electrons.

Electron trigger efficiency. The systematic uncertainty on the efficiency of single- and dielectron triggers is calculated using the official tool that is built on results from [14]. Correlated variations of $\pm 1\sigma$ of the trigger efficiency are applied on an event-by-event basis and propagated through the full analysis chain up to the exclusive cross section calculation using signal MC events.

Table 9.2 summarizes the electron-related systematic uncertainties. An overall contribution of these uncertainties to the exclusive cross section measurement is below 3%.

9.3 Pile-up description

A possible systematic effect due to the pile-up description in MC events is studied by comparing the p_{T}- and η-dependent distribution of charged-particle tracks originating from pile-up, measured at sufficiently large distances from the dilepton vertex. The same technique as in [10] is used. The tracks are selected as described in Section 6.1, with the only exclusion that instead of the standard impact parameter cuts, tracks are required to have $d_0^{\mathrm{BS}} < 1.5$ mm and $|z_0^{\mathrm{trk}} - z_{\mathrm{vtx}}^{\ell\ell}| > 20$ mm. The first requirement selects tracks of charged particles produced in interactions on the beam spot (BS), and the second one suppresses the contribution of particles produced in the hard process. A comparison of $d^2N_{\mathrm{trk}}/\mathrm{d}\eta\ \mathrm{d}p_{\mathrm{T}}$ distributions between the data and MC for pile-up tracks is shown in Figure 9.1. Good data-to-simulation agreement (below 5%) is observed for charged-particle tracks with $p_{\mathrm{T}} < 1$ GeV. For $p_{\mathrm{T}} > 1$ GeV, $|\eta| < 2.3$ MC simulation underestimates the spectrum by ≈10%, whereas for $p_{\mathrm{T}} > 1$ GeV, $2.3 < |\eta| < 2.5$ a disagreement is reaching 20%.

The same effect is observed for the integrated pile-up track density distribution. Figure 9.2 shows pile-up track multiplicity in the vertex with closest distance to the dimuon vertex. A distribution in MC simulation is slightly shifted comparing to data, which results in the underestimation of mean pile-up track density per event. Pile-up description in MC is affected by the systematic uncertainty related with the track reconstruction inefficiency, originating mainly from uncertainties in detector material description in MC simulations. This was estimated in [61] to be from 2% for charged particles with

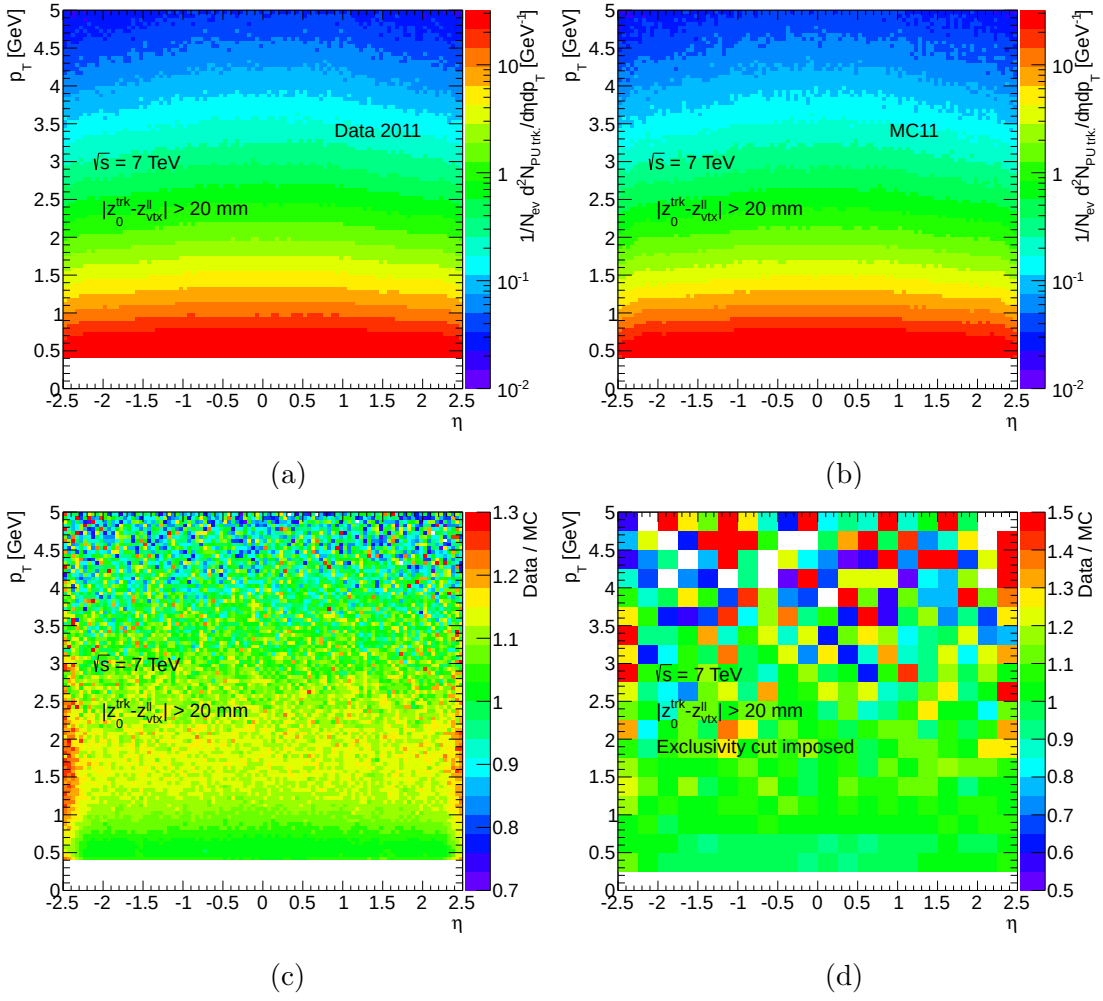

FIGURE 9.1: Comparison of reconstructed charged-particle track density originating from pile-up, $\mathrm{d}^2N_{\mathrm{trk}}/\mathrm{d}\eta\ \mathrm{d}p_{\mathrm{T}}$, between the (a) data and (b) MC simulations for events satisfying preselection criteria. The ratio of (a) and (b) distributions is shown in (c). The ratio of similar distributions for events after exclusive selection is shown in (d).

$0.5 < p_{\mathrm{T}} < 10$ GeV, $|\eta| < 2.3$ to 7% at $0.5 < p_{\mathrm{T}} < 10$ GeV, $|2.3 < \eta| < 2.5$ and 10% at $p_{\mathrm{T}} > 10$ GeV. These numbers are consistent with the differences observed between the data and MC simulations.

To estimate the effect of this uncertainty on the final results, the loss of the efficiency is simulated by randomly removing (or adding) from 2% to 20% of reconstructed pile-up tracks in the signal MC sample. This results in a maximum of 0.5% change of the exclusive signal yield values in both channels, which is taken as a systematic uncertainty.

As discussed in Section 7.3, MC events are corrected using the pile-up reweighting procedure, in order to reproduce the average number of interactions per bunch crossing, $\langle\mu\rangle$, observed in data. A good agreement between the data and MC simulation for $\langle\mu\rangle$ distributions is observed, but not for the number of reconstructed vertices in the

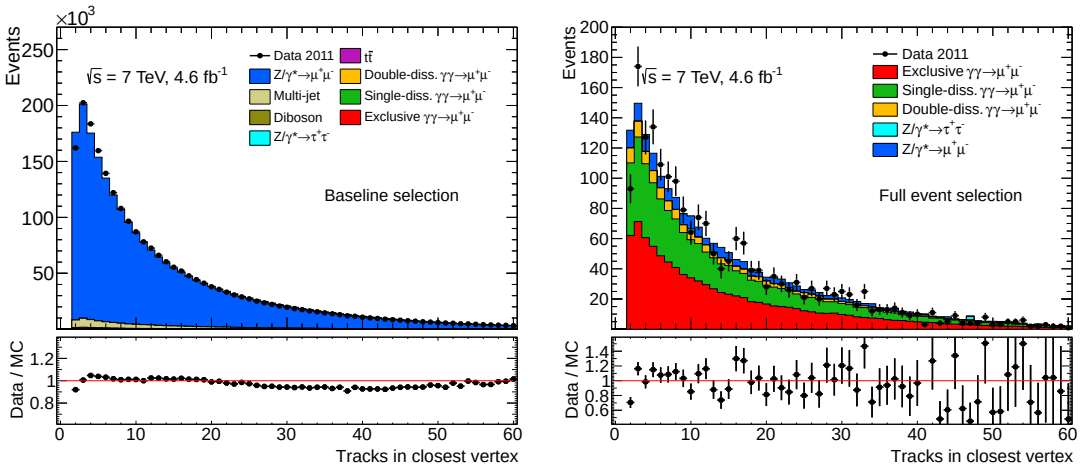

(a) (b)

FIGURE 9.2: Reconstructed charged-particle track multiplicity associated with the vertex with closest distance to the dimuon vertex for events (a) after preselection, and (b) after full event selection.

high vertex-multiplicity region. In order to estimate the systematic uncertainty from the pile-up reweighting, on top of the event selection, the reweighting that use the number of reconstructed vertices is applied. The ratio between the data and MC simulation in the number of reconstructed vertices is used as an additional weight for the signal MC events. The difference in the exclusive cross section with and without applying the additional vertex weight is below 0.1% for both analysis channels. Therefore, this effect is considered negligible.

As an additional check, events with exactly one additional track attached to the dilepton vertex are used to extract the exclusive event scale factor. Since this region is dominated by the Drell–Yan (DY) events, $p_{\mathrm{T}}^{\ell^+\ell^-} < 1$ GeV cut is imposed and the Z region (70 GeV $< m_{\ell^+\ell^-} <$ 105 GeV) is removed. Figure 9.3 presents the transverse and longitudinal impact parameter distributions for muon channel after these selection criteria are applied. One can observe that the exclusive events contribute with a track that has uniformly distributed z_0 component. This component reflects the random association of a pile-up track to the purely exclusive dilepton vertex. On the other hand, track from the Z/γ^* event originates essentially from the hard interaction vertex, which creates a peaked structure. Therefore, the DY events can be further suppressed requiring $|z_0 \sin\theta| > 0.5$ for the additional track.

With the tightened event selection described in the preceding paragraph, exclusive event yield is extracted by performing a binned log-likelihood fit to the dilepton acoplanarity distribution. Best-fit distributions are shown in Figure 9.4. The extracted exclusive signal scale factors, $f^{\mathrm{excl.}}_{\gamma\gamma\to\mu^+\mu^-} = 0.832^{+0.192}_{-0.184}(\mathrm{stat.})$ and $f^{\mathrm{excl.}}_{\gamma\gamma\to\mathrm{e}^+\mathrm{e}^-} = 0.852^{+0.275}_{-0.301}(\mathrm{stat.})$,

are in a good agreement with the values obtained when using events passing the default event selection requirements.

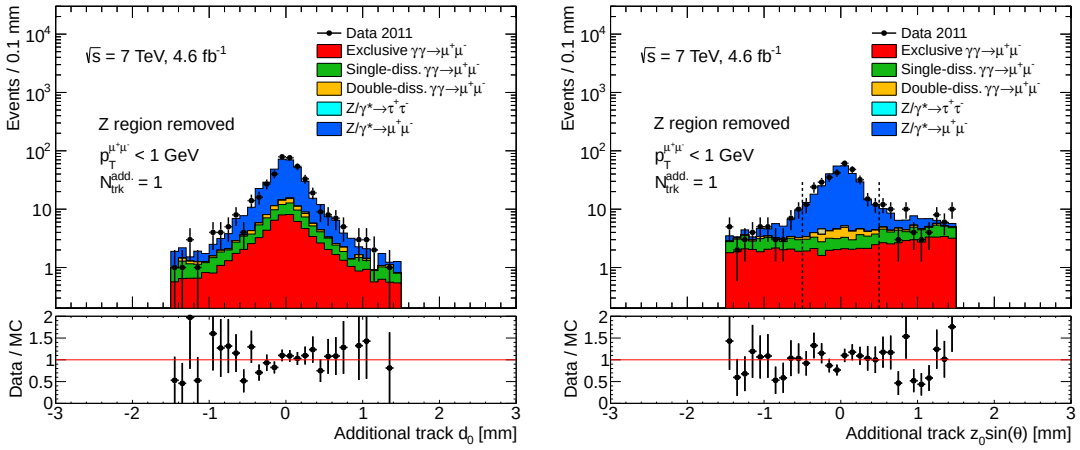

(a) (b)

FIGURE 9.3: (a) Transverse and (b) longitudinal impact parameter distributions for additional reconstructed charged-particle track associated with the dimuon vertex. Events with exactly one additional reconstructed track are considered. To enhance the relative signal contribution, $p_T^{\ell^+\ell^-} < 1$ GeV cut is imposed with Z region being removed.

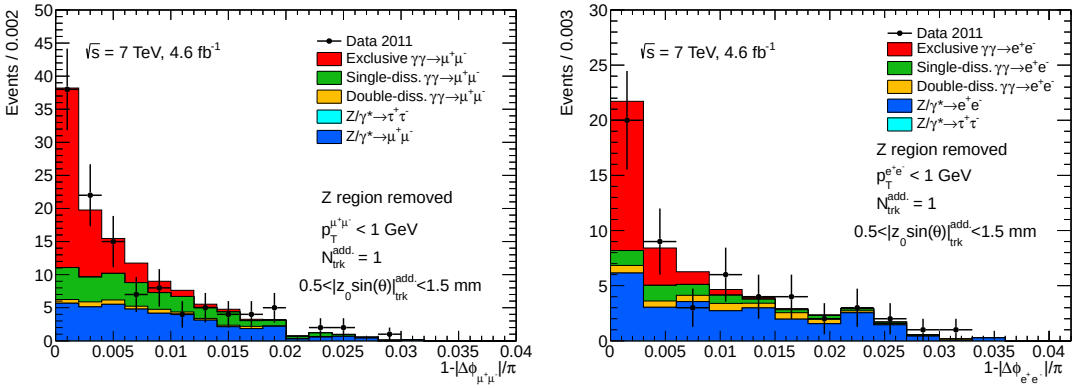

(a) (b)

FIGURE 9.4: Best-fit acoplanatrity distribution for events with exactly one additional track associated with the dilepton vertex for (a) muon and (b) electron channels. Cuts imposed to reduce the DY contamination are detailed in the text.

9.4 Exclusivity veto efficiency

The 3 mm exclusivity veto efficiency (described in Section 8.1.3) as a function of pile-up intensity can be extracted directly from data and compared with MC simulations. This can be done by analysing relevant distribution shapes (like $\langle\mu\rangle$, e.g. in Figure 7.2a) before and after exclusivity veto is applied. This is presented in Figure 9.5. Each distribution

is normalized to the respective total number of events. It is expected that the presence of additional pile-up tracks will decrease the exclusivity veto efficiency. The effect is strongest for high pile-up intensities, thus changing the initial $\langle\mu\rangle$ distribution shape.

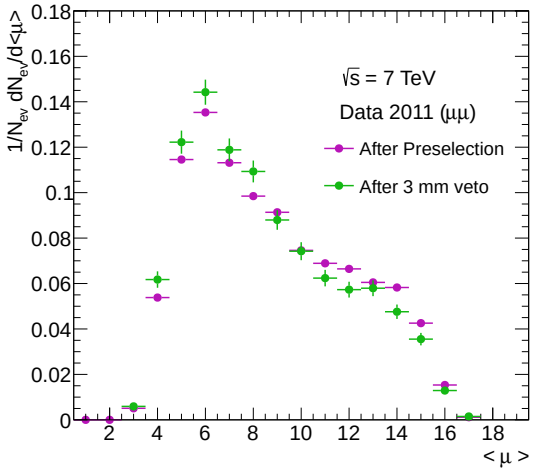

FIGURE 9.5: Average number of interactions per bunch crossing in data (muon channel) for events before and after 3 mm exclusivity veto is applied. Each distribution is normalized to the respective total number of events.

Taking the ratios of data distributions shown in Figure 9.5, it is possible to recover the shape of the exclusivity veto efficiency distribution as a function of pile-up intensity. A missing normalization factor can be also extracted from data. Information about the density of pile-up tracks at a random point z_i with the minimum distance $|z_i - z_{\text{vtx}}^{\ell^+\ell^-}| >$ 20 mm from the dilepton vertex is used. This requirement suppresses the contribution of charged particles produced in the hard process and only pile-up tracks are counted. The normalization factor is given by the probability to have no tracks (or vertices) within 3 mm from the point z_i, which has the same z_{BS} distribution, as the dilepton vertex. This probability is calculated as follows. Firstly, the point z_i is randomly generated from the gaussian distribution, with a parameters corresponding to the 2011 beam spot conditions: $\sigma_{z_{\text{BS}}} = 56.7$ mm and $\langle z_{\text{BS}}\rangle = -7.9$ mm. For each event, the random generation procedure is repeated until z_i will pass the minimum distance from the dilepton vertex requirement ($|z_i - z_{\text{vtx}}^{\ell^+\ell^-}| > 20$ mm). Then, the relevant probability is calculated, by taking the ratio of events having no tracks (or vertices) within 3 mm from the point z_i, to the total number of events. The extracted probability using this type of *random sampling* for 3 mm veto size is $p_{\text{data}} = 0.713$ and $p_{\text{MC}} = 0.722$ for data and MC events, respectively.

Figure 9.6 shows the comparison of exclusive selection efficiency as a function of the average interactions per bunch crossing, $\langle\mu\rangle$, extracted from the data and MC simulations. Good agreement between the data and simulation shapes is observed.

A comparison of exclusive selection efficiency (extracted using random sampling procedure) as a function of z-coordinate of the reference point for 3 mm veto size is shown in Figure 9.7a. In Figure 9.7b the same efficiency is presented as a function of different exclusivity veto sizes. Here, a systematic discrepancy is observed, with a maximum deviation of 1.2%. Therefore, this 1.2% difference is taken as a systematic uncertainty for the exclusivity veto efficiency.

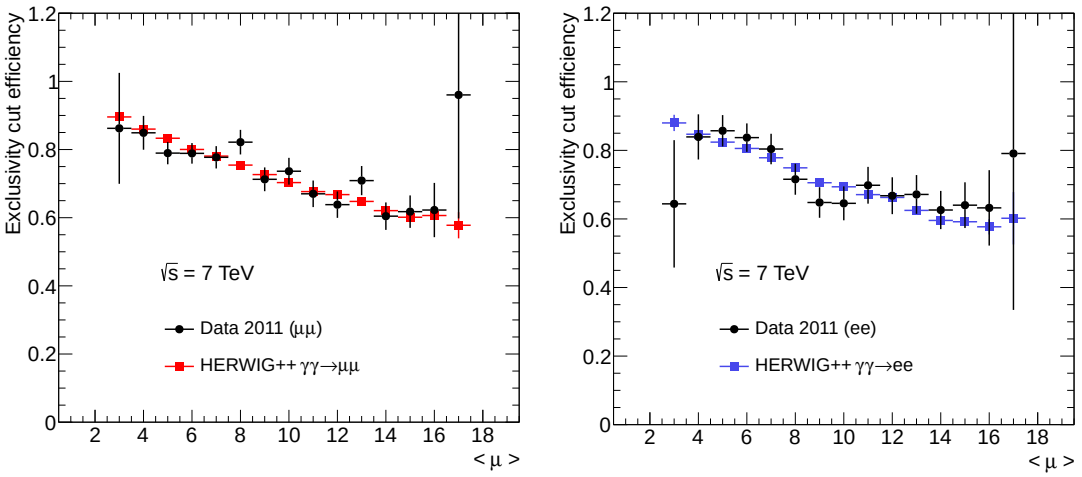

(a) (b)

FIGURE 9.6: Exclusivity veto efficiency extracted from the data (black points) as a function of average interactions per bunch crossing for (a) $\mu^+\mu^-$ and (b) e^+e^- channels. Comparison with MC simulation is also shown (red and blue markers, respectively). Data distributions are built according to the differences in shape between the events passing preselection and 3 mm veto selection cuts. For data, additional normalization factor is also applied, using random sampling procedure.

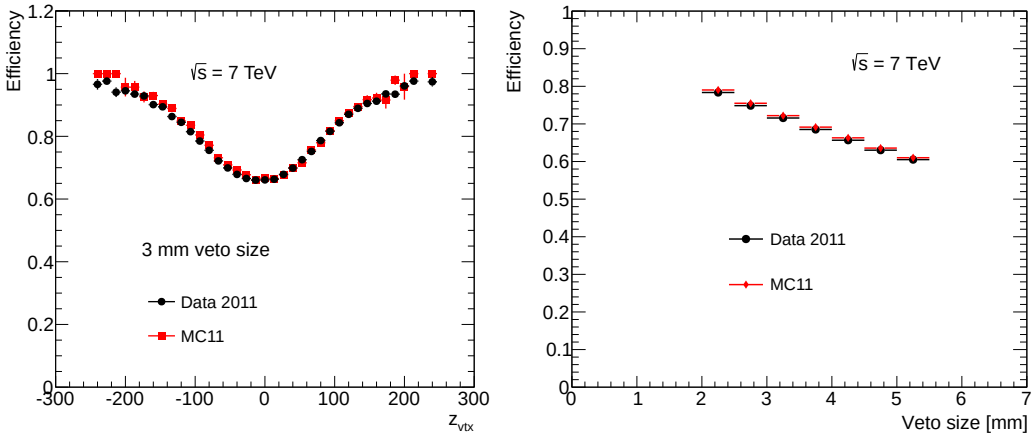

(a) (b)

FIGURE 9.7: Exclusivity veto efficiency extracted from the data (black points) and MC simulations (red points) as a function of (a) z-coordinate of the reference point for 3 mm exclusivity veto size and (b) as a function of different exclusivity veto size.

9.5 Background estimation

The maximum-likelihood fit procedure fixes the yields of the double-dissociative and DY events. In order to estimate the systematic effect related with the background modelling, the fit is repeated with each of these background contributions varied independently.

e^+e^- and $\mu^+\mu^-$ Drell–Yan. DY background contamination is well controlled by checking the lepton kinematic distributions in the Z region. Figure 9.8 shows the dimuon acoplanarity distribution for events in the Z-peak region after 3 mm exclusivity veto. MC simulation gives a perfect agreement in the entire kinematic range.

An uncertainty of 20% on the contribution of DY background processes is assumed. This value is considered conservative and accounts for the uncertainties coming from the data/MC simulation disagreement, related with the track multiplicity (≈10%) and $p_{\mathrm{T}}^{\ell^+\ell^-}$ (≈5%) reweighting procedures. Moreover, this includes 5% statistical uncertainty on the Z/γ^* MC sample after event selection. Additional 5% uncertainty for the PDFs and scale in Z/γ^* processes is also assumed. Because of the similar shapes of the DY and single proton-dissociative components in the fitted distribution, this variation is partly absorbed by the single-dissociative contribution. A ±20% variation results in a 1% change of the exclusive signal yield in the fit procedure for the muon and 1.2% for the electron channel.

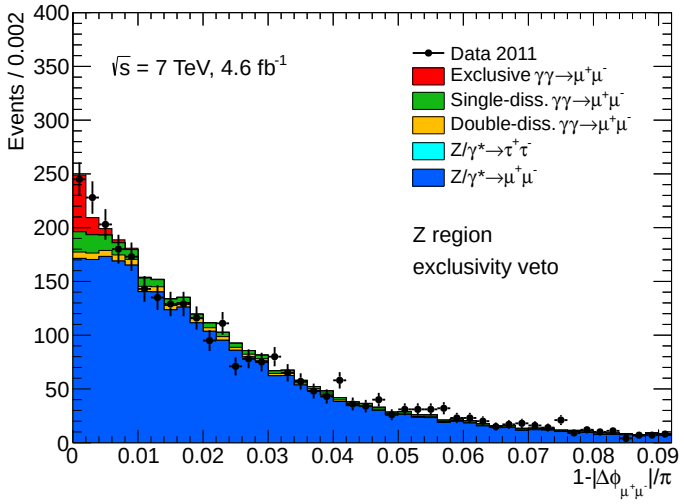

FIGURE 9.8: Acoplanarity of the dimuon system in the Z region after 3 mm exclusivity veto being imposed.

Double-dissociative $\gamma\gamma \to \ell^+\ell^-$. The default photon-PDF set used in double-dissociative $\gamma\gamma \to \ell^+\ell^-$ PYTHIA 8 sample is NNPDF2.3QED. It is found that this set describes very well the kinematic distributions of the lepton pairs. In order to estimate

the double-dissociative background uncertainty on the measurement, the 68% confidence level (CL) range for the photon-PDFs are built. This is done using the standard set of $N = 100$ replicas available. The photon-PDFs are affected by sizeable uncertainties, typically of order 50% [30]. This is shown in Figure 9.9, where the PDFs are shown, together with the 68% CL ranges at typical values of Q^2. The maximum fit variation for the double-dissociative background uncertainty obtained in this way is 1.7% for the muon and 1.9% for the electron channel, which is considered as a systematic effect.

Additional systematic checks using MRST2004QED PDFs with PYTHIA 8 double-dissociative events, as well as the predictions from LPAIR MC generator agrees within the 68% CL range of NNPDF2.3QED PDF set. Therefore, no additional systematic effect is assigned for double-dissociative background uncertainty.

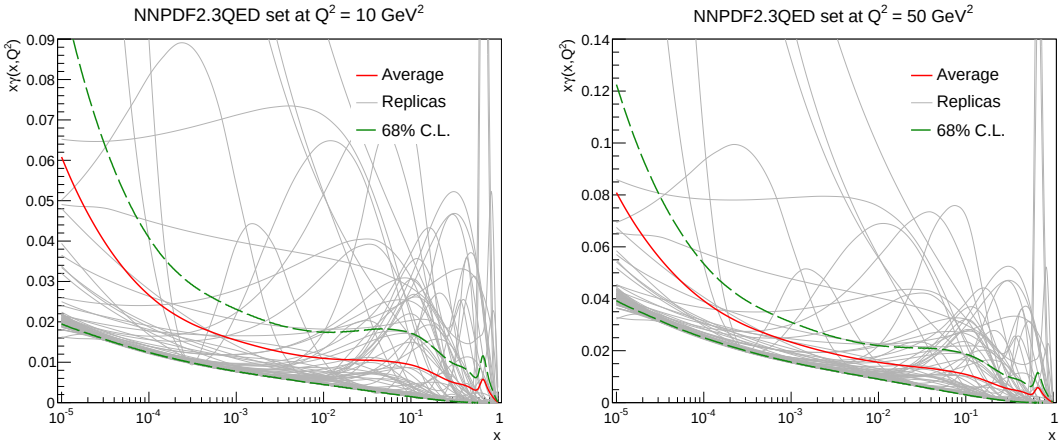

(a) (b)

FIGURE 9.9: The NNPDF2.3QED photon-PDFs at different energy scales: (a) $\mu^2 = 10$ GeV^2 and (b) $\mu^2 = 50$ GeV^2, presented as a function of the proton energy fraction carried by the photon. The 100 replicas are shown, along with the mean and the 68% CL ranges.

$\tau^+\tau^-$ Drell–Yan. After all selection criteria are applied, 3 ($\mu^+\mu^-$) and 2 (e^+e^- channel) events from $Z/\gamma^* \to \tau^+\tau^-$ processes are expected from MC simulation in the selected sample. Varying this background contribution by a factor of 2 results in 0.1% change in the fitted exclusive signal yield. Therefore, this contribution to the systematic uncertainty is considered negligible.

Exclusive $\gamma\gamma \to \tau^+\tau^-$. The contribution from exclusive $\gamma\gamma \to \tau^+\tau^-$ with fully leptonic decay of the taus is also considered. It is calculated using HERWIG++ MC generator. The estimated cross section for $\gamma\gamma \to \tau^+\tau^- \to \mu^+\mu^-(e^+e^-)$ is 1.7 fb for $m_{\mu^+\mu^-(e^+e^-)} > 20$ GeV range. Including the same selection requirements as in the nominal analysis, it gives the value of 0.2 fb, which has a negligible effect.

Exclusive $\gamma\gamma \to W^+W^-$. A cross section for exclusive W pair production is estimated to be 41 fb using HERWIG++ generator. Including the branching fraction to e^+e^- or $\mu^+\mu^-$ final states gives 1.2 fb. Additionally, requiring $p_T^{\ell^+\ell^-} < 1.5$ GeV reduces the cross section below 0.1 fb, which has a negligible effect on the analysis.

SPE/DPE Drell–Yan. Another source of possible background is the Single- (SPE) and Double-Pomeron Exchange (DPE) production of the lepton pairs via the Z/γ^* boson production. This contribution is estimated with FPMC [62] generator, with a default setup being used.

FPMC prediction for the cross section is 2 pb for SPE $Z/\gamma^* \to e^+e^-(\mu^+\mu^-)$ production, after including the assumed 3% gap survival probability [63] and using standard requirements on lepton kinematics. However, in SPE processes, only one intact proton is produced, where on the other side the standard (inclusive) proton-remnant hadronization occurs. This effect produces additional charged particles in the central detector acceptance region. A requirement vetoing the events with additional charged particles with $|\eta| < 2.5$ and $p_T > 400$ MeV reduces the SPE DY cross section to the values below 0.5 fb.

For DPE $Z/\gamma^* \to e^+e^-(\mu^+\mu^-)$ events, the predicted cross section is 1.2 pb for leptons with standard kinematic cuts applied at the preselection step. However, the effective cross section (when multiplied by the gap survival probability and including the elastic selection) is below 1 fb. Therefore, the contributions from SPE/DPE DY processes is considered as negligible.

Cosmic background. The possible contamination of cosmic-ray muons is also studied. Those may fake a signal, since they will not be correlated with other charged-particle tracks in the event. A possible contamination from cosmic muons is studied by comparing the vertex position and three-dimensional opening angle, θ_{3D}, in data and simulation. The cut $\theta_{3D} > 0.95\pi$, which requires almost collinear back-to-back muons, is used to enhance the relative cosmic-ray contribution. No difference between the vertex position distributions is observed between the events passing (or failing) θ_{3D} cut. Therefore, this effect is considered negligible.

9.6 LHC beam effects

The LHC beam energy uncertainty is evaluated in [64] to be 0.7%. This affects the exclusive cross sections by 0.4% and is considered as a systematic effect.

The non-zero crossing angle of the LHC beams in the ATLAS interaction point leads to a boost of the dilepton system in the y-direction. As a result, the kinematic distributions of the lepton pairs in MC simulation should undergo additional smearing effect. A proper Lorentz boost for collisions in the $y-z$ plane can be expressed as:

$$\begin{bmatrix} E' \\ p'_x \\ p'_y \\ p'_z \end{bmatrix} = \begin{bmatrix} \cos^{-1}(\theta_c/2) & 0 & \tan(\theta_c/2) & 0 \\ 0 & 1 & 0 & 0 \\ \sin(\theta_c/2) & 0 & 1 & -\sin(\theta_c/2) \\ \sin(\theta_c/2)\tan(\theta_c/2) & 0 & \tan(\theta_c/2) & \cos(\theta_c/2) \end{bmatrix} \times \begin{bmatrix} E \\ p_x \\ p_y \\ p_z \end{bmatrix} , \tag{9.1}$$

where $\theta_c/2$ is the half-crossing angle in the $y-z$ plane. Using a half-angle of 142 µrad and approximating Equations (9.1) to the linear terms, the smearing is equivalent to the set of equations:

$$\begin{aligned} E' &= E + 2.5 \cdot 10^{-6} p_y \ , \\ p'_x &= p_x \ , \\ p'_y &= 2.5 \cdot 10^{-6} E + p_y - 2.5 \cdot 10^{-6} p_z \ , \\ p'_z &= 2.5 \cdot 10^{-6} p_y + p_z \ . \end{aligned} \tag{9.2}$$

The effect is estimated by applying a correction for the Lorentz boost to truth-level lepton kinematics in the exclusive signal sample. Figure 9.10 shows the effect of beam crossing for truth dliepton transverse momentum distribution. As a result, the fitted value of the exclusive scale factors change by 0.3% from nominal fit value after applying this correction.

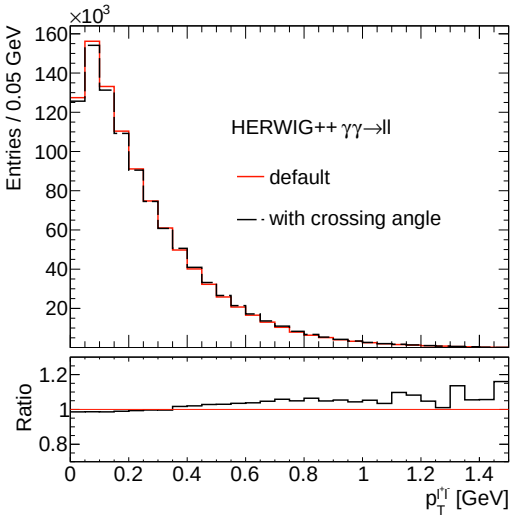

FIGURE 9.10: Truth-level dilepton transverse momentum distribution for exclusive $\gamma\gamma \to \ell^+\ell^-$ MC events. Comparison between the default setup and the one with the beam crossing angle enabled is shown.

9.7 Template shapes

The uncertainty arising from the choice of the template acoplanarity shapes in the signal extraction procedure is evaluated by refitting the data with different template distributions.

Various elastic electron–proton scattering experiments report a small deviation of proton elastic form factors from the standard dipole parametrization. This is presented in Figure 9.12, where the world data from proton elastic form factors measurements is fitted to the model with QCD corrections [65]. The model curves differ form the standard dipole by 1% at $Q^2 = 0.2$ GeV^2 and the effect is smaller for lower Q^2, where the density of equivalent photons is highest, following the exclusive cross section formula. The impact of this effect on the exclusive cross section measurements is evaluated by reweighting the equivalent photon spectra in signal MC events, according to the model predictions. Figure 9.13 shows the difference in dilepton acoplanarity signal shape when, instead of the standard dipole, a best-fit parametrized functions from Figure 9.12 are applied. A small proton elastic form factors deviation from the standard dipole parametrization used in the simulations has a 0.2% effect on the exclusive cross sections.

The impact of possible mis-modelling of acoplanarity shape in single-dissociative template distribution is evaluated using reweighted single-dissociative MC events. So-called exponential modification factor is applied to the shape of the $p_{\mathrm{T}}^{\ell^+\ell^-}$ distribution and the reweighted single-dissociative events are used in the signal extraction procedure. The exponential modification factor is characterized by the parameter a, using the expression:

$$e^{-a\left(p_{\mathrm{T}}^{\ell^+\ell^-}\right)^2} . \tag{9.3}$$

The modification parameter accounts for possible absorptive effects not included in the single-dissociative process simulation. It is extracted by fitting the shape of $p_{\mathrm{T}}^{\ell^+\ell^-}$ distribution to data using single-dissociative MC distribution. The binned maximum-likelihood fit is performed for events satisfying exclusive selection criteria, except for $p_{\mathrm{T}}^{\ell^+\ell^-}$ cut, in the range 1.5 GeV $< p_{\mathrm{T}}^{\ell^+\ell^-} <$ 5 GeV, where the contribution from single-dissociative processes is dominant. The best-fit results are: $a_{\mu^+\mu^-} = 0.05 \pm 0.01$ GeV^{-2} for the muon and $a_{\mathrm{e}^+\mathrm{e}^-} = 0.01 \pm 0.02$ GeV^{-2} for the electron channel. Figure 9.11 shows the comparison between the default and exponentially modified modelling of the $p_{\mathrm{T}}^{\ell^+\ell^-}$ distribution for the muon channel. The maximum $p_{\mathrm{T}}^{\ell^+\ell^-}$ shape deviation can be obtained using exponential modification factor with $a_{\mu^+\mu^-}$ parameter, which is then applied as a weight for single-dissociative MC events in both analysis channels. For single-dissociative events after $p_{\mathrm{T}}^{\ell^+\ell^-} <$ 1.5 GeV cut, this weight modifies the shape of the acoplanarity distribution by at most 2%. This results in a 0.9% change of the exclusive

yields in the signal extraction procedure. As an additional cross-check, the modification factor is extracted with DY and double-dissociative template distributions simultaneously varied by $\pm 1\sigma$. The maximal value of the modification parameter obtained in that way is observed for muon channel and $+1\sigma$ check: $a_{\mu^+\mu^-} = 0.06 \pm 0.01$ GeV^{-2}.

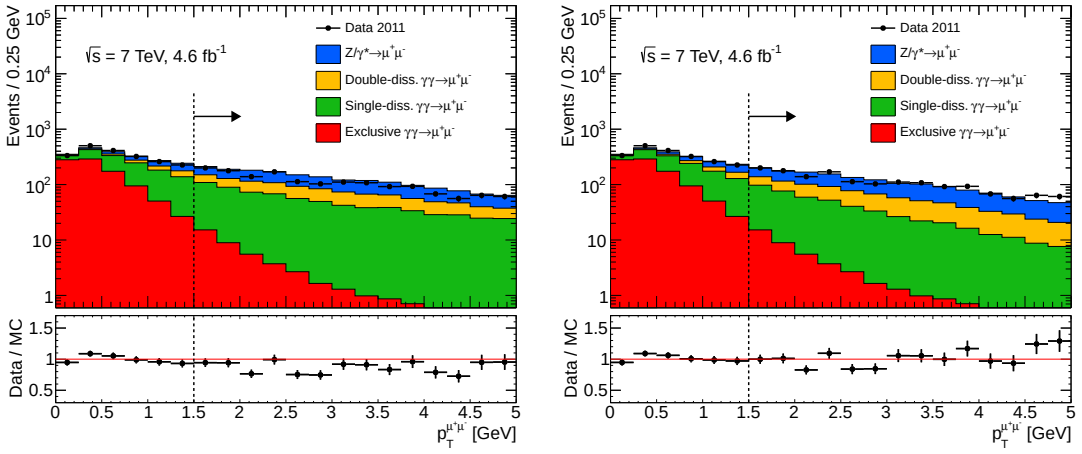

FIGURE 9.11: Comparison between the (a) default and (b) the exponentially modified modelling of the $p_{\mathrm{T}}^{\ell^+\ell^-}$ distribution for muon channel. The modification factor with parameter $a = 0.05$ GeV^{-2} is applied to the single-dissociative MC events.

The effect of a possible mis-description of the detector resolution [66] on the measurements of η^ℓ and ϕ^ℓ angles has been also studied. The resolution in the MC simulations on both angles is enlarged by 20% and the impact on the measured exclusive cross section calculated. A change of the resolution on η^ℓ has no impact on the signal shape and measured cross section. On the other hand, a change of the resolution on ϕ^ℓ has an impact on the measured cross section of 0.2% for the muon and 0.3% for the electron channel.

9.8 QED FSR and other NLO effects

Although the effect of QED final-state radiation (FSR) - and the other NLO contributions - is predicted to be small in $\gamma\gamma \to \ell^+\ell^-$ reactions [67], it may be a source of potential experimental issue, affecting e.g. lepton efficiencies and dilepton acoplanarity resolution. Here it is worth to mention that the HERWIG++ used to generate signal events, does not include NLO QED+EW effects. For the kinematic cuts used in the analysis, the effect of QED FSR is at the level of 0.8% and does not depend on the dilepton invariant mass (for details, see [67]).

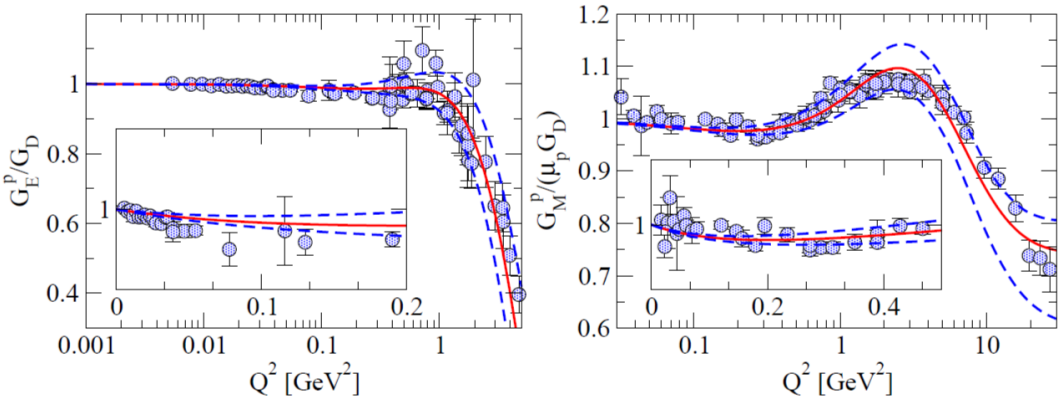

FIGURE 9.12: The proton elastic form factors extracted from the world data and compared to the model with QCD corrections. The solid line represents the best-fit to the data, while the dashed lines indicate the 1σ error band. Figure taken from [65].

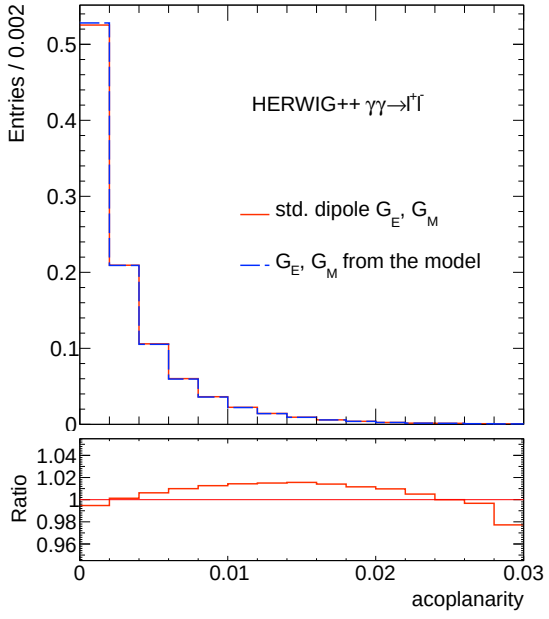

FIGURE 9.13: Truth-level dilepton acoplanarity distribution for exclusive $\gamma\gamma \to \ell^+\ell^-$ events. Comparison between the proton elastic form factors with the standard-dipole parametrization applied and the ones parametrized as in [65] is shown.

In order to estimate the effect of QED FSR on the lepton efficiencies, Z/γ^* MC events are used with two standard reference points. *Bare* reference point is using the lepton momenta after QED FSR. On the other hand, the *dressed* level includes also the momenta of all FSR photons with $E > 10$ MeV, which are radiated off the lepton in a cone of $\Delta R < 0.1$ around the bare lepton direction.

A possible bias of QED FSR on the electron efficiencies is studied by comparing electron pair reconstruction efficiency in Z/γ^* MC events for nominal scenario and the events with no QED FSR photon being emitted. This is presented in Figure 9.14. Electron pair efficiency accounts for the trigger, reconstruction and identification efficiencies of both electrons, as well as for the LAr crack removal procedure. The efficiency is calculated for $m_{e^+e^-} > 24$ GeV, $p_{\mathrm{T}}^{e} > 12$ GeV, $|\eta_e| < 2.4$ truth-level requirements applied on QED *Born* level. One can observe from Figure 9.14 that the effect is strongest in the vicinity of the Z-peak region, where the interference effects are present. However, since the Z region (70 GeV $< m_{\ell^+\ell^-} <$ 105 GeV) is not used in the exclusive cross section determination procedure, the overall impact of this effect is relatively small. Indeed, when convoluting the differences in the electron pair reconstruction efficiency with the exclusive signal events, this results in a 0.8% change in the signal yield. This is taken as a systematic uncertainty.

To check the size of this effect on a fitted acoplanarity distribution, bare and dressed reference points in Z/γ^* MC are compared in the lepton track azimuthal resolution, with a presence of at least one QED FSR photon. This is shown in Figure 9.15. Generally, the QED FSR is the source of additional smearing also for the track-based observables. The effect is estimated by applying additional smearing to one of the reconstructed lepton azimuthal angle for 0.7% randomly chosen signal events. A relative change below 0.1% in the fitted signal yield is observed in both analysis channels. Moreover, the result of this effect is partially included by varying lepton angular resolution (see the Sec. 9.7).

Finally, the effect of higher-order virtual EW corrections is considered. It is also estimated in [67]. For exclusive lepton pair production the weak corrections are negligible below the weak bosons scale ($\lesssim 2m_W$).

9.9 Luminosity

Systematic uncertainties on the absolute luminosity calibration have been evaluated in [19]. For the 2011 proton–proton runs, the uncertainty is dominated by the accuracy of the vdM calibration procedure. The total systematic uncertainty for the luminosity determination in 2011 is 1.8%.

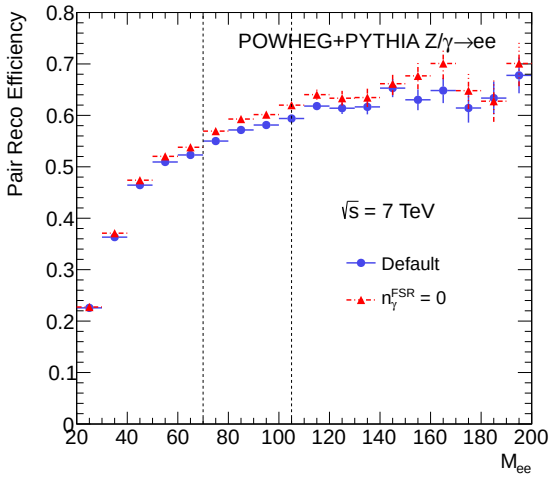

FIGURE 9.14: Electron pair reconstruction efficiency as a function of truth invariant mass of the dielectron system. Default scenario is compared to the events with no QED FSR photon being emitted. For details, see the text.

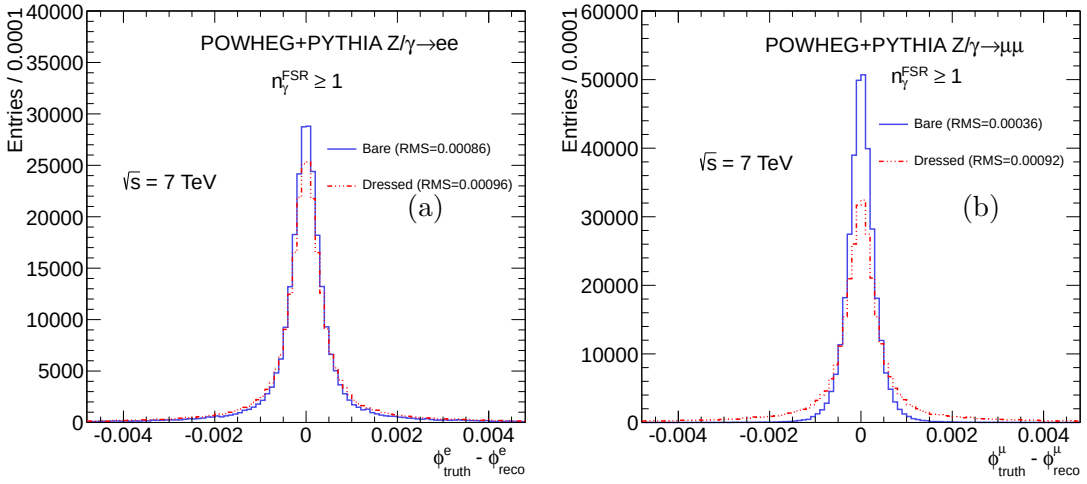

FIGURE 9.15: Lepton track azimuthal resolution for events with at least one QED FSR photon emitted for (a) electrons and (b) muons. Z/γ^* MC events are used to calculate the effective smearing (difference between the bare and dressed reference points).

9.10 Additional cross-checks

Additional checks of the maximum-likelihood fit stability are performed by comparing different bin widths and fit ranges. Starting from the nominal number of 30 bins in the fit range $0 \leq 1 - |\Delta\phi_{\ell^+\ell^-}|/\pi \leq 0.06$, variations in the bin width (0.002 ± 0.001) and fit range ($[0 - 0.03]$, $[0 - 0.09]$) show relative deviations by at most 0.9% with respect to the nominal exclusive yield.

As an alternative set of elastic cuts, for systematic cross-checks, several configurations are studied. They include various types of requirements for acoplanarity and transverse

Cut	Definition	Fitted distribution	$f^{\text{excl.}}$	$f^{\text{s-diss.}}$
1 (def.)	$p_{\text{T}}^{\mu^+\mu^-} < 1.5$ GeV	$1 - \left\|\Delta\phi_{\mu^+\mu^-}\right\|/\pi$	$0.791^{+0.041}_{-0.040}$	$0.762^{+0.049}_{-0.048}$
2	$\Delta p_{\text{T}}^{\mu^+\mu^-} < 1$ GeV	$p_{\text{T}}^{\mu^+\mu^-}$	$0.848^{+0.047}_{-0.046}$	$0.737^{+0.057}_{-0.056}$
3	$1 - \left\|\Delta\phi_{\mu^+\mu^-}\right\|/\pi < 0.008$	$\Delta p_{\text{T}}^{\mu^+\mu^-}$	$0.805^{+0.068}_{-0.068}$	$0.751^{+0.134}_{-0.131}$
1 (def.)	$p_{\text{T}}^{\text{e}^+\text{e}^-} < 1.5$ GeV	$1 - \left\|\Delta\phi_{\text{e}^+\text{e}^-}\right\|/\pi$	$0.863^{+0.070}_{-0.069}$	$0.759^{+0.080}_{-0.078}$
2	$\Delta p_{\text{T}}^{\text{e}^+\text{e}^-} < 1$ GeV	$p_{\text{T}}^{\text{e}^+\text{e}^-}$	$0.916^{+0.094}_{-0.093}$	$0.736^{+0.090}_{-0.088}$
3	$1 - \left\|\Delta\phi_{\text{e}^+\text{e}^-}\right\|/\pi < 0.008$	$\Delta p_{\text{T}}^{\text{e}^+\text{e}^-}$	$1.04^{+0.17}_{-0.18}$	$0.60^{+0.27}_{-0.25}$

TABLE 9.3: Elastic cut definitions used for additional cross-checks. First cut is used as a default option. Fit results for the muon and electron channels are also shown, with the corresponding statistical uncertainties.

momentum difference of the lepton pairs. Detailed description for each set of requirements is summarized in Table 9.3. The scale factor predictions for exclusive and single dissociative contributions are also shown. Good agreement for the fitted yields is observed for all control regions. For each elastic region definition, the best-fit curve and exclusive signal yield are consistent with the default fit procedure within the statistical uncertainties. For electrons, the smearing in the energy (transverse momentum) is much higher than for the muons and the shapes of the exclusive and single-dissociative distributions are thus very similar. This results in large uncertainties from the fit procedure.

Since all of these variations are strongly correlated with the statistical uncertainties, no additional systematic uncertainties are assigned in this case.

9.11 Summary of systematic uncertainties

Table 9.4 summarizes the contributions from different sources of systematic uncertainties to the measured exclusive cross section for the muon and electron channels. A total systematic uncertainty, including contribution from luminosity determination, is 3.3% for the muon and 4.3% for the electron channel.

Source	Variation from nominal yield	
	Muon channel	Electron channel
Muon reconstruction efficiency	0.2%	-
Muon momentum scale and resolution	0.5%	-
Muon trigger efficiency	0.6%	-
Electron reconstruction and identification efficiency	-	1.9%
Electron energy scale and smearing	-	1.4%
Electron trigger efficiency	-	0.7%
Pile-up description	0.5%	0.5%
Exclusivity veto efficiency	1.2%	1.2%
Backgrounds	2.0%	2.3%
LHC beam effects	0.5%	0.5%
Template shapes	0.9%	1.0%
QED final-state radiation	-	0.8%
Luminosity	1.8%	1.8%
Total systematic uncertainty	3.3%	4.3%
Statistical uncertainty	5.1%	8.2%

TABLE 9.4: Summary of systematic uncertainties on the exclusive cross section measurements for the muon and electron channels. The data statistical uncertainties are also given for comparison.

Chapter 10

Results

The exclusive $\gamma\gamma \to \ell^+\ell^-$ cross sections are restricted to the fiducial regions defined in Table 10.1. The fitted value of exclusive fraction, $f^{\text{excl.}}$, for muon and electron channels, are converted to a fiducial cross section defined as:

$$\sigma^{\text{excl.}} = f^{\text{excl.}} \cdot \sigma^{\text{EPA}} \tag{10.1}$$

where σ^{EPA} is a cross section predicted by HERWIG++ in the phase-space region considered: $\sigma^{\text{EPA}}_{\gamma\gamma\to e^+e^-} = 0.496 \pm 0.008$ pb and $\sigma^{\text{EPA}}_{\gamma\gamma\to\mu^+\mu^-} = 0.794 \pm 0.013$ pb. The uncertainties in both theoretical values include uncertainties related with proton elastic form factors (1.6%), and those originating from the higher order electroweak corrections [67] not included in the calculations (0.7%). The proton form factors uncertainty is evaluated using parametrizations from [65] that include QCD corrections in the calculations. The uncertainty is estimated by reweighting the equivalent photon spectra in signal MC events, according to the form factors uncertainty band. It is found that the -1σ line gives the maximum deviation of exclusive cross sections (1.6%) and it is taken as a theory uncertainty related with proton elastic form factors. This procedure covers small form factors deviation from the standard dipole formula. It is also found that the uncertainties on the proton magnetic form factor have no impact on the theory cross section uncertainty. This is due to the fact that the proton magnetic form factor contributes to the 10% of the total exclusive cross section in the fiducial regions considered.

Variable	Electron channel	Muon channel
p_{T}^{ℓ}	> 12 GeV	> 10 GeV
$\lvert\eta^{\ell}\rvert$	< 2.4	< 2.4
$m_{\ell^+\ell^-}$	> 24 GeV	> 20 GeV

TABLE 10.1: Definition of the electron and muon channel fiducial regions for which the exclusive cross sections are evaluated.

10.1 Exclusive cross sections

The resulting visible exclusive cross section for the muon channel is measured to be

$$\sigma^{\mathrm{excl.}}_{\gamma\gamma\to\mu^+\mu^-} = 0.628 \pm 0.032\ (\mathrm{stat.})^{1} \pm 0.021\ (\mathrm{syst.})\ \mathrm{pb}$$

for $m_{\mu^+\mu^-} > 20$ GeV, $p_{\mathrm{T}}^{\mu} > 10$ GeV, $|\eta^{\mu}| < 2.4$. This value can be compared with the theoretical predictions, including correction for proton absorptive effects: $\sigma^{\mathrm{EPA,\ corr.}}_{\gamma\gamma\to\mu^+\mu^-} = 0.638 \pm 0.013$ pb. For the electron channel, the visible cross section is measured to be

$$\sigma^{\mathrm{excl.}}_{\gamma\gamma\to\mathrm{e}^+\mathrm{e}^-} = 0.428 \pm 0.035\ (\mathrm{stat.}) \pm 0.018\ (\mathrm{syst.})\ \mathrm{pb}$$

for electrons with $m_{e^+e^-} > 24$ GeV, $p_{\mathrm{T}}^{e} > 12$ GeV and $|\eta^{e}| < 2.4$. This measured value can be compared with the theoretical predictions containing proton survival factor: $\sigma^{\mathrm{EPA,\ corr.}}_{\gamma\gamma\to\mathrm{e}^+\mathrm{e}^-} = 0.398 \pm 0.007$ pb. The uncertainty of each corrected prediction includes an additional 0.8% uncertainty related to the modelling of proton absorptive corrections. It is evaluated by varying the effective transverse size of the proton by 3%, according to [68].

10.2 Control distributions

Kinematic distributions for muons after all cuts and best fit procedure are shown in Figures 10.1, 10.2 and 10.3. Here the additional acoplanarity requirement, $1 - |\Delta\phi_{\ell^+\ell^-}|/\pi < 0.008$, is also applied. This is done for additional cross-check and for illustration how to further enrich the sample in elastic events. Similar plots for the electrons are presented in Figures 10.4, 10.5 and 10.6. For distributions from Figures 10.2 and 10.5, the acoplanarity requirement is imposed, instead of standard elastic selection. A very good agreement between the data and MC simulations is observed for each kinematic variable.

[1] The statistical uncertainties on the measured exclusive cross sections are symmetrized with respect to the uncertainties on the exclusive scale factors

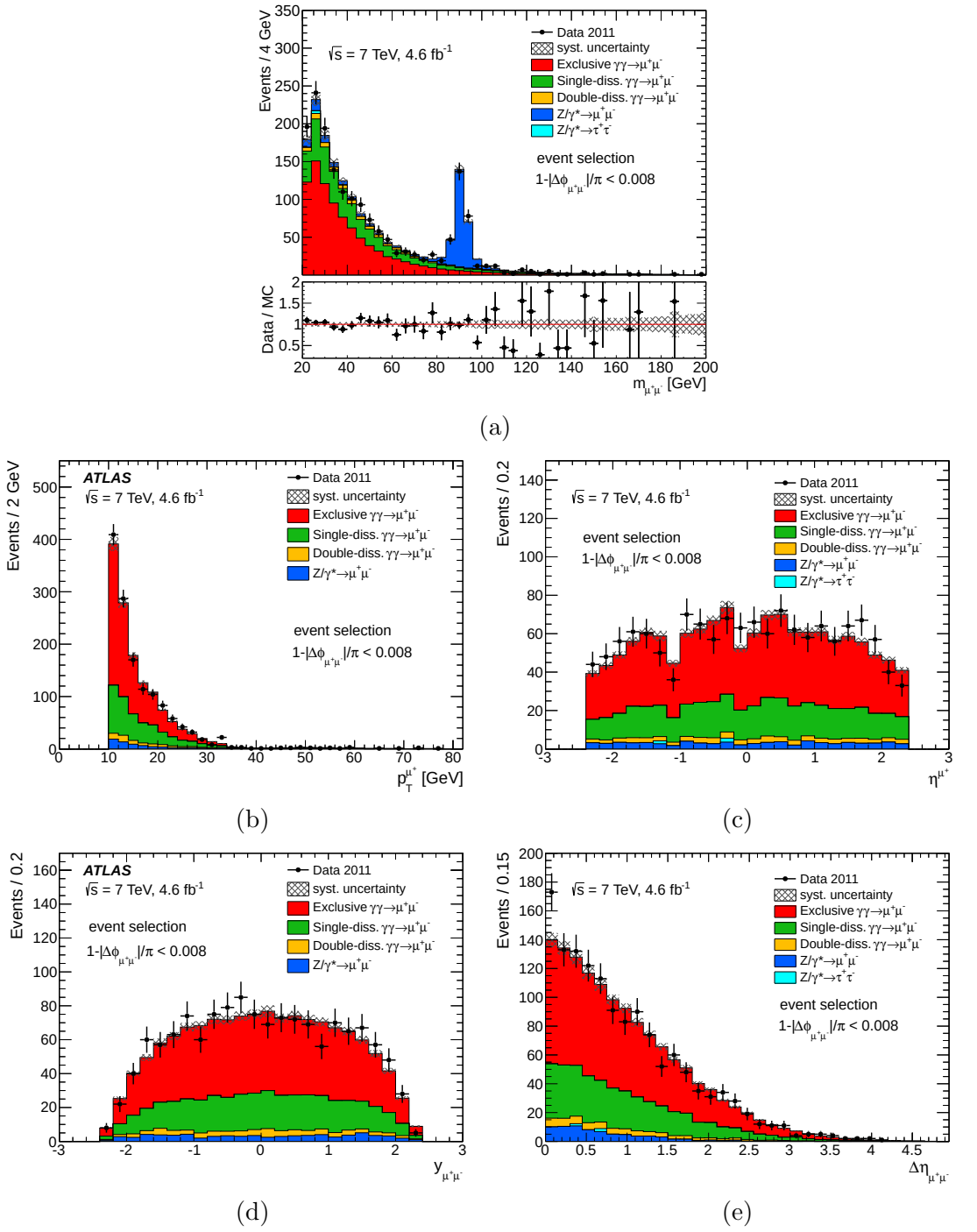

FIGURE 10.1: Control distributions of kinematic variables in the muon channel for events passing the exclusivity veto together with the other selection criteria, and satisfying a cut on the dilepton acoplanarity ($1 - |\Delta\phi_{\ell^+\ell^-}|/\pi < 0.008$). Data are shown as points with statistical error bars, while the histograms represent the simulated exclusive signal (solid red line), and the single-dissociative (green dashed line), double-dissociative (orange) and DY (blue) backgrounds. Systematic uncertainties on the signal events are shown by the black-hashed regions. The exclusive and single-dissociative yields are determined from the fit described in the text.

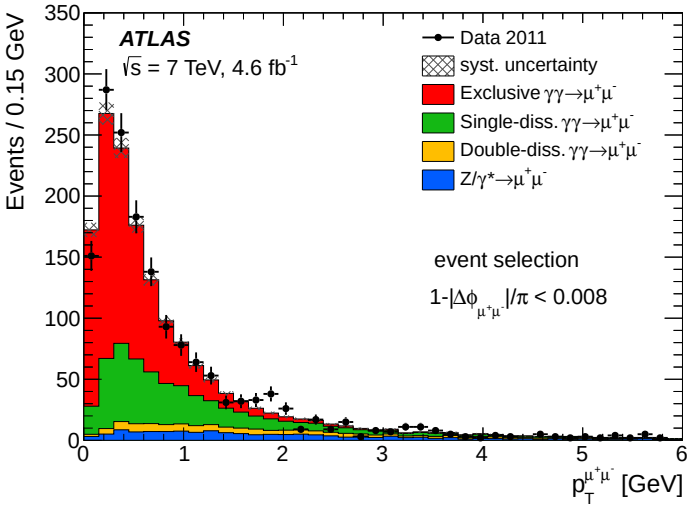

(a)

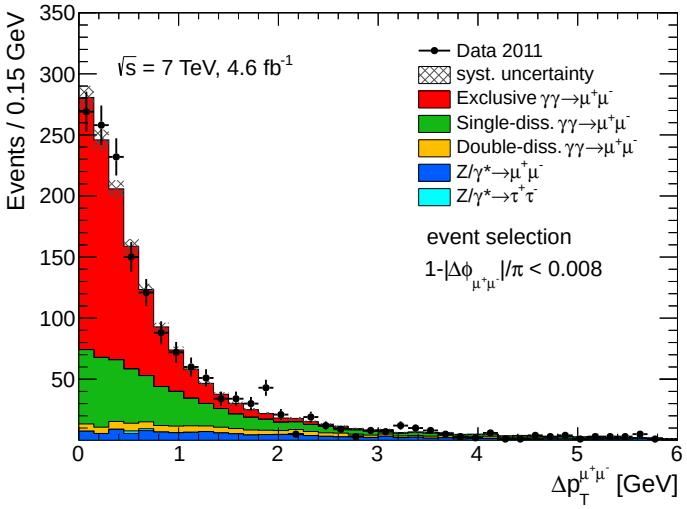

(b)

FIGURE 10.2: Control distributions of (a) the dimuon transverse momentum and (b) the muon transverse momentum difference ($|p_{\mathrm{T}}^{\mu^+} - p_{\mathrm{T}}^{\mu^-}|$) for events passing the exclusivity veto together with the other selection criteria, and passing a cut on the dilepton acoplanarity ($1 - |\Delta\phi_{\ell^+\ell^-}|/\pi < 0.008$), instead of the total transverse momentum. Data are shown as points with statistical error bars, while the histograms, in top-to-bottom order, represent the simulated exclusive signal, and the single-dissociative, double-dissociative and DY backgrounds. Systematic uncertainties on the signal events are shown by the black-hashed regions. The exclusive and single-dissociative yields are determined from the fit described in the text.

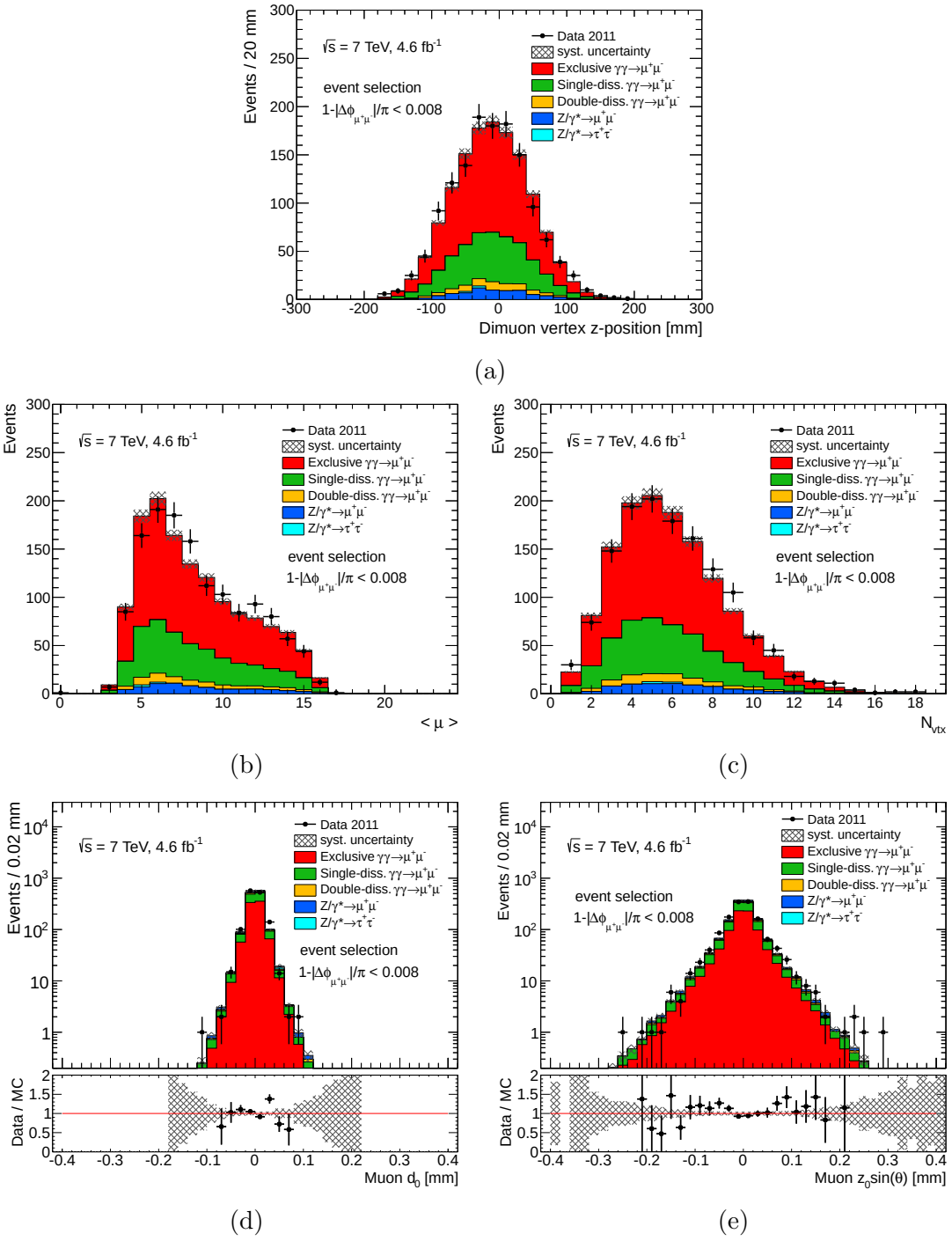

FIGURE 10.3: Additional control distributions of dimuon event variables for events passing the exclusivity veto together with the other selection criteria, and satisfying a cut on the dilepton acoplanarity ($1 - |\Delta\phi_{\ell^+\ell^-}|/\pi < 0.008$). Data are shown as points with statistical error bars, while the histograms represent the simulated exclusive signal (solid red line), and the single-dissociative (green dashed line), double-dissociative (orange) and DY (blue) backgrounds. Systematic uncertainties on the signal events are shown by the black-hashed regions. The exclusive and single-dissociative yields are determined from the fit described in the text.

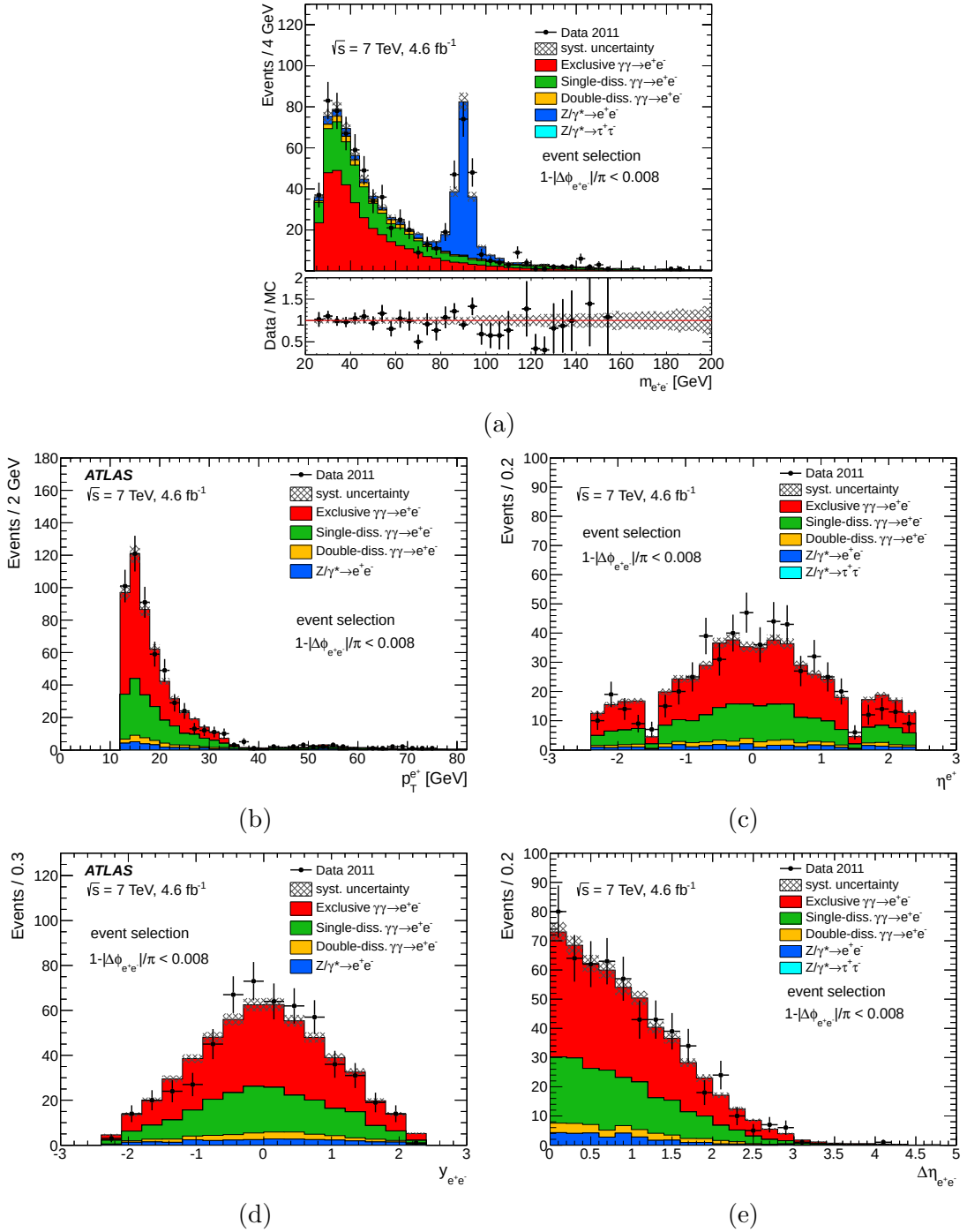

FIGURE 10.4: Control distributions of kinematic variables in the electron channel for events passing the exclusivity veto together with the other selection criteria, and satisfying a cut on the dilepton acoplanarity ($1 - |\Delta\phi_{\ell^+\ell^-}|/\pi < 0.008$). Data are shown as points with statistical error bars, while the histograms represent the simulated exclusive signal (solid red line), and the single-dissociative (green dashed line), double-dissociative (orange) and DY (blue) backgrounds. Systematic uncertainties on the signal events are shown by the black-hashed regions. The exclusive and single-dissociative yields are determined from the fit described in the text.

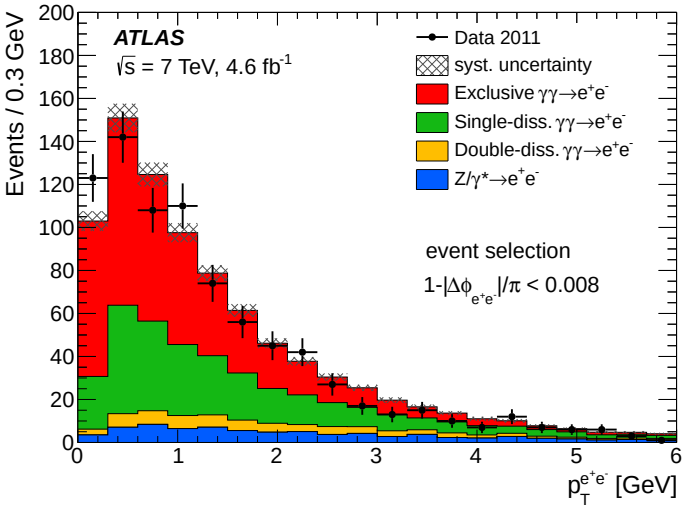

(a)

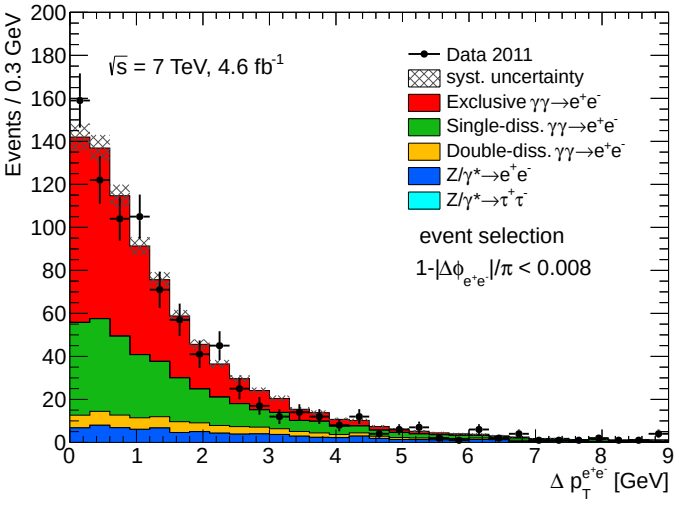

(b)

FIGURE 10.5: Control distributions of (a) the dielectron transverse momentum and (b) the electron transverse momentum difference ($|p_{\mathrm{T}}^{e^+} - p_{\mathrm{T}}^{e^-}|$) for events passing the exclusivity veto together with the other selection criteria, and passing a cut on the dilepton acoplanarity ($1 - |\Delta\phi_{\ell^+\ell^-}|/\pi < 0.008$), instead of the total transverse momentum. Data are shown as points with statistical error bars, while the histograms, in top-to-bottom order, represent the simulated exclusive signal, and the single-dissociative, double-dissociative and DY backgrounds. Systematic uncertainties on the signal events are shown by the black-hashed regions. The exclusive and single-dissociative yields are determined from the fit described in the text.

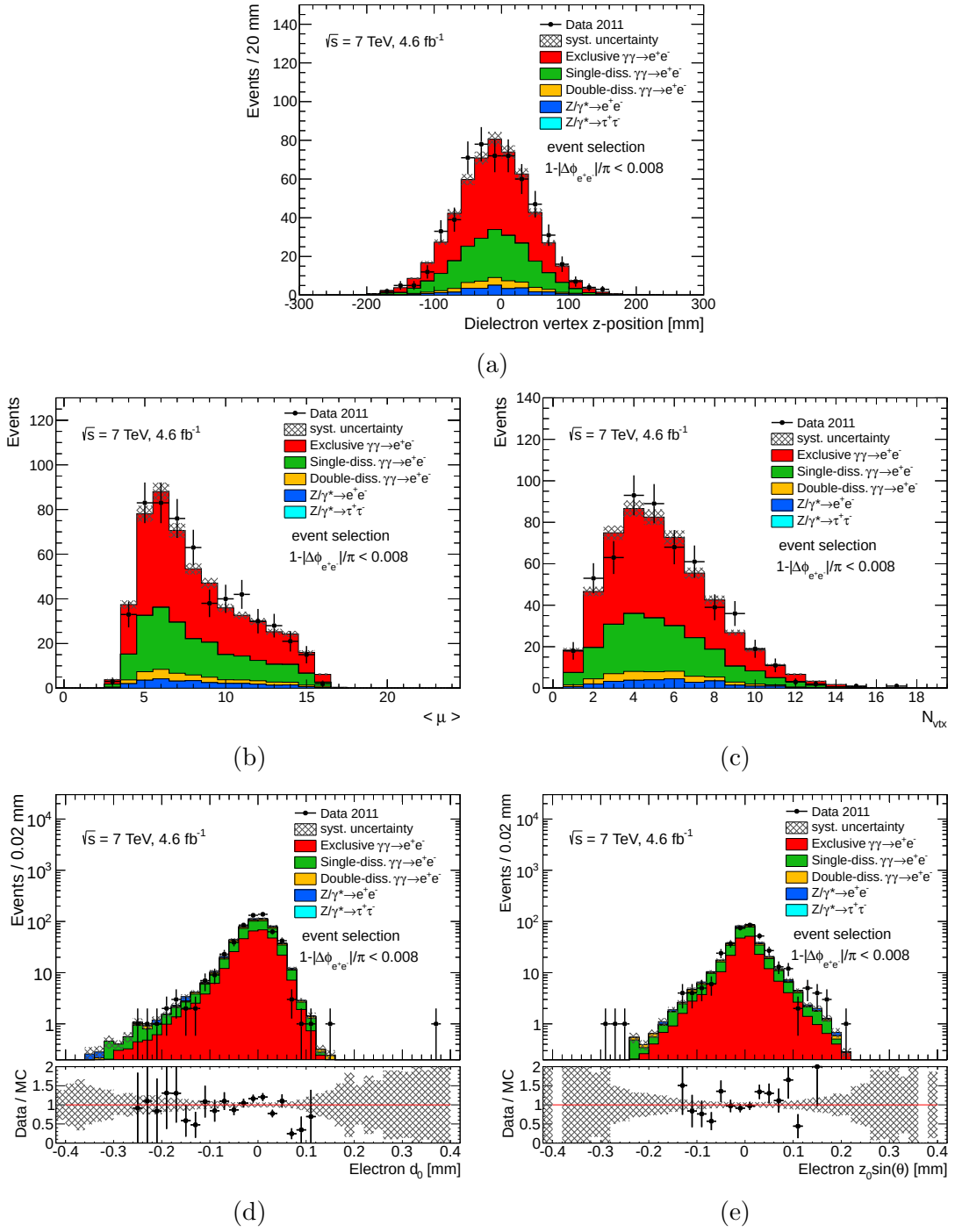

FIGURE 10.6: Additional control distributions of dielectron event variables for events passing the exclusivity veto together with the other selection criteria, and satisfying a cut on the dilepton acoplanarity ($1 - |\Delta\phi_{\ell^+\ell^-}|/\pi < 0.008$). Data are shown as points with statistical error bars, while the histograms represent the simulated exclusive signal (solid red line), and the single-dissociative (green dashed line), double-dissociative (orange) and DY (blue) backgrounds. Systematic uncertainties on the signal events are shown by the black-hashed regions. The exclusive and single-dissociative yields are determined from the fit described in the text.

10.3 Event displays

Figure 10.7 shows a reconstructed candidate for exclusive $\gamma\gamma \to \mu^+\mu^-$ event in data with the overlaid model of the ATLAS detector prepared using the VP1 event display software [69]. Two back-to-back muons with reconstructed invariant mass of 25.6 GeV have no additional charged-particle tracks associated with its vertex. Tracks and vertices originating from pile-up interactions are also visible.

Similar visualization prepared for exclusive $\gamma\gamma \to e^+e^-$ event candidate is presented in Figure 10.8. Here the energy deposits in the ATLAS Electromagnetic Calorimeter are visualized as yellow boxes.

10.4 Comparison with CMS results

Exclusive two-photon production of muon pairs have been recently studied by the CMS experiment in pp collisions at $\sqrt{s} = 7$ TeV. For muon pairs with invariant mass greater than 11.5 GeV, transverse momentum $p_{\mathrm{T}} > 4$ GeV and pseudorapidity $|\eta| < 2.1$ the exclusive cross section is measured and compared with the LPAIR predictions. In particular, the CMS exclusive signal yield ratio is $0.83^{+0.14}_{-0.13}$(stat.). However, one cannot compare the results directly, before imposing the correction due to the finite-size effects of the proton. Indeed, the CMS dimuon exclusive yield scale factor is measured in much lower invariant mass range, where the proton absorptive effects are smaller.

The ratio of measured exclusive signal scale factor (f^{excl}) to predicted proton survival factor ($S^2_{\gamma\gamma}$) is directly related with the ratio of measured ($\sigma^{\mathrm{excl.}}$) to predicted ($\sigma^{\mathrm{EPA,\ corr.}}$) exclusive cross section:

$$\sigma^{\mathrm{excl.}} \ / \ \sigma^{\mathrm{EPA,\ corr.}} = f^{\mathrm{excl}} \ / \ S^2_{\gamma\gamma} \ . \tag{10.2}$$

Figure 10.9 shows a comparison between the scale factors for both analysis channels and the CMS measurement after imposing the proton absorptive correction for the exclusive event scale factor. Here the corrected exclusive and uncorrected[2] single-dissociative scale factors are presented.

Figure 10.10 presents the ratios of the measured and predicted cross sections to the uncorrected EPA calculations. The measurements are in agreement with the predicted values corrected for absorptive effects. The figure also includes a similar CMS cross section measurement.

[2]There are currently no theoretical models of absorptive corrections available for single-dissociative reactions

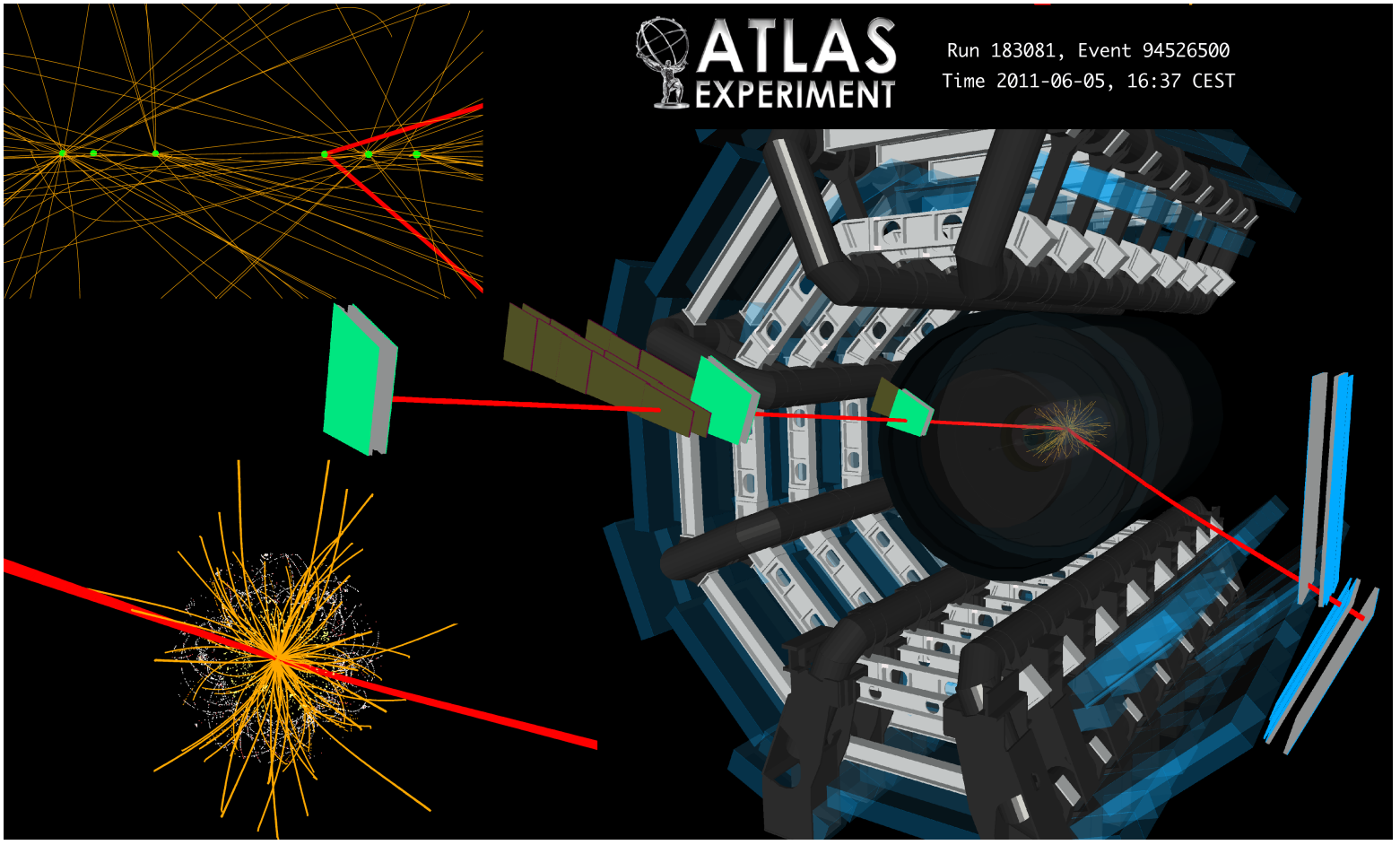

FIGURE 10.7: Event display for exclusive $\gamma\gamma \to \mu^+\mu^-$ candidate. Event 94526500 from run 183081 recorded on 2011.06.05 at 16:37:10 is shown. Two back-to-back muons with an invariant mass of 25.6 GeV have no additional charged-particle tracks associated with its vertex. Tracks and vertices originating from pile-up interactions are also visible. The figure is prepared using VP1 [69].

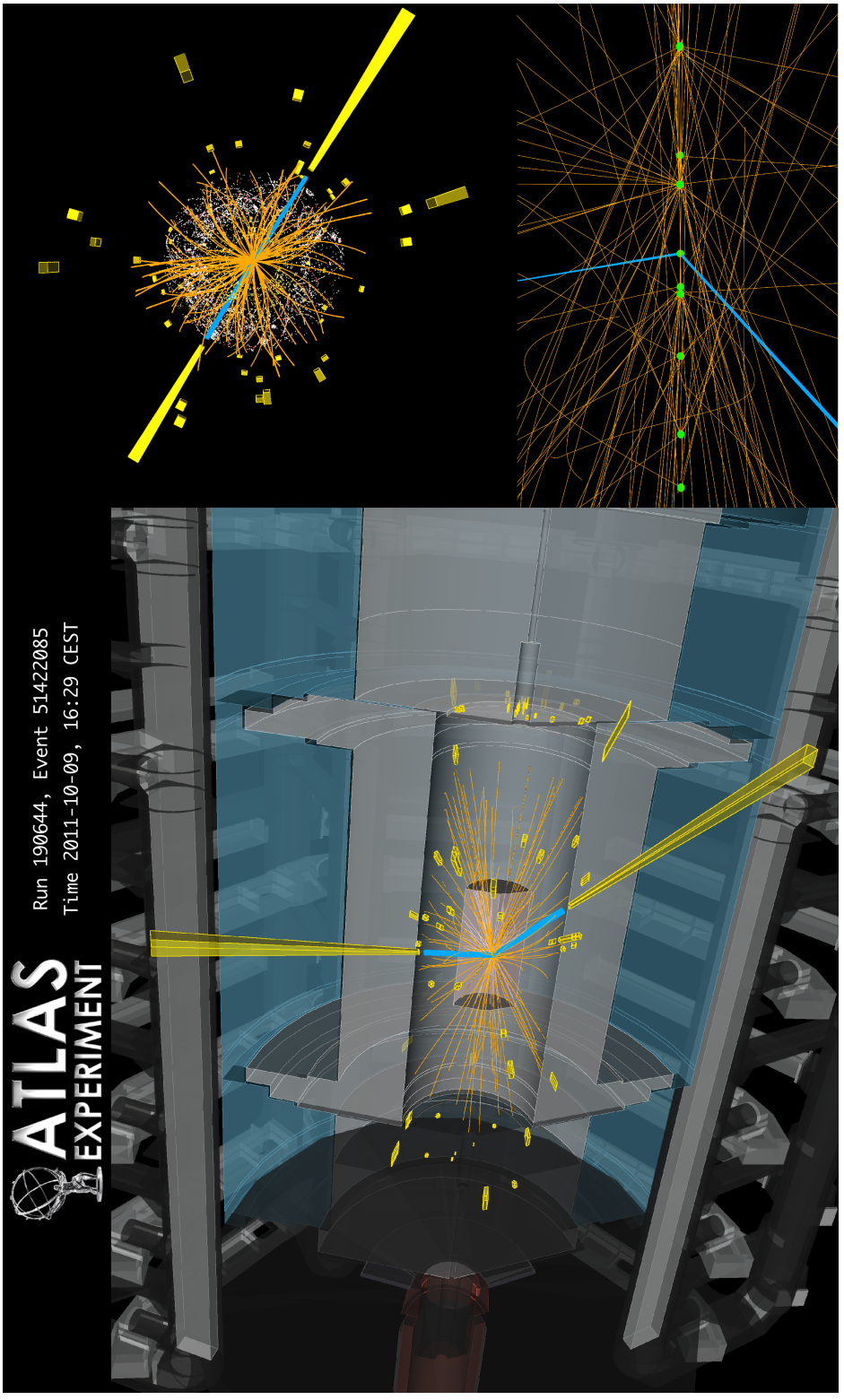

FIGURE 10.8: Event display for exclusive $\gamma\gamma \to e^+e^-$ candidate. Event 51422085 from run 190644 recorded on 2011.10.09 at 16:29:20 is shown. Two back-to-back electrons with an invariant mass of 150.7 GeV have no additional charged-particle tracks associated with its vertex. Tracks and vertices originating from pile-up interactions are also visible. The figure is prepared using VP1 [69].

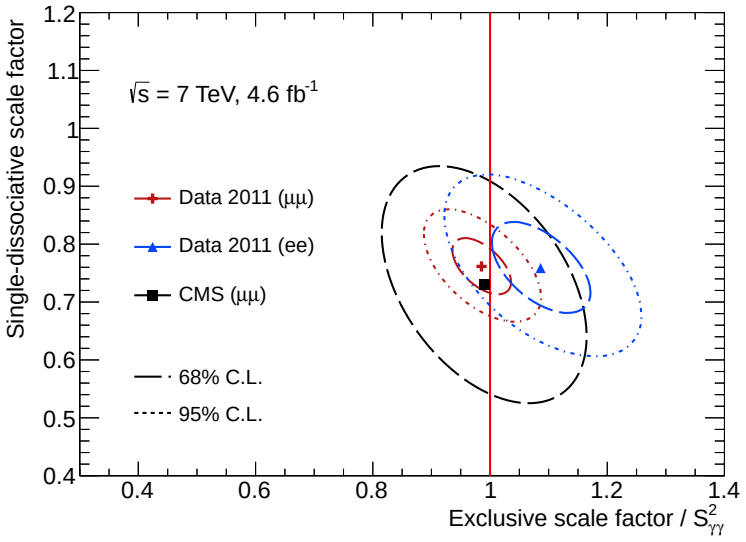

FIGURE 10.9: 68% and 95% CL contour plots for the signal vs. single-dissociative yield scale factors in the fitted parameter plane. The contours represent the statistical uncertainties on the measurement and the points indicate the best-fit values. Results for muon and electron channels are compared with the similar CMS measurement after imposing the proton absorptive correction for exclusive yield scale factor.

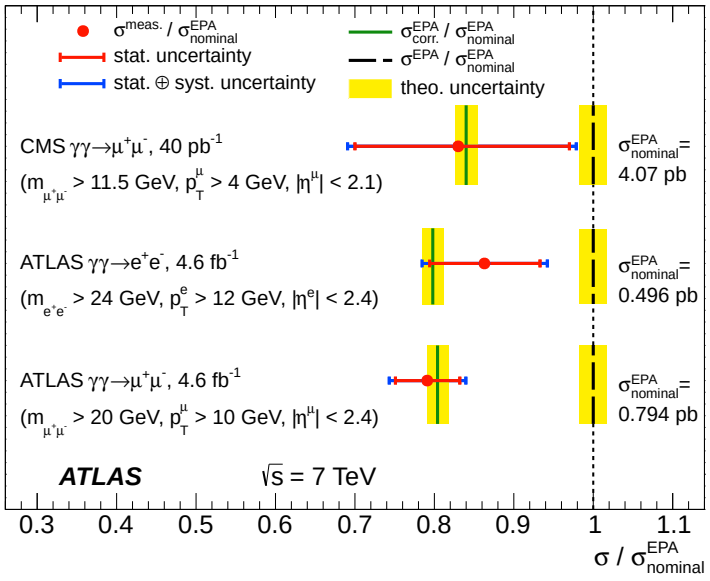

FIGURE 10.10: Comparison of the ratios of measured (red points) and predicted (solid green lines) cross sections to the uncorrected EPA calculations (black dashed lines). Results for the muon and electron channels are also compared with a similar CMS measurement [70]. The inner red error bar represents the statistical error, and the blue bar represents the total error on each measurement. The yellow band represents the theoretical uncertainty of 1.8% (1.7%) on the predicted (uncorrected EPA) cross sections, assumed to be uniform in the phase space of the measurements.

10.5 Unfolded acoplanarity distributions

In order to allow comparison of data with the external single-dissociative models, relevant acoplanarity distributions have to be corrected for detector effects. Due to the detector resolution in lepton azimuthal-angle reconstruction, the measured acoplanarity spectrum is slightly smeared causing migrations between the bins with respect to the generator-level spectrum. Figure 10.11 shows distributions of true acoplanarity over the reconstructed acoplanarity bins due to detector resolution effects. They are called the *response matrices*. Acoplanarity bins purity, defined as a fraction of the reconstructed MC events that originate from the same acoplanarity bins at the generator-level, is shown in Figure 10.12. One can observe that the effect of bin migrations is very small.

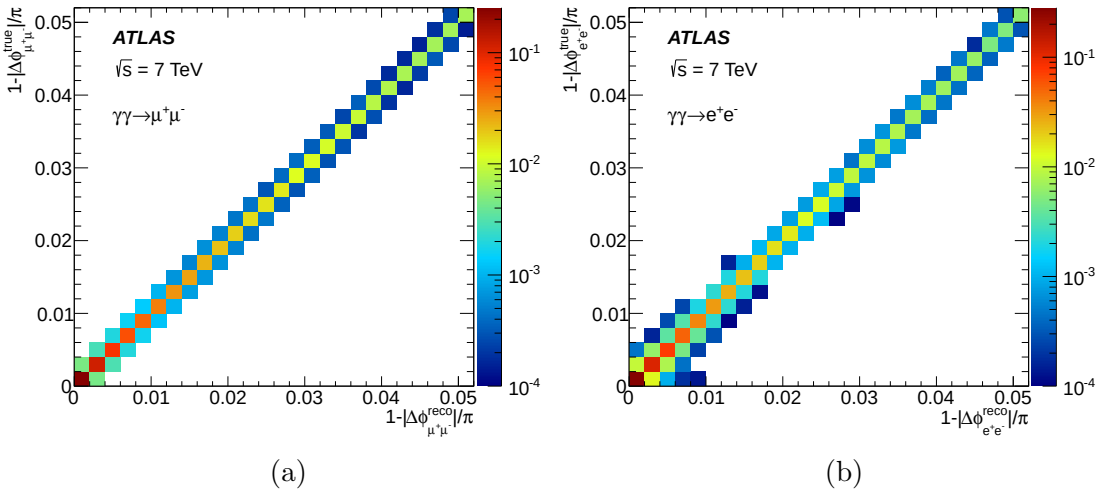

(a) (b)

FIGURE 10.11: Detector response matrix for the acoplanarity variable for (a) the muon and (b) the electron channel. The exclusive and single-dissociative MC events after all selection criteria applied are used to extract the matrices.

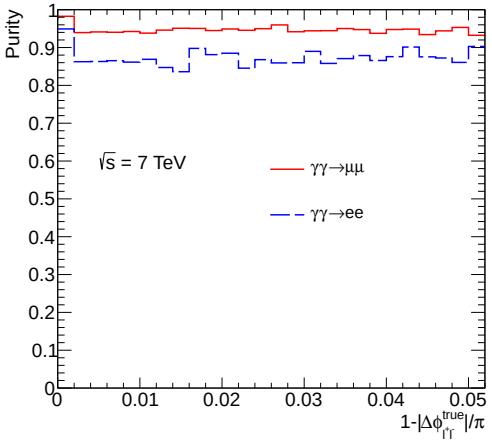

FIGURE 10.12: Acoplanarity bins purity for muon and electron channels.

The `RooUnfold` [58] package is used to perform the unfolding of acoplanarity distribution for detector resolution effects. In the unfolding procedure both exclusive and single-dissociative MC distributions are added together according to the scaling factors obtained from the fit procedure. Drell–Yan and double-dissociative $\gamma\gamma \to \ell^+\ell^-$ contributions are treated as the background processes and are subtracted from the data.

Figure 10.13 shows unfolded data acoplanarity distributions, corrected also for the lepton pair trigger, reconstruction and identification efficiencies. One can notice that it is impossible to further unfold these distributions from the effect of exclusivity veto efficiency. This is related with the precise knowledge of underlying nature of single-dissociative reactions, that remains still unknown. Obviously, to determine experimentally the detailed nature of proton-dissociative processes, one can use single-proton tagging to measure accurately the single-dissociative part. This would also give the access to the photon-PDFs of the proton - a quantities that are still poorly known at the LHC energies.

For additional information, the exclusivity veto efficiencies for signal and single-dissociative MC events are provided as a function of dilepton invariant mass $m_{\ell^+\ell^-}$ and rapidity $|y_{\ell^+\ell^-}|$, as shown in Figures 10.14 and 10.14, respectively.

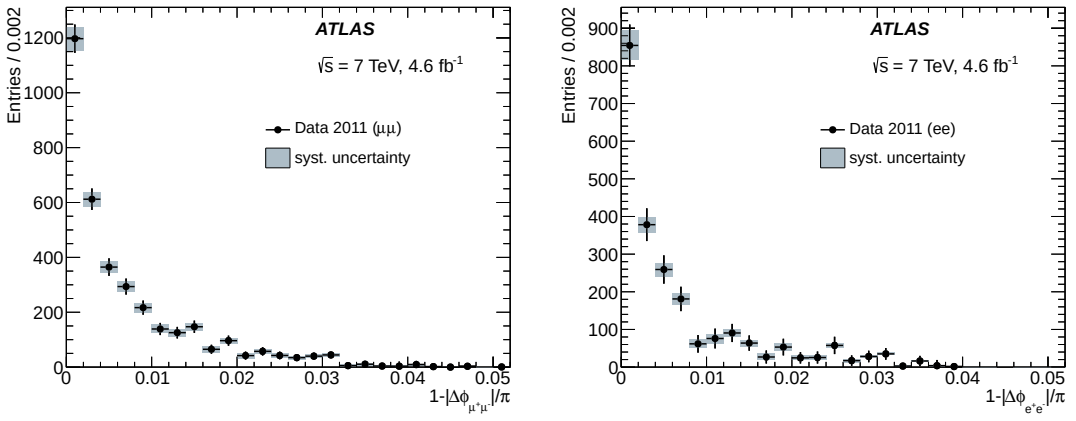

(a) (b)

FIGURE 10.13: Acoplanarity distributions for the selected data sample unfolded for detector resolution, and lepton pair trigger, reconstruction and identification efficiencies for (a) the muon and (b) the electron channel. Drell–Yan and double-dissociative background events are subtracted from the data. Statistical uncertainties are shown as bars and systematic uncertainties as dark regions.

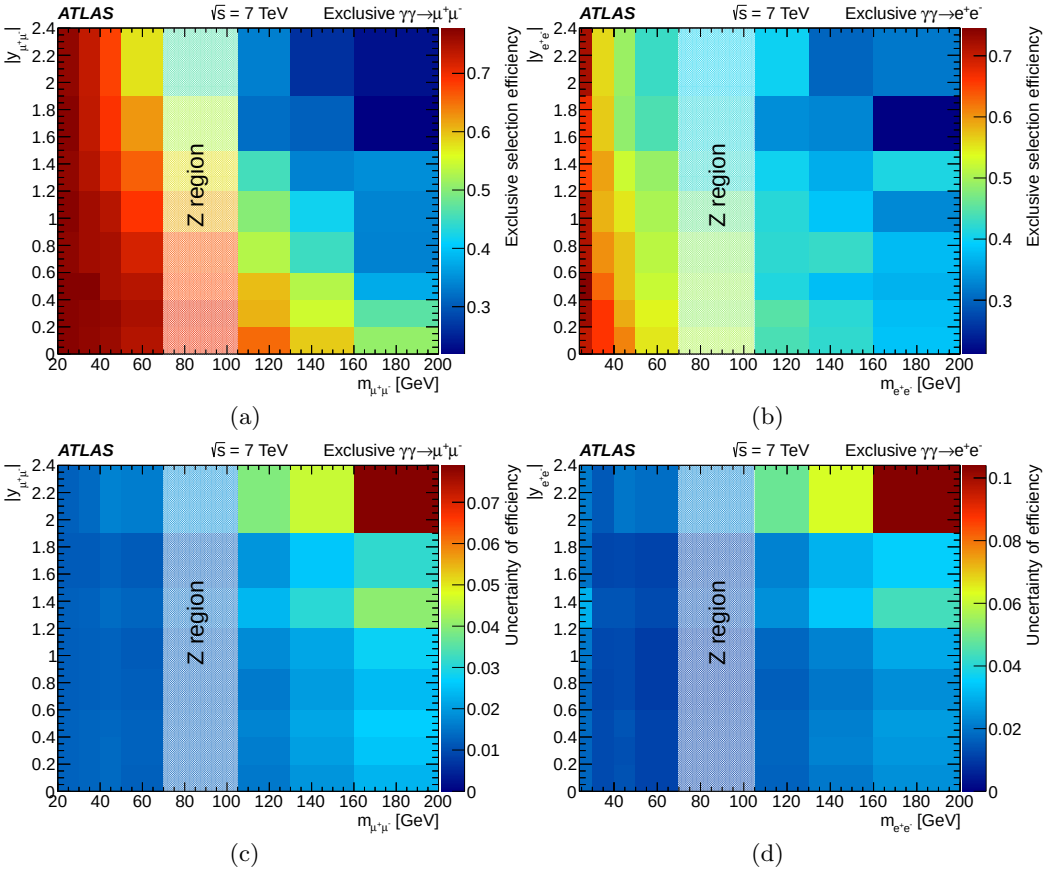

FIGURE 10.14: The lepton pair exclusive selection efficiency in the fiducial region for signal MC events as a function of $m_{\ell^+\ell^-}$ and $|y_{\ell^+\ell^-}|$ for (a) muons and (b) electrons. The efficiency includes Z region (70 GeV $< m_{\ell^+\ell^-} <$ 105 GeV) removal. The total uncertainties on these efficiencies are also shown (c, d).

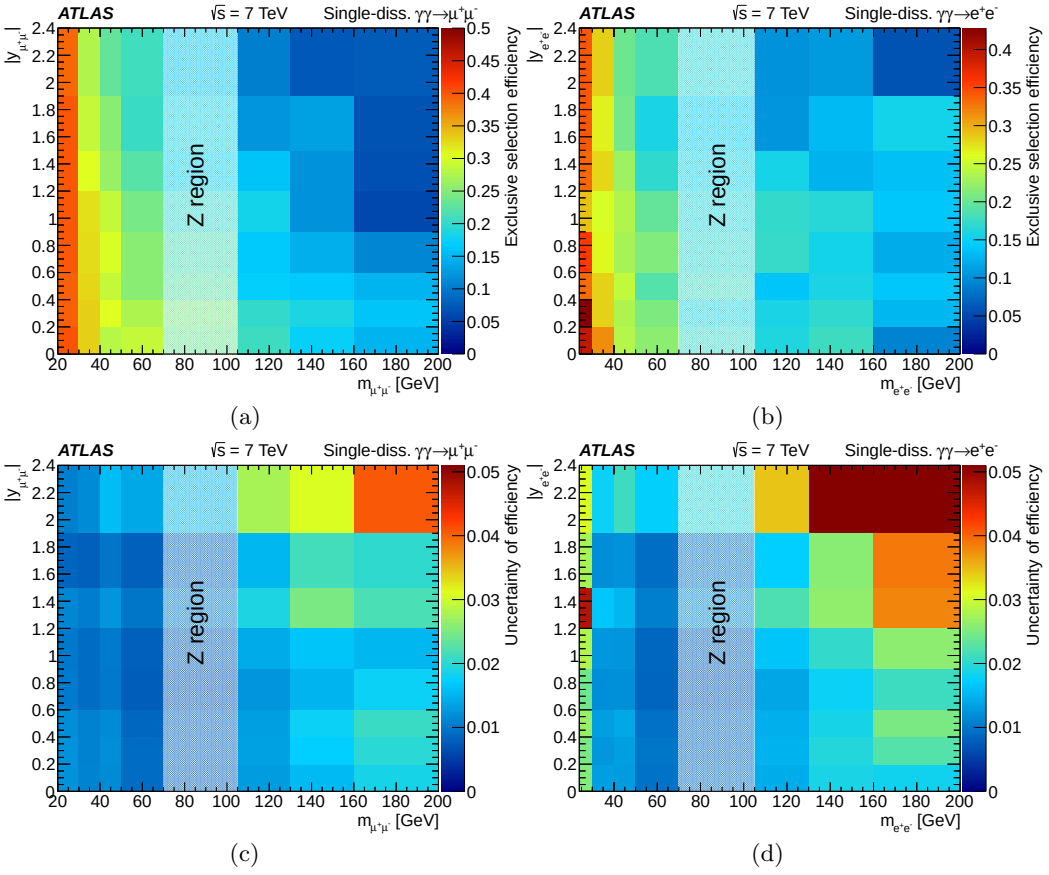

FIGURE 10.15: The lepton pair exclusive selection efficiency in the fiducial region for single-dissociative MC events as a function of $m_{\ell^+\ell^-}$ and $|y_{\ell^+\ell^-}|$ for (a) muons and (b) electrons. The efficiency includes Z region (70 GeV $< m_{\ell^+\ell^-} <$ 105 GeV) removal. The total uncertainties on these efficiencies are also shown (c, d).

Summary and conclusion

As a significant part of the thesis, measurement of exclusive $\gamma\gamma \to \ell^+\ell^-$ ($\ell = e, \mu$) production in proton–proton collisions at a center-of-mass energy of 7 TeV is presented using 4.6 fb^{-1} of data collected by the ATLAS experiment at the LHC. The exclusive production of lepton pairs represents an essential class of reactions at the LHC, mediated through photon–photon interactions. The interest of such processes is due to their well-known initial conditions and simple final state. For these reactions, it is known that the proton absorptive corrections have a sizeable impact on the predicted cross sections, encoded in what one can call the survival factor. The effect is larger when the dilepton invariant mass becomes larger. A better experimental understanding of such effects is essential for all photon–photon interactions in proton–proton collisions at the LHC energies. This is the main conclusion of the measurement detailed in this thesis.

The resulting fiducial cross section for exclusive two-photon production of muon pairs is measured to be

$$\sigma^{\text{excl.}}_{\gamma\gamma\to\mu^+\mu^-} = 0.628 \ \pm \ 0.032 \text{ (stat.)} \ \pm \ 0.021 \text{ (syst.) pb} ,$$

for $m_{\mu^+\mu^-} > 20$ GeV, $p^{\mu}_{\text{T}} > 10$ GeV and $|\eta^{\mu}| < 2.4$. This value is found to be in good agreement with the theoretical predictions, including proton absorptive corrections: $\sigma^{\text{EPA, corr.}}_{\gamma\gamma\to\mu^+\mu^-} = 0.638 \ \pm \ 0.013$ pb. For the electron channel, the fiducial cross section is measured to be

$$\sigma^{\text{excl.}}_{\gamma\gamma\to\text{e}^+\text{e}^-} = 0.428 \ \pm \ 0.035 \text{ (stat.)} \ \pm \ 0.018 \text{ (syst.) pb} ,$$

with $m_{e^+e^-} > 24$ GeV, $p^{e}_{\text{T}} > 12$ GeV, $|\eta^{e}| < 2.4$. A direct comparison to the theory predictions with absorptive corrections gives also a reasonable agreement with the uncertainties: $\sigma^{\text{EPA, corr.}}_{\gamma\gamma\to\text{e}^+\text{e}^-} = 0.398 \pm 0.007$ pb. In addition, these results are in good agreement with previous measurement of exclusive $\gamma\gamma \to \mu^+\mu^-$ production in pp collisions realized by the CMS collaboration.

A possible future improvement of the analysis can be reached using dedicated, very forward proton taggers. The AFP project promises a significant extension to the physics reach of ATLAS by tagging and measuring the momentum and emission angle of very forward protons during nominal LHC runs. This enables even more precise measurement of a range of (photon-induced) processes, where one or both protons remain intact. Here the significant work has been made in order to simulate the performance of fully integrated ATLAS+AFP detector setup. The results of theses studies were crucial for approval of the AFP project as an official ATLAS upgrade.

Bibliography

[1] T. Cornelissen et al., *Concepts, Design and Implementation of the ATLAS New Tracking (NEWT)*, ATL-SOFT-PUB-2007-007, ATL-COM-SOFT-2007-002 (2007).

[2] R. E. Kalman, *A New Approach to Linear Filtering and Prediction Problems*, Trans. of the ASME–Journal of Basic Engineering **82D** (1960) 35–45.

[3] R. Fruhwirth, *Application of Kalman filtering to track and vertex fitting*, Nucl. Instrum. Meth. **A262** (1987) 444–450.

[4] P. F. Akesson et al., *ATLAS Tracking Event Data Model*, ATL-SOFT-PUB-2006-004, ATL-COM-SOFT-2006-005 (2006).

[5] R. Fruhwirth, W. Waltenberger and P. Vanlaer, *Adaptive vertex fitting*, J. Phys. **G34** (2007) N343.

[6] ATLAS Collaboration, *Characterization of Interaction-Point Beam Parameters Using the pp Event-Vertex Distribution Reconstructed in the ATLAS Detector at the LHC*, ATLAS-CONF-2010-027, ATLAS-COM-CONF-2010-027 (2010).

[7] ATLAS Experiment Beamspot Public Results. `twiki.cern.ch/twiki/bin/view/AtlasPublic/BeamSpotPublicResults`.

[8] ATLAS Experiment Luminosity Public Results. `twiki.cern.ch/twiki/bin/view/AtlasPublic/LuminosityPublicResults`.

[9] ATLAS Collaboration, *Measurement of the underlying event in jet events from 7 TeV proton-proton collisions with the ATLAS detector*, Eur. Phys. J. **C74** no. 8, (2014) 2965, `arXiv:1406.0392 [hep-ex]`.

[10] ATLAS Collaboration, *Measurement of distributions sensitive to the underlying event in inclusive Z-boson production in pp collisions at* $\sqrt{s} = 7$ *TeV with the ATLAS detector*, Eur. Phys. J. **C74** no. 12, (2014) 3195, `arXiv:1409.3433 [hep-ex]`.

[11] ATLAS Collaboration, *Measurement of the muon reconstruction performance of the ATLAS detector using 2011 and 2012 LHC proton-proton collision data*, Eur. Phys. J. **C74** no. 11, (2014) 3130, arXiv:1407.3935 [hep-ex].

[12] S. Hassani et al., *A muon identification and combined reconstruction procedure for the ATLAS detector at the LHC using the (MUONBOY, STACO, MuTag) reconstruction packages*, Nucl. Instrum. Meth. **A572** (2007) 77–79.

[13] ATLAS Collaboration, *Electron performance measurements with the ATLAS detector using the 2010 LHC proton-proton collision data*, Eur. Phys. J. **C72** (2012) 1909, arXiv:1110.3174 [hep-ex].

[14] ATLAS Collaboration, *Electron reconstruction and identification efficiency measurements with the ATLAS detector using the 2011 LHC proton-proton collision data*, Eur. Phys. J. **C74** (2014) 2941, arXiv:1404.2240 [hep-ex].

[15] R. Frühwirth, *Track fitting with nonGaussian noise*, Comput. Phys. Commun. **100** (1997) 1–16.

[16] ATLAS Collaboration, *Improved electron reconstruction in ATLAS using the Gaussian Sum Filter-based model for bremsstrahlung*, ATLAS-CONF-2012-047, ATLAS-COM-CONF-2012-068 (2012).

[17] ATLAS Collaboration, *ATLAS first level trigger: Technical design report*, CERN-LHCC-98-14, ATLAS-TDR-12 (1998).

[18] ATLAS Collaboration, *ATLAS high-level trigger, data acquisition and controls: Technical design report*, CERN-LHCC-2003-022, ATLAS-TRD-016 (2003).

[19] ATLAS Collaboration, *Improved luminosity determination in pp collisions at $\sqrt{s} = 7$ TeV using the ATLAS detector at the LHC*, Eur. Phys. J. **C73** (2013) 2518, arXiv:1302.4393 [hep-ex].

[20] S. van der Meer, *Calibration of the Effective Beam Height in the ISR*, CERN-ISR-PO-68-31 (1968).

[21] C. Rubbia, *Measurement of the luminosity of $p\overline{p}$ collider with a (generalized) Van der Meer Method*, Tech. Rep. CERN-$p\overline{p}$-Note-38, 1977.

[22] M. Bähr et al., *Herwig++ Physics and Manual*, Eur. Phys. J. **C58** (2008) 639–707, arXiv:0803.0883 [hep-ph].

[23] J. Vermaseren, *Two Photon Processes at Very High-Energies*, Nucl. Phys. **B229** (1983) 347.

[24] S. Baranov et al., *LPAIR: A generator for lepton pair production*, Proc. of Phys. at HERA (1991) 1478.

[25] A. Suri and D. R. Yennie, *The space-time phenomenology of photon absorption and inelastic electron scattering*, Annals Phys. **72** no. 1, (1972) 243 – 292.

[26] F. Brasse et al., *Parametrization of the q^2 dependence of $\gamma_V p$ total cross sections in the resonance region*, Nucl. Phys. **B110** (1976) 413.

[27] T. Sjöstrand, *High-energy physics event generation with PYTHIA 5.7 and JETSET 7.4*, Comput. Phys. Commun. **82** (1994) 74–90.

[28] B. Andersson et al., *Parton Fragmentation and String Dynamics*, Phys. Rept. **97** (1983) 31–145.

[29] T. Sjöstrand, S. Mrenna and P. Z. Skands, *A Brief Introduction to PYTHIA 8.1*, Comput. Phys. Commun. **178** (2008) 852–867, arXiv:0710.3820 [hep-ph].

[30] NNPDF Collaboration (R. D. Ball et al.), *Parton distributions with QED corrections*, Nucl. Phys. **B877** (2013) 290–320, arXiv:1308.0598 [hep-ph].

[31] R. Corke and T. Sjöstrand, *Multiparton Interactions and Rescattering*, JHEP **1001** (2010) 035, arXiv:0911.1909 [hep-ph].

[32] P. Nason, *A New method for combining NLO QCD with shower Monte Carlo algorithms*, JHEP **0411** (2004) 040, arXiv:hep-ph/0409146 [hep-ph].

[33] S. Frixione, P. Nason and C. Oleari, *Matching NLO QCD computations with Parton Shower simulations: the POWHEG method*, JHEP **0711** (2007) 070, arXiv:0709.2092 [hep-ph].

[34] S. Alioli et al., *NLO vector-boson production matched with shower in POWHEG*, JHEP **0807** (2008) 060, arXiv:0805.4802 [hep-ph].

[35] H.-L. Lai et al., *New parton distributions for collider physics*, Phys. Rev. **D82** (2010) 074024, arXiv:1007.2241 [hep-ph].

[36] T. Sjöstrand, S. Mrenna and P. Z. Skands, *PYTHIA 6.4 Physics and Manual*, JHEP **0605** (2006) 026, arXiv:hep-ph/0603175 [hep-ph].

[37] J. Pumplin et al., *New generation of parton distributions with uncertainties from global QCD analysis*, JHEP **0207** (2002) 012, arXiv:hep-ph/0201195 [hep-ph].

[38] ATLAS Collaboration, *ATLAS tunes of PYTHIA 6 and Pythia 8 for MC11*, Tech. Rep. ATL-PHYS-PUB-2011-009, 2011.

[39] A. Sherstnev and R. Thorne, *Parton Distributions for LO Generators*, Eur. Phys. J. **C55** (2008) 553–575, arXiv:0711.2473 [hep-ph].

[40] S. Frixione and B. R. Webber, *Matching NLO QCD computations and parton shower simulations*, JHEP **0206** (2002) 029, arXiv:hep-ph/0204244 [hep-ph].

[41] S. Frixione, P. Nason and B. R. Webber, *Matching NLO QCD and parton showers in heavy flavor production*, JHEP **0308** (2003) 007, arXiv:hep-ph/0305252 [hep-ph].

[42] G. Corcella et al., *HERWIG 6.5 release note*, arXiv:hep-ph/0210213 [hep-ph].

[43] P. Golonka and Z. Was, *PHOTOS Monte Carlo: A Precision tool for QED corrections in Z and W decays*, Eur. Phys. J. **C45** (2006) 97–107, arXiv:hep-ph/0506026 [hep-ph].

[44] C. Anastasiou et al., *High precision QCD at hadron colliders: Electroweak gauge boson rapidity distributions at NNLO*, Phys. Rev. **D69** (2004) 094008, arXiv:hep-ph/0312266 [hep-ph].

[45] R. Gavin et al., *FEWZ 2.0: A code for hadronic Z production at next-to-next-to-leading order*, Comput. Phys. Commun. **182** (2011) 2388–2403, arXiv:1011.3540 [hep-ph].

[46] A. Martin et al., *Parton distributions for the LHC*, Eur. Phys. J. **C63** (2009) 189–285, arXiv:0901.0002 [hep-ph].

[47] M. Czakon and A. Mitov, *Top++: A Program for the Calculation of the Top-Pair Cross-Section at Hadron Colliders*, Comput. Phys. Commun. **185** (2014) 2930, arXiv:1112.5675 [hep-ph].

[48] M. Czakon and A. Mitov, *NNLO corrections to top-pair production at hadron colliders: the all-fermionic scattering channels*, JHEP **1212** (2012) 054, arXiv:1207.0236 [hep-ph].

[49] M. Czakon, P. Fiedler and A. Mitov, *Total Top-Quark Pair-Production Cross Section at Hadron Colliders Through* $O(\alpha_S^4)$, Phys. Rev. Lett. **110** (2013) 252004, arXiv:1303.6254 [hep-ph].

[50] J. M. Campbell, R. K. Ellis and D. L. Rainwater, *Next-to-leading order QCD predictions for W + 2 jet and Z + 2 jet production at the CERN LHC*, Phys. Rev. **D68** (2003) 094021, arXiv:hep-ph/0308195 [hep-ph].

[51] ATLAS Collaboration, *Measurement of the transverse momentum distribution of* Z/γ^* *bosons in proton-proton collisions at* $\sqrt{s} = 7$ *TeV with the ATLAS detector*, Phys. Lett. **B705** (2011) 415–434, arXiv:1107.2381 [hep-ex].

[52] F. Landry et al., *Tevatron Run-1 Z boson data and Collins-Soper-Sterman resummation formalism*, Phys. Rev. **D67** (2003) 073016, arXiv:hep-ph/0212159 [hep-ph].

[53] ATLAS Collaboration, *Measurement of angular correlations in Drell-Yan lepton pairs to probe Z/γ^* boson transverse momentum at $\sqrt{s} = 7$ TeV with the ATLAS detector*, Phys. Lett. **B720** (2013) 32–51, arXiv:1211.6899 [hep-ex].

[54] ATLAS Collaboration, *Measurement of the Z/γ^* boson transverse momentum distribution in pp collisions at $\sqrt{s} = 7$ TeV with the ATLAS detector*, JHEP **1409** (2014) 145, arXiv:1406.3660 [hep-ex].

[55] ATLAS Collaboration, *Measurement of the low-mass Drell-Yan differential cross section at $\sqrt{s} = 7$ TeV using the ATLAS detector*, JHEP **1406** (2014) 112, arXiv:1404.1212 [hep-ex].

[56] ATLAS Collaboration, *Measurement of the production cross section of jets in association with a Z boson in pp collisions at $\sqrt{s} = 7$ TeV with the ATLAS detector*, JHEP **1307** (2013) 032, arXiv:1304.7098 [hep-ex].

[57] ATLAS Collaboration, *Electron and photon energy calibration with the ATLAS detector using LHC Run 1 data*, Eur. Phys. J. **C74** no. 10, (2014) 3071, arXiv:1407.5063 [hep-ex].

[58] T. Adye, *Unfolding algorithms and tests using RooUnfold*, arXiv:1105.1160 [physics.data-an].

[59] F. James and M. Roos, *Minuit - a system for function minimization and analysis of the parameter errors and correlations*, Comput. Phys. Commun. **10** no. 6, (1975) 343 – 367.

[60] ATLAS Collaboration, *Muon reconstruction efficiency in reprocessed 2010 LHC proton-proton collision data recorded with the ATLAS detector*, Tech. Rep. ATLAS-CONF-2011-063, 2011.

[61] ATLAS Collaboration, *Charged-particle multiplicities in pp interactions measured with the ATLAS detector at the LHC*, New J. Phys. **13** (2011) 053033, arXiv:1012.5104 [hep-ex].

[62] M. Boonekamp et al., *FPMC: A Generator for forward physics*, arXiv:1102.2531 [hep-ph].

[63] J. Bjorken, *Rapidity gaps and jets as a new physics signature in very high-energy hadron hadron collisions*, Phys. Rev. **D47** (1993) 101–113.

[64] ATLAS Collaboration, *Simultaneous measurements of the $t\bar{t}$, W^+W^-, and $Z/\gamma^* \to \tau\tau$ production cross-sections in pp collisions at $\sqrt{s} = 7$ TeV with the ATLAS detector*, Phys. Rev. **D91** (2015) 052005, arXiv:1407.0573 [hep-ex].

[65] M. Belushkin, H.-W. Hammer and U.-G. Meissner, *Dispersion analysis of the nucleon form-factors including meson continua*, Phys. Rev. **C75** (2007) 035202, arXiv:hep-ph/0608337 [hep-ph].

[66] ATLAS Collaboration, *The ATLAS Inner Detector commissioning and calibration*, Eur. Phys. J. **C70** (2010) 787–821, arXiv:1004.5293 [physics.ins-det].

[67] A. Denner and S. Dittmaier, *Production of light fermion anti-fermion pairs in gamma gamma collisions*, Eur. Phys. J. **C9** (1999) 425–435, arXiv:hep-ph/9812411 [hep-ph].

[68] H1 Collaboration (F. D. Aaron et al.), *Deeply Virtual Compton Scattering and its Beam Charge Asymmetry in $e^{\pm}p$ Collisions at HERA*, Phys. Lett. **B681** (2009) 391–399, arXiv:0907.5289 [hep-ex].

[69] T. H. Kittelmann et al., *The virtual point 1 event display for the ATLAS experiment*, J. Phys. Conf. Ser. **219** (2010) 032012.

[70] CMS Collaboration, *Exclusive photon-photon production of muon pairs in proton-proton collisions at $\sqrt{s} = 7$ TeV*, JHEP **1201** (2012) 052, arXiv:1111.5536 [hep-ex].

Appendix A

Summary in French

Introduction

Une fraction importante des collisions proton–proton à haute énergie au LHC (*Large Hadron Collider*) impliquent des réactions médiées par des photons. Cette fraction est dominée par des collisions élastiques avec un seul photon échangé lors de la réaction proton–proton. Des photons quasi-réels peuvent aussi être émis par chacun des deux protons. Ces photons peuvent ensuite interagir pour générer une large variété d'états finals. Pour ces processus, les collisions proton–proton peuvent ainsi être considérées comme des collisions photon–photon. Au LHC, ce type de réactions peut être étudiée expérimentalement avec une bonne précision.

Ce travail de thèse présente ma contribution dans le développement de la compréhension des processus photon–photon à haute énergie en utilisant les données du LHC. La thèse est divisée en trois grandes parties. Ce document est une synthèse en langue française, évidemment courte, qui reprend les résultats importants du travail de thèse. Les différentes étapes des analyses n'y sont que brièvement mentionnées. L'ensemble du travail est décrit beaucoup plus largement dans la thèse originale en langue anglaise.

La partie 1 décrit le LHC et ses principales caractéristiques. Je détaille particulièrement les détecteurs dits à l'avant, en particulier le projet AFP (ATLAS forward proton). Ces détecteurs permettent de mesurer la trajectoire des protons issus de la collision (primaire) proton–proton lorsque ceux-ci ressortent quasiment intacts de cette collision. C'est le cas lorsque les deux protons émettent des photons, lesquels interagissent ensuite dans une réaction photon–photon. Mon travail de qualification en tant qu'auteur de ALTAS a consisté dans l'écriture du code de simulation pour les détecteurs AFP.

La partie 2 contient une introduction théorique. En plus d'une présentation rapide du Modèle Standard de la physique des particules, le cadre théorique des interactions photon–photon en collisions proton–proton est expliqué. En particulier, un aspect délicat est discuté en détail: il concerne les effets de taille finie du proton (autrement appelées corrections d'absorption). Cette étude a constitué l'une de mes contributions à cette physique au travers d'une publication théorique.

La partie 3 décrit les résultat de la mesure expérimentale de la production exclusive de paires de leptons lors d'une collision photon–photon au LHC, avec toutes les données accumulées en 2011 par l'expérience ATLAS, à une énergie dans le centre de masse de $\sqrt{s} = 7$ TeV. J'ai conduit cette analyse au sein de la collaboration. Avec une luminosité de 4.6 fb^{-1}, les sections efficaces fiducielles de la production exclusive de paires de leptons on été mesurées et comparées aux prédictions théoriques, telles que décrites dans la partie 2.

Tous ces travaux ont été publiés:

- ATLAS Collaboration (G. Aad et al.), *Measurement of exclusive $\gamma\gamma \to \ell^+\ell^-$ production in proton–proton collisions at $\sqrt{s} = 7$ TeV with the ATLAS detector*, Phys. Lett. B749 (2015) 242-261.
- M. Dyndal and L. Schoeffel, *The role of finite-size effects on the spectrum of equivalent photons in proton–proton collisions at the LHC*, Phys. Lett. B741 (2015) 66-70.
- ATLAS Collaboration (G. Aad et al.), *Technical Design Report for the ATLAS Forward Proton Detector*, CERN-LHCC-2015-009; ATLAS-TDR-024.
- M. Dyndal (on behalf of the ATLAS Collaboration), *Standard Model measurements with ATLAS*, The XXII International Workshop High Energy Physics and Quantum Field Theory, 24 Jun – 01 Jul 2015, Samara, Russia, ATL-PHYS-SLIDE-2015-353.
- M. Dyndal (on behalf of the ATLAS Collaboration), *The tracking system of the AFP detector*, 2$^{\text{nd}}$ Workshop on Detectors for Forward Physics at LHC, 28–30 May 2014, La Biodola, Isola d'Elba, Italy, ATL-FWD-SLIDE-2014-231.

Partie 1

L'expérience ATLAS au LHC

Le LHC *Large Hadron Collider* [1] est actuellement le plus grand et le plus puissant accélérateur au monde. Il est situé au CERN, à coté de Genève, au voisinage des frontières suisse et française.

C'est un collisionneur circulaire de protons placé à 40–170 m sous la surface du sol, logé dans un tunnel de 27 km de circonférence, construit à l'origine pour les expériences du LEP [2], conduites entre 1989 et 2000. Le LHC peut produire des collisions de protons jusqu'à une énergie dans le centre de masse de $\sqrt{s} = 14$ TeV avec une luminosité instantanée de 10^{34} cm^{-2}s^{-1}. De plus, il permet aussi de réaliser des collisions entre ions lourds.

Le complexe d'accélérateurs du CERN est représenté sur la figure 1.1. Le LHC en est le dernier élément.

L'expérience ATLAS (*A Toroidal LHC ApparatuS*) [3] est l'une des expériences de physique des particules installée sur l'anneau du LHC. Sa conception est usuelle pour ce type d'expérience avec des détecteurs de traces, des calorimètres, des chambres à muons etc. Une représentation schématique est illustrée sur la figure 1.3.

L'expérience ATLAS dispose de plusieurs sous-détecteurs localisés à grand angle (dans le système de référence de ATLAS), dans la direction de vol des protons. Ces détecteurs sont par nature dédiés à la mesure des trajectoires des protons lorsque ceux-ci resortent quasiment intacts de la collision proton–proton. La couverture angulaire de ces détecteurs est illustrée sur la figure 1.2.

Mon travail de qualification en tant qu'auteur de ATLAS a été dédié à la simulation d'un groupe de ces détecteurs à l'avant, le projet AFP (*ATLAS Forward Proton*) [9], dont l'installation est prévue à la fin de l'année 2015 pour une première prise de données en

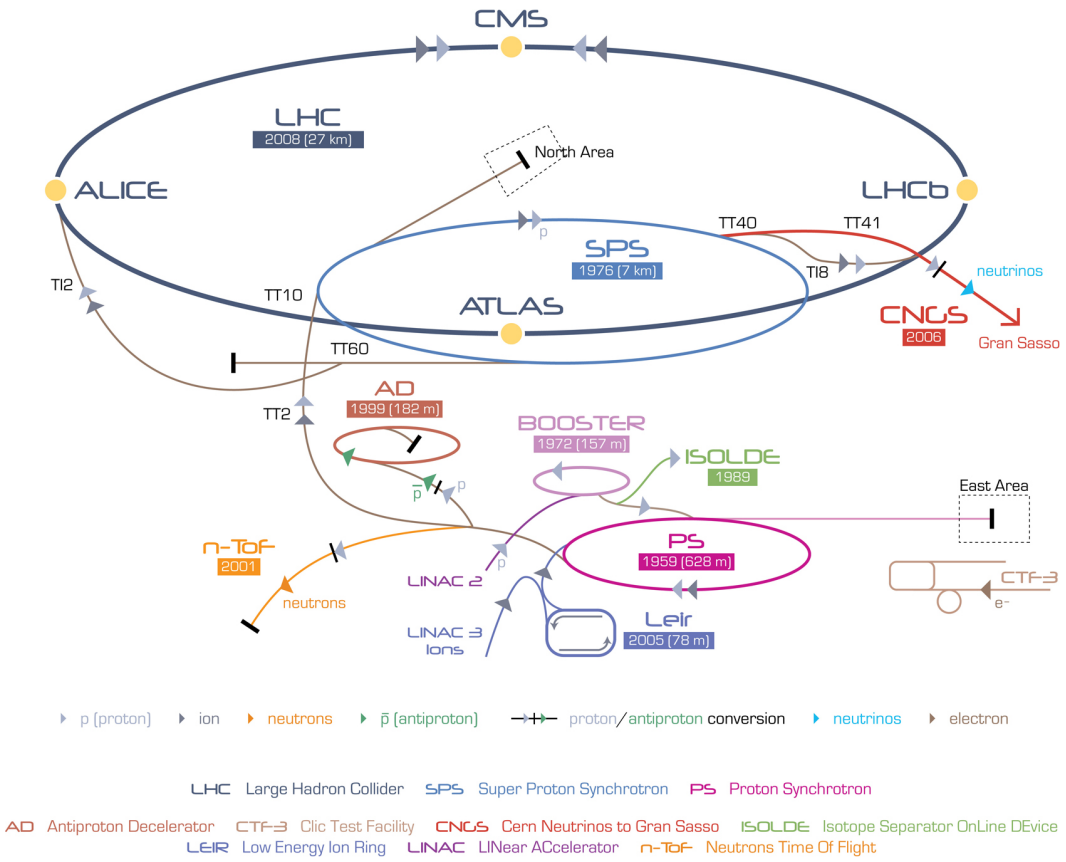

FIGURE 1.1

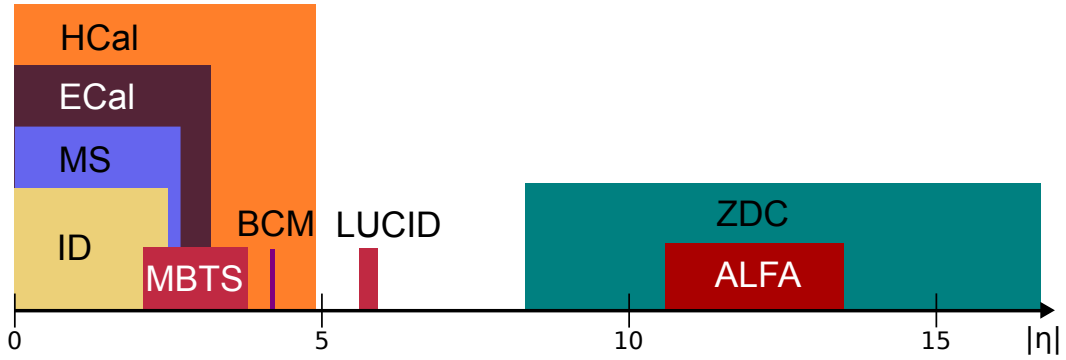

FIGURE 1.2

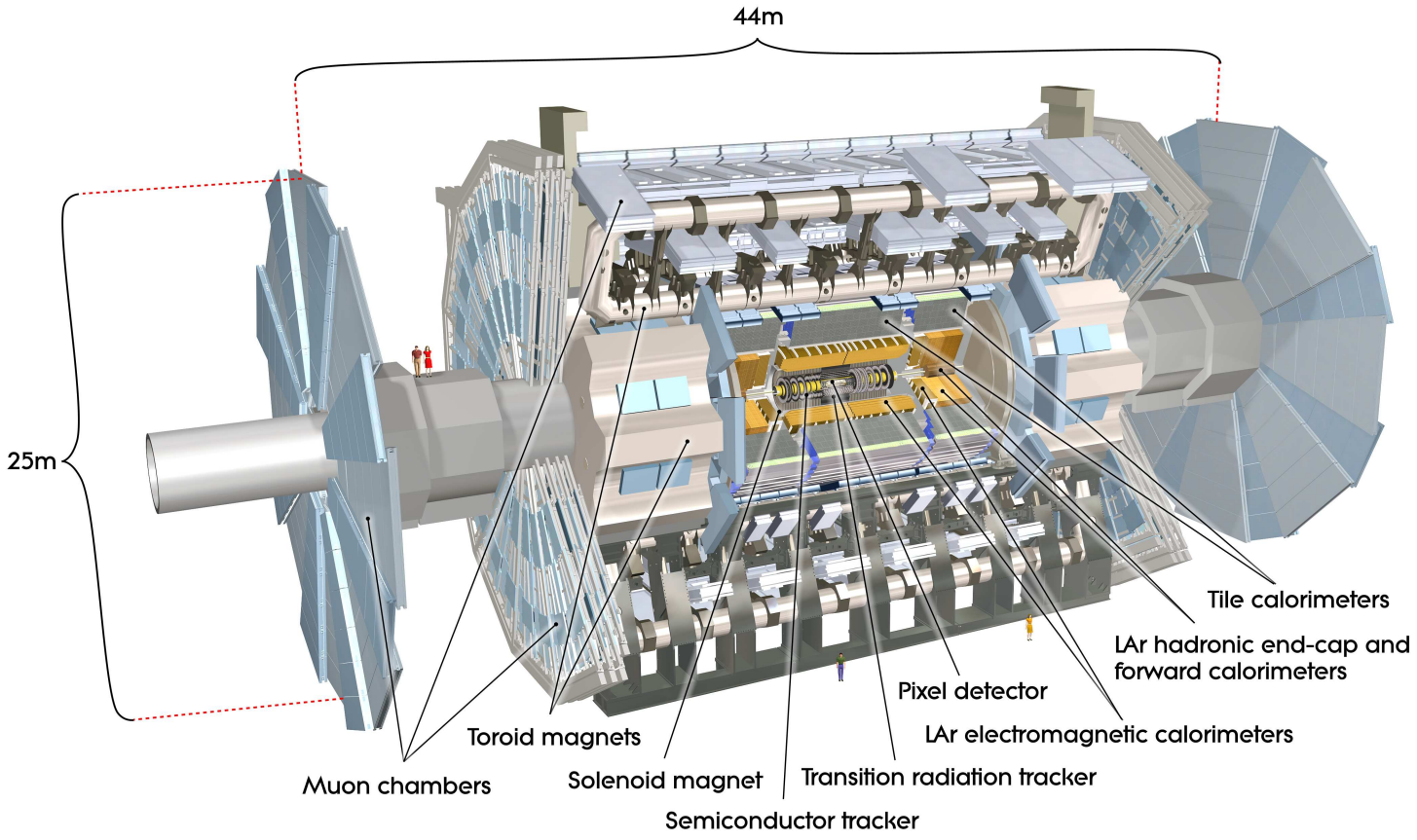
44m
25m
Tile calorimeters
LAr hadronic end-cap and
forward calorimeters
Pixel detector
LAr electromagnetic calorimeters
Toroid magnets
Muon chambers
Solenoid magnet
Transition radiation tracker
Semiconductor tracker

FIGURE 1.3

2016. Ces détecteurs sont indiqués sur la figure 1.4, où l'on peut voir leurs positions par rapport à l'ensembe des autres composants dits à l'avant de ATLAS (dans la direction de vol des protons).

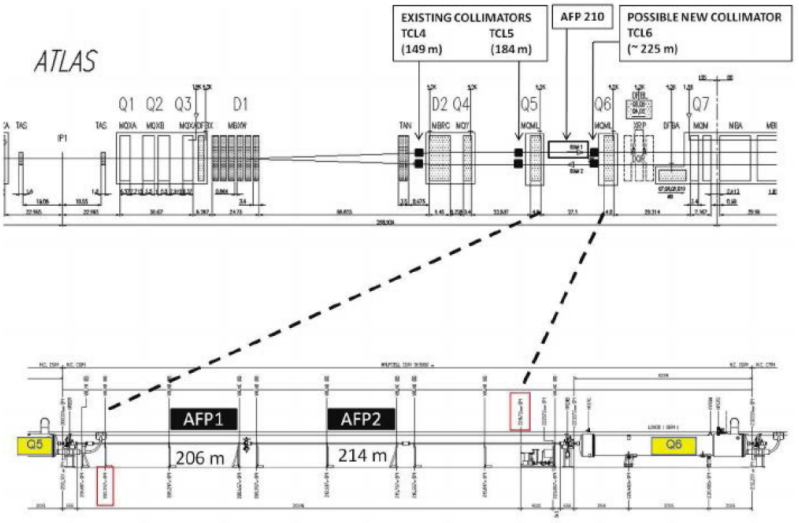

FIGURE 1.4

Ci-dessous, un résultat de ce travail sur la simulation des détecteurs AFP. La figure 1.5 présente un histogramme 2D des positions en x, y pour les traces des protons dans les stations AFP (à 212 m) avant et après sélection d'une bonne trace.

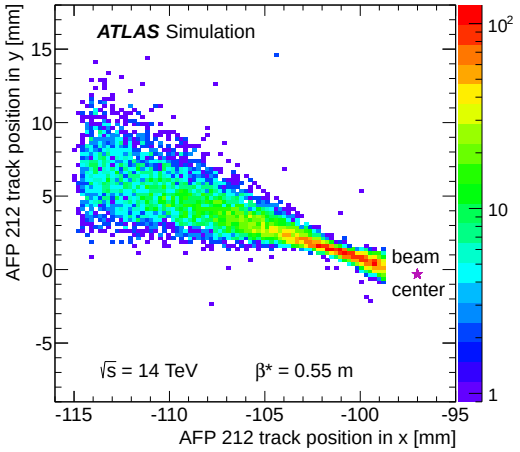

FIGURE 1.5

Bibliographie

[1] L. Evans and P. Bryant, *LHC Machine*, JINST **3** (2008) S08001.

[2] R. Assmann, M. Lamont and S. Myers, *A brief history of the LEP collider*, Nucl. Phys. Proc. Suppl. **109B** (2002) 17–31.

[3] ATLAS Collaboration, *The ATLAS Experiment at the CERN Large Hadron Collider*, JINST **3** (2008) S08003.

[4] P. Jenni and M. Nessi, *ATLAS Forward Detectors for Luminosity Measurement and Monitoring*, Tech. Rep. CERN-LHCC-2004-010, 2004.

[5] ATLAS Collaboration, *Zero degree calorimeters for ATLAS*, Tech. Rep. CERN-LHCC-2007-01, 2007.

[6] ATLAS Collaboration, *ATLAS Forward Detectors for Measurement of Elastic Scattering and Luminosity*, Tech. Rep. CERN-LHCC-2008-004, ATLAS-TDR-18, 2008.

[7] V. Cindro et al., *The ATLAS beam conditions monitor*, JINST **3** (2008) P02004.

[8] ATLAS Collaboration, *Performance of the Minimum Bias Trigger in p-p Collisions at* $\sqrt{s} = 7$ *TeV*, Tech. Rep. ATLAS-CONF-2010-068, 2010.

[9] ATLAS Collaboration, *Technical Design Report for the ATLAS Forward Proton Detector*, Tech. Rep. CERN-LHCC-2015-009, ATLAS-TDR-024, 2015.

Partie 2

Eléments théoriques

Le Modèle Standard

Le Modèle Standard (MS) de la physique des particules est la théorie la plus complète qui résume notre compréhension des constituants fondamentaux de la matière et de leurs interactions. Les forces fondamentales décrites par la théorie sont la force électromagnétique, la force faible et la force forte. Le MS est une théorie quantique relativiste des champs, c'est-à-dire qu'il associe les principes fondamentaux de la mécanique quantique avec ceux de la relativité restreinte. Notons que la gravité est la seule force fondamentale non incluse dans le MS. Il n'y a actuellement pas de théorie quantique pleinement satisfaisante de gravité.

Dans ce résumé de la thèse, je ne rentre pas plus avant dans la description des particules et de leurs interactions. Rappelons simplement que le MS a été étudié expérimentalement avec une très grande précision, voir par exemple [1]. Au LHC, en plus de la découverte du boson de Higgs, de nombreuses mesures ont été effectuées pour tester la compatibilité des mesures expérimentales avec le MS. Elles sont résumées dans la figure 2.1.

Interactions photon–photon au LHC

Les interactions photon–photon ($\gamma\gamma$) au LHC peuvent être rangées dans la classe des processus pour lesquels les photons sont émis à partir des deux particules chargées relativistes qui entrent en collision, les deux protons dans le cas du LHC. Le proton qui émet un photon peut rester quasiment intact et, dans cette hypothèse, il est diffusé

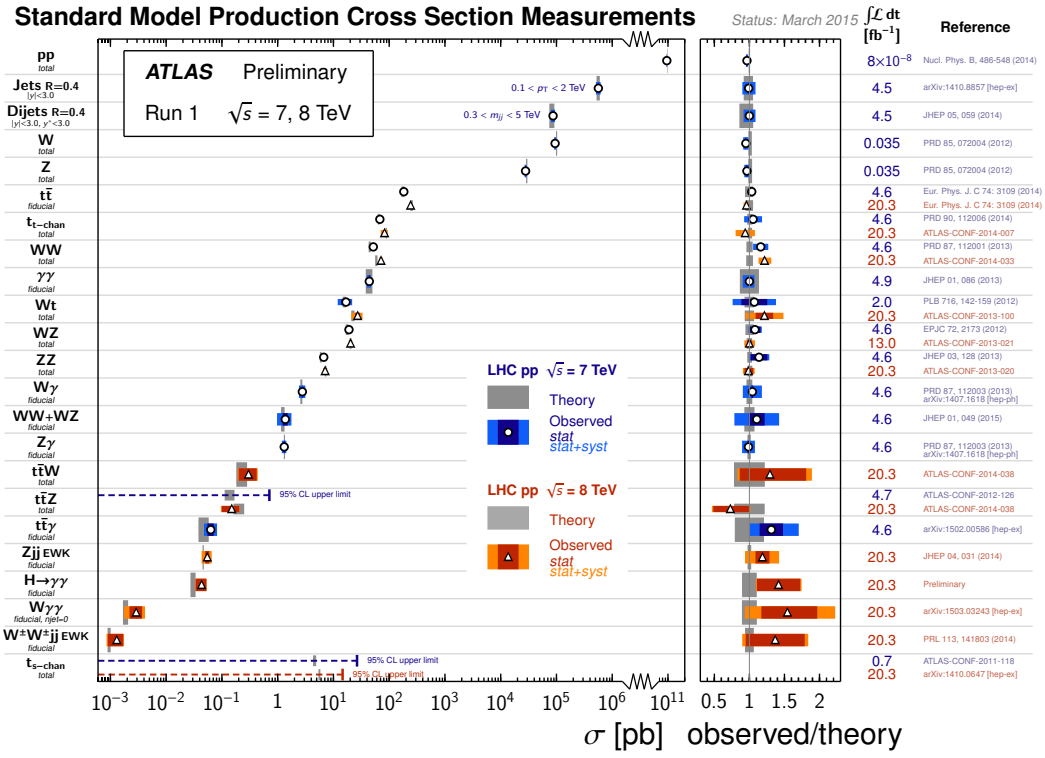

FIGURE 2.1

dans sa ligne de vol (émission élastique), ou bien ce proton peut se dissocier en un état hadronique (émission inélastique). Un seul ou les deux protons peuvent subir une dissociation inélastique lors d'une collision. Si les deux protons sont émis élastiquement (i.e. qu'ils restent intacts lors de la collisions) on parle de processus exclusif. Ces différentes possibilités sont représentées sur la figure 2.2. Ensuite, c'est une interaction photon-photon qui se produit, pour donner un ensemble de particules que l'on note collectivement X. De plus, la section efficace du processus microscopique $\gamma\gamma \to X$ peut être calculée dans le cadre de la théorie électrofaible (Modèle Standard).

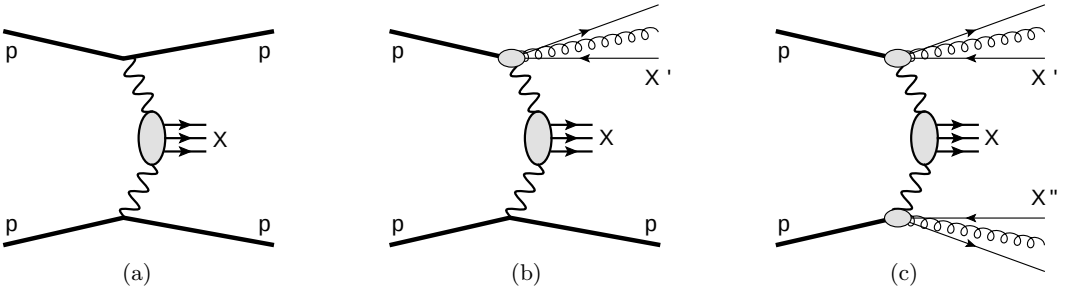

FIGURE 2.2

Les réactions les plus simples dans les catégories ci-dessus concernent la production de paires de leptons chargés (électrons ou muons) [3–5]. On peut écrire leurs sections efficaces comme:

$$\sigma(\gamma\gamma \to \ell^+\ell^-) = \frac{4\pi\alpha_{em}^2}{W_{\gamma\gamma}^2}\left[\left(1+\frac{4m_\ell^2}{W_{\gamma\gamma}^2}-\frac{8m_\ell^4}{W_{\gamma\gamma}^4}\right)2\ln\left(\frac{W_{\gamma\gamma}}{2m_\ell}+\sqrt{\frac{W_{\gamma\gamma}^2}{4m_\ell^2}-1}\right)\right.$$
$$\left.-\left(1+\frac{4m_\ell^2}{W_{\gamma\gamma}^2}\right)\sqrt{1-\frac{4m_\ell^2}{W_{\gamma\gamma}^2}}\right]\Theta\left(W_{\gamma\gamma}^2-4m_\ell^2\right)\ , \qquad (2.1)$$

où m_ℓ est la masse du lepton et $W_{\gamma\gamma}$ la masse invariante du système photon–photon. Cette relation (2.1) inclus les diagrammes à l'ordre dominant illustrés sur la figure 2.3.

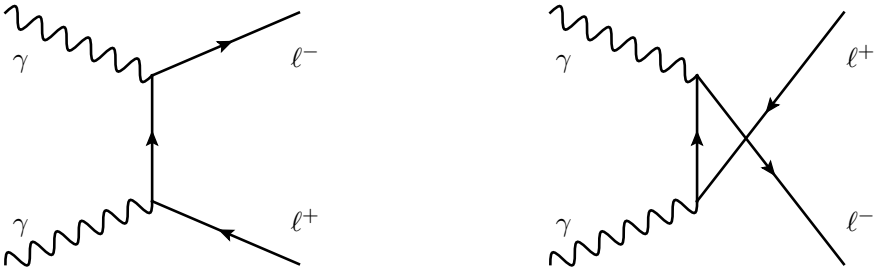

FIGURE 2.3

Une complication intervient lorsque l'on doit prendre en compte le fait que le proton est de taille finie (au contraire d'un lepton qui est un constituant élémentaire ponctuel). Alors, la section efficace ci-dessus (2.1) doit être modifiée. En pratique, cela revient à la multiplier par un terme (dit de suppression) qui s'écrit comme suit en fonction des nombres de photons équivalents pour chaque proton:

$$S_{\gamma\gamma}^2 = \frac{\int_{b_1>r_p}\int_{b_2>r_p} \mathrm{d}^2\vec{b}_1\mathrm{d}^2\vec{b}_2\ n(\vec{b}_1,\omega_1)n(\vec{b}_2,\omega_2)\ P_{\text{non-inel}}(|\vec{b}_1-\vec{b}_2|)}{\int_{b_1>0}\int_{b_2>0}\ \mathrm{d}^2\vec{b}_1\mathrm{d}^2\vec{b}_2\ n(\vec{b}_1,\omega_1)n(\vec{b}_2,\omega_2)}\ , \qquad (2.2)$$

où le numérateur contient les effets de taille finie incorporés dans la fonction $P_{\text{non-inel}}(b)$ et les bornes d'intégration sur les paramètres d'impact $\vec{b}_1$ and $\vec{b}_2$ [6]. Ce terme $S_{\gamma\gamma}^2$ est bien évidemment plus petit que l'unité. Nous le représentons sur les figures 2.4 (haut et bas) en fonction de plusieurs variables cinématiques.

L'obtention de cette formule (2.2) ainsi que son étude en fonction de différentes variables cinématiques (figure 2.4) est une contribution personnelle [6]. Comme on le voit sur la figure 2.4, lors d'une mesure au LHC, on s'attend à une réduction d'environ 20 % de la section efficace par rapport à celle prédite par la théorie. Et ceci, du fait des effets de taille finie du proton. C'est ce que l'analyse expérimentale qui va suivre (chapitre 3) nous permettra de vérifier.

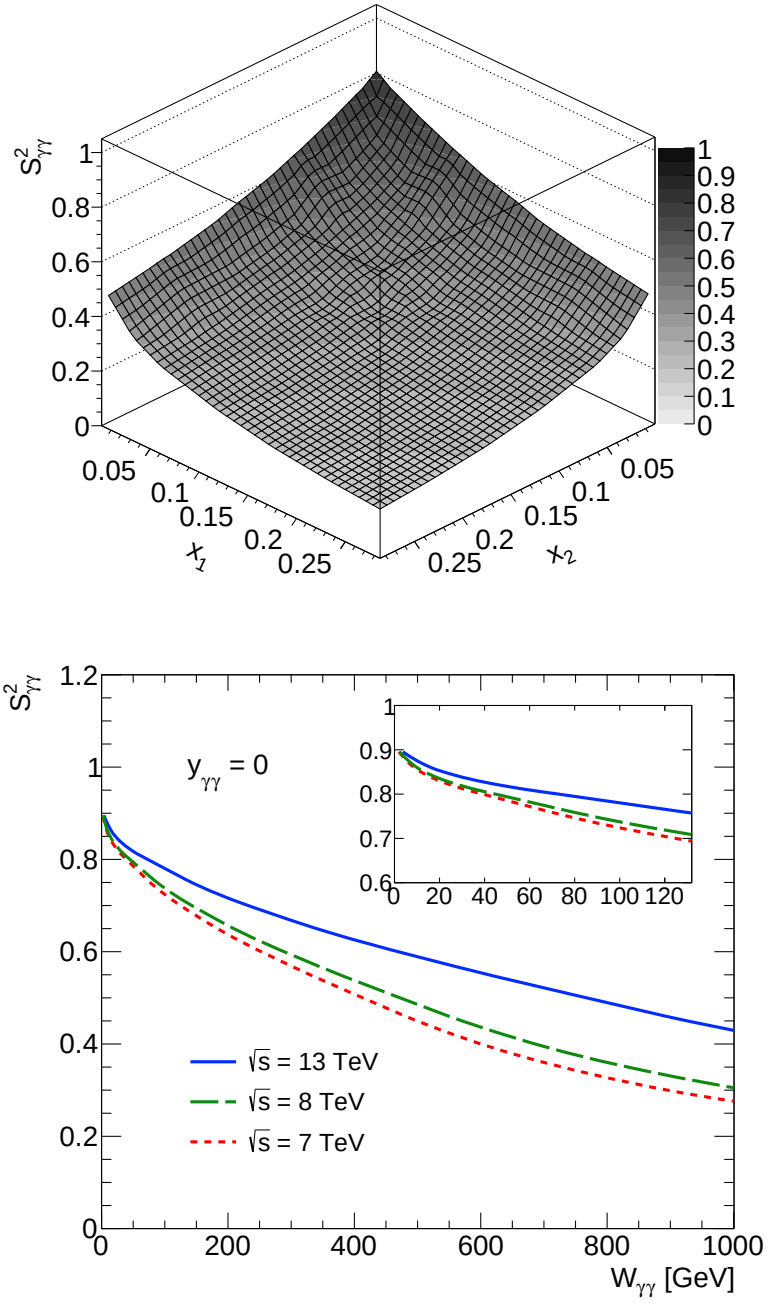
$S^2_{\gamma\gamma}$
1
0.8
0.6
0.4
0.2
0
0.05
0.1
0.15
0.2
0.25
x_1
x_2
1
0.9
0.8
0.7
0.6
0.5
0.4
0.3
0.2
0.1
0
$y_{\gamma\gamma} = 0$
$\sqrt{s}$ = 13 TeV
$\sqrt{s}$ = 8 TeV
$\sqrt{s}$ = 7 TeV
0
20
40
60
80
100
120
200
400
600
800
1000
$W_{\gamma\gamma}$ [GeV]

FIGURE 2.4

Bibliographie

[1] ALEPH and CDF and D0 and DELPHI and L3 and OPAL and SLD and LEP Electroweak Working Group and Tevatron Electroweak Working Group and SLD Electroweak and Heavy Flavour Groups Collaborations, *Precision Electroweak Measurements and Constraints on the Standard Model*, arXiv:1012.2367 [hep-ex].

[2] ATLAS Experiment Standard Model Results. twiki.cern.ch/twiki/bin/view/AtlasPublic/StandardModelPublicResults.

[3] M.-S. Chen et al., *Lepton pair production from two-photon processes*, Phys. Rev. **D7** (1973) 3485–3502.

[4] V. Budnev et al., *The process $pp \to ppe^+e^-$ and the possibility of its calculation by means of quantum electrodynamics only*, Nucl. Phys. **B63** (1973) 519–541.

[5] F. Krauss, M. Greiner and G. Soff, *Photon and gluon induced processes in relativistic heavy ion collisions*, Prog. Part. Nucl. Phys. **39** (1997) 503–564.

[6] M. Dyndal and L. Schoeffel, *The role of finite-size effects on the spectrum of equivalent photons in proton-proton collisions at the LHC*, Phys. Lett. **B741** (2015) 66 – 70, arXiv:1410.2983 [hep-ph].

Partie 3

L'analyse expérimentale avec les données de ATLAS

Dans ce court résumé de la thèse, je ne rentre dans aucun détail de l'analyse expérimentale. Cette analyse et ses résultats, qui constituent le coeur de la thèse sont publiés dans:
ATLAS Collaboration (G. Aad et al.), *Measurement of exclusive* $\gamma\gamma \to \ell^+\ell^-$ *production in proton–proton collisions at* $\sqrt{s} = 7$ *TeV with the ATLAS detector*,
Phys. Lett. B749 (2015) 242-261.

La base de l'analyse est d'effectuer une sélection des événements de type Drell-Yan (DY) avec deux leptons dans l'état final, ceci avec une paire de muons et une paire d'électrons. Des distributions de contrôle pour diverses variables cinématiques sont représentées sur les figures 3.1 pour le canal en muons et 3.2 pour le canal en électrons.

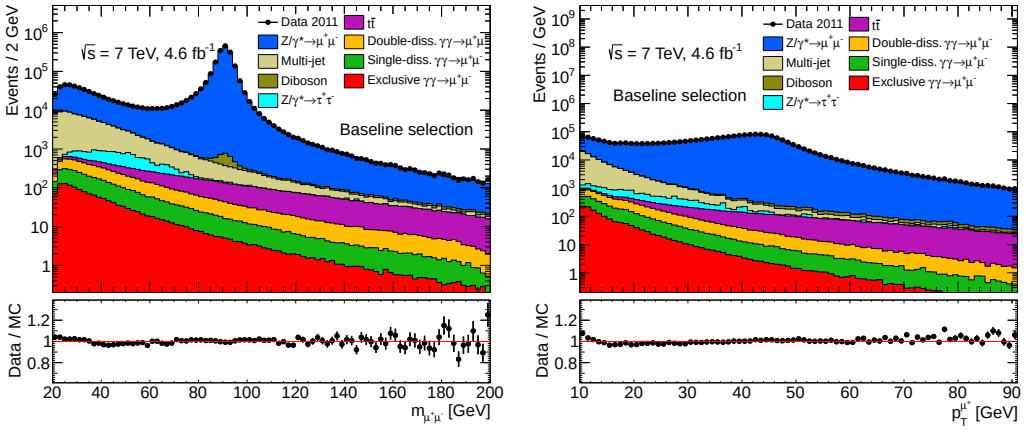

(a) (b)

FIGURE 3.1

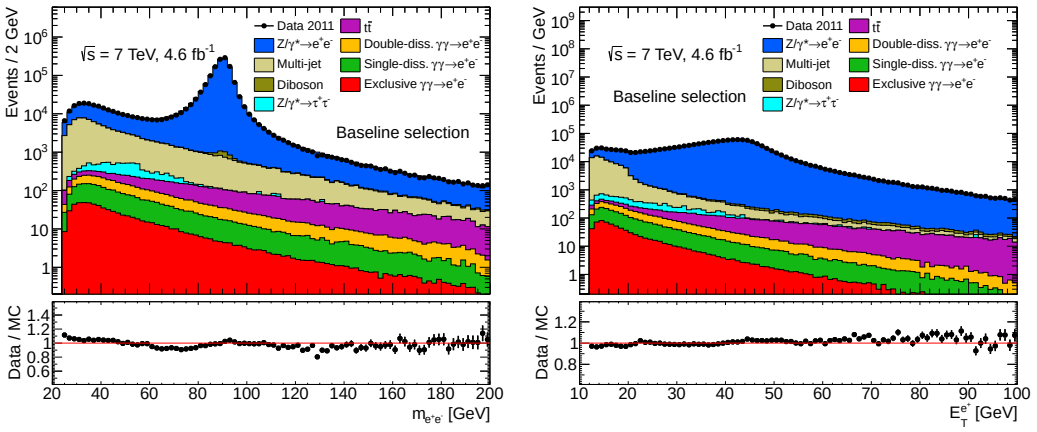

(a) (b)

FIGURE 3.2

Ces deux analyses (pour les canaux en muons et électrons) sont en fait indépendantes du fait des critères de déclenchement (*triggers*) pour chaque cas. Ceci étant, les figures 3.1 et 3.2 donnent le résultat de cette pré-sélection de type DY. On observe le pic du boson Z_0 très largement dominé par les interactions DY (en bleues) sur les figures. Ce que l'on doit ensuite sélectionner, ce sont les événements exclusifs (interactions photon–photon) qui correspondent aux parties (rouges) des figures ci-dessus (3.1 et 3.2).

Le principe de la sélection repose sur une observation très simple: les événements issus des réactions de DY ont en général de très nombreuses traces associées au point d'émission des deux leptons (appelé le vertex de l'interaction), alors que les événements produits par des réactions exclusives (interactions photon–photon) n'ont que deux (et seulement deux traces) associées à ce vertex Ce sont les deux traces associées aux deux leptons émis. Le principe général de l'analyse est donc celui-ci: repérer les événements qui ont deux traces (et seulement deux traces) associées à un vertex bien défini. Cette topologie d'événement n'est possible que dans le cas d'une interaction photon–photon. De plus, même s'il y a d'autres événements (issus d'autres interactions proton–proton du même *bunch* de protons) qui se superposent à l'événement exclusif identifié, ces événements présenteront un vertex d'interaction différent de l'événement de physique qui nous intéresse. Ainsi, si ce taux d'événements supplémentaires n'est pas trop élevé, le principe général de sélection mentionné ci-dessus restera valide et très robuste.

Après la sélection exclusive (2 traces associées à un vertex bien identifié), des distributions de contrôle pour des variables cinématiques standards sont représentées sur les figures 3.3 et 3.4, pour les canaux en muons et électrons respectivement. La masse invariante des deux leptons ainsi que l'impulsion transverse de la paire de ces deux leptons sont illustrées pour chaque canal. Ce que l'on remarque c'est que sur les

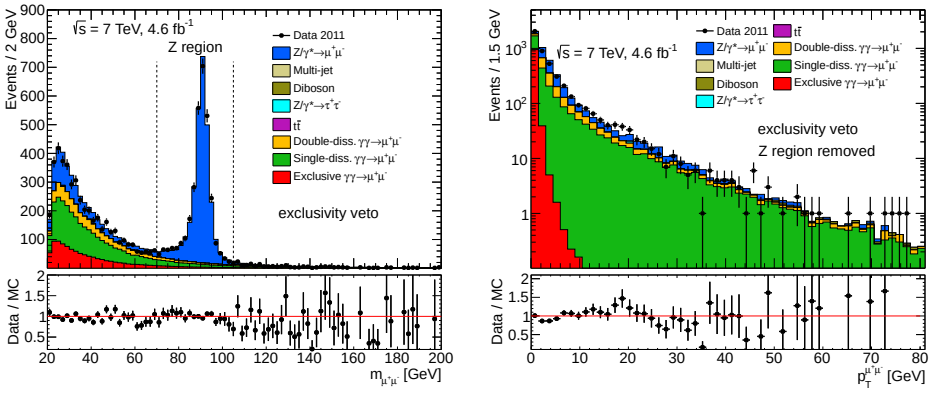

FIGURE 3.3

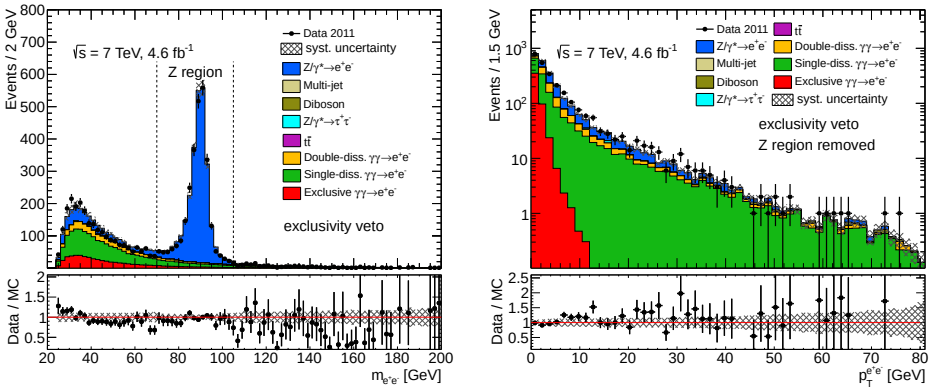

FIGURE 3.4

masses invariantes (pour les canaux en muons et électrons), on peut supprimer encore beaucoup d'événements de type DY en supprimant le domaine en masse autour de la masse du boson Z^0, comme indiqué sur les figures 3.3 et 3.4. De plus, on observe que l'impulsion transverse pour le système des deux leptons est dominée par les réactions inélastiques dès que cette impulsion transverse est plus grande que 1.5 GeV/c. Comme nous nous intéressons essentiellement aux interactions photon–photon élastiques, nous allons sélectionner les événements à petite impulsion transverse pour le système des deux leptons.

Après ces deux nouveaux critères de sélection, on obtient les distributions de masse invariante présentées sur la figure 3.5. On constate que cette fois-ci, que nous avons très clairement enrichi la sélection en événements exclusifs élastiques, ce que cherchions depuis le début de l'analyse. Avec les événements où un seul proton est dissocié, ils dominent la sélection ainsi effectuée (figure 3.5). Ceci est illustré également sur la distribution dite d'acoplanarité (figure 3.6).

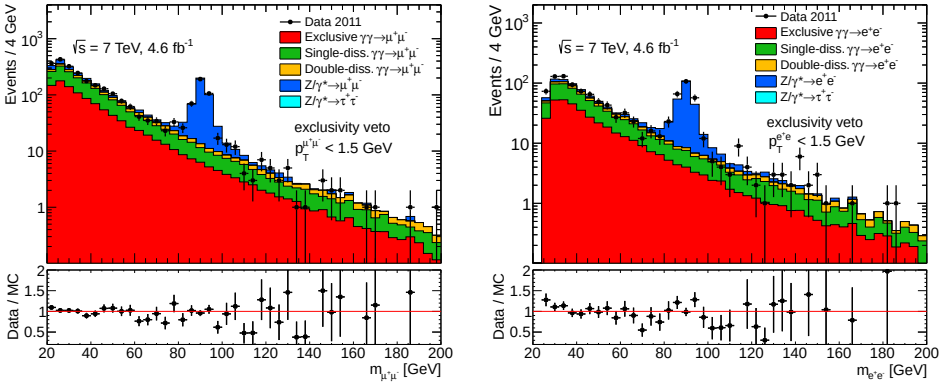

(a) (b)

FIGURE 3.5

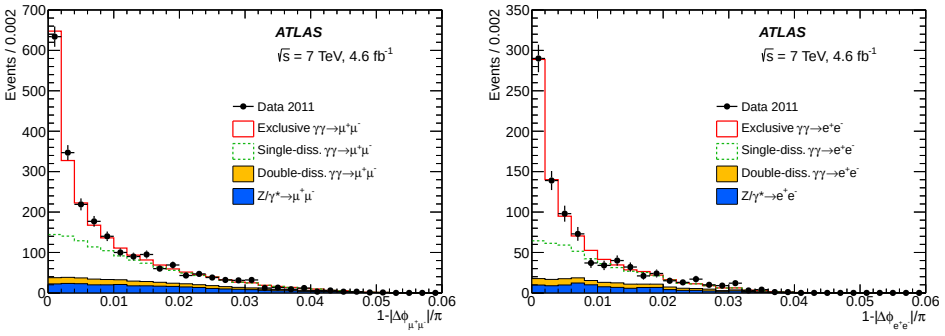

FIGURE 3.6

Une fois la sélection d'événements exclusifs réalisées dans les canaux en muons et en électrons, il est possible d'en déduire la mesure de la la section efficace exclusive. Lorsque la paire de leptons est une paire de muons, on trouve:

$$\sigma^{\text{excl.}}_{\gamma\gamma\to\mu^+\mu^-} = 0.628 \ \pm \ 0.032 \text{ (stat.)} \ \pm \ 0.021 \text{ (syst.) pb}$$

pour le domaine cinématique suivant: $m_{\mu^+\mu^-} > 20$ GeV, $p_{\text{T}}^{\mu} > 10$ GeV, $|\eta^{\mu}| < 2.4$. Cette valeur doit être comparée aux prédictions théoriques (de la partie précédente), qui incluent les effets de taille finie des protons: $\sigma^{\text{EPA, corr.}}_{\gamma\gamma\to\mu^+\mu^-} = 0.638 \ \pm \ 0.013$ pb.

Lorsque la paire de leptons est une paire d'électrons, nous avons obtenu:

$$\sigma^{\text{excl.}}_{\gamma\gamma\to e^+e^-} = 0.428 \ \pm \ 0.035 \text{ (stat.)} \ \pm \ 0.018 \text{ (syst.) pb}$$

pour $m_{e^+e^-} > 24$ GeV, $p_{\text{T}}^{e} > 12$ GeV and $|\eta^{e}| < 2.4$. La prédiction théorique (corrigée des effets de taille finie des protons) étant: $\sigma^{\text{EPA, corr.}}_{\gamma\gamma\to e^+e^-} = 0.398 \ \pm \ 0.007$ pb.

La figure 3.8 montre un exemple d'événement exclusif tel qu'enregistré par les détecteurs de ATLAS.

Conclusion

Si maintenant nous calculons le rapport entre les sections efficaces exclusives mesurées (en canal muons ou en canal électrons) et les prédictions théoriques nominales (sans prendre en compte les effets de taille finie des protons), nous devrions obtenir environ un résultat d'environ 0.8. En effet, si la théorie du chapitre 2 est correcte, on devrait observer que le rapport entre la section efficace exclusive mesurée et la prédiction nominale est proche du facteur de suppression ($S^2_{\gamma\gamma}$) introduit au chapitre précédent. Soit:

$$\sigma^{\text{excl.,mesure}} \; / \; \sigma^{\text{EPA,nominale}} \simeq S^2_{\gamma\gamma}.$$

Avec les valeurs expérimentales obtenues plus haut, nous avons tout ce qui est nécessaire pour cette vérification. Les résultats sont présentés sur la figure 3.7. Cette figure confirme que la mesure que nous avons brièvement décrite dans ce chapitre 3 est en accord avec ce que l'on attend de la théorie que nous avons développée au chapitre 2. Cette figure 3.7 inclut également les résultat de l'expérience CMS en canal muons. Enfin, un événement exclusif tel qu'enregistré dans les différents détecteurs de ATLAS est illustré sur la figure 3.8.

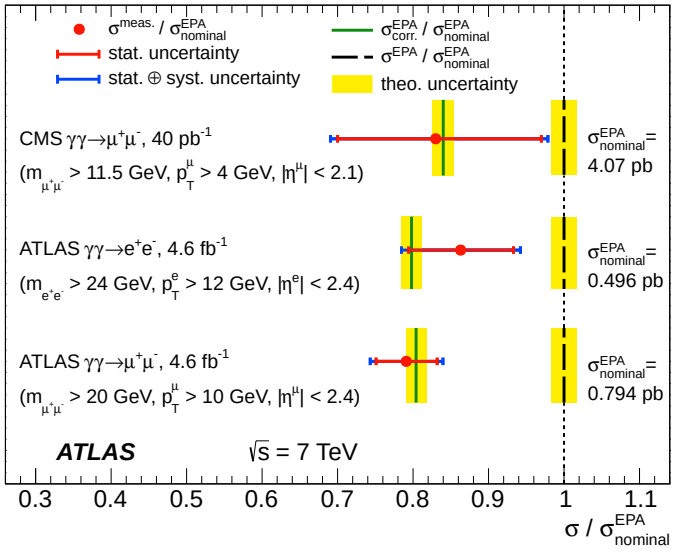

FIGURE 3.7

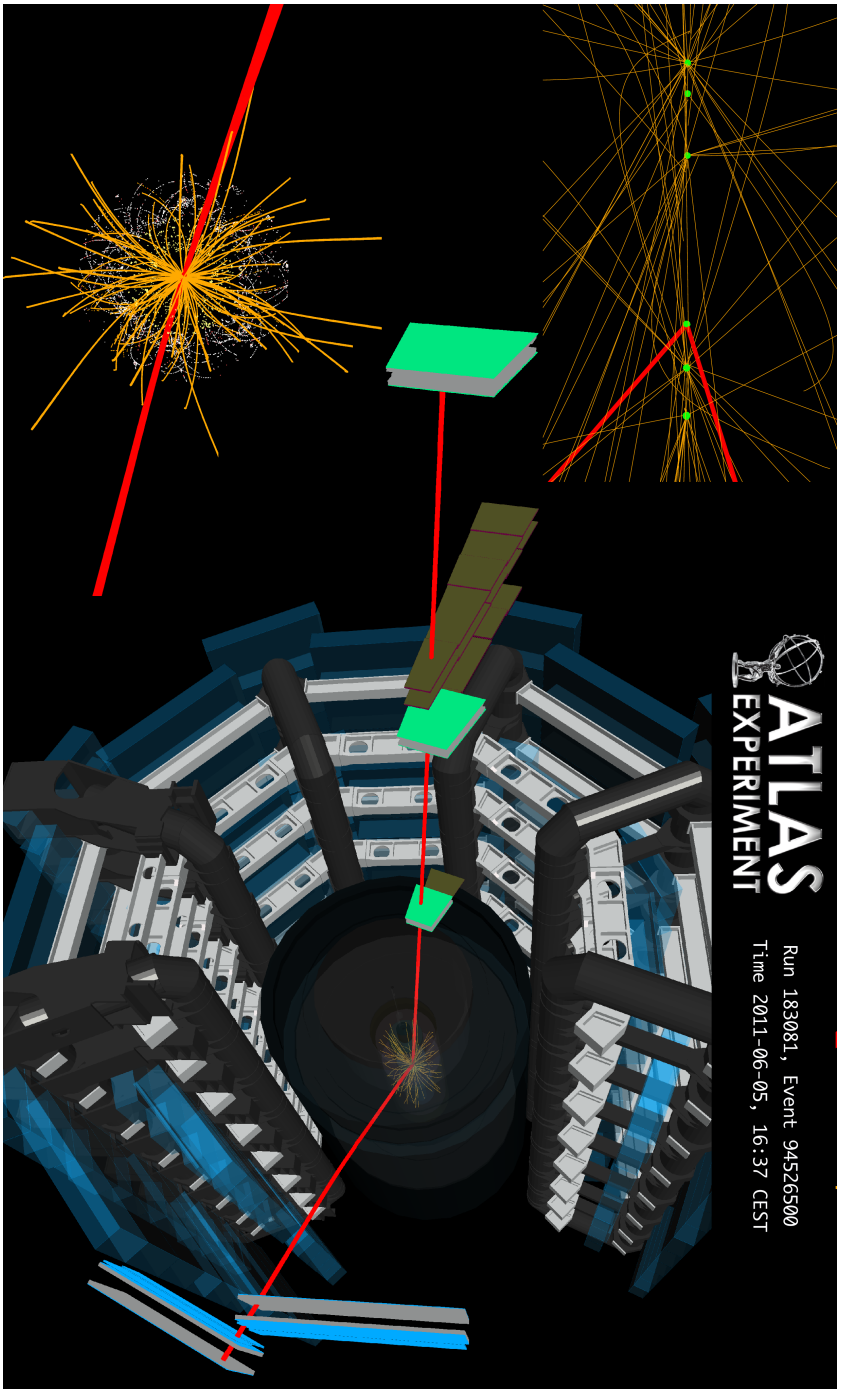
ATLAS
EXPERIMENT
Run 183081, Event 94526500
Time 2011-06-05, 16:37 CEST

FIGURE 3.8

Appendix B

Phenomenological paper

Here follow the phenomenological studies presented in this thesis as published in

Phys. Lett. **B741** (2015) 66–70.

Physics Letters B 741 (2015) 66–70

Contents lists available at ScienceDirect

Physics Letters B

www.elsevier.com/locate/physletb

The role of finite-size effects on the spectrum of equivalent photons in proton–proton collisions at the LHC

Mateusz Dyndal [a,b], Laurent Schoeffel [b,*]

[a] AGH University of Science and Technology, Cracow, Poland
[b] CEA Saclay, Irfu/SPP, Gif-sur-Yvette, France

ARTICLE INFO

Article history:
Received 17 October 2014
Received in revised form 24 November 2014
Accepted 6 December 2014
Available online 11 December 2014
Editor: J.-P. Blaizot

ABSTRACT

Photon–photon interactions represent an important class of physics processes at the LHC, where quasi-real photons are emitted by both colliding protons. These reactions can result in the exclusive production of a final state X, $p+p \to p+p+X$. When computing such cross sections, it has already been shown that finite size effects of colliding protons are important to consider for a realistic estimate of the cross sections. These first results have been essential in understanding the physics case of heavy-ion collisions in the low invariant mass range, where heavy ions collide to form an exclusive final state like a J/Ψ vector meson. In this paper, our purpose is to present some calculations that are valid also for the exclusive production of high masses final states in proton–proton collisions, like the production of a pair of W bosons or the Higgs boson. Therefore, we propose a complete treatment of the finite size effects of incident protons irrespective of the mass range explored in the collision. Our expectations are shown to be in very good agreement with existing experimental data obtained at the LHC.

1. Introduction

A significant fraction of proton–proton collisions at large energies involves quasi-real photon interactions. This fraction is dominated by elastic scattering, with a single Born-level photon exchange. The photons can also be emitted by both protons, where a variety of central final states can be produced. The proton–proton collision is then transformed into a photon–photon interaction and the protons are deflected at small angles. At the LHC, these reactions can be measured at the energies well beyond the electroweak energy scale. This offers an interesting field of research linked to photon–photon interactions, where the available effective luminosity is small, relative to parton–parton interactions, but is compensated by better known initial conditions and usually simpler final states. Indeed, for high energetic proton–proton collisions, at a center of mass energy s, the idea is to search for the exclusive production of a final state X through the reaction $p+p \to p+p+X$. Therefore, the initial state formed by both photons is well-defined, while the final state formed by X with no other hadronic activity is much simpler than in a standard inelastic proton–proton interaction. In the following, we write this reaction as $pp(\gamma\gamma) \to ppX$.

In order to compute the cross section for the process $pp(\gamma\gamma) \to ppX$, we need to consider that each of the two incoming protons emits a quasi-real photon which fuse to give a centrally produced final state X ($\gamma+\gamma \to X$). This calculation relies on the so-called equivalent photon approximation (EPA) [1–5]. The EPA is based on the property that the electromagnetic (EM) field of a charged particle, here a proton, moving at high velocities becomes more and more transverse with respect to the direction of propagation. As a consequence, an observer in the laboratory frame cannot distinguish between the EM field of the relativistic proton and its transverse component, which can be labeled as the transverse EM field of equivalent photons. This implies that the total cross section of the reaction $pp(\gamma\gamma) \to ppX$ can be approximately described as a photon–photon fusion cross section ($\gamma\gamma \to X$) folded with the equivalent photon distributions $f(.)$ for the two protons

$$\sigma(p+p \to p+p+X) = \iint f(\omega_1) f(\omega_2) \sigma_{\gamma\gamma \to X}(\omega_1, \omega_2) \frac{d\omega_1}{\omega_1} \frac{d\omega_2}{\omega_2}, \quad (1)$$

where $\omega_{1,2}$ represent the energies of the photons and are integrated over. For each photon, the maximum energy is obviously the energy of the incident proton $\sqrt{s}/2$. However, there is also the constraint that the highest available energy for one photon is of the order of the inverse Lorentz contracted radius of the proton, γ/r_p, where r_p represents the proton radius. Let us note that

* Corresponding author.
E-mail address: laurent.schoeffel@cea.fr (L. Schoeffel).

http://dx.doi.org/10.1016/j.physletb.2014.12.019

the two photon center-of-mass energy squared is $W^2_{\gamma\gamma} = 4\omega_1\omega_2$, and the rapidity of the two photons system is defined as $y_{\gamma\gamma} = 0.5 \ln[\omega_1/\omega_2]$.

In Eq. (1), the photon distributions $f(.)$ are already integrated over the virtuality ($Q^2_{1,2}$) of the photons. As this dependence is of the order of $1/Q^2_{1,2}$, this justifies the approximation that both photons are quasi-real.

We can remark that for practical issues, the situation may be more complex. Indeed, each proton can either survive and, then, is scattered at a small angle, as considered above. This is the case of elastic emission. Elastic two-photon processes yield very clean event topologies at the LHC: two very forward protons measured away from the interaction point and a few centrally produced particles (forming the final state X). But, it is also possible that one or both protons dissociate into a hadronic state. This is the case of inelastic emission. In this paper, we restrict the discussion to the elastic case.

Let us note also that the calculations presented in this paper are commonly used for heavy-ion collisions, where the EPA approximation can be applied similarly. Only the charges and the radii of the incident particles are modified in this case.

Previous studies have been done using Eq. (1) in order to compute cross sections at LHC energies for various photon–photon processes in proton–proton collisions, $pp(\gamma\gamma) \to ppX$, corresponding to different final states X [6,7]. Some results are displayed in Fig. 1. The exclusive production of pairs of muons and pairs of W bosons have been generated using the Herwig++ generator [8]. The exclusive production of pairs of photons has been generated using the FPMC generator [9] at large $W_{\gamma\gamma}$ where the $\gamma\gamma \to \gamma\gamma$ cross section is dominated by one-loop diagrams involving W bosons [10]. Finally, the exclusive production of the Higgs boson is computed according to higgs effective field theory (HEFT) [11]. Obviously, this last reaction appears as a point in Fig. 1, representing the total cross section, at the Higgs mass.

In this paper, our purpose is to generalize Eq. (1) to the physics case where the impact parameter dependence of the interaction cannot be neglected [12]. In particular, we show that this approach is needed when we take in consideration the finite size of colliding protons (or heavy-ions) in the calculations. This is not new in the sense that these finite size effects have already been encoded in the Starlight Monte Carlo [13] dedicated to heavy-ion collisions. Let us note that Starlight is not restricted to photon–photon interactions but can also be used in photon–Pomeron configurations, as it is done at LHCb [14]. However, Starlight is focused mainly on the low invariant mass domain around the mass of the J/Ψ, which justifies some approximations made for example by neglecting the magnetic form factors.

In the following we develop some calculations that are valid also for the exclusive production of high masses final states in proton–proton collisions, like the production of a pair of W bosons or the Higgs boson. Therefore, our purpose in this paper is to propose a complete treatment of the finite size effects of incident protons irrespective of the mass range explored in the collision. In Section 2, these calculations are presented extensively. Then, results are discussed in Section 3 and compared to existing measurements.

2. Impact parameter dependent equivalent photon method

Deriving the expression of the equivalent photon distribution of the fast moving proton without neglecting the impact parameter dependence means that we determine this distribution as a function of the energy of the photon and the distance $\vec{b}$ to the proton trajectory. This distance is defined in the plane transverse to the proton trajectory. Therefore we speak of transverse distance.

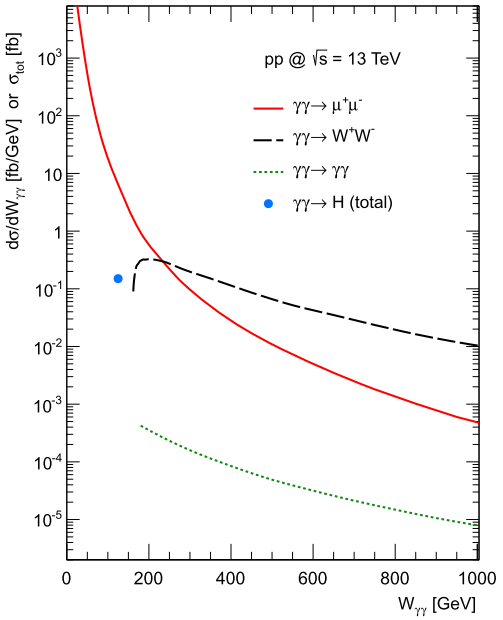

Fig. 1. Cross sections of various processes $pp(\gamma\gamma) \to ppX$, differential in the photon–photon center of mass energy. For the exclusive Higgs production, the total cross section is shown. The exclusive production of pairs of photons has been generated at large $W_{\gamma\gamma}$ where the cross section is dominated by one-loop diagrams involving W bosons.

This last dependence is not present in the approach based on formula (1). Following calculations presented in [15,16], the general equivalent photon distribution read

$$n(b,\omega) = \frac{\alpha_{EM}}{\pi^2\omega}\left|\int dk_\perp k_\perp^2 \frac{F\left(k_\perp^2 + \frac{\omega^2}{\gamma^2}\right)}{k_\perp^2 + \frac{\omega^2}{\gamma^2}} J_1(bk_\perp)\right|^2 \tag{2}$$

where γ is the Lorentz contraction factor, ω and $\vec{k}_\perp$ represent the energy and transverse momentum of photons respectively. In this expression, $F(.)$ is the proton form factor, electric and magnetic, that we develop explicitly below. Let us note that $n(b,\omega)$ depends only on the modulus of the impact parameter as obviously this quantity does not depend on the orientation of $\vec{b}$. We can introduce the virtuality of the photon $Q^2 = -k^2 = k_\perp^2 + \frac{\omega^2}{\gamma^2}$. Then, expression (2) becomes

$$n(b,\omega) = \frac{\alpha_{EM}}{\pi^2\omega}\left|\int dk_\perp k_\perp^2 \frac{F(Q^2)}{Q^2} J_1(bk_\perp)\right|^2, \tag{3}$$

After developing the complete expression of the form factor $F(.)$, we get

$$n(b,\omega) = \frac{\alpha_{EM}}{\pi^2\omega}\left|\int dk_\perp k_\perp^2 \frac{G_E(Q^2)}{Q^2} \times \left[(1-x)\frac{4m_p^2 + Q^2\mu_p^2}{4m_p^2 + Q^2} + \frac{1}{2}x^2\frac{Q^2}{k_\perp^2}\mu_p^2\right]^{\frac{1}{2}} J_1(bk_\perp)\right|^2, \tag{4}$$

where x is the energy fraction of the proton carried by the photon, given by $x = 2\omega/\sqrt{s}$. Let us note that the electromagnetic coupling strength α_{EM} is taken to be $\alpha_{EM}(Q^2 \simeq 0\ \text{GeV}^2) = 1/137.036$

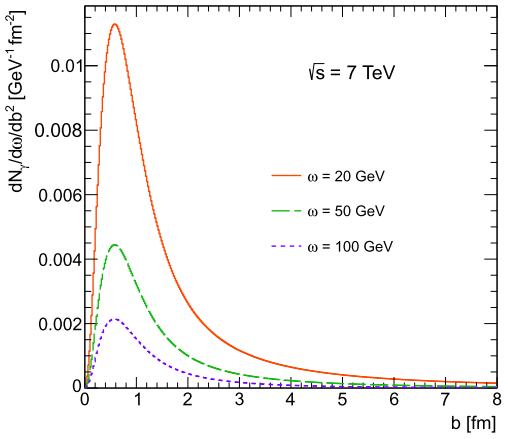

Fig. 2. Equivalent photon distributions of the fast moving proton for different energies of the photon, as function of the transverse distance b (see text).

throughout our calculations, following the property that the photons entering the interaction are quasi-real (see Section 1).

The relation (4) for $n(b,\omega)$ corresponds to the equivalent photon distribution (for one proton) when the impact parameter dependence is taken into account. Equivalent photon distributions are presented in Fig. 2, as a function of the impact parameter for different energies of the photon. The overall shapes of these distributions can be understood easily. At very large b values, $n(b,\omega)$ behaves asymptotically as $\frac{1}{b}e^{-2\omega b/\gamma}$ for what concerns its b dependence. At very small b values, the photon distributions are damped due to the effects of form factors and finite size of the proton. We can remark that Eq. (1) can be re-derived from expression (4) after replacing $f(\omega_1)$ by the integral of $n(\vec{b}_1,\omega_1)$ for all $\vec{b}_1$, and similarly for the second photon variables independently. Indeed

$$f(\omega) = \frac{e^2}{\pi\omega}\int \frac{d^2\vec{k}_\perp}{(2\pi)^2}\left(\frac{F\left(k_\perp^2+\frac{\omega^2}{\gamma^2}\right)}{k_\perp^2+\frac{\omega^2}{\gamma^2}}\right)^2 |\vec{k}_\perp|^2,$$

where we have used the generic expression for the form factor of the proton, as in Eq. (2).

The full expression (4) is necessary when we want to take into account effects that depend directly on the transverse space variables of the reaction. Therefore, when we consider the finite sizes of colliding protons, we need to do the replacement

$$f(\omega_1)f(\omega_2) \to \iint n(\vec{b}_1,\omega_1)n(\vec{b}_2,\omega_2)d^2\vec{b}_1 d^2\vec{b}_2, \qquad (5)$$

where the bounds of integrations on the transverse distances $\vec{b}_1$ and $\vec{b}_2$ prevent from performing the integrations independently. Indeed, there are important geometrical constraints to encode: the two photons need to interact at the same point outside the two protons, of radii r_p, while the proton-halos do not overlap. This implies minimally that $b_1 > r_p$, $b_2 > r_p$ and $|\vec{b}_1 - \vec{b}_2| > 2r_p$ (see Fig. 3). The last condition clearly breaks the factorization in the variables $\vec{b}_1$ and $\vec{b}_2$ of the integral (5). In these conditions, the proton radius r_p is the two-dimensional radius, determined in the transverse plane, that will be taken to be 0.64 ± 0.02, as measured in the H1 experiment [17]. Let us note that it would be possible to keep the factorization by imposing stronger constraints, like $b_{1,2} > 2r_p$. However, this last condition prevents configurations where the two protons are very close and produce very energetic photon–photon collisions. This is not what we want.

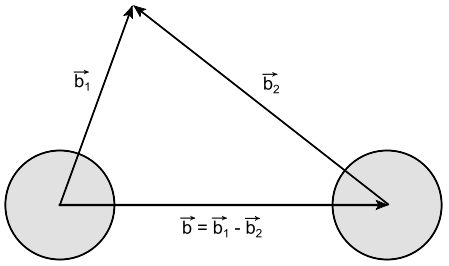

Fig. 3. Schematic view of the two protons and the transverse distances $\vec{b}_1$ and $\vec{b}_2$. The difference $\vec{b} = \vec{b}_1 - \vec{b}_2$ is also pictured. This is clear from this view that the geometrical non-overlapping condition of the two protons corresponds to $|\vec{b}_1 - \vec{b}_2| > 2r_p$.

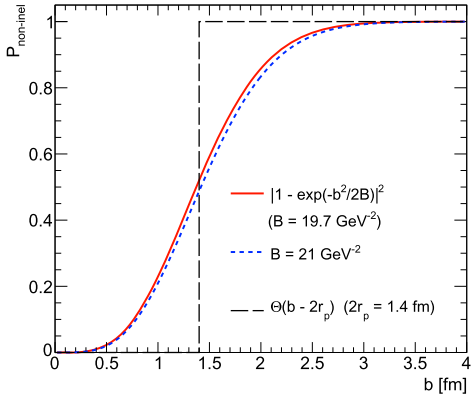

Fig. 4. Function $P_{non\text{-}inel}(b) = |1 - \Gamma(b)|^2$ compared with the step function $\Theta(b-2R)$. $P(b)$ represents the probability for no inelastic interaction in a proton–proton collision at impact parameter b.

Eq. (5) is a first step towards encoding finite size effects. It can be refined by including the proton–proton interaction probability, which depends explicitly on the transverse variables, $P_{non\text{-}inel}(|\vec{b}_1 - \vec{b}_2|)$. Then, Eq. (5) becomes

$$f(\omega_1)f(\omega_2) \to \iint n(\vec{b}_1,\omega_1)n(\vec{b}_2,\omega_2)P_{non\text{-}inel}(|\vec{b}_1 - \vec{b}_2|)d^2\vec{b}_1 d^2\vec{b}_2, \qquad (6)$$

where the bounds of integrations are still $b_1 > r_p$, $b_2 > r_p$. The non-overlapping condition $|\vec{b}_1 - \vec{b}_2| > 2r_p$ is not needed any longer. It follows as a consequence of the effect of the function $P_{non\text{-}inel}(|\vec{b}_1 - \vec{b}_2|)$. Indeed, this function represents the probability that there is no interaction (no overlap) between the two colliding protons in impact parameter space. Following [18], we make the natural assumption that a probabilistic approximation gives a reasonable estimate of the absorption effects. Then, we can write [18]

$$P_{non\text{-}inel}(b) = \left|1 - \exp\left(-b^2/(2B)\right)\right|^2,$$

where the value of $B = 19.7$ GeV^{-2} is taken from a measurement at $\sqrt{s} = 7$ TeV by the ATLAS experiment [19] (see Fig. 4). At $\sqrt{s} = 13$ TeV, we will use the extrapolated value $B = 21$ GeV^{-2}. In Fig. 4, we compare $P_{non\text{-}inel}(b)$ with the step function $\Theta(b-2r_p)$, which is the first approximation that we have described above to quantify a non-overlapping condition between both protons. We see that both functions are roughly comparable. However, we can expect

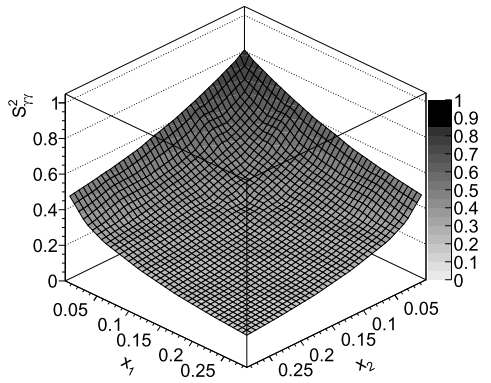

Fig. 5. The survival factor as a function of the energy fractions of the protons carried by the interacting photons, x_1 and x_2.

some deviations when performing more accurate computations of cross sections using $P_{non\text{-}inel}(b)$ in Eq. (6), and then in Eq. (1).

3. Results

Following the previous section, the first important issue is to quantify the size of the correction when we take into account the finite size of colliding protons. We define the survival factor as

$$S^2_{\gamma\gamma} = \frac{\int_{b_1>r_p}\int_{b_2>r_p} n(\vec{b}_1,\omega_1)n(\vec{b}_2,\omega_2)P_{non\text{-}inel}(|\vec{b}_1-\vec{b}_2|)d^2\vec{b}_1 d^2\vec{b}_2}{\int_{b_1>0}\int_{b_2>0} n(\vec{b}_1,\omega_1)n(\vec{b}_2,\omega_2)d^2\vec{b}_1 d^2\vec{b}_2}, \tag{7}$$

where the numerator contains the finite size effects encoded in the function $P_{non\text{-}inel}(b)$ and dedicated bounds of the integrations over $\vec{b}_1$ and $\vec{b}_2$, whereas the denominator represents the integral over all impact parameters with no constraint.

Trivially, this factor will always be smaller than unity. Then, the deviation with respect to unity will quantify the overestimation done when the finite size effects are neglected. This is first illustrated in Fig. 5, where we present the two-dimensional dependence of $S^2_{\gamma\gamma}$ as a function of x_1 and x_2, the energy fractions of the protons carried by the interacting photons. Then, the survival factor is displayed as a function of experimentally measurable variables in Figs. 6 and 7. Fig. 6 presents the behavior of the survival factor as a function of the center of mass energy of the photon–photon system ($W_{\gamma\gamma}$) at zero rapidity. Different curves are displayed corresponding to the different center of mass energies for the proton–proton collision. We observe a common feature. For all curves, the survival factor is decreasing as a function of $W_{\gamma\gamma}$, to reach values of 0.3 at $W_{\gamma\gamma} = 1$ TeV for $\sqrt{s} = 7$ or 8 TeV and 0.43 at $W_{\gamma\gamma} = 1$ TeV for $\sqrt{s} = 13$ TeV. This is a large effect, due to the fact that for larger values of $W_{\gamma\gamma}$, smaller values of $b = |\vec{b}_1 - \vec{b}_2|$ are probed, and thus the integral at the numerator of the survival factor (7) becomes smaller. Indeed, when the photon–photon energy becomes larger and larger, this is understandable that the probability of no inelastic interaction becomes smaller and smaller. Fig. 6 illustrates the behavior of the survival factor as a function of the rapidity of the photon–photon system, for different $W_{\gamma\gamma}$. Obviously, we observe the same effect as in Fig. 6, that when $W_{\gamma\gamma}$ increases the survival factor decreases. In addition, this figure shows the small dependence as a function of the rapidity $y_{\gamma\gamma}$. Let us note that for possible measurements at the LHC, the rapidity domain covered is close to zero. Therefore, the dependence in $y_{\gamma\gamma}$ is a marginal effect.

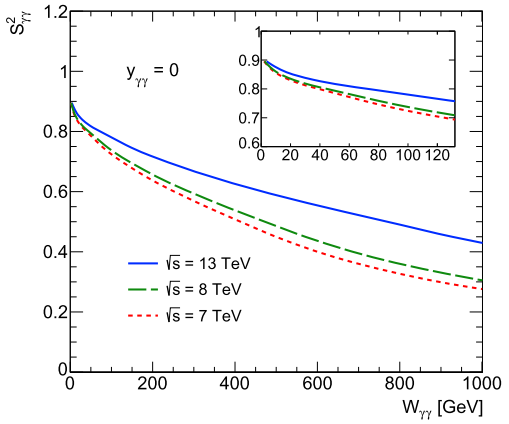

Fig. 6. The survival factor at zero rapidity as a function of the photon–photon center of mass energy.

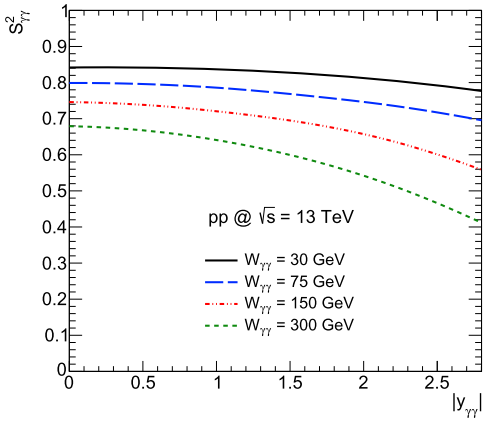

Fig. 7. The survival factor for different the photon–photon center of mass energies displayed as a function of the rapidity of the photon–photon system.

Table 1
Comparison of total cross sections at $\sqrt{s} = 13$ TeV for different processes $pp(\gamma\gamma) \to ppX$ with and without proton survival factor applied.

Process	σ_{tot}	$\sigma_{tot} \otimes S^2_{\gamma\gamma}$	$\langle S^2_{\gamma\gamma} \rangle$
$\gamma\gamma \to H$ ($M_H = 125$ GeV)	0.15 fb	0.11 fb	0.74
$\gamma\gamma \to \mu^+\mu^-$ ($W_{\gamma\gamma} > 40$ GeV)	12 pb	10 pb	0.8
$\gamma\gamma \to \mu^+\mu^-$ ($W_{\gamma\gamma} > 160$ GeV)	36 fb	25 fb	0.7
$\gamma\gamma \to W^+W^-$	82 fb	53 fb	0.65
$\gamma\gamma \to \gamma\gamma$ ($W_{\gamma\gamma} > 200$ GeV)	0.06 fb	0.04 fb	0.64

As a second step, we can compute cross sections for various processes $pp(\gamma\gamma) \to ppX$ taking correctly into account the finite size effects of incident protons and thus the survival factor. As discussed in the previous section, this requires Eq. (1) with the replacement (6). A set of predictions is presented in Table 1, where total cross sections are shown, cumulative in $W_{\gamma\gamma}$ above the bounds indicated in Table 1. For the exclusive production of pairs of W bosons, this is the natural bound which applies of $2M_W$.

Finally, we can compare our results with the experimental measurements available. Recently, the CMS experiment has measured exclusive pair of muons production [20] and has reported the value of $S^2_{\gamma\gamma}$ to be 0.83 ± 0.15 for invariant masses of the photon–

photon system above 11.5 GeV. This is consistent with our expectations from Fig. 6, which, convoluted with the elementary cross section in this kinematic range, gives a survival factor of 0.84. In addition, in the analysis of the exclusive production of pairs of W bosons by the CMS experiment [21], using exclusive muons production as a benchmark, the measured survival factor $S^2_{\gamma\gamma}$ is found to be about 10% smaller that the one above for invariant masses above 40 GeV. This is also consistent with our expectations ($S^2_{\gamma\gamma} = 0.76$ in this kinematic domain).

4. Conclusion

The exclusive production of a final state X, $pp(\gamma\gamma) \to ppX$, represents an essential class of reactions at the LHC, mediated through photon–photon interactions. The interest of such processes is due to their well-known initial conditions and simple final state. In this paper, we have presented a complete treatment of finite size effects of colliding protons, needed to compute the corresponding cross sections for these reactions. We have derived a survival factor that quantifies the deviation of the complete treatment with respect to no size effect.

We have shown that the survival factor is decreasing as a function of mass of the photon–photon system ($W_{\gamma\gamma}$), to reach values of 0.3 at $W_{\gamma\gamma} = 1$ TeV for $\sqrt{s} = 7$ or 8 TeV and 0.43 at $W_{\gamma\gamma} = 1$ TeV for $\sqrt{s} = 13$ TeV. This is a large effect, due to the fact that for larger values of $W_{\gamma\gamma}$, the probability of no inelastic interaction becomes smaller and smaller and so the survival factor. The key point of our approach is that it is valid for the full spectrum of invariant masses produced in the final state, and thus for high masses final states, like the production of a pair of W bosons or the Higgs boson. This allows a direct comparison with experimental results already obtained at the LHC beyond the electroweak scale, where a very good agreement has been observed between our expectations and the measurements.

Finally, we remind that these calculations are commonly used for the physics case of heavy-ion collisions. For example, this already exists with some approximations in the Starlight Monte Carlo, mainly focused on the low invariant mass domain around the mass of the J/Ψ. A complication, properly taken into account in Starlight, arises in such collisions, due to the large value of the charges of the ions. Then, photon–photon interactions may be accompanied by additional electromagnetic reactions, such as photo-nuclear interactions, and the ions that come out from the collisions may be produced with some neutrons.

Acknowledgements

This work was partly supported by the Polish National Science Centre under contract No. UMO-2012/05/B/ST2/02480.

References

[1] E. Fermi, Z. Phys. 29 (1) (1924) 315–327.
[2] E. Williams, Phys. Rev. 45 (1934) 729–730.
[3] M.S. Chen, I.J. Muzinich, H. Terazawa, T.P. Cheng, Phys. Rev. D 7 (1973) 3485.
[4] H. Terazawa, Rev. Mod. Phys. 45 (1973) 615.
[5] V. Budnev, I. Ginzburg, G. Meledin, V. Serbo, Nucl. Phys. B 63 (1973) 519–541.
[6] D. d'Enterria, M. Klasen, K. Piotrzkowski, Nucl. Phys. Proc. Suppl. 179B (2008) 1.
[7] J. de Favereau de Jeneret, V. Lemaitre, Y. Liu, S. Ovyn, T. Pierzchala, K. Piotrzkowski, X. Rouby, N. Schul, et al., arXiv:0908.2020 [hep-ph].
[8] M. Bahr, S. Gieseke, M.A. Gigg, D. Grellscheid, K. Hamilton, O. Latunde-Dada, S. Platzer, P. Richardson, et al., Eur. Phys. J. C 58 (2008) 639, arXiv:0803.0883 [hep-ph].
[9] M. Boonekamp, A. Dechambre, V. Juranek, O. Kepka, M. Rangel, C. Royon, R. Staszewski, arXiv:1102.2531 [hep-ph].
[10] S. Atag, S.C. Inan, I. Sahin, J. High Energy Phys. 1009 (2010) 042, arXiv:1005.4792 [hep-ph].
[11] M.A. Shifman, A.I. Vainshtein, M.B. Voloshin, V.I. Zakharov, Sov. J. Nucl. Phys. 30 (1979) 711;
B.A. Kniehl, M. Spira, Z. Phys. C 69 (1995) 77;
S. Dawson, R. Kauffman, Phys. Rev. D 49 (1994) 2298.
[12] A. Szczurek, Acta Phys. Pol. B 45 (2014) 7, arXiv:1404.0896 [nucl-th], 1597.
[13] S.R. Klein, J. Nystrand, Phys. Rev. Lett. 92 (2004) 142003, arXiv:hep-ph/0311164.
[14] R. Aaij, et al., LHCb Collaboration, J. Phys. G 40 (2013) 045001, arXiv:1301.7084 [hep-ex].
[15] M. Vidovic, M. Greiner, C. Best, G. Soff, Phys. Rev. C 47 (1993) 2308.
[16] A.J. Baltz, Y. Gorbunov, S.R. Klein, J. Nystrand, Phys. Rev. C 80 (2009) 044902, arXiv:0907.1214 [nucl-ex].
[17] F.D. Aaron, et al., H1 Collaboration, Phys. Lett. B 681 (2009) 391, arXiv:0907.5289 [hep-ex].
[18] L. Frankfurt, C.E. Hyde, M. Strikman, C. Weiss, Phys. Rev. D 75 (2007) 054009, arXiv:hep-ph/0608271.
[19] G. Aad, et al., ATLAS Collaboration, arXiv:1408.5778 [hep-ex].
[20] S. Chatrchyan, et al., CMS Collaboration, J. High Energy Phys. 1201 (2012) 052, arXiv:1111.5536 [hep-ex].
[21] S. Chatrchyan, et al., CMS Collaboration, J. High Energy Phys. 1307 (2013) 116, arXiv:1305.5596 [hep-ex].

Appendix C

Experimental paper

Here follow the experimental studies presented in this thesis as published in

Phys. Lett. **B749** (2015) 242–261.

EUROPEAN ORGANISATION FOR NUCLEAR RESEARCH (CERN)

Submitted to: Phys. Lett. B.

CERN-PH-EP-2015-134
18th August 2015

Measurement of exclusive $\gamma\gamma \to \ell^+\ell^-$ production in proton–proton collisions at $\sqrt{s} = 7$ TeV with the ATLAS detector

The ATLAS Collaboration

Abstract

This Letter reports a measurement of the exclusive $\gamma\gamma \to \ell^+\ell^-$ ($\ell = e,\ \mu$) cross-section in proton–proton collisions at a centre-of-mass energy of 7 TeV by the ATLAS experiment at the LHC, based on an integrated luminosity of 4.6 fb^{-1}. For the electron or muon pairs satisfying exclusive selection criteria, a fit to the dilepton acoplanarity distribution is used to extract the fiducial cross-sections. The cross-section in the electron channel is determined to be $\sigma^{\text{excl.}}_{\gamma\gamma\to e^+e^-} = 0.428 \pm 0.035\,(\text{stat.}) \pm 0.018\,(\text{syst.})$ pb for a phase-space region with invariant mass of the electron pairs greater than 24 GeV, in which both electrons have transverse momentum $p_{\text{T}} > 12$ GeV and pseudorapidity $|\eta| < 2.4$. For muon pairs with invariant mass greater than 20 GeV, muon transverse momentum $p_{\text{T}} > 10$ GeV and pseudorapidity $|\eta| < 2.4$, the cross-section is determined to be $\sigma^{\text{excl.}}_{\gamma\gamma\to\mu^+\mu^-} = 0.628 \pm 0.032\,(\text{stat.}) \pm 0.021\,(\text{syst.})$ pb. When proton absorptive effects due to the finite size of the proton are taken into account in the theory calculation, the measured cross-sections are found to be consistent with the theory prediction.

Contents

1 Introduction

A considerable fraction of proton–proton (pp) collisions at high energies involve reactions mediated by photons. This fraction is dominated by elastic scattering, with a single photon exchange. Quasi-real photons can also be emitted by both protons, with a variety of final states produced. In these processes the pp collision can be then considered as a photon–photon ($\gamma\gamma$) collision. At the LHC, these reactions can be studied at energies well beyond the electroweak energy scale [1]. The cross-section of the $pp(\gamma\gamma) \to \ell^+\ell^- X$ process has been predicted to increase with energy [2] and constitutes a non-negligible background to Drell–Yan (DY) reactions [3].

The exclusive two-photon production of lepton pairs ($pp(\gamma\gamma) \to \ell^+\ell^- pp$, referred to as exclusive $\gamma\gamma \to \ell^+\ell^-$) can be calculated in the framework of quantum electrodynamics (QED) [4, 5], within uncertainties of less than 2% associated with the proton elastic form-factors. Exclusive dilepton events have a clean signature that helps discriminate them from background: there are only two identified muons or electrons, without any other activity in the central detectors, and the leptons are back-to-back in azimuthal angle. Furthermore, due to the very small photon virtualities involved, the incident protons are scattered at almost zero-degree angles. Consequently, the measurement of exclusive $\gamma\gamma \to \ell^+\ell^-$ reactions was proposed for precise absolute luminosity measurement at hadron colliders [5–8]. However, this process requires significant corrections (of the order of 20%) due to additional interactions between the elastically scattered protons [9, 10].

At hadron colliders exclusive $\gamma\gamma \to \ell^+\ell^-$ events have been observed in ep collisions at HERA [11], in $p\bar{p}$ collisions at the Tevatron [12–14] and in nucleus–nucleus collisions at RHIC [15, 16] and the LHC [17]. The exclusive two-photon production of lepton pairs in pp collisions at the LHC was studied recently by the CMS collaboration [18, 19].

This Letter reports a measurement of exclusive dilepton production in pp collisions at $\sqrt{s} = 7$ TeV. The measurement of exclusive dilepton production cross-section is compared to the QED-based prediction with and without proton absorptive corrections.

2 The ATLAS detector

The ATLAS experiment [20] at the LHC is a multi-purpose particle detector with a forward-backward symmetric cylindrical geometry and nearly 4π coverage in solid angle.[1] It consists of inner tracking devices surrounded by a superconducting solenoid, electromagnetic and hadronic calorimeters, and a muon spectrometer. The inner detector (ID) provides charged-particle tracking in the pseudorapidity region $|\eta| < 2.5$ and vertex reconstruction. It comprises a silicon pixel detector, a silicon microstrip tracker, and a straw-tube transition radiation tracker. The ID is surrounded by a solenoid that produces a 2 T axial magnetic field. Lead/liquid-argon (LAr) sampling calorimeters provide electromagnetic (EM) energy measurements with high granularity. A hadron (iron/scintillator-tile) calorimeter covers the central pseudorapidity range $|\eta| < 1.7$. The end-cap and forward regions are instrumented with LAr calorimeters for both the EM and hadronic energy measurements up to $|\eta| = 4.9$. The muon spectrometer (MS) is operated in a magnetic field provided by air-core superconducting toroids and includes tracking chambers for precise muon momentum measurements up to $|\eta| = 2.7$ and trigger chambers covering the range $|\eta| < 2.4$.

A three-level trigger system is used to select interesting events. The first level is implemented in custom electronics and is followed by two software-based trigger levels, referred to collectively as the High-Level Trigger.

3 Theoretical background and event simulation

Calculations of the cross-section for exclusive two-photon production of lepton pairs in pp collisions are based on the Equivalent Photon Approximation (EPA) [4, 5, 21–24]. The EPA relies on the property that the EM field of a charged particle, here a proton, moving at high velocity becomes more and more transverse with respect to the direction of propagation. As a consequence, an observer in the laboratory frame cannot distinguish between the EM field of a relativistic proton and the transverse component of the EM field associated with equivalent photons. Therefore, using the EPA, the cross-section for the reaction above can be written as

$$\sigma^{\mathrm{EPA}}_{pp(\gamma\gamma)\to\ell^+\ell^- pp} = \iint P(x_1)\, P(x_2)\, \sigma_{\gamma\gamma\to\ell^+\ell^-}(m^2_{\ell^+\ell^-})\, \mathrm{d}x_1\, \mathrm{d}x_2 \,,$$

where $P(x_1)$ and $P(x_2)$ are the equivalent photon spectra for the protons, x_1 and x_2 are the fractions of the proton energy carried away by the emitted photons and $m_{\ell^+\ell^-}$ is the invariant mass of the lepton pair. These variables are related by $m^2_{\ell^+\ell^-}/s = x_1 x_2$ where s is the pp centre-of-mass energy squared. The symbol $\sigma_{\gamma\gamma\to\ell^+\ell^-}$ refers to the cross-section for the QED sub-process. As discussed previously, the photons are quasi-real, which means that their virtuality Q^2 is very small compared to $m^2_{\ell^+\ell^-}$. In this kinematic region the EPA gives the same predictions as full leading-order (LO) QED calculations [4, 5].

In the reaction $pp(\gamma\gamma) \to \ell^+\ell^- X$ the protons scattering can be: elastic, $X = pp$; single-dissociative, $X = pX'$; or double-dissociative, $X = X'X''$ (the symbols X', X'' denote any additional final state produced in

[1] ATLAS uses a right-handed coordinate system with its origin at the nominal interaction point in the centre of the detector and the z-axis coinciding with the axis of the beam pipe. The x-axis points from the interaction point to the centre of the LHC ring, and the y-axis points upward. The pseudorapidity is defined in terms of the polar angle θ as $\eta = -\ln\tan(\theta/2)$, and ϕ is the azimuthal angle around the beam pipe with respect to the x-axis. The angular distance is defined as $\Delta R = \sqrt{(\Delta\eta)^2 + (\Delta\phi)^2}$. The transverse momentum is defined relative to the beam axis.

the event). Unless both outgoing protons are detected, the proton dissociative events form an irreducible background to the fully elastic production.

Such photon-induced reactions, in particular exclusive $\gamma\gamma \to \ell^+\ell^-$ production, require significant corrections due to proton absorptive effects. These effects are mainly related to pp strong-interaction exchanges that accompany the two-photon interaction and that lead to the production of additional hadrons in the final state. Recent phenomenological studies suggest that the exclusive $\gamma\gamma \to \ell^+\ell^-$ cross-section is suppressed by a factor that depends on the mass and rapidity of the system produced [10]. For the kinematic range relevant for this measurement the suppression factor is about 20%. This factor includes both the strong pp absorptive correction (~8% suppression) and the photon–proton (γp) coherence condition ($b_{\gamma p} > r_p$, where $b_{\gamma p}$ is the γp impact parameter and r_p the transverse size of the proton).

Simulated event samples are generated in order to estimate the background and to correct the signal yields for detector effects. The signal event samples for exclusive $\gamma\gamma \to \ell^+\ell^-$ production are generated using the Herwig++ 2.6.3 [25] Monte Carlo (MC) event generator, which implements the EPA formalism in pp collisions. The dominant background, photon-induced single-dissociative dilepton production, is simulated using Lpair 4.0 [26] with the Brasse [27] and Suri–Yennie [28] structure functions for proton dissociation. For photon virtualities $Q^2 < 5$ GeV^2 and masses of the dissociating system, $m_N < 2$ GeV, low-multiplicity states from the production and decays of Δ resonances are usually created. For higher Q^2 or m_N, the system decays to a variety of resonances, which produce a large number of forward particles. The Lpair package is interfaced to JetSet 7.408 [29], where the Lund [30] fragmentation model is implemented. The Herwig++ and Lpair generators do not include any corrections to account for proton absorptive effects.

For double-dissociative reactions, Pythia 8.175 [31] is used with the NNPDF2.3QED [32] parton distribution functions (PDF). The NNPDF2.3QED set uses LO QED and next-to-next-to-leading-order (NNLO) QCD perturbative calculations to construct the photon PDF, starting from the initial scale $Q_0^2 = 2$ GeV^2. Depending on the multiplicity of the dissociating system, the default Pythia 8 string or mini-string fragmentation model is used for proton dissociation. The absorptive effects in double-dissociative MC events are taken into account using the default multi-parton interactions model in Pythia 8 [33].

The Powheg 1.0 [34–36] MC generator is used with the CT10 [37] PDF to generate both the DY $Z/\gamma^* \to e^+e^-$ and $Z/\gamma^* \to \mu^+\mu^-$ events. It is interfaced with Pythia 6.425 [38] using the CTEQ6L1 [39] PDF set and the AUET2B [40] values of the tunable parameters to simulate the parton shower and the underlying event (UE). These samples are referred to as Powheg+Pythia. The DY $Z/\gamma^* \to \tau^+\tau^-$ process is generated using Pythia 6.425 together with the MRST LO* [41] PDF. The transverse momentum of lepton pairs in Powheg+Pythia samples is reweighted to a Resbos [42] prediction, which is found to yield good agreement with the transverse momentum distribution of Z bosons observed in data [43, 44]. The production of top-quark pair ($t\bar{t}$) events is modelled using MC@NLO 3.42 [45, 46] and diboson (W^+W^-, $W^\pm Z$, ZZ) processes are simulated using Herwig 6.520 [47]. The event generators used to model Z/γ^*, $t\bar{t}$ and diboson reactions are interfaced to Photos 3.0 [48] to simulate QED final-state radiation (FSR) corrections.

Multiple interactions per bunch crossing (pile-up) are accounted for by overlaying simulated minimum-bias events, generated with Pythia 6.425 using the AUET2B tune and CTEQ6L1 PDF, and reweighting the distribution of the average number of interactions per bunch crossing in MC simulation to that observed in data. Furthermore, the simulated samples are weighted such that the z-position distribution of reconstructed pp interaction vertices matches the distribution observed in data. The ATLAS detector

response is modelled using the GEANT4 toolkit [49, 50] and the same event reconstruction as that used for data is performed.

4 Event reconstruction, preselection and background estimation

The data used in this analysis were collected during the 2011 LHC pp run at a centre-of-mass energy of $\sqrt{s} = 7$ TeV. After application of data-quality requirements, the total integrated luminosity is 4.6 fb^{-1} with an uncertainty of 1.8% [51]. Events from these pp collisions are selected by requiring at least one collision vertex with at least two charged-particle tracks with $p_{\mathrm{T}} > 400$ MeV. Events are then required to have at least two lepton candidates (electrons or muons), as defined below.

Events in the electron channel were selected online by requiring a single-electron or di-electron trigger. For the single-electron trigger, the transverse momentum threshold was increased during data-taking from 20 GeV to 22 GeV in response to the increased LHC instantaneous luminosity. The di-electron trigger required a minimum transverse momentum of 12 GeV for each electron candidate. Electron candidates are reconstructed from energy deposits in the calorimeter matched to ID tracks. Electron reconstruction uses track refitting with a Gaussian-sum filter to be less sensitive to bremsstrahlung losses and improve the estimates of the electron track parameters [52, 53]. The electrons are required to have a transverse momentum $p_{\mathrm{T}}^{e} > 12$ GeV and pseudorapidity $|\eta^{e}| < 2.4$ with the calorimeter barrel/end-cap transition region $1.37 < |\eta^{e}| < 1.52$ excluded. Electron candidates are required to meet "medium" identification criteria based on shower shape and track-quality variables [54].

Events in the muon channel were selected online by a single-muon or di-muon trigger, with a transverse momentum threshold of 18 GeV or 10 GeV, respectively. Muon candidates are identified by matching complete tracks in the MS to tracks in the ID [55], and are required to have $p_{\mathrm{T}}^{\mu} > 10$ GeV and $|\eta^{\mu}| < 2.4$. Only isolated muons are selected by requiring the scalar sum of the p_{T} of the tracks with $p_{\mathrm{T}} > 1$ GeV in a $\Delta R = 0.2$ cone around the muon to be less than 10% of the muon p_{T}.

Di-electron (di-muon) events are selected by requiring two oppositely charged same-flavour leptons with an invariant mass $m_{e^+e^-} > 24$ GeV for the electron channel and $m_{\mu^+\mu^-} > 20$ GeV for the muon channel. After these preselection requirements 1.57×10^6 di-electron and 2.42×10^6 di-muon candidate events are found in the data.

The background to the exclusive signal includes contributions from single- and double-proton dissociative $\gamma\gamma \to \ell^+\ell^-$ production, as well as Z/γ^*, diboson, $t\bar{t}$ and multi-jet production. The contribution from $\gamma\gamma \to W^+W^-$ and $\gamma\gamma \to \tau^+\tau^-$ processes is considered negligible. Single- and double-dissociative background contributions are estimated using MC simulations. The electroweak (Z/γ^*, diboson) and top-quark pair background contributions are also estimated from simulations and normalised to the respective inclusive cross-sections calculated at high orders in perturbative QCD (pQCD), as in Ref. [56]. Scale factors are applied to the simulated samples to correct for the small differences from data in the trigger, reconstruction and identification efficiencies for electrons and muons [54–56]. MC events are also corrected to take into account differences from data in lepton energy, momentum scale and resolution [55, 57].

The multi-jet background is determined using data-driven methods, similarly to Refs. [44, 58]. For the e^+e^- channel, the multi-jet sample is obtained by applying the full nominal preselection but requiring the electron candidates to not satisfy the medium identification criteria. For the $\mu^+\mu^-$ channel, it is extracted using same-charge muon pairs that satisfy the remaining preselection criteria. The normalisation of the multi-jet background is determined by fitting the invariant mass spectrum of the electron (muon) pair

in the data to a sum of expected contributions, including MC predictions of the signal and the other backgrounds.

5 Exclusive event selection and signal extraction

In order to select exclusive $\gamma\gamma \to \ell^+\ell^-$ candidates, a veto on additional charged-particle track activity is applied. This exclusivity veto requires that no additional charged-particle tracks with $p_{\mathrm{T}} > 400$ MeV be associated with the dilepton vertex, and that no additional tracks or vertices be found within a 3 mm longitudinal isolation distance, $\Delta z_{\mathrm{vtx}}^{\mathrm{iso}}$, from the dilepton vertex. These conditions are primarily motivated by the rejection of the Z/γ^* and multi-jet events, which typically have many tracks originating from the same vertex.

The charged-particle multiplicity distribution in Z/γ^* MC events is reweighted to match the UE observed in data, following the same procedure as in Ref. [59]. Uncorrected Z/γ^* MC models overestimate the charged-particle multiplicity distributions observed in data by 50% for low-multiplicity events. In order to estimate the relevant weight, the events in the Z-peak region, defined as 70 GeV $< m_{\ell^+\ell^-} <$ 105 GeV, are used. This region is expected to include a large DY component. The correction procedure also accounts for the effect of tracks originating from pile-up and ID track reconstruction inefficiency. The requirement of no additional tracks associated with the dilepton vertex completely removes multi-jet, $t\bar{t}$, and diboson backgrounds.

The $\Delta z_{\mathrm{vtx}}^{\mathrm{iso}}$ distribution for events with no additional tracks at the dilepton vertex is presented in Figure 1(a). The structure observed at small $\Delta z_{\mathrm{vtx}}^{\mathrm{iso}}$ values is due to the vertex finding algorithm, which identifies the vertex as two close vertices in high-multiplicity DY events: the two-track vertex formed from the lepton tracks and the vertex from the UE tracks. The 3 mm cut significantly suppresses the DY background, at the cost of a 26% reduction in signal yield. The inefficiency is related to tracks and vertices originating from additional pp interactions.

Contributions from the DY $\mathrm{e^+e^-}$ and $\mu^+\mu^-$ processes can be further reduced by excluding events with a dilepton invariant mass in the Z-peak region. The invariant mass distribution of muon pairs for events satisfying the exclusivity veto (exactly two tracks at the dilepton vertex, $\Delta z_{\mathrm{vtx}}^{\mathrm{iso}} > 3$ mm) is presented in Figure 1(b) (where the excluded Z-peak region is indicated by dashed lines). The figure shows that the MC description of the $m_{\mu^+\mu^-}$ distribution is satisfactory. To further suppress the proton dissociative backgrounds, the lepton pair is required to have small total transverse momentum ($p_{\mathrm{T}}^{\ell^+\ell^-} < 1.5$ GeV). This is shown in Figure 1(c), which displays the di-muon transverse momentum distribution for events outside the Z region that satisfy the exclusivity veto. The $p_{\mathrm{T}}^{\ell^+\ell^-}$ resolution below 1.5 GeV is approximately 0.3 GeV for the electron channel and 0.2 GeV for the muon channel.

The result of each step of the exclusive selection applied to the data, signal and background samples is shown in Table 1. After all selection criteria are applied, 869 events remain for the electron channel, and 2124 events are selected in the muon channel. From simulations, approximately half are expected to originate from exclusive production. The number of selected events in the data is below the expectation from the simulation, with an observed yield that is approximately 80% of the sum of simulated signal and background processes (see discussion in Section 7).

After the final exclusive event selection, there is still a significant contamination from DY, single- and double-dissociative processes. Scaling factors for signal and background processes are estimated by a binned maximum-likelihood fit of the sum of the simulated distributions contained in the MC templates

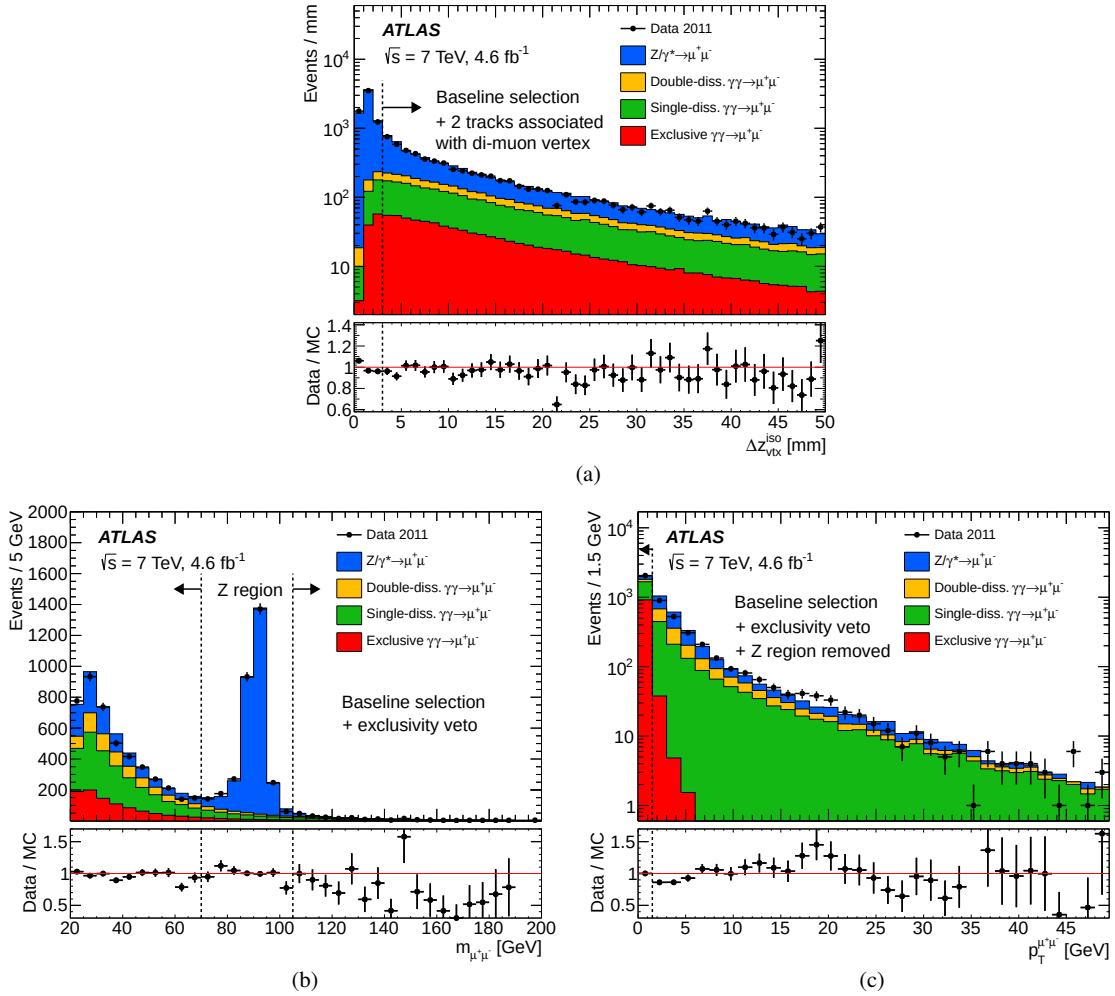

Figure 1: Illustration of exclusive event selection in the muon channel (see text). (a) Longitudinal distance between the di-muon vertex and any other tracks or vertices, (b) di-muon invariant mass, and (c) transverse momentum of the di-muon system, after application of subsequent selection criteria (indicated by the dashed lines). Data are shown as points with statistical error bars, while the histograms represent the expected signal and background levels, corrected using the scale factors described in the text.

for the various processes, to the measured dilepton acoplanarity $(1 - |\Delta\phi_{\ell^+\ell^-}|/\pi)$ distribution. The fit determines two scaling factors, defined as the ratios of the number of observed to the number of expected events based on the MC predictions, for the exclusive ($R^{\text{excl.}}$) and single-dissociative ($R^{\text{s-diss.}}$) templates. The double-dissociative and DY contributions are fixed to the MC predictions in the fit procedure. Contributions from other background processes are found to be negligible.

Figure 2 shows the e^+e^- and $\mu^+\mu^-$ acoplanarity distributions in data overlaid with the result of the fit to the shapes from MC simulations for events satisfying all selection requirements. The results from the best fit to the data for the electron channel are: $R^{\text{excl.}}_{\gamma\gamma\to e^+e^-} = 0.863 \pm 0.070$ (stat.) for the signal scaling factor and $R^{\text{s-diss.}}_{\gamma\gamma\to e^+e^-} = 0.759 \pm 0.080$ (stat.) for the single-dissociative scaling factor. Similarly, for the muon channel the results are: $R^{\text{excl.}}_{\gamma\gamma\to\mu^+\mu^-} = 0.791 \pm 0.041$ (stat.) and $R^{\text{s-diss.}}_{\gamma\gamma\to\mu^+\mu^-} = 0.762 \pm 0.049$ (stat.).

Table 1: Effect of sequential selection requirements on the number of events selected in data, compared to the number of predicted signal and background events for electron and muon channels. Predictions for exclusive and single-dissociative event yields do not take into account proton absorptive corrections.

Selection	$\gamma\gamma \to \ell^+\ell^-$			Z/γ^*	Multi-	Z/γ^*		Di-	Total	
	Signal	S-diss.	D-diss.	$\to \ell^+\ell^-$	jet	$\to \tau^+\tau^-$	$t\bar{t}$	boson	predicted	Data
Electron channel ($\ell = e$)										
Preselection	898	2096	2070	1 460 000	83 000	3760	4610	1950	1 560 000	1 572 271
Exclusivity veto	661	1480	470	3140	0	9	0	5	5780	5410
Z region removed	569	1276	380	600	0	8	0	3	2840	2586
$p_{\mathrm{T}}^{\ell^+\ell^-} < 1.5$ GeV	438	414	80	100	0	2	0	0	1030	869
Muon channel ($\ell = \mu$)										
Preselection	1774	3964	4390	2 300 000	98 000	7610	6710	2870	2 420 000	2 422 745
Exclusivity veto	1313	2892	860	3960	3	8	0	6	9040	7940
Z region removed	1215	2618	760	1160	3	8	0	3	5760	4729
$p_{\mathrm{T}}^{\ell^+\ell^-} < 1.5$ GeV	1174	1085	160	210	0	3	0	0	2630	2124

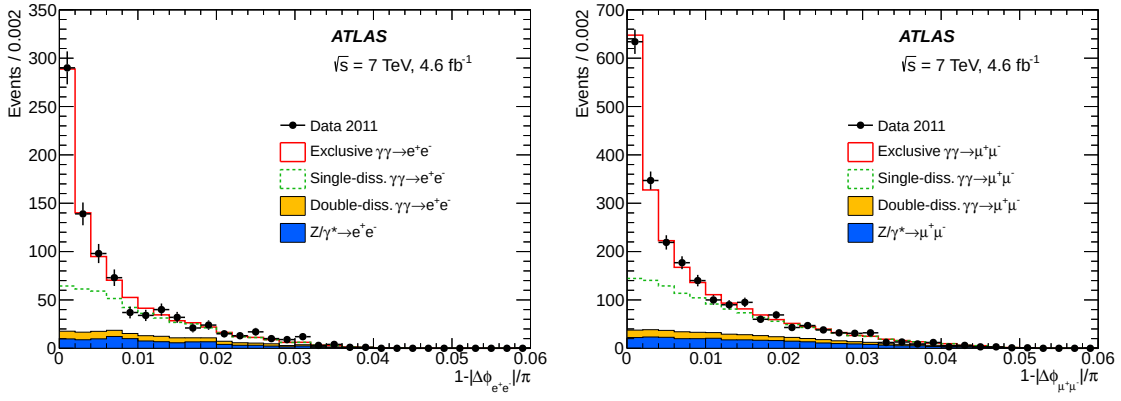

(a) (b)

Figure 2: (a) Di-electron and (b) di-muon acoplanarity distributions for the selected sample after exclusivity requirements. Data are shown as points with statistical error bars. The stacked histograms, in top-to-bottom order, represent the simulated exclusive signal, and the single-dissociative, double-dissociative and DY backgrounds. The exclusive and single-dissociative yields are determined from the fit described in the text.

The central values and statistical uncertainties on $R^{\text{excl.}}$ are strongly correlated with the central values and uncertainties on $R^{\text{s-diss.}}$, respectively.

6 Systematic uncertainties and cross-checks

The different contributions to the systematic uncertainties are described below. The dominant sources of systematic uncertainty for both the electron and muon channels are related to background modelling.

The uncertainty on the electron and muon selection includes uncertainties on the electron energy or muon momentum scale and resolution, as well as uncertainties on the scale factors applied to the simulation

in order to reproduce the trigger, reconstruction and identification efficiencies for electrons or muons measured in the data. The lepton energy or momentum scale correction uncertainties are obtained from a comparison of the Z boson invariant mass distribution in data and simulation, while the uncertainties on the scale factors are derived from a comparison of tag-and-probe results in data and simulations [54–57]. The overall effect on the exclusive $\gamma\gamma \to \ell^+\ell^-$ cross-sections is approximately 1–3%, where the dominant electron uncertainties originate from the electron reconstruction and identification and the dominant muon uncertainty originates from the trigger.

The uncertainty on the contribution of DY processes mainly accounts for disagreements between data and simulations which are related to the reweighting procedures of the charged-particle multiplicity (10%) and $p_{\mathrm{T}}^{\ell^+\ell^-}$ (5%) distributions. It also includes a 5% contribution for the PDF and scale uncertainties in modelling DY processes, as well as a 5% statistical uncertainty on the Z/γ^* MC samples after event selection. An overall normalisation uncertainty of 20% is assigned to cover all these effects. Because of the similar shapes of the DY and single-proton dissociative $\gamma\gamma \to \ell^+\ell^-$ components in the fitted acoplanarity distribution, this uncertainty on the DY normalisation is partly absorbed by the single-dissociative contribution. The 20% uncertainly has a 1.2% effect on the exclusive cross-section for the electron channel and 1% for the muon channel.

In order to estimate the double-proton dissociative $\gamma\gamma \to \ell^+\ell^-$ uncertainty, this contribution is varied according to the photon PDF uncertainties, defined at 68% confidence level and evaluated using NNPDF2.3QED replicas [32]. The photon PDF are affected by sizeable uncertainties, typically of the order of 50%. The resulting uncertainty on the exclusive cross-sections related to double-dissociative background uncertainty is 1.9% for the electron channel and 1.7% for the muon channel.

The uncertainty arising from the choice of acoplanarity shapes in the fit procedure is evaluated by refitting the data with different template distributions. A small deviation of the proton elastic form-factors [60] from the standard dipole parameterisation used in the simulations has a 0.2% effect on the exclusive cross-sections. This effect is estimated by reweighting the equivalent photon spectra in signal MC events to agree with the model predictions. The impact of the shape uncertainty in the single-dissociative template is evaluated by reweighting the corresponding MC events with an exponential modification factor $\propto \exp\left[-a(p_{\mathrm{T}}^{\ell^+\ell^-})^2\right]$. A value of $a = 0.05$ GeV^{-2} is extracted from the data (before the $p_{\mathrm{T}}^{\ell^+\ell^-} < 1.5$ GeV selection) to improve the shape agreement with the simulation, shown in Figure 1(c). Propagating these weights to the acoplanarity distribution and the signal extraction results in a 0.9% change of signal yields.

Possible mis-modelling of the angular resolution of the tracking detectors [61] measuring the lepton tracks could also distort the shape of the signal template, and leads to uncertainties of up to 0.3% (0.2%) in the electron (muon) channel.

The systematic effect related to the pile-up description is estimated from data-to-MC comparisons of the p_{T}- and η-dependent density of tracks originating from pile-up, as in Ref. [59]. The resulting uncertainty on the cross-sections is 0.5%.

The dilepton vertex isolation efficiency is studied by comparing the spatial distribution of tracks originating from pile-up in MC simulations and in data. The effect of mis-modelling of the vertex isolation efficiency is determined by comparing the efficiency in data and simulations for different $\Delta z_{\mathrm{vtx}}^{\mathrm{iso}}$ values (varied between 2 mm and 5 mm, where the sensitivity of the measurements to the level of background is

Table 2: Summary of systematic uncertainties on the exclusive cross-section measurement for the electron and muon channels. The data statistical uncertainties are also given for comparison.

	Uncertainty [%]	
Source of uncertainty	$\gamma\gamma \to e^+e^-$	$\gamma\gamma \to \mu^+\mu^-$
Electron reconstruction and identification efficiency	1.9	-
Electron energy scale and resolution	1.4	-
Electron trigger efficiency	0.7	-
Muon reconstruction efficiency	-	0.2
Muon momentum scale and resolution	-	0.5
Muon trigger efficiency	-	0.6
Backgrounds	2.3	2.0
Template shapes	1.0	0.9
Pile-up description	0.5	0.5
Vertex isolation efficiency	1.2	1.2
LHC beam effects	0.5	0.5
QED FSR in DY e^+e^-	0.8	-
Luminosity	1.8	1.8
Total systematic uncertainty	4.3	3.3
Data statistical uncertainty	8.2	5.1

maximal). The relative variations between the data and simulations are found to be at most 1.2%, which is taken as a systematic uncertainty.

The LHC beam energy uncertainty is evaluated to be 0.7%, following Ref. [62]. This affects the exclusive cross-sections by 0.4% and is considered as a systematic effect. The impact of the non-zero crossing angles of the LHC beams at the ATLAS interaction point is estimated by applying a relevant Lorentz transformation to generator-level lepton kinematics for signal MC events. This results in a 0.3% variation and is taken as a systematic uncertainty.

The effect of QED FSR is predicted to be small (below 1%) in exclusive $\gamma\gamma \to \ell^+\ell^-$ reactions [63]. However, as experimental corrections for electrons are derived from $Z/\gamma^* \to e^+e^-$ and $W \to e\nu$ processes including significant QED FSR effects, these corrections may not be directly applicable to the exclusive dilepton signal MC events without QED FSR simulation. A possible bias in the electron efficiencies is studied by comparing DY e^+e^- MC events with and without QED FSR photons being emitted. The observed difference in the efficiency to trigger, reconstruct and identify electron pairs is 0.8%, which is taken as a systematic uncertainty.

Additional tests of the maximum-likelihood fit stability are performed by comparing different bin widths and fit ranges. Starting from the nominal number of 30 bins in the fit range $0 \leq 1 - |\Delta\phi_{\ell^+\ell^-}|/\pi \leq 0.06$, variations of the bin width (0.002 ± 0.001) and fit range from [0, 0.03] to [0, 0.09] produce relative changes of at most 0.9%. Since these variations are strongly correlated with the statistical uncertainties, no additional systematic uncertainty is assigned in this case.

Table 2 summarises the contributions to the systematic uncertainty on the exclusive cross-sections from the different sources. The total systematic uncertainty is formed by adding the individual contributions

in quadrature for each analysis channel, including the uncertainty on the integrated luminosity. Control distributions of the dilepton transverse momentum for events satisfying the selection criteria listed in Table 1 are shown in Figure 3, with the exclusive and single-dissociative yields normalised according to the fit results. Here an additional cut on the dilepton acoplanarity ($1 - |\Delta\phi_{\ell^+\ell^-}|/\pi < 0.008$) is used, instead of the cut on total transverse momentum ($p_{\mathrm{T}}^{\ell^+\ell^-} < 1.5$ GeV). The MC predictions for the shapes of dilepton distributions are found to be in good agreement with the data.

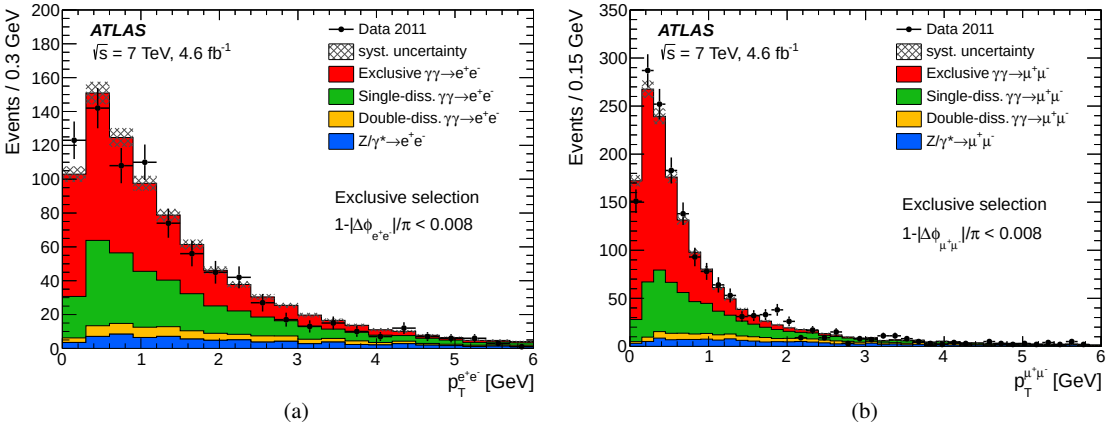

Figure 3: Control distributions of (a) the di-electron and (b) the di-muon transverse momentum for events passing the exclusivity veto together with the other selection criteria described in Section 5, and passing a cut on the dilepton acoplanarity ($1 - |\Delta\phi_{\ell^+\ell^-}|/\pi < 0.008$), instead of the total transverse momentum. Data are shown as points with statistical error bars, while the histograms, in top-to-bottom order, represent the simulated exclusive signal, and the single-dissociative, double-dissociative and DY backgrounds. Systematic uncertainties on the signal events are shown by the black-hashed regions. The exclusive and single-dissociative yields are determined from the fit described in the text.

7 Results and comparison to theory

The exclusive $\gamma\gamma \to \ell^+\ell^-$ cross-sections reported in this article are restricted to the fiducial regions defined in Table 3. The event selection results in an acceptance times efficiency of 19% for the electron channel and 32% for the muon channel. The fiducial cross-sections are given by the product of the measured signal scale factors by the exclusive cross-sections predicted, in the fiducial region considered, by the EPA calculation:

$$\sigma^{\mathrm{excl.}}_{\gamma\gamma\to\ell^+\ell^-} = R^{\mathrm{excl.}}_{\gamma\gamma\to\ell^+\ell^-} \cdot \sigma^{\mathrm{EPA}}_{\gamma\gamma\to\ell^+\ell^-} \, .$$

For the $\mathrm{e^+e^-}$ channel,

$$\begin{aligned} R^{\mathrm{excl.}}_{\gamma\gamma\to\mathrm{e^+e^-}} &= 0.863 \pm 0.070\ (\mathrm{stat.}) \pm 0.037\ (\mathrm{syst.}) \pm 0.015\ (\mathrm{theor.}) \, , \\ \sigma^{\mathrm{EPA}}_{\gamma\gamma\to\mathrm{e^+e^-}} &= 0.496 \ \pm \ 0.008\ (\mathrm{theor.})\ \mathrm{pb} \, . \end{aligned}$$

The theoretical uncertainties are fully correlated between $R^{\mathrm{excl.}}_{\gamma\gamma\to\mathrm{e^+e^-}}$ and $\sigma^{\mathrm{EPA}}_{\gamma\gamma\to\mathrm{e^+e^-}}$, and cancel each other in the cross-section extraction procedure. They are related to the proton elastic form-factors (1.6%) and to the higher-order electroweak corrections [63] not included in the calculations (0.7%). The proton form-factor uncertainty is conservatively estimated by taking the full difference between the calculations using

Table 3: Definition of the electron and muon channel fiducial regions for which the exclusive cross-sections are evaluated.

Variable	Electron channel	Muon channel
p_{T}^{ℓ}	> 12 GeV	> 10 GeV
$\lvert\eta^{\ell}\rvert$	< 2.4	< 2.4
$m_{\ell^+\ell^-}$	> 24 GeV	> 20 GeV

the standard dipole form-factors and the improved model parameterisation including pQCD corrections from Ref. [60]. The latter includes a fit uncertainty and the prediction furthest away from the dipole form-factors is chosen.

Similarly, for the $\mu^+\mu^-$ channel,

$$\begin{aligned} R^{\text{excl.}}_{\gamma\gamma\to\mu^+\mu^-} &= 0.791 \pm 0.041\ (\text{stat.}) \pm 0.026\ (\text{syst.}) \pm 0.013\ (\text{theor.})\ , \\ \sigma^{\text{EPA}}_{\gamma\gamma\to\mu^+\mu^-} &= 0.794\ \pm\ 0.013\ (\text{theor.})\ \text{pb}\ . \end{aligned}$$

The resulting fiducial cross-section for the electron channel is measured to be

$$\sigma^{\text{excl.}}_{\gamma\gamma\to e^+e^-} = 0.428\ \pm\ 0.035\ (\text{stat.})\ \pm\ 0.018\ (\text{syst.})\ \text{pb}\ .$$

This value can be compared to the theoretical prediction, including absorptive corrections to account for the finite size of the proton [10]:

$$\sigma^{\text{EPA, corr.}}_{\gamma\gamma\to e^+e^-} = 0.398\ \pm\ 0.007\ (\text{theor.})\ \text{pb}\ .$$

For the muon channel, the fiducial cross-section is measured to be

$$\sigma^{\text{excl.}}_{\gamma\gamma\to\mu^+\mu^-} = 0.628\ \pm\ 0.032\ (\text{stat.})\ \pm\ 0.021\ (\text{syst.})\ \text{pb}\ ,$$

to be compared with [10]:

$$\sigma^{\text{EPA, corr.}}_{\gamma\gamma\to\mu^+\mu^-} = 0.638\ \pm\ 0.011\ (\text{theor.})\ \text{pb}\ .$$

The uncertainty of each prediction includes an additional 0.8% uncertainty related to the modelling of proton absorptive corrections. It is evaluated by varying the effective transverse size of the proton by 3%, according to Ref. [64]. Figure 4 shows the ratios of the measured cross-sections to the EPA calculations and to the prediction with the inclusion of absorptive corrections. The measurements are in agreement with the predicted values corrected for proton absorptive effects. The figure includes a similar CMS cross-section measurement [18].

8 Conclusion

Using 4.6 fb^{-1} of data from pp collisions at a centre-of-mass energy of 7 TeV the fiducial cross-sections for exclusive $\gamma\gamma \to \ell^+\ell^-$ ($\ell = e,\ \mu$) reactions have been measured with the ATLAS detector at the LHC. Comparisons are made to the theory predictions based on EPA calculations, as included in the Herwig++ MC generator. The corresponding data-to-EPA signal ratios for the electron and muon channels

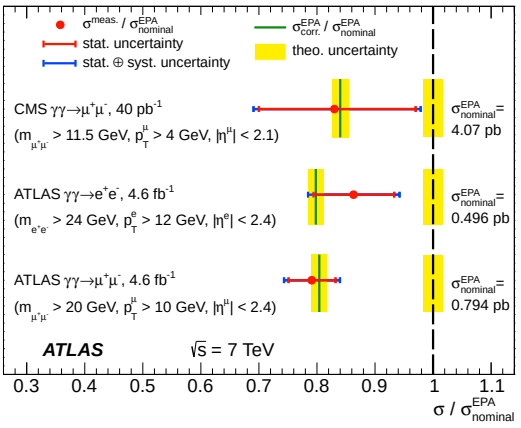

Figure 4: Comparison of the ratios of measured (red points) and predicted (solid green lines) cross-sections to the uncorrected EPA calculations (black dashed line). Results for the muon and electron channels are also compared with a similar CMS measurement [18]. The inner red error bar represents the statistical error, and the blue bar represents the total error on each measurement. The yellow band represents the theoretical uncertainty of 1.8% (1.7%) on the predicted (uncorrected EPA) cross-sections, assumed to be uniform in the phase space of the measurements.

are consistent with the recent CMS measurement and indicate a suppression of the exclusive production mechanism in data with respect to EPA prediction. The observed cross-sections are about 20% below the nominal EPA prediction, and consistent with the suppression expected due to proton absorption contributions. The MC predictions for the shapes of the dilepton kinematic distributions, including both the exclusive signal and the background dominated by two-photon production of lepton pairs with single-proton dissociation, are also found to be in good agreement with the data. With its improved statistical precision compared to previous measurements, this analysis provides a better understanding of the physics of two-photon interactions at hadron colliders.

Acknowledgements

We thank CERN for the very successful operation of the LHC, as well as the support staff from our institutions without whom ATLAS could not be operated efficiently.

We acknowledge the support of ANPCyT, Argentina; YerPhI, Armenia; ARC, Australia; BMWFW and FWF, Austria; ANAS, Azerbaijan; SSTC, Belarus; CNPq and FAPESP, Brazil; NSERC, NRC and CFI, Canada; CERN; CONICYT, Chile; CAS, MOST and NSFC, China; COLCIENCIAS, Colombia; MSMT CR, MPO CR and VSC CR, Czech Republic; DNRF, DNSRC and Lundbeck Foundation, Denmark; EPLANET, ERC and NSRF, European Union; IN2P3-CNRS, CEA-DSM/IRFU, France; GNSF, Georgia; BMBF, DFG, HGF, MPG and AvH Foundation, Germany; GSRT and NSRF, Greece; RGC, Hong Kong SAR, China; ISF, MINERVA, GIF, I-CORE and Benoziyo Center, Israel; INFN, Italy; MEXT and JSPS, Japan; CNRST, Morocco; FOM and NWO, Netherlands; BRF and RCN, Norway; MNiSW and NCN, Poland; GRICES and FCT, Portugal; MNE/IFA, Romania; MES of Russia and NRC KI, Russian Federation; JINR; MSTD, Serbia; MSSR, Slovakia; ARRS and MIZŠ, Slovenia; DST/NRF, South Africa; MINECO, Spain; SRC and Wallenberg Foundation, Sweden; SER, SNSF and Cantons of Bern

and Geneva, Switzerland; NSC, Taiwan; TAEK, Turkey; STFC, the Royal Society and Leverhulme Trust, United Kingdom; DOE and NSF, United States of America.

The crucial computing support from all WLCG partners is acknowledged gratefully, in particular from CERN and the ATLAS Tier-1 facilities at TRIUMF (Canada), NDGF (Denmark, Norway, Sweden), CC-IN2P3 (France), KIT/GridKA (Germany), INFN-CNAF (Italy), NL-T1 (Netherlands), PIC (Spain), ASGC (Taiwan), RAL (UK) and BNL (USA) and in the Tier-2 facilities worldwide.

References

[1] CMS Collaboration, *Study of exclusive two-photon production of W^+W^- in pp collisions at $\sqrt{s} = 7$ TeV and constraints on anomalous quartic gauge couplings*, JHEP **1307** (2013) 116, arXiv:1305.5596 [hep-ex].

[2] C. Carimalo, P. Kessler and J. Parisi, *$\gamma\gamma$ Background of the Drell-Yan Process*, Phys. Rev. **D18** (1978) 2443.

[3] ATLAS Collaboration, *Measurement of the high-mass Drell–Yan differential cross-section in pp collisions at $\sqrt{s} = 7$ TeV with the ATLAS detector*, Phys. Lett. **B725** (2013) 223–242, arXiv:1305.4192 [hep-ex].

[4] M.-S. Chen et al., *Lepton pair production from two-photon processes*, Phys. Rev. **D7** (1973) 3485–3502.

[5] V. Budnev et al., *The process $pp \to ppe^+e^-$ and the possibility of its calculation by means of quantum electrodynamics only*, Nucl. Phys. **B63** (1973) 519–541.

[6] V. A. Khoze et al., *Luminosity monitors at the LHC*, Eur. Phys. J. **C19** (2001) 313–322, arXiv:hep-ph/0010163 [hep-ph].

[7] A. Shamov and V. I. Telnov, *Precision luminosity measurement at LHC using two photon production of $\mu^+\mu^-$ pairs*, Nucl. Instrum. Meth. **A494** (2002) 51–56, arXiv:hep-ex/0207095 [hep-ex].

[8] M. Krasny, J. Chwastowski and K. Slowikowski, *Luminosity measurement method for LHC: The Theoretical precision and the experimental challenges*, Nucl. Instrum. Meth. **A584** (2008) 42–52, arXiv:hep-ex/0610052 [hep-ex].

[9] W. Schafer and A. Szczurek, *Exclusive photoproduction of J/ψ in proton-proton and proton-antiproton scattering*, Phys. Rev. **D76** (2007) 094014, arXiv:0705.2887 [hep-ph].

[10] M. Dyndal and L. Schoeffel, *The role of finite-size effects on the spectrum of equivalent photons in proton–proton collisions at the LHC*, Phys. Lett. **B741** (2015) 66–70, arXiv:1410.2983 [hep-ph].

[11] A. Aktas et al., H1 Collaboration, *Muon pair production in ep collisions at HERA*, Phys. Lett. **B583** (2004) 28–40, arXiv:hep-ex/0311015 [hep-ex].

[12] A. Abulencia et al., CDF Collaboration, *Observation of Exclusive Electron-Positron Production in Hadron-Hadron Collisions*, Phys. Rev. Lett. **98** (2007) 112001, arXiv:hep-ex/0611040 [hep-ex].

[13] T. Aaltonen et al., CDF Collaboration, *Search for exclusive Z boson production and observation of high mass $p\bar{p} \to \gamma\gamma \to p + \ell\ell + \bar{p}$ events in $p\bar{p}$ collisions at $\sqrt{s} = 1.96$ TeV*, Phys. Rev. Lett. **102** (2009) 222002, arXiv:0902.2816 [hep-ex].

[14] T. Aaltonen et al., CDF Collaboration, *Observation of exclusive charmonium production and $\gamma + \gamma$ to $\mu^+\mu^-$ in $p\bar{p}$ collisions at $\sqrt{s} = 1.96$ TeV*, Phys. Rev. Lett. **102** (2009) 242001, arXiv:0902.1271 [hep-ex].

[15] J. Adams et al., STAR Collaboration, *Production of e^+e^- pairs accompanied by nuclear dissociation in ultra-peripheral heavy ion collision*, Phys. Rev. **C70** (2004) 031902, arXiv:nucl-ex/0404012 [nucl-ex].

[16] A. Afanasiev et al., PHENIX Collaboration, *Photoproduction of J/psi and of high mass e+e- in ultra-peripheral Au+Au collisions at $\sqrt{s} = 200$ GeV*, Phys. Lett. **B679** (2009) 321–329, arXiv:0903.2041 [nucl-ex].

[17] E. Abbas et al., ALICE Collaboration, *Charmonium and e^+e^- pair photoproduction at mid-rapidity in ultra-peripheral Pb-Pb collisions at $\sqrt{s_{\rm NN}}$=2.76 TeV*, Eur. Phys. J. **C73**.11 (2013) 2617, arXiv:1305.1467 [nucl-ex].

[18] CMS Collaboration, *Exclusive photon-photon production of muon pairs in proton-proton collisions at $\sqrt{s} = 7$ TeV*, JHEP **1201** (2012) 052, arXiv:1111.5536 [hep-ex].

[19] CMS Collaboration, *Search for exclusive or semi-exclusive photon pair production and observation of exclusive and semi-exclusive electron pair production in pp collisions at $\sqrt{s} = 7$ TeV*, JHEP **1211** (2012) 080, arXiv:1209.1666 [hep-ex].

[20] ATLAS Collaboration, *The ATLAS Experiment at the CERN Large Hadron Collider*, JINST **3** (2008) S08003.

[21] C. von Weizsacker, *Radiation emitted in collisions of very fast electrons*, Z. Phys. **88** (1934) 612–625.

[22] E. Williams, *Nature of the high-energy particles of penetrating radiation and status of ionization and radiation formulae*, Phys. Rev. **45** (1934) 729–730.

[23] H. Terazawa, *Two photon processes for particle production at high-energies*, Rev. Mod. Phys. **45** (1973) 615–662.

[24] V. Budnev et al., *The Two photon particle production mechanism. Physical problems. Applications. Equivalent photon approximation*, Phys. Rept. **15** (1975) 181–281.

[25] M. Bähr et al., *Herwig++ Physics and Manual*, Eur. Phys. J. **C58** (2008) 639–707, arXiv:0803.0883 [hep-ph].

[26] J. Vermaseren, *Two Photon Processes at Very High-Energies*, Nucl. Phys. **B229** (1983) 347.

[27] F. Brasse et al., *Parametrization of the q^2 dependence of $\gamma_V p$ total cross sections in the resonance region*, Nucl. Phys. **B110** (1976) 413.

[28] A. Suri and D. R. Yennie, *The space-time phenomenology of photon absorption and inelastic electron scattering*, Annals Phys. **72** (1972) 243 –292.

[29] T. Sjöstrand, *High-energy physics event generation with PYTHIA 5.7 and JETSET 7.4*, Comput. Phys. Commun. **82** (1994) 74–90.

[30] B. Andersson et al., *Parton Fragmentation and String Dynamics*, Phys. Rept. **97** (1983) 31–145.

[31] T. Sjöstrand, S. Mrenna and P. Z. Skands, *A Brief Introduction to PYTHIA 8.1*, Comput. Phys. Commun. **178** (2008) 852–867, arXiv:0710.3820 [hep-ph].

[32] R. D. Ball et al., NNPDF Collaboration, *Parton distributions with QED corrections*, Nucl. Phys. **B877** (2013) 290–320, arXiv:1308.0598 [hep-ph].

[33] R. Corke and T. Sjöstrand, *Multiparton Interactions and Rescattering*, JHEP **1001** (2010) 035, arXiv:0911.1909 [hep-ph].

[34] P. Nason, *A New method for combining NLO QCD with shower Monte Carlo algorithms*, JHEP **0411** (2004) 040, arXiv:hep-ph/0409146 [hep-ph].

[35] S. Frixione, P. Nason and C. Oleari, *Matching NLO QCD computations with Parton Shower simulations: the POWHEG method*, JHEP **0711** (2007) 070, arXiv:0709.2092 [hep-ph].

[36] S. Alioli et al., *NLO vector-boson production matched with shower in POWHEG*, JHEP **0807** (2008) 060, arXiv:0805.4802 [hep-ph].

[37] H.-L. Lai et al., *New parton distributions for collider physics*, Phys. Rev. **D82** (2010) 074024, arXiv:1007.2241 [hep-ph].

[38] T. Sjöstrand, S. Mrenna and P. Z. Skands, *PYTHIA 6.4 Physics and Manual*, JHEP **0605** (2006) 026, arXiv:hep-ph/0603175 [hep-ph].

[39] J. Pumplin et al., *New generation of parton distributions with uncertainties from global QCD analysis*, JHEP **0207** (2002) 012, arXiv:hep-ph/0201195 [hep-ph].

[40] ATLAS Collaboration, *ATLAS tunes of PYTHIA 6 and Pythia 8 for MC11*, ATL-PHYS-PUB-2011-009, URL: http://cds.cern.ch/record/1363300.

[41] A. Sherstnev and R. Thorne, *Parton Distributions for LO Generators*, Eur. Phys. J. **C55** (2008) 553–575, arXiv:0711.2473 [hep-ph].

[42] F. Landry et al., *Tevatron Run-1 Z boson data and Collins-Soper-Sterman resummation formalism*, Phys. Rev. **D67** (2003) 073016, arXiv:hep-ph/0212159 [hep-ph].

[43] ATLAS Collaboration, *Measurement of angular correlations in Drell-Yan lepton pairs to probe Z/γ^* boson transverse momentum at $\sqrt{s} = 7$ TeV with the ATLAS detector*, Phys. Lett. **B720** (2013) 32–51, arXiv:1211.6899 [hep-ex].

[44] ATLAS Collaboration, *Measurement of the Z/γ^* boson transverse momentum distribution in pp collisions at $\sqrt{s} = 7$ TeV with the ATLAS detector*, JHEP **1409** (2014) 145, arXiv:1406.3660 [hep-ex].

[45] S. Frixione and B. R. Webber, *Matching NLO QCD computations and parton shower simulations*, JHEP **0206** (2002) 029, arXiv:hep-ph/0204244 [hep-ph].

[46] S. Frixione, P. Nason and B. R. Webber, *Matching NLO QCD and parton showers in heavy flavor production*, JHEP **0308** (2003) 007, arXiv:hep-ph/0305252 [hep-ph].

[47] G. Corcella et al., *HERWIG 6.5 release note* (2002), arXiv:hep-ph/0210213 [hep-ph].

[48] P. Golonka and Z. Was,
PHOTOS Monte Carlo: A Precision tool for QED corrections in Z and W decays,
Eur. Phys. J. **C45** (2006) 97–107, arXiv:hep-ph/0506026 [hep-ph].

[49] S. Agostinelli et al., GEANT4 Collaboration, *GEANT4: A Simulation toolkit*,
Nucl. Instrum. Meth. **A506** (2003) 250–303.

[50] ATLAS Collaboration, *The ATLAS Simulation Infrastructure*, Eur. Phys. J. **70** (2010) 823–874,
arXiv:1005.4568 [physics.ins-det].

[51] ATLAS Collaboration, *Improved luminosity determination in pp collisions at $\sqrt{s}$ = 7 TeV using the ATLAS detector at the LHC*, Eur. Phys. J. **C73** (2013) 2518, arXiv:1302.4393 [hep-ex].

[52] R. Frühwirth, *Track fitting with non-Gaussian noise*, Comput. Phys. Commun. **100** (1997) 1–16.

[53] ATLAS Collaboration, *Improved electron reconstruction in ATLAS using the Gaussian Sum Filter-based model for bremsstrahlung*, ATLAS-CONF-2012-047,
URL: http://cds.cern.ch/record/1449796.

[54] ATLAS Collaboration, *Electron reconstruction and identification efficiency measurements with the ATLAS detector using the 2011 LHC proton-proton collision data*,
Eur. Phys. J. **C74** (2014) 2941, arXiv:1404.2240 [hep-ex].

[55] ATLAS Collaboration, *Measurement of the muon reconstruction performance of the ATLAS detector using 2011 and 2012 LHC proton-proton collision data*,
Eur. Phys. J. **C74**.11 (2014) 3130, arXiv:1407.3935 [hep-ex].

[56] ATLAS Collaboration, *Measurement of the low-mass Drell-Yan differential cross section at $\sqrt{s}$ = 7 TeV using the ATLAS detector*, JHEP **1406** (2014) 112, arXiv:1404.1212 [hep-ex].

[57] ATLAS Collaboration,
Electron and photon energy calibration with the ATLAS detector using LHC Run 1 data,
Eur. Phys. J. **C74**.10 (2014) 3071, arXiv:1407.5063 [hep-ex].

[58] ATLAS Collaboration, *Measurement of the production cross section of jets in association with a Z boson in pp collisions at $\sqrt{s}$ = 7 TeV with the ATLAS detector*, JHEP **1307** (2013) 032,
arXiv:1304.7098 [hep-ex].

[59] ATLAS Collaboration, *Measurement of distributions sensitive to the underlying event in inclusive Z-boson production in pp collisions at $\sqrt{s}$ = 7 TeV with the ATLAS detector*,
Eur. Phys. J. **C74**.12 (2014) 3195, arXiv:1409.3433 [hep-ex].

[60] M. Belushkin, H.-W. Hammer and U.-G. Meissner,
Dispersion analysis of the nucleon form-factors including meson continua,
Phys. Rev. **C75** (2007) 035202, arXiv:hep-ph/0608337 [hep-ph].

[61] ATLAS Collaboration, *The ATLAS Inner Detector commissioning and calibration*,
Eur. Phys. J. **C70** (2010) 787–821, arXiv:1004.5293 [physics.ins-det].

[62] ATLAS Collaboration, *Simultaneous measurements of the $t\bar{t}$, W^+W^-, and $Z/\gamma^* \to \tau\tau$ production cross-sections in pp collisions at $\sqrt{s}$ = 7 TeV with the ATLAS detector*,
Phys. Rev. **D91** (2015) 052005, arXiv:1407.0573 [hep-ex].

[63] A. Denner and S. Dittmaier,
Production of light fermion anti-fermion pairs in gamma gamma collisions,
Eur. Phys. J. **C9** (1999) 425–435, arXiv:hep-ph/9812411 [hep-ph].

[64] F. Aaron et al., H1 Collaboration,
Measurement of deeply virtual Compton scattering and its t-dependence at HERA,
Phys. Lett. **B659** (2008) 796–806, arXiv:0709.4114 [hep-ex].

The ATLAS Collaboration

G. Aad[85], B. Abbott[113], J. Abdallah[151], O. Abdinov[11], R. Aben[107], M. Abolins[90], O.S. AbouZeid[158], H. Abramowicz[153], H. Abreu[152], R. Abreu[116], Y. Abulaiti[146a,146b], B.S. Acharya[164a,164b,a], L. Adamczyk[38a], D.L. Adams[25], J. Adelman[108], S. Adomeit[100], T. Adye[131], A.A. Affolder[74], T. Agatonovic-Jovin[13], J. Agricola[54], J.A. Aguilar-Saavedra[126a,126f], S.P. Ahlen[22], F. Ahmadov[65,b], G. Aielli[133a,133b], H. Akerstedt[146a,146b], T.P.A. Åkesson[81], A.V. Akimov[96], G.L. Alberghi[20a,20b], J. Albert[169], S. Albrand[55], M.J. Alconada Verzini[71], M. Aleksa[30], I.N. Aleksandrov[65], C. Alexa[26a], G. Alexander[153], T. Alexopoulos[10], M. Alhroob[113], G. Alimonti[91a], L. Alio[85], J. Alison[31], S.P. Alkire[35], B.M.M. Allbrooke[149], P.P. Allport[74], A. Aloisio[104a,104b], A. Alonso[36], F. Alonso[71], C. Alpigiani[76], A. Altheimer[35], B. Alvarez Gonzalez[30], D. Álvarez Piqueras[167], M.G. Alviggi[104a,104b], B.T. Amadio[15], K. Amako[66], Y. Amaral Coutinho[24a], C. Amelung[23], D. Amidei[89], S.P. Amor Dos Santos[126a,126c], A. Amorim[126a,126b], S. Amoroso[48], N. Amram[153], G. Amundsen[23], C. Anastopoulos[139], L.S. Ancu[49], N. Andari[108], T. Andeen[35], C.F. Anders[58b], G. Anders[30], J.K. Anders[74], K.J. Anderson[31], A. Andreazza[91a,91b], V. Andrei[58a], S. Angelidakis[9], I. Angelozzi[107], P. Anger[44], A. Angerami[35], F. Anghinolfi[30], A.V. Anisenkov[109,c], N. Anjos[12], A. Annovi[124a,124b], M. Antonelli[47], A. Antonov[98], J. Antos[144b], F. Anulli[132a], M. Aoki[66], L. Aperio Bella[18], G. Arabidze[90], Y. Arai[66], J.P. Araque[126a], A.T.H. Arce[45], F.A. Arduh[71], J-F. Arguin[95], S. Argyropoulos[42], M. Arik[19a], A.J. Armbruster[30], O. Arnaez[30], V. Arnal[82], H. Arnold[48], M. Arratia[28], O. Arslan[21], A. Artamonov[97], G. Artoni[23], S. Asai[155], N. Asbah[42], A. Ashkenazi[153], B. Åsman[146a,146b], L. Asquith[149], K. Assamagan[25], R. Astalos[144a], M. Atkinson[165], N.B. Atlay[141], B. Auerbach[6], K. Augsten[128], M. Aurousseau[145b], G. Avolio[30], B. Axen[15], M.K. Ayoub[117], G. Azuelos[95,d], M.A. Baak[30], A.E. Baas[58a], M.J. Baca[18], C. Bacci[134a,134b], H. Bachacou[136], K. Bachas[154], M. Backes[30], M. Backhaus[30], P. Bagiacchi[132a,132b], P. Bagnaia[132a,132b], Y. Bai[33a], T. Bain[35], J.T. Baines[131], O.K. Baker[176], E.M. Baldin[109,c], P. Balek[129], T. Balestri[148], F. Balli[84], E. Banas[39], Sw. Banerjee[173], A.A.E. Bannoura[175], H.S. Bansil[18], L. Barak[30], E.L. Barberio[88], D. Barberis[50a,50b], M. Barbero[85], T. Barillari[101], M. Barisonzi[164a,164b], T. Barklow[143], N. Barlow[28], S.L. Barnes[84], B.M. Barnett[131], R.M. Barnett[15], Z. Barnovska[5], A. Baroncelli[134a], G. Barone[23], A.J. Barr[120], F. Barreiro[82], J. Barreiro Guimarães da Costa[57], R. Bartoldus[143], A.E. Barton[72], P. Bartos[144a], A. Basalaev[123], A. Bassalat[117], A. Basye[165], R.L. Bates[53], S.J. Batista[158], J.R. Batley[28], M. Battaglia[137], M. Bauce[132a,132b], F. Bauer[136], H.S. Bawa[143,e], J.B. Beacham[111], M.D. Beattie[72], T. Beau[80], P.H. Beauchemin[161], R. Beccherle[124a,124b], P. Bechtle[21], H.P. Beck[17,f], K. Becker[120], M. Becker[83], S. Becker[100], M. Beckingham[170], C. Becot[117], A.J. Beddall[19b], A. Beddall[19b], V.A. Bednyakov[65], C.P. Bee[148], L.J. Beemster[107], T.A. Beermann[175], M. Begel[25], J.K. Behr[120], C. Belanger-Champagne[87], W.H. Bell[49], G. Bella[153], L. Bellagamba[20a], A. Bellerive[29], M. Bellomo[86], K. Belotskiy[98], O. Beltramello[30], O. Benary[153], D. Benchekroun[135a], M. Bender[100], K. Bendtz[146a,146b], N. Benekos[10], Y. Benhammou[153], E. Benhar Noccioli[49], J.A. Benitez Garcia[159b], D.P. Benjamin[45], J.R. Bensinger[23], S. Bentvelsen[107], L. Beresford[120], M. Beretta[47], D. Berge[107], E. Bergeaas Kuutmann[166], N. Berger[5], F. Berghaus[169], J. Beringer[15], C. Bernard[22], N.R. Bernard[86], C. Bernius[110], F.U. Bernlochner[21], T. Berry[77], P. Berta[129], C. Bertella[83], G. Bertoli[146a,146b], F. Bertolucci[124a,124b], C. Bertsche[113], D. Bertsche[113], M.I. Besana[91a], G.J. Besjes[36], O. Bessidskaia Bylund[146a,146b], M. Bessner[42], N. Besson[136], C. Betancourt[48], S. Bethke[101], A.J. Bevan[76], W. Bhimji[15], R.M. Bianchi[125], L. Bianchini[23], M. Bianco[30], O. Biebel[100], D. Biedermann[16], S.P. Bieniek[78], M. Biglietti[134a], J. Bilbao De Mendizabal[49], H. Bilokon[47], M. Bindi[54], S. Binet[117], A. Bingul[19b], C. Bini[132a,132b], S. Biondi[20a,20b], C.W. Black[150], J.E. Black[143], K.M. Black[22], D. Blackburn[138], R.E. Blair[6], J.-B. Blanchard[136], J.E. Blanco[77], T. Blazek[144a], I. Bloch[42], C. Blocker[23], W. Blum[83,*], U. Blumenschein[54], G.J. Bobbink[107], V.S. Bobrovnikov[109,c], S.S. Bocchetta[81], A. Bocci[45],

C. Bock[100], M. Boehler[48], J.A. Bogaerts[30], D. Bogavac[13], A.G. Bogdanchikov[109], C. Bohm[146a], V. Boisvert[77], T. Bold[38a], V. Boldea[26a], A.S. Boldyrev[99], M. Bomben[80], M. Bona[76], M. Boonekamp[136], A. Borisov[130], G. Borissov[72], S. Borroni[42], J. Bortfeldt[100], V. Bortolotto[60a,60b,60c], K. Bos[107], D. Boscherini[20a], M. Bosman[12], J. Boudreau[125], J. Bouffard[2], E.V. Bouhova-Thacker[72], D. Boumediene[34], C. Bourdarios[117], N. Bousson[114], A. Boveia[30], J. Boyd[30], I.R. Boyko[65], I. Bozic[13], J. Bracinik[18], A. Brandt[8], G. Brandt[54], O. Brandt[58a], U. Bratzler[156], B. Brau[86], J.E. Brau[116], H.M. Braun[175,*], S.F. Brazzale[164a,164c], W.D. Breaden Madden[53], K. Brendlinger[122], A.J. Brennan[88], L. Brenner[107], R. Brenner[166], S. Bressler[172], K. Bristow[145c], T.M. Bristow[46], D. Britton[53], D. Britzger[42], F.M. Brochu[28], I. Brock[21], R. Brock[90], J. Bronner[101], G. Brooijmans[35], T. Brooks[77], W.K. Brooks[32b], J. Brosamer[15], E. Brost[116], J. Brown[55], P.A. Bruckman de Renstrom[39], D. Bruncko[144b], R. Bruneliere[48], A. Bruni[20a], G. Bruni[20a], M. Bruschi[20a], N. Bruscino[21], L. Bryngemark[81], T. Buanes[14], Q. Buat[142], P. Buchholz[141], A.G. Buckley[53], S.I. Buda[26a], I.A. Budagov[65], F. Buehrer[48], L. Bugge[119], M.K. Bugge[119], O. Bulekov[98], D. Bullock[8], H. Burckhart[30], S. Burdin[74], B. Burghgrave[108], S. Burke[131], I. Burmeister[43], E. Busato[34], D. Büscher[48], V. Büscher[83], P. Bussey[53], J.M. Butler[22], A.I. Butt[3], C.M. Buttar[53], J.M. Butterworth[78], P. Butti[107], W. Buttinger[25], A. Buzatu[53], A.R. Buzykaev[109,*c*], S. Cabrera Urbán[167], D. Caforio[128], V.M. Cairo[37a,37b], O. Cakir[4a], N. Calace[49], P. Calafiura[15], A. Calandri[136], G. Calderini[80], P. Calfayan[100], L.P. Caloba[24a], D. Calvet[34], S. Calvet[34], R. Camacho Toro[31], S. Camarda[42], P. Camarri[133a,133b], D. Cameron[119], R. Caminal Armadans[165], S. Campana[30], M. Campanelli[78], A. Campoverde[148], V. Canale[104a,104b], A. Canepa[159a], M. Cano Bret[33e], J. Cantero[82], R. Cantrill[126a], T. Cao[40], M.D.M. Capeans Garrido[30], I. Caprini[26a], M. Caprini[26a], M. Capua[37a,37b], R. Caputo[83], R. Cardarelli[133a], F. Cardillo[48], T. Carli[30], G. Carlino[104a], L. Carminati[91a,91b], S. Caron[106], E. Carquin[32a], G.D. Carrillo-Montoya[8], J.R. Carter[28], J. Carvalho[126a,126c], D. Casadei[78], M.P. Casado[12], M. Casolino[12], E. Castaneda-Miranda[145b], A. Castelli[107], V. Castillo Gimenez[167], N.F. Castro[126a,*g*], P. Catastini[57], A. Catinaccio[30], J.R. Catmore[119], A. Cattai[30], J. Caudron[83], V. Cavaliere[165], D. Cavalli[91a], M. Cavalli-Sforza[12], V. Cavasinni[124a,124b], F. Ceradini[134a,134b], B.C. Cerio[45], K. Cerny[129], A.S. Cerqueira[24b], A. Cerri[149], L. Cerrito[76], F. Cerutti[15], M. Cerv[30], A. Cervelli[17], S.A. Cetin[19c], A. Chafaq[135a], D. Chakraborty[108], I. Chalupkova[129], P. Chang[165], J.D. Chapman[28], D.G. Charlton[18], C.C. Chau[158], C.A. Chavez Barajas[149], S. Cheatham[152], A. Chegwidden[90], S. Chekanov[6], S.V. Chekulaev[159a], G.A. Chelkov[65,*h*], M.A. Chelstowska[89], C. Chen[64], H. Chen[25], K. Chen[148], L. Chen[33d,*i*], S. Chen[33c], X. Chen[33f], Y. Chen[67], H.C. Cheng[89], Y. Cheng[31], A. Cheplakov[65], E. Cheremushkina[130], R. Cherkaoui El Moursli[135e], V. Chernyatin[25,*], E. Cheu[7], L. Chevalier[136], V. Chiarella[47], G. Chiarelli[124a,124b], J.T. Childers[6], G. Chiodini[73a], A.S. Chisholm[18], R.T. Chislett[78], A. Chitan[26a], M.V. Chizhov[65], K. Choi[61], S. Chouridou[9], B.K.B. Chow[100], V. Christodoulou[78], D. Chromek-Burckhart[30], J. Chudoba[127], A.J. Chuinard[87], J.J. Chwastowski[39], L. Chytka[115], G. Ciapetti[132a,132b], A.K. Ciftci[4a], D. Cinca[53], V. Cindro[75], I.A. Cioara[21], A. Ciocio[15], Z.H. Citron[172], M. Ciubancan[26a], A. Clark[49], B.L. Clark[57], P.J. Clark[46], R.N. Clarke[15], W. Cleland[125], C. Clement[146a,146b], Y. Coadou[85], M. Cobal[164a,164c], A. Coccaro[138], J. Cochran[64], L. Coffey[23], J.G. Cogan[143], L. Colasurdo[106], B. Cole[35], S. Cole[108], A.P. Colijn[107], J. Collot[55], T. Colombo[58c], G. Compostella[101], P. Conde Muiño[126a,126b], E. Coniavitis[48], S.H. Connell[145b], I.A. Connelly[77], S.M. Consonni[91a,91b], V. Consorti[48], S. Constantinescu[26a], C. Conta[121a,121b], G. Conti[30], F. Conventi[104a,*j*], M. Cooke[15], B.D. Cooper[78], A.M. Cooper-Sarkar[120], T. Cornelissen[175], M. Corradi[20a], F. Corriveau[87,*k*], A. Corso-Radu[163], A. Cortes-Gonzalez[12], G. Cortiana[101], G. Costa[91a], M.J. Costa[167], D. Costanzo[139], D. Côté[8], G. Cottin[28], G. Cowan[77], B.E. Cox[84], K. Cranmer[110], G. Cree[29], S. Crépé-Renaudin[55], F. Crescioli[80], W.A. Cribbs[146a,146b], M. Crispin Ortuzar[120], M. Cristinziani[21], V. Croft[106], G. Crosetti[37a,37b], T. Cuhadar Donszelmann[139], J. Cummings[176], M. Curatolo[47], C. Cuthbert[150], H. Czirr[141], P. Czodrowski[3], S. D'Auria[53], M. D'Onofrio[74], M.J. Da Cunha Sargedas De Sousa[126a,126b], C. Da Via[84], W. Dabrowski[38a],

A. Dafinca[120], T. Dai[89], O. Dale[14], F. Dallaire[95], C. Dallapiccola[86], M. Dam[36], J.R. Dandoy[31], N.P. Dang[48], A.C. Daniells[18], M. Danninger[168], M. Dano Hoffmann[136], V. Dao[48], G. Darbo[50a], S. Darmora[8], J. Dassoulas[3], A. Dattagupta[61], W. Davey[21], C. David[169], T. Davidek[129], E. Davies[120,l], M. Davies[153], P. Davison[78], Y. Davygora[58a], E. Dawe[88], I. Dawson[139], R.K. Daya-Ishmukhametova[86], K. De[8], R. de Asmundis[104a], A. De Benedetti[113], S. De Castro[20a,20b], S. De Cecco[80], N. De Groot[106], P. de Jong[107], H. De la Torre[82], F. De Lorenzi[64], L. De Nooij[107], D. De Pedis[132a], A. De Salvo[132a], U. De Sanctis[149], A. De Santo[149], J.B. De Vivie De Regie[117], W.J. Dearnaley[72], R. Debbe[25], C. Debenedetti[137], D.V. Dedovich[65], I. Deigaard[107], J. Del Peso[82], T. Del Prete[124a,124b], D. Delgove[117], F. Deliot[136], C.M. Delitzsch[49], M. Deliyergiyev[75], A. Dell'Acqua[30], L. Dell'Asta[22], M. Dell'Orso[124a,124b], M. Della Pietra[104a,j], D. della Volpe[49], M. Delmastro[5], P.A. Delsart[55], C. Deluca[107], D.A. DeMarco[158], S. Demers[176], M. Demichev[65], A. Demilly[80], S.P. Denisov[130], D. Derendarz[39], J.E. Derkaoui[135d], F. Derue[80], P. Dervan[74], K. Desch[21], C. Deterre[42], P.O. Deviveiros[30], A. Dewhurst[131], S. Dhaliwal[23], A. Di Ciaccio[133a,133b], L. Di Ciaccio[5], A. Di Domenico[132a,132b], C. Di Donato[104a,104b], A. Di Girolamo[30], B. Di Girolamo[30], A. Di Mattia[152], B. Di Micco[134a,134b], R. Di Nardo[47], A. Di Simone[48], R. Di Sipio[158], D. Di Valentino[29], C. Diaconu[85], M. Diamond[158], F.A. Dias[46], M.A. Diaz[32a], E.B. Diehl[89], J. Dietrich[16], S. Diglio[85], A. Dimitrievska[13], J. Dingfelder[21], P. Dita[26a], S. Dita[26a], F. Dittus[30], F. Djama[85], T. Djobava[51b], J.I. Djuvsland[58a], M.A.B. do Vale[24c], D. Dobos[30], M. Dobre[26a], C. Doglioni[81], T. Dohmae[155], J. Dolejsi[129], Z. Dolezal[129], B.A. Dolgoshein[98,*], M. Donadelli[24d], S. Donati[124a,124b], P. Dondero[121a,121b], J. Donini[34], J. Dopke[131], A. Doria[104a], M.T. Dova[71], A.T. Doyle[53], E. Drechsler[54], M. Dris[10], E. Dubreuil[34], E. Duchovni[172], G. Duckeck[100], O.A. Ducu[26a,85], D. Duda[107], A. Dudarev[30], L. Duflot[117], L. Duguid[77], M. Dührssen[30], M. Dunford[58a], H. Duran Yildiz[4a], M. Düren[52], A. Durglishvili[51b], D. Duschinger[44], M. Dyndal[38a], C. Eckardt[42], K.M. Ecker[101], R.C. Edgar[89], W. Edson[2], N.C. Edwards[46], W. Ehrenfeld[21], T. Eifert[30], G. Eigen[14], K. Einsweiler[15], T. Ekelof[166], M. El Kacimi[135c], M. Ellert[166], S. Elles[5], F. Ellinghaus[175], A.A. Elliot[169], N. Ellis[30], J. Elmsheuser[100], M. Elsing[30], D. Emeliyanov[131], Y. Enari[155], O.C. Endner[83], M. Endo[118], J. Erdmann[43], A. Ereditato[17], G. Ernis[175], J. Ernst[2], M. Ernst[25], S. Errede[165], E. Ertel[83], M. Escalier[117], H. Esch[43], C. Escobar[125], B. Esposito[47], A.I. Etienvre[136], E. Etzion[153], H. Evans[61], A. Ezhilov[123], L. Fabbri[20a,20b], G. Facini[31], R.M. Fakhrutdinov[130], S. Falciano[132a], R.J. Falla[78], J. Faltova[129], Y. Fang[33a], M. Fanti[91a,91b], A. Farbin[8], A. Farilla[134a], T. Farooque[12], S. Farrell[15], S.M. Farrington[170], P. Farthouat[30], F. Fassi[135e], P. Fassnacht[30], D. Fassouliotis[9], M. Faucci Giannelli[77], A. Favareto[50a,50b], L. Fayard[117], P. Federic[144a], O.L. Fedin[123,m], W. Fedorko[168], S. Feigl[30], L. Feligioni[85], C. Feng[33d], E.J. Feng[6], H. Feng[89], A.B. Fenyuk[130], L. Feremenga[8], P. Fernandez Martinez[167], S. Fernandez Perez[30], J. Ferrando[53], A. Ferrari[166], P. Ferrari[107], R. Ferrari[121a], D.E. Ferreira de Lima[53], A. Ferrer[167], D. Ferrere[49], C. Ferretti[89], A. Ferretto Parodi[50a,50b], M. Fiascaris[31], F. Fiedler[83], A. Filipčič[75], M. Filipuzzi[42], F. Filthaut[106], M. Fincke-Keeler[169], K.D. Finelli[150], M.C.N. Fiolhais[126a,126c], L. Fiorini[167], A. Firan[40], A. Fischer[2], C. Fischer[12], J. Fischer[175], W.C. Fisher[90], E.A. Fitzgerald[23], N. Flaschel[42], I. Fleck[141], P. Fleischmann[89], S. Fleischmann[175], G.T. Fletcher[139], G. Fletcher[76], R.R.M. Fletcher[122], T. Flick[175], A. Floderus[81], L.R. Flores Castillo[60a], M.J. Flowerdew[101], A. Formica[136], A. Forti[84], D. Fournier[117], H. Fox[72], S. Fracchia[12], P. Francavilla[80], M. Franchini[20a,20b], D. Francis[30], L. Franconi[119], M. Franklin[57], M. Frate[163], M. Fraternali[121a,121b], D. Freeborn[78], S.T. French[28], F. Friedrich[44], D. Froidevaux[30], J.A. Frost[120], C. Fukunaga[156], E. Fullana Torregrosa[83], B.G. Fulsom[143], T. Fusayasu[102], J. Fuster[167], C. Gabaldon[55], O. Gabizon[175], A. Gabrielli[20a,20b], A. Gabrielli[132a,132b], G.P. Gach[38a], S. Gadatsch[107], S. Gadomski[49], G. Gagliardi[50a,50b], P. Gagnon[61], C. Galea[106], B. Galhardo[126a,126c], E.J. Gallas[120], B.J. Gallop[131], P. Gallus[128], G. Galster[36], K.K. Gan[111], J. Gao[33b,85], Y. Gao[46], Y.S. Gao[143,e], F.M. Garay Walls[46], F. Garberson[176], C. García[167], J.E. García Navarro[167], M. Garcia-Sciveres[15], R.W. Gardner[31], N. Garelli[143], V. Garonne[119], C. Gatti[47], A. Gaudiello[50a,50b], G. Gaudio[121a], B. Gaur[141],

L. Gauthier[95], P. Gauzzi[132a,132b], I.L. Gavrilenko[96], C. Gay[168], G. Gaycken[21], E.N. Gazis[10], P. Ge[33d], Z. Gecse[168], C.N.P. Gee[131], D.A.A. Geerts[107], Ch. Geich-Gimbel[21], M.P. Geisler[58a], C. Gemme[50a], M.H. Genest[55], S. Gentile[132a,132b], M. George[54], S. George[77], D. Gerbaudo[163], A. Gershon[153], S. Ghasemi[141], H. Ghazlane[135b], B. Giacobbe[20a], S. Giagu[132a,132b], V. Giangiobbe[12], P. Giannetti[124a,124b], B. Gibbard[25], S.M. Gibson[77], M. Gilchriese[15], T.P.S. Gillam[28], D. Gillberg[30], G. Gilles[34], D.M. Gingrich[3,d], N. Giokaris[9], M.P. Giordani[164a,164c], F.M. Giorgi[20a], F.M. Giorgi[16], P.F. Giraud[136], P. Giromini[47], D. Giugni[91a], C. Giuliani[48], M. Giulini[58b], B.K. Gjelsten[119], S. Gkaitatzis[154], I. Gkialas[154], E.L. Gkougkousis[117], L.K. Gladilin[99], C. Glasman[82], J. Glatzer[30], P.C.F. Glaysher[46], A. Glazov[42], M. Goblirsch-Kolb[101], J.R. Goddard[76], J. Godlewski[39], S. Goldfarb[89], T. Golling[49], D. Golubkov[130], A. Gomes[126a,126b,126d], R. Gonçalo[126a], J. Goncalves Pinto Firmino Da Costa[136], L. Gonella[21], S. González de la Hoz[167], G. Gonzalez Parra[12], S. Gonzalez-Sevilla[49], L. Goossens[30], P.A. Gorbounov[97], H.A. Gordon[25], I. Gorelov[105], B. Gorini[30], E. Gorini[73a,73b], A. Gorišek[75], E. Gornicki[39], A.T. Goshaw[45], C. Gössling[43], M.I. Gostkin[65], D. Goujdami[135c], A.G. Goussiou[138], N. Govender[145b], E. Gozani[152], H.M.X. Grabas[137], L. Graber[54], I. Grabowska-Bold[38a], P. Grafström[20a,20b], K-J. Grahn[42], J. Gramling[49], E. Gramstad[119], S. Grancagnolo[16], V. Grassi[148], V. Gratchev[123], H.M. Gray[30], E. Graziani[134a], Z.D. Greenwood[79,n], K. Gregersen[78], I.M. Gregor[42], P. Grenier[143], J. Griffiths[8], A.A. Grillo[137], K. Grimm[72], S. Grinstein[12,o], Ph. Gris[34], J.-F. Grivaz[117], J.P. Grohs[44], A. Grohsjean[42], E. Gross[172], J. Grosse-Knetter[54], G.C. Grossi[79], Z.J. Grout[149], L. Guan[89], J. Guenther[128], F. Guescini[49], D. Guest[176], O. Gueta[153], E. Guido[50a,50b], T. Guillemin[117], S. Guindon[2], U. Gul[53], C. Gumpert[44], J. Guo[33e], Y. Guo[33b], S. Gupta[120], G. Gustavino[132a,132b], P. Gutierrez[113], N.G. Gutierrez Ortiz[53], C. Gutschow[44], C. Guyot[136], C. Gwenlan[120], C.B. Gwilliam[74], A. Haas[110], C. Haber[15], H.K. Hadavand[8], N. Haddad[135e], P. Haefner[21], S. Hageböck[21], Z. Hajduk[39], H. Hakobyan[177], M. Haleem[42], J. Haley[114], D. Hall[120], G. Halladjian[90], G.D. Hallewell[85], K. Hamacher[175], P. Hamal[115], K. Hamano[169], M. Hamer[54], A. Hamilton[145a], G.N. Hamity[145c], P.G. Hamnett[42], L. Han[33b], K. Hanagaki[118], K. Hanawa[155], M. Hance[15], P. Hanke[58a], R. Hanna[136], J.B. Hansen[36], J.D. Hansen[36], M.C. Hansen[21], P.H. Hansen[36], K. Hara[160], A.S. Hard[173], T. Harenberg[175], F. Hariri[117], S. Harkusha[92], R.D. Harrington[46], P.F. Harrison[170], F. Hartjes[107], M. Hasegawa[67], S. Hasegawa[103], Y. Hasegawa[140], A. Hasib[113], S. Hassani[136], S. Haug[17], R. Hauser[90], L. Hauswald[44], M. Havranek[127], C.M. Hawkes[18], R.J. Hawkings[30], A.D. Hawkins[81], T. Hayashi[160], D. Hayden[90], C.P. Hays[120], J.M. Hays[76], H.S. Hayward[74], S.J. Haywood[131], S.J. Head[18], T. Heck[83], V. Hedberg[81], L. Heelan[8], S. Heim[122], T. Heim[175], B. Heinemann[15], L. Heinrich[110], J. Hejbal[127], L. Helary[22], S. Hellman[146a,146b], D. Hellmich[21], C. Helsens[12], J. Henderson[120], R.C.W. Henderson[72], Y. Heng[173], C. Hengler[42], A. Henrichs[176], A.M. Henriques Correia[30], S. Henrot-Versille[117], G.H. Herbert[16], Y. Hernández Jiménez[167], R. Herrberg-Schubert[16], G. Herten[48], R. Hertenberger[100], L. Hervas[30], G.G. Hesketh[78], N.P. Hessey[107], J.W. Hetherly[40], R. Hickling[76], E. Higón-Rodriguez[167], E. Hill[169], J.C. Hill[28], K.H. Hiller[42], S.J. Hillier[18], I. Hinchliffe[15], E. Hines[122], R.R. Hinman[15], M. Hirose[157], D. Hirschbuehl[175], J. Hobbs[148], N. Hod[107], M.C. Hodgkinson[139], P. Hodgson[139], A. Hoecker[30], M.R. Hoeferkamp[105], F. Hoenig[100], M. Hohlfeld[83], D. Hohn[21], T.R. Holmes[15], M. Homann[43], T.M. Hong[125], L. Hooft van Huysduynen[110], W.H. Hopkins[116], Y. Horii[103], A.J. Horton[142], J-Y. Hostachy[55], S. Hou[151], A. Hoummada[135a], J. Howard[120], J. Howarth[42], M. Hrabovsky[115], I. Hristova[16], J. Hrivnac[117], T. Hryn'ova[5], A. Hrynevich[93], C. Hsu[145c], P.J. Hsu[151,p], S.-C. Hsu[138], D. Hu[35], Q. Hu[33b], X. Hu[89], Y. Huang[42], Z. Hubacek[128], F. Hubaut[85], F. Huegging[21], T.B. Huffman[120], E.W. Hughes[35], G. Hughes[72], M. Huhtinen[30], T.A. Hülsing[83], N. Huseynov[65,b], J. Huston[90], J. Huth[57], G. Iacobucci[49], G. Iakovidis[25], I. Ibragimov[141], L. Iconomidou-Fayard[117], E. Ideal[176], Z. Idrissi[135e], P. Iengo[30], O. Igonkina[107], T. Iizawa[171], Y. Ikegami[66], K. Ikematsu[141], M. Ikeno[66], Y. Ilchenko[31,q], D. Iliadis[154], N. Ilic[143], T. Ince[101], G. Introzzi[121a,121b], P. Ioannou[9], M. Iodice[134a], K. Iordanidou[35], V. Ippolito[57], A. Irles Quiles[167], C. Isaksson[166], M. Ishino[68],

M. Ishitsuka[157], R. Ishmukhametov[111], C. Issever[120], S. Istin[19a], J.M. Iturbe Ponce[84], R. Iuppa[133a,133b], J. Ivarsson[81], W. Iwanski[39], H. Iwasaki[66], J.M. Izen[41], V. Izzo[104a], S. Jabbar[3], B. Jackson[122], M. Jackson[74], P. Jackson[1], M.R. Jaekel[30], V. Jain[2], K. Jakobs[48], S. Jakobsen[30], T. Jakoubek[127], J. Jakubek[128], D.O. Jamin[114], D.K. Jana[79], E. Jansen[78], R. Jansky[62], J. Janssen[21], M. Janus[170], G. Jarlskog[81], N. Javadov[65,b], T. Javůrek[48], L. Jeanty[15], J. Jejelava[51a,r], G.-Y. Jeng[150], D. Jennens[88], P. Jenni[48,s], J. Jentzsch[43], C. Jeske[170], S. Jézéquel[5], H. Ji[173], J. Jia[148], Y. Jiang[33b], S. Jiggins[78], J. Jimenez Pena[167], S. Jin[33a], A. Jinaru[26a], O. Jinnouchi[157], M.D. Joergensen[36], P. Johansson[139], K.A. Johns[7], K. Jon-And[146a,146b], G. Jones[170], R.W.L. Jones[72], T.J. Jones[74], J. Jongmanns[58a], P.M. Jorge[126a,126b], K.D. Joshi[84], J. Jovicevic[159a], X. Ju[173], C.A. Jung[43], P. Jussel[62], A. Juste Rozas[12,o], M. Kaci[167], A. Kaczmarska[39], M. Kado[117], H. Kagan[111], M. Kagan[143], S.J. Kahn[85], E. Kajomovitz[45], C.W. Kalderon[120], S. Kama[40], A. Kamenshchikov[130], N. Kanaya[155], S. Kaneti[28], V.A. Kantserov[98], J. Kanzaki[66], B. Kaplan[110], L.S. Kaplan[173], A. Kapliy[31], D. Kar[53], K. Karakostas[10], A. Karamaoun[3], N. Karastathis[10,107], M.J. Kareem[54], M. Karnevskiy[83], S.N. Karpov[65], Z.M. Karpova[65], K. Karthik[110], V. Kartvelishvili[72], A.N. Karyukhin[130], L. Kashif[173], R.D. Kass[111], A. Kastanas[14], Y. Kataoka[155], A. Katre[49], J. Katzy[42], K. Kawagoe[70], T. Kawamoto[155], G. Kawamura[54], S. Kazama[155], V.F. Kazanin[109,c], R. Keeler[169], R. Kehoe[40], J.S. Keller[42], J.J. Kempster[77], H. Keoshkerian[84], O. Kepka[127], B.P. Kerševan[75], S. Kersten[175], R.A. Keyes[87], F. Khalil-zada[11], H. Khandanyan[146a,146b], A. Khanov[114], A.G. Kharlamov[109,c], T.J. Khoo[28], V. Khovanskiy[97], E. Khramov[65], J. Khubua[51b,t], H.Y. Kim[8], H. Kim[146a,146b], S.H. Kim[160], Y. Kim[31], N. Kimura[154], O.M. Kind[16], B.T. King[74], M. King[167], S.B. King[168], J. Kirk[131], A.E. Kiryunin[101], T. Kishimoto[67], D. Kisielewska[38a], F. Kiss[48], K. Kiuchi[160], O. Kivernyk[136], E. Kladiva[144b], M.H. Klein[35], M. Klein[74], U. Klein[74], K. Kleinknecht[83], P. Klimek[146a,146b], A. Klimentov[25], R. Klingenberg[43], J.A. Klinger[139], T. Klioutchnikova[30], E.-E. Kluge[58a], P. Kluit[107], S. Kluth[101], J. Knapik[39], E. Kneringer[62], E.B.F.G. Knoops[85], A. Knue[53], A. Kobayashi[155], D. Kobayashi[157], T. Kobayashi[155], M. Kobel[44], M. Kocian[143], P. Kodys[129], T. Koffas[29], E. Koffeman[107], L.A. Kogan[120], S. Kohlmann[175], Z. Kohout[128], T. Kohriki[66], T. Koi[143], H. Kolanoski[16], I. Koletsou[5], A.A. Komar[96,*], Y. Komori[155], T. Kondo[66], N. Kondrashova[42], K. Köneke[48], A.C. König[106], T. Kono[66], R. Konoplich[110,u], N. Konstantinidis[78], R. Kopeliansky[152], S. Koperny[38a], L. Köpke[83], A.K. Kopp[48], K. Korcyl[39], K. Kordas[154], A. Korn[78], A.A. Korol[109,c], I. Korolkov[12], E.V. Korolkova[139], O. Kortner[101], S. Kortner[101], T. Kosek[129], V.V. Kostyukhin[21], V.M. Kotov[65], A. Kotwal[45], A. Kourkoumeli-Charalampidi[154], C. Kourkoumelis[9], V. Kouskoura[25], A. Koutsman[159a], R. Kowalewski[169], T.Z. Kowalski[38a], W. Kozanecki[136], A.S. Kozhin[130], V.A. Kramarenko[99], G. Kramberger[75], D. Krasnopevtsev[98], M.W. Krasny[80], A. Krasznahorkay[30], J.K. Kraus[21], A. Kravchenko[25], S. Kreiss[110], M. Kretz[58c], J. Kretzschmar[74], K. Kreutzfeldt[52], P. Krieger[158], K. Krizka[31], K. Kroeninger[43], H. Kroha[101], J. Kroll[122], J. Kroseberg[21], J. Krstic[13], U. Kruchonak[65], H. Krüger[21], N. Krumnack[64], A. Kruse[173], M.C. Kruse[45], M. Kruskal[22], T. Kubota[88], H. Kucuk[78], S. Kuday[4b], S. Kuehn[48], A. Kugel[58c], F. Kuger[174], A. Kuhl[137], T. Kuhl[42], V. Kukhtin[65], Y. Kulchitsky[92], S. Kuleshov[32b], M. Kuna[132a,132b], T. Kunigo[68], A. Kupco[127], H. Kurashige[67], Y.A. Kurochkin[92], V. Kus[127], E.S. Kuwertz[169], M. Kuze[157], J. Kvita[115], T. Kwan[169], D. Kyriazopoulos[139], A. La Rosa[137], J.L. La Rosa Navarro[24d], L. La Rotonda[37a,37b], C. Lacasta[167], F. Lacava[132a,132b], J. Lacey[29], H. Lacker[16], D. Lacour[80], V.R. Lacuesta[167], E. Ladygin[65], R. Lafaye[5], B. Laforge[80], T. Lagouri[176], S. Lai[54], L. Lambourne[78], S. Lammers[61], C.L. Lampen[7], W. Lampl[7], E. Lançon[136], U. Landgraf[48], M.P.J. Landon[76], V.S. Lang[58a], J.C. Lange[12], A.J. Lankford[163], F. Lanni[25], K. Lantzsch[30], A. Lanza[121a], S. Laplace[80], C. Lapoire[30], J.F. Laporte[136], T. Lari[91a], F. Lasagni Manghi[20a,20b], M. Lassnig[30], P. Laurelli[47], W. Lavrijsen[15], A.T. Law[137], P. Laycock[74], T. Lazovich[57], O. Le Dortz[80], E. Le Guirriec[85], E. Le Menedeu[12], M. LeBlanc[169], T. LeCompte[6], F. Ledroit-Guillon[55], C.A. Lee[145b], S.C. Lee[151], L. Lee[1], G. Lefebvre[80], M. Lefebvre[169], F. Legger[100], C. Leggett[15], A. Lehan[74], G. Lehmann Miotto[30], X. Lei[7], W.A. Leight[29], A. Leisos[154,v], A.G. Leister[176], M.A.L. Leite[24d], R. Leitner[129], D. Lellouch[172],

B. Lemmer[54], K.J.C. Leney[78], T. Lenz[21], B. Lenzi[30], R. Leone[7], S. Leone[124a,124b], C. Leonidopoulos[46], S. Leontsinis[10], C. Leroy[95], C.G. Lester[28], M. Levchenko[123], J. Levêque[5], D. Levin[89], L.J. Levinson[172], M. Levy[18], A. Lewis[120], A.M. Leyko[21], M. Leyton[41], B. Li[33b,w], H. Li[148], H.L. Li[31], L. Li[45], L. Li[33e], S. Li[45], Y. Li[33c,x], Z. Liang[137], H. Liao[34], B. Liberti[133a], A. Liblong[158], P. Lichard[30], K. Lie[165], J. Liebal[21], W. Liebig[14], C. Limbach[21], A. Limosani[150], S.C. Lin[151,y], T.H. Lin[83], F. Linde[107], B.E. Lindquist[148], J.T. Linnemann[90], E. Lipeles[122], A. Lipniacka[14], M. Lisovyi[58b], T.M. Liss[165], D. Lissauer[25], A. Lister[168], A.M. Litke[137], B. Liu[151,z], D. Liu[151], H. Liu[89], J. Liu[85], J.B. Liu[33b], K. Liu[85], L. Liu[165], M. Liu[45], M. Liu[33b], Y. Liu[33b], M. Livan[121a,121b], A. Lleres[55], J. Llorente Merino[82], S.L. Lloyd[76], F. Lo Sterzo[151], E. Lobodzinska[42], P. Loch[7], W.S. Lockman[137], F.K. Loebinger[84], A.E. Loevschall-Jensen[36], A. Loginov[176], T. Lohse[16], K. Lohwasser[42], M. Lokajicek[127], B.A. Long[22], J.D. Long[89], R.E. Long[72], K.A. Looper[111], L. Lopes[126a], D. Lopez Mateos[57], B. Lopez Paredes[139], I. Lopez Paz[12], J. Lorenz[100], N. Lorenzo Martinez[61], M. Losada[162], P. Loscutoff[15], P.J. Lösel[100], X. Lou[33a], A. Lounis[117], J. Love[6], P.A. Love[72], N. Lu[89], H.J. Lubatti[138], C. Luci[132a,132b], A. Lucotte[55], F. Luehring[61], W. Lukas[62], L. Luminari[132a], O. Lundberg[146a,146b], B. Lund-Jensen[147], D. Lynn[25], R. Lysak[127], E. Lytken[81], H. Ma[25], L.L. Ma[33d], G. Maccarrone[47], A. Macchiolo[101], C.M. Macdonald[139], J. Machado Miguens[122,126b], D. Macina[30], D. Madaffari[85], R. Madar[34], H.J. Maddocks[72], W.F. Mader[44], A. Madsen[166], S. Maeland[14], T. Maeno[25], A. Maevskiy[99], E. Magradze[54], K. Mahboubi[48], J. Mahlstedt[107], C. Maiani[136], C. Maidantchik[24a], A.A. Maier[101], T. Maier[100], A. Maio[126a,126b,126d], S. Majewski[116], Y. Makida[66], N. Makovec[117], B. Malaescu[80], Pa. Malecki[39], V.P. Maleev[123], F. Malek[55], U. Mallik[63], D. Malon[6], C. Malone[143], S. Maltezos[10], V.M. Malyshev[109], S. Malyukov[30], J. Mamuzic[42], G. Mancini[47], B. Mandelli[30], L. Mandelli[91a], I. Mandić[75], R. Mandrysch[63], J. Maneira[126a,126b], A. Manfredini[101], L. Manhaes de Andrade Filho[24b], J. Manjarres Ramos[159b], A. Mann[100], P.M. Manning[137], A. Manousakis-Katsikakis[9], B. Mansoulie[136], R. Mantifel[87], M. Mantoani[54], L. Mapelli[30], L. March[145c], G. Marchiori[80], M. Marcisovsky[127], C.P. Marino[169], M. Marjanovic[13], D.E. Marley[89], F. Marroquim[24a], S.P. Marsden[84], Z. Marshall[15], L.F. Marti[17], S. Marti-Garcia[167], B. Martin[90], T.A. Martin[170], V.J. Martin[46], B. Martin dit Latour[14], M. Martinez[12,o], S. Martin-Haugh[131], V.S. Martoiu[26a], A.C. Martyniuk[78], M. Marx[138], F. Marzano[132a], A. Marzin[30], L. Masetti[83], T. Mashimo[155], R. Mashinistov[96], J. Masik[84], A.L. Maslennikov[109,c], I. Massa[20a,20b], L. Massa[20a,20b], N. Massol[5], P. Mastrandrea[148], A. Mastroberardino[37a,37b], T. Masubuchi[155], P. Mättig[175], J. Mattmann[83], J. Maurer[26a], S.J. Maxfield[74], D.A. Maximov[109,c], R. Mazini[151], S.M. Mazza[91a,91b], L. Mazzaferro[133a,133b], G. Mc Goldrick[158], S.P. Mc Kee[89], A. McCarn[89], R.L. McCarthy[148], T.G. McCarthy[29], N.A. McCubbin[131], K.W. McFarlane[56,*], J.A. Mcfayden[78], G. Mchedlidze[54], S.J. McMahon[131], R.A. McPherson[169,k], M. Medinnis[42], S. Meehan[145a], S. Mehlhase[100], A. Mehta[74], K. Meier[58a], C. Meineck[100], B. Meirose[41], B.R. Mellado Garcia[145c], F. Meloni[17], A. Mengarelli[20a,20b], S. Menke[101], E. Meoni[161], K.M. Mercurio[57], S. Mergelmeyer[21], P. Mermod[49], L. Merola[104a,104b], C. Meroni[91a], F.S. Merritt[31], A. Messina[132a,132b], J. Metcalfe[25], A.S. Mete[163], C. Meyer[83], C. Meyer[122], J-P. Meyer[136], J. Meyer[107], R.P. Middleton[131], S. Miglioranzi[164a,164c], L. Mijović[21], G. Mikenberg[172], M. Mikestikova[127], M. Mikuž[75], M. Milesi[88], A. Milic[30], D.W. Miller[31], C. Mills[46], A. Milov[172], D.A. Milstead[146a,146b], A.A. Minaenko[130], Y. Minami[155], I.A. Minashvili[65], A.I. Mincer[110], B. Mindur[38a], M. Mineev[65], Y. Ming[173], L.M. Mir[12], T. Mitani[171], J. Mitrevski[100], V.A. Mitsou[167], A. Miucci[49], P.S. Miyagawa[139], J.U. Mjörnmark[81], T. Moa[146a,146b], K. Mochizuki[85], S. Mohapatra[35], W. Mohr[48], S. Molander[146a,146b], R. Moles-Valls[21], K. Mönig[42], C. Monini[55], J. Monk[36], E. Monnier[85], J. Montejo Berlingen[12], F. Monticelli[71], S. Monzani[132a,132b], R.W. Moore[3], N. Morange[117], D. Moreno[162], M. Moreno Llácer[54], P. Morettini[50a], M. Morgenstern[44], D. Mori[142], M. Morii[57], M. Morinaga[155], V. Morisbak[119], S. Moritz[83], A.K. Morley[150], G. Mornacchi[30], J.D. Morris[76], S.S. Mortensen[36], A. Morton[53], L. Morvaj[103], M. Mosidze[51b], J. Moss[111], K. Motohashi[157], R. Mount[143], E. Mountricha[25], S.V. Mouraviev[96,*], E.J.W. Moyse[86], S. Muanza[85], R.D. Mudd[18],

F. Mueller[101], J. Mueller[125], R.S.P. Mueller[100], T. Mueller[28], D. Muenstermann[49], P. Mullen[53], G.A. Mullier[17], J.A. Murillo Quijada[18], W.J. Murray[170,131], H. Musheghyan[54], E. Musto[152], A.G. Myagkov[130,aa], M. Myska[128], O. Nackenhorst[54], J. Nadal[54], K. Nagai[120], R. Nagai[157], Y. Nagai[85], K. Nagano[66], A. Nagarkar[111], Y. Nagasaka[59], K. Nagata[160], M. Nagel[101], E. Nagy[85], A.M. Nairz[30], Y. Nakahama[30], K. Nakamura[66], T. Nakamura[155], I. Nakano[112], H. Namasivayam[41], R.F. Naranjo Garcia[42], R. Narayan[31], T. Naumann[42], G. Navarro[162], R. Nayyar[7], H.A. Neal[89], P.Yu. Nechaeva[96], T.J. Neep[84], P.D. Nef[143], A. Negri[121a,121b], M. Negrini[20a], S. Nektarijevic[106], C. Nellist[117], A. Nelson[163], S. Nemecek[127], P. Nemethy[110], A.A. Nepomuceno[24a], M. Nessi[30,ab], M.S. Neubauer[165], M. Neumann[175], R.M. Neves[110], P. Nevski[25], P.R. Newman[18], D.H. Nguyen[6], R.B. Nickerson[120], R. Nicolaidou[136], B. Nicquevert[30], J. Nielsen[137], N. Nikiforou[35], A. Nikiforov[16], V. Nikolaenko[130,aa], I. Nikolic-Audit[80], K. Nikolopoulos[18], J.K. Nilsen[119], P. Nilsson[25], Y. Ninomiya[155], A. Nisati[132a], R. Nisius[101], T. Nobe[155], M. Nomachi[118], I. Nomidis[29], T. Nooney[76], S. Norberg[113], M. Nordberg[30], O. Novgorodova[44], S. Nowak[101], M. Nozaki[66], L. Nozka[115], K. Ntekas[10], G. Nunes Hanninger[88], T. Nunnemann[100], E. Nurse[78], F. Nuti[88], B.J. O'Brien[46], F. O'grady[7], D.C. O'Neil[142], V. O'Shea[53], F.G. Oakham[29,d], H. Oberlack[101], T. Obermann[21], J. Ocariz[80], A. Ochi[67], I. Ochoa[78], J.P. Ochoa-Ricoux[32a], S. Oda[70], S. Odaka[66], H. Ogren[61], A. Oh[84], S.H. Oh[45], C.C. Ohm[15], H. Ohman[166], H. Oide[30], W. Okamura[118], H. Okawa[160], Y. Okumura[31], T. Okuyama[66], A. Olariu[26a], S.A. Olivares Pino[46], D. Oliveira Damazio[25], E. Oliver Garcia[167], A. Olszewski[39], J. Olszowska[39], A. Onofre[126a,126e], P.U.E. Onyisi[31,q], C.J. Oram[159a], M.J. Oreglia[31], Y. Oren[153], D. Orestano[134a,134b], N. Orlando[154], C. Oropeza Barrera[53], R.S. Orr[158], B. Osculati[50a,50b], R. Ospanov[84], G. Otero y Garzon[27], H. Otono[70], M. Ouchrif[135d], E.A. Ouellette[169], F. Ould-Saada[119], A. Ouraou[136], K.P. Oussoren[107], Q. Ouyang[33a], A. Ovcharova[15], M. Owen[53], R.E. Owen[18], V.E. Ozcan[19a], N. Ozturk[8], K. Pachal[142], A. Pacheco Pages[12], C. Padilla Aranda[12], M. Pagáčová[48], S. Pagan Griso[15], E. Paganis[139], F. Paige[25], P. Pais[86], K. Pajchel[119], G. Palacino[159b], S. Palestini[30], M. Palka[38b], D. Pallin[34], A. Palma[126a,126b], Y.B. Pan[173], E. Panagiotopoulou[10], C.E. Pandini[80], J.G. Panduro Vazquez[77], P. Pani[146a,146b], S. Panitkin[25], D. Pantea[26a], L. Paolozzi[49], Th.D. Papadopoulou[10], K. Papageorgiou[154], A. Paramonov[6], D. Paredes Hernandez[154], M.A. Parker[28], K.A. Parker[139], F. Parodi[50a,50b], J.A. Parsons[35], U. Parzefall[48], E. Pasqualucci[132a], S. Passaggio[50a], F. Pastore[134a,134b,*], Fr. Pastore[77], G. Pásztor[29], S. Pataraia[175], N.D. Patel[150], J.R. Pater[84], T. Pauly[30], J. Pearce[169], B. Pearson[113], L.E. Pedersen[36], M. Pedersen[119], S. Pedraza Lopez[167], R. Pedro[126a,126b], S.V. Peleganchuk[109,c], D. Pelikan[166], O. Penc[127], C. Peng[33a], H. Peng[33b], B. Penning[31], J. Penwell[61], D.V. Perepelitsa[25], E. Perez Codina[159a], M.T. Pérez García-Estañ[167], L. Perini[91a,91b], H. Pernegger[30], S. Perrella[104a,104b], R. Peschke[42], V.D. Peshekhonov[65], K. Peters[30], R.F.Y. Peters[84], B.A. Petersen[30], T.C. Petersen[36], E. Petit[42], A. Petridis[146a,146b], C. Petridou[154], P. Petroff[117], E. Petrolo[132a], F. Petrucci[134a,134b], N.E. Pettersson[157], R. Pezoa[32b], P.W. Phillips[131], G. Piacquadio[143], E. Pianori[170], A. Picazio[49], E. Piccaro[76], M. Piccinini[20a,20b], M.A. Pickering[120], R. Piegaia[27], D.T. Pignotti[111], J.E. Pilcher[31], A.D. Pilkington[84], J. Pina[126a,126b,126d], M. Pinamonti[164a,164c,ac], J.L. Pinfold[3], A. Pingel[36], B. Pinto[126a], S. Pires[80], H. Pirumov[42], M. Pitt[172], C. Pizio[91a,91b], L. Plazak[144a], M.-A. Pleier[25], V. Pleskot[129], E. Plotnikova[65], P. Plucinski[146a,146b], D. Pluth[64], R. Poettgen[146a,146b], L. Poggioli[117], D. Pohl[21], G. Polesello[121a], A. Poley[42], A. Policicchio[37a,37b], R. Polifka[158], A. Polini[20a], C.S. Pollard[53], V. Polychronakos[25], K. Pommès[30], L. Pontecorvo[132a], B.G. Pope[90], G.A. Popeneciu[26b], D.S. Popovic[13], A. Poppleton[30], S. Pospisil[128], K. Potamianos[15], I.N. Potrap[65], C.J. Potter[149], C.T. Potter[116], G. Poulard[30], J. Poveda[30], V. Pozdnyakov[65], P. Pralavorio[85], A. Pranko[15], S. Prasad[30], S. Prell[64], D. Price[84], L.E. Price[6], M. Primavera[73a], S. Prince[87], M. Proissl[46], K. Prokofiev[60c], F. Prokoshin[32b], E. Protopapadaki[136], S. Protopopescu[25], J. Proudfoot[6], M. Przybycien[38a], E. Ptacek[116], D. Puddu[134a,134b], E. Pueschel[86], D. Puldon[148], M. Purohit[25,ad], P. Puzo[117], J. Qian[89], G. Qin[53], Y. Qin[84], A. Quadt[54], D.R. Quarrie[15], W.B. Quayle[164a,164b], M. Queitsch-Maitland[84], D. Quilty[53], S. Raddum[119],

V. Radeka[25], V. Radescu[42], S.K. Radhakrishnan[148], P. Radloff[116], P. Rados[88], F. Ragusa[91a,91b], G. Rahal[178], S. Rajagopalan[25], M. Rammensee[30], C. Rangel-Smith[166], F. Rauscher[100], S. Rave[83], T. Ravenscroft[53], M. Raymond[30], A.L. Read[119], N.P. Readioff[74], D.M. Rebuzzi[121a,121b], A. Redelbach[174], G. Redlinger[25], R. Reece[137], K. Reeves[41], L. Rehnisch[16], H. Reisin[27], M. Relich[163], C. Rembser[30], H. Ren[33a], A. Renaud[117], M. Rescigno[132a], S. Resconi[91a], O.L. Rezanova[109,c], P. Reznicek[129], R. Rezvani[95], R. Richter[101], S. Richter[78], E. Richter-Was[38b], O. Ricken[21], M. Ridel[80], P. Rieck[16], C.J. Riegel[175], J. Rieger[54], M. Rijssenbeek[148], A. Rimoldi[121a,121b], L. Rinaldi[20a], B. Ristić[49], E. Ritsch[30], I. Riu[12], F. Rizatdinova[114], E. Rizvi[76], S.H. Robertson[87,k], A. Robichaud-Veronneau[87], D. Robinson[28], J.E.M. Robinson[42], A. Robson[53], C. Roda[124a,124b], S. Roe[30], O. Røhne[119], S. Rolli[161], A. Romaniouk[98], M. Romano[20a,20b], S.M. Romano Saez[34], E. Romero Adam[167], N. Rompotis[138], M. Ronzani[48], L. Roos[80], E. Ros[167], S. Rosati[132a], K. Rosbach[48], P. Rose[137], P.L. Rosendahl[14], O. Rosenthal[141], V. Rossetti[146a,146b], E. Rossi[104a,104b], L.P. Rossi[50a], R. Rosten[138], M. Rotaru[26a], I. Roth[172], J. Rothberg[138], D. Rousseau[117], C.R. Royon[136], A. Rozanov[85], Y. Rozen[152], X. Ruan[145c], F. Rubbo[143], I. Rubinskiy[42], V.I. Rud[99], C. Rudolph[44], M.S. Rudolph[158], F. Rühr[48], A. Ruiz-Martinez[30], Z. Rurikova[48], N.A. Rusakovich[65], A. Ruschke[100], H.L. Russell[138], J.P. Rutherfoord[7], N. Ruthmann[48], Y.F. Ryabov[123], M. Rybar[165], G. Rybkin[117], N.C. Ryder[120], A.F. Saavedra[150], G. Sabato[107], S. Sacerdoti[27], A. Saddique[3], H.F-W. Sadrozinski[137], R. Sadykov[65], F. Safai Tehrani[132a], M. Saimpert[136], T. Saito[155], H. Sakamoto[155], Y. Sakurai[171], G. Salamanna[134a,134b], A. Salamon[133a], M. Saleem[113], D. Salek[107], P.H. Sales De Bruin[138], D. Salihagic[101], A. Salnikov[143], J. Salt[167], D. Salvatore[37a,37b], F. Salvatore[149], A. Salvucci[106], A. Salzburger[30], D. Sammel[48], D. Sampsonidis[154], A. Sanchez[104a,104b], J. Sánchez[167], V. Sanchez Martinez[167], H. Sandaker[119], R.L. Sandbach[76], H.G. Sander[83], M.P. Sanders[100], M. Sandhoff[175], C. Sandoval[162], R. Sandstroem[101], D.P.C. Sankey[131], M. Sannino[50a,50b], A. Sansoni[47], C. Santoni[34], R. Santonico[133a,133b], H. Santos[126a], I. Santoyo Castillo[149], K. Sapp[125], A. Sapronov[65], J.G. Saraiva[126a,126d], B. Sarrazin[21], O. Sasaki[66], Y. Sasaki[155], K. Sato[160], G. Sauvage[5,*], E. Sauvan[5], G. Savage[77], P. Savard[158,d], C. Sawyer[131], L. Sawyer[79,n], J. Saxon[31], C. Sbarra[20a], A. Sbrizzi[20a,20b], T. Scanlon[78], D.A. Scannicchio[163], M. Scarcella[150], V. Scarfone[37a,37b], J. Schaarschmidt[172], P. Schacht[101], D. Schaefer[30], R. Schaefer[42], J. Schaeffer[83], S. Schaepe[21], S. Schaetzel[58b], U. Schäfer[83], A.C. Schaffer[117], D. Schaile[100], R.D. Schamberger[148], V. Scharf[58a], V.A. Schegelsky[123], D. Scheirich[129], M. Schernau[163], C. Schiavi[50a,50b], C. Schillo[48], M. Schioppa[37a,37b], S. Schlenker[30], E. Schmidt[48], K. Schmieden[30], C. Schmitt[83], S. Schmitt[58b], S. Schmitt[42], B. Schneider[159a], Y.J. Schnellbach[74], U. Schnoor[44], L. Schoeffel[136], A. Schoening[58b], B.D. Schoenrock[90], E. Schopf[21], A.L.S. Schorlemmer[54], M. Schott[83], D. Schouten[159a], J. Schovancova[8], S. Schramm[49], M. Schreyer[174], C. Schroeder[83], N. Schuh[83], M.J. Schultens[21], H.-C. Schultz-Coulon[58a], H. Schulz[16], M. Schumacher[48], B.A. Schumm[137], Ph. Schune[136], C. Schwanenberger[84], A. Schwartzman[143], T.A. Schwarz[89], Ph. Schwegler[101], H. Schweiger[84], Ph. Schwemling[136], R. Schwienhorst[90], J. Schwindling[136], T. Schwindt[21], F.G. Sciacca[17], E. Scifo[117], G. Sciolla[23], F. Scuri[124a,124b], F. Scutti[21], J. Searcy[89], G. Sedov[42], E. Sedykh[123], P. Seema[21], S.C. Seidel[105], A. Seiden[137], F. Seifert[128], J.M. Seixas[24a], G. Sekhniaidze[104a], K. Sekhon[89], S.J. Sekula[40], D.M. Seliverstov[123,*], N. Semprini-Cesari[20a,20b], C. Serfon[30], L. Serin[117], L. Serkin[164a,164b], T. Serre[85], M. Sessa[134a,134b], R. Seuster[159a], H. Severini[113], T. Sfiligoj[75], F. Sforza[30], A. Sfyrla[30], E. Shabalina[54], M. Shamim[116], L.Y. Shan[33a], R. Shang[165], J.T. Shank[22], M. Shapiro[15], P.B. Shatalov[97], K. Shaw[164a,164b], S.M. Shaw[84], A. Shcherbakova[146a,146b], C.Y. Shehu[149], P. Sherwood[78], L. Shi[151,ae], S. Shimizu[67], C.O. Shimmin[163], M. Shimojima[102], M. Shiyakova[65], A. Shmeleva[96], D. Shoaleh Saadi[95], M.J. Shochet[31], S. Shojaii[91a,91b], S. Shrestha[111], E. Shulga[98], M.A. Shupe[7], S. Shushkevich[42], P. Sicho[127], P.E. Sidebo[147], O. Sidiropoulou[174], D. Sidorov[114], A. Sidoti[20a,20b], F. Siegert[44], Dj. Sijacki[13], J. Silva[126a,126d], Y. Silver[153], S.B. Silverstein[146a], V. Simak[128], O. Simard[5], Lj. Simic[13], S. Simion[117], E. Simioni[83], B. Simmons[78], D. Simon[34], R. Simoniello[91a,91b], P. Sinervo[158],

N.B. Sinev[116], M. Sioli[20a,20b], G. Siragusa[174], A.N. Sisakyan[65,*], S.Yu. Sivoklokov[99], J. Sjölin[146a,146b], T.B. Sjursen[14], M.B. Skinner[72], H.P. Skottowe[57], P. Skubic[113], M. Slater[18], T. Slavicek[128], M. Slawinska[107], K. Sliwa[161], V. Smakhtin[172], B.H. Smart[46], L. Smestad[14], S.Yu. Smirnov[98], Y. Smirnov[98], L.N. Smirnova[99,af], O. Smirnova[81], M.N.K. Smith[35], R.W. Smith[35], M. Smizanska[72], K. Smolek[128], A.A. Snesarev[96], G. Snidero[76], S. Snyder[25], R. Sobie[169,k], F. Socher[44], A. Soffer[153], D.A. Soh[151,ae], C.A. Solans[30], M. Solar[128], J. Solc[128], E.Yu. Soldatov[98], U. Soldevila[167], A.A. Solodkov[130], A. Soloshenko[65], O.V. Solovyanov[130], V. Solovyev[123], P. Sommer[48], H.Y. Song[33b], N. Soni[1], A. Sood[15], A. Sopczak[128], B. Sopko[128], V. Sopko[128], V. Sorin[12], D. Sosa[58b], M. Sosebee[8], C.L. Sotiropoulou[124a,124b], R. Soualah[164a,164c], A.M. Soukharev[109,c], D. South[42], B.C. Sowden[77], S. Spagnolo[73a,73b], M. Spalla[124a,124b], F. Spanò[77], W.R. Spearman[57], D. Sperlich[16], F. Spettel[101], R. Spighi[20a], G. Spigo[30], L.A. Spiller[88], M. Spousta[129], T. Spreitzer[158], R.D. St. Denis[53,*], S. Staerz[44], J. Stahlman[122], R. Stamen[58a], S. Stamm[16], E. Stanecka[39], C. Stanescu[134a], M. Stanescu-Bellu[42], M.M. Stanitzki[42], S. Stapnes[119], E.A. Starchenko[130], J. Stark[55], P. Staroba[127], P. Starovoitov[42], R. Staszewski[39], P. Stavina[144a,*], P. Steinberg[25], B. Stelzer[142], H.J. Stelzer[30], O. Stelzer-Chilton[159a], H. Stenzel[52], G.A. Stewart[53], J.A. Stillings[21], M.C. Stockton[87], M. Stoebe[87], G. Stoicea[26a], P. Stolte[54], S. Stonjek[101], A.R. Stradling[8], A. Straessner[44], M.E. Stramaglia[17], J. Strandberg[147], S. Strandberg[146a,146b], A. Strandlie[119], E. Strauss[143], M. Strauss[113], P. Strizenec[144b], R. Ströhmer[174], D.M. Strom[116], R. Stroynowski[40], A. Strubig[106], S.A. Stucci[17], B. Stugu[14], N.A. Styles[42], D. Su[143], J. Su[125], R. Subramaniam[79], A. Succurro[12], Y. Sugaya[118], C. Suhr[108], M. Suk[128], V.V. Sulin[96], S. Sultansoy[4c], T. Sumida[68], S. Sun[57], X. Sun[33a], J.E. Sundermann[48], K. Suruliz[149], G. Susinno[37a,37b], M.R. Sutton[149], S. Suzuki[66], M. Svatos[127], S. Swedish[168], M. Swiatlowski[143], I. Sykora[144a], T. Sykora[129], D. Ta[90], C. Taccini[134a,134b], K. Tackmann[42], J. Taenzer[158], A. Taffard[163], R. Tafirout[159a], N. Taiblum[153], H. Takai[25], R. Takashima[69], H. Takeda[67], T. Takeshita[140], Y. Takubo[66], M. Talby[85], A.A. Talyshev[109,c], J.Y.C. Tam[174], K.G. Tan[88], J. Tanaka[155], R. Tanaka[117], S. Tanaka[66], B.B. Tannenwald[111], N. Tannoury[21], S. Tapprogge[83], S. Tarem[152], F. Tarrade[29], G.F. Tartarelli[91a], P. Tas[129], M. Tasevsky[127], T. Tashiro[68], E. Tassi[37a,37b], A. Tavares Delgado[126a,126b], Y. Tayalati[135d], F.E. Taylor[94], G.N. Taylor[88], W. Taylor[159b], F.A. Teischinger[30], M. Teixeira Dias Castanheira[76], P. Teixeira-Dias[77], K.K. Temming[48], H. Ten Kate[30], P.K. Teng[151], J.J. Teoh[118], F. Tepel[175], S. Terada[66], K. Terashi[155], J. Terron[82], S. Terzo[101], M. Testa[47], R.J. Teuscher[158,k], T. Theveneaux-Pelzer[34], J.P. Thomas[18], J. Thomas-Wilsker[77], E.N. Thompson[35], P.D. Thompson[18], R.J. Thompson[84], A.S. Thompson[53], L.A. Thomsen[176], E. Thomson[122], M. Thomson[28], R.P. Thun[89,*], M.J. Tibbetts[15], R.E. Ticse Torres[85], V.O. Tikhomirov[96,ag], Yu.A. Tikhonov[109,c], S. Timoshenko[98], E. Tiouchichine[85], P. Tipton[176], S. Tisserant[85], K. Todome[157], T. Todorov[5,*], S. Todorova-Nova[129], J. Tojo[70], S. Tokár[144a], K. Tokushuku[66], K. Tollefson[90], E. Tolley[57], L. Tomlinson[84], M. Tomoto[103], L. Tompkins[143,ah], K. Toms[105], E. Torrence[116], H. Torres[142], E. Torró Pastor[167], J. Toth[85,ai], F. Touchard[85], D.R. Tovey[139], T. Trefzger[174], L. Tremblet[30], A. Tricoli[30], I.M. Trigger[159a], S. Trincaz-Duvoid[80], M.F. Tripiana[12], W. Trischuk[158], B. Trocmé[55], C. Troncon[91a], M. Trottier-McDonald[15], M. Trovatelli[169], P. True[90], L. Truong[164a,164c], M. Trzebinski[39], A. Trzupek[39], C. Tsarouchas[30], J.C-L. Tseng[120], P.V. Tsiareshka[92], D. Tsionou[154], G. Tsipolitis[10], N. Tsirintanis[9], S. Tsiskaridze[12], V. Tsiskaridze[48], E.G. Tskhadadze[51a], I.I. Tsukerman[97], V. Tsulaia[15], S. Tsuno[66], D. Tsybychev[148], A. Tudorache[26a], V. Tudorache[26a], A.N. Tuna[122], S.A. Tupputi[20a,20b], S. Turchikhin[99,af], D. Turecek[128], R. Turra[91a,91b], A.J. Turvey[40], P.M. Tuts[35], A. Tykhonov[49], M. Tylmad[146a,146b], M. Tyndel[131], I. Ueda[155], R. Ueno[29], M. Ughetto[146a,146b], M. Ugland[14], M. Uhlenbrock[21], F. Ukegawa[160], G. Unal[30], A. Undrus[25], G. Unel[163], F.C. Ungaro[48], Y. Unno[66], C. Unverdorben[100], J. Urban[144b], P. Urquijo[88], P. Urrejola[83], G. Usai[8], A. Usanova[62], L. Vacavant[85], V. Vacek[128], B. Vachon[87], C. Valderanis[83], N. Valencic[107], S. Valentinetti[20a,20b], A. Valero[167], L. Valery[12], S. Valkar[129], E. Valladolid Gallego[167], S. Vallecorsa[49], J.A. Valls Ferrer[167], W. Van Den Wollenberg[107], P.C. Van Der Deijl[107], R. van der Geer[107],

H. van der Graaf[107], R. Van Der Leeuw[107], N. van Eldik[152], P. van Gemmeren[6], J. Van Nieuwkoop[142], I. van Vulpen[107], M.C. van Woerden[30], M. Vanadia[132a,132b], W. Vandelli[30], R. Vanguri[122], A. Vaniachine[6], F. Vannucci[80], G. Vardanyan[177], R. Vari[132a], E.W. Varnes[7], T. Varol[40], D. Varouchas[80], A. Vartapetian[8], K.E. Varvell[150], F. Vazeille[34], T. Vazquez Schroeder[87], J. Veatch[7], L.M. Veloce[158], F. Veloso[126a,126c], T. Velz[21], S. Veneziano[132a], A. Ventura[73a,73b], D. Ventura[86], M. Venturi[169], N. Venturi[158], A. Venturini[23], V. Vercesi[121a], M. Verducci[132a,132b], W. Verkerke[107], J.C. Vermeulen[107], A. Vest[44], M.C. Vetterli[142,d], O. Viazlo[81], I. Vichou[165], T. Vickey[139], O.E. Vickey Boeriu[139], G.H.A. Viehhauser[120], S. Viel[15], R. Vigne[62], M. Villa[20a,20b], M. Villaplana Perez[91a,91b], E. Vilucchi[47], M.G. Vincter[29], V.B. Vinogradov[65], I. Vivarelli[149], F. Vives Vaque[3], S. Vlachos[10], D. Vladoiu[100], M. Vlasak[128], M. Vogel[32a], P. Vokac[128], G. Volpi[124a,124b], M. Volpi[88], H. von der Schmitt[101], H. von Radziewski[48], E. von Toerne[21], V. Vorobel[129], K. Vorobev[98], M. Vos[167], R. Voss[30], J.H. Vossebeld[74], N. Vranjes[13], M. Vranjes Milosavljevic[13], V. Vrba[127], M. Vreeswijk[107], R. Vuillermet[30], I. Vukotic[31], Z. Vykydal[128], P. Wagner[21], W. Wagner[175], H. Wahlberg[71], S. Wahrmund[44], J. Wakabayashi[103], J. Walder[72], R. Walker[100], W. Walkowiak[141], C. Wang[151], F. Wang[173], H. Wang[15], H. Wang[40], J. Wang[42], J. Wang[33a], K. Wang[87], R. Wang[6], S.M. Wang[151], T. Wang[21], X. Wang[176], C. Wanotayaroj[116], A. Warburton[87], C.P. Ward[28], D.R. Wardrope[78], M. Warsinsky[48], A. Washbrook[46], C. Wasicki[42], P.M. Watkins[18], A.T. Watson[18], I.J. Watson[150], M.F. Watson[18], G. Watts[138], S. Watts[84], B.M. Waugh[78], S. Webb[84], M.S. Weber[17], S.W. Weber[174], J.S. Webster[31], A.R. Weidberg[120], B. Weinert[61], J. Weingarten[54], C. Weiser[48], H. Weits[107], P.S. Wells[30], T. Wenaus[25], T. Wengler[30], S. Wenig[30], N. Wermes[21], M. Werner[48], P. Werner[30], M. Wessels[58a], J. Wetter[161], K. Whalen[116], A.M. Wharton[72], A. White[8], M.J. White[1], R. White[32b], S. White[124a,124b], D. Whiteson[163], F.J. Wickens[131], W. Wiedenmann[173], M. Wielers[131], P. Wienemann[21], C. Wiglesworth[36], L.A.M. Wiik-Fuchs[21], A. Wildauer[101], H.G. Wilkens[30], H.H. Williams[122], S. Williams[107], C. Willis[90], S. Willocq[86], A. Wilson[89], J.A. Wilson[18], I. Wingerter-Seez[5], F. Winklmeier[116], B.T. Winter[21], M. Wittgen[143], J. Wittkowski[100], S.J. Wollstadt[83], M.W. Wolter[39], H. Wolters[126a,126c], B.K. Wosiek[39], J. Wotschack[30], M.J. Woudstra[84], K.W. Wozniak[39], M. Wu[55], M. Wu[31], S.L. Wu[173], X. Wu[49], Y. Wu[89], T.R. Wyatt[84], B.M. Wynne[46], S. Xella[36], D. Xu[33a], L. Xu[33b,aj], B. Yabsley[150], S. Yacoob[145a], R. Yakabe[67], M. Yamada[66], Y. Yamaguchi[118], A. Yamamoto[66], S. Yamamoto[155], T. Yamanaka[155], K. Yamauchi[103], Y. Yamazaki[67], Z. Yan[22], H. Yang[33e], H. Yang[173], Y. Yang[151], W-M. Yao[15], Y. Yasu[66], E. Yatsenko[5], K.H. Yau Wong[21], J. Ye[40], S. Ye[25], I. Yeletskikh[65], A.L. Yen[57], E. Yildirim[42], K. Yorita[171], R. Yoshida[6], K. Yoshihara[122], C. Young[143], C.J.S. Young[30], S. Youssef[22], D.R. Yu[15], J. Yu[8], J.M. Yu[89], J. Yu[114], L. Yuan[67], S.P.Y. Yuen[21], A. Yurkewicz[108], I. Yusuff[28,ak], B. Zabinski[39], R. Zaidan[63], A.M. Zaitsev[130,aa], J. Zalieckas[14], A. Zaman[148], S. Zambito[57], L. Zanello[132a,132b], D. Zanzi[88], C. Zeitnitz[175], M. Zeman[128], A. Zemla[38a], K. Zengel[23], O. Zenin[130], T. Ženiš[144a], D. Zerwas[117], D. Zhang[89], F. Zhang[173], H. Zhang[33c], J. Zhang[6], L. Zhang[48], R. Zhang[33b], X. Zhang[33d], Z. Zhang[117], X. Zhao[40], Y. Zhao[33d,117], Z. Zhao[33b], A. Zhemchugov[65], J. Zhong[120], B. Zhou[89], C. Zhou[45], L. Zhou[35], L. Zhou[40], N. Zhou[163], C.G. Zhu[33d], H. Zhu[33a], J. Zhu[89], Y. Zhu[33b], X. Zhuang[33a], K. Zhukov[96], A. Zibell[174], D. Zieminska[61], N.I. Zimine[65], C. Zimmermann[83], S. Zimmermann[48], Z. Zinonos[54], M. Zinser[83], M. Ziolkowski[141], L. Živković[13], G. Zobernig[173], A. Zoccoli[20a,20b], M. zur Nedden[16], G. Zurzolo[104a,104b], L. Zwalinski[30].

[1] Department of Physics, University of Adelaide, Adelaide, Australia

[2] Physics Department, SUNY Albany, Albany NY, United States of America

[3] Department of Physics, University of Alberta, Edmonton AB, Canada

[4] (a) Department of Physics, Ankara University, Ankara; (b) Istanbul Aydin University, Istanbul; (c) Division of Physics, TOBB University of Economics and Technology, Ankara, Turkey

[5] LAPP, CNRS/IN2P3 and Université Savoie Mont Blanc, Annecy-le-Vieux, France

[6] High Energy Physics Division, Argonne National Laboratory, Argonne IL, United States of America
[7] Department of Physics, University of Arizona, Tucson AZ, United States of America
[8] Department of Physics, The University of Texas at Arlington, Arlington TX, United States of America
[9] Physics Department, University of Athens, Athens, Greece
[10] Physics Department, National Technical University of Athens, Zografou, Greece
[11] Institute of Physics, Azerbaijan Academy of Sciences, Baku, Azerbaijan
[12] Institut de Física d'Altes Energies and Departament de Física de la Universitat Autònoma de Barcelona, Barcelona, Spain
[13] Institute of Physics, University of Belgrade, Belgrade, Serbia
[14] Department for Physics and Technology, University of Bergen, Bergen, Norway
[15] Physics Division, Lawrence Berkeley National Laboratory and University of California, Berkeley CA, United States of America
[16] Department of Physics, Humboldt University, Berlin, Germany
[17] Albert Einstein Center for Fundamental Physics and Laboratory for High Energy Physics, University of Bern, Bern, Switzerland
[18] School of Physics and Astronomy, University of Birmingham, Birmingham, United Kingdom
[19] [(a)] Department of Physics, Bogazici University, Istanbul; [(b)] Department of Physics Engineering, Gaziantep University, Gaziantep; [(c)] Department of Physics, Dogus University, Istanbul, Turkey
[20] [(a)] INFN Sezione di Bologna; [(b)] Dipartimento di Fisica e Astronomia, Università di Bologna, Bologna, Italy
[21] Physikalisches Institut, University of Bonn, Bonn, Germany
[22] Department of Physics, Boston University, Boston MA, United States of America
[23] Department of Physics, Brandeis University, Waltham MA, United States of America
[24] [(a)] Universidade Federal do Rio De Janeiro COPPE/EE/IF, Rio de Janeiro; [(b)] Electrical Circuits Department, Federal University of Juiz de Fora (UFJF), Juiz de Fora; [(c)] Federal University of Sao Joao del Rei (UFSJ), Sao Joao del Rei; [(d)] Instituto de Fisica, Universidade de Sao Paulo, Sao Paulo, Brazil
[25] Physics Department, Brookhaven National Laboratory, Upton NY, United States of America
[26] [(a)] National Institute of Physics and Nuclear Engineering, Bucharest; [(b)] National Institute for Research and Development of Isotopic and Molecular Technologies, Physics Department, Cluj Napoca; [(c)] University Politehnica Bucharest, Bucharest; [(d)] West University in Timisoara, Timisoara, Romania
[27] Departamento de Física, Universidad de Buenos Aires, Buenos Aires, Argentina
[28] Cavendish Laboratory, University of Cambridge, Cambridge, United Kingdom
[29] Department of Physics, Carleton University, Ottawa ON, Canada
[30] CERN, Geneva, Switzerland
[31] Enrico Fermi Institute, University of Chicago, Chicago IL, United States of America
[32] [(a)] Departamento de Física, Pontificia Universidad Católica de Chile, Santiago; [(b)] Departamento de Física, Universidad Técnica Federico Santa María, Valparaíso, Chile
[33] [(a)] Institute of High Energy Physics, Chinese Academy of Sciences, Beijing; [(b)] Department of Modern Physics, University of Science and Technology of China, Anhui; [(c)] Department of Physics, Nanjing University, Jiangsu; [(d)] School of Physics, Shandong University, Shandong; [(e)] Department of Physics and Astronomy, Shanghai Key Laboratory for Particle Physics and Cosmology, Shanghai Jiao Tong University, Shanghai; [(f)] Physics Department, Tsinghua University, Beijing 100084, China
[34] Laboratoire de Physique Corpusculaire, Clermont Université and Université Blaise Pascal and CNRS/IN2P3, Clermont-Ferrand, France
[35] Nevis Laboratory, Columbia University, Irvington NY, United States of America
[36] Niels Bohr Institute, University of Copenhagen, Kobenhavn, Denmark
[37] [(a)] INFN Gruppo Collegato di Cosenza, Laboratori Nazionali di Frascati; [(b)] Dipartimento di Fisica,

Università della Calabria, Rende, Italy
[38] [(a)] AGH University of Science and Technology, Faculty of Physics and Applied Computer Science, Krakow; [(b)] Marian Smoluchowski Institute of Physics, Jagiellonian University, Krakow, Poland
[39] Institute of Nuclear Physics Polish Academy of Sciences, Krakow, Poland
[40] Physics Department, Southern Methodist University, Dallas TX, United States of America
[41] Physics Department, University of Texas at Dallas, Richardson TX, United States of America
[42] DESY, Hamburg and Zeuthen, Germany
[43] Institut für Experimentelle Physik IV, Technische Universität Dortmund, Dortmund, Germany
[44] Institut für Kern- und Teilchenphysik, Technische Universität Dresden, Dresden, Germany
[45] Department of Physics, Duke University, Durham NC, United States of America
[46] SUPA - School of Physics and Astronomy, University of Edinburgh, Edinburgh, United Kingdom
[47] INFN Laboratori Nazionali di Frascati, Frascati, Italy
[48] Fakultät für Mathematik und Physik, Albert-Ludwigs-Universität, Freiburg, Germany
[49] Section de Physique, Université de Genève, Geneva, Switzerland
[50] [(a)] INFN Sezione di Genova; [(b)] Dipartimento di Fisica, Università di Genova, Genova, Italy
[51] [(a)] E. Andronikashvili Institute of Physics, Iv. Javakhishvili Tbilisi State University, Tbilisi; [(b)] High Energy Physics Institute, Tbilisi State University, Tbilisi, Georgia
[52] II Physikalisches Institut, Justus-Liebig-Universität Giessen, Giessen, Germany
[53] SUPA - School of Physics and Astronomy, University of Glasgow, Glasgow, United Kingdom
[54] II Physikalisches Institut, Georg-August-Universität, Göttingen, Germany
[55] Laboratoire de Physique Subatomique et de Cosmologie, Université Grenoble-Alpes, CNRS/IN2P3, Grenoble, France
[56] Department of Physics, Hampton University, Hampton VA, United States of America
[57] Laboratory for Particle Physics and Cosmology, Harvard University, Cambridge MA, United States of America
[58] [(a)] Kirchhoff-Institut für Physik, Ruprecht-Karls-Universität Heidelberg, Heidelberg; [(b)] Physikalisches Institut, Ruprecht-Karls-Universität Heidelberg, Heidelberg; [(c)] ZITI Institut für technische Informatik, Ruprecht-Karls-Universität Heidelberg, Mannheim, Germany
[59] Faculty of Applied Information Science, Hiroshima Institute of Technology, Hiroshima, Japan
[60] [(a)] Department of Physics, The Chinese University of Hong Kong, Shatin, N.T., Hong Kong; [(b)] Department of Physics, The University of Hong Kong, Hong Kong; [(c)] Department of Physics, The Hong Kong University of Science and Technology, Clear Water Bay, Kowloon, Hong Kong, China
[61] Department of Physics, Indiana University, Bloomington IN, United States of America
[62] Institut für Astro- und Teilchenphysik, Leopold-Franzens-Universität, Innsbruck, Austria
[63] University of Iowa, Iowa City IA, United States of America
[64] Department of Physics and Astronomy, Iowa State University, Ames IA, United States of America
[65] Joint Institute for Nuclear Research, JINR Dubna, Dubna, Russia
[66] KEK, High Energy Accelerator Research Organization, Tsukuba, Japan
[67] Graduate School of Science, Kobe University, Kobe, Japan
[68] Faculty of Science, Kyoto University, Kyoto, Japan
[69] Kyoto University of Education, Kyoto, Japan
[70] Department of Physics, Kyushu University, Fukuoka, Japan
[71] Instituto de Física La Plata, Universidad Nacional de La Plata and CONICET, La Plata, Argentina
[72] Physics Department, Lancaster University, Lancaster, United Kingdom
[73] [(a)] INFN Sezione di Lecce; [(b)] Dipartimento di Matematica e Fisica, Università del Salento, Lecce, Italy
[74] Oliver Lodge Laboratory, University of Liverpool, Liverpool, United Kingdom

[75] Department of Physics, Jožef Stefan Institute and University of Ljubljana, Ljubljana, Slovenia
[76] School of Physics and Astronomy, Queen Mary University of London, London, United Kingdom
[77] Department of Physics, Royal Holloway University of London, Surrey, United Kingdom
[78] Department of Physics and Astronomy, University College London, London, United Kingdom
[79] Louisiana Tech University, Ruston LA, United States of America
[80] Laboratoire de Physique Nucléaire et de Hautes Energies, UPMC and Université Paris-Diderot and CNRS/IN2P3, Paris, France
[81] Fysiska institutionen, Lunds universitet, Lund, Sweden
[82] Departamento de Fisica Teorica C-15, Universidad Autonoma de Madrid, Madrid, Spain
[83] Institut für Physik, Universität Mainz, Mainz, Germany
[84] School of Physics and Astronomy, University of Manchester, Manchester, United Kingdom
[85] CPPM, Aix-Marseille Université and CNRS/IN2P3, Marseille, France
[86] Department of Physics, University of Massachusetts, Amherst MA, United States of America
[87] Department of Physics, McGill University, Montreal QC, Canada
[88] School of Physics, University of Melbourne, Victoria, Australia
[89] Department of Physics, The University of Michigan, Ann Arbor MI, United States of America
[90] Department of Physics and Astronomy, Michigan State University, East Lansing MI, United States of America
[91] [(a)] INFN Sezione di Milano; [(b)] Dipartimento di Fisica, Università di Milano, Milano, Italy
[92] B.I. Stepanov Institute of Physics, National Academy of Sciences of Belarus, Minsk, Republic of Belarus
[93] National Scientific and Educational Centre for Particle and High Energy Physics, Minsk, Republic of Belarus
[94] Department of Physics, Massachusetts Institute of Technology, Cambridge MA, United States of America
[95] Group of Particle Physics, University of Montreal, Montreal QC, Canada
[96] P.N. Lebedev Institute of Physics, Academy of Sciences, Moscow, Russia
[97] Institute for Theoretical and Experimental Physics (ITEP), Moscow, Russia
[98] National Research Nuclear University MEPhI, Moscow, Russia
[99] D.V. Skobeltsyn Institute of Nuclear Physics, M.V. Lomonosov Moscow State University, Moscow, Russia
[100] Fakultät für Physik, Ludwig-Maximilians-Universität München, München, Germany
[101] Max-Planck-Institut für Physik (Werner-Heisenberg-Institut), München, Germany
[102] Nagasaki Institute of Applied Science, Nagasaki, Japan
[103] Graduate School of Science and Kobayashi-Maskawa Institute, Nagoya University, Nagoya, Japan
[104] [(a)] INFN Sezione di Napoli; [(b)] Dipartimento di Fisica, Università di Napoli, Napoli, Italy
[105] Department of Physics and Astronomy, University of New Mexico, Albuquerque NM, United States of America
[106] Institute for Mathematics, Astrophysics and Particle Physics, Radboud University Nijmegen/Nikhef, Nijmegen, Netherlands
[107] Nikhef National Institute for Subatomic Physics and University of Amsterdam, Amsterdam, Netherlands
[108] Department of Physics, Northern Illinois University, DeKalb IL, United States of America
[109] Budker Institute of Nuclear Physics, SB RAS, Novosibirsk, Russia
[110] Department of Physics, New York University, New York NY, United States of America
[111] Ohio State University, Columbus OH, United States of America
[112] Faculty of Science, Okayama University, Okayama, Japan

[113] Homer L. Dodge Department of Physics and Astronomy, University of Oklahoma, Norman OK, United States of America
[114] Department of Physics, Oklahoma State University, Stillwater OK, United States of America
[115] Palacký University, RCPTM, Olomouc, Czech Republic
[116] Center for High Energy Physics, University of Oregon, Eugene OR, United States of America
[117] LAL, Université Paris-Sud and CNRS/IN2P3, Orsay, France
[118] Graduate School of Science, Osaka University, Osaka, Japan
[119] Department of Physics, University of Oslo, Oslo, Norway
[120] Department of Physics, Oxford University, Oxford, United Kingdom
[121] [(a)] INFN Sezione di Pavia; [(b)] Dipartimento di Fisica, Università di Pavia, Pavia, Italy
[122] Department of Physics, University of Pennsylvania, Philadelphia PA, United States of America
[123] National Research Centre "Kurchatov Institute" B.P.Konstantinov Petersburg Nuclear Physics Institute, St. Petersburg, Russia
[124] [(a)] INFN Sezione di Pisa; [(b)] Dipartimento di Fisica E. Fermi, Università di Pisa, Pisa, Italy
[125] Department of Physics and Astronomy, University of Pittsburgh, Pittsburgh PA, United States of America
[126] [(a)] Laboratório de Instrumentação e Física Experimental de Partículas - LIP, Lisboa; [(b)] Faculdade de Ciências, Universidade de Lisboa, Lisboa; [(c)] Department of Physics, University of Coimbra, Coimbra; [(d)] Centro de Física Nuclear da Universidade de Lisboa, Lisboa; [(e)] Departamento de Fisica, Universidade do Minho, Braga; [(f)] Departamento de Fisica Teorica y del Cosmos and CAFPE, Universidad de Granada, Granada (Spain); [(g)] Dep Fisica and CEFITEC of Faculdade de Ciencias e Tecnologia, Universidade Nova de Lisboa, Caparica, Portugal
[127] Institute of Physics, Academy of Sciences of the Czech Republic, Praha, Czech Republic
[128] Czech Technical University in Prague, Praha, Czech Republic
[129] Faculty of Mathematics and Physics, Charles University in Prague, Praha, Czech Republic
[130] State Research Center Institute for High Energy Physics, Protvino, Russia
[131] Particle Physics Department, Rutherford Appleton Laboratory, Didcot, United Kingdom
[132] [(a)] INFN Sezione di Roma; [(b)] Dipartimento di Fisica, Sapienza Università di Roma, Roma, Italy
[133] [(a)] INFN Sezione di Roma Tor Vergata; [(b)] Dipartimento di Fisica, Università di Roma Tor Vergata, Roma, Italy
[134] [(a)] INFN Sezione di Roma Tre; [(b)] Dipartimento di Matematica e Fisica, Università Roma Tre, Roma, Italy
[135] [(a)] Faculté des Sciences Ain Chock, Réseau Universitaire de Physique des Hautes Energies - Université Hassan II, Casablanca; [(b)] Centre National de l'Energie des Sciences Techniques Nucleaires, Rabat; [(c)] Faculté des Sciences Semlalia, Université Cadi Ayyad, LPHEA-Marrakech; [(d)] Faculté des Sciences, Université Mohamed Premier and LPTPM, Oujda; [(e)] Faculté des sciences, Université Mohammed V-Agdal, Rabat, Morocco
[136] DSM/IRFU (Institut de Recherches sur les Lois Fondamentales de l'Univers), CEA Saclay (Commissariat à l'Energie Atomique et aux Energies Alternatives), Gif-sur-Yvette, France
[137] Santa Cruz Institute for Particle Physics, University of California Santa Cruz, Santa Cruz CA, United States of America
[138] Department of Physics, University of Washington, Seattle WA, United States of America
[139] Department of Physics and Astronomy, University of Sheffield, Sheffield, United Kingdom
[140] Department of Physics, Shinshu University, Nagano, Japan
[141] Fachbereich Physik, Universität Siegen, Siegen, Germany
[142] Department of Physics, Simon Fraser University, Burnaby BC, Canada
[143] SLAC National Accelerator Laboratory, Stanford CA, United States of America

[144] [(a)] Faculty of Mathematics, Physics & Informatics, Comenius University, Bratislava; [(b)] Department of Subnuclear Physics, Institute of Experimental Physics of the Slovak Academy of Sciences, Kosice, Slovak Republic
[145] [(a)] Department of Physics, University of Cape Town, Cape Town; [(b)] Department of Physics, University of Johannesburg, Johannesburg; [(c)] School of Physics, University of the Witwatersrand, Johannesburg, South Africa
[146] [(a)] Department of Physics, Stockholm University; [(b)] The Oskar Klein Centre, Stockholm, Sweden
[147] Physics Department, Royal Institute of Technology, Stockholm, Sweden
[148] Departments of Physics & Astronomy and Chemistry, Stony Brook University, Stony Brook NY, United States of America
[149] Department of Physics and Astronomy, University of Sussex, Brighton, United Kingdom
[150] School of Physics, University of Sydney, Sydney, Australia
[151] Institute of Physics, Academia Sinica, Taipei, Taiwan
[152] Department of Physics, Technion: Israel Institute of Technology, Haifa, Israel
[153] Raymond and Beverly Sackler School of Physics and Astronomy, Tel Aviv University, Tel Aviv, Israel
[154] Department of Physics, Aristotle University of Thessaloniki, Thessaloniki, Greece
[155] International Center for Elementary Particle Physics and Department of Physics, The University of Tokyo, Tokyo, Japan
[156] Graduate School of Science and Technology, Tokyo Metropolitan University, Tokyo, Japan
[157] Department of Physics, Tokyo Institute of Technology, Tokyo, Japan
[158] Department of Physics, University of Toronto, Toronto ON, Canada
[159] [(a)] TRIUMF, Vancouver BC; [(b)] Department of Physics and Astronomy, York University, Toronto ON, Canada
[160] Faculty of Pure and Applied Sciences, University of Tsukuba, Tsukuba, Japan
[161] Department of Physics and Astronomy, Tufts University, Medford MA, United States of America
[162] Centro de Investigaciones, Universidad Antonio Narino, Bogota, Colombia
[163] Department of Physics and Astronomy, University of California Irvine, Irvine CA, United States of America
[164] [(a)] INFN Gruppo Collegato di Udine, Sezione di Trieste, Udine; [(b)] ICTP, Trieste; [(c)] Dipartimento di Chimica, Fisica e Ambiente, Università di Udine, Udine, Italy
[165] Department of Physics, University of Illinois, Urbana IL, United States of America
[166] Department of Physics and Astronomy, University of Uppsala, Uppsala, Sweden
[167] Instituto de Física Corpuscular (IFIC) and Departamento de Física Atómica, Molecular y Nuclear and Departamento de Ingeniería Electrónica and Instituto de Microelectrónica de Barcelona (IMB-CNM), University of Valencia and CSIC, Valencia, Spain
[168] Department of Physics, University of British Columbia, Vancouver BC, Canada
[169] Department of Physics and Astronomy, University of Victoria, Victoria BC, Canada
[170] Department of Physics, University of Warwick, Coventry, United Kingdom
[171] Waseda University, Tokyo, Japan
[172] Department of Particle Physics, The Weizmann Institute of Science, Rehovot, Israel
[173] Department of Physics, University of Wisconsin, Madison WI, United States of America
[174] Fakultät für Physik und Astronomie, Julius-Maximilians-Universität, Würzburg, Germany
[175] Fachbereich C Physik, Bergische Universität Wuppertal, Wuppertal, Germany
[176] Department of Physics, Yale University, New Haven CT, United States of America
[177] Yerevan Physics Institute, Yerevan, Armenia
[178] Centre de Calcul de l'Institut National de Physique Nucléaire et de Physique des Particules (IN2P3),

Villeurbanne, France
[a] Also at Department of Physics, King's College London, London, United Kingdom
[b] Also at Institute of Physics, Azerbaijan Academy of Sciences, Baku, Azerbaijan
[c] Also at Novosibirsk State University, Novosibirsk, Russia
[d] Also at TRIUMF, Vancouver BC, Canada
[e] Also at Department of Physics, California State University, Fresno CA, United States of America
[f] Also at Department of Physics, University of Fribourg, Fribourg, Switzerland
[g] Also at Departamento de Fisica e Astronomia, Faculdade de Ciencias, Universidade do Porto, Portugal
[h] Also at Tomsk State University, Tomsk, Russia
[i] Also at CPPM, Aix-Marseille Université and CNRS/IN2P3, Marseille, France
[j] Also at Universita di Napoli Parthenope, Napoli, Italy
[k] Also at Institute of Particle Physics (IPP), Canada
[l] Also at Particle Physics Department, Rutherford Appleton Laboratory, Didcot, United Kingdom
[m] Also at Department of Physics, St. Petersburg State Polytechnical University, St. Petersburg, Russia
[n] Also at Louisiana Tech University, Ruston LA, United States of America
[o] Also at Institucio Catalana de Recerca i Estudis Avancats, ICREA, Barcelona, Spain
[p] Also at Department of Physics, National Tsing Hua University, Taiwan
[q] Also at Department of Physics, The University of Texas at Austin, Austin TX, United States of America
[r] Also at Institute of Theoretical Physics, Ilia State University, Tbilisi, Georgia
[s] Also at CERN, Geneva, Switzerland
[t] Also at Georgian Technical University (GTU),Tbilisi, Georgia
[u] Also at Manhattan College, New York NY, United States of America
[v] Also at Hellenic Open University, Patras, Greece
[w] Also at Institute of Physics, Academia Sinica, Taipei, Taiwan
[x] Also at LAL, Université Paris-Sud and CNRS/IN2P3, Orsay, France
[y] Also at Academia Sinica Grid Computing, Institute of Physics, Academia Sinica, Taipei, Taiwan
[z] Also at School of Physics, Shandong University, Shandong, China
[aa] Also at Moscow Institute of Physics and Technology State University, Dolgoprudny, Russia
[ab] Also at Section de Physique, Université de Genève, Geneva, Switzerland
[ac] Also at International School for Advanced Studies (SISSA), Trieste, Italy
[ad] Also at Department of Physics and Astronomy, University of South Carolina, Columbia SC, United States of America
[ae] Also at School of Physics and Engineering, Sun Yat-sen University, Guangzhou, China
[af] Also at Faculty of Physics, M.V.Lomonosov Moscow State University, Moscow, Russia
[ag] Also at National Research Nuclear University MEPhI, Moscow, Russia
[ah] Also at Department of Physics, Stanford University, Stanford CA, United States of America
[ai] Also at Institute for Particle and Nuclear Physics, Wigner Research Centre for Physics, Budapest, Hungary
[aj] Also at Department of Physics, The University of Michigan, Ann Arbor MI, United States of America
[ak] Also at University of Malaya, Department of Physics, Kuala Lumpur, Malaysia
[*] Deceased